Research in Optoelectronics (A)

Reprints published in 2005

by

Professor Larry A. Coldren

and Collaborators

Published as

Technical Report # ECE 06-01

of

The Department of Electrical & Computer Engineering

The University of California

Santa Barbara, CA 93106

Phone: (805) 893-4486

Fax: (805) 893-4500

E-mail: coldren@ece.ucsb.edu

www.ece.ucsb.edu/Faculty/Coldren

Introduction:

The 2005 edition of Research in Optoelectronics (A) contains conference and journal articles published by Prof. Coldren, together with his students and post docs, and other collaborators. These generally focus on III-V semiconductor lasers and related photonic integrated circuits. The work spans efforts from basic materials and processing technology, through device physics and design, to device formation, characterization, and insertion into systems demonstrations.

The reprints have been grouped into four areas: **I. Photonic Integrated Circuits and Related Technology; II. InP-based Vertical-Cavity Lasers; III. Avalanche Photodetectors and SOA-PIN Receivers; and IV. Terahertz Technology, Microcavities, and Quantum Coherence**. The majority of the work is in the first area, which has been further subdivided into *A. Quantum-well-intermixed PICs; B. Widely-Tunable Transmitter PICs; C. Wavelength Converter Technology; and D. 980nm Edge-Emitter Technology.* The 980nm edge-emitter technology and Section **IV** are based upon an MBE-grown GaAs materials platform, while all of the rest is grown on InP substrates either via MOCVD or MBE. The epitaxial growth activity is strongly supported by Prof. DenBaars (MOCVD) and Prof. Gossard (MBE), who co-advise the students involved in these areas. Thus, their contributions have been invaluable to the research, even when they do not appear as co-authors on the device oriented papers.

The work was performed with funding from several grants from industry and government, some gift funds from industry, and support from the Kavli Endowed Chair in Optoelectronics and Sensors. Specific projects included one on photocurrent-driven widely-tunable wavelength converters supported by DARPA via the CSWDM program; a second on wavelength converters and fiber-based buffers under the DARPA DoDN program; two projects to create very high-efficiency optical interconnects for ICs using either edge-emitting short-cavity laser-modulators (supported by the DARPA C2OI program) or directly-modulated vertical-cavity surface-emitting lasers (supported by MARCO as part of the Interconnect Focus Center). A UC-MICRO project with leveraging funding from Intel supported work on quantum-well intermixing for more advanced Photonic ICs.

The first group of reprints (*IA. Quantum-well-intermixed PICs*) summarizes efforts to make highly-functional and efficient widely-tunable transmitters, receivers and transceivers using the recently developed QWI technology. This technique provides for an accurate post-growth shift of the active region absorption edge to higher energies by various amounts at specified locations on the wafer. Thus, optimized gain, modulator, passive waveguide, and tuning regions can be formed from the initially grown centered-MQW active region without any additional regrowths. In 2005 this technology was also extended to add offset gain and absorber regions for high-saturation power SOAs and photodetectors. Figure 1 illustrates a cross section of a portion of a QWI-PIC that contains a high-gain, high-saturation power optical receiver. It includes a two-section SOA—a high-gain preamp (as grown c-MQW) and a high-power postamp (o-MQW above intermixed c-MQW)—as well as a uni-traveling carrier (UTC) photodiode. Such

chips have achieved gains in excess of 20 dB with saturation powers in excess of 20dBm. The experimental results illustrate the small-signal RF-response for several input powers and eye-diagrams at 40Gb/s for two different biases.

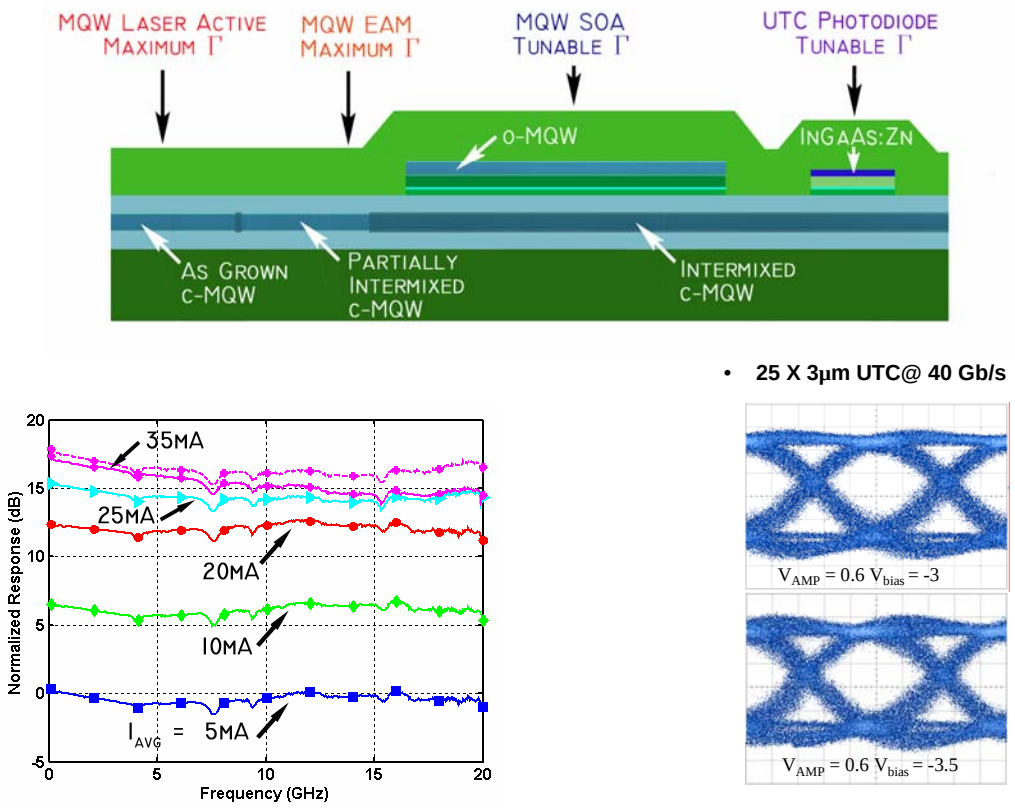

Figure 1. (top) Schematic of Photonic IC formed with quantum-well intermixing (QWI) and MOCVD regrowth. The centered multiple-quantum well (c-MQW) active region is intermixed by two differing amounts to form either passive waveguides or electro-absorption modulators (EAMs) as well as the as-grown gain region at various places on the chip. The EAM is not typically incorporated in a receiver, but rather in a transmitter stage that would exist in an integrated transceiver. (bottom-left) Small-signal frequency response for several input powers (indicated by the dc currents they create), and (bottom-right) 40Gb/s NRZ eye-diagrams.

The next two sections (*IB. Widely-Tunable Transmitter PICs and IC Wavelength Converter Technology*) include papers using the more-conventional off-set gain integration platform, in which a MQW active layer is grown on top of a common waveguide, and this is then removed in regions where passive waveguides or modulators are desired. Most of this work involves combining a widely-tunable Sampled-Grating Distributed-Bragg-Reflector (SGDBR) laser with monolithically integrated amplifiers (SOAs), modulators (both EA and MZ), waveguide splitters (MMIs), and photodetectors. In Fig. 2 results from a photocurrent-driven wavelength converter are illustrated. In this case the common waveguide also contains quantum-wells with a higher energy gap to enhance the efficiency of the electro-absorption modulators (EAMs) to be incorporated in the transmitter stage. This so-called 'dual quantum-well' design has enabled wavelength

converters to have overall chip gain (more signal out than in) as well as good operation up to 10Gb/s across the full 32 nm tuning range of the SGDBR-EAM transmitter. Flared amplifiers and tapered photodiodes are used to increase the saturation power of both the SOA receiver preamps and the photodetectors in order to have sufficient signal to obtain good extinction in the EAM.

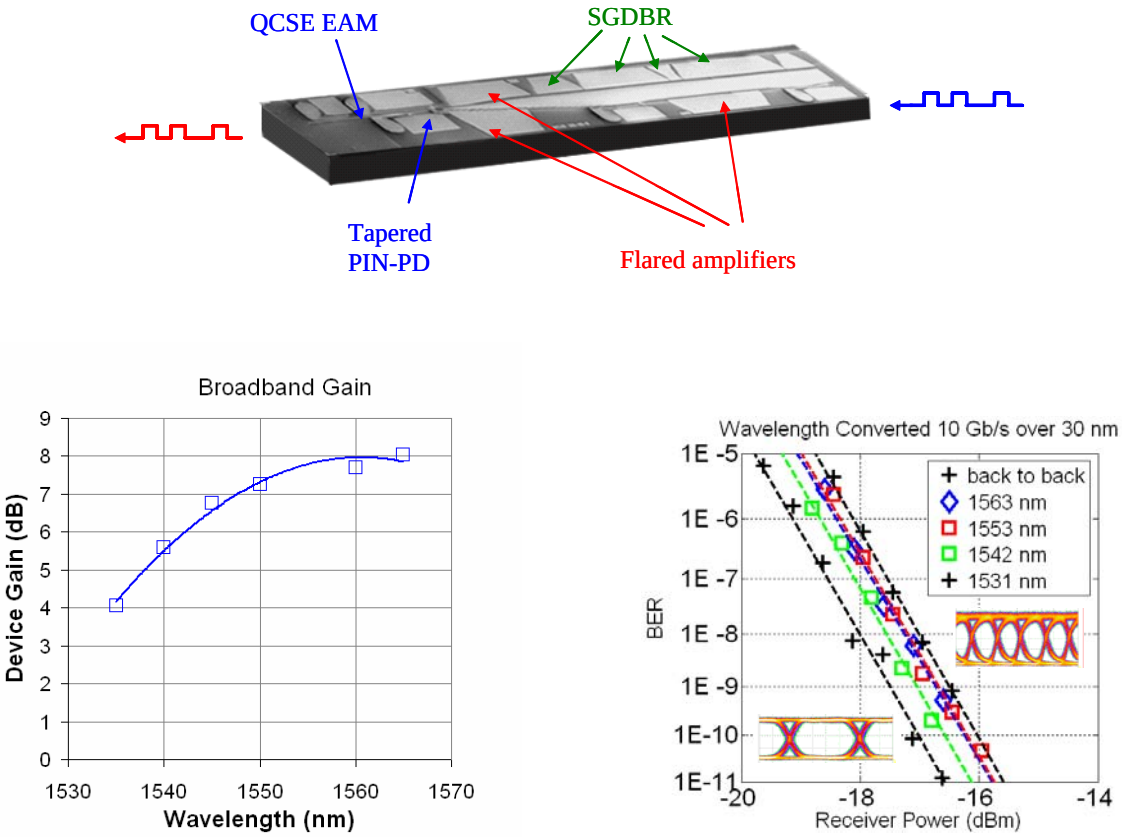

Figure 2. (top) Schematic of photocurrent driven wavelength converter (or transceiver) chip that uses the dual quantum-well integration platform to provide EAMs enhanced by the quantum-confined Stark effect (QCSE). (bottom-left) Device gain across the wavelength tuning range; (bottom-right) bit-error-rate at 10Gb/s for several wavelengths together with example input and transmitted eye-diagrams.

Figure 3 gives another example of a photocurrent-driven wavelength converter, which in this case uses a series-connected Mach-Zehnder modulator (MZM) in the transmitter stage. This more complex design requires the use of a semi-insulating substrate and an on-chip capacitor to enable the phase modulators in the two arms of the MZM to be electrically connected in series. It also incorporates integrated NiCr load resistors so that no RF is required to be coupled off the chip. The bandwidth in this case is limited by the receiver stage as well as some unwanted resistance in the connection to the n-type layers next to the substrate. These and other unnecessary parasitics lead to an unwanted dip in the small frequency response, which limit good results to RZ data.

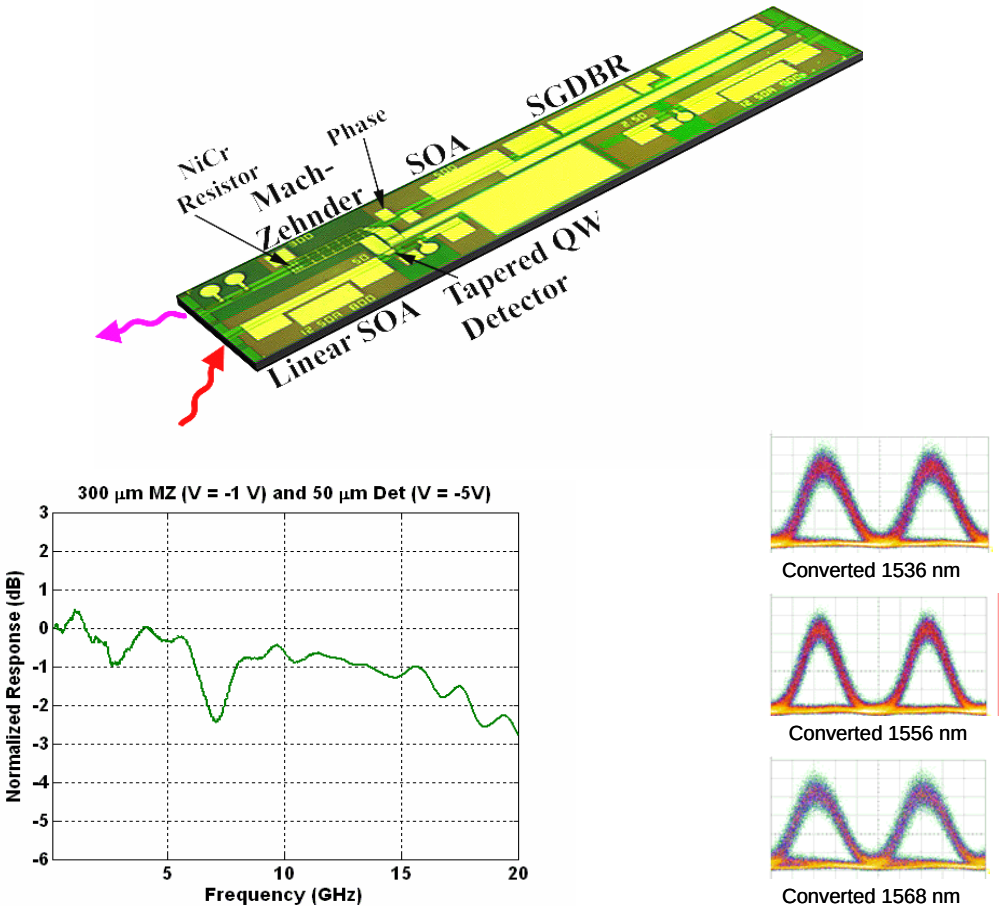

Figure 3. (top) Schematic of a photocurrent wavelength converter that uses a series-connected MZM in the transmitter stage. (bottom-left) Small-signal frequency response, and (bottom-right) 10Gb/s RZ eye-diagrams.

As another example of work in the photonic networking area, Fig. 4 illustrates results from the optical buffering of 40Gb/s RZ data for times up to 12.6 μs. As illustrated this approach uses fiber-Bragg-gratings (FBGs) to selectively reflect different wavelengths. The complete buffer consists of a wavelength converter in front of the optical circulator to select the wavelength of the data and thus the delay it will undergo in traveling down the fiber, reflecting off the respective FBG, and then traveling back again. For times up to 1 μs, standard fiber could be used without too much pulse spreading. For greater times, dispersion-compensated fiber (DCF) was necessary to avoid intolerable pulse spreading. The very low loss of fiber (<0.2 dB/km), the quality of the FBGs, and the fast reconfiguration time of our wavelength converters (< 10ns) makes this approach one of the best alternatives for obtaining rapidly programmable delays from nanoseconds to tens of microseconds in a small relatively cheap package. Using a wavelength converter with a 40 nm tuning range and assuming 100GHz channel spacing, we can obtain up to 50 different selectable delays.

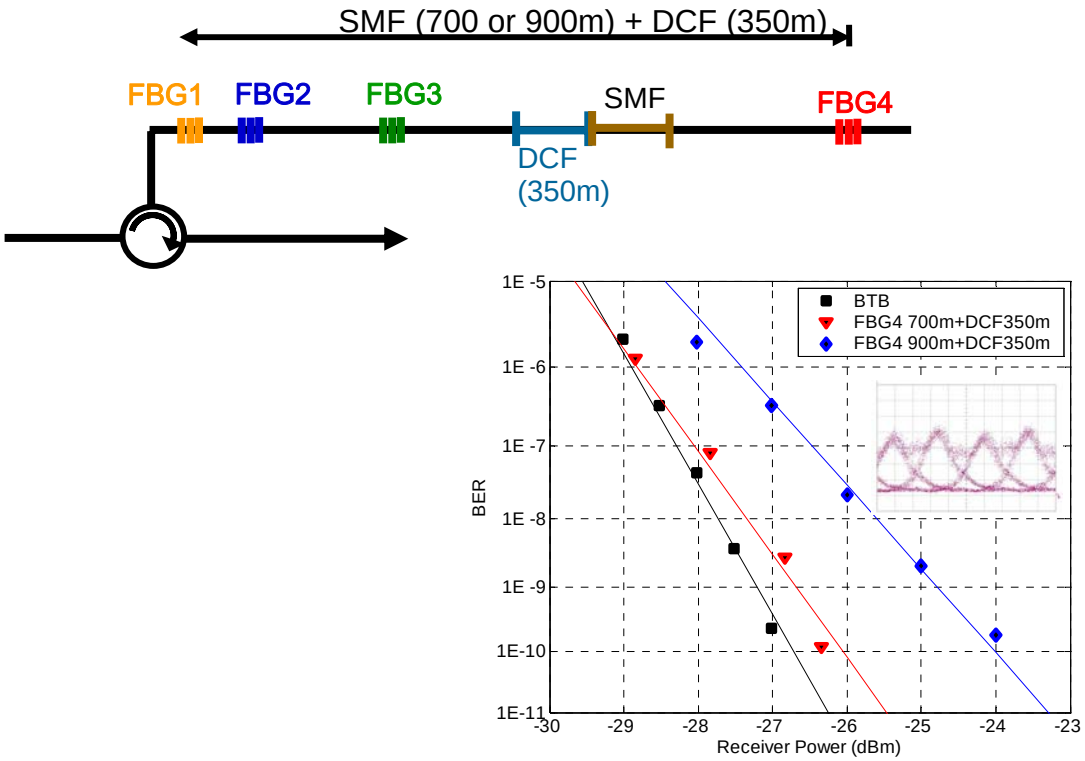

Figure 4. (top) Schematic of optical buffer consisting of an optical circulator and an array of FBGs within a single fiber. A wavelength converter is used in front of this for delay selection. In this case the delays to the FBGs 1-4 were (1)-133ns, (2)-161ns, (3)-1.19 μs and (4)-either 10.09 or 12.6 μs, respectively. (bottom) Bit-error-rate for 40Gb/s RZ for back-to-back (BTB) and FBG4 with two different delays. The BER for the shorter delays showed nearly zero power penalty.

The second general area of research is on high-performance long wavelength InP-based Vertical-Cavity Surface-Emitting Lasers (VCSELs): **II. InP-based VCSELs**. The focus of the effort is to create all-epitaxial VCSELs in a single MBE growth using AlGaAsSb alloys for the mirrors and InGaAlAs MQW active regions. Both 1310 and 1550 nm VCSELs with good characteristics have been demonstrated. The papers in 2005 bring to a culmination much of the work of the past several years with numerous results for devices in the 1310 nm range. It is now clear that this material structure can provide a single vehicle for VCSELs across the entire 1300 -1600 nm wavelength range. The new work has incorporated low-loss optical apertures for improved differential quantum efficiency. Figure 5 illustrates a schematic of the VCSEL structure as well as light out and voltage vs. the drive current for an example device. The results show record high differential quantum efficiencies of 64% and relatively good temperature behavior. In this case the optical aperture was formed by etching out the tunnel junction that connected the n-type InP contact layer to the p-type side of the gain region.

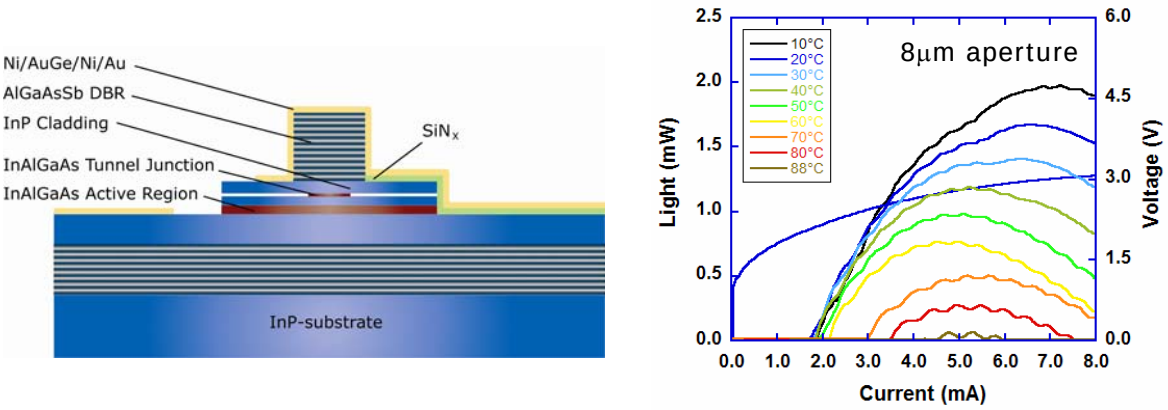

Figure 5. Schematic and PIV results for a 1310 nm all-epitaxial VCSEL grown on InP.

Work on **III. Avalanche Photodetectors and SOA-PIN Receivers** contains a number of papers summarizing work done in collaboration with Prof. Joseph C. Campbell of the University of Texas at Austin. Prof. Coldren's group grew the materials used by MBE. One paper on high-saturation power SOA-PIN receivers in also included. This describes the nature of flared-waveguide receivers used in some of the wavelength converters discussed above.

The final group of papers, **IV. Terahertz Technology, Microcavities, and Quantum Coherence,** summarizes a collection of efforts utilizing GaAs-based MBE material grown by Prof. Coldren's group. The microcavity activity has grown out of our GaAs-based VCSEL activity in which we have demonstrated record low optical losses. Here this is being utilized to enable enhanced quantum microcavity effects. The Terahertz and quantum-coherence efforts are centered in the Physics Department, and our contribution has been to create novel epitaxial structures via MBE that have been designed by others.

Back Row (from left): Steve Nicholes, Uppili Krishnamachari, Jon Barton, Chad Wang, James Raring, Matt Sysak, Jon Klamkin, Leif Johansson

Front Row: Janet Chen, Anna Tauke-Pedretti, Matt Dummer, Yan Zheng, Larry Coldren, Joseph Chang, Nick Stoltz, Jill Nolde, Abbey Keck

Not Pictured: Dave Buell, Danny Feezell, John Hutchinson, Gordon Morrison

Professor Coldren's Group

I. *Visiting Researchers*

J. Barton	Post Doctoral Researcher, UCSB
B. Fimland	Visiting Researcher, Norwegian University of Science and Technology
J. Getty	Post Doctoral Researcher, UCSB, now at Raytheon
J. Hutchinson	Visiting Researcher, Intel Corporation
L. Johansson	Post Doctoral Researcher, UCSB
G. Morrison	Post Doctoral Researcher, UCSB, now at III-V

II. *Students*

D. Buell	Ph.D. Program, now at CNRS
Y. Chang	Ph.D. Program
C. Chen	Ph.D. Program
M. Dummer	Ph.D. Program
D. Feezell	Ph.D. Program, now Post Doctoral Researcher, UCSB (Nakamura)
J. Klamkin	Ph.D. Program
J. Raring	Ph.D. Program
N. Stoltz	Ph.D. Program
M. Sysak	Ph.D. Program, now Post Doctoral Researcher, UCSB (Bowers)
A. Tauke-Pedretti	Ph.D. Program
C. Wang	Ph.D. Program

III. *Staff*

D. Cohen	Principal Development Engineer
A. Keck	Project Manager, OTC

Collaborators

I. *Faculty*

D. Blumenthal	UCSB
D. Bouwmeester	UCSB
J. Campbell	University of Texas, Austin
D. Citrin	Georgia Tech University
S. DenBaars	UCSB
A. Gossard	UCSB
E. Hu	UCSB
P. Petroff	UCSB
J. Piprek	UCSB
M. Sherwin	UCSB

II. *Researchers*

P. Abraham	Agility Communications, Inc.
Y. Akulova	Agility Communications, Inc.
J. Beck	DRS Infrared Technologies, LP, Dallas
C. Coldren	Agility Communications, Inc.
J. Decobert	Alcatel R&L
G. Fish	Agility Communications, Inc.
E. Hall	Agility Communications, Inc
E. Hegblom	Agility Communications, Inc.
A. Huntington	Voxtel
M. Kinch	DRS Infrared Technologies, LP, Dallas
R. Koda	Sony Corporation
M. Larson	Agility Communications, Inc.
D. Lofgreen	Raytheon
H. Marchand	Agility Communications, Inc.
M. Mašanović	Post Doctoral Researcher, UCSB (Blumenthal)
A. Maslov	NASA Ames Research Center

L. Rau	Post Doctoral Researcher, UC Irvine (Allbritton)
E. Skogen	Sandia National Laboratories
T. Strand	Agility Communications, Inc.
S. Strauf	Post Doctoral Researcher, UCSB (Bouwmeester)
N. Tscherptner	Alcatel R&L
C. Turner	Agility Communications, Inc.
H. Xu	Agility Communications, Inc.

Collaborating Students

A. Badolato	UCSB (Petroff)
A. Beck	University of Texas, Austin (Campbell)
V. Birkedal née Ciulin	UCSB (Sherwin)
S. Carter	UCSB (Sherwin)
S. Demiguel	University of Texas, Austin (Campbell)
W. Donat	UCSB (Blumenthal)
N. Duan	University of Texas, Austin (Campbell)
X. Guo	University of Texas, Austin (Campbell)
M. Hanson	UCSB (Gossard)
K. Hennessy	UCSB (Hu)
Z. Hu	UCSB (Blumenthal)
V. Lal	UCSB (Blumenthal)
N. Li	University of Texas, Austin (Campbell)
X. Li	University of Texas, Austin (Campbell)
F. Ma	University of Texas, Austin (Campbell)
M. Rakher	UCSB (Bouwmeester)
J. Summers	UCSB (Blumenthal)
S. Wang	University of Texas, Austin (Campbell)
X. Zheng	University of Texas, Austin (Campbell)

Table of Contents:

I. Photonic Integrated Circuits (PICs) and Related Technology Page

IA. Quantum-well-intermixed PICs

J.W. Raring, E.J. Skogen, L.A. Johansson, M.N. Sysak, S.P. DenBaars, and L.A. Coldren, "Widely Tunable Negative-Chirp SG-DBR Laser/EA-Modulated Transmitter," *Journal of Lightwave Technology*, **23**, (1), pp. 80-86 (January 2005) 3

G.B. Morrison, J.W. Raring, E.J. Skogen, C.S. Wang, and L.A. Coldren, "Photocurrent Spectroscopy Analysis of Widely Tunable Negative-Chirp Quantum-Well Intermixed Laser-Modulator Transmitters," *Applied Physics Letters*, **86**, (07118), pp. 1-3 (February 2005) 10

E.J. Skogen, J.W. Raring, G.B. Morrison, C.S. Wang, V. Lal, M.L. Mašanović, and L.A. Coldren, "Monolithically Integrated Active Components: A Quantum-Well Intermixing Approach," *IEEE Journal of Selected Topics in Quantum Electronics*, **11**, (2), pp. 343-355 (March/April 2005) INVITED PAPER 13

E.J. Skogen, L.A. Coldren, J.W. Raring, and S.P. DenBaars, "Multiple-Band-Edge Quantum-Well Intermixing in the InGaAs/InGaAsP/InGaP Material System," *Applied Physics Letters*, **86**, (241117), (June 13, 2005) 26

J.W. Raring, E.J. Skogen, J.S. Barton, S.P. DenBaars, and L.A. Coldren, "Quantum Well Intermixing and MOCVD Regrowth for the Monolithic Integration of UTC Type Detectors with Quantum Well Based Components," *Proc. Electronic Materials Conference,* paper no. NN6, Santa Barbara, CA (June 22-24, 2005) ABSTRACT ONLY 29

G.B. Morrison, J.W. Raring, C.S. Wang, E.J. Skogen, and L.A. Coldren, "Band-Edge Characterization of Intermixed InGaAsP/InP and InGaAs/GaAs Quantum Wells," *Proc. Electronic Materials Conference*, paper no. U4, Santa Barbara, CA (June 22-24, 2005) ABSTRACT ONLY 30

G.B. Morrison, E.J. Skogen, C.S. Wang, J.W. Raring, Y.-C. Chang, M.N. Sysak, and L.A. Coldren, "Photocurrent Spectroscopy for Quantum-Well Intermixed Photonic Integrated Circuit Design," *IEEE Photonics Technology Letters*, **17**, (7), pp. 1414-1416 (July 2005) 31

J.W. Raring, E.J. Skogen, J.S. Barton, C.S. Wang, S.P. DenBaars, and L.A. Coldren, "Quantum Well Intermixing and MOCVD Regrowth for the Monolithic Integration of 40 Gb/s UTC Type Detectors with Quantum Well Based Components," *Electronics Letters*, **41**, (18), pp. 1033-1034 (September 1, 2005) 34

J.W. Raring, E.J. Skogen, M.L. Mašanović, S.P. DenBaars, and L.A. Coldren, "Demonstration of High Saturation Power/High Gain SOAs using Quantum Well Intermixing Based Integration Platform," *Electronics Letters*, **41**, (24), pp. 1345-1346 (November 2005) 36

IB. Widely-Tunable Transmitter PICs

L.A. Johansson, Z. Hu, D.J. Blumenthal, L.A. Coldren, Y.A. Akulova, and G.A. Fish, "40 GHz Dual Mode-Locked Widely Tunable Sampled-Grating DBR Laser," *IEEE Photonics Technology Letters*, **17**, (2), pp. 285-287 (February 2005) 41

L.A. Johansson and L.A. Coldren, "Wavelength-Tunable Receiver Channel Selection and Filtering using SG-DBR Laser Injection-Locking," *Proc. OFC/NFOEC 2005*, paper no. OFM7, Anaheim, CA (March 6-11, 2005) 44

J.T. Getty, L.A. Johansson, and L.A. Coldren, "Novel Segmented Cascade Electroabsorption Modulator with Improved Bandwidth-Extinction Tradeoff," *Proc. OFC/NFOEC 2005*, paper no. OWE6, Anaheim, CA (March 6-11, 2005) 47

Y.A. Akulova, G.A. Fish, H. Xu, E. Hall, M.C. Larson, P. Abraham, H. Marchand, C. Turner, C.W. Coldren, E. Hegblom, T.A. Strand, and L.A. Coldren, "Monolithic Integrated Tunable Transmitters," *Proc. Integrated Photonics Research and Applications 2005*, paper no. IWF4, San Diego, CA (April 11-15, 2005) 50

M.L. Mašanović, J.S. Barton, V. Lal, M.N. Sysak, J.W. Raring, E.J. Skogen, D.J. Blumenthal, and L.A. Coldren, "Integration Techniques for InP-Based High-Functionality Photonic Integrated Circuits," *Proc. Integrated Photonics Research and Applications 2005*, paper no. IMC1, San Diego, CA (April 11-15, 2005) INVITED PAPER 53

L.A. Coldren, E.J. Skogen, J.W. Raring, J.S. Barton, D.D. Lofgreen, L.A. Johansson, and J.T. Getty, "Active Photonic Integrated Circuits," *Proc. 17th International Conference on Indium Phosphide and Related Materials,* Glasgow, Scotland (May 8-12, 2005) INVITED PAPER 56

L.A. Coldren, J.W. Raring, J.S. Barton, M.N. Sysak, and L.A. Johansson, "Widely-Tunable Transmitters and Photonic Integrated Circuits," *Proc. 63rd Device Research Conference*, **1**, pp. 11-14, Santa Barbara, CA (June 20-22, 2005) INVITED PAPER 59

J. Klamkin, J.M. Hutchinson, J.T. Getty, L.A. Johansson, E.J. Skogen, and L.A. Coldren, "High Efficiency Widely Tunable SGDBR Lasers for Improved Direct Modulation Performance," *IEEE Journal of Selected Topics in Quantum Electronics*, **11**, (4), pp. 931-938 (July/August 2005) 63

A. Tauke-Pedretti, M.N. Sysak, J.S. Barton, J.W. Raring, M. Dummer, and L.A. Coldren, "Monolithic Dual-Quantum-Well 10 Gb/s Mach-Zehnder Transmitter," *Proc. LEOS 2005, The 18th Annual Meeting of the IEEE,* paper no. TuBB3, pp. 408-409, Sydney, Australia (October 23-27, 2005) 71

IC. Wavelength Converter Technology

C.-H. Chen, L.A. Johansson, V. Lal, M.L. Mašanović, D.J. Blumenthal, and L.A. Coldren, "Programmable Optical Buffering using Fiber Bragg Gratings Combined with a Widely Tunable Wavelength Converter," *Proc. OFC/NFOEC 2005*, paper no. OWK4, Anaheim, CA (March 6-11, 2005) 75

M.N. Sysak, J.S. Barton, J.W. Raring, M. Dummer, A. Tauke-Pedretti, D.J. Blumenthal, and L.A. Coldren, "10 Gb/s Photocurrent Driven, Widely Tunable Electroabsorption Modulator Based Wavelength Converter," *Proc. OFC/NFOEC 2005*, paper no. OtuM4, Anaheim, CA (March 6-11, 2005) 78

M.L. Mašanović, V. Lal, J.A. Summers, J.S. Barton, E.J. Skogen, L.G. Rau, L.A. Coldren, and D.J. Blumenthal, "Widely Tunable Monolithically Integrated All-Optical Wavelength Converters in InP," *Journal of Lightwave Technology,* **23**, (3), pp. 1350-1362 (March 2005) 81

J. Piprek, V. Lal, J.M. Hutchinson, A. Tauke-Pedretti, M. Dummer, and L.A. Coldren, "Device Physics of an Optoelectronic Integrated Wavelength Converter," *Proc. SPIE Photonics West*, **5729**, pp. 170-176, San Jose, CA (March 2005) INVITED PAPER 94

J.S. Barton, M.N. Sysak, A. Tauke-Pedretti, M. Dummer, J. Klamkin, J.T. Getty, E.J. Skogen, J.W. Raring, L.A. Johansson, M.L. Mašanović, and L.A. Coldren, "Widely-Tunable Photocurrent-Driven Wavelength Converters," *Proc. SPIE Photonics West*, **5729**, pp. 177-191, San Jose, CA (March 2005) 101

J.A. Summers, V. Lal, M.L. Mašanović, L.A. Coldren, and D.J. Blumenthal, "Widely-Tunable All-Optical Wavelength Converter Monolithically Integrated with a Total Internal Reflection Corner Mirror Delay Line for 40Gbps RZ Operation," *Proc. Integrated Photonics Research and Applications 2005*, paper no. IMC5, San Diego, CA (April 11-15, 2005) 116

V. Lal, M.L. Mašanović, E.J. Skogen, J.W. Raring, J.A. Summers, L.A. Coldren, and D.J. Blumenthal, "10Gbps Monolithically-Integrated Widely-Tunable Wavelength Converter using Quantum Well Intermixing," *Proc. Integrated Photonics Research and Applications 2005*, paper no. IMC3, San Diego, CA (April 11-15, 2005) 119

V. Lal, J.A. Summers, M.L. Mašanović, L.A. Coldren, and D.J. Blumenthal, "Novel Compact InP-Based Monolithic Widely Tunable Differential Mach-Zehnder Interferometer Wavelength Converter for 40Gbps Operation," *Proc. 17th International Conference on Indium Phosphide and Related Materials,* Glasgow, Scotland (May 8-12, 2005) 122

V. Lal, M.L. Mašanović, E.J. Skogen, J.W. Raring, J.A. Summers, L.A. Coldren, and D.J. Blumenthal, "Quantum-Well-Intermixed Monolithically Integrated Widely Tunable All-Optical Wavelength Converter Operating at 10 Gb/s," *IEEE Photonics Technology Letters*, **17**, (8), pp. 1689-1691 (August 2005) 125

J.S. Barton, A. Tauke-Pedretti, M. Dummer, M.N. Sysak, M.L. Mašanović, J.W. Raring, E.J. Skogen, and L.A. Coldren, "10Gbit/s Wavelength Conversion using a Widely-Tunable Series Push-Pull Photocurrent-Driven Transmitter," *IEEE Photonics Technology Letters,* **17**, (9), pp. 1902-1904 (September 2005) 128

V. Lal, W. Donat, A. Tauke-Pedretti, L.A. Coldren, D.J. Blumenthal, and J. Piprek, "Broadband Rate-Equation Model Including Many-Body Gain for WDM Traveling –Wave SOAs," *Proc. IEEE/LEOS International Conference, Numerical Simulation of Optoelectronic Devices (NUSOD)*, paper no. ThC2, Berlin, Germany (September 2005) 131

J.A. Summers, M.L. Mašanović, V. Lal, L.A. Coldren, and D.J. Blumenthal, "Monolithic Widely-Tunable All-Optical Wavelength Converter with Spatial Filtering of Input and Output Signals for 10Gbps NRZ Operation," *Proc. LEOS 2005, The 18th Annual Meeting of the IEEE,* paper no. TuT2, Sydney, Australia (October 23-27, 2005) 133

M.L. Mašanović, V. Lal, E.J. Skogen, J.S. Barton, J.A. Summers, J.W. Raring, L.A. Coldren, and D.J. Blumenthal, "Cross-Phase Modulation Efficiency in Offset Quantum-Well and Centered Quantum-Well Semiconductor Optical Amplifiers," *IEEE Photonics Technology Letters,* **17**, (11), pp. 2364-2366 (November 2005) 135

ID. 980nm Edge-Emitter Technology

G.B. Morrison, C.S. Wang, E.J. Skogen, D.D. Lofgreen, and L.A. Coldren, "980 nm DBR Lasers Monolithically Integrated with EA Modulators for Optical Interconnect Applications," *Proc. Integrated Photonics Research and Applications 2005*, paper no. IWF2, San Diego, CA (April 11-15, 2005) 141

C.S. Wang, G.B. Morrison, E.J. Skogen, and L.A. Coldren, "Fabrication and MBE Regrowth of First Order, High Contrast AlGaAs/GaAs Gratings," *Proc. 23rd North American Conference on Molecular Beam Epitaxy*, paper no. WD-1, Santa Barbara, CA (September 11-14, 2005) ABSTRACT ONLY 144

II. InP-Based Vertical Cavity Lasers

C.S. Wang, R. Koda, A.S. Huntington, A.C. Gossard, and L.A. Coldren, ">100% Output Differential Efficiency 1.55-μm VCSELs Using Submonolayer Superlattices Digital-Alloy Multiple-Active-Regions Grown by MBE on InP," *Journal of Crystal Growth*, **277**, (1-4), pp. 13-20 (April 2005) 147

R. Koda, C.S. Wang, D.D. Lofgreen, and L.A. Coldren, "High-Differential-Quantum-Efficiency, Long-Wavelength Vertical-Cavity Lasers Using Five-Stage Bipolar-Cascade Active Regions," *Applied Physics Letters*, **86**, (211104), (May 23, 2005) 155

D. Feezell, D.A. Buell, L.A. Johansson, and L.A. Coldren, "High Differential Efficiency (>60%) Continuous-Wave Operation of 1.3μm InP-Based VCSELs with Sb-Based DBRs," *Proc. 63rd Device Research Conference*, post deadline paper, Santa Barbara, CA (June 20-22, 2005) 158

D.A. Buell, D. Feezell, and L.A. Coldren, "Defect Reduction at the AlGaAsSb/InP Interface for Optimized Long Wavelength Vertical Cavity Lasers," *Proc. Electronic Materials Conference*, paper no. NN7, Santa Barbara, CA (June 22-24, 2005) ABSTRACT ONLY 160

D. Feezell, D.A. Buell, and L.A. Coldren, "Continuous-Wave Operation of All-Epitaxial InP-Based 1.3μm VCSELs with 57% Differential Quantum Efficiency," *Electronics Letters,* **41**, (14), pp. 803-804 (July 7, 2005) 161

D.A. Buell, D. Feezell, B.-O. Fimland, and L.A. Coldren, "Molecular Beam Epitaxy of InP-Based Alloys for Long-Wavelength Vertical-Cavity Lasers," *Proc. 23rd North American Conference on Molecular Beam Epitaxy*, paper no. WC-1, Santa Barbara, CA (September 11-14, 2005) 163

D. Feezell, D.A. Buell, and L.A. Coldren, "InP-Based 1.3 – 1.6 μm VCSELs with Selectively Etched Tunnel-Junction Apertures on a Wavelength Flexible Platform," *IEEE Photonics Technology Letters,* **17**, (10), pp. 2017-2019 (October 2005) 179

D. Feezell, L.A. Johansson, D.A. Buell, and L.A. Coldren, "Efficient Modulation of InP-Based 1.3-*μ*m VCSELs with AsSb-Based DBRs," *IEEE Photonics Technology Letters,* **17**, (11), pp. 2253-2255 (November 2005) 182

III. Avalanche Photodetectors and SOA-PIN Receivers

N. Duan, S. Wang, X.G. Zheng, X. Li, N. Li, J.C. Campbell, C.S. Wang, and L.A. Coldren, "Detrimental Effect of Impact Ionization in the Absorption Region on the Frequency Response and Excess Noise Performance of InGaAs-InAlAs SACM Avalanche Photodiodes," *IEEE Journal of Quantum Electronics*, **41**, (4), pp. 568-572 (April 2005) 187

N. Duan, S. Wang, F. Ma, N. Li, J.C. Campbell, C.S. Wang, and L.A. Coldren, "High-Speed and Low-Noise SACM Avalanche Photodiodes With an Impact-Ionization-Engineered Multiplication Region," *IEEE Photonics Technology Letters*, **17**, (8), pp. 1719-1721 (August 2005) 192

A. Tauke-Pedretti, M. Dummer, J.S. Barton, M.N. Sysak, J.W. Raring, and L.A. Coldren, "High Saturation Power and High Gain Integrated Photoreceivers," *IEEE Photonics Technology Letters,* **17**, (10), pp. 2167-2169 (October 2005) 195

J.C. Campbell, S. Demiguel, F. Ma, A. Beck, X. Guo, S. Wang, X. Zheng, X. Li, J.D. Beck, M.A. Kinch, A.S. Huntington, L.A. Coldren, J. Decobert, and N. Tscherptner, "Correction to 'Recent Advances in Avalanche Photodiodes,'" *IEEE Journal of Selected Topics in Quantum Electronics*, **10**, (6), pp. 1446-1447 (November/December 2004) 198

IV. Terahertz Technology, Microcavities, and Quantum Coherence

M. Rakher, S. Strauf, N.G. Stoltz, K. Hennessy, A. Badolato, E. Hu, L.A. Coldren, P.M. Petroff, and D. Bouwmeester, "Cavity Quantum Electrodynamics with Single Quantum Dots in Microcavities," *Proc. 2005 American Physical Society March Meeting,* abstract no. C1.00011, Los Angeles, CA (March 21-25, 2005) ABSTRACT ONLY 203

S.G. Carter, V. Ciulin, M.S. Sherwin, C.S. Wang, L.A. Coldren, and A.V. Maslov, "Excitonic Autler-Townes Splitting Induced by an Intense Terahertz Field," *Proc. International Quantum Electronics Conference*, paper no. QTuI1, Baltimore, MD (May 22-27, 2005) 204

N.G. Stoltz, M. Rakher, S. Strauf, A. Badolato, D.D. Lofgreen, P.M. Petroff, L.A. Coldren, and D. Bouwmeester, "High-Quality Factor Optical Microcavities Using Oxide Apertured Micropillars," *Applied Physics Letters,* **87**, (031105), (July 12, 2005) 207

S.G. Carter, V. Birkedal, C.S. Wang, L.A. Coldren, A.V. Maslov, D.S. Citrin, and M.S. Sherwin, "Quantum Coherence in an Optical Modulator," *Science*, **310**, (5748), pp. 651-653 (October 28, 2005) 210

S.G. Carter, V. Ciulin, M. Hanson, A.S. Huntington, C.S. Wang, A.C. Gossard, L.A. Coldren, and M.S. Sherwin, "Terahertz-Optical Mixing in Undoped and Doped GaAs Quantum Wells: From Excitonic to Electronic Intersubband Transitions," *Physical Review B*, **72**, (155309), (October 2005) 213

I. Photonic Integrated Circuits (PICs) and Related Technology

A. Quantum-well-intermixed PICs

Widely Tunable Negative-Chirp SG-DBR Laser/EA-Modulated Transmitter

J. W. Raring, *Student Member, IEEE*, E. J. Skogen, *Member, IEEE*, L. A. Johansson, *Member, IEEE*, M. N. Sysak, *Student Member, IEEE*, S. P. DenBaars, *Member, IEEE*, and L. A. Coldren, *Fellow, IEEE*

***Abstract*—Ten Gb/s low power penalty (< 0.5 dB) error-free transmission was achieved through 75 km using a high-performance sampled-grating (SG) distributed Bragg reflector (DBR) laser/EAM transmitter. Large signal chirp measurements show negative chirp operation across the entire tuning range of the devices. An integration-oriented quantum-well-intermixing (QWI) process was employed for the realization of these devices.**

***Index Terms*—Chirp, electroabsorption modulators (EAMs), ion implantation, laser tuning, optical fiber communication, quantum-well intermixing (QWI), semiconductor lasers, wavelength division multiplexing (WDM).**

I. Introduction

ELECTROABSORPTION-MODULATED widely tunable transmitters are candidate sources for optical metropolitan area network applications, as they are compact and potentially low cost. The monolithic integration of electroabsorption modulators (EAM) with widely tunable lasers allows for inventory reduction and wavelength agile functionality. A common method used to realize this integration employs an offset quantum-well (QW) epitaxial architecture, in which the QW active region is grown on top of a bulk waveguide. For EAM definition, the QWs are selectively etched away and an upper cladding regrowth is performed [1]. This process produces Franz-Keldysh type modulators with a positive chirp factor, not suitable for 10 Gb/s transmission through standard fiber over distances required in metro networks. If QWs are used in the EAM, the quantum-confined stark effect can be exploited, and negative chirp factors can be achieved. Power-penalty-free transmission through over 100 km of standard fiber using QW EAMs has been reported [2]. The traditional method for the realization of monolithically integrated diode laser/QW-EAM transmitter involves the selective removal of the as-grown waveguide/multiple QW (MQW) region followed by the regrowth of waveguide/MQW material with the desired band edge. This tedious method is commonly referred to as butt-joint regrowth [3]. Although the butt-joint regrowth process does allow each integrated component to possess a unique band edge, the difficulty associated with matching thickness and achieving the desired composition to avoid reflection and loss at the interface is great. Another technique used to realize multiple band edges across a wafer is selective area growth. However, as discussed in [4] the abruptness of the transition region is limited by the surface diffusion of the growth constituents, which may be on the order of tens of microns. Additionally, the optical mode overlap with the MQW may not be ideal in all sections due to the thickness variation. The relatively simple QWI process employed in this paper enables for the precise placement of the band edge of each component within the device, allowing for blue-shifted QWs to remain in the modulator while leaving the axial waveguide undisturbed.

For the first time, a widely tunable transmitter demonstrating negative chirp performance at 10 Gb/s over its entire tuning range has been fabricated. A simple, robust quantum-well-intermixing (QWI) processing platform was employed for the fabrication. The transmitter consists of a quantum-well electroabsorption modulator (QW-EAM) monolithically integrated with a widely tunable sampled grating (SG) distributed Bragg reflector (DBR) laser. Less than 0.5 dB power penalty was measured for transmission at 10 Gb/s through 75 km of standard fiber. Time resolved large signal chirp measurements demonstrated negative chirp characteristics over the 27–nm tuning range of the device in operating regimes providing over 10 dB of RF extinction and reasonable insertion loss. The QWI process avoids much of the complexity usually associated with the fabrication of laser/EAMs having negative chirp.

II. Background

A. QWI Integration Platform

This paper employs a modified ion-implantation enhanced QWI process described in [4], as the fabrication platform. In this process, vacancies are created by ion implantation into an InP buffer layer over the MQW active region. During a high temperature anneal, the vacancies are diffused through the MQW region, promoting the interdiffusion of group V-atoms between the wells and barriers. The interdiffusion reshapes the QW profile by distorting the QW/barrier interface. The result is a shift in the quantized energy levels in the well, and hence a shift in the band edge energy [4].

B. Device Architecture

The device architecture [Fig. 1(a)] consists of a five section widely tunable SG distributed Bragg reflector (DBR) laser followed by an EAM. The five sections of the SG-DBR laser are, from left to right in Fig. 1(a); backside absorber, rear mirror,

Manuscript received May 26, 2004; revised October 22, 2004. This work was supported by DARPA/MTO CS-WDM by Grant N66001-02-C-8026 and by Intel Corporation by Grant TXA001630000.

J. W. Raring and S. P. DenBaars are with the Materials Department, University of California, Santa Barbara, CA 93106 USA (e-mail: jraring@engineering.ucsb.edu).

E. J. Skogen, L. A. Johansson, M. N. Sysak, and L. A. Coldren are with the Electrical and Computer Engineering Department, University of California, Santa Barbara, CA 93106 USA.

Digital Object Identifier 10.1109/JLT.2004.840330

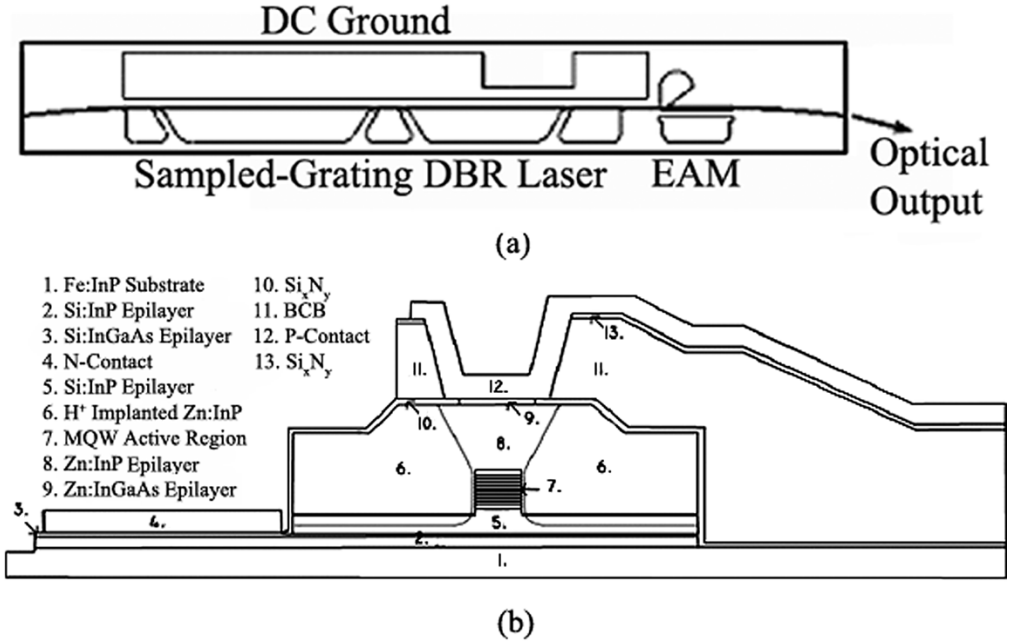

Fig. 1. (a) Top view schematic of the transmitter device architecture. (b) Cross-sectional schematic of modulator sections.

phase, gain, and front mirror. A buried ridge stripe waveguide design was employed with a curved/flared output to reduce the demands on the antireflection coating.

C. SG-DBR Laser

The SG DBR mirror is a special form of DBR mirror, where the gratings are periodically blanked to create a comb-like reflectivity spectrum [5]. The lithographically defined SG mirrors and the relatively simple process used to render the phase and mirror sections passive, make this device ideal for monolithic integration.

The sampling periods in the front and back mirrors differ, which provides the front and back mirrors with a different peak reflectivity spacing, so that only one set of reflectivity peaks is aligned within the desired tuning range. By differentially tuning the front and back mirrors a small amount, adjacent reflectivity peaks can be aligned, and the laser will operate at this new widely spaced wavelength. The simultaneous tuning of front and back mirrors allow wavelength coverage between mirror reflectivity peaks. The phase section provides cavity mode tuning, which ensures that the laser cavity mode is aligned with the mirror reflectivity peaks. The tuning in the mirrors and phase sections is based on carrier injection, producing a negative change in refractive index. To keep the loss to a minimal level over the desired wavelength operating range, the tuning sections make use of higher bandgap material or MQW regions whose quantized energy state is greater than that of the active region.

D. Electroabsorption Modulator

In an EAM, a reverse bias is used to shift the band edge of the modulator section to lower energy, thereby increasing the absorption of that region. In our case, QWI only smears the interfaces between the quantum wells and barriers, such that the quantum wells still remain after the intermixing, although slightly shallower and rounded. Allowing QWs to remain in the EAM enables the exploitation of the quantum-confined Stark effect in the EAM. The rounded shape of the intermixed quantum well also contributes to increased absorption efficiency in the modulator [6].

In this paper, several design and processing measures were taken to reduce parasitic capacitance in the EAM regions to achieve 10 Gb/s operation. The epilayer base structure was grown on a semiinsulating substrate. A 3-μm-thick layer of benzocyclobutene (BCB) was defined below the EAM bond pads to serve as a low-K dielectric. An angled proton implantation described in [7] was performed adjacent to the buried ridge to eliminate the parasitic capacitance associated with the homojunction. The implant was designed such that proton concentration was maintained at a level greater than 2E19 cm^{-2} to a depth beyond the InP homojunction on either side of the buried ridge. Fig. 1(b) is a schematic cross-sectional view of the EAM, illustrating these described features.

III. Process

The epitaxial base structure contained an n-contact InGaAs layer 1 μm below a multiquantum well (MQW) active region centered within a 1.1Q waveguide. The MQW consists of 15 InGaAsP 8.0 nm compressively strained (0.6%) quantum wells, separated by 8.0 nm tensile strained (0.3%) InGaAsP barriers grown on an Fe-doped InP substrate using a Thomas Swan horizontal-flow rotating-disk MOCVD reactor. Following the active region, a 15 nm InP stop etch, a 20-nm 1.3Q stop etch, and a 450-nm InP implant buffer layer was grown.

A 500-nm $\mathrm{Si}_x\mathrm{N}_y$, mask layer was deposited using plasma-enhanced chemical vapor deposition and lithographically patterned such that it remained over only the active regions of the chip. Next, ion implantation was performed using P^+ at an energy of 100 keV, yielding a range of 90 nm, with a dose of 5E14

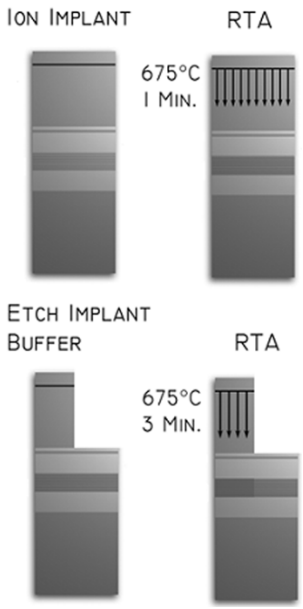

Fig. 2. Schematic of the intermixing process. From left to right on top; ion implantation followed by rapid thermal annealing. From left to right on bottom; selective removal of vacancy point defects required for blue-shifting, followed by an additional anneal.

cm^{-2}, at a substrate temperature of 200 °C [4]. The point defects created during the P^{+} implant were then partially diffused through the structure during a 60-s, 675 °C rapid thermal anneal (RTA), yielding the desired, 1510-nm photoluminescence band edge for the EAM. The implant buffer layer above the EAM sections was removed using a wet etching process, stopping on the 1.3Q stop etch layer. The sample was then subjected to an additional 180-s rapid thermal anneal, further blue-shifting the regions where the implant buffer layer remained. This second anneal was used to obtain desired band edge of 1450 nm for the mirror and phase sections. A schematic illustrating the intermixing process and the photoluminescence of the active, EAM, and passive regions are shown in Figs. 2 and 3, respectively.

The remainder of the process was carried out as described in [4] with the modifications for top-side n-contacts and the addition of BCB beneath the EAM contacts. The wafers were thinned, the devices were cleaved into bars and antireflection coated. The die were separated, soldered to aluminum nitride carriers, and wire bonded for characterization. A scanning electron micrograph of a completed devices mounted on a carrier is shown in Fig. 4.

IV. Device Results

The SG-DBR lasers demonstrated low threshold currents of 13 mA, with output powers of 10 mW captured in an integrating sphere at a gain section current of 100 mA as shown in Fig. 5. At this operating point, a side mode suppression ratio (SMSR) greater than 35 dB was achieved. By placing the MQW region in between a symmetrical waveguide maximum modal overlap is achieved, increasing the confinement factor by 50% over the traditional SG-DBR laser offset QW architecture [8].

The EAM 175 μm demonstrated over 40 dB of dc extinction for wavelengths of 1558, 1570, and 1580 nm, with efficiencies

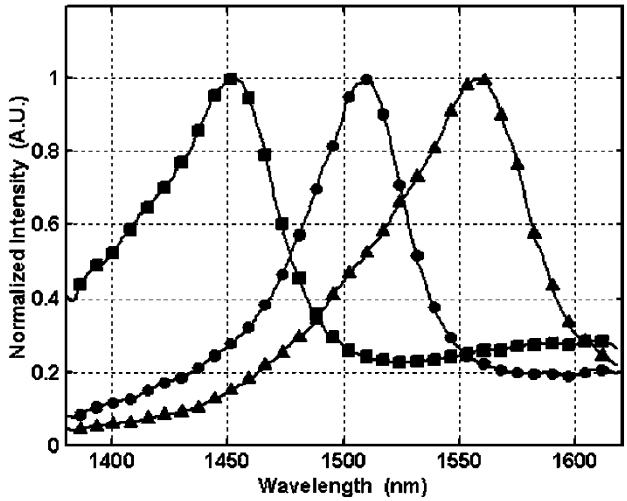

Fig. 3. Photoluminescence spectra of active section (triangles), modulator section (circles), and passive sections (squares).

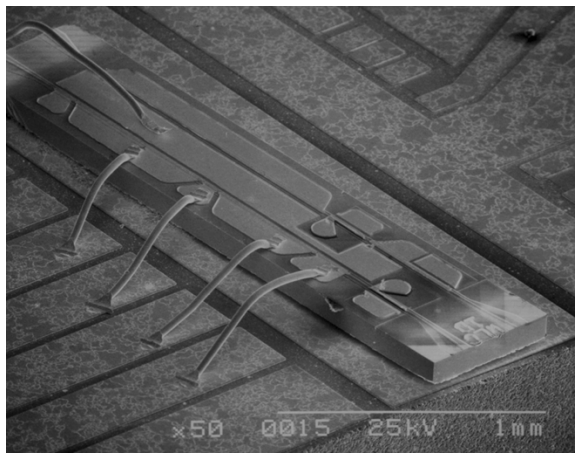

Fig. 4. Electron micrograph of transmitter device.

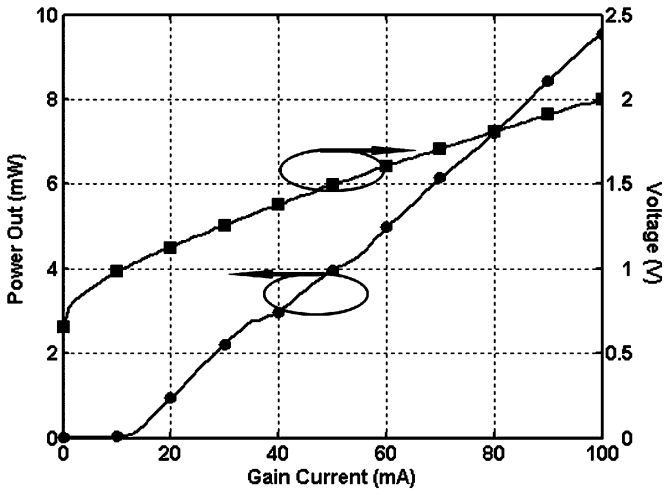

Fig. 5. Power out and gain section voltage versus applied current to SG-DBR laser gain section.

greater than 20 dB/V as shown in Fig. 6. The insertion loss of this EAM was found to be 1–2 dB at a wavelength of 1575 nm. The efficient extinction properties are due to the combination of the centered QW design and the intermixing process that allows

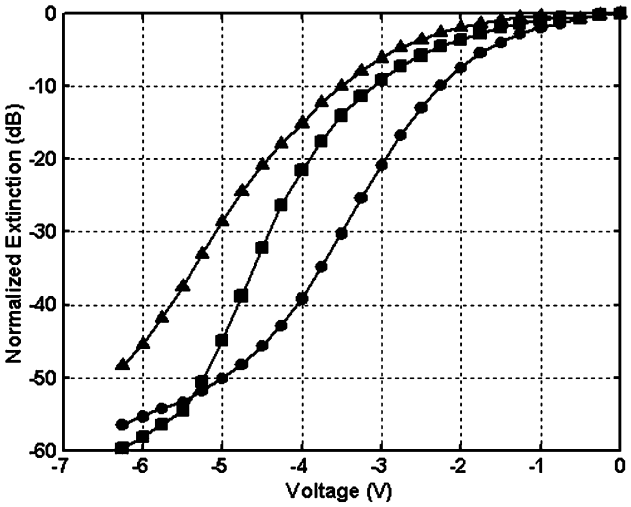

Fig. 6. DC extinction of a 175 μm modulator for wavelengths of 1558 nm (circles), 1570 nm (squares), and 1580 nm (triangles).

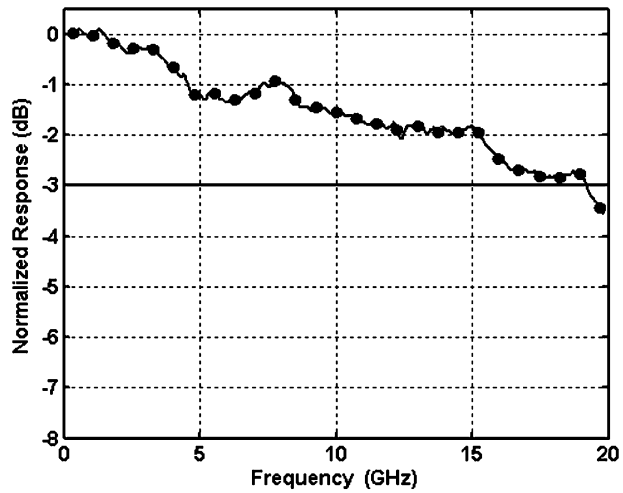

Fig. 7. Electrical to optical frequency response of a 175-μm modulator. The circular markers represent every 30th data point.

for precise placement of the modulator band edge. The 3-dB bandwidth, shown in Fig. 7, of the same modulator was greater than 19 GHz.

To demonstrate operation and transmission at 10 Gb/s, eye-diagrams were taken and bit-error rate (BER) testing was performed through various fiber lengths for the SG-DBR/EAM transmitters. The device was placed on a gold plated copper stage and cooled to 17 °C by a thermoelectric cooler. Light was coupled from the output facet of the transmitter device into a conical-tipped lensed fiber. The EAM was terminated with a 50-ohm resistor mounted directly on the ground-signal probes such that it was in parallel with the diode. A capacitor was placed in series with the termination resistor to eliminate dc power dissipation. The direct probing scheme was used to avoid the parasitics associated with the carrier and/or wire bonding. Back to back eye diagrams at 10 Gb/s were taken over the tuning range of the SG-DBR laser demonstrating RF extinction ratios greater than 10 dB using a dc driving voltage between 2.4 and 3.4 V with a 2.2-V peak to peak swing. The test setup and eye diagrams are shown in Figs. 8 and 9, respectively.

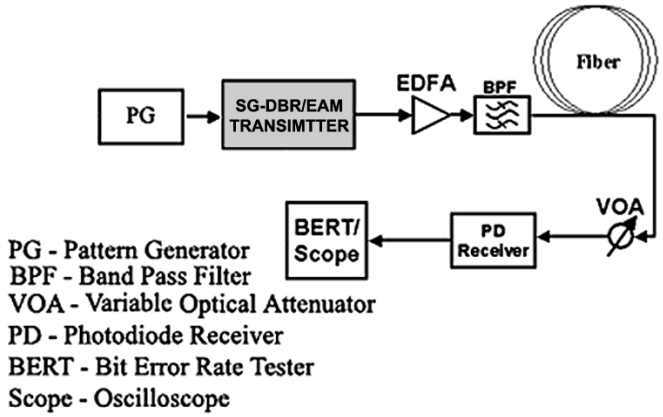

Fig. 8. Test set used to obtain BER and eye-diagrams from transmitter.

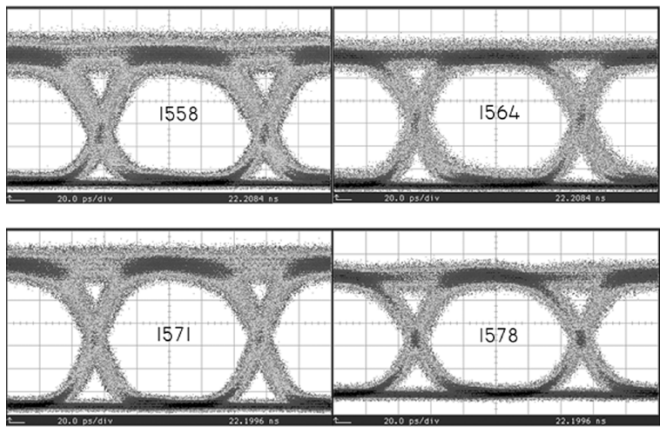

Fig. 9. Back-to-back eye diagrams from transmitter at wavelengths of 1558, 1564, 1571, and 1578 nm.

Transmission experiments at 10 Gb/s were performed using a nonreturn-to-zero (NRZ) pseudorandom-bit-sequence (PRBS) of $2^{31}-1$. A booster erbium doped fiber amplifier (EDFA) was used to launch optical powers on the order of 30 mW through Corning SMF-28 fiber. A variable optical attenuator was used to regulate the optical power into a nonpreamplified receiver. The complete test setup is shown in Fig. 8. Bit error rate (BER) curves through 25, 50, and 75 km of fiber at a wavelength of 1564 nm are shown in Fig. 4(b). Error-free operation was achieved through 75 km of fiber with a power penalty of less than 0.5 dB. The shaping of the eye diagrams due to dispersion is clearly seen in the insets of Fig. 10 where the optical eye diagrams are shown after transmission through fiber. The noise performance for transmission through 75 km is limited by the signal attenuation of the fiber and the noise of the oscilloscope optical receiver.

The low dispersion penalty for 10 Gb/s transmission demonstrated in Fig. 10 is indicative of negative chirp characteristics. For confirmation, the small-signal chirp parameter of the same device was extracted using the fiber-response method described in [9] for various EAM bias points at 1563 nm, as shown in Fig. 11. As expected, the EAM did exhibit negative chirp characteristics, with the transition from a positive to a negative chirp parameter occurring at -3.5 V

To demonstrate the capability for efficient 10 Gb/s transmission across the wide tuning range of these transmitters, the large

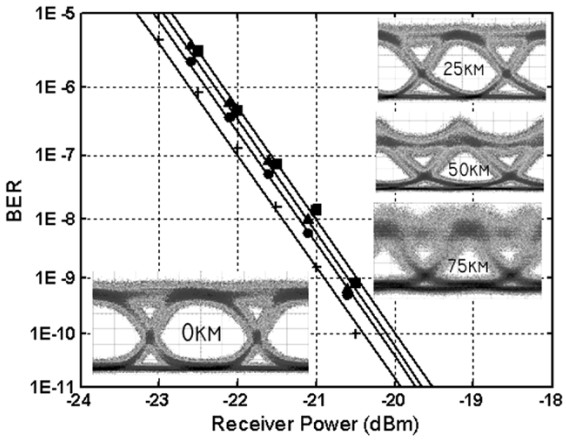

Fig. 10. BER curves and respective eye diagrams for back-to-back (cross), and transmission through 25 km (circles), 50 km (triangles), and 75 km (squares) of fiber at a wavelength of 1564 nm.

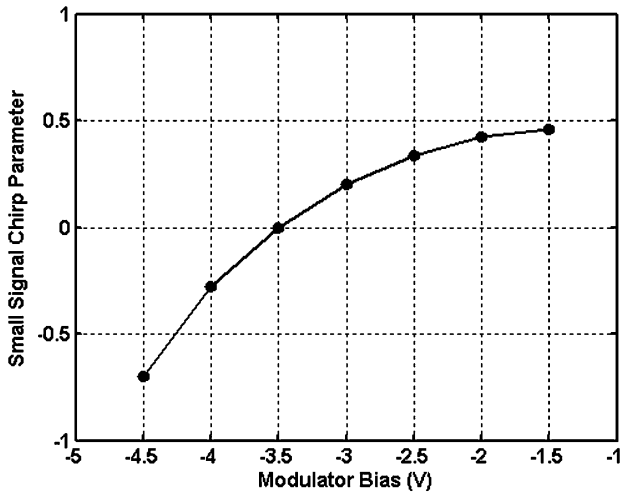

Fig. 11. The small signal chirp parameter characteristics versus reverse bias at 1563 nm.

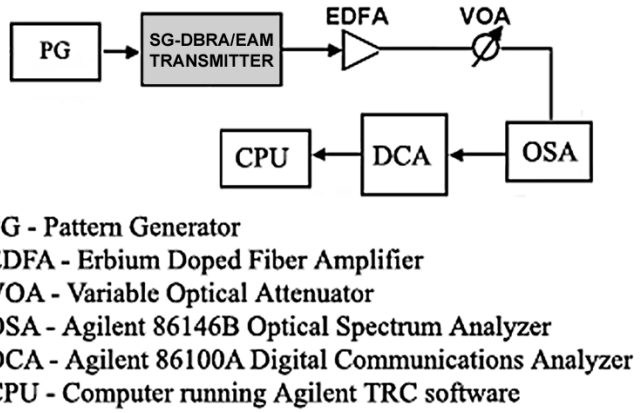

Fig. 12. Test setup used to extract time resolved large signal chirp parameter.

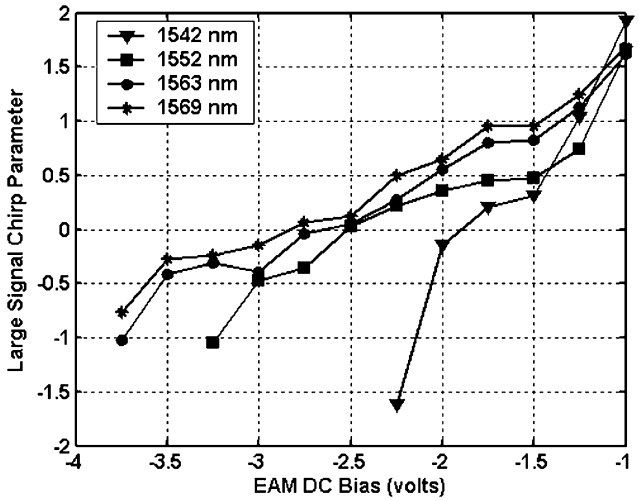

Fig. 13. Large signal chirp parameter as a function of EAM bias at 1542, 1552, 1562, and 1569 nm.

signal chirp parameter was extracted on a separate device at various wavelengths across its 27-nm tuning range. The large signal measurement is a better determination of the chirp characteristics of EAMs because it accounts for the full dynamic operating range essential for efficient transmission. That is the measurements can be made with an ac voltage swing necessary for > 10 dB signal extinction.

Large signal chirp measurements were made using Agilent's Time Resolved Chirp (TRC) software coupled with the required Agilent 86 146B optical spectrum analyzer and 86 100 A digital communications analyzer. The complete test setup is illustrated in Fig. 12. The chirp parameter was measured as a function of the dc bias applied to the EAM for wavelengths of 1542, 1552, 1562, and 1569 nm. The laser gain section was biased at 50 mA with the appropriate mirror section currents to achieve each wavelength while the peak-to-peak voltage swing applied to the EAM was 2 V. As shown in Fig. 13, a larger reverse bias is required to achieve a negative chirp parameter at longer wavelengths. The measured chirp parameters were found to transition from positive to negative for all wavelengths, occurring at 1.9 V at 1542 nm and 2.8 V at 1569 nm.

Considering the proximity of the modulator band edge to the laser operating wavelength, it is clear that a larger reverse bias is required to achieve efficient absorption at longer wavelengths. The onset of absorption with reverse voltage increases and the absorption efficiency decreases somewhat with increasing wavelength, however, the general shape of the extinction curves remain similar. In view of the fact that the chirp parameter is related to the operating point on the modulator extinction curve, and the fact that similar extinction characteristics are observed for all wavelengths, our demonstration of a negative chirp parameter over the wide tuning range of the SG-DBR laser is perfectly reasonable.

To demonstrate that the negative chirp characteristics of the transmitter can be achieved within an operating regime providing sufficient signal extinction and reasonable output power across its tuning range, the modal extinction characteristics were evaluated with respect to the large signal chirp data at each wavelength. By comparing the extinction characteristics in Fig. 14 with the chirp characteristics of the same device in Fig. 13, the modulator extinction ratio and insertion loss can be estimated for a given chirp parameter at all tested wavelengths. The intersections of the dashed and dotted lines on in Fig. 14 represent the on-state operating voltage of the EAM to achieve

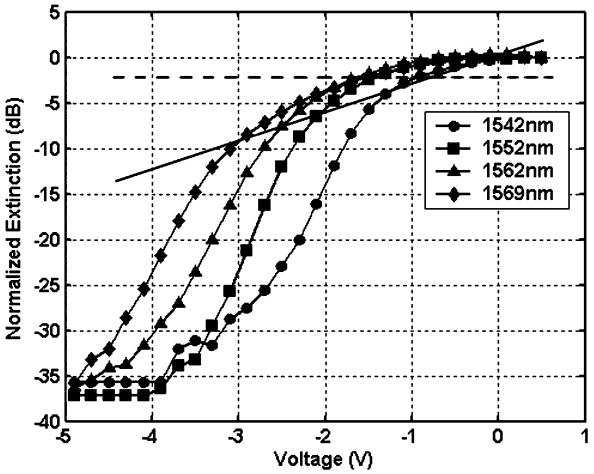

Fig. 14. DC extinction of the 175 μm modulator for wavelengths from 1542 to 1569 nm from the same modulator in which the large signal chirp was extracted from. The dashed and solid lines indicate the approximate EAM on state dc bias to achieve a chirp parameter of 0 and -0.7, respectively, with a 2 V peak to peak swing.

chirp parameters of 0 and -0.7, respectively. The on-state operating voltage was calculated by adding 1/2 of the peak to peak voltage swing (1 V) to the dc bias necessary to achieve the chirp parameter values in question. It is clear that for both chirp parameter values, a 2-V swing on the EAM provides over 10 dB extinction at all tested wavelengths. Fig. 14 indicates that to achieve a chirp parameter of 0, the modulator must be biased such that there is only $\sim$2 dB of on-state signal extinction for all tested wavelengths. To achieve a chirp parameter of -0.7, the on-state signal extinction ranged from 3.5 dB at 1542 nm to 9 dB at 1569 nm. With these extinction values, the total insertion loss of the EAM can be estimated at each wavelength for operation at both chirp parameter values by adding the unbiased insertion loss, which we have extracted to be 1-2 dB at 1575 nm. Although the unbiased insertion loss will increase with decreasing operation wavelength, the signal extinction required for negative chirp is decreased with decreasing wavelength. The key point is that to achieve chirp parameter values necessary for low penalty 10 Gb/s transmission the EAMs are not forced to operate at a bias point along the extinction curve which provides unacceptable insertion loss or insufficient extinction.

V. Conclusion

For the first time, we have realized a high performance widely tunable laser/EAM transmitter capable of negative chirp operation across its entire tuning range. The transmitter demonstrated error-free low-power-penalty operation through 75 km of standard fiber at 10 Gb/s. The large signal chirp parameter was shown to transition to a negative value at larger reverse biases for increasing operation wavelength. Furthermore, it was shown that the operation regime required for negative chirp characteristics provided sufficient signal extinction and reasonable insertion loss. The 3-dB bandwidth of this transmitter was shown to be over 19 GHz with an RF extinction greater than 10 dB. This work was made possible by the use of a simple, robust QWI processing platform for the monolithic integration of blue-shifted QW-EAMs with SG-DBR lasers.

References

[1] Y. Akulova, G. Fish, P. Koh, C. Schow, P. Kozodoy, A. Dahl, S. Nakagawa, M. Larson, M. Mack, T. Strand, C. Coldren, E. Hegblom, S. Penniman, T. Wipiejewski, and L. Coldren, "Widely tunable electroabsorption-modulated sampled grating DBR laser transmitter," *IEEE J. Sel. Topics Quantum Electron.*, vol. 8, pp. 1349–1357, Nov./Dec. 2002.

[2] K. Morito, R. Sahara, K. Sato, and Y. Kotaki, "Penalty free 10 Gb/s NRZ transmission over 100 km of standard fiber at 1.55 μm with a blue-chirp modulator integrated DFB laser," *IEEE Photon. Technol. Lett.*, vol. 8, pp. 431–433, 1996.

[3] J. Binsma, P. Thijs, T. VanDongen, E. Jansen, A. Staring, G. VanDenHoven, and L. Tiemeijer, "Characterization of butt-joint InGaAsP waveguides and their application to 1310 nm DBR-type MQW ganin-clamped semiconductor optical amplifiers," *IEICE Trans. Electron.*, vol. E80-C, pp. 675–681, 1997.

[4] E. Skogen, J. Raring, J. Barton, S. DenBaars, and L. Coldren, "Post-growth control of the quantum well band edge for the monolithic integration of widely tunable lasers and electroabsorption modulators," IEEE J. Sel. Topics Quantum Electron., 2004, to be published.

[5] V. Jayaraman, Z. Chuang, and L. Coldren, "Theory, design, and performance of extended tuning range semiconductor lasers with sampled gratings," *IEEE J. Quantum Electron.*, vol. 29, pp. 1824–1834, 1993.

[6] S. Charbonneau, E. Kotels, P. Poole, J. He, G. Aers, J. Haysom, M. Buchanan, Y. Feng, A. Delage, F. Yang, M. Davies, R. Goldberg, P. Piva, and I. Mitchell, "Photonic integrated circuits fabricated using ion implantation," *IEEE J. Sel. Topics Quantum Electron.*, vol. 4, pp. 772–793, 1998.

[7] J. Raring, E. Skogen, L. Johansson, and L. Coldren, "Enhanced frequency response in buried ridge quantum well intermixed SGDBR laser modulators," in *Conf. Lasers Electro-Optics*, San Francisco, CA, May 16–21, 2004.

[8] B. Mason, J. Barton, G. Fish, and L. Coldren, "Design of sampled grating DBR lasers with integrated semiconductor optical amplifiers," *IEEE Photon. Technol. Lett.*, vol. 12, pp. 762–764, 2000.

[9] B. Dvaux, Y. Sorel, and J. F. Kerdiles, "Simple measurement of fiber dispersion and of chirp parameter of intensity modulated light emitter," *J. Lightw. Technol.*, vol. 11, no. 12, pp. 1937–1940, Dec. 1993.

James W. Raring (S'03) was born in Ramsey, NJ, in 1978. He received the B.S. degree from the Materials Engineering Department, California Polytechnic State University, San Luis Obispo, in 2001.

He is currently pursuing the Ph.D. degree in materials science from the University of California, Santa Barbara. His current research focuses on the monolithic integration of widely tunable diode lasers into high-speed photonic integrated circuits with the use of quantum-well intermixing and MOCVD growth.

Erik J. Skogen (M'99) was born in Minneapolis, MN, in 1975. He received the B.S. degree from Iowa State University in 1997, and the M.S. and Ph.D. degrees from the University of California, Santa Barbara, in 1999 and 2003, respectively.

His current research interests include widely tunable semiconductor lasers, monolithic integration for photonic integrated circuits, growth aspects in the InGaAsP material system using MOCVD, and quantum-well intermixing.

Leif A. Johanasson (M'04) received the Ph.D. degree in engineering from University College London in 2002.

He continued with a Postdoctoral position with the University of California, Santa Barbara, in 2002. His current research interests include design and characterization of integrated photonic devices for analog and digital applications.

Mathew N. Sysak (M'03) was born in Smithtown, NY, in 1976. He received the B.S. degree from Pennsylvania State University in chemical engineering in 1998 and the M.S. degree from the University of California, Santa Barbara, in electrical and computer engineering.

His current research interests include the monolithic integration of widely tunable semiconductor lasers with semiconductor optical amplifiers, electroabsorption modulators, and photodetectors in the InGaAsP material system.

Steven P. DenBaars (M'91) from 1988 to 1991, he was a member of Technical Staff at Hewlett-Packard where he was involved in the fabrication of high brightness LEDs. In 1991 he joined the faculty of the University of California, Santa Barbara (UCSB), as a Professor of materials and electrical engineering, where he is developing new solid-state optoelectronic devices. His research also involves MOCVD growth of GaN- and InP-based tunable lasers and detectors. Currently, he is an Associate Director of the solid-state lighting and display center (SSLDC) at UCSB, which is developing new more-energy efficient light sources. Special interests include the effect of materials properties on device performance, blue VCSEL lasers, and microwave power transistors. He has authored more than 200 technical publications, three book chapters, 100 conference presentations, and more than seven patents.

Dr. DenBaars has received a NSF Young Scientist Award (1995) and the Young Scientist Award from the International Symposium on Compound Semiconductors in 1998.

Larry A. Coldren (F'80) received the Ph.D. degree in electrical engineering from Stanford University, Stanford, CA, in 1972.

He is the Fred Kavli Professor of Optoelectronics and Sensors at the University of California (UCSB), Santa Barbara. He is also Chairman and Chief Technology Officer of Agility Communications, Inc. After 13 years in the research area at Bell Laboratories, he joined UCSB in 1984 where he now holds appointments in Materials and Electrical and Computer Engineering, and is Director of the Optoelectronics Technology Center. In 1990 he cofounded Optical Concepts, later acquired as Gore Photonics, to develop novel VCSEL technology; and in 1998 he cofounded Agility Communications to develop widely tunable integrated transmitters. At Bell Labs, he initially worked on waveguided surface-acoustic-wave signal processing devices and coupled-resonator filters. He later developed tunable coupled-cavity lasers using novel reactive-ion etching (RIE) technology that he created for the then new InP-based materials. At UCSB he continued work on multiple-section tunable lasers, in 1988 inventing the widely tunable multielement mirror concept, which is now fundamental to many of Agility's products. During the late 1980s, he also developed efficient vertical-cavity multiple-quantum-well modulators, which led to novel vertical-cavity surface-emitting laser (VCSEL) designs that provided unparalleled levels of performance. He continues to be active in developing new photonic integrated circuit (PIC) and VCSEL technology, including the underlying materials growth and fabrication techniques. In recent years, for example, he has been involved in the creation of vertical and in-plane GaN-based emitters, efficient all-epitaxial InP-based VCSELs, and a variety of PICs incorporating numerous optical elements for widely tunable integrated transmitters, receivers, and wavelength converters. He has authored or coauthored more than 700 papers, five book chapters, one textbook, and has been issued 36 patents.

Professor Coldren has presented dozens of invited and plenary talks at major conferences. He is a fellow of the OSA and IEE, the recipient of the 2004 John Tyndall Award, and a member of the National Academy of Engineering.

Photocurrent spectroscopy analysis of widely tunable negative-chirp quantum-well intermixed laser-modulator transmitters

G. B. Morrison[a)]
Department of Electrical and Computer Engineering, University of California–Santa Barbara, Santa Barbara, California 93106

J. W. Raring
Materials Department, University of California–Santa Barbara, Santa Barbara, California 93106

E. J. Skogen and C. S. Wang
Department of Electrical and Computer Engineering, University of California–Santa Barbara, Santa Barbara, California 93106

L. A. Coldren
Department of Electrical and Computer Engineering and Materials Department, University of California–Santa Barbara, Santa Barbara, California 93106

(Received 3 September 2004; accepted 20 December 2004; published online 10 February 2005)

High-speed laser-modulator transmitters fabricated using InGaAsP quantum-well intermixing exhibit negative chirp over a wavelength range of more than 30 nm. Photocurrent spectroscopy is used to examine the multiple band edges in these devices. An exciton peak is found in the photocurrent data, and the evolution of the band edge as a function of quantum-well intermixing and applied bias voltage is revealed. The photocurrent data are then exploited to verify and explain the negative chirp characteristics of the wavelength-agile transmitters. © *2005 American Institute of Physics*. [DOI: 10.1063/1.1865330]

Widely tunable laser-electro-absorption modulator (EAM) transmitters are ideal sources for next-generation optical networks. These monolithic wavelength-agile components promise cost savings in the form of inventory reduction, and are a key to technologies such as wavelength-routing and dynamic provisioning for future wavelength-division-multiplexing networks. Monolithic integration of separate laser and modulator band edges has been accomplished by numerous methods, but quantum-well intermixing (QWI) is an especially elegant approach, and is one of the simplest to implement.[1] QWI also allows simultaneous integration of passive waveguide sections, thereby reducing mirror loss. Using InGaAsP based QWI we have designed and fabricated widely tunable laser-EAMs that exhibit negative chirp and good extinction ratios over a wavelength range of more than 30 nm.[2] We attribute the excellent performance of the wavelength-agile modulator to the presence of a band edge exciton peak that is associated with the quantum confined stark effect (QCSE).[3] Quantum-well intermixing, however, is known to smooth out quantum well definition and to make the quantum wells broader and shallower,[4] altering, and potentially weakening or even extinguishing the exciton peak.[5] The degree of influence that QWI has on the QCSE in InGaAsP materials is not yet well established experimentally. In this letter, we use photocurrent spectroscopy to demonstrate that the QWI process can be exploited to obtain multiple band edges orthogonal to the growth direction while still retaining a strong exciton peak. The photocurrent data show the effect of QWI on the exciton peak in InGaAsP QW over a wide range of applied bias voltages. Furthermore, we model the large-signal chirp, starting with the photocurrent data, and demonstrate that the model is in good agreement with data collected from our widely tunable laser-EAM devices. The negative chirp of the widely tunable laser-EAM transmitter is thereby shown to be a direct result of the QWI band edge.

The laser-EAM transmitter device consists of a five-section sampled grating (SG) distributed Bragg reflector (DBR) laser, followed by an EAM. The five sections in the SGDBR, starting at the rear facet, are the back side absorber, the passive rear mirror, the passive phase section, the gain section, and a passive front mirror. The phase and mirror sections are used to tune the wavelength of the laser. The transmitter uses a buried ridge stripe architecture containing 15 InGaAsP 80 Å compressively strained (0.6%) quantum wells separated by 80 Å tensile-strained (0.3%) InGaAsP barriers. The quantum wells are centered within a 1.1Q waveguide that is 1.0 μm above an *n*-contact InGaAs layer that is grown on an Fe-doped InP substrate. Above the active region, a 15 nm InP regrowth layer, a 20 nm 1.3Q etch stop, and a 450 nm InP implant buffer layer were grown.

Gain and absorber sections of the transmitter were masked with 5000 Å of Si_xN_y and the wafer was exposed to a 5E14 cm^{-2} P^+ implant at 100 keV. The sample was then annealed at 675 °C until the desired band edge was obtained in the EAM sections. The photoluminescent peak (λ_{pl}) for the EAM QWI material was measured to be approximately 1510 nm. The implant layer in the EAM region was etched, and further annealing was performed on the wafer, causing the phase, mirror, and passive waveguide sections to shift to $\lambda_{pl} \approx 1450$ nm. The remaining implant layer was removed, stop etches were removed, and the wafer was submitted for metalorganic chemical vapor deposition (MOCVD) regrowth as described in Ref. 1. A more detailed description of the transmitter design and fabrication is available in Ref. 2. A schematic of the laser-modulator transmitter, and a cross-

[a)]Electronic mail: gmorrison@ece.ucsb.edu

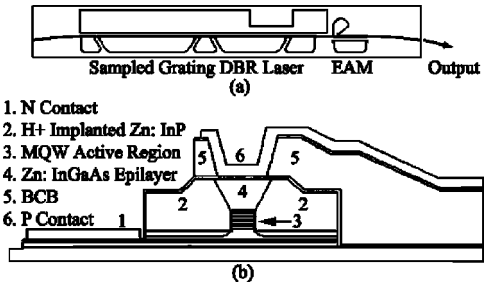

FIG. 1. (a) Diagram of the SGDBR laser module and electroabsorption modulator. (b) Cross-sectional schematic of the modulator component analyzed in this letter.

sectional view of the modulator, are shown in Figs. 1(a) and 1(b), respectively.

Identical material from the same MOCVD growth as was used for transmitter fabrication was simultaneously fabricated into circular photodiodes with radii ranging from 50 to 400 μm. These photodiodes were fabricated for the photocurrent spectroscopy characterization of the material. QWI was performed to obtain four different band edges for the photodiodes, with λ_{pl} at approximately 1554, 1527, 1508, and 1480 nm. The circular photodiode mesas were reactive-ion etched through the waveguide and quantum wells. The top InGaAs *p*-contact was thinner (750 Å) than on the transmitter devices in order to minimize absorption of input light. A 2000 Å layer of Si_xN_y was deposited, and circular vias were etched to expose the mesa contact layers. Ti/Pt/Au ring contacts and bonding pads were laid down and annealed at 420 °C for 30 s. A diagram of the basic structure of the photodiode is shown in Fig. 2.

Photodiodes were placed in a Varian Cary 500 spectrophotometer behind a 500 μm radius, position-adjustable aperture. The aperture served to sample a specific part of the spectrophotometer input beam, and input power was then easily calibrated using a Newport 1835 C optical power meter. A Kiethly 2400 L-V source meter was used to bias the photodiodes over a range of 0 to −6 V in −0.5 V increments. An EG&G lock-in Amplifier with a 1 s time constant was used in conjunction with a 3 kHz chopper to filter the photocurrent signal from leakage current and other noise. The entire system is automated. Reflectance and transmittance measurements on the spectrophotometer have been used to quantify the absorption of input light in the InGaAs *p*-contact material.

Photodiodes with 250 μm radii were found to be ideal candidates for easy alignment with the aperture, while coupling enough input light to generate a photocurrent signal well above the noise floor. A Ti/Pt/Au layer was deposited

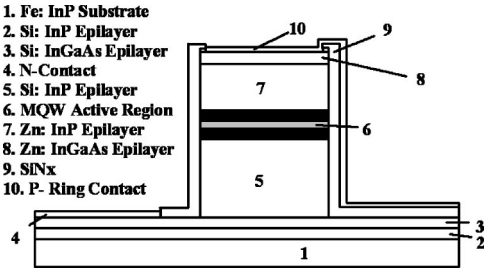

FIG. 2. Side view of the photodiode structure used for photocurrent spectroscopy.

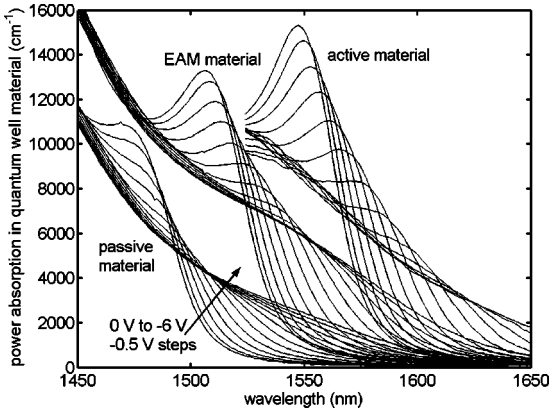

FIG. 3. Active, modulator, and passive absorption edges, obtained by ion-implant quantum-well intermixing. Curves are shown for biases ranging from 0 to −6 V in −0.5 V increments.

on the back side of the devices to prevent significant photocurrent contribution from backscattered light. Figure 3 shows the evolution of the band edge as a function of QWI and applied bias voltage. Band edges for as-grown material ($\lambda_{pl} \approx 1554$ nm), EAM material ($\lambda_{pl} \approx 1508$ nm), and passive material ($\lambda_{pl} \approx 1480$ nm) are shown. Note that the exciton peak for the QWI EAM material is strong, and that even the passive material exhibits an identifiable exciton peak. The carrier confinement in the quantum wells, however, is clearly reduced by QWI. The exciton is extinguished (i.e., electrons tunnel out of conduction band wells) at weaker biases when quantum-well intermixing is performed.

Starting with the absorption data for the EAM modulator in Fig. 3, differences in absorption between the band edge at 0 V and the band edges at each of the reverse biases are easily obtained. Application of the Kramers–Kronig transform, as described in Ref. 6, yields the index change as a function of voltage change. Although data in Fig. 3 are shown over a 200 nm range only, data spanning a full 280 nm was used for the truncated Kramers–Kronig transform. Figure 4 shows absorption changes ($\Delta\alpha$) and index changes (Δn) that are expected with −2 V change in potential, centered at bias voltages ranging from −1.5 to −5.0 V (e.g., a −2 V change in potential, centered at a bias voltage of −1.5 V, is from −0.5 to −2.5 V). With these −2 V changes, positive absorption changes ($\Delta\alpha$) are clearly seen

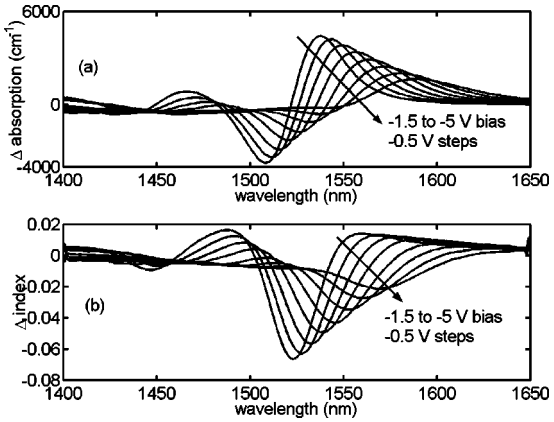

FIG. 4. (a) Changes in absorption with −2 V changes in potential that are centered at bias voltages ranging from −1.5 to −5 V. (b) Change in index with −2 V changes in potential that are centered at bias voltages ranging from −1.5 to −5 V.

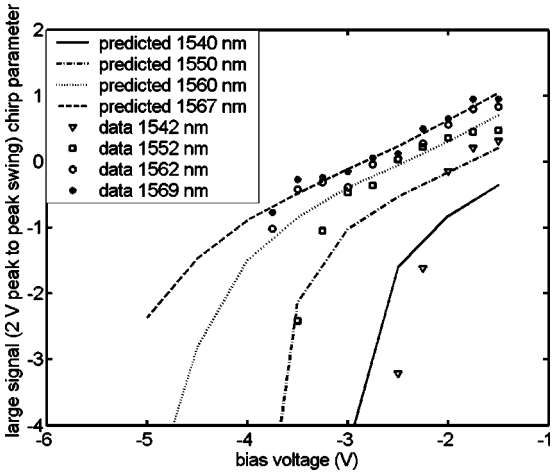

FIG. 5. Data points show measured chirp as a function of bias voltage at 1542, 1552, 1562, and 1569 nm. Lines show chirps predicted using photocurrent spectroscopy at 1540, 1550, 1560, and 1567 nm.

throughout the operating range of the transmitter, as expected. At shorter wavelengths, in the vicinity of the exciton peak, negative absorption change ($\Delta\alpha$) occurs with a −2 V change in bias voltage. These trends directly influence the shape of the Δn curves [shown directly below Fig. 4(a) for comparison] by way of the Kramers–Kronig transform.

The $\Delta\alpha$ and Δn curves of Fig. 4 are in turn used to calculate the large-signal chirp.[7] Figure 5 compares the large-signal chirp, as calculated from photocurrent spectroscopy, at wavelengths of 1540, 1550, 1560, and 1567 nm, with the chirp measured in the buried-ridge modulators at wavelengths of 1542, 1552, 1562, and 1569 nm. The 2 nm differences between the wavelengths are included to account for the fact that the photocurrent diodes were intermixed to $\lambda_{pl} \approx 1508$ nm, whereas the transmitter EAMs were intermixed to $\lambda_{pl} \approx 1510$ nm. Chirp measurements were made on the transmitters using Agilent's Time Resolved Chirp software coupled with the required Agilent 86146B optical spectrum analyzer. The insertion loss of the modulator depends on the bias voltage and operating wavelength. For this device, a chirp of 0 can be obtained at all wavelengths in Fig. 5 (1542–1569 nm) with total insertion loss ranging from 3 to 4 dB, depending on the wavelength. Negative chirp of −0.7 can be obtained at all wavelengths in Fig. 5 with total insertion loss ranging from 3.5 to 9 dB, depending on the operating wavelength.[8]

In Fig. 5, the measured chirp parameter and the chirp parameter that is calculated directly from photocurrent spectroscopy are in reasonable agreement. There are no fitting parameters for the calculated curves. Clearly, the negative chirp performance of these wavelength-agile transmitters can be directly attributed to the QCSE band edge that is found in the QWI material from which the EAMs are fabricated. The QWI process that was used to shift the band edge in the EAM section of the device did not significantly detract from the exciton confinement. We therefore assert that QWI is a promising integration platform for implementation of high performance, widely tunable, negative chirp, laser-EAM transmitter devices.

In summary, quantum-well intermixing by ion implantation is a widely used technique for obtaining multiple band edges on a single wafer. We have presented detailed data examining the effect of QWI on InGaAsP quantum well band edges, over a wide range of bias voltages. We have used the data with the Kramers–Kronig transformation to experimentally verify that QWI laser-EAM transmitters can exhibit negative chirp over a range of 30 nm. The QWI process that was used to obtain the EAM band edge does not significantly detract from the exciton confinement, and thus the negative chirp exhibited by as-grown wells for a wide range of wavelengths is also exhibited in the QWI modulator wells. Quantum-well intermixing is therefore an excellent method for fabrication of integrated laser-EAM transmitters. We consider photocurrent spectroscopy to be an essential tool for understanding, designing, and analyzing complex QWI photonic integrated circuits.

[1] E. J. Skogen, J. W. Raring, J. S. Barton, S. P. Denbaars, and L. A. Coldren, IEEE J. Sel. Top. Quantum Electron. **9**, 1183 (2003).
[2] J. W. Raring, E. J. Skogen, L. A. Johansson, M. N. Sysak, J. S. Barton, M. L. Mašanovic, and L. A. Coldren, IEEE Photonics Technol. Lett. **16**, 1613 (2004).
[3] T. Yamanka, K. Wakita, and K. Yokoyama, Appl. Phys. Lett. **70**, 87 (1997).
[4] D. Hofstetter, B. Maisenhölder, and H. P. Zappe, IEEE J. Sel. Top. Quantum Electron. **4**, 794 (1998).
[5] E. H. Li and W. C. H. Choy, J. Appl. Phys. **82**, 3861 (1991).
[6] C. H. Henry, R. A. Logan, and K. A. Bertness, J. Appl. Phys. **52**, 4457 (1981).
[7] J. A. J. Fells, I. H. White, M. A. Gibbon, R. V. Penty, G. B. H. Thompson, A. P. Wright, R. A. Saunders, and C. J. Armistead, Electron. Lett. **30**, 2066 (1994).
[8] J. W. Raring, E. J. Skogen, S. P. DenBaars, and L. A. Coldren, Electron. Lett. **40**, 1599 (2004).

Monolithically Integrated Active Components: A Quantum-Well Intermixing Approach

Erik J. Skogen, *Member, IEEE*, James W. Raring, *Student Member, IEEE*, Gordon B. Morrison, *Member, IEEE*, Chad S. Wang, Vikrant Lal, *Student Member, IEEE*, Milan L. Mašanović, *Student Member, IEEE*, and Larry A. Coldren, *Fellow, IEEE*

Invited Paper

***Abstract*—As the demand for bandwidth increases, the communications industry is faced with a paradigm shift. Photonic integration is a key technology that will facilitate this shift. Monolithic integration allows for the realization of highly functional optical components, called photonic integrated circuits. Herein, we discuss the advantages and potential applications of photonic integration, and after a brief overview of various integration techniques, provide a detailed look at our work using a novel quantum well intermixing processing platform.**

***Index Terms*—Ion implantation, laser tuning, semiconductor lasers, wavelength division multiplexing (WDM).**

I. Introduction

MONOLITHIC integration of optoelectronic components is the key to realizing low-cost, high-functionality devices that have the capability to revolutionize the communications industry. Although not a new concept, monolithic integration of various optical functions now appears to be feasible, and perhaps the only way to truly revitalize the optical component industry. With today's technology, the generation, detection, modulation, switching, and transport of light on chip enables cost reduction, but it will also allow for a new generation of high functionality photonic integrated circuits (PICs) with reduced size and power dissipation.

Of course, monolithic integration has already occurred in the electronics industry, allowing the once discrete transistor, resistor, and capacitor to reside on the same chip, the electronic integrated circuit (IC). The advent of the IC allowed for electronic devices to be smaller and cheaper than their discrete counterparts, and most importantly, gave rise to a set of high functionality ICs that discrete components could not emulate. The field of optoelectronics faces a similar shift from discrete to integrated components, where the concepts and potential payoffs are similar to that in the electronics industry, yet the monolithic integration of optoelectronic components cannot be compared so simply to that of electronic devices.

Currently, the majority of optoelectronic components in use in the field are of a discrete nature. That is, each component is designed to perform one specific task. In practice, several components with differing functions are then interconnected, typically via fiber splices, in order to achieve the desired operation. This method has one advantage in that each component is optimized for one specific function, enabling that device to perform its task flawlessly. However, there are several shortcomings involved with this method of system construction. One is the difficulty in coupling light on and off each discrete chip. Advances in the coupling between the semiconductor chip and a fiber optic cable using mode converters is a significant step in reducing the coupling loss, yet it is still a dominant source of optical loss. Another is the expense involved with the discrete packaging of each component. The packaging of optoelectronic devices is the major cost source for the component.

A reduction of the packaging cost can be accomplished by using a method called copackaging. Copackaging involves the integration of discrete optoelectronic chips within the same package. Each component is still fabricated discretely and is designed for one specific task. However, the coupling problem continues to exist, although it is device-to-device not device-to-fiber.

A. Benefits of Photonic Integration

The monolithic integration of the optoelectronic devices on the same chip offers the potential to completely eliminate the device-to-device coupling problem. This can provide a significant reduction in packaging cost and package size as well as increased reliability and reduced power dissipation. Increased reliability results from the elimination of possible mechanical movements amongst the elements of an optical train and the reduced driving currents allowed by the reduction in optical coupling loss between elements. The power dissipation is reduced for this same reason. Furthermore, the potential for high functionality components such as widely tunable transmitters and chip scale wavelength conversion devices will open new avenues for wavelength division multiplexing (WDM) applications such as dynamic provisioning, reconfigurable optical

Manuscript received September 30, 2004; revised February 1, 2005.

E. J. Skogen was with the Department of Electrical and Computer Engineering, University of California, Santa Barbara, CA 93106 USA. He is now with Sandia National Laboratories, Albuquerque, NM 87123 USA (e-mail: ejskoge@sandia.gov).

J. W. Raring, G. B. Morrison, C. S. Wang, V. Lai, M. L. Mašanović, and L. A. Coldren are with the Department of Electrical and Computer Engineering, University of California, Santa Barbara, CA 93106 USA.

Digital Object Identifier 10.1109/JSTQE.2005.846525

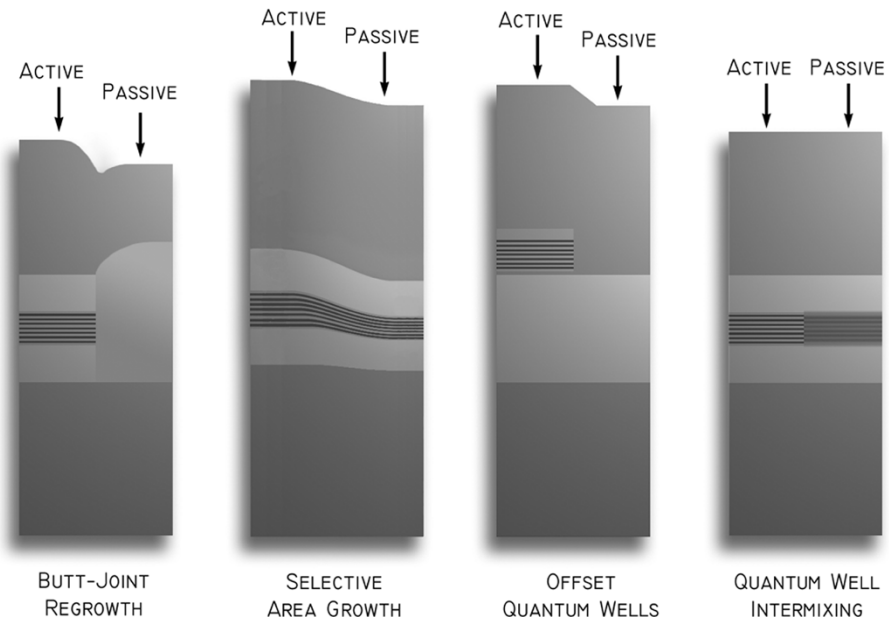

Fig. 1. Various techniques for achieving active and passive sections orthogonal to the growth direction.

add/drop multiplexers (ROADMs), wavelength routing, and optical packet switching.

The potential drawback, however, is the fact that each component must now be fabricated on the same chip, and to do so is technologically difficult. Compromises in device performance or increases in fabrication complexity must be avoided or at least minimized. There are several techniques that have been used in the past, such as the use of offset quantum wells, butt-joint regrowth, selective area growth (SAG) and quantum-well intermixing (QWI) to enable numerous components to be formed on the same chip with a common fabrication process. However, before trying to evaluate the advantages of these approaches, we will review the requirements and present some general guidelines for monolithic integration.

B. Guidelines for Photonic Integration

There are some general requirements that must be fulfilled when monolithically integrating optoelectronic components. First, each integrated component must function as intended. The performance of each integrated device does not necessarily have to meet the performance characteristics of a discrete component, but must still operate in a way that is suitable for the operation of the circuit as a whole. The second requirement states that the operation of one device must not adversely effect the operation of another. This stems from the fact that each component in an integrated circuit, whether it be electronic or optoelectronic, should be isolated from the other components on chip and function as if it were a discrete component. These requirements allow for the design of PICs using optoelectronic building blocks, that is, discrete components that share a common growth and processing platform that can be arranged in such a way that a more complex device or PIC can be obtained.

There are also a few general guidelines to bear in mind when implementing a method for monolithic integration. First, the method used should not be prohibitively time consuming or expensive. This is the key to realizing the cost reduction over existing discrete components. Second, the integration should not lead to device compromises. This is a difficult task due to the fact that each discrete device was designed with a single function in mind and, therefore, the device structure evolved on an individual basis. However, as stated earlier, the integrated component must only perform as intended, it does not necessarily need to match the performance of a discrete device. This affords some flexibility in the design of the device in terms of the device structure, possibly allowing devices with differing functionalities to be fabricated using the same growth and processing platform. Lastly, the process complexity should remain constant as the number of integrated components increases. An additional processing step or the substitution of one step for one that is more complex can increase the manufacturing cost and, in the case of complex processing/growth can lead to yield reduction. A review of some of the integration methods used in the past are given in the following section.

II. Integration Background

There has been some great success in producing simple PICs based on various methods. As illustrated in Fig. 1, such methods include, but are not limited to, a butt-joint regrowth technique [1], selective area growth (SAG) methods [2], the use of an offset quantum-well active region [3], and QWI [4]–[7]. The first, butt-joint regrowth involves the selective removal of waveguide core material followed by the regrowth of an alternate waveguide core using different material composition. This process is inherently difficult involving a precise etch of the original waveguide core, followed by a regrowth of waveguide material with composition and thickness variables.

Another process, the SAG process, involves the selective growth using a mask. In this process, a mask is patterned on the surface of the wafer prior to epitaxial growth. The geometry of the mask has a role in determining the growth near the vicinity

of the mask and can be used to obtain different compositions and thickness across the wafer. This method is useful in fabricating several quantum-well band edges across the wafer, but due to the fact that the thickness is inherently coupled with the band edge in these regions, the optical confinement factor cannot be independently optimized.

The use of offset quantum wells, where the quantum wells are grown above the waveguide and selectively removed in various regions post-growth, has been used with great success in fabricating various integrated structures, sampled-grating distributed Bragg reflector (SG-DBR) lasers with integrated electro-absorption modulators (EAMs) [8], SG-DBR lasers with integrated semiconductor optical amplifiers (SOAs) [9], SG-DBR lasers with integrated Mach-Zehnder modulators [10], optical receivers, and wavelength converters. The drawback of the offset quantum-well method, however, is the limitation of each integrated component to one of two band edges, not allowing for the flexibility necessary for the fabrication of complex, high-performance PICs.

QWI has been used in the past to fabricate a multitude of devices. There are a great deal of techniques that have evolved over the years to accomplish selective intermixing, such as impurity-induced disordering (IID) [11], impurity-free vacancy-enhanced disordering (IFVD) [12], photoabsorption-induced disordering (PAID) [13], and implantation-enhanced interdiffusion [14] to name just a few.

QWI makes use of the metastable nature of the compositional gradient found at heterointerfaces. The natural tendency for materials to interdiffuse is the basis for the intermixing process. The rate at which this process takes place can be enhanced with the introduction of a catalyst. Using a lithographically definable catalyst patterning process, the QWI process can be made selective. This is the process by which virtually all selective QWI is performed, whether it is by the introduction of impurities or by the creation of vacancies.

We have developed a method to further control the QWI process, to achieve any number of quantum-well band edges in the structure. The method is based on the selective removal of the catalyst. This process fits ideally with the suggested guidelines for monolithic integration. It is not prohibitively time consuming or expensive, it is versatile enough that is does not lead to device compromises, and the process complexity remains simple such as not to increase cost or decrease yield. Using this method we have fabricated short-cavity DBR lasers with integrated modulators, widely-tunable multisection SG-DBR lasers with integrated modulators, and chip-scale wavelength converters.

The various QWI techniques all benefit from their relative simplicity; however the flexibility of each is not equal. For example, the IID technique commonly uses dopants as the impurity to accelerate intermixing. This can have a detrimental effect on the electrical nature of the device. Another example involves the method that the technique is applied. For instance, the IFVD and implantation enhanced intermixing techniques can be applied to full device structures or partially grown epitaxial base structures. Asserting that there are several methods by which QWI can be applied, the degree of desired flexibility determines the combination of technique and method used.

III. Method for Integration

As described earlier, a technique that offers great potential for large scale monolithic integration is QWI. A unique QWI processing platform was developed to fulfill the requirements and guidelines for monolithic integration. In the following section, the QWI processing platform is described, the process details given, and the characterization methods and results will be presented.

A. QWI Processing Platform

In this paper, we employ the implant-enhanced interdiffusion technique, which relies on the diffusion of point defects created during an ion implantation. This method has also been shown to have good spatial resolution, and be controllable using anneal time, temperature, and implant dose [14]. Wide ranges of implant energies have been used in this process from the mega-electronvolt range down to tens of kiloelectronvolts. Commonly, these implants are performed on full lasers structures, where the vacancies are created in the upper cladding, and must diffuse long distances before reaching the quantum wells. Although this is not detrimental to the intermixing itself, the device performance may be hindered due to the redistribution of dopants which control the electrical nature of the device. This can be avoided by using a partially grown laser structure with a sacrificial cap layer, which can be subsequently removed, and the upper cladding regrown as described in [15]. While [15] demonstrated such a concept, the process was not optimized, as multiple implant and anneal cycles were required to achieve significant intermixing.

The implant dose can be used to control the extent of intermixing using a single anneal step [7]. Such an effect would allow the formation of several band edges across the wafer, which is useful for the monolithic integration of several optoelectronic components. However, to achieve three band edges, two ion implants are required. With the majority of ion implants being farmed out to specialty houses, the task can be time consuming and expensive. Furthermore, each additional desired band edge requires an additional ion implant, a process that begins to show limitations.

The QWI method developed in this paper uses the selective removal of the vacancies created during the ion implant to effectively halt the intermixing process at the desired level. This method requires a single ion implant followed by a rapid thermal anneal. The extent of intermixing can be controlled using the anneal time. Once the desired band edge is reached, the anneal is stopped and the vacancies are removed in that region. The anneal is then continued until the desired band edge is reached another section, at which point the vacancies are removed in this section. As will be shown, this process can be repeated to achieve any number of band edges across the wafer.

B. QWI Process Details

The epitaxial base structure was designed, not only to perform intermixing experiments, but also to facilitate the fabrication of DBR based lasers. In this respect, the base structure was designed with multiple stop etch layers to allow access to the high

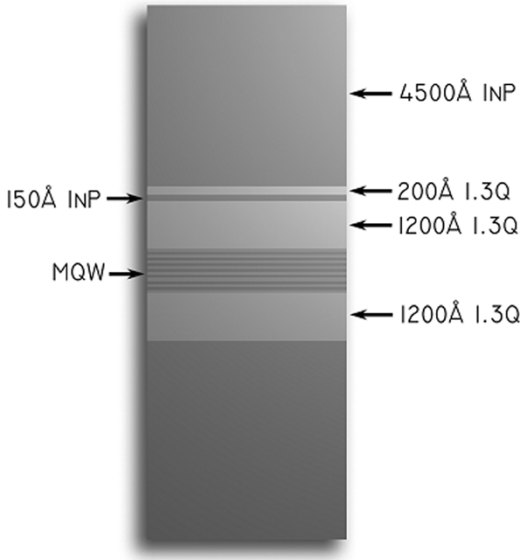

Fig. 2. Epitaxial base structure with both seven or ten quantum-well active region and 4500 Å InP implant buffer layer.

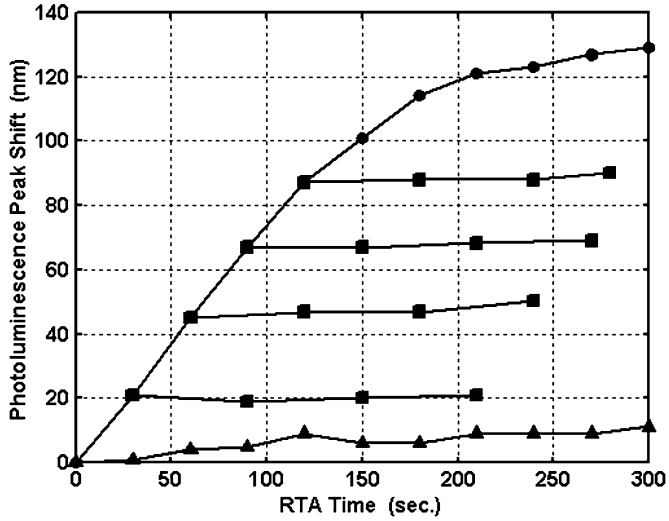

Fig. 3. Peak photoluminescence peak shift as a function of anneal time, showing the initial linear increase in the peak shift and the complete halting of the peak shift for samples for which the implant buffer layer has been etched. Symbols indicate nonimplanted (triangles), implanted (circles), and samples with partial anneal followed by the removal of the implant buffer layer (squares).

field region of the optical mode, which allows for the formation of the high index contrast gratings used in the DBR mirrors.

The base structure, shown in Fig. 2, was grown on a sulfur doped InP wafer using a Thomas Swan horizontal flow rotating-disc metal-organic chemical vapor deposition (MOCVD) reactor. The base structure consists of seven 6.5-nm quantum wells, eight 8.0-nm barriers, sandwiched between 120-nm-thick 1.3Q (InGaAsP $\lambda_g = 1.3$ μm) layers, making up the waveguide layer. The MQW active region was designed to have an emission wavelength of 1560 nm. Above the waveguide, a 15-nm InP stop etch layer, and a 20-nm 1.3Q stop etch layer was followed by a 450-nm InP layer. The top most InP layer, herein called the implant buffer layer, was designed to capture a low energy ion implant, thereby creating vacancies far from the MQW active region.

The base structure was subjected to an ion implant using P^+ at an energy of 100 keV, yielding a range of 90 nm, with a dose of 5E14 cm^{-2}. The substrate temperature during the implant was held at 200 °C to aid in point defect(s) formation [5].

The unique intermixing process was investigated using several samples cleaved from an implanted base structure, as described in the previous section. These samples were annealed at 675 °C for various times ranging from 30 to 300 s at 30-s intervals and the extent of the intermixing was measured by room-temperature photoluminescence. As the point defect(s) front moves through the quantum-well region, the blue-shift increases linearly. Once the point defect(s) front has moved through the quantum-well region the blue-shifting ceases. This saturation of the blue-shift can be observed above 120 nm ,as shown in Fig. 3. After the 30-, 60-, 90-, 120-s anneals, the implant buffer layer was removed from the respective samples. These samples were then subjected to additional anneal cycles. We found that removing the implant buffer layer halted the blue-shift during these anneals. The arrest of the blue-shift is the result of the removal of the abundance of vacancies, necessary for intermixing, along with the implant buffer layer. With this process, it is possible to achieve any number of band edges across the wafer, limited only by the practical number of lithographic process steps [16].

C. QWI Characterization

In order to characterize the intermixed quantum-well material, several experiments have been performed to investigate properties and extract parameters that have implications for PICs. The modal loss of the QWI material is an important parameter in the design of PICs. It is shown in the following section that the waveguide modal loss of QWI material is inversely proportional to the extent of intermixing. Another important aspect of the intermixed quantum wells has to do with the quantum confined Stark effect (QCSE). We have observed a strong exciton peak in the intermixed quantum wells; we also show for the first time the shift of the exciton peak as a function of reverse bias. We show that the QWI material is an ideal candidate for negative chirp parameter electroabsorption modulators by relating the change in absorption to the change in refractive index through the Kramers–Kronig relation.

Using active/passive devices, where the passive region is composed of intermixed quantum wells, the modal loss can be extracted. This is done by plotting the differential efficiency of the active/passive device as a function of passive region length. The passive waveguide loss was measured for several sets of devices each with a different magnitude of photoluminescence shift. The modal loss of the structure is dependent on the configuration of the waveguide; the modal loss is dependent on the optical mode overlap with sources of loss. In this experiment, active/passive buried ridge stripe (BRS) Fabry–Perot (FP) laser devices were tested under pulsed conditions, initially with a passive waveguide length of 2500 μm, cleaved back in steps of 500 μm. The active/passive laser differential efficiency was extracted from laser light versus current measurements, assuming equal reflectivity for the front and back facet. Once

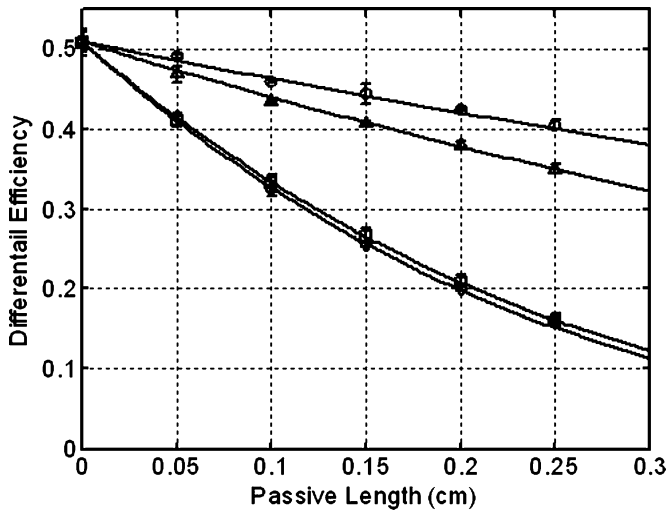

Fig. 4. Differential efficiency of active/passive lasers as a function of passive region length. Symbols indicate data with passive region photoluminescence peaks at 1428 (circles), 1448 (triangles), 1485 (squares), and 1488 nm (diamonds). Solid lines are curve fits used for extracting passive region modal loss, 1.5 (circles), 2.3 (triangles), 6.4 (squares), and 6.7 cm^{-1} (diamonds).

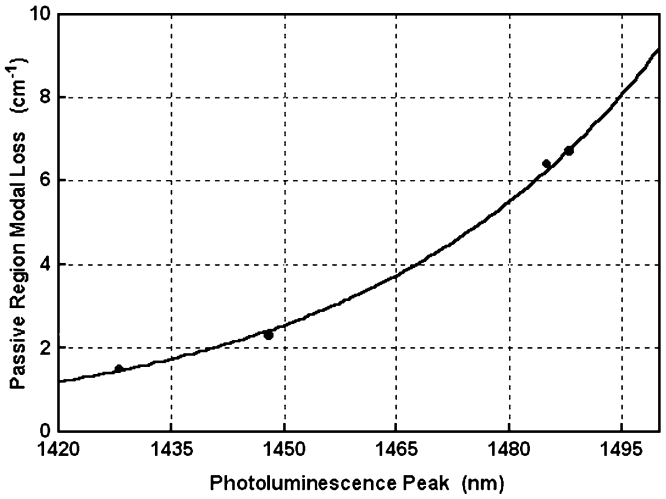

Fig. 5. Passive region modal loss as a function of photoluminescence peak wavelength. Solid line indicates an exponential curve fit, while symbols indicate modal loss data extracted from active/passive lasers.

the all-active BRS, FP lasers have been pulse tested and the laser characteristics extracted, the theoretical active/passive differential efficiency can be plotted as a function of passive region length and the modal loss computed [7]. Fig. 4 shows data and curve fits for several sets of active/passive devices each with a different magnitude of intermixing applied. The passive region loss was plotted as a function of photoluminescence peak wavelength, shown in Fig. 5. An exponential curve provides a good fit with the data. As evident from Fig. 5, the passive region modal loss is strongly dependent on the relative position of the intermixed band edge. The modal loss in the passive region can be minimized by maximizing the magnitude of intermixing.

It was implied that QWI material be used in the SG-DBR mirrors that are used to create the cavity of the widely-tunable SG-DBR laser. Here, intermixed quantum wells are used as the tuning medium, where quantized energy states remain. The

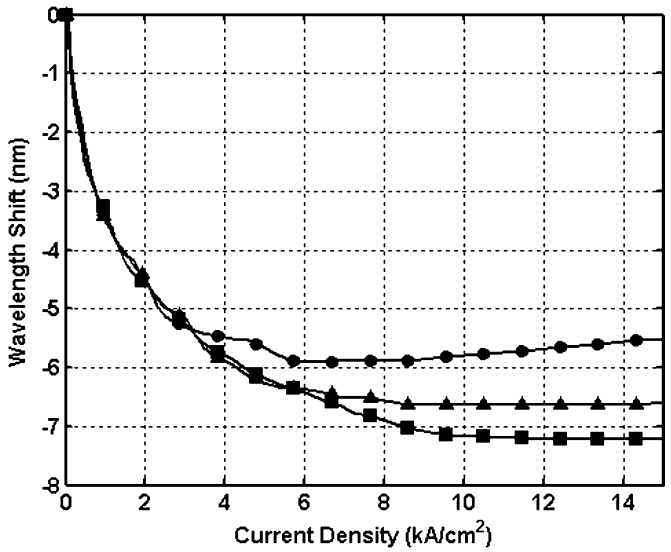

Fig. 6. Experimental tuning curve for samples with differing extents of intermixing. Symbols indicate wavelength shifts of 1475 (circles), 1446 (squares), and 1423 nm (triangles).

presence of quantized energy states allows the mirror to achieve a high tuning efficiency in a small volume of material. This is made possible by a more efficient band filling mechanism resulting from the step-function density of states [17].

The carrier induced refractive index change can be measured by biasing the gain region of an SG-DBR laser below threshold and observing the shift of the transmission notches as a function of injected current. Once the wavelength shift is found as a function of current injection, the wavelength shift can be translated to refractive index shift using the following:

$$\Delta \overline{n}_g = \overline{n}_g \cdot \frac{\Delta \lambda}{\lambda} \tag{1}$$

The variables in (1) indicate the change in modal group refractive index $\Delta \overline{n}_g$ the modal group index in the untuned waveguide $\overline{n}_g$ the change in wavelength $\Delta \lambda$ and the initial wavelength λ. We have previously shown that intermixed quantum wells provide sufficient refractive index shift by carrier injection to cover the full tuning range of the SG-DBR laser [16]. Fig. 6 shows the tuning results for three magnitudes of intermixed quantum wells.

Another simple tool for extracting material band edge absorption is photocurrent spectroscopy. The band edge absorption data can be exploited for design, optimization and performance-analysis of QWI integrated laser-modulators. We also present a detailed characterization of the evolution of band-edge absorption as a function of the degree of QWI in InGaAsP–based quantum wells. The ability to directly measure the QWI band edge, and to use this measurement for analysis of potential transmitter designs, will enable the engineering of superior, highly optimized integrated laser-modulator transmitters for telecommunications applications.

The photodiodes used in our photocurrent spectroscopy experiments are simple devices that can be rapidly fabricated for material characterization. The QWI process, as described earlier, is used to create three band edges on a single wafer—one as-grown and two intermixed. Each of the intermixed regions

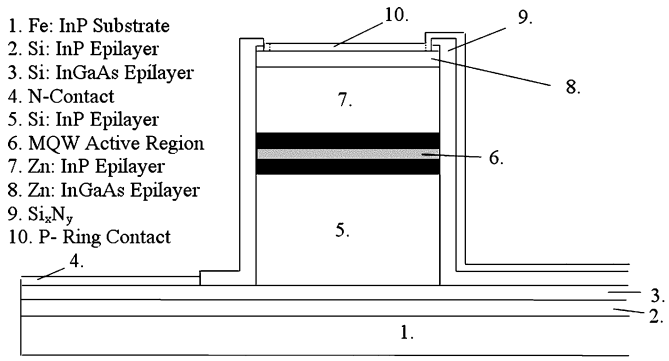

Fig. 7. Cross-sectional side view of a typical photodiode structure.

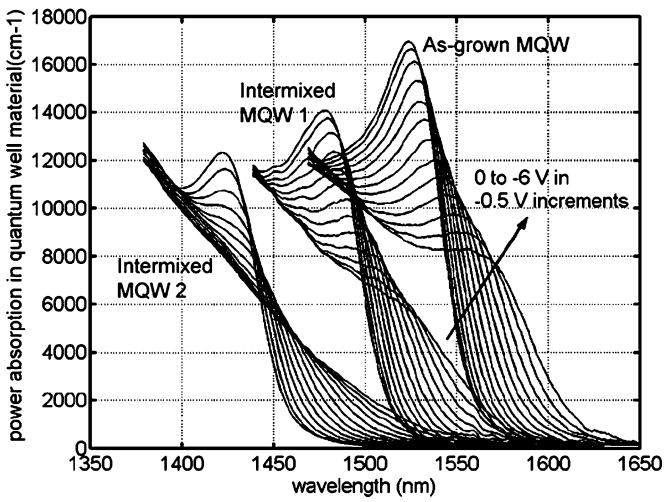

Fig. 8. Power absorption versus wavelength for as-grown and two regions whose quantum wells are intermixed to different levels.

are blue-shifted by a different amount. The three band edges are referred to quantitatively by the wavelengths, in nanometers, of their photoluminescence peaks.

Once each band edge was patterned, circular mesas ranging from 50 to 400 μm in radius were etched. The mesa etch is performed by reactive ion etching through the waveguide and into the n-type substrate. Some devices are grown on semi-insulating substrates, in which case reactive ion etching is used to remove the active region and waveguide, after which a wet etch is used to stop on the n contact InGaAs layer. A 2000-Å layer of SiNx is deposited by plasma-enhanced chemical vapor depostion (PECVD), and circular vias are patterned onto the mesas. Ti/Pt/Au ring contacts were deposited. The contacts are annealed at 410 °C for 30 s. Devices are wire bonded to AlN carriers. Fig. 7 shows a schematic of the simple photodiodes used in photocurrent spectroscopy experiments.

The photodiodes were characterized using a Varian Cary 500 spectrophotometer. A description of the test apparatus is given in [18]. Simple calculations are performed to extract an absorption coefficient from the photocurrent data. Measured incident power is reduced to account for reflection and p-contact absorption, and is converted to units of photons/s. Light incident to the photodiode surface is transverse-electric (TE) polarized. Transverse-magnetic (TM) light is not considered because in-plane laser devices operate with TE polarization. We have determined that back-scattered light is negligible due to scattering and absorption by the Ti/Pt/Au backside contact. The measured photocurrent is converted to electrons/second, and each electron is the result of one absorbed photon. Absorption is then obtained as

$$\alpha = \frac{-\ln\left(\frac{P_{\rm in}-P_{\rm out}}{P_{\rm in}}\right)}{L} \tag{2}$$

where $P_{\rm in}$ is the input power in photons per second, $\rm P_{out}$ is the output photocurrent in photons per second, and L is the total length of quantum-well material through which the light passes.

Fig. 8 shows representative band edge measurements obtained by photocurrent spectroscopy. The epitaxial material used for devices shown in Fig. 7 contained seven 65-Å compressively strained quantum wells and eight 80-Å barriers sandwiched between two 120-nm waveguides. The effect of QWI on the exciton peak is made clear by comparison of the band edges for the photodiodes fabricated from the as-grown MQW material versus those fabricated from intermixed MQW material. The diodes were biased from 0 to −6 V in −0.5 V increments. The band edges shown in Fig. 8 have photoluminescence peaks ($\lambda_{\rm pl}$) at 1537, 1483, and 1429 nm. As the degree of intermixing increases, and the exciton peaks shift to shorter wavelengths, the exciton magnitude decays significantly. With increased intermixing, the exciton peaks also decay more rapidly as a function of applied bias voltage.

The intermixing process results in group V atoms diffusing across the as-grown material boundaries, causing quantum wells to develop rounded edges, and become wider and shallower. This is consistent with the observed behavior of the exciton peaks, which are expected to decay more rapidly with applied voltage when the quantum wells are made shallower by QWI.

Absorption band edge data, such as that shown in Fig. 8, offer great potential for use in optimizing, analyzing, and understanding laser-EAM transmitters and photonic integrated circuits. Later in this paper, predictions of device performance are made using the absorption band edge data. These predictions are compared directly to the performance of actual laser-EAM transmitters. The predictions are shown to be in good agreement with the data.

IV. Integrated Devices

In this section, several of the active component integrated devices will be introduced and discussed. These devices make use of the QWI method discussed in the previous sections. Described herein are the short-cavity DBR laser with integrated electroabsorption modulator, the widely-tunable SG-DBR laser with integrated electroabsorption modulator, and two types of wavelength converter with on-chip widely-tunable continuous-wave laser source. In the past, there have been some analogous examples using one or more of the integration techniques described in Section II. For example, integrated DFB-EAMs have been very successful as commercial sources for moderate reach fiber links. These have used butt-joint [18] and SAG [19].

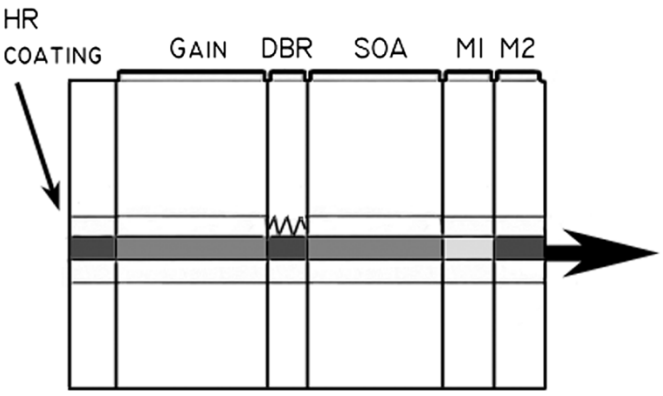

Fig. 9. Side-view schematic of the integrated short cavity DBR laser/EAM device.

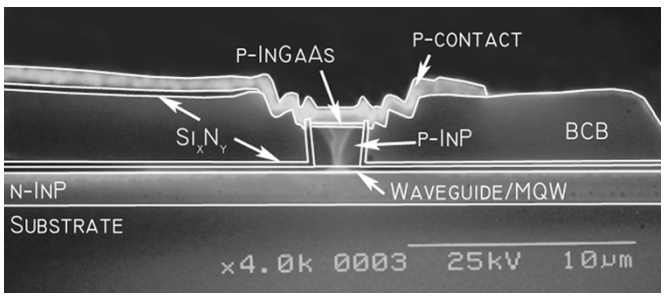

Fig. 10. End-on-view cross-sectional stain etch of the integrated short cavity DBR laser/EAM device.

A. Short Cavity DBR Laser With Integrated EAM

In designing a short-cavity DBR laser, considerations and tradeoffs have to be made regarding the mirror reflectivity, operating current, and temperature rise in the device. First, the cavity requires the length to be sufficiently short such that the mode spacing is wide enough on the DBR stopband to maintain single mode emission. With a high reflectivity (HR) back mirror, the front mirror needs to be optimized for low current operation in the laser at high powers (>10 mW). Here, we chose to design a short-cavity DBR laser with a HR coated back mirror, short gain section (150 μm), and a front DBR mirror (40 μm). The short front mirror is enabled by deep gratings resulting in a high coupling coefficient ($\kappa = 250$ cm^{-1}). This does not adversely affect the laser performance since it lies outside the gain region. A side-view schematic of the designed device is shown in Fig. 9, which, for demonstration, includes an integrated SOA and two-section EAM.

As described previously, a QWI processing platform was applied to optimize the band edge of each integrated device. For example, the gain and SOA sections were left at the as-grown band edge of $\lambda_{\rm pl} = 1540$ nm, the EAM was intermixed to $\lambda_{\rm pl} = 1500$ nm, and the DBRs and passive waveguides were further intermixed to $\lambda_{\rm pl} = 1430$ nm. The amount of intermixing for the EAM section was optimized by photocurrent spectroscopy for optimum extinction performance [20]. Following the top p-cladding regrowth, standard ridge lasers were fabricated [21]. To facilitate high-speed operation of the integrated EAM, benzocyclobutene (BCB) was patterned beneath the EAM contact metal for low pad capacitance. A cross section of the EAM is shown in Fig. 10.

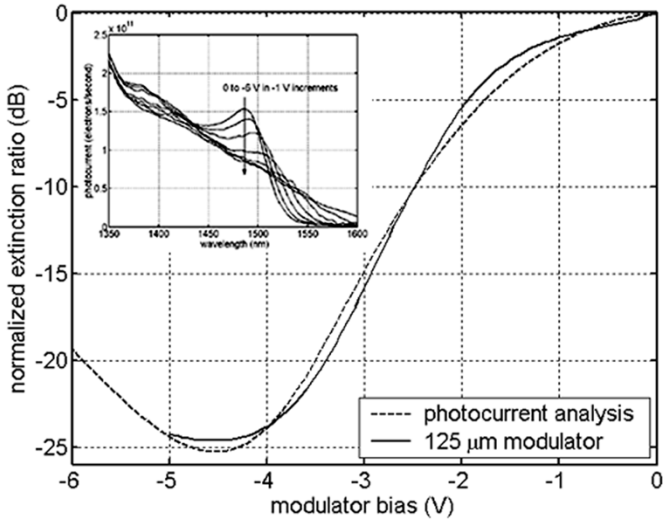

Fig. 11. DC extinction characteristic of a 125-μm integrated EAM computed with a simulation using photocurrent spectroscopy data from identical material. Inset shows photocurrent data used in extinction simulation.

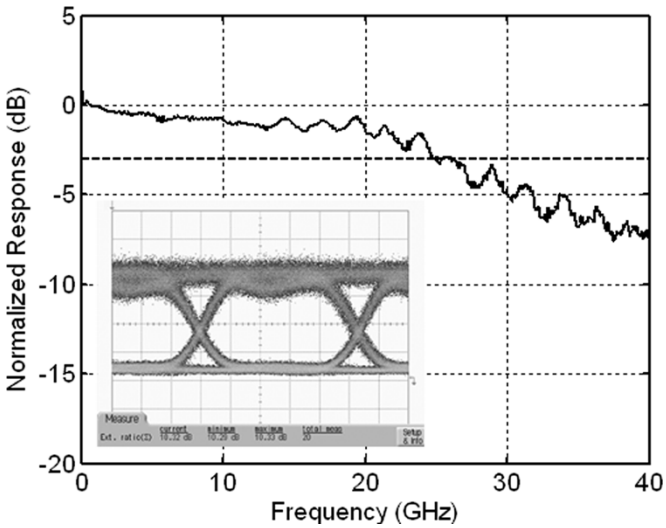

Fig. 12. Bandwidth of a 125-μm integrated EAM demonstrating 25 GHz. Inset is a 10-Gb/s eye diagram showing grater than 10-dB extinction with a 0.6-V swing.

The devices demonstrated good characteristics in terms of output power, efficiency, and side mode suppression ratio (SMSR) [22]. A threshold current of 7 mA was measured, and output powers greater than 10 mW were achieved with a gain section current of 30 mA [22].

The integrated EAM demonstrated greater than 20 dB optical extinction with >13-dB/V extinction efficiency for a 125 μm modulator, as shown in Fig. 11. The inset shows measured photocurrent spectroscopy data for this QWI material. This excellent performance is easily verified using absorption data taken by photocurrent spectroscopy from a similar device. Starting with a spline interpolation of absorption as a function of voltage, simple calculations, which account for optical overlap with the quantum wells and the effective index and length of the waveguide, lead to predicted DC extinction ratios for an EAM. In Fig. 11, the dotted line shows the simulated DC extinction of the 125-μm EAM at 1542 nm. Clearly, the photocurrent measurements allow reasonable estimation of

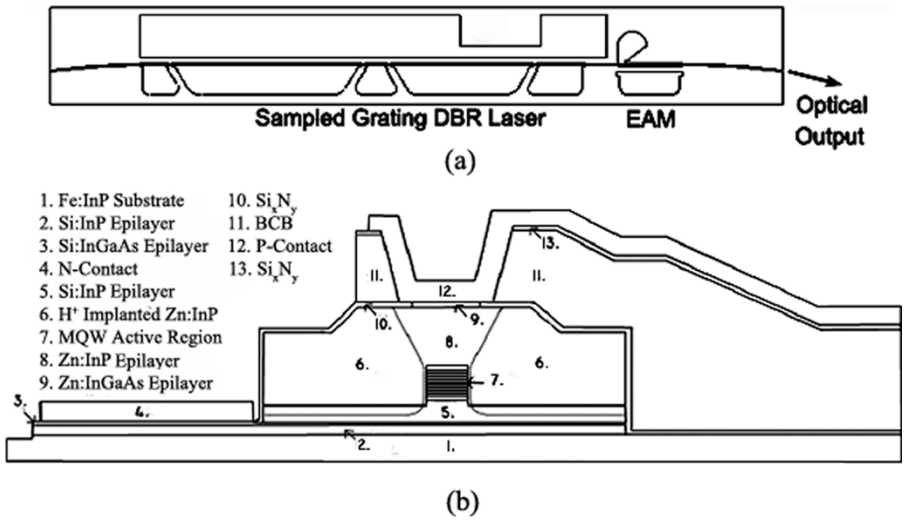

Fig. 13. (a) Top view schematic of the SG-DBR laser/EAM transmitters device architecture. (b) Cross-sectional schematic of modulator sections.

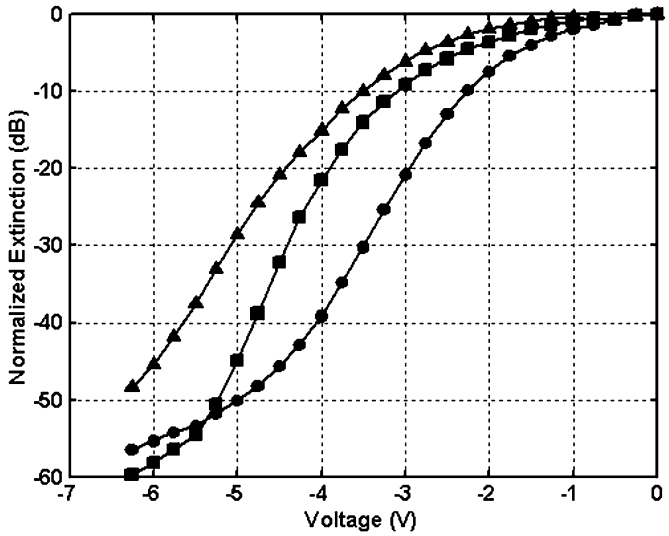

Fig. 14. DC extinction of a 175-μm modulator for wavelengths of 1558 (circles), 1570 (squares), and 1580 nm (triangles).

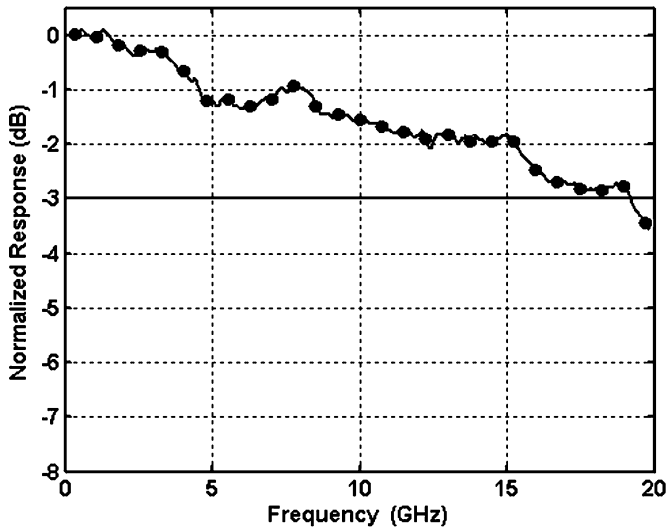

Fig. 15. Electrical to optical frequency response of a 175-μm modulator. The circular markers represent every 30th data point.

modulator performance. These results suggest that photocurrent spectroscopy can be used as a powerful tool for predicting device performance. The 3-dB modulation bandwidth was measured to be 25 GHz, as shown in Fig. 12. The inset shows open eye diagrams were achieved at 10 Gb/s with greater than 10-dB dynamic extinction at a DC bias of -3 V and a 0.6-V swing. From these data, it is clear that the QWI material in modulator sections can be controlled, and is of high optical and electrical quality.

B. SG-DBR Laser With Integrated EAM

Electroabsorption-modulated widely-tunable lasers are candidate sources for optical metropolitan area network applications, as they are compact and potentially low-cost. For efficient 10 Gb/s transmission, it is essential that the EAM demonstrate negative chirp behavior such that the dispersion penalty can be minimized. This characteristic may be achieved by exploiting the quantum confined stark effect (QCSE) with the use quantum wells as the EAM absorption medium.

The simple, robust QWI method described earlier provides an ideal integration platform for the fabrication of widely-tunable laser/QW-EAM transmitters. The ability to define multiple precisely tuned band-edges across a single chip, allows for the independent optimization of the EAM and passive components. The band-edge of the EAM can be blue-shifted such that it maintains a high absorption coefficient, reasonable insertion loss, and without severe degradation to the exciton peak. The passive component band-edge can be further blue-shifted for minimum loss. With the use of QWI, we have for the first time, fabricated a widely-tunable transmitter demonstrating negative chirp characteristics at 10 Gb/s over its entire tuning range.

The transmitter device, shown in Fig. 13, consists of a five section widely tunable SG-DBR laser followed by an EAM. The five sections of the SG-DBR laser are, from rear facet to front facet: 1) backside absorber; 2) rear mirror; 3) phase; 4) gain; and 5) front mirror. The phase and mirror sections function to

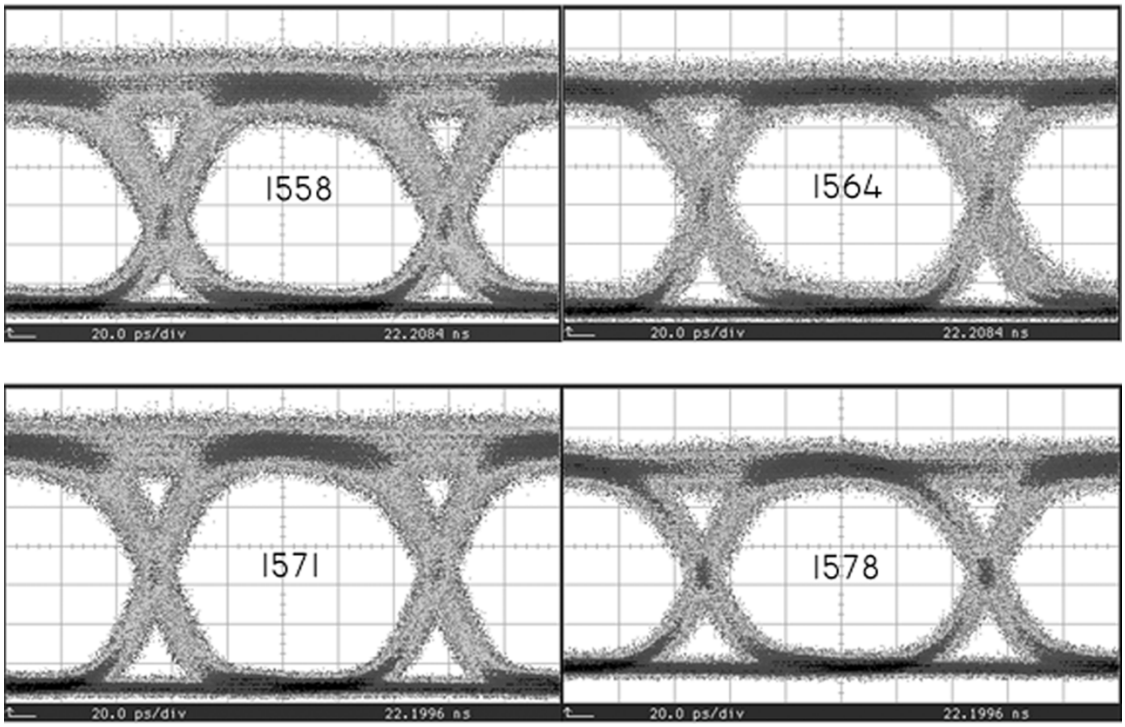

Fig. 16. 10-Gb/s back-to-back eye diagrams from transmitter at wavelengths of 1558, 1564, 1571, and 1578 nm.

tune the wavelength of the laser [7]. The lithographically defined mirrors make the SG-DBR laser ideal for monolithic integration due to the fact that no facets are required for operation. The process of these devices is described elsewhere [23].

The SG-DBR laser demonstrated a threshold current of 13 mA, with an output power of 10 mW at a gain section current of 100 mA. At this operating point, a side mode suppression ratio (SMSR) greater than 35 dB was achieved.

The EAM (175 μm) demonstrated over 40 dB of dc extinction for wavelengths of 1558, 1570, and 1580 nm, with efficiencies greater than 20 dB/V, as shown in Fig. 14. The efficient extinction properties are due to the combination of the centered quantum-well design and the intermixing process that allows for precise placement of the modulator band edge. The 3-dB bandwidth, shown in Fig. 15, of the same modulator was greater than 19 GHz. Eye diagrams, shown in Fig. 16, were taken at wavelengths of 1558, 1564, 1571, and 1578 nm with dc biases ranging from -2.1 to -3.8 V and peak-to-peak voltage swings ranging from 2.2 V to 3.4 V. Greater than 10-dB extinction was achieved at all wavelengths.

Transmission experiments at 10 Gb/s were performed using a nonreturn to zero (NRZ) pseudorandom-bit-sequence (PRBS) of $2^{31}-1$. A booster erbium doped fiber amplifier (EDFA) was used to launch the signal through Corning SMF-28 fiber. A variable optical attenuator was used to regulate the optical power into a optical receiver. Bit-error rate (BER) curves through 25, 50, and 75 km of fiber at a wavelength of 1564 nm are shown in Fig. 17. The EAM was biased at -3.5 V with a 2.0-V peak to peak swing. Error-free operation was achieved through 75 km of fiber with a power penalty of less than 0.5 dB. The shaping of the eye diagrams due to dispersion is clearly seen in the insets of Fig. 17 where the optical eye diagrams are shown after transmission through fiber. The noise performance for transmission through 75 km is limited by the signal attenuation of the fiber and the noise of the oscilloscope optical receiver.

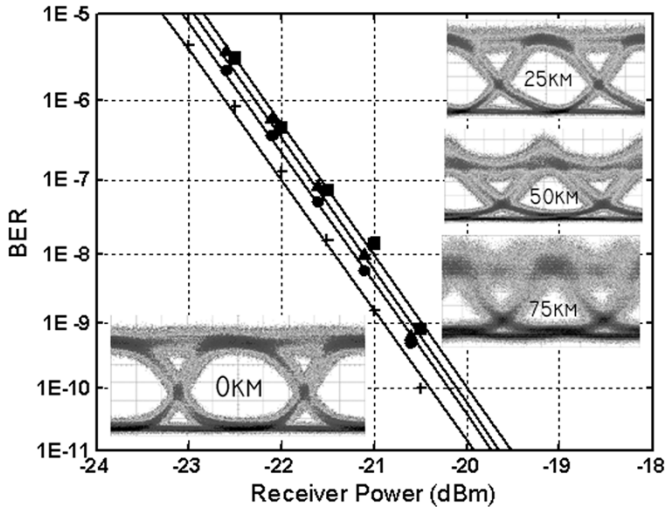

Fig. 17. BER curves and respective eye diagrams for back-to-back (cross), and transmission through 25 (circles), 50 (triangles), and 75 km (squares) of fiber at a wavelength of 1564 nm.

The low dispersion penalty for 10-Gb/s transmission demonstrated in Fig. 17 is indicative of negative chirp characteristics. In order to verify the chirp behavior of the modulator, the large signal chirp parameter was measured on the EAM and analysis was performed on the photocurrent data similar to that shown in Fig. 8 obtained from identical material as the transmitters. With the photocurrent data, differences in absorption between the band edge at 0 V and the band edges at each of the reverse biases are easily obtained. Application of the Kramers–Kronig transform to the absorption data, as described in [24], yields the index change as a function of voltage change.

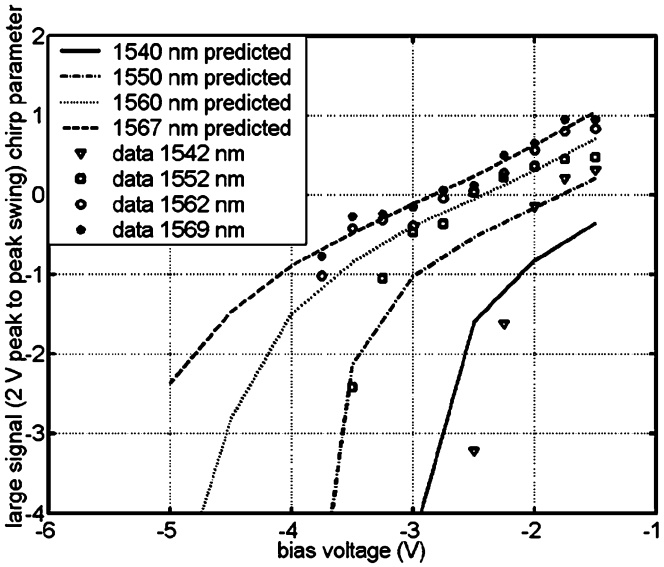

Fig. 18. Data points show measured large signal chirp as a function of bias voltage at 1542, 1552, 1562, and 1569 nm. Lines show predicted chirps at 1540, 1550, 1560, and 1567 nm.

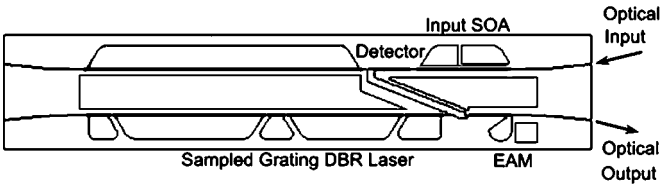

Fig. 19. (a) Top-view schematic of the OEIC wavelength converter architecture with the receiver ridge (upper) and transmitter ridge (lower).

With knowledge of index change as a function of voltage, and absorption change as a function of chirp, the large signal chirp can be calculated [25]. Fig. 18 compares the large signal chirp, as calculated from photocurrent spectroscopy, at wavelengths of 1540, 1550, 1560, and 1567 nm, with the chirp measured in the buried-ridge modulators at wavelengths of 1542, 1552, 1562, and 1569 nm. The 2-nm difference in wavelengths has been included to account for the fact that the photocurrent diodes were intermixed to $\lambda_{\rm pl} \approx 1508$ nm, whereas the transmitter EAMs were intermixed to $\lambda_{\rm pl} \approx 1510$ nm. Chirp measurements were made on the transmitters using Agilent's Time Resolved Chirp (TRC) software coupled with the required Agilent 86 146B optical spectrum analyzer. The measured dynamic chirp parameter, and the chirp parameter that is calculated directly from photocurrent spectroscopy, are in reasonable agreement. Clearly, the wavelength-agile negative chirp performance of the transmitters can be directly attributed to the band edge that is found in the QWI material from which the EAMs are fabricated. The QWI process that was used to shift the band edge in the EAM section of the device did not significantly detract from the exciton confinement. We, therefore, assert that QWI is a promising fabrication platform for implementation of high performance, widely tunable, negative chirp, 10-Gb/s laser-EAM transmitter devices.

C. Wavelength Converters

The integration of an optical receiver with a widely-tunable transmitter can provide wavelength conversion functionality, making applications such as wavelength routing and ROADMs possible. Using the same QWI integration platform as the laser/EAM transmitter, wavelength converters were fabricated. The device architecture, shown in Fig. 19, consists of two adjacent parallel buried ridges, with one ridge operating as an optical receiver and the adjacent ridge operating as an optical transmitter. The receiving ridge consists of a semiconductor optical amplifier (SOA) and a photodetector for the amplification and detection of the input optical signal, respectively. The adjacent ridge consists of the same SG-DBR laser/EAM architecture as the transmitter.

In this photocurrent-driven wavelength converter, the detector and EAM electrodes are joined by a coplanar strip (CPS) interconnect. In this configuration, the photocurrent generated in the detector by the input optical signal will pass through a termination load, resulting in the small signal voltage swing across the EAM identical to that of the input data sequence. The EAM functions to write the data on the continuous wave output of the SG-DBR laser operating at any wavelength within the tuning band hence wavelength conversion is achieved.

The optical to optical frequency response of a wavelength converter with a 225 μm photodetector interconnected to a 175-μm modulator demonstrated a 3-dB bandwidth of over 12 GHz with a 25-Ω termination. To demonstrate 10-Gb/s operation, eye diagrams were taken for wavelength conversion from 1550 nm to 1555, 1562, 1569, and 1575 nm, as shown in Fig. 20. Although error-free operation was achieved, insufficient extinction ($\sim$2 dB) resulted in high power penalties ($\sim$8 dB). The insufficient extinction was a result of receiver inefficiencies such as inadequate photocurrent generation and saturation effects. These aspects of the device are being addressed with higher saturation power SOAs and photodetectors.

For example, higher extinction ratios and lower power penalties were observed in other wavelength-converter experiments, which used an offset quantum-well integration platform and higher saturation power SOAs and photodetectors in the receiver stage. One version used the integration of a slightly higher saturation power SOA-PIN receiver with an EAM-modulated SG-DBR to demonstrate 10-dB extinction and 2.5-dB power penalties back-to-back at 10 Gb/s over a wide tuning range [26]. A second wired a separate high-power SOA-PIN receiver with a MZ-modulated SG-DBR to demonstrate 12 dB of extinction, capable of positive and negative chirp, and 1.2 dB of power penalty at 10 Gb/s over 75 km of Corning SMF-28 fiber the 35-nm tuning range [27].

The QWI platform has also been used to fabricate monolithic tunable all-optical wavelength converters (TAO-WCs). These devices are among the most elaborate photonic integrated circuits fabricated to date in terms of the number of functional elements integrated into a single device. The devices, illustrated in Fig. 21, consist of a widely-tunable SG-DBR laser monolithically integrated with a semiconductor optical amplifier-based Mach-Zehnder Interferometer (MZI) wavelength converter. A schematic of the device is shown in Fig. 21.

The device works on the principle of optically induced index change in a SOA due to carrier density modulation. The cross phase modulation that results from the index change is then used

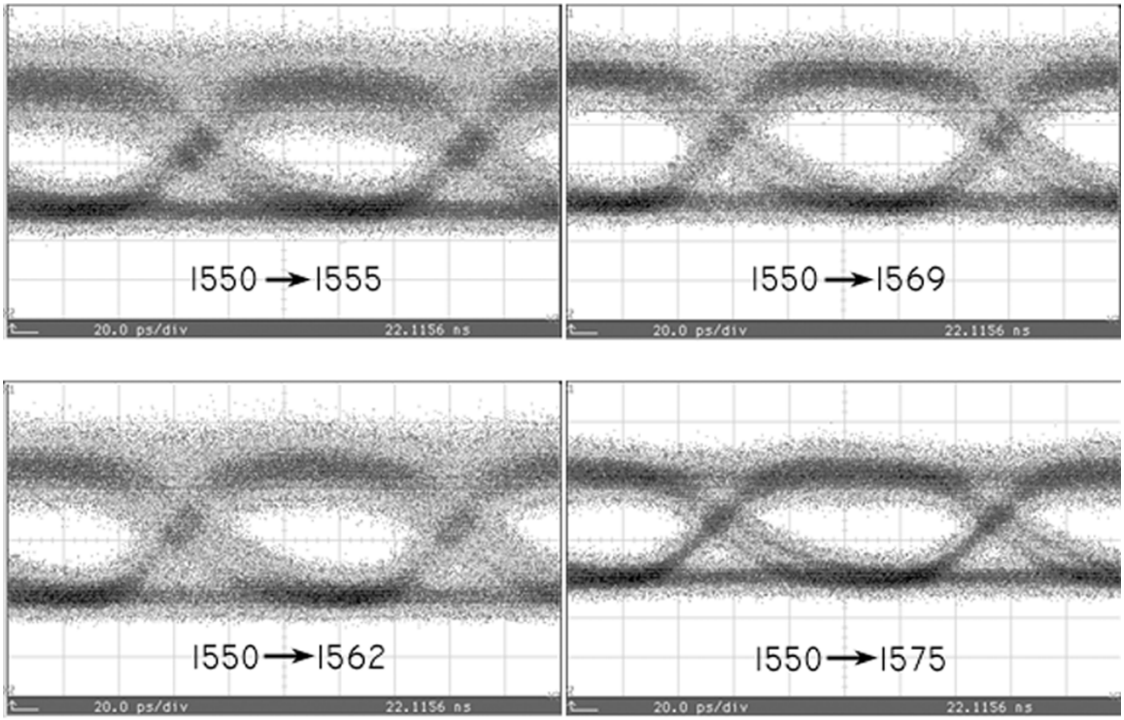

Fig. 20. The 10-Gb/s eye diagrams for wavelength conversion from 1550 to 1555 nm, 1562, 1569, and 1575 nm.

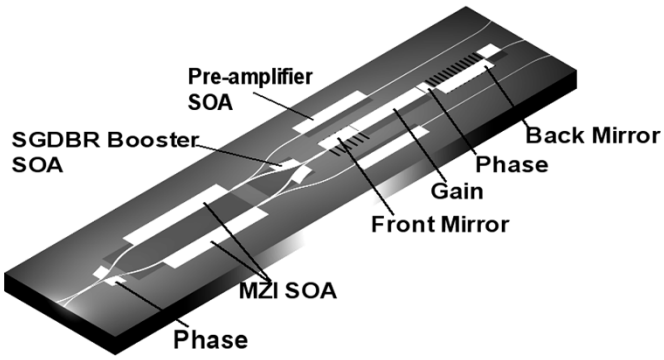

Fig. 21. QWI TAO-WC.

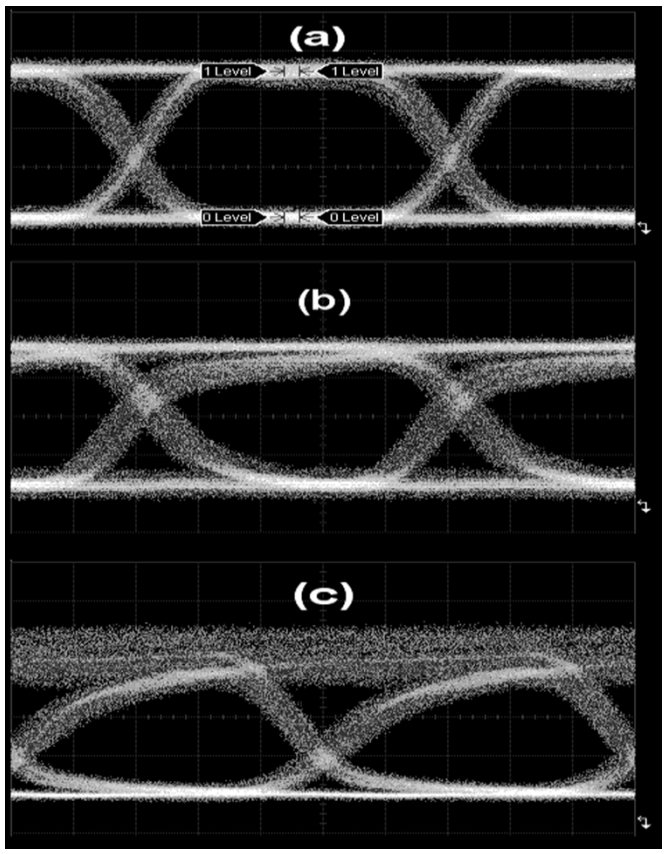

Fig. 22. (a) Input data to the device at 10 Gb/s. Wavelength converted data in the (b) noninverting and (c) inverting mode of operation.

to gate the SGDBR output using a MZI [29]–[31]. Fig. 22 shows the eye diagrams of the wavelength converted data in both the inverted and noninverted mode of operation. The current devices are capable of converting from any input wavelength to any output wavelength across the entire C-band (over 30-nm tuning range).

To maximize the speed of operation of this wavelength converter, it is important to reduce the carrier lifetimes in the SOA's in the MZI. This lifetime governed by the saturation properties and the material parameters of the SOA, i.e., carrier concentration, differential gain, the optical confinement factor, as well as the optical power in the SOA and the length of the SOA through the effects of high-pass filtering. Our earlier work on TAO-WCs [29]–[31] employed an offset quantum-well platform to fabricate the device, with inherent modal confinement factor of around 6%, which limited the minimum carrier lifetime attainable [30]. The QWI-based platform allows us to overcome this limitation and further reduce the carrier lifetime by using centered quantum wells with a significantly increased the confinement factor of over 9% in our current design. The value of the confinement factor can be tailored by the choice of the number of quantum wells.

Along with the benefit it offers, the increase in the confinement factor also creates additional challenges. The SOA saturation power reduction results in the enhancement of pattern dependence in the preamplifier SOAs. Optimizing the preamplifier designs in the QWI platform to get linear, high power amplification is a work in progress.

V. Conclusion

The development of photonic integrated circuits is key to the advancement of the fiber optic communications field. The introduction of new highly functional devices and systems must stem from innovation. This manuscript focused on the ability to monolithically integrate optoelectronic components through a novel QWI processing platform. Such a processing method allows for the optimization of the quantum well band edge for each integrated component. This allows designers to break many, but not all design tradeoffs in pursuit of high functionality photonic integrated circuits.

A QWI process has been developed which allows for the formation of multiple quantum-well band edges across the wafer. The use of an implant buffer layer not only prevented the implanted ions from damaging the quantum wells, but facilitated the development of a cyclic etch and anneal process enabling the strategic placement of the quantum well band edge for integrated devices.

There are an almost limitless number of applications for QWI in the development of high functionality photonic integrated circuits. The capability to monolithically integrate a number of devices each with a unique quantum-well band edge is an advancement that must be exploited. Although device improvement is certainly on the forefront of the QWI horizon, the real driving force for QWI applies to those devices and integration schemes that will be made possible in the future, and have yet to come.

References

[1] J. Binsma, P. Thijs, T. VanDongen, E. Jansen, A. Staring, G. VanDenHoven, and L. Tiemeijer, "Characterization of butt-joint InGaAsP waveguides and their application to 1310 nm DBR-Type MQW ganin-clamped semiconductor optical amplifiers," *IEICE Trans. Electron.*, vol. E80-C, pp. 675–681, 1997.

[2] M. Aoki, M. Suzuki, H. Sano, T. Kawano, T. Ido, T. Taniwatari, K. Uomi, and A. Takai, "InGaAs/InGaAsP MQW electroabsorption modulator integrated with a DFB laser fabricated by band-gap energy control selective area MOCVD," *IEEE J Quantum Electron.*, vol. 29, no. 6, pp. 2088–2096, Jun. 1993.

[3] B. Mason, G. Fish, S. DenBaars, and L. Coldren, "Ridge waveguide sampled grating DBR lasers with 22-nm quasi-continuous tuning range," *IEEE Photon. Technol. Lett.*, vol. 10, no. 9, pp. 1211–1213, Sep. 1998.

[4] S. McDougall, O. Kowalski, C. Hamilton, F. Camacho, B. Qiu, M. Ke, R. De La Rue, A. Bryce, and J. Marsh, "Monolithic integration via a universal damage enhanced quantum-well intermixing technique," *IEEE J. Sel. Topics Quantum Electron.*, vol. 4, no. 4, pp. 636–646, Jul./Aug. 1998.

[5] S. Charbonneau, E. Kotels, P. Poole, J. He, G. Aers, J. Haysom, M. Buchanan, Y. Feng, A. Delage, F. Yang, M. Davies, R. Goldberg, P. Piva, and I. Mitchell, "Photonic integrated circuits fabricated using ion implantation," *IEEE J. Sel. Topics Quantum Electron.*, vol. 4, no. 4, pp. 772–793, Jul./Aug. 1998.

[6] D. Hofstetter, B. Maisenholder, and H. Zappe, "Quantum-well intermixing for fabrication of lasers and photonic integrated circuits," *IEEE J. Sel. Topics Quantum Electron.*, vol. 4, no. 4, pp. 794–802, Jul./Aug. 1998.

[7] E. Skogen, J. Barton, S. DenBaars, and L. Coldren, "A quantum-well-intermixing process for wavelength-agile photonic integrated circuits," *IEEE J. Sel. Topics in Quantum Electron.*, vol. 8, no. 4, pp. 863–869, Jul./Aug. 2002.

[8] B. Mason, G. Fish, S. DenBaars, and L. Coldren, "Widely tunable sampled grating DBR lasers with integrated electroabsorption modulator," *IEEE Photon. Technol. Lett.*, vol. 11, no. 6, pp. 638–640, Jun. 1999.

[9] B. Mason, J. Barton, G. Fish, and L. Coldren, "Design of sampled grating DBR lasers with integrated semiconductor optical amplifiers," *IEEE Photon. Technol. Lett.*, vol. 12, no. 7, pp. 762–764, Jul. 2000.

[10] J. Barton, M. Mašanovic, E. Skogen, and L. Coldren, "Widely-tunable high-speed transmitters using integrated SGDBRs and Mach-Zehnder modulators," *IEEE J. Sel. Topics Quantum Electron.*, vol. 9, no. 5, pp. 1113–1117, Sep./Oct. 2003.

[11] D. Deppe and N. Holonyak, Jr., "Atom diffusion and impurity-induced layer disordering in quantum well III-V semiconductor heterostructures," *J. Appl. Phys.*, vol. 64, pp. 93–113, 1988.

[12] S. K. Si, D. H. Yeo, K. H. Yoon, and S. J. Kim, "Area selectivity of InGaAsP-InP multiquantum-well intermixing by impurity-free vacancy diffusion," *IEEE J. Sel. Topics Quantum Electron.*, vol. 4, no. 4, pp. 619–623, Jul./Aug. 1998.

[13] B. Qui, A. Bryce, R. De La Rue, and J. Marsh, "Monolithic integration in InGaAs-InGaAsP multiquantum-well structure using laser processing," *IEEE Photon. Technol. Lett.*, vol. 10, no. 6, pp. 769–771, Jun. 1998.

[14] S. Charbonneau, P. Poole, Y. Feng, G. Aers, M. Dion, M. Davies, R. Goldberg, and I. Mitchell, "Band-gap tuning of InGaAs/InGaAsP/InP laser using high energy ion implantation," *Appl. Phys. Lett.*, vol. 67, pp. 2954–2956, 1995.

[15] M. Paquette, J. Beauvais, J. Beerens, P. Poole, S. Charbonneau, C. Miner, and C. Blaauw, "Blueshifting of InGaAsP/InP laser diodes by low-energy ion implantation," *Appl. Phys. Lett.*, vol. 71, pp. 3749–3751, 1997.

[16] E. Skogen, J. Raring, J. Barton, S. DenBaars, and L. Coldren, "Post-growth control of the quantum-well band edge for the monolithic integration of widely-tunable lasers and electroabsorption modulators," *IEEE J. Sel. Topics Quantum Electron.*, vol. 9, no. 5, pp. 1183–1190, Sep./Oct. 2003.

[17] J. Shim, M. Yamaguchi, P. Delansay, and M. Kitamura, "Refractive index and loss changes produced by current injection in InGaAs(P)-InGaAsP Multiple Quantum-Well (MQW) waveguides," *IEEE J. Sel. Topics Quantum Electron.*, vol. 1, no. 2, pp. 408–415, Jun. 1995.

[18] H. Takeuchi, K. Tsuzki, K. Sato, M. Yamamoto, Y. Itaya, A. Sano, M. Yoneyama, and T. Otsuji, "Very high-speed light-source module up to 40 Gb/s containing an MQW electroabsorption modulator integrated with a DFB laser," *IEEE J. Sel. Topics Quantum Electron.*, vol. 3, pp. 336–343, Apr. 1997.

[19] H. Haisch, W. Baumert, C. Hache, E. Kühn, M. Klenk, K. Satzke, M. Schilling, J. Weber, and E. Zielinski, "10 Gbit/s standard fiber TDM transmission at 1.55 μm with low chirp monolithically integrated MQW electroabsorption modulator/DFB-laser realized by selective area MOVPE," in *Proc. 20th Eur. Conf. Optical Communication*, 1994, pp. 801–804.

[20] G. Morrison, E. Skogen, C. Wang, J. Raring, Y. Chang, M. Sysak, and L. Coldren, "Photocurrent spectroscopy for quantum-well intermixed photonic integrated circuit design," *IEEE Photon. Technol. Lett*, submitted for publication.

[21] E. Skogen, C. Wang, J. Raring, G. Morrison, and L. Coldren, "Small-footprint, high-efficiency, integrated transmitters for high-speed optical interconnect applications," presented at the *Proc. Integrated Photonics Research Conf.*, San Francisco, CA, June 30–July 2 2004, paper no. IThD2.

[22] C. Wang, E. Skogen, J. Raring, G. Morrison, and L. Coldren, "Short-cavity 1.55 μm DBR lasers integrated with high-speed EAM modulators," in *Proc. 19th Annu. IEEE Int. Semiconductor Laser Conf.*, Matsueshi, Simane, Japan, 2004.

[23] J. Raring, E. Skogen, L. Johansson, M. Sysak, J. Barton, M. Mašanović, and L. Coldren, "Demonstration of widely-tunable single-chip 10 GB/s laser-modulators using multiple-bandgap InGaAsP quantum-well intermixing," *IEEE Photon. Technol. Lett.*, vol. 16, no. 7, pp. 1613–1615, Jul. 2004.

[24] C. Henery, R. Logan, and K. Bertness, "Spectral dependence of the change in refractive index due to carrier injection in GaAs lasers," *J. Appl. Phys.*, vol. 52, no. 7, pp. 4457–4461, 1981.

[25] J. Fells, I. White, M. Gibbon, R. Penty, G. Thompson, A. Wright, R. Saunders, and C. Armistead, "Controlling the chirp in electroabsorption modulators under digital modulation," *Electron. Lett.*, vol. 30, no. 24, pp. 2066–2067, 1994.

[26] M. Sysak, J. Barton, J. Raring, M. Dummer, A. Tauke-Pedretti, D. Blumenthal, and L. Coldren, "10 Gb/s photocurrent driven, widely tunable electroabsorption modulator based wavelength converter," in *Proc. Optical Fiber Conf.*, 2005, submitted for publication.

[27] J. Barton, A. Tauke-Pedretti, M. Dummer, M. Sysak, M. Masanovic, J. Raring, E. Skogen, and L. Coldren, "10 Gbit/s wavelength conversion using a widely tunable series push-pull photocurrent-driven transmitter," *IEEE Photon. Technol. Lett.*, submitted for publication.
[28] V. Lal, M. Mašanović, E. Skogen, J. Summers, L. Coldren, and D. Blumenthal, "Widely tunable all-optical wavelength converter based on monolithic integration of a SGDBR and Mach-Zehnder interferometer using quantum well intermixing," IEEE Photon. Technol. Lett., submitted for publication.
[29] M. Mašanović, V. Lal, J. Barton, E. Skogen, L. Coldren, and D. Blumenthal, "Monolithically integrated Mach-Zehnder interferometer wavelength converter and widely-tunable laser in InP," *IEEE Photon. Technol. Lett.*, vol. 15, pp. 1117–1119, 2003, submitted for publication.
[30] M. L. Mašanović, V. Lal, J. A. Summers, J. S. Barton, E. J. Skogen, L. A. Coldren, and D. J. Blumenthal, "Design and performance of a monolithically-integrated widely-tunable all-optical wavelength converter with independent phase control," *IEEE Photonics Technology Letters*, vol. 16, no. 10, pp. 2299–2301, Oct. 2004.
[31] M. Mašanović, V. Lal, J. A. Summers, J. Barton, E. Skogen, L. Rau, L. Coldren, and D. Blumenthal, "Widely-tunable monolithically-integrated all-optical wavelength converters in InP," *IEEE J. Lightw. Technol.*, submitted for publication.

Erik J. Skogen received the B.S. degree from Iowa State University, Ames, in 1997, and the M.S. and Ph.D. degrees from the University of California at Santa Barbara (UCSB) in 1999 and 2003, respectively. His dissertation work involved the development and application of quantum-well intermixing techniques to widely-tunable sampled-grating DBR lasers and photonic integrated circuits (PICs).

He was a Postdoctoral Researcher with UCSB from 2003 to 2005, where he investigated advanced PICs. In 2005, he joined Sandia National Laboratories, Albuquerque, NM, as a Senior Member of the Technical Staff. His current research interests include monolithic integration techniques for next-generation PICs.

James W. Raring (S'02) was born in New Jersey in 1978. He received the B.S. degree from the Materials Engineering Department, California Polytechnic State University, San Luis Obispo, in 2001. He is currently working toward the Ph.D. degree in materials science from the University of California at Santa Barbara.

His research interests include the monolithic integration of widely tunable diode lasers into high-speed photonic integrated circuits with the use of quantum-well intermixing.

Gordon B. Morrison was born in Portsmouth, U.K., in 1973. He obtained his B.A.Sc. degree in engineering physics from Simon Fraser University, Vancouver, BC, Canada, in 1997, and the Ph.D. from the Department of Engineering Physics, McMaster University, Hamilton, ON, Canada, in 2002.

He is currently a Postdoctoral Researcher with the Department of Electrical and Computer Engineering, University of California at Santa Barbara (UCSB). His research interests at McMaster University included modeling the spectra of semiconductor lasers, fitting models to spectra for parameter extraction, and modeling gain in quantum well lasers. At UCSB, he has been involved in the design and characterization of integrated laser/modulator transmitters that are fabricated using quantum-well intermixing.

Chad S. Wang (S'99) was born in Racine, WI, in 1979. He received the B.S. degree from The University of Texas at Austin, in 2001, and the M.S. degree in 2002 from the University of California, Santa Barbara, where he is currently working toward the Ph.D. degree in electrical and computer engineering.

His research interests include the development of integrated laser-modulators for optical interconnect applications. He is also involved in molecular beam epitaxy growth of III-V semiconductor vertical cavity lasers and avalanche photodetectors.

Vikrant Lal received the B.S. degree in electrical engineering from the Indian Institute of Technology, Delhi, India, 1999, and the M.S. degree majoring in communications engineering in electrical and computer engineering from the University of Maryland, College Park, in 2001. He is currently working toward the Ph.D. degree student in electrical and computer engineering at the University of California at Santa Barbara.

His research interests include photonic integrated circuits and all-optical switching.

Milan L. Mašanović graduated as a valedictorian from the School of Electrical Engineering, University of Belgrade, Belgrade, Yugoslavia, in 1998. He received the M.S. degree and Ph.D. degree in electrical engineering from the Department of Electrical and Computer Engineering, University of California at Santa Barbara in 2000 and 2004, respectively.

His research interests include InP photonic integrated circuits with emphasis on integrated tunable wavelength converters and their applications in novel all-optical networks.

Dr. Mašanović is the winner of numerous awards and fellowships including the 2004 IEEE-Laser and Electro-Optics Society Graduate Student Fellowship Award and the 2003 Best Student Paper Award at the Indium Phosphide and Related Materials Conference.

Larry A. Coldren (S'67–M'72–SM'77–F'82) received the Ph.D. degree in electrical engineering from Stanford University, Stanford, CA, in 1972.

After 13 years in the research area at Bell Laboratories, he was appointed Professor of Electrical and Computer Engineering at the University of California at Santa Barbara (UCSB) in 1984. In 1986, he assumed a joint appointment with Materials and ECE, and in 2000, the Fred Kavli Chair in Optoelectronics and Sensors. He is also Chairman and Chief Technology Officer of Agility Communications, Inc. At UCSB, his efforts have included work on novel guided-wave and vertical-cavity modulators and lasers, as well as the underlying materials growth and fabrication technology. He is now investigating the integration of various optoelectronic devices, including optical amplifiers and modulators, tunable lasers, wavelength-converters, and surface-emitting lasers. He has authored or coauthored over 500 papers, five book chapters, one textbook, and has been issued 32 patents.

Dr. Coldren is a past Vice-President of the IEEE Lasers and Electro-Optics Society and a Fellow of the Optical Society of America.

Multiple-band-edge quantum-well intermixing in the InGaAs/InGaAsP/InGaP material system

Erik J. Skogen[a] and Larry A. Coldren
Electrical and Computer Engineering Department, University of California, Santa Barbara, California 93106

James W. Raring and Steven P. DenBaars
Materials Department, University of California, Santa Barbara, California 93106

(Received 6 December 2004; accepted 4 May 2005; published online 9 June 2005)

The development of photonic integrated circuits lattice matched to GaAs are desirable for the manufacture of high-power, high-efficiency optical components. In this letter we investigate and describe a process technique based on quantum-well intermixing to achieve multiple band edges in the Al-free 980 nm InGaAs/InGaAsP/InGaP material system. © *2005 American Institute of Physics*. [DOI: 10.1063/1.1946903]

As the InP- and GaAs-based optoelectronics field matures, it is desirable to monolithically integrate multiple components onto a single chip. These photonic integrated circuits (PICs) will allow for reduced cost, improved performance, and increased functionality over discrete components. The realization of an optimally performing PIC is the primary challenge, as each integrated component requires differing materials and architectural features based on its specific function, and to do so is technologically difficult.

Selective area quantum-well intermixing (QWI) has been shown to be a promising method of tailoring the quantum-well band edge in optoelectronic devices. There have been reports of complex PICs fabricated using selective QWI in the InP material system.[1–3]

This work focuses on QWI in the GaAs material system. In the past, many 980 nm components made use of InGaAs/GaAs/AlGaAs-based structures, and there have been many reports of achieving QWI in such active regions.[3,4] However, InGaAs/InGaAsP/InGaP-based devices offer numerous advantages over the InGaAs/GaAs/AlGaAs based devices.[5,6] For instance, the InGaAsP material has a direct band gap throughout its compositional range, donor related *DX* centers are not as significant as in AlGaAs, and the reliability may also be improved due to the absence of dark line defects and catastrophic mirror facet damage due to oxidation. Fundamental improvements in the carrier confinement in the quantum wells have been observed in InGaAs/InGaAsP active regions over InGaAs/GaAs active regions, leading to increased differential efficiency and improved thermal characteristics of lasers.[6] The InGaAs/InGaAsP/InGaP-based devices are also more desirable from an integration standpoint as the selective wet chemical etching of InGaP over GaAs allows for simple process techniques. Furthermore, exposed surfaces utilizing materials with minimal tendency for oxidation are well suited for epitaxial regrowths.

It is shown that multiple-quantum-well (MQW) active regions based on an InGaAs/InGaAsP constant-*x* design are more stable at elevated temperatures than those comprised of an InGaAs/GaAs constant-*y* design when subjected to impurity-free vacancy diffusion (IFVD) using plasma-enhanced chemical vapor deposited SiO_xN_y. This suggests that the intermixing employing the IFVD method using a dielectric cap is occurring largely on the group-III sublattice. When InGaAs/InGaAsP MQW active regions are subjected to ion-implantation-enhanced QWI, we show that intermixing occurs, suggesting that point defects generated during the implant are capable of interdiffusing on the group-V sublattice. It is also shown that multiple band edges across the wafer can be achieved using a cyclic etch and anneal process, a result similar to that previously reported in InP material system.[1]

In this experiment, five epitaxial base structures were grown each with different combinations of MQW and implant buffer layer, as shown in Fig. 1. The base structures were grown using a Thomas Swan Scientific Equipment Ltd. horizontal-flow rotating-disk metalorganic chemical vapor deposition (MOCVD) system on (100) GaAs misoriented 2° towards ⟨111⟩A. The MQW regions were composed of 8- or 9-nm InGaAs quantum wells (In=0.185) and either GaAs or 0.76*Q* (InGaAsP λ_g=0.76 μm) tensile strained 0.15% barriers 10 or 11 nm thick. In the case of the InGaAs/InGaAsP MQW the structure is a constant-*x* design. That is, the same

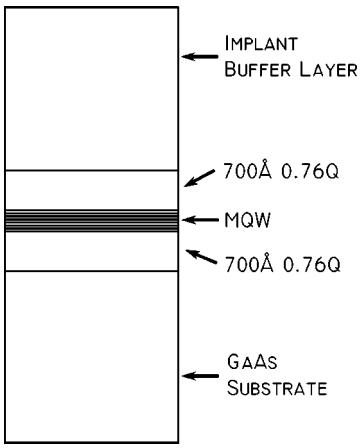

FIG. 1. Epitaxial base structure with either (InGaAs/InGaAsP) MQW or (InGaAs/GaAs) MQW active region, and GaAs or InGaP implant buffer layer.

[a]Author is now with Sandia National Laboratories, P.O. Box 5800 MS 0603, Albuquerque, New Mexico 87185-0603; electronic mail: ejskoge@sandia.gov

TABLE I. Epitaxial base structures used in the intermixing experiments. Samples A through D use an implant buffer layer thickness of 200 nm; sample E uses a 500 nm implant buffer layer. Samples A through D use a MQW consisting of 9-nm wells and 11-nm barriers, while sample E uses 8-nm wells and 10-nm barriers.

Sample	MQW	Implant buffer layer
A	InGaAs/GaAs	GaAs
B	InGaAs/GaAs	InGaP
C	InGaAs/InGaAsP	GaAs
D	InGaAs/InGaAsP	InGaP
E	InGaAs/InGaAsP	InGaP

group-III composition is used in the wells and barriers. The MQW was centered within a symmetric waveguide structure consisting of 70 nm of 0.76*Q* on either side of the MQW. An implant buffer layer was grown above the structure and designed to capture the ion implant, creating point defects above the active region, and consisted of either 200 nm GaAs, 200 nm of InGaP, or 500 nm of InGaP. In those base structures using the InGaP implant buffer layers, the implant buffer layer can be selectively removed. The base structures are summarized in Table I.

The samples were cleaved and a portion of each was ion implanted. Phosphorus was implanted at an energy of 100 keV and a dose of 2×10^{14} cm^{-2}, the implant was carried out at a temperature of 200 °C, yielding a range of 110 nm in InGaP and 93 nm in GaAs. Both implanted and nonimplanted samples were encapsulated with 40 nm of SiO_xN_y to protect the sample surface and subjected to rapid thermal processing for various temperatures and times ranging from 650 to 900 °C, and 15 to 180 s, respectively. The SiO_xN_y was removed using buffered HF and the wavelength of the MQW emission measured using room-temperature photoluminescence with a pump wavelength of 785 nm.

The peak photoluminescence wavelength shifts for samples that are not implanted are plotted as a function of rapid thermal anneal (RTA) temperature, shown in Fig. 2. The RTA time for these samples is 120-seconds. This demonstrates the temperature at which interfaces that have dielectric caps, yet have not been subjected to the implantation process, begin to interdiffuse. The two samples, which use an InGaAs/GaAs MQW, show an appreciable shift in the quantized energy state within the temperature range tested. In contrast, the samples which employ an InGaAs/InGaAsP MQW do not shift to such an extent.

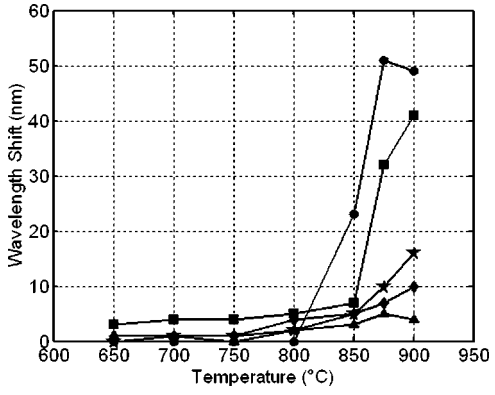

FIG. 2. Photoluminescence peak wavelength shift vs RTA temperature for nonimplanted base structures. Sample A (InGaAs/GaAs) MQW with a GaAs cap (circles), sample B (InGaAs/GaAs) MQW with a InGaP cap (squares), sample C (InGaAs/InGaAsP) MQW with a GaAs cap (triangles), sample D (InGaAs/InGaAsP) MQW with an InGaP cap (diamonds), and sample E (InGaAs/InGaAsP) MQW with a 500 nm InGaP cap (stars).

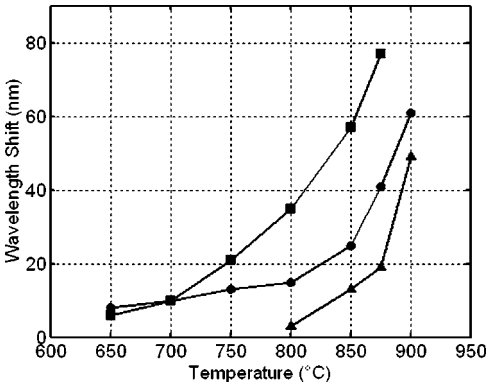

FIG. 3. Photoluminescence peak wavelength shift vs RTA temperature for implanted base structures. Sample D (InGaAs/InGaAsP) MQW with a 200 nm InGaP cap (circles), sample E (InGaAs/InGaAsP) MQW with a 500 nm InGaP cap (squares), and sample E with an InGaP cap removed prior to annealing (triangles).

The photoluminescence peak wavelength shifts of samples subjected to implantation are shown in Fig. 3. The RTA time for these samples was again 120 s. The photoluminescence response of the samples that incorporate a GaAs implant buffer layer are not visible due to the damage from the implant in the GaAs layer, thereby blocking the photoexcited carriers from reaching the MQW, whereas for the samples with an InGaP cap the photoluminescence signal is present because the photocarriers are generated at the MQW due to the fact that InGaP is transparent at the pump wavelength. For this reason, only those samples that utilize an InGaP implant buffer layer are shown. Furthermore, it is only those samples that use the InGaAs/InGaAsP MQW that are stable at elevated temperatures when encapsulated with SiO_xN_y, and are of interest; therefore, only samples employing the InGaAsP barriers are shown, samples D and E. Sample D uses a 200 nm InGaP implant buffer layer, while sample E uses a 500 nm InGaP implant buffer layer. Also shown in Fig. 3 is the photoluminescence peak wavelength shift of sample E, which has been implanted, and had the implanted InGaP buffer layer etched away prior to annealing.

All heterointerfaces are metastable by nature, and with enough input energy compositional gradients will interdiffuse without the need for a catalyst. For conservation of the as-grown MQW, it is essential that sharp heterointerfaces remain intact at elevated temperatures. As demonstrated in Fig. 2, the samples using InGaAs/GaAs MQWs have a tendency to interdiffuse at lower temperatures than those samples that use InGaAs/InGaAsP MQWs. This is due to the introduction of group-III vacancies at the sample/dielectric interface which have a tendency to interdiffuse species residing on the group-III sublattice only.[7] In the case of the InGaAs/GaAs MQW the intermixing takes place on the group-III sublattice, while in the InGaAs/InGaAsP MQWs, because the same group-III composition is used in the wells and barriers the compositional gradient is only on the group-V sublattice and therefore remains intact in the presence of group-III vacancies. Therefore, we conclude that the group-V sublattice is more stable and less likely to interdiffuse at elevated temperatures than the group-III sublattice in samples encapsulated by SiO_xN_y.

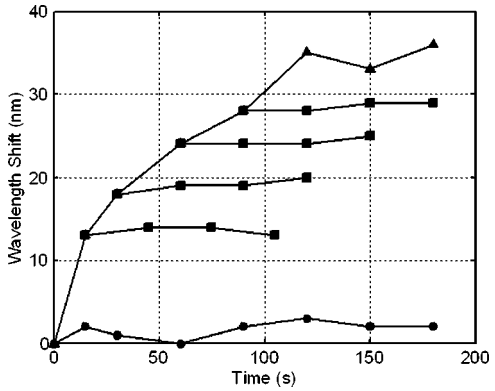

FIG. 4. Isothermal, 800 °C, photoluminescence peak wavelength shift as a function of RTA time demonstrating multiple band edges using a single-ion implant. Symbols indicate nonimplanted (circles), implanted (triangles), and samples with partial anneal followed by the removal of the implant buffer layer (squares) followed by further anneals.

When considering the implanted structures, it is clear that the InGaAs/InGaAsP MQWs readily interdiffuse due to the introduction of point defects that are created in the InGaP layer during implantation. A more substantial shift of the photoluminescence peak wavelength is observed in sample E, a 500 nm thick implant buffer layer, than observed for sample D, a 200 nm thick implant buffer layer. The origin of the difference is not understood at this time, however, we speculate that the proximity of the implant to the MQW and/or strain in the implant buffer layer could play a role. Nevertheless, the transport of point defects through InGaP is readily achievable in either structure.

An important aspect of the implant enhanced intermixing is the extent to which the wells and barriers interdiffuse once the implant buffer layer is removed. A lack of blueshift of the emission wavelength implies the MQW will be stable during future high-temperature processing, such as further anneals and MOCVD regrowth. As shown in Fig. 3, significant intermixing begins to occur at 850 °C for the sample with the implant buffer layer removed. Thus, in order to ensure the MQW will not interdiffuse, the anneal temperature should be kept below 850 °C.

With this information, it is possible to construct a process for the achievement of multiple band edges across the wafer using a single implantation process. This process is demonstrated in Fig. 4, where isothermal annealing at 800 °C was performed for various times. Both implanted and nonimplanted samples were annealed for times ranging from 15 to 180 s, as shown in the figure. After the 15, 30, 60, and 90 second anneals, the implant buffer layer was removed from the respective samples. These samples were then subjected to additional anneal cycles. We found that removing the implant buffer layer halted the blue-shift during these anneals. The arrest of the blueshift is the result of the removal of the abundance of point defects which reside in the implant buffer layer, which are necessary for intermixing. With this process it is possible to achieve any number of band edges across the wafer, limited only by the practical number of lithographic process steps.

Implantation-enhanced QWI in the GaAs material system has been investigated. Several combinations of MQW and implant buffer layer have been studied. It was found that constant-x InGaAs/InGaAsP MQWs are more stable at elevated temperatures than InGaAs/GaAs MQWs when encapsulated with SiO_xN_y. This supports the fact that interdiffusion occurs more readily on the group-III sublattice than on the group-V sublattice in the presence of group-III vacancies. This stability is desirable for the development of a selective QWI process.

Significant interdiffusion enhancement in the InGaAs/InGaAsP was achieved using ion implantation into an InGaP implant buffer layer followed by rapid thermal processing. It was found that point defects readily diffuse through the InGaP allowing for intermixing to occur in the MQW. The ability for the InGaAs/InGaAsP MQW to remain stable without the introduction of point defects, while readily diffusing when point defects are present make this material system ideal for the development of a selective QWI process.

A selective QWI process was developed and demonstrated using a sacrificial implant buffer layer. Using a single-ion implant, multiple band edges can be achieved by ceasing the anneal prior to the saturation of blue-shift, removing the implant buffer layer in those regions where the desired blueshift has been reached, and continuing the anneal. In those regions were the implant buffer layer was removed, the blueshift was halted, whereas in those regions the implant buffer layer remained the intermixing continued. This result shows the feasibility of creating high-performance PICs in this material system.

[1]E. Skogen, J. Raring, J. Barton, S. DenBaars, and L. Coldren, IEEE J. Sel. Top. Quantum Electron. **9**, 1183 (2003).
[2]S. McDougall, O. Kowalski, C. Hamilton, F. Camacho, B. Qiu, M. Ke, R. De La Rue, A. Bryce, and J. Marsh, IEEE J. Sel. Top. Quantum Electron. **4**, 636 (1998).
[3]S. Charbonneau, E. Kotels, P. Poole, J. He, G. Aers, J. Haysom, M. Buchanan, Y. Feng, A. Delage, F. Yang, M. Davies, R. Goldberg, P. Piva, and I. Mitchell, IEEE J. Sel. Top. Quantum Electron. **4**, 772 (1998).
[4]A. Helmy, J. Aitchison, and J. Marsh, Appl. Phys. Lett. **71**, 2998 (1997).
[5]M. Ohjubo, S. Namiki, T. Ijichi, A. Iketani, and T. Kikuta, IEEE J. Quantum Electron. **29**, 1932 (1993).
[6]G. Zhang, A. Ovtchinnikov, J. Nappi, H. Asonen, and M. Pessa, IEEE J. Quantum Electron. **29**, 1943 (1993).
[7]A. Helmy, J. Aitchison, and J. Marsh, IEEE J. Sel. Top. Quantum Electron. **4**, 653 (1998).

Proc. Electronic Materials Conference, paper no. NN6, Santa Barbara, CA (June 22-24, 2005)

Quantum Well Intermixing and MOCVD Regrowth for the Monolithic Integration of UTC Type Detectors with Quantum Well Based Components

J. W. Raring, E. J. Skogen, J. S. Barton, S. P. DenBaars, and L. A. Coldren

The traditional limitations of a 1-dimensional growth platform and a 2-dimensional fabrication scheme makes the monolithic integration of optimal photonic circuits a great challenge due to the common waveguide architecture and material compositions that the individual components within the circuit are often forced to share. Here we present an innovative fabrication/growth scheme using quantum well intermixing (QWI) and blanket MOCVD regrowth for the realization of a unique waveguide architecture and material composition in the photodetector region of an integrated circuit. Through the use of QWI, we blue-shift the as-grown InGaAsP base structure QWs in regions where low loss waveguides or alternative component architectures are desired. An MOCVD regrowth is then performed in which the layer structure necessary for an InGaAs uni-traveling-carrier (UTC) type photodetector is grown. The UTC layer structure is then selectively removed such that mesas remain only in detector regions with blue-shifted, transparent QWs below. Following a thin p-InP regrowth and dry etch ridge definition, a p-InP cladding is grown to yield a buried ridge stripe (BRS) device with three distinct regions: The as grown InGaAsP QWs for use in components such as diode lasers, blue-shifted QWs for low loss waveguides, and UTC type detectors with blue-shifted QWs below. The benefits offered by the InGaAs UTC type detector over that of a detector making use of the as-grown base structure QWs are threefold: The redshifted bandedge relative to the input wavelengths reduces the bias dependence of the absorption coefficient. Without the limitation of hole transport within the UTC the saturation current density is increased allowing for smaller diode areas and hence increased bandwidth.

In recent work, we have demonstrated the ability to achieve high quality QW material grown short distances above a regrowth interface subjected to defect diffusion during the QWI process. Here, we build off this capability by developing the necessary MOCVD growth conditions and processing techniques to enable the fabrication of a BRS device containing UTC type detectors and components employing the base structure QWs. We study the effects of growth rate and growth temperature on the resulting profile at the sidewalls of the UTC mesas, which suffer from undercutting during wet etch definition. Since ridges must be defined and buried across these sidewalls, the regrowth profile is a key aspect to successful device fabrication. We found that using a two-stage temperature profile at a rate of 3.8 Å/s provided an optimum growth profile. Finally, by fabricating both UTC type and QW pin type photodetectors on the same chip, we demonstrate a 2X and 4X increase in large-signal voltage amplitude from UTC detectors with 1/5 and 3/5 the diode area, respectively, as the QW pin detectors.

Proc. Electronic Materials Conference, paper no. U4, Santa Barbara, CA (June 22-24, 2005)

Band-Edge Characterization of Intermixed InGaAsP/InP and InGaAs/GaAs Quantum Wells

G.B. Morrison, J.W. Raring, C.S. Wang, E.J. Skogen, and L.A. Coldren

Quantum well intermixing (QWI) has been widely demonstrated as an elegant method for creating multiple band edges in photonic integrated circuits (PICs). Despite the popularity of QWI, quantitative experimental studies of the effect of intermixing on quantum well band edges are scarce. This study makes extensive use of photocurrent spectroscopy to probe the band edge characteristics of intermixed quantum wells in both the 1550 nm InGaAsP/InP material system and the 980 nm InGaAs/GaAs material system. The photocurrent data is generated using simple photodiodes designed specifically for photocurrent spectroscopy. The photocurrent is collected as a function of both wavelength and bias voltage, and is then transformed into a measurement of absorption at the band edge. Band edge absorption measurements are used to compare quantum well designs for QWI PICs, and also to suggest optimal QWI band shifts for electro-absorption modulators (EAMs). Predictions of EAM chirp by application of the Kramers-Kronig transform are also demonstrated. By comparing the absorption edges of as-grown quantum wells with the absorption edges of intermixed quantum wells, the effect of QWI on the absorption edge is made clear. The effects of intermixing on device performance, such as EAM insertion loss, extinction, and extinction efficiency, are explained. As expected, the QWI process reduces carrier confinement, and can significantly weaken the exciton peak. A weakened exciton peak translates to lower extinction in modulator applications. In the InGaAsP/InP material system, we compare a 65 Å wide well having conduction band depth of 120 meV, to an 80 Å wide well having conduction band depth of 85 meV. Both designs exhibit satisfactory exciton confinement for a QWI modulator, but the 80 Å design is shown to be shallower than is optimal for the overall PIC. For the wells considered in the InGaAsP/InP material system, a band edge shift of approximately 40-50 nm is ideal for modulator components. In the GaAs/InGaAs 980 nm material, an 80 Å well with conduction band depth of 147 meV is examined. A 20-30 nm blue shift by QWI is shown to be appropriate for modulators in this material system. Unfortunately, the QWI process seriously degrades the exciton peaks in these wells. For 980 nm applications, moving to a different material system that allows deeper wells (e.g. InGaAs/AlGaAs or InGaAsP/GaAs) may be necessary. Alternatively, for optimization at 980 nm in the InGaAs/GaAs system, red shifting the laser frequency from the gain peak by about 10 nm would allow a smaller degree of QWI (e.g. 10 nm) in the modulator, resulting in improved modulator performance.

[1] J.W. Raring, E.J. Skogen, L.A. Johansson, M.N. Sysak, J.S. Barton, M.L. Mašanovic, and L.A. Coldren, IEEE Photon. Technol. Lett., **16**, 1613 (2004).
[2] S. Charbonneau, E.S. Koteles, P.J. Poole, J.J. He, G. C. Aers, J. Haysom, M. Buchanan, Y. Feng, A. Delage, F, Yang, M. Davies, R.D. Godberf, P.G. Piva, and I.V. Mitchell, IEEE J. Sel. Topics in Quantum Electron, vol 4, July/August 1998 pp772-793.
[3] E. Skogen, J. Raring, J. Barton, S. DenBaars, and L. Coldren, J. Sel. Topics in Quantum Electron., vol. 9, September/October, 2003 pp. 1183-1190.
[4] G. B. Morrison, C.S. Wang, E. Skogen and L.A. Coldren, Submitted to IPRA 2005.

Photocurrent Spectroscopy for Quantum-Well Intermixed Photonic Integrated Circuit Design

Gordon B. Morrison, *Member, IEEE*, Erik J. Skogen, *Member, IEEE*, Chad S. Wang, *Student Member, IEEE*, James W. Raring, Yu-Chia Chang, Matt Sysak, and Larry A. Coldren, *Fellow, IEEE*

***Abstract*—Photocurrent spectroscopy is used to characterize band edges in quantum-well intermixed InGaAsP material lattice matched to InP. The band edge absorption data is used as a design tool to predict the dc performance of electroabsorption modulators, and is shown to agree well with data obtained from actual devices. In addition, we demonstrate the presence of an exciton peak in InGaAsP quantum wells, and present its evolution as a function of quantum-well intermixing and reverse bias voltage.**

***Index Terms*—Electroabsorption modulators (EAMs), excitons, laser tuning, photoconductivity, photodiodes, quantum-well intermixing (QWI), semiconductor lasers.**

I. Introduction

PHOTONIC integrated circuits with monolithic integration of multiple optoelectronic components are highly desirable for next-generation optical networks. Monolithic integration of components such as lasers, electroabsorption modulators (EAM), and passive waveguides, requires multiple band edges. Quantum-well intermixing (QWI) is a popular and simple method for achieving multiple band edges on a single wafer, orthogonal to the growth direction [1]–[4]. The wavelengths of these band edges must be carefully tailored for optimal performance of the integrated photonic circuit. In this letter, we apply band edge photocurrent measurements to the design and performance-analysis of QWI integrated laser modulators. We also present a detailed characterization of the evolution of band edge absorption as a function of the degree of QWI in an InGaAsP quantum well. Photocurrent spectroscopy data for QWI InGaAsP wells have been presented in the literature previously [1], [3], but here we present detailed observation of exciton peaks at multiple biases and with multiple degrees of intermixing. The ability to directly measure the QWI band edge, and to use this measurement for analysis of potential transmitter designs, will enable the engineering of superior highly optimized integrated laser-modulator transmitters for telecommunications applications [5].

Manuscript received August 26, 2004; revised February 17, 2005. This work was supported in part by ARMY Grant DAAD19-03-1-0058. The work of G. B. Morrison was supported in part by an Natural Sciences and Engineering Research Council of Canada (NSERC) PDF.

G. B. Morrison was with the Department of Electrical and Computer Engineering, University of California, Santa Barbara, CA 93106 USA. He is now with III-V Photonics, Houten 3994 DB, The Netherlands (e-mail: tallest_dwarf@hotmail.com).

E. J. Skogen was with the Department of Electrical and Computer Engineering, University of California, Santa Barbara, CA 93106 USA. He is now with Sandia National Laboratories, Albuquerque, NM 87123 USA.

C. S. Wang, J. W. Raring, Y.-C. Chang, M. Sysak, and L. A. Coldren are with the Department of Electrical and Computer Engineering, University of California, Santa Barbara, CA 93106 USA.

Digital Object Identifier 10.1109/LPT.2005.848543

II. Fabrication

Photodiodes for photocurrent spectroscopy were fabricated from a wafer that initially consisted of seven 65-Å compressively strained quantum wells (conduction band well depth 120 meV) and eight 80-Å barriers sandwiched between two 120-nm waveguide layers grown on InP by metal–organic chemical vapor deposition (MOCVD). This structure was designed for the fabrication of small-footprint chip-to-chip laser-modulator transmitters [4]. A 15-nm InP layer, 20-nm $1.3Q$ etch stop, and a 450-nm InP implant buffer were grown on top of the waveguide. A 5000-Å SiN_x mask layer was deposited, patterned, and removed in regions where implant was desired. A 100-keV 5e14-cm^{-2} dose of P^+ was implanted into the buffer layer. Rapid thermal annealing at 675 °C was performed to accomplish intermixing [2]. Different levels of intermixing were obtained across the wafer by halting the anneal process and removing the InP implant buffer layer prior to further annealing. By this method, we retained the active (unshifted) band edge, and created three QWI band edges, each blue-shifted by a different amount. The band edges are referred to quantitatively by the wavelengths, in nanometers, of their photoluminescence peaks. The remaining implant layer was removed, and the sample was submitted for MOCVD regrowth of 750 nm of p-type InP above the waveguide, a 750-Å InGaAs contact layer, and a 200-nm InP protective cap.

Each band edge was patterned and etched with circular mesas ranging from 50 to 400 μm in radius. The mesa etch was performed through the waveguide and into the n-type substrate. A 2000-Å layer of SiN_x was deposited by plasma-enhanced chemical vapor deposition, and circular vias were patterned onto the mesas. The protective InP cap was removed, and Ti–Pt–Au ring contacts were deposited. The contacts were annealed at 410 °C for 30 s. Devices were wire bonded to AlN carriers.

III. Experiment

The wavelength-tunable light source used in our photocurrent measurements is a Varian Cary 500 spectrophotometer. Measurements are taken at 1-nm intervals and the wavelength resolution is 2 nm. An EG&G 5210 lock-in amplifier is used with a 3-kHz chopper and 1-s time constant to extract the photocurrent signal from leakage current. Leakage current for most devices is less than 10 μA at -6 V. A Newport 1835C optical power meter is used to measure the optical power input to the device. An example of data acquired by this method from a 100-μm

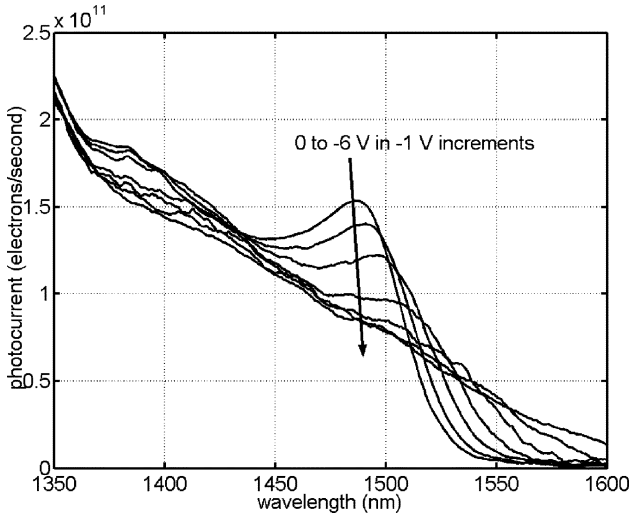

Fig. 1. Photocurrent versus wavelength in device at biases of 0 through −6 V in −1-V increments.

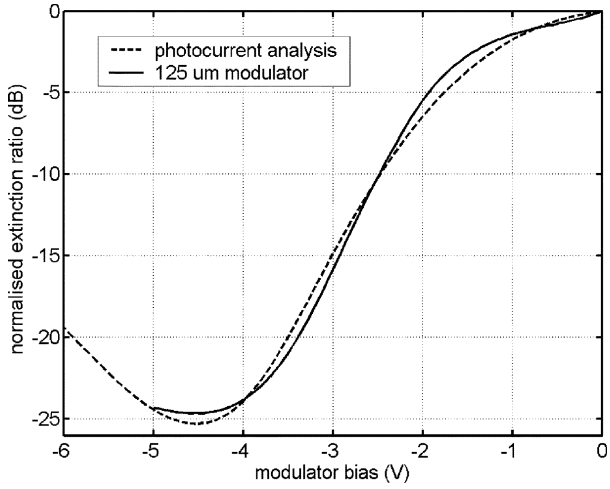

Fig. 2. DC extinction curve for a 125-μm integrated EAM compared with a simulation using photocurrent spectroscopy data from identical material.

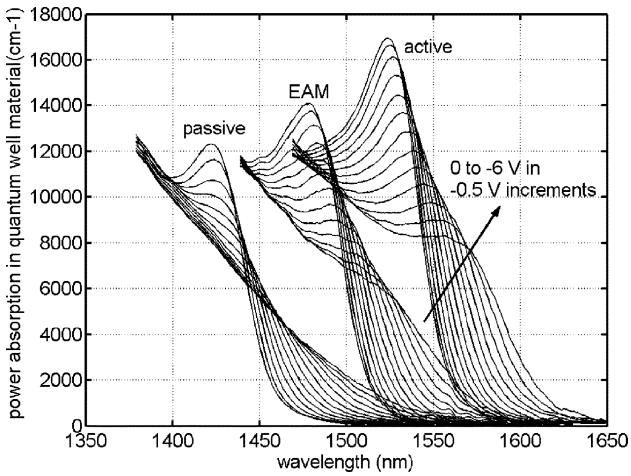

Fig. 3. Active, modulator, and passive absorption edges, obtained by ion-implant QWI. Curves are shown for biases ranging from 0 to −6 V in −0.5-V increments.

radius device is shown in Fig. 1. This device was intermixed to approximately 1495 nm from an as-grown band edge of approximately 1540 nm.

The Cary 500 spectrophotometer is useful for calibrating the photocurrent diodes. The absorption of a doped InGaAs contact layer has been determined by measuring transmittance through a 5360-Å layer grown on undoped InP, and comparing this transmittance to that obtained upon removal of the 5360-Å layer.

IV. Results and Discussion

Simple calculations are performed to extract an absorption coefficient from the photocurrent data. Measured incident power is reduced to account for reflection and p-contact absorption. Light incident to the photodiode surface is transverse-electric (TE) polarized. Transverse-magnetic light is not considered because the devices in this letter operate with TE polarization.

Back-scattered light is negligible due to scattering and absorption by the Ti–Pt–Au backside contact. This surprising result was determined by comparing photocurrent magnitude from similar devices on semi-insulating (SI) substrates with and without a Ti–Pt–Au layer annealed on the backside. The magnitudes of photocurrent from doped and SI substrates were the same within experimental error, provided the Ti–Pt–Au layer was annealed on the back side of the SI material. Without the Ti–Pt–Au backside layer, photocurrent is increased by approximately 35% due to back-scattered light.

The measured photocurrent is converted to electrons/second, and each electron is the result of one absorbed photon. Absorption is then obtained as

$$\alpha = \frac{-\ln\left(\frac{P\text{in}-P\text{out}}{P\text{in}}\right)}{L} \tag{1}$$

where $P\text{in}$ is the input power in photons per second, $P\text{out}$ is the output photocurrent in photons per second, and L is the total length of quantum well material through which the light passes. For these devices, the length was $7{*}65\ \text{Å} = 455\ \text{Å}$.

The absorption data is useful for analyzing device performance. Starting with a spline interpolation of the absorption as a function of wavelength from data in Fig. 1, simple calculations, which account for optical overlap with the quantum wells and the effective index and length of the waveguide, lead to predicted dc extinction ratios for an EAM. In Fig. 2, the dc extinction of a 125-μm EAM is simulated at 1542 nm using data from Fig. 1. Also shown for comparison is the dc extinction at 1543 nm of an actual device that was fabricated from the same material intermixed to 1500 nm, and integrated with a 150-μm distributed Bragg reflector laser [4]. Clearly, the photocurrent measurements allow accurate estimation of modulator performance.

Figs. 1 and 2 demonstrate the useful nature of photocurrent spectroscopy for design of integrated photonic circuits. Of special interest is the strong exciton peak in the QWI InGaAsP material in Fig. 1. The exciton peak is especially important for achieving good dc extinction, as well as negative chirp.

The effect of QWI on the exciton peak is shown in Fig. 3, with band edges for the active, modulator, and passive sections of a photonic integrated circuit. The diodes were biased from 0 to −6 V in −0.5 V increments. The band edges shown in Fig. 3 have photoluminescence peaks at 1537, 1483, and 1429 nm. As

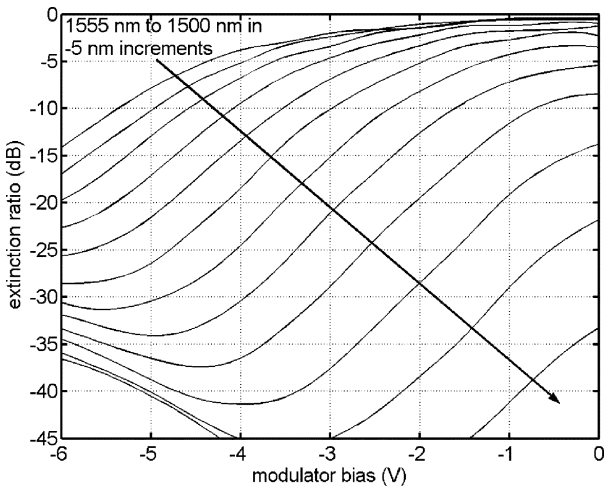

Fig. 4. Predicted dc extinction curves for input light ranging from 1500 to 1555 nm for a 125-μm modulator fabricated from the 1483-nm QWI material of Fig. 3.

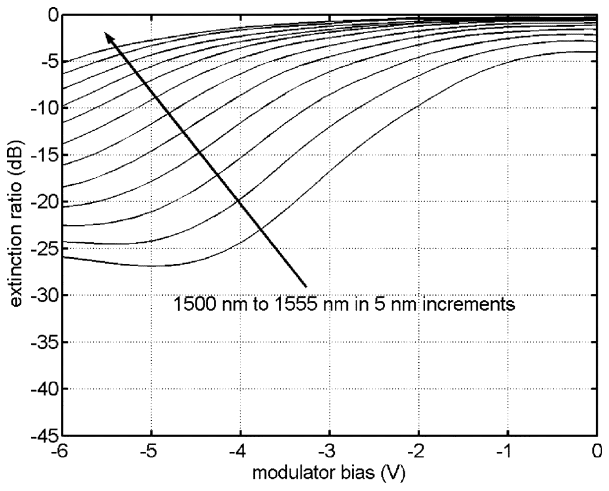

Fig. 5. Predicted dc extinction curves for input light ranging from 1500 to 1555 nm for a 125-μm modulator fabricated from 1460-nm QWI material.

the degree of intermixing increases, and the exciton peaks shift to shorter wavelengths, the exciton magnitude decays significantly [3], [6]. With increased intermixing, the exciton peaks also decay more rapidly as a function of applied bias voltage.

The intermixing process results in group V atoms diffusing across the as-grown material boundaries, causing quantum wells to develop rounded edges, and become wider and shallower. This is consistent with the observed behavior of the exciton peaks, which are expected to decay more rapidly with applied voltage when the quantum wells are made shallower by QWI.

In addition to the 1483-nm band edge shown in Fig. 3, there was also a 1460-nm band edge fabricated. These two band edges are both potentially suitable for use in the modulator component of a quantum well intermixed device. In Fig. 4, we compare the simulated dc extinction ratios of 125-μm EAMs operating at wavelengths ranging from 1505 to 1560 nm, using data from the 1483-nm materials. At short wavelengths, the simulated modulator suffers from high insertion loss (high extinction ratio at 0 V), whereas at longer wavelengths, the modulator has a poor extinction ratio. It appears that the ideal operating wavelength for this modulator would be between 1520 and 1540 nm, where extinction ratios larger than 20 dB are obtainable with maximum slopes of up to 10 dB/V, and insertion loss is less than 5 dB.

Simulated dc extinction ratios for EAMs fabricated from the 1460-nm material are shown in Fig. 5. The operating wavelengths are the same as those in Fig. 4, but the 23 nm of additional QWI has a profound effect on the characteristics of the EAM. The performance of the simulated 1460-nm QWI 125-μm modulator is similar to that of the 1483-nm QWI modulator, but the optimal operating point is now at approximately 1500 nm. The maximum extinction ratio obtainable with low ($<$5 dB) insertion loss is about 20% less for the 1460-nm QWI device, due to reduced carrier confinement caused by increased QWI. A QWI blue shift of about 45 nm is optimal for the structures studied in this letter, and would allow low insertion loss and maximum extinction ratio near the gain peak of the active section of the laser-modulator integrated device. We have reached the same conclusions for QWI InGaAsP wells of different design (80 Å wide, 30% shallower), and thus suggest that 40–50 nm of intermixing is a reasonable criteria that can be extended to many different InGaAsP quantum-well designs. Naturally, different results would be expected for very different quantum wells and for quantum wells in other material systems.

V. Conclusion

With the advent of QWI as a popular method for monolithic integration of optoelectronic components comes the difficulty of specifically tailoring the various band edges in order to optimize device performance. We have demonstrated that photocurrent data can be exploited to accurately predict extinction ratios for QWI modulators in integrated laser-modulator devices. The influence of QWI on EAM modulator dc extinction ratios at various wavelengths has been presented, and an optimal degree of QWI has been suggested for a range of designs of laser/EAM transmitters in the InGaAsP material system. Photocurrent spectroscopy is an important tool for the engineering of highly optimized photonic integrated circuits.

References

[1] S. Charbonneau, E. S. Koteles, P. J. Poole, J. J. He, G. C. Aers, J. Haysom, M. Buchanan, Y. Feng, A. Delage, F. Yang, M. Davies, R. D. Goldberg, P. G. Piva, and I. V. Mitchell, "Photonic integrated circuits fabricated using ion implantation," *IEEE J. Sel. Topics Quantum Electron.*, vol. 4, no. 4, pp. 772–793, Jul./Aug. 1998.

[2] E. Skogen, J. Raring, J. Barton, S. DenBaars, and L. Coldren, "Post-growth control of the quantum-well band edge for the monolithic integration of widely-tunable lasers and electroabsorption modulators," *J. Sel. Topics Quantum Electron.*, vol. 9, no. 5, pp. 1183–1190, Sep./Oct. 2003.

[3] A. Ramdane, P. Krauz, E. V. K. Rao, A. Hamoudi, A. Ougazzaden, D. Robein, A. Gloukhian, and M. Carré, "Monolithic integration of InGaAsP-InP strained layer distributed feedback laser and external modulator by selective quantum-well interdiffusion," *IEEE Photon. Technol. Lett.*, vol. 7, no. 9, pp. 1016–1018, Sep. 1995.

[4] C. S. Wang, E. J. Skogen, J. W. Raring, G. B. Morrison, and L. A. Coldren, "Short-cavity 1.55 μm DBR lasers integrated with high-speed EAM modulators," presented at the 19th Ann. IEEE Int. Semiconductor Laser Conf., Matsue-shi, Simane, Japan, 2004.

[5] T. H. Wood, "Direct measurement of the electric-field-dependent absorption coefficient in GaAs/AlGaAs multiple quantum wells," *Appl. Phys. Lett.*, vol. 48, pp. 1413–1415, 1986.

[6] J. E. Zucker, K. L. Jones, B. Tell, K. Brown-Goebeler, C. H. Joyner, B. I. Miller, and M. G. Young, "InGaAsP/InP quantum well buried heterostructure waveguides produced by ion implantation," *Electron. Lett.*, vol. 28, pp. 853–855, 1992.

Quantum well intermixing and MOCVD regrowth for the monolithic integration of 40 Gb/s UTC type photodiodes with QW based components

J. W. Raring, E. J. Skogen, J. S. Barton, C.S. Wang, S. P. DenBaars, and L. A. Coldren

In this letter we present a novel fabrication method for uni-traveling carrier (UTC) type photodiodes using quantum well (QW) intermixing (QWI) and MOCVD regrowth. The fabrication scheme will enable the monolithic integration of the photodiodes with high gain laser diodes, high efficiency electroabsorption modulators (EAM), and high saturation power semiconductor optical amplifiers (SOA). The photodiodes fabricated on intermixed quantum wells presented here exhibit excellent photocurrent handling capabilities, minimal response roll-off over the 20 GHz of our testing capability, and open 40 Gb/s eye diagrams.

Introduction: Monolithic integration of photonic circuits presents tremendous opportunities for the attainment of high-functionality, efficient, compact, and cost effective components for next generation optical networks. Various methods for manipulating the material properties to achieve several QW band edges within a single photonic integrated circuit (PIC) have been reported [1-3]. Beyond this, highly complex PICs will require differing gain or optical confinement at the same or similar wavelength, and in some cases, a radically different internal structure. High-performance multiple QW band-edge widely-tunable PICs have been demonstrated using QWI [4]. With the addition of a single blanket MOCVD step for the growth of an offset multiple QW (o-MQW) active region over an intermixed centered multiple QW (c-MQW) region, we achieved regions of both low and high optical confinement on the same chip [5]. Here we expand on this integration scheme with the demonstration of a uni-traveling carrier (UTC) photodiode fabricated over an intermixed c-MQW active region. This scheme will enable the monolithic integration of the photodiodes with high gain laser diodes, high efficiency EAMs, and high saturation power SOAs. The photodiodes fabricated on intermixed quantum wells exhibit excellent photocurrent handling capabilities, minimal response roll-off over the 20 GHz of our testing capability, and open 40 Gb/s eye diagrams.

With the emergence of fiber amplifiers and the development of SOAs for use in receivers, the demands on photodetectors have drastically increased since they are forced to handle the higher generated photocurrents. The photocurrent handling capabilities of the traditional pin type photodetector is intrinsically limited by the space charge effect, which is a result of the slow carrier transport time associated with the photogenerated holes. The UTC photodiode has been developed specifically to eliminate the influence of hole transport on the performance of the detector. In this type of photodiode, charge transport is governed completely by electrons. The fundamental layers of the UTC are the neutral InGaAs:Zn absorption layer and the depleted wide bandgap InP electron collection layer. Under normal operation, carriers are photogenerated in the absorber layer. The minority carriers (electrons) diffuse towards the collector layer where they accelerate to their overshoot velocity and drift across the collector layer. The escape time of the majority carriers (holes) from the absorption layer is negligible since it is set by the dielectric relaxation time [6]. Thus the carrier transport properties are set solely by electron transport, the space charge effect associated with pin photodiodes is avoided, and saturation current densities 4-6 times higher than that in pin photodiodes are theoretically possible [6].

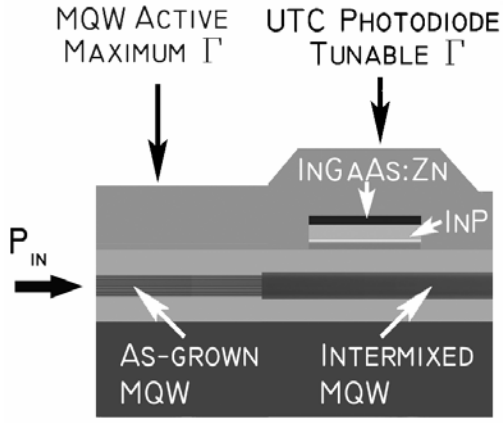

Fig. 1 *Side view schematic of the device structure showing the high confinement c-MQW (left), and the UTC structure grown over regions in which the c-MQW has been intermixed (right).*

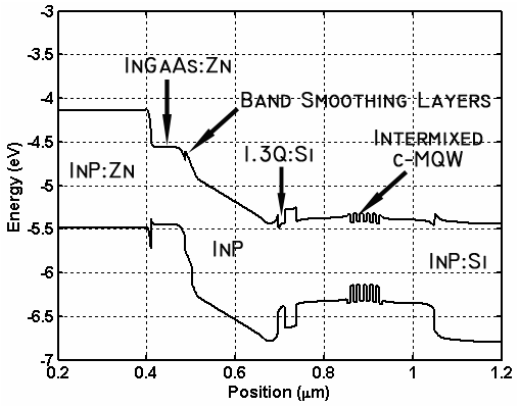

Fig. 2 *Simulated 0 V band diagram for our proposed integrated UTC structure showing the placement of the InGaAs:Zn absorber, conduction band smoothing layers, and InP collector with respect to the intermixed c-MQW.*

Experiment: The epitaxial base structure is grown on a conducting InP substrate using a Thomas Swan Scientific Equipment Ltd. horizontal-flow rotating-disc MOCVD reactor. The active region consists of ten 6.5 nm compressively strained (1.0%) quantum wells, separated by 8.0 nm tensile strained (0.3%) barriers, centered within two InGaAsP:Si (1.3Q:Si) layers designed to maximize the optical confinement in the quantum wells. Following the active region, a 15 nm InP:Si regrowth layer, a 20 nm 1.3Q:Si stop etch, and a 450 nm InP implant buffer layer is grown.

The sample is patterned with Si_xN_y and selectively implanted with P+ for intermixing. Following the implant, the samples are subjected to our QWI process as described in [1]. In the QWI process, the as grown c-MQW is shifted in peak photoluminescence wavelength from 1530 nm to 1410nm in regions where passive waveguide or UTC type detectors are desired. Following the QWI process, the implant buffer layer and 1.3Q stop etch layers are removed using selective wet chemical etching. An MOCVD regrowth is then performed for the growth of a thin InP:Si layer followed by a 1.3Q:Si stop etch layer, a 30nm InP:Si subcollector layer, a 150nm InP collector layer, conduction band smoothing layers, a 50nm InGaAs:Zn absorber layer, and a 200nm InP:Zn cap layer. The epitaxial structure associated with the UTC was based largely on that presented in [6] by Ishibashi et al. The absorber and collector thicknesses were designed to provide 90% quantum efficiency and 3 dB bandwidths in the range of 30 – 40 GHz for a 3 by 25μm diode. Following the regrowth, the sample is patterned with SixNy and a selective wet chemical etch process

is carried out such that the UTC structure remains in regions where it is desired with the blue-shifted c-MQW below. A final MOCVD regrowth is performed to grow the p-type InP:Zn cladding and p-contact InGaAs:Zn layers. A schematic side view illustrating both the high confinement active c-MQW and UTC structure over the intermixed c-MQW regions is presented in Fig. 1. The resulting non-biased band diagram for the UTC region is shown in Fig. 2.

Following the growth of the p-cladding, surface ridge waveguides were defined, photo-benzocyclobutene (BCB) was defined such that it would remain underneath the p-contacts, and p-metal was deposited. The wafers were thinned, back-side n-metalwas deposited, the die were separated into 3 by 25μm diodes, soldered to aluminum nitride carriers, and wire bonded to a matched load of 50 Ω on a coplanar transmission line for RF characterization.

Results: The quantum efficiency of the detectors was estimated by separately reverse biasing two photodetectors configured optically in series. The first detector in the pair is the 25μm detector in question and the second detector is much longer at 250μm such that essentially all optical power escaping the first detector is absorbed. A quantum efficiency of ~90% was estimated by taking the fraction of photocurrent detected in the 25μm detector over the sum of photocurrents in both detectors.

The frequency response of the photodiodes was characterized using a 20 GHz Agilent Lightwave Component Analyzer (LCA). The optical signal from the LCA was fed through an erbium doped fiber amplifier (EDFA) and then coupled into the photodiode waveguide using a tapered fiber. In Fig. 3 the normalized response of the photodiode is shown for various average detected photocurrent levels at a reverse bias of 3 volts. As can be seen in the figure, the 20 GHz response demonstrates under 0.5 dB of roll-off with average photocurrents up to 20 mA. At an average photocurrent of 25mA, the roll off is somewhat increased to 0.75 dB and at 35mA the 20 GHz roll-off is increased to slightly over 2 dB. However, when increasing the reverse bias to 4V (dashed line) at the same average photocurrent, the roll of is decreased to below 1dB.

To examine the large signal characteristics of the photdiodes, eye diagrams were taken at 40 Gb/s in a non-return to zero (NRZ) format using a pseudo-random-bit-sequence (PRBS) of 2^{31}-1. The modulated light was fed through an EDFA and into the waveguide of the photodiode using a tapered fiber. Fig. 4a shows the eye diagrams taken at a 2.5V reverse bias for two different input powers driving a voltage amplitude of 0.33 and 0.41V. As can be seen from the figure, the eye diagrams are open and demonstrate no difference in shape for the two input power levels. In Fig. 4b, eye diagrams are shown for a constant input power at reverse biases of 2.5 and 3.0V. The higher crossing point of the eye diagram driving a voltage amplitude of 0.53V at a reverse bias of 2.5V is indicative of the onset of saturation. However, upon increasing the reverse bias to 3.0V, the voltage amplitude is increased to 0.6V and the crossing point returns to its normal position. The 0.6V amplitude provided by the photodiode at 3V is indicative of a minimum peak current of 24mA in the photodiode.

Conclusion: We have demonstrated UTC type photodiodes using a fabrication scheme ideal for integration with high gain laser diodes, high efficiency EAMs, and high saturation power SOAs using QWI and MOCVD regrowth. The 3 by 25μm photodiodes demonstrated minimal response roll-off over the 20 GHz of our testing capability at a 3V reverse bias and an average photocurrent of 25mA. Open 40 Gb/s eye diagrams were achieved with an amplitude voltage of 0.6V.

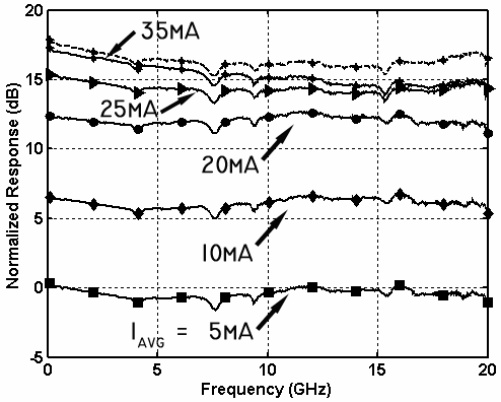

Fig. 3 Optical to electrical response of detector for average photocurrents of 5 (squares), 10 (diamonds), 20 (circles), 25 (triangles), and 35 mA (stars) with a 3V reverse bias (solid lines) and 35mA at a –4V reverse bias (dashed line). Response is normalized to 5mA data set. Markers represent every 80th data point.

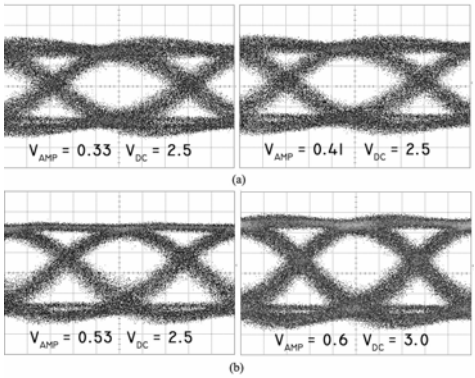

Fig. 4 40 Gb/s eye diagrams from a 25 μm detector at a (a) constant reverse bias of 2.5V and (b) constant input power.

References

[1] E. Skogen, J. Raring, J. Barton, S. DenBaars, and L. Coldren, "Post-Growth Control of the Quantum-Well Band Edge for the Monolithic Integration of Widely-Tunable Lasers and Electroabsorption Modulators," *IEEE J. Sel. Topics in Quantum Electron.*, vol. 9, pp. 1183-1190, September/October, 2003.

2 J. Binsma, P. Thijs, T. VanDongen, E. Jansen, A. Staring, G. VanDenHoven, and L. Tiemeijer, "Characterization of Butt-Joint InGaAsP Waveguides and Their Application to 1310 nm DBR-Type MQW Ganin-Clamped Semiconductor Optical Amplifiers," *IEICE Trans. Electron.*, vol. E80-C, pp. 675-681, 1997.

3 M. Aoki, M. Suzuki, H. Sano, T. Kawano, T. Ido, T. Taniwatari, K. Uomi, and A. Takai, "InGaAs/InGaAsP MQW Electroabsorption Mofulator Integrated with a DFB Laser Fabricated by Band-Gap Energy Control Selective Area MOCVD," *IEEE J Quantum Electron.*, vol. 29, pp. 2088-2096, 1993.

4 J. Raring, E. Skogen, S. DenBaars, and L. Coldren, "Demonstration of negative chirp characteristics over wide wavelength range using monolithically integrated SG-DBR laser electroabsorption modulator," *IEEE Electronics Letts.* vol.40, pp. 1599-1600 ,2004

5 E. Skogen, J. Raring, S. DenBaars, and L. Coldren, "Integration of High-Gain and High-Saturation Power Active Regions using Quantum Well Intermixing and Offset-Quantum Well Regrowth," *Electron. Lett.*, Vol. 40, pp. 993-94, 2004.

6 T. Ishibashi, T. Furuta, H. Fushimi, S. Kodama, H. Ito, T. Nagatsuma, N. Shimizu, and Y. Miyamoto. InP/InGaAs Uni-Traveling-Carrier Photodiodes. *IEICE Trans. Elelctron.*, vol. E83-C, no.6 June 2000

Demonstration of high saturation power/high gain SOAs using quantum well intermixing based integration platform

J. W. Raring, E. J. Skogen, M. L. Mašanović, S. P. DenBaars, and L. A. Coldren

In this letter we report the performance of semiconductor optical amplifiers (SOA) employing regions of high and low optical confinement designed for high saturation power and high gain using a novel quantum well (QW) intermixing (QWI) and MOCVD regrowth fabrication scheme. The scheme enables the monolithic integration of the high performance SOAs with high gain laser diodes, high efficiency electroabsorption modulators (EAM), and high saturation power photodiodes. The SOAs presented here exhibit saturation powers in the 19-20 dBm range with nearly 15 dB of gain.

Introduction: High functionality, high efficiency, and size reduction offered by single chip photonic circuits inspires the present effort towards increased levels of monolithic integration. The performance of the photonic integrated circuit (PIC) as a whole is ultimately limited by the performance of the individual components within the circuit. High functionality active PICs can require multiple QW band edges, differing gain or optical confinement at similar wavelengths, and radically different internal structures for components such as high saturation power photodiodes. Integration schemes that enable high flexibility for the independent optimization of the individual components within the PIC are essential for monolithic circuits to operate at the performance levels offered by circuits comprised of discrete components.

High-performance multiple QW band-edge widely-tunable transmitters have been demonstrated using our quantum well intermixing (QWI) integration platform [1]. With the addition of simple blanket MOCVD regrowth steps, we have extended the QWI integration platform to achieve QW active regions of both low and high optical confinement and high saturation power photodiodes operating at 40 Gb/s [2, 3]. In this work we exploit the capability of achieving both high and low optical confinement on a single chip for the demonstration of high saturation power/high gain SOAs.

Low optical confinement (LOC) MQW active regions are an attractive choice for employment in SOAs requiring high saturation power since the photon density within the QWs can be kept relatively low. Using the LOC-QW scheme, impressive saturation powers of +23 dBm and +28 dBm have been reported (4, 5). It should be noted that until recently the record SOA saturation power was +17 dBm (6). Here we report SOAs exhibiting 19-20 dBm saturation output powers with nearly 15 dB of chip gain using a fabrication scheme that will enable the SOAs to be placed in highly functional PICs containing widely tunable lasers, QW EAMs, and high saturation power photodiodes.

Experiment and Theory: Device fabrication initiates on an MOCVD grown epitaxial base structure consisting of ten 6.5 nm compressively strained QWs, separated by 8.0 nm tensile strained barriers, centered within two InGaAsP:Si (1.3Q:Si) layers designed to maximize the optical confinement at ~12.6% in the QWs. The samples are subjected to our QWI process as described in [7], in which the as-grown c-MQW is shifted in peak photoluminescence wavelength from 1530 nm to 1410nm in regions where passive waveguide, low optical confinement QWs, or high saturation power photodiodes are desired. An MOCVD regrowth is then performed for the growth of a thin InP:Si layer followed by a 1.3Q:Si stop etch layer, a 145nm InP:Si confinement tuning layer (CTL), a 5 o-MQW with similar compositions and thicknesses to that of the c-MQW, and a InP:Zn cap layer. Since the CTL layer functions to move the active wells away from the peak of the optical mode, the layer thickness is a key aspect in the design. In this work it was chosen such

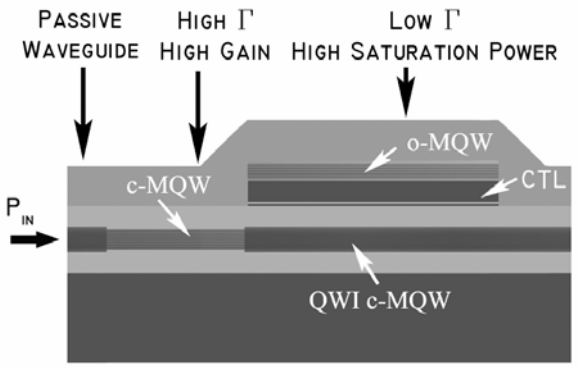

Fig. 1 *Side view schematic of the SOA device structure illustrating the c-MQW high modal gain region (left), and the o-MQW with reduced modal gain (right) for the realization of a high saturation power/ high gain SOA.*

that the optical confinement factor in the o-MQW was ~1.3% to achieve saturation output powers in the 20 dBm range. Following the o-MQW regrowth, wet etching was used to selectively remove the o-MQW structure in regions it is not desired, a similar sequence was performed for the realization of high saturation power photodiodes [3], and the p-type InP:Zn cladding and p-contact InGaAs:Zn layers were grown. A thorough discussion of the theory and growth aspects can be found in [8]. Standard lithography methods were used to define 5μm wide surface ridge SOA devices with varying lengths. The three unique waveguide sections in the resulting SOA structures are shown in Fig. 1:

Results: The cleave back method was used to characterize Fabry Perot ridge lasers to extract the injection efficiency and optical loss of both active region types. The injection efficiency was found to be 70% and 73 % in the c-MQW and o-MQW active regions, respectively. The optical loss was found to be 20 cm^{-1} and 3 cm^{-1} in the c-MQW and o-MQW active regions, respectively. A two-parameter fit was used to plot the threshold modal gain versus current density as shown in Fig. 2. The fit yielded a modal gain parameter of 94.1 cm^{-1} in the o-MQW active region and 9.1 cm^{-1} in the o-MQW active region, which is in good agreement with the simulated difference in optical confinement factor.

The SOA devices employed curved/flared passive input waveguides for reduced facet reflections. Single section low confinement SOAs with lengths of 1000μm and 1500μm along with a dual section SOA containing 150μm high optical confinement section followed by 1350μm of low optical confinement section were soldered to AlN carriers, wirebonded, and placed on a copper stage cooled to 18˚C for characterization. A continuous wave (CW) 1550 nm light source was fed through a polarization controller and coupled into the SOA waveguide using a tapered fiber. The TE polarization state was used during all testing due to the polarization sensitivity of the compressively strained QWs. The coupled chip power was determined by reverse biasing the

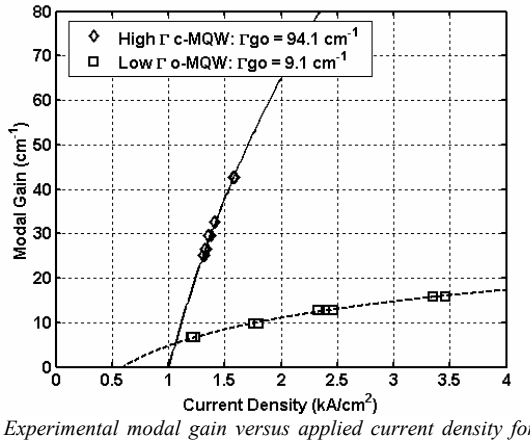

Fig. 2 *Experimental modal gain versus applied current density for 3μm wide Fabry Perot lasers employing high confinement c-MQW (diamonds) and low confinement o-MQW (squares) active regions.*

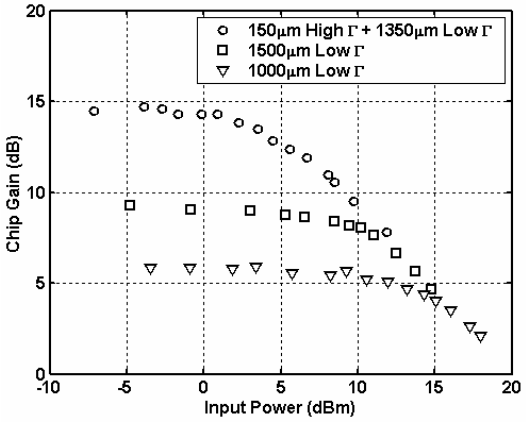

(a)

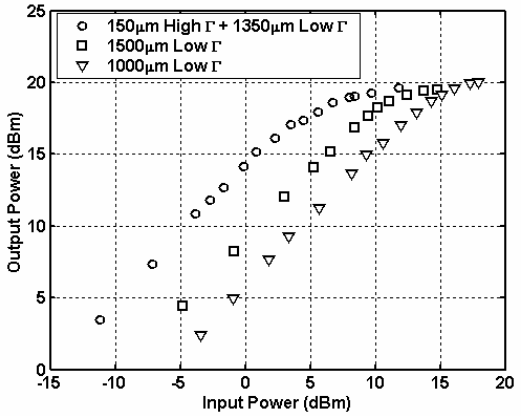

(b)

Fig. 3 *(a) Chip gain versus input power and (b) output power versus input power for SOA devices at 1550nm. The applied current density was 9 kA/cm^2 in the low-Γ o-MQW sections and 20 kA/cm^2 in the high-Γ c-MQW sections.*

SOA and measuring the generated photocurrent. The long length of the SOAs was such that unity internal quantum efficiency could be assumed. The SOA was then forward biased at various current densities and the generated output power and chip gain were determined by the generated photocurrent in an integrated photodiode. The amplified spontaneous emission (ASE) was subtracted out such that it was not included in the output power or gain calculation.

The chip gain versus input power and output power versus input power characteristics are shown for the three SOA types in Fig. 3a and Fig. 3b, respectively. In all figures, the operating electrode current density was 9 kA/cm^2 in the o-MQW regions and 20 kA/cm^2 in the c-MQW regions. As can be seen in Fig. 3, a 1000μm long single section o-MQW device provides 6 dB of gain with a saturation output power of over 20 dBm while a 1500μm long single section device provides over 9 dB of chip gain with a saturation output power of 19.5 dBm. By placing a 150μm c-MQW high gain section in front of a 1350μm o-MQW section, the device gain is increased to nearly 15 dB while maintaining a saturation output power of over 19 dBm at 1550nm. Over 13.5 dB of gain was maintained for wavelengths from 1530 to 1560nm. Based on the results of this experiment, optimum o-MQW section lengths, c-MQW section lengths, and CTL thickness can be determined for improved device gain/saturation characteristics.

Conclusion: In this work we demonstrate high saturation power SOAs fabricated using an integration platform ideal for the monolithic integration of the SOAs with widely-tunable lasers, high performance QW EAMs, and high saturation power photodiodes. The SOAs presented here demonstrate saturation output powers in the 19-20 dBm range and chip gains of nearly 15 dB.

References

1 J. Raring, E. Skogen, S. DenBaars, and L. Coldren, "Demonstration of negative chirp characteristics over wide wavelength range using monolithically integrated SG-DBR laser electroabsorption modulator," *IEEE Electronics Letts*. vol.40, pp. 1599-1600 ,2004

2 E. Skogen**,** J. Raring, S. DenBaars, and L. Coldren, "Integration of High-Gain and High-Saturation Power Active Regions using Quantum Well Intermixing and Offset-Quantum Well Regrowth," *Electron. Lett*., Vol. 40, pp. 993-94, 2004.

3 J. Raring, E. Skogen, C. Wang, J. Barton, S. DenBaars, and L. Coldren, "Quantum well intermixing and MOCVD regrowth for the monolithic integration of 40 Gb/s UTC type photodiodes with QW based components," To be published *IEEE Electronics Letts*. 2005.

4 K. Morito, S. Tanaka, S. Tomabechi, and A. Kuramata, "A broadband MQW semiconductor optical amplifier with high saturation output power and low noise figure". Semiconductor Optical Amplifiers and their Applications Meeting. PD1-1. San Francisco, CA June 30 2004.

5 P. W. Juodawlkis, J. J. Plant, R. K. Huang, L. J Missaggia, and J. P. "High Power 1.5μm InGaAsP-InP Slab-Coupled Optical Waveguide Amplifier*," IEEE Photon. Technol. Letts*. vol. 17, Feb, 2005.

6 K. Morito, N. Ekawa, T. Watanabe, and Y. Kotaki, "High-output-power polarization-insensitive semiconductor optical amplifier", *J. Lightw. Technol.,* vol. 21, no. 1, pp. 176-181, Jan. 2003.

7 E. Skogen, J. Raring, J. Barton, S. DenBaars, and L. Coldren, "Post-Growth Control of the Quantum-Well Band Edge for the Monolithic Integration of Widely-Tunable Lasers and Electroabsorption Modulators," *J. Sel. Topics in Quantum Electron.*, vol. 9, September/October, 2003.

8. J. Raring, E. Skogen, S. Denbaars, and L. Coldren: "A Study of Regrowth Interface and Material Quality for a Novel InP Based Architecture," *Journal of Crystal Growth. vol.* 273/1-2 pp. 26-37 Dec. 2004.

I. Photonic Integrated Circuits (PICs) and Related Technology

B. Widely-Tunable Transmitter PICs

40-GHz Dual-Mode-Locked Widely Tunable Sampled-Grating DBR Laser

L. A. Johansson, *Member, IEEE*, Zhaoyang Hu, D. J. Blumenthal, *Fellow, IEEE*, L. A. Coldren, *Fellow, IEEE*, Y. A. Akulova, and G. A. Fish, *Member, IEEE*

***Abstract*—Generation of 40-GHz alternate-phase pulses is demonstrated using a dual-mode-locked sampled-grating distributed Bragg reflector laser. More than 10-dB extinction and >20-dB sidemode suppression ratio is measured over the >40-nm tuning range of the laser. Based on captured phase noise spectra, the timing jitter is estimated in the 0.35–0.41-ps range. The demonstrated dual-mode laser would form an attractive basis for an integrated 40-Gb/s return-to-zero transmitter.**

***Index Terms*—Dual-mode lasers, integrated optoelectronics, optical communications, optical pulse generation, sampled-grating distributed Bragg reflector (SG-DBR) lasers.**

I. Introduction

HIGH-SPEED optical communications systems with transmission rates of 40 Gb/s have been developed for future wavelength multiplexed high-capacity systems. It has been found that using return-to-zero (RZ) modulation format instead of the nonreturn-to-zero counterpart is advantageous in terms of tolerance to fiber nonlinearity [1] and receiver sensitivity [2]. Usually, transmitters with RZ modulation format require pulse-carving and data encoding. An attractive option is to use a dual-mode-locked laser for optical pulse generation, where two lasing modes are synchronized either by optical or electrical injection of a clock reference. All generated optical power here contributes to the generated pulse train, eliminating the insertion loss unavoidable using a modulator based approach. Further, spectrally compact alternate-phase pulses, also termed carrier suppressed RZ optical pulses, are formed. Although several dual-mode optical sources have been demonstrated for 40-GHz applications [3]–[6], none has to date demonstrated wide wavelength tunability in a monolithically integrated source.

In this letter, we demonstrate a widely tunable dual-mode pulse source based on a sampled-grating distributed Bragg reflector (SG-DBR) laser, integrated with a semiconductor optical amplifier (SOA), producing a 40-GHz clock source over a tuning range exceeding 40 nm. Similar devices have previously been monolithically integrated with a Mach–Zehnder modulator [7], and in an extended perspective, the source described in this letter can be monolithically integrated with a fast Mach–Zehnder modulator to form a widely tunable RZ transmitter for either amplitude or phase encoded pulses. Alternative potential applications include wavelength-agile optical clock recovery [8], or carrier-generation for millimeter-wave analog applications [9].

Manuscript received July 27, 2004; revised October 15, 2004.

L. A. Johansson, Z. Hu, D. J. Blumenthal, and L. A. Coldren are with the Department of Electrical and Computer Engineering, University of California, Santa Barbara, CA 93106 USA (e-mail: leif@ece.ucsb.edu; huby@ece.ucsb.edu; danb@ece.ucsb.edu; coldren@ece.ucsb.edu).

Y. A. Akulova and G. A. Fish are with the Agility Communications, Inc., Santa Barbara, CA 93117 USA (e-mail: yakulova@agility.com; gfish@agility.com).

Digital Object Identifier 10.1109/LPT.2004.840819

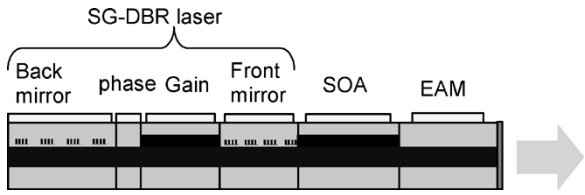

Fig. 1. Device schematic including the SG-DBR laser, semiconductor amplifier, and modulator.

II. Experiment

The device used for this demonstration is a widely tunable SG-DBR laser, integrated with an SOA and an electroabsorption modulator (EAM). A schematic of the device is shown in Fig. 1. The device uses a common bulk quaternary waveguide for all sections. Passive sections, such as modulator and laser tuning sections are defined by selective removal of an offset quantum-well layer. Wide tunability of the laser is achieved by imposing a different periodicity of the comblike reflection spectra of the sampled grating mirrors, such that only one pair of reflection peaks can overlap at a time. A small change in mirror tuning current will allow a different set of reflection peaks to come into alignment, resulting in a large shift in wavelength, i.e., the Vernier effect. A phase section is used for fine alignment of Fabry–Pérot cavity modes with the mirror reflection peaks. An SOA and an EAM are also integrated with the SG-DBR. The former is employed to allow wavelength independent power leveling. The latter could be used for data encoding, but here it is designed for 2.5-GHz operation. More details about the device are given in [10]. Typical performance of an SG-DBR laser integrated with an SOA is more than 20-mW fiber-coupled output power, lower than 2-MHz linewidth, lower than −140-dB/Hz relative intensity noise, and more than 40-dB sidemode suppression ratio over more than 40-nm wavelength tuning range.

The sampled grating mirrors are designed so that only one single stable axial mode can be supported at a time. Mode jumps between cavity modes can be achieved by tuning the phase section of the SG-DBR laser, and unstable operation is observed at the boundary due to mode competition. When the device is used in dual-mode operation for pulse generation, the phase section is reversed biased and will function as a Franz–Keldysh

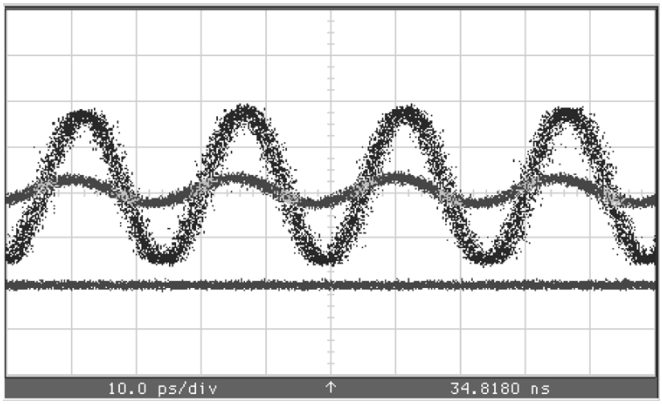

Fig. 2. Captured waveforms showing enhanced small signal modulation at the cavity mode-spacing and single-mode operation, pulse-generation by synchronized dual-mode operation, and the zero level.

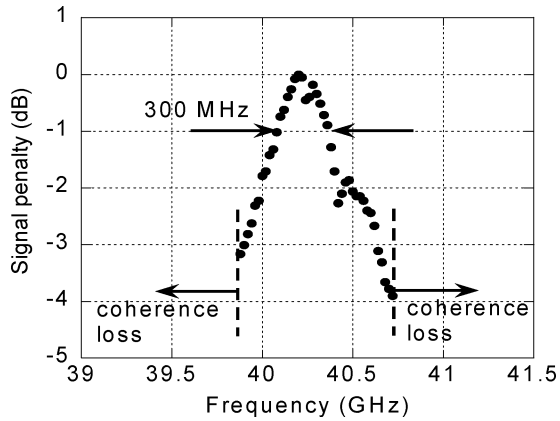

Fig. 3. Measured penalty in generated signal as a function of RF frequency at 1548 nm with 1-dB frequency locking range and synchronization frequency range indicated.

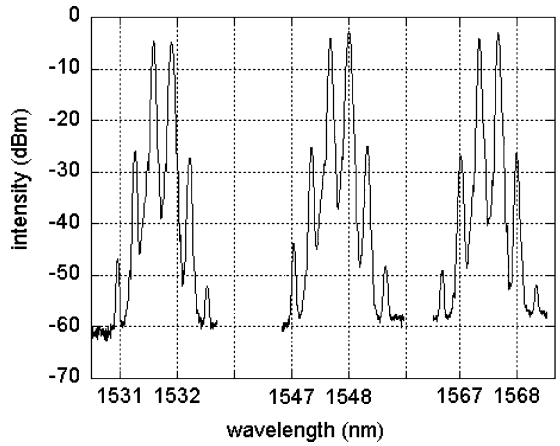

Fig. 4. Captured dual-mode optical spectra at low, center, and high laser wavelength. Resolution bandwidth: 0.08 nm.

modulator, with a higher bandgap than that of the gain section. The phase between the cavity modes is then adjusted by the combination of mirror tuning and gain section tuning. Ideally, a separate modulator section would have to be included in the cavity for improved operation. In an optimized device, front and back mirror sections are also optimized for a wide stable dual-mode operation range, while retaining high sidemode suppression ratio. When injecting a radio-frequency (RF) carrier into the phase section, enhanced small signal modulation is generated if the modulation frequency matches to the cavity mode-spacing, illustrated by the captured oscilloscope trace shown in Fig. 2. After adjusting the phase between two cavity modes, stable dual-mode operation is now achieved and synchronized by the injected RF carrier. The two modes will result in an envelope modulation with high modulation index. An extinction ratio better than 10 dB is estimated from Fig. 2, where the zero-level is limited by the bandwidth of the oscilloscope and the photodetector used to capture the waveform, both specified at 50 GHz. Because the phase section has not been designed for either high-speed or efficient loss-modulation, the required RF power is here large, up to +20 dBm, even to achieve the small modulation depth needed for mode synchronization. In principle, using a modulator section designed for high-speed electroabsorption modulation, a smaller modulation signal is sufficient for pulse generation, compared to that needed when an external optical modulator is used. Because of the asymmetric location of the modulator within the laser cavity, these two modes can be locked at two different phases, corresponding to forward and backward-traveling waves. Even though single phase is observed under most operating conditions, simultaneous dual-mode locking at the two different locked phases can be observed at a balancing point.

III. Results

Mode synchronization is achieved in a narrow frequency range centered on the cavity-mode spacing, in this particular device centered around 40.2 GHz. As the injected RF frequency is detuned, the extinction ratio is reduced and the amplitude balance between the two modes is shifted until dual-mode synchronization is no longer possible, as illustrated by Fig. 3. The 1-dB frequency range is around 300 MHz, and the frequency range with mode-synchronization is 900 MHz.

Dual-mode-locking is possible at any wavelength within the tuning range of the laser. However, after tuning the wavelength, dual-mode operation will need to be reoptimized by a combination of gain and mirror tuning. When tuning the gain section, the resulting shift in cavity phase will first unbalance the power of the two modes and eventually transition to single-mode behavior. The 1-dB gain section tuning range is about 10 mA, sufficiently large for stable long-term dual-mode operation. Fig. 4 shows captured optical spectra for low, center, and high wavelength. In all cases, the sidemode suppression ratio is better than 20 dB. Like other mode-locked lasers where the mode-spacing is defined by the effective cavity length, the range of locking frequencies is determined and limited by device design. The center frequency remains well within the 1-dB frequency range throughout the tuning range of the laser. Similar frequency tolerance was observed with changing chip temperature. The output power variations over the tuning range is consistent to what is observed during conventional single-mode laser operation, the gain and SOA bias held constant.

Fig. 5 shows the captured RF spectrum at 100-kHz frequency span centered around 40.2-GHz signal and reveals the generation of a pure tone with little excess noise. At larger spans some

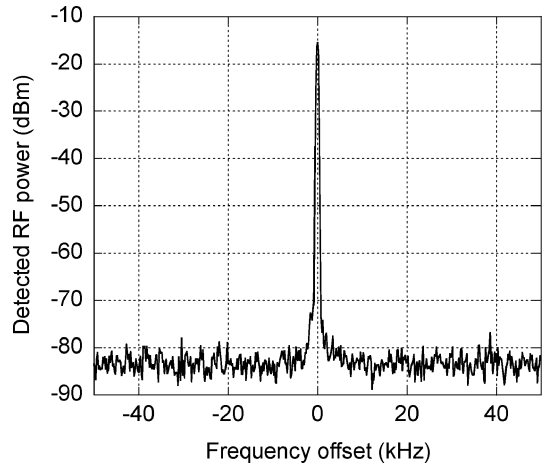

Fig. 5. Detected RF spectrum at 40.2-GHz and 100-kHz span. Resolution bandwidth: 1 kHz.

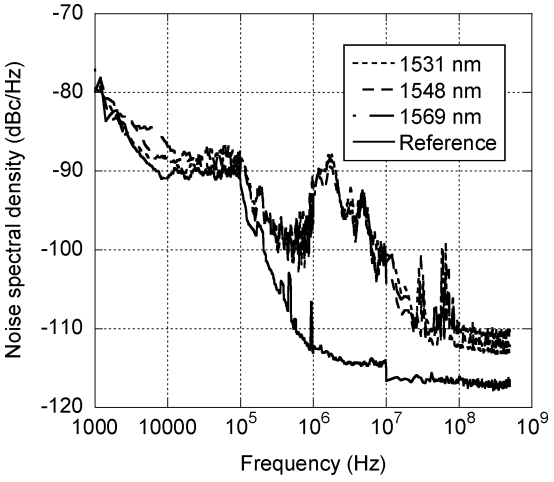

Fig. 6. Detected single-sideband phase-noise spectral density for low, center, and high wavelength, and for the RF reference.

minor noise peaks can be observed in the megahertz (MHz) region. This noise is due to random modulation of laser tuning sections originating from current sources and free-space RF pickup. The magnitude of these noise peaks will be reduced if a shielded package and decoupling capacitors are used. This enhancement of noise in the MHz region can be seen in Fig. 6, where the phase noise spectral densities measured at three wavelengths; 1531, 1548, and 1569 nm are compared to that of the injected RF carrier. The phase noise of the generated signal follows that of the reference down to >100 kHz, after which the excess noise is clearly visible. Integrating the phase noise from 1 kHz to 500 MHz, a total timing jitter of 0.41, 0.35, and 0.38 ps were obtained for 1531, 1548, and 1569 nm, respectively. The timing jitter of the reference was 0.19 ps, obtained in the same manner. Even though the timing jitter obtained from the phase noise spectra does not accurately represent all sources of timing jitter present in a real 40-GHz system, it serves well in giving a comparison to other sources when timing jitter has been obtained in a similar manner.

IV. Summary

For the first time, a monolithically integrated source combining more than 40-nm-wide tunability with 40-GHz pulse-generation is demonstrated. The device consists of an SG-DBR laser where an intracavity EAM is formed by reverse biasing the phase section. Alternate-phase pulses are then generated by locking two cavity modes to an injected 40-GHz RF signal. The extinction ratio is estimated to be better than 10 dB and the sidemode suppression ratio is better than 20 dB throughout the tuning range of the laser. Timing jitter is calculated by integrating phase noise spectra and is in the 0.35–0.41-ps range. Improved jitter performance will be obtained using proper packaging of the device. The robust frequency tolerance to temperature and wavelength variation would enable the design of a practical pulse source for 40- or 43-Gb/s applications with only minor design modifications compared to present devices. Further, the device is readily integrated with high-speed modulators and semiconductor amplifiers, to potentially form a compact, monolithically integrated 40-Gb/s RZ transmitter.

References

[1] R. Ludwig, U. Feiste, E. Dietrich, H. G. Weber, D. Breuer, M. Martin, and F. Kuppers, "Experimental comparison of 40 Gb/s RZ and NRZ transmission over standard singlemode fiber," *Electron. Lett.*, vol. 35, no. 25, pp. 2216–2218, 1999.

[2] P. J. Winzer and A. Kalmár, "Sensitivity enhancement of optical receivers by impulsive RZ coding," *J. Lightw. Technol.*, vol. 12, no. 2, pp. 171–177, Feb. 1999.

[3] C. Bobbert, J. Kreissl, L. Molle, F. Raub, M. Rohde, and B. Sartorius. Novel compact 40 GHz RZ-pulse-source based on self-pulsating phaseCOMB lasers. presented at *Optical Fiber Communication Conf.*. [CD-ROM]Paper WL5

[4] K. Sato, A. Hirano, N. Shimizu, T. Ohno, and H. Ishii, "Dual mode operation of semiconductor mode-locked lasers for anti-phase pulse generation," in *Proc. Optical Fiber Communication (OFC 2000)*, Baltimore, MD, Mar. 7–10, 2000, Paper ThW3.

[5] H. C. Bao, Y. J. Wen, H. F. Liu, and A. Nirmalathas, "Multichannel dual-mode-based optical pulse source from a single laser diode," *IEEE Photon. Technol. Lett.*, vol. 16, no. 3, pp. 894–896, Mar. 2004.

[6] Z. Hu, H. F. Chou, J. E. Bowers, and D. J. Blumenthal, "40-GHz optical pulse generation using strong external light injection of a gain-switched high-speed DBR laser diode," *IEEE Photon. Technol. Lett.*, vol. 15, no. 12, pp. 1767–1769, Dec. 2003.

[7] Y. A. Akulova, G. A. Fish, P. Koh, P. Kozodoy, M. Larson, C. Schow, E. Hall, H. Marchand, P. Abraham, and L. A. Coldren. 10 Gb/s Mach-Zehnder modulator integrated with widely-tunable sampled grating DBR Laser. presented at *Optical Fiber Communication Conf.* [CD-ROM]Paper TuE4

[8] C. Bornholdt, B. Sartorius, S. Schelbase, M. Mohrle, and S. Bauer, "Self-pulsating DFB laser for all-optical clock recovery at 40 Gbit/s," *Electron. Lett.*, vol. 36, no. 4, pp. 327–328, Feb. 2000.

[9] D. Wake, C. R. Lima, and P. A. Davies, "Optical generation of millimeter-wave signals for fiber-radio systems using a dual-mode DFB semiconductor laser," *IEEE Trans. Microw. Theory Tech.*, vol. 43, no. 9, pp. 2270–2276, Sep. 1995.

[10] Y. A. Akulova, G. A. Fish, P. C. Koh, C. Schow, P. Kozodoy, A. Dahl, S. Nakagawa, M. Larson, M. Mack, T. Strand, C. Coldren, E. Hegblom, S. Penniman, T. Wipiejewski, and L. A. Coldren, "Widely tunable electroabsorption-modulated sampled grating DBR laser transmitter," *IEEE J. Sel. Topics Quantum Electron.*, vol. 8, no. 6, pp. 1349–1357, Nov./Dec. 2002.

Wavelength-Tunable Receiver Channel Selection and Filtering Using SG-DBR Laser injection-Locking

L.A. Johansson and L.A. Coldren
Department of Electrical and Computer Engineering, University of California, Santa Barbara, CA 93106.
Tel: (805) 893 8489, Fax: (805) 893 4500, Email: leif@ece.ucsb.edu

Abstract: An injection-locked SGDBR laser is used for wavelength-tunable receiver channel selection and filtering. Successful phase tracking of a 2Gbps DPSK modulated signal at 10 GHz channel spacing was achieved.

OCIS codes: (060.1660) Coherent communications; (060.5060) Phase modulation; (140.3600) Lasers, tunable; (140.3520) Lasers, injection-locked.

1. Introduction

Coherent techniques and systems for optical communications have traditionally been considered due to increased receiver sensitivity, compared to conventional intensity modulation -direct detection (IMDD) optical transmission. With the introduction of the erbium-doped fiber amplifier (EDFA), most interest for coherent optical transmission consequently waned, as nearly all optical transmission needs could now be satisfied using IMDD links. However, during the recent years there has been a renewed interest in coherent techniques, mainly driven by the improved fiber transmission properties of high bit rate phase modulated coding schemes, e.g. DPSK, QPSK and related. Another area where coherent coding schemes can be of benefit is increased spectral efficiency, where using multilevel modulation formats can either increase channel bit rate, or lead to closer channel spacing.

Even considering recent interest in coherent modulation techniques, further benefits, and greater challenges arises when an optical communications system fully taking advantage of coherent techniques is considered. Drawing a parallel with aspects of the development of radio and wireless systems; optical communications have much to catch up with in order to reach a comparable functionality in terms such as efficient use of spectral resources, frequency agility, multiple access, efficient multiservice usage and secure transmission. These are aspects that will be relevant for applications like multifunctional optical systems, sharing analog/digital communication, sensing applications and other functions. Particular areas where coherent techniques can contribute are exact wavelength and band-limited channel forming, agile and high precision channel selection and filtering and wavelength conversion of phase or frequency modulated signals, all operating in a highly dynamic optical environment. One interesting note is that the originally most interesting aspect using coherent techniques; receiver sensitivity is still offset by the availability of optical amplification, most recently SOA-preamplified receivers.

In this paper, a channel selection scheme is proposed and demonstrated where optical injection locking of a widely tunable laser can be used to pick out a phase-modulated signal in a closely-spaced WDM environment. Although not investigated in this paper, this technique, combined with ns wavelength switching [1], can be used in a fast frequency-hopping optical communications scheme where secure communications are of importance.

2. Channel selection scheme

In the proposed channel selection scheme, an optical signal, consisting of several closely-spaced wavelength components, is injected into a semiconductor laser, illustrated by the schematic in Fig. 1. The laser will track the frequency and phase of any signal falling within the injection locking-range of the laser, and reject any signal falling outside. By using a widely tunable sampled-grating (SG) DBR laser, the laser will be able to pick out any wavelength window within typically a 40nm wavelength tuning range. Using this channel selection scheme, the out-of-channel rejection ratio has been theoretically and experimentally investigated for CW multiline injection [2]. It is found that only closely-spaced wavelength channels will cause significant channel crosstalk.

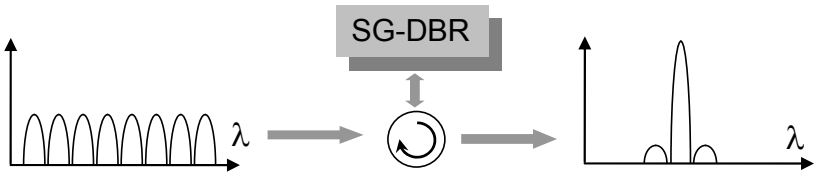

Fig. 1: Schematic of channel selection and filtering scheme.

If the injected signal is being phase or frequency modulated, the injection locked-laser will track any modulation falling within a bandwidth determined by the injection locking range. A more precise expression for the phase-tracking capabilities of an injection-locked laser is given in [3].

Further, by using injection-locking for wavelength stabilization, an SG-DBR laser has been used to demonstrate switching times in the ns-range [1]. Combined with the above capabilities, a multifunctional device is obtained that simultaneously can track, filter and amplify a channel-hopping optical signal with moderate bandwidth phase or frequency encoding. For this vision to be realized, careful control of the laser free-running wavelength and injection ratio need to be implemented as indicated by the results presented below. One technique to stabilize the free-running wavelength would be combining optical injection-locking and an optical phase-lock loop, as described in [3].

3. Experimental verification

To verify the principle, an SGDBR laser with a tuning range exceeding 40 nm, integrated to an optical amplifier and electroabsorption modulator, is used for injection-locking. More details about the device are found in [4]. Figure 2a shows the CW injection locking characteristics of the SGDBR laser, including locking range and areas within the locking range where chaotic or resonant behavior is observed. In these following experiments, the injection ratio with the widest stable locking range is used; between -25 dB to -20 dB.

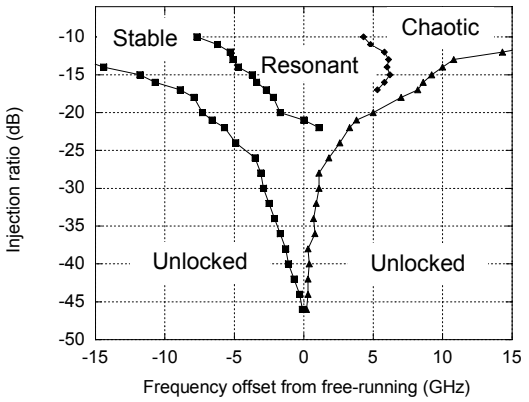

Fig. 2a: SGDBR laser injection locking characteristics.

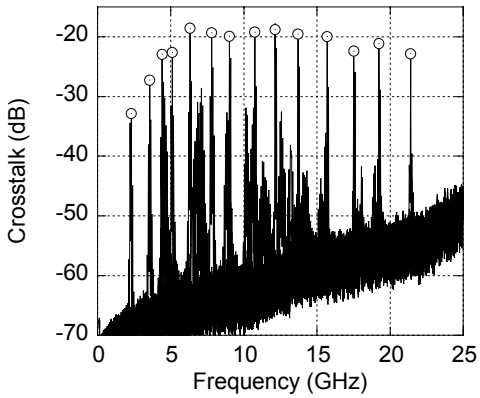

Fig. 2b: Channel crosstalk values at different channel spacing.

The neighboring channel-rejection ratio is experimentally investigated by injecting two CW optical wavelengths with equal power corresponding to -23dB injection ratio each into the SG-DBR laser. The laser output is then detected and the beat between the main locked line and interfering line is displayed using a spectrum analyzer. The channel-rejection ratio is defined as the resulting power ratio between the selected channel and the rejected channel and is calculated based on the power of the detected beat-signal and the optical received power. The result is shown in Fig. 2b, where the crosstalk, calculated from multiple spectrum analyzer traces, is shown. With closer channel spacing, a weak trend of increasing values of crosstalk is observed down to the laser resonance frequency, 7 GHz, below which the crosstalk is dropping rapidly, more rapidly than predicted compared to the analysis in [2]. The difference can be partly attributed to increased instability and appearance of harmonics at these lower frequencies. The spurious, unmarked peaks seen in the overlapped spectra are harmonics that appears when the channel spacing is lower than the resonance frequency of the laser.

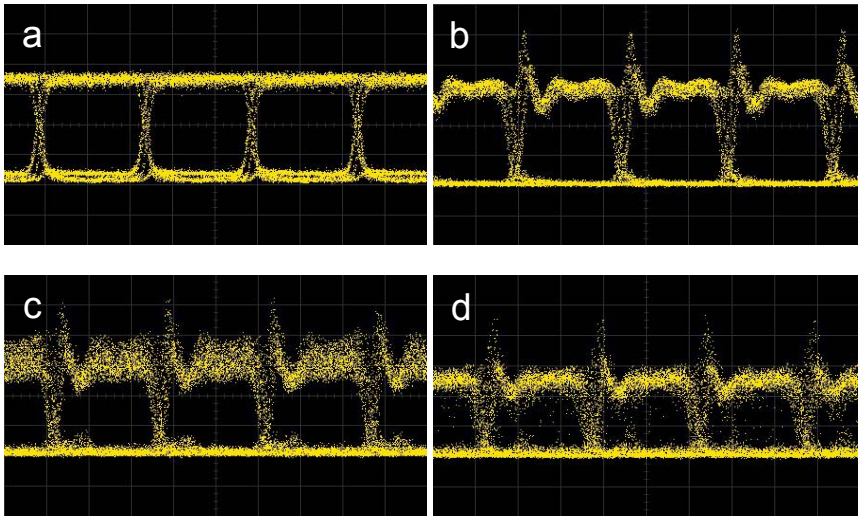

Fig. 3: Captured demodulated eye diagrams for a: back-to-back, b: single channel injection, c: dual channel injection, 10 GHz spacing and d: dual channel injection, 5 GHz spacing

In order to investigate the viability using the channel-selection scheme to select a modulated input, a 2Gbps DPSK modulated signal was generated using push-pull modulation of a Mach-Zehnder modulator. The bit-rate was selected to match the fiber-delay line DPSK demodulator used. Figure 3a shows the back-to-back demodulated eye diagram. Injecting the modulated signal into the SG-DBR laser, the phase of the injection-locked laser will track that of the injected signal, as evident by the recovered eye after injection, shown in Fig. 3b. The resonance in the demodulated eye matches that of the laser. Figure 3c and 3d shows demodulated eyes when an interfering channel is added just above resonance, at 10GHz offset, and just below resonance frequency, at 5GHz offset. A slight degradation in SNR, mainly due to more critical stable locking range, can be seen in the eye at 10 GHz channel spacing, though not sufficient to prevent error-free operation. At 5 GHz spacing, further degradation of the eye is observed, both in terms of added SNR and increased distortion, as expected by the increased distortion below resonance frequency seen in Fig. 2b.

Viewed from a tunable optical filter perspective, the injection-locked laser has the advantage of having adjustable filter bandwidth in the form of varying locking-range with injection ratio, such that varying channel spacing can be dynamically adjusted for by regulating injection ratio and laser bias point, for optimum resonance frequency. In combination with the potential for faster wavelength switching than most optical filters, this results in a highly flexible tool for optical channel selection. One limitation is the inability to track amplitude modulation, which will interfere with successful phase tracking. A second limiting factor is the high degree of required control that the high degree of flexibility brings. Free-running wavelength, injection ratio and laser bias must be adjusted for optimal phase tracking. In these experiments, BER testing was not possible due to a combination of master and slave laser wavelength wandering and demodulator drift. By using optical injection in combination with a simple optical phase-lock loop [3], and using a more stable commercial demodulator the system stability should improve.

4. Conclusion

We successfully used optical injection locking of an SG-DBR laser to select and track a 2 Gbps DPSK modulated optical signal. Open eye diagrams were obtained both for single injected optical channel and dual injected channels at 10 GHz offset. Based on obtained data, one interesting prospect would be the selection and tracking of a well-filtered 10 Gbps DPSK modulated signal at 10 GHz channel spacing. A second promising prospect is the application in a rapidly frequency hopping secure communications scenario, using fast wavelength switching techniques.

5. References

[1] C.C. Renaud, *et al, IEEE Photon. Technol. Lett.,* Vol. 16, pp: 903– 905, March 2004 .
[2] B. Cai, *et al, J. Lightwave Technol.*,Vol. 21, pp:3029- 3036, Dec. 2003.
[3] L.A. Johansson, *et al, J. Lightwave Technol.*, Vol: 21, pp: 511-520, Feb. 2003.
[4] Y. A. Akulova, *et al, IEEE J. Selec. Top. in Quantum Electron.*, 8, 1349-1357, Nov/Dec 2002.

Novel Segmented Cascade Electroabsorption Modulator with Improved Bandwidth-Extinction Product

Jonathan T. Getty, Leif A. Johansson, Larry A. Coldren
ECE Department, Univ. of California, Santa Barbara, 93106
Tel: (805) 893-7163; Fax (805)893-4500; Email: beans@mrows.org

Abstract: A new configuration for electroabsorption modulators is presented and demonstrated. Compared to a conventional device of the same length, a three-stage cascaded modulator triples the RC-bandwidth while maintaining the same extinction and insertion loss.

OCIS codes: (130.0250) Optoelectronics, (230.4110) Modulators

1. Introduction

Standard lumped-element Electroabsorption Modulators (EAMs) are the workhorse of InP integrated modulation, due to their simple operation and small size. A short length of passive waveguide is appended to a laser [1] or other photonic circuit, and driven with a variable negative voltage. A voltage-dependent Franz-Keldysh absorption, similar to that shown in Fig. 1, modulates the optical input.

A large digital extinction ratio can be achieved either by swinging a large voltage, biasing at a more negative voltage, or using a longer modulator. While the first solution may be practical (up to a point!) in some applications, it can be very difficult to generate a large voltage on-chip in integrated circuits, as will be discussed below.

Setting a more negative bias causes unavoidable, and often severe, insertion loss, necessitating high-power pre-amplifiers with large power budgets and heating problems. Lengthening the modulator proportionally increases the extinction ratio (and the insertion loss, emphasizing the importance of a low bias), but increases the area and capacitance across the depletion region of the reverse-biased EAM diode. While this is an acceptable (and common) tradeoff at modest bit-rates, the diode capacitance becomes a serious consideration for 10GHz and higher bandwidths, although diode capacitance can be reduced with clever doping and epitaxial schemes [2]. This capacitance is typically driven either by a 50Ω RF driver, or an on-chip voltage created by limited photocurrent across a resistor [3]; in either case, the resultant RF circuit is a low-pass RC filter.

Finally, while traveling-wave modulator structures can be used to enhance the bandwidth of InP modulators [4], fundamental limitations, such as impedance matching and junction RF-loss limits both the maximum useful electrode length and overall available improvement in performance.

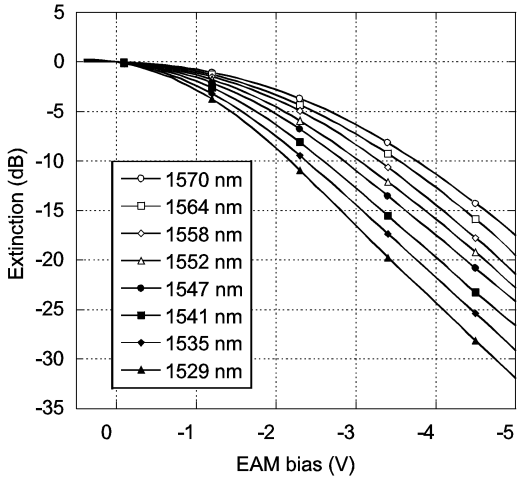

Fig.1. Voltage and wavelength dependence of a typical EAM. A larger extinction is achieved with a large voltage swing, or a more negative bias, with high insertion loss.

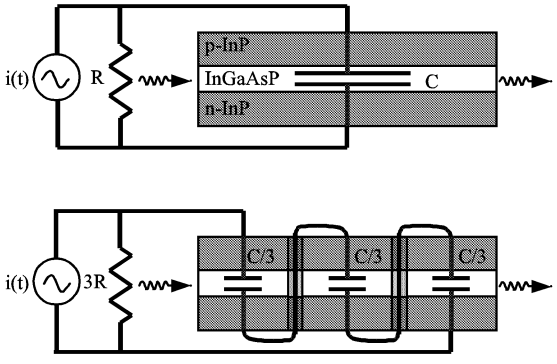

Fig. 2. RF Equivalent circuit of a conventional EAM (above), and a 3-stage segmented cascade EAM (below) of the same total length. Adjacent sections are electrically isolated by ion implantation.

2. Operating principle

This paper proposes and demonstrates that the EAM can be extended to much higher bandwidths with the configuration shown in Fig. 2. A single EAM waveguide is divided into N

electrically disconnected sections, which are then wired in series. It can be seen that for a modulator of fixed length, each stage will have capacitance C_0/N (where C_0 is the capacitance of the unsegmented modulator), and the assembly will have capacitance C_0/N^2. The N-stage EAM will require N times the voltage (or N times the length) to achieve the same extinction ratio as the unsegmented modulator; if the voltage is increased by driving a proportionally larger resistor, bandwidth will still increase a factor of N. Alternatively, if N sections of constant section length each is series-connected, the modulation voltage will remain approximately the same, but with an N-fold increase in bandwidth. Table 1 summarizes the extinction and bandwidth for two different segmentation schemes, comparing them to a single-section conventional device.

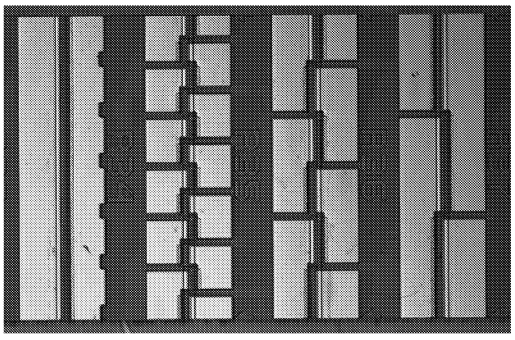

Fig. 3. Micrograph of a 600 μm-long bar of devices. From left, 1-stage control (R34), 12 -stage (R35), 6 -stage (R36), and 3 -stage (R37) cascaded devices are shown.

Number of Stages	Capacitance per Stage	Total Capacitance	Series Resistance	RC Bandwidth	Extinction Ratio
1	C	C	R	$B \equiv 2\pi/RC$	ER
N	C/N	C/N^2	R	BN^2	ER/N
N	C/N	C/N^2	NR	BN	ER

Table 1. Summary of scaling in the conventional (1 stage) and cascade EAM, with and without increased resistance

It is interesting to note that the series-connected device design requires current conservation: the photocurrent, i.e. the absorbed optical power, must be evenly distributed over each section such that the power handling of a segmented EAM is improved compared to a single section modulator, where most of the absorption is taking place close to the front end of the modulator. If uniform voltage distribution is required, instead of using a single load resistor, each modulator segment must be connected in parallel with a separate load resistor, adding up to the total required load.

3. Experimental verification

To verify the principle, segmented EAM's and single-stage control modulators were fabricated side-by-side using a mask and process borrowed from segmented laser design.[5] A passive InP ridge waveguide was fabricated atop an insulating substrate; H^+ and He^+ are implanted from the surface through to the substrate, creating insulating planes that isolate adjacent regions better than 400kΩ. Adjacent contacts are series-connected as shown in Fig. 3; the large, capacitive Au interconnects are unnecessary, but lower the bandwidths to values we can more easily measure. Finally, the material was cleaved into 600μm bars, soldered to a submount, and wire-bonded to its contacts.

Modulation bandwidth and extinction characteristics were characterized using a broadband optical source to cancel out modulator Fabry-Perot effects arising due to straight, uncoated facets. Fig. 4 shows the extinction for one and three stage modulators of 600μm total length. As expected, three times the voltage is needed to achieve, in three series-connected diodes, the same absorption as the control.

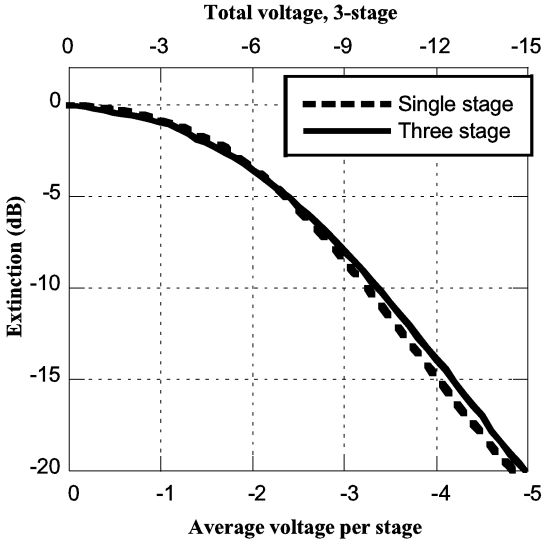

Fig. 4. DC Extinction vs. Voltage for single-stage conventional and three-stage cascaded EAM's. The voltages across the three-stage modulator balance so that each generates the same photocurrent.

However, the three-stage modulator has nine times the bandwidth of the control, as shown in Fig. 5. If the larger RF signal needed to drive the three-stage EAM is achieved by tripling the resistance, the bandwidth is still increased by a factor of three, as shown by the dashed line. Higher-bandwidth EAM's fabricated by increasing the dielectric thickness under the pads, appear to demonstrate bandwidths over 20GHz, but are limited by the probing technology. We hope to report on these, and more advanced, integrated modulators at the conference.

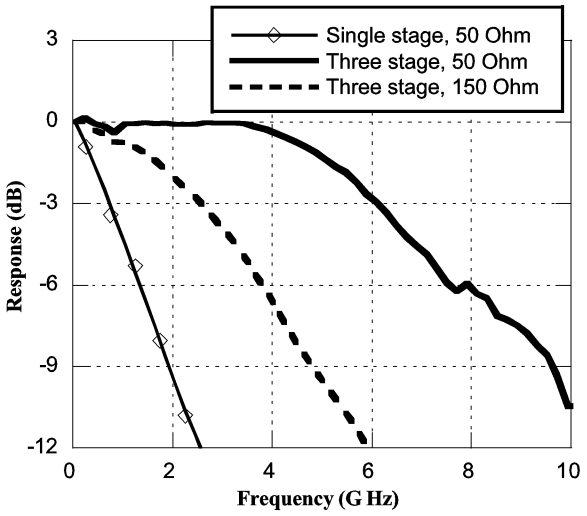

Fig. 5. Bandwidth measurements for conventional and cascaded EAM's. When the three-stage modulator is driven by a current across 150Ω, it has the same extinction characteristic as a single-section across 50Ω. Thus, the bandwidth is improved at no cost to extinction.

4. Conclusions

We have described the first demonstration of a segmented cascade EAM, allowing modulator bandwidth to be increased without sacrificing extinction or insertion loss. The division of a modulator into three segmented stages improved the bandwidth as predicted, with no apparent side effects. While we make no claim to have made a record-breakingly fast modulator, the segmented cascade can enhance nearly *any* EAM, and represents a much easier way to triple performance than epitaxial or other optimizations.

5. References

1. A. Ramdane, A. Ougazzaden, F. Devaux, F. Delorme, M. Schneider, J. Landreau, "Very simple approach for high performance DFB laser-electroabsorption modulator monolithic integration," *Electronics Letters,* **30**, pp.1980-1 (1994).

2. J.W. Raring, E.J. Skogen, L.A. Johansson, J.S. Barton, M.L. Masanovic, L.A. Coldren, "Demonstration of Widely Tunable Single-Chip 10-Gb/s Laser-Modulators Using Multiple-Bandgap InGaAsP Quantum-Well Intermixing," *IEEE Photon. Technol. Lett.,* **16**, 1613-15 (2004).

3. R. Lewén, S. Irmscher., U. Westergren, L. Thylén and U. Eriksson,"Traveling-wave electrode electroabsorption modulators toward 100 Gb/s," in Optical Fiber Communication Conference on CD-ROM (Optical Society of America, Washington, DC, 2004), Paper FL1 (2004).

4. G.L. Li, C.K. Sun, S.A. Pappert, W.X. Chen, P.K.L. Yu, "Ultrahigh-speed traveling-wave electroabsorption modulator-design and analysis," *IEEE Trans. Microwave Theory and Techniques*, **47**, 1177-83 (1999).

5. J.T.Getty, E.J. Skogen, L.A. Johansson, L.A. Coldren, "CW operation of 1.55μ m bipolar cascade laser with record differential efficiency, low threshold, and 50Ω matching," *IEEE Photonics Technology Letters*, 15, 1513-15 (2003).

Proc. Integrated Photonics Research and Applications 2005, paper no. IWF4, San Diego, CA (April 11-15, 2005)

Monolithic integrated tunable transmitters

Y. A. Akulova, G. A. Fish, H. Xu, E. Hall, M. C. Larson, P. Abraham, H. Marchand, C. Turner, C. Coldren, E. Hegblom, T. A. Strand, and L. A. Coldren
Agility Communications, Inc., 475 Pine Ave, Santa Barbara, CA 93117
yakulova@agility.com

Abstract: Monolithic widely-tunable transmitters are key enablers in reducing the component size, power consumption, and simplifying DWDM network provisioning. We discuss design and performance of monolithic transmitters based on SGDBR laser and electroabsorption or Mach-Zehnder modulators.

OCIS codes: (250.5300) Photonic integrated circuits; (140.5960) Semiconductor lasers; (140.3600) Lasers, tunable

1. Introduction

A compact, high-performance widely-tunable integrated laser/modulator chip is a key component of a tunable transmitter that can dramatically lower the barriers to deployment and operation of high capacity DWDM networks. Optical networking applications for tunable, modulated, lasers range from one time wavelength provisioning and sparing to dynamic wavelength provisioning in re-configurable optical add/drop multiplexers, photonic cross-connects, and all-optical regenerators. Transmitters with full band coverage (C or L) enable wavelength-agile networking concepts in addition to simplifying provisioning and inventory control. Telecom applications impose stringent requirements on transmitter tuning range, wavelength stability, output power, side-mode suppression ratio (SMSR), linewidth, extinction ratio, chirp, tuning speed, and reliability. The application of monolithic tunable transmitters will be limited unless all of the requirements listed above are met.

In this paper, we present details of the design and performance characteristics of widely-tunable monolithic optical transmitters based on Sampled-Grating Distributed Bragg Reflector (SG-DBR) laser integrated with Semiconductor Optical Amplifier (SOA) and electroabsorption (EA) or Mach-Zehnder (MZ) modulators. We demonstrate that these chips fabricated using simple manufacturable offset quantum well technology meet stringent system requirements across 40 nm wavelength range at 2.5 and 10 Gb/s.

2. Device design

As illustrated in Fig. 1, the device consists of a four-section SG-DBR laser, an SOA, and an EA or MZ modulator, all integrated on the same InP chip. The SG-DBR laser includes gain and phase sections positioned between two "sampled grating" distributed reflectors. This laser architecture described in details in [1] utilizes Vernier enhanced current injection tuning mechanism and combines the advantages of wide tuning range (>40 nm), fast tuning (a few tens of nanoseconds), and simplicity for integration with other components. For optical networking applications, lasing on an absolute discrete frequency grid is achieved through calibration at the time of assembly. Employing an integrated SOA for power control allows the gain section current to be held constant across channels, allowing the laser to be biased far enough above threshold to ensure adequate spectral properties and also eliminating a source of parasitic thermally-induced wavelength tuning. The SOA also allows for additional functionality, such as variable optical attenuation (VOA) and beam blanking during wavelength switching.

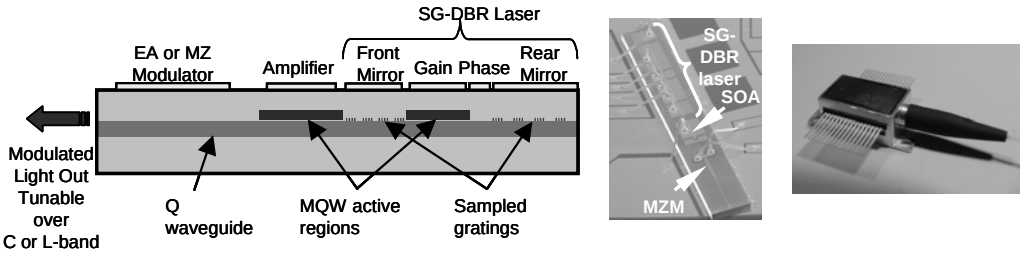

Fig. 1. Schematic crossection of an SG-DBR laser integrated with SOA and EA or MZ modulator; SEM of an SGDBR-SOA-MZM chip mounted on ceramic carrier, and optical image of a packaged integrated optical transmitter.

The chip-scale integration of a widely tunable SG-DBR laser with an SOA and a modulator is accomplished using the same offset quantum-well structure and fabrication technology as used for manufacturing of an SG-DBR alone. In this simple integration technology the active region of the modulator uses the same bulk quaternary waveguide as the tuning sections of the laser. The composition, doping, and thickness of the bulk waveguide can be optimized to achieve high tuning efficiency for the laser and a target extinction ratio for EAM or desired V_π for MZ modulator over the wide spectral bandwidth. The footprint of the monolithic transmitter chip is compatible with packaging into standard hermetic butterfly module (Fig. 1) or transmitter optical subassembly (TOSA).

3. Performance characteristics

Figure 2a) presents typical CW characteristics of an SGDBR-SOA chip. The output power in excess of 80 mW and SMSR better than 40 dB can be maintained across 40 nm tuning range. For the EA-integrated devices modulated time-averaged powers in excess of 5 dBm and *RF* extinction ratios > 10 dB across a 40 nm tuning range have been achieved (Fig. 2b). Fig. 3 shows filtered back-to-back eye diagrams and bit-error-rate (BER) characteristics for several representative channels across the C-band at 2.5Gb/s. Error-free transmission at 2.5 Gb/s has been demonstrated for 350 km of standard single mode fiber. This transmission distance is limited by transient chirp of the bulk EA modulator which remains slightly positive at the used operating conditions.

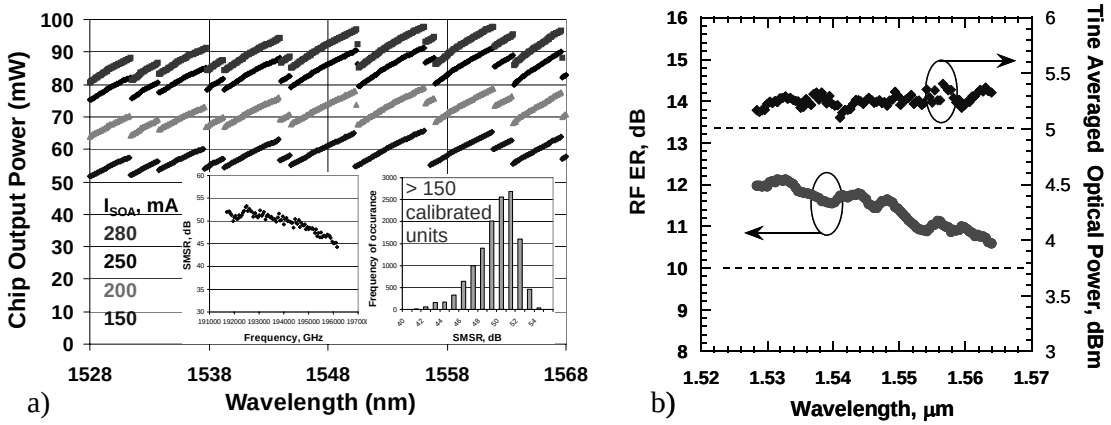

Fig. 2. a) Output power of SG-DBR-SOA chip at several SOA currents; gain section current is 150 mA. The inserts show SMSR as a function of lasing frequency measured with 0.1 nm resolution bandwidth and distribution of SMSR measured for more than 150 calibrated tunable transmitters. b) RF ER and time-averaged fiber-coupled output power for EAM modulated transmitter at 2.5 Gb/s.

The output power vs. wavelength for an SGDBR-SOA-MZM chip is shown in Fig. 4a). For this measurement the nominally π-phase shifted MZM is biased to produce differential phase shift of 0 radians between the two arms. The integrated chips are capable of producing more than 20 mW of power across 40 nm tuning range in the C-band. The insert in Figure 4a) shows normalized transfer function for a packaged SG-DBR-SOA-MZM chip at three wavelength across C-band. DC ER in excess of 20 dB is achieved with less than 3.3 V. The key for achieving uniform transmission performance of the integrated SG-DBR-SOA-MZM transmitter over wide wavelength range is in eliminating optical and electrical crosstalk and precise control of the transient chirp of the modulator. For a π-shifted MZM the dual-drive condition results in "zero" chirp configuration, while single-ended operation results in "negative" chirp. In single-ended drive configuration RF ER of 12 dB was measured across 40 nm tuning range with less than 4 V peak-to-peak modulation voltage (Fig. 4b). The output eye diagrams at 10 Gb/s shown in Figure 5a) pass mask test with 10% margin. The BER data presented in Fig. 5b) for three representative channels shows error free transmission for 1600-1800 ps/nm dispersion for 1535-1563 nm wavelength range.

4. Summary

In summary, widely-tunable SG-DBR lasers are well-positioned for next generation DWDM transmission systems. Compared to their fixed-wavelength counterparts, they exhibit comparable performance characteristics and reliability, with the additional functionality of full band coverage tunability. Simple, robust manufacturing technology has been developed for integration of widely-tunable SG-DBR lasers with SOAs and modulators. The

monolithic widely tunable transmitter chips meet stringent system requirements at 2.5 and 10 Gb/s. The developed chip-scale integration technology is compatible with further enhancement of the performance characteristics (power, tuning range, bit rate) and provides essential building blocks to realize various photonic circuits with increased functionality.

5. References

[1] V. Jayaraman, Z.-M. Chuang, L. A. Coldren, "Theory, Design, and Performance of Extended Tuning Range Semiconductor Laser with Sampled Grating", *IEEE J. of Quantum Electron*., 29, pp. 1824 –1834, 1993.

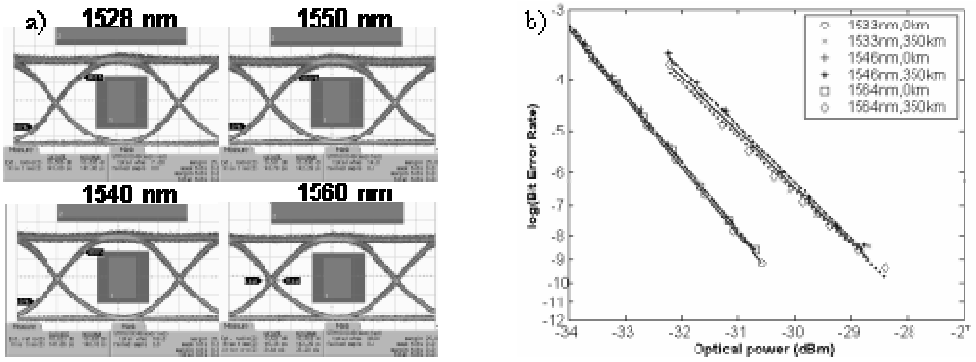

Fig. 3. a) Output eye diagrams of SG-DBR-EAM optical transmitter for several representative wavelength channels at 2.5Gb/s (PRBS 2^{31}-1); overimposed is SONET mask with 25% margin. b) BER curves measured BtB and after 350 km of standard single mode fiber.

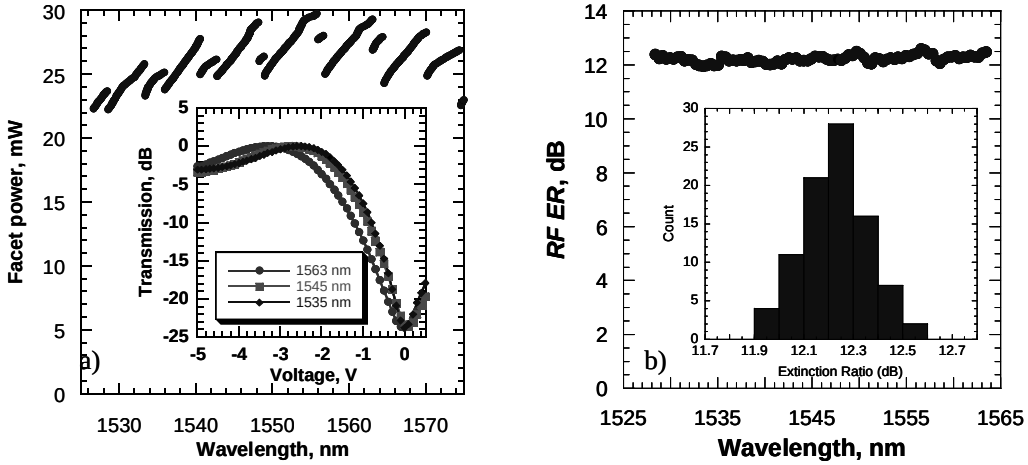

Fig. 4. a) Output power of an SGDBR-SOA-MZM chip as a function of wavelength; the insert shows normalized MZ transfer function at three wavelength. b) RF ER at 10 Gb/s as a function of wavelength measured for 88 ITU channels.

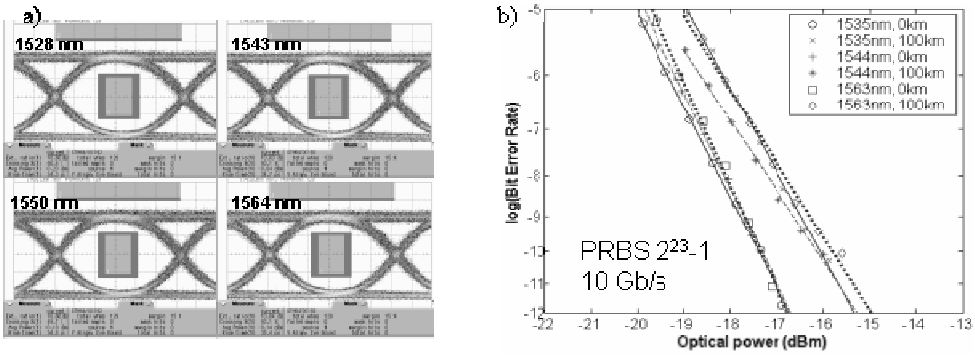

Fig. 5. a) Output eye diagram of an SGDBR-SOA-MZM transmitter at 10 Gb/s. b) BER curves measured BtB and after 100 km of standard single mode fiber.

Proc. Integrated Photonics Research and Applications 2005, paper no. IMC1, San Diego, CA (April 11-15, 2005)

Integration techniques for InP-based high-functionality photonic integrated circuits (Invited)

Milan L. Mašanović, Jonathon S. Barton, Vikrant Lal, Matthew N. Sysak, James W. Raring, Erik J. Skogen, Daniel J. Blumenthal, Larry A. Coldren
Electrical and Computer Engineering and Materials Departments, University of California Santa Barbara, USA
mashan@ece.ucsb.edu

Abstract: High-performance photonic integrated circuits require flexible yet robust integration platforms. In this paper, we discuss issues related to various integration platforms and techniques in InP used at UC Santa Barbara. These platforms include the traditional offset quantum well approach as well as novel integration methods using quantum well intermixing or dual quantum wells. Testing results of some of out latest devices are presented, including a tunable all-optical wavelength converter operating at 40 Gbps RZ, tunable Mach-Zehnder modulator transmitter operating at 40 Gbps NRZ, and a photocurrent-driven tunable wavelength converter operating at 10 Gbps NRZ.

OCIS codes: (250.5300) Photonic integrated circuits; (230.5590) Quantum-well devices;

1. Introduction

With ever increasing requirements for high performance, high reliability, low cost optical network modules that execute complex optical network functions, it is becoming increasingly difficult to fulfill all the demands without reverting to photonic integration and photonic integrated circuits (PICs). The primary objectives of optoelectronic and photonic integration are similar to those of electronic integration: enhancing the performance, reliability, robustness and increasing the functionality while lowering the manufacturing cost. Integrated optical components rely on both the optical and electronic properties of their constituent materials and they critically depend on heteroepitaxially grown material with accurately controlled composition and dimensions to achieve optimum performance. While the feature sizes of most photonic integrated circuits are still on a scale of a micrometer, which is a factor of 10 above the limits of standard fabrication processes used in electronic integration, the main challenge in photonic integration comes from the fact that in their most versatile form, PICs are built up from components that are fundamentally different in functionality: light emitters, passive waveguides, modulators and detectors. Each of these different components in principle requires a differently optimized material heterostructure to achieve the desired maximum performance. Growth techniques like butt-joint growth (BJG) [1] can address the issue of separate component optimization, at the expense of growth and fabrication process complexity, yield, and ultimately cost. Therefore, other integration platforms are of interest, where post-growth control of the semiconductor bandgap is possible.

2. Integration platforms in InP

A basic photonic integration platform needs to allow for design and fabrication of at least three different waveguide types: optically-active waveguides, passive interconnect waveguides and grating-containing waveguides. In a more complex platform, several different active sections may be required (for example, for separate optimization of the laser gain section and the optical amplifiers), as well as different passive sections that could be used for photonic interconnection components (low loss) or optical modulators (high controllable absorption/index change). Integrating a (tunable) laser on the same chip poses significant challenges on its own. The design requirements are for a laser that does not utilize a facet reflection to form a cavity. Another challenge to consider is the suppression of coherent reflections into the laser which can be detrimental for the chip performance.

Various photonic integration platforms in InP material system have been reported in the past. Those include BJG [1] and selective area growth (SAG) [2] based platforms. Our work at UC Santa Barbara has traditionally been focused around a simple offset quantum well integration platform [3] (Figure 1 (a))., where the multiple quantum well active region is located on top of an InGaAsP waveguide, and can be selectively removed using wet chemical etching. Devices of various complexities have been successfully

fabricated at UCSB over time using this platform, including Sampled-grating DBR tunable lasers, which have been commercialized. Lately, tunable transmitters operating at 40 Gbps [4] and tunable all-optical and photocurrent-driven wavelength converters [3,5-7] operating at speeds up to 40 Gbps have been demonstrated using this platform (Fig. 2 and 3).

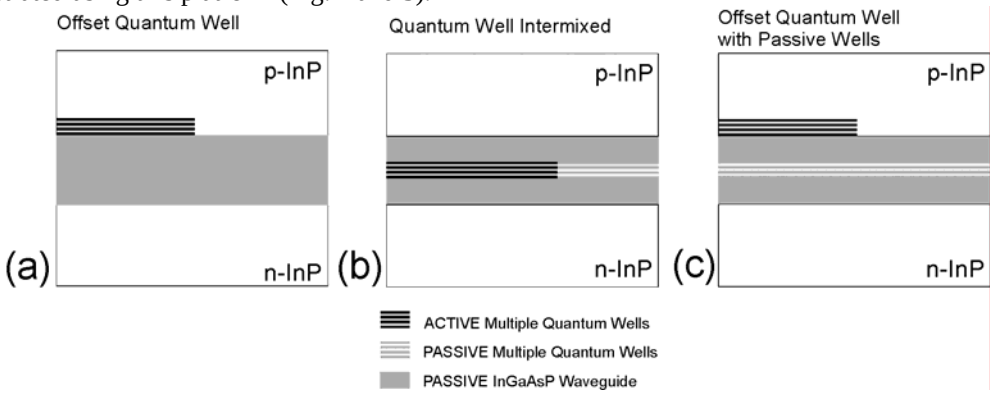

Fig. 1. Different photonic integration platforms for high-functionality integration (a) Offset quantum well (b) Quantum well intermixed (c) Offset quantum well with passive wells

Recently, quantum well intermixing (QWI) has emerged as a powerful new fabrication process for post growth band edge control in photonic circuit integration [8]. Applicable to quantum well-based active regions, this process achieves intermixing of the quantum wells with the barriers to increase the bandgap of the quantum well region and make it non-absorbing. The mechanism of intermixing is based on the fact that quantum wells represent an inherently metastable system due to a large concentration gradient of atomic species at the quantum well/barrier interface. To increase the intermixing process efficiency, the surface of a semiconductor is implanted with impurities or phosphorus (to create vacancies) [8], and those are thermally propagated through the quantum well active region of the wafer. The impurities/vacancies cause the redistribution of atoms from the quantum wells and barriers, effectively raising the band edge, and rendering the material transparent. Using phosphorus-enhanced intermixing, at UCSB we have demonstrated that by controlling the diffusion length of the vacancies, it is possible to create multiple bandgaps on the wafer [9]. Initial concerns existed about the device reliability due to the impurity and defect introduction, however, studies have shown that no significant differences in device lifetimes exist, and this technology has been commercialized as well [8]. At the moment, QWI integration platforms in InP seem to offer the best tradeoffs in terms of the device design flexibility and process complexity. Devices like tunable transmitters, tunable photocurrent-driven (Fig. 3 (b)) and all-optical wavelength converters operating at 10 Gbps have been successfully demonstrated in this platform [10,11].

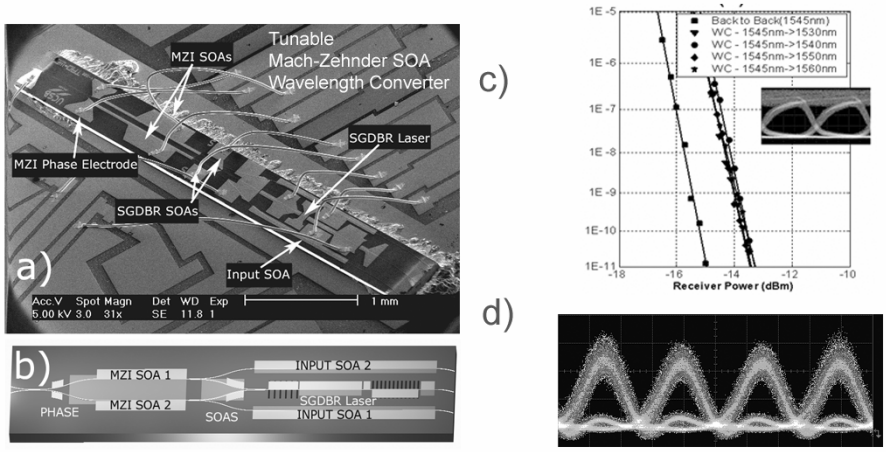

Fig. 2. Monolithic tunable all-optical wavelength converter realized using OQW and QWI at UCSB (a) Electron micrograph (b) Device schematic (c) Bit-error rate curves for 10 Gbps NRZ operation (d) Eye diagram for 40 Gbps RZ operation

Another new integration platform that has been used to solve some of the efficiency issues related to the photocurrent-driven tunable wavelength converters is shown in Fig. 1 (c). The epi-layer structure

incorporates a dual quantum well stack design. A set of offset quantum wells is used to provide gain in the laser and the amplifiers (Photoluminescence = 1550 nm) while a separate set of quantum wells, centered in the InGaAsP quaternary waveguide (PL = 1300 nm) provides broadband modulation efficiency when reverse biased in the EAM. An efficient transmitter operating at 10 Gbps and a hybrid wavelength converter at the same bit-rate have been demonstrated using this platform [12]. Though currently the receiver and transmitter are not monolithically integrated, the fact that both sections have identical InP regrowth and fabrication steps shows that the dual quantum well base structure should be well suited for an efficient single-chip photocurrent driven wavelength converter.

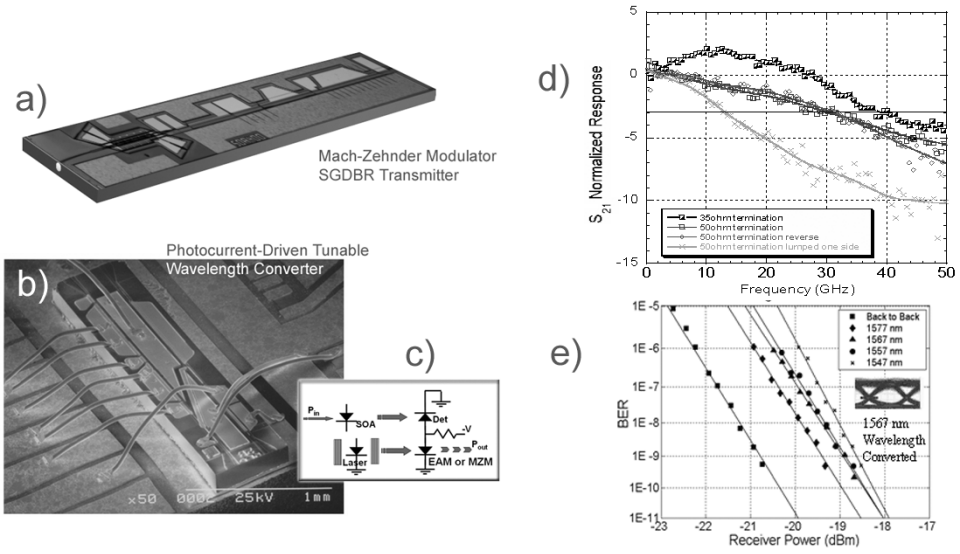

Fig. 3. (a) Traveling-wave tunable Mach-Zehnder modulator (TW-MZM) transmitter (b) Photocurrent-driven tunable wavelength converter (PD-TWC) (c) Schematic of a EAM and MZM PD-TWC (d) 40 Ghz bandwidth of the TW-MZM transmitter (e) Bit-error rate curves for the PD-TWC at 10 Gbps NRZ

3. References

[1] B. Stoltz, M. Dasler, and O. Sahlen, "Low threshold-current, wide tuning-range, butt-joint DBB laser grown with four MOVPE steps," ElectronicsLetters, vol. 29, pp. 700-2, 1993.

[2] C. H. Joyner, S. Chandrasekhar, J. W. Sulhoff, and A. G. Dentai, "Extremely large band gap shifts for MQW structures by selective epitaxy on SiO/sub 2/ masked substrates," IEEE Photonics Technology Letters, vol. 4, pp. 1006-9, 1992.

[3] M. L. Masanovic, V. Lal, J. S. Barton, E. J. Skogen, J. A. Summers, L. Rau, L. A. Coldren, and D. J. Blumenthal, "Widely-Tunable Monolithically-Integrated All-Optical Wavelength Converters in InP," IEEE Journal of Lightwave Technology, March 2005.

[4] J. S. Barton, M. L. Masanovic, A. Tauke-Pedretti, E. J. Skogen, and L. A. Coldren, "Monolithically-integrated 40Gbit/s widely-tunable transmitter using series push-pull Mach-Zehnder modulator SOA and Sampled-Grating DBR laser," presented at Optical Fiber Communications Conference, Anaheim, 2005.

[5] V. Lal, M. L. Masanovic, J. A. Summers, L. A. Coldren, and D. J. Blumenthal, "40Gbps Operation of an Offset Quantum Well Active Region Based Widely-Tunable All-Optical Wavelength Converter," presented at Optical Fiber Communication Conference, Anaheim, 2005.

[6] J. S. Barton, M. L. Masanovic, M. N. Sysak, J. M. Hutchinson, E. J. Skogen, D. J. Blumenthal, and L. A. Coldren, "2.5-Gb/s error-free wavelength conversion using a monolithically integrated widely tunable SGDBR-SOA-MZ transmitter and integrated photodetector," *IEEE Photonics Technology Letters*, vol. 16, pp. 1531-3, 2004.

[7] M. L. Masanovic, V. Lal, J. A. Summers, J. S. Barton, E. J. Skogen, L. A. Coldren, and D. J. Blumenthal, "Design and Performance of a Monolithically-Integrated Widely-Tunable All-Optical Wavelength Converter with Independent Phase Control," *IEEE Photonics Technology Letters*, vol. 16, pp. 2299-2301, 2004.

[8] J. H. Marsh, "Quantum well intermixing," Semiconductor Science & Technology, vol. 8, pp. 1136-55, 1993.

[9] E. J. Skogen, J. S. Barton, S. P. Denbaars, L. A. Coldren, "A quantum-well-intermixing process for wavelength-agile photonic integrated circuits" IEEE journal of Sel. Topics in Quantum Elec. , 8 , No. 4, 863-869 (2002)

[10] J. W. Raring, E. J. Skogen, L. A. Johansson, M. N. Sysak, J. S. Barton, M. L. Masanovic, and L. A. Coldren, "Quantum Well Intermixing for Monolithic Integration: A Demonstration of Novel Widely-Tunable 10Gb/s Transmitters and Wavelength Converters," presented at Integrated Photonics Research Conference, San Francisco, California, USA, 2004.

[11] M. L. Masanovic, V. Lal, E. J. Skogen, J. S. Barton, J. A. Summers, L. A. Coldren, and D. J. Blumenthal, "Detailed Comparison of Cross-phase Modulation Efficiency in Offset Quantum Well and Centered Quantum Well Intermixed Monolithically Integrated Widely-Tunable MZI-SOA Wavelength Converters," presented at Optical Fiber Communication Conference, Anaheim, 2005.

[12] Matthew N. Sysak, Jonathon S. Barton, James W. Raring, Matthew Dummer, Anna Tauke-Pedretti, Daniel J. Blumenthal, Larry A. Coldren, "10 Gb/s Photocurrent Driven, Widely Tunable Electroaborption Modulator Based Wavelength Converter", presented at Optical Fiber Communication Conference, Anaheim, 2005.

Proc. 17th International Conference on Indium Phosphide and Related Materials, Glasgow, Scotland (May 8-12, 2005)

Active Photonic Integrated Circuits

Larry A. Coldren, Erik J. Skogen, James W. Raring, Jonathon S. Barton, Dan Lofgreen, Leif Johansson, and Jonathan T. Getty

Electrical &Computer Engineering and Materials Departments, University of California Santa Barbara, CA 93106 USA

coldren@ece.ucsb.edu

INVITED PAPER

Abstract: Recent advances in photonic integration technology on InP and related materials have enabled continued growth in the scale, performance and quality of active photonic integrated circuits. Complex widely-tunable transmitters, transceivers, and wavelength converters with state-of-the-art performance have been demonstrated.

1. Introduction

Photonic integration has long been sought after as the next big step toward low-cost, low-size, and low-power dissipation chips with increased capability. This dream has gone largely unrealized over the past couple of decades, during which time significant effort in this direction was undertaken. However, within the past several years there has been a resurgence of effort as well as significant progress in realizing practical photonic integrated circuits (PICs). This is despite the huge reduction in research effort in the area of optical communications components. It would appear that at least some of this is due to a few research breakthroughs that have enabled such integration to be more robust.

In this paper we shall review some of the recent advances that have been carried out at UCSB in developing new integration approaches[1-11]. Seamless transitions in absorption edge, which require no regrowths for the various elements of widely-tunable lasers, transmitters, and wavelength converters, have been provided by selective removal of quantum-wells as well as via novel quantum-well intermixing approaches. A variety of optical waveguide elements are involved, including gain regions, phase and amplitude modulators, grating reflectors, passive waveguides, semiconductor-optical-amplifiers (SOAs) variable-optical-attenuators (VOAs), and photodetectors. In principle, there is no limit to the scale of the PICs that can be created, once these elements can be integrated with high yield. These PICs achieve a high level of functionality by using only photonic components with no electronics or the interconnections to such electronics required. For example, optical amplifiers (SOAs) are used for power gain and pre-amplification of weak signals, in many cases obviating the need for any electronic components in the entire sub-system.

2. Technology Advances: Quantum-well intermixing

Figure 1 illustrates how quantum-well intermixing (QWI) works and details the process of the novel approach used at UCSB for InGaAsP/InP[1]. In this case, low-energy P^+ ions are implanted near the surface of a sacrificial InP layer to create vacancies, and in a subsequent rapid-thermal-annealing (RTA) step, these are then diffused through this layer and then across the multiple-quantum-well (MQW) active region to intermix this MQW region and increase its effective bandgap energy. Multiple bandgaps are formed by performing multiple short RTAs with intermediate selective etching steps to remove the implanted sacrificial InP, and thus vacancy source, in regions where the bandgap is to be frozen. Finally, all of the sacrificial InP is removed, other processing such as grating formation is performed if desired, and then the top waveguide cladding layers are regrown. Thus, only a single regrowth step, as required for grating reflector formation, is typically carried out.

Figure 2 shows new results for similar processes in a GaAs-based technology. Although QWI in GaAs-based materials has been reported for many years, robust processes for Al-free layer structures[10] as well as reproducible large bandgap shifts in InGaAs/GaAs/AlGaAs [9] have not been developed.

3. Example Device Advances: Photonic ICs

Figure 3 illustrates a widely-tunable transmitter in the 1550nm wavelength band formed with the QWI process. It includes a widely-tunable laser, a back-side absorber/detector, an electro-absorption-modulator (EAM), and a curved-waveguide output coupler, all monolithically integrated on the same chip with the process described

above[5,6]. High output power, full C-band tunability, and negative chirp capability is demonstrated with three different QWI bandgaps formed from the single MQW growth.

Figure 4 illustrates an array of other PICs that have been created with the QWI or 'offset quantum-well' integration platform. The offset QW technique is the same basic platform as used commercially in supplying large numbers of widely-tunable lasers and transmitters to dense-WDM networks[12]. This collage of configurations includes an array of tunable SGDBR lasers having a bipolar-cascaded gain stage[2] for differential efficiencies > 1, a single-chip biosensor[4] that heterodynes two DBRs to provide a base-band output with out any light coupling to or from the chip, and a transceiver (or wavelength converter) that uses the photocurrent from a receiver stage to directly drive a laser or external modulator such as in a Mach-Zehnder modulator-SGDBR laser based transmitter without any need for rf to enter or leave the chip[3,11].

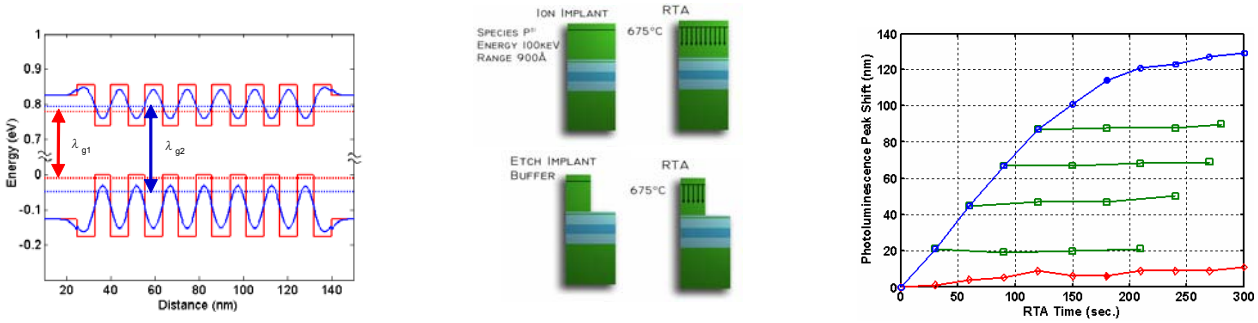

Figure 1. Schematic of QWI in InGaAsP/InP; procedure for multiple bandgaps from one implant; experimental bandgaps vs RTA time after sequential etch steps to remove vacancy source[1].

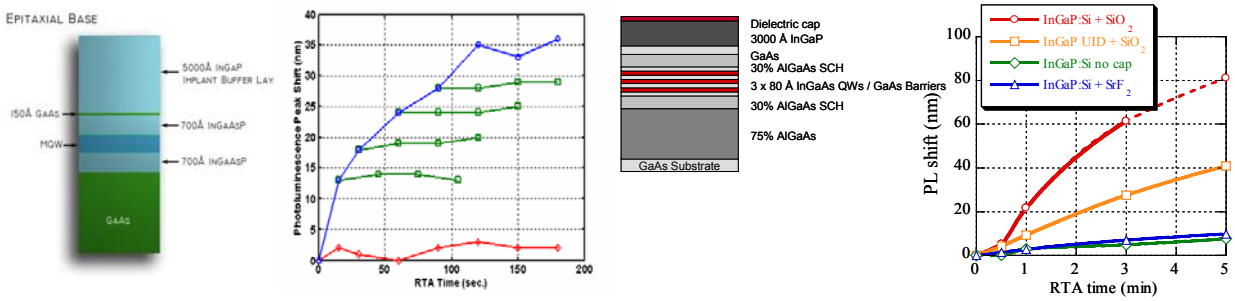

Figure 2. GaAs QWI: (left) 980 nm Al-free showing results after sequential RTA and etch removal of implant layer[10]; (right) 980 nm AlGaAs/GaAs/InGaAs case oxide deposition as vacancy source and surface fluoridation to inhibit QWI in desired areas [9].

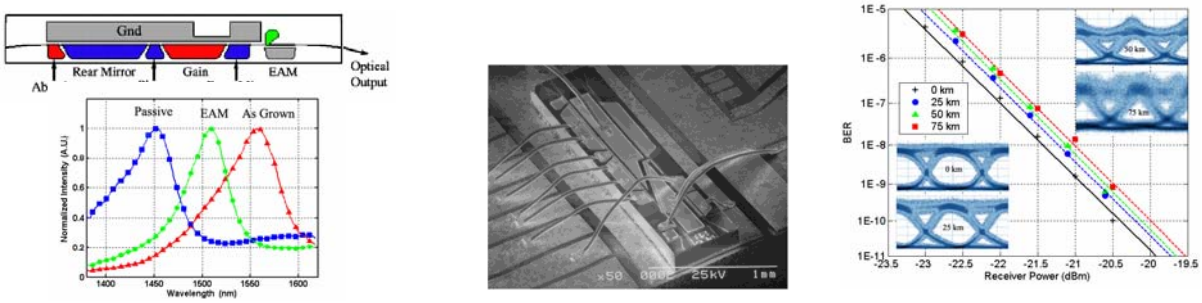

Figure 3. QWI-SGDBR-EAM full C-band single-chip transmitter (and wavelength converter with SOA-PIN receiver in SEM). Low power penalty 10Gb/s transmission over 75 km of standard fiber illustrates negative chirp that is available across the band[5,6].

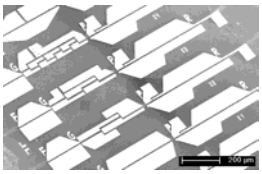

Bipolar cascade SGDBR array

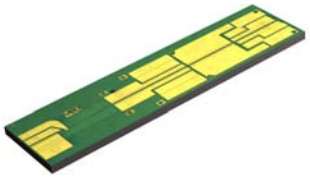

Biosensors w/heterodyned lasers

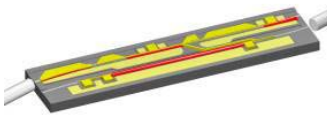

Photocurrent driven wavelength converters

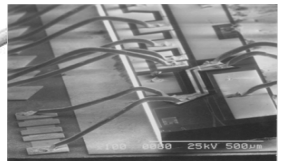

Mach-Zehnder modulator-SGDBR laser transmitter

Figure 4. Various other PICs that have been formed. The bipolar cascade [2] also uses the QWI integration platform. The others use the offset quantum-well integration platform[4, 3, 8, 11].

References

1. E. Skogen, J. Raring, J. Barton, S. DenBaars, and L. Coldren, "Post-Growth Control of the Quantum-Well Band Edge for the Monolithic Integration of Widely-Tunable Lasers and Electroabsorption Modulators," *IEEE J. Sel. Topics in Quantum Electron*., vol. 9, pp. 1183-1190, September/October 2003.
2. J.T. Getty, L.A. Johansson, E.J. Skogen, and L.A. Coldren, "1.55µm Bipolar Cascade Segmented Ridge Lasers", *IEEE Jour. Of Selected Topics in Quant. Elec*., **9**, (5), pp. 1138-1145 (September/October 2003*)*
3. Jonathon S. Barton, Erik J. Skogen, Milan L. Masanovic, Steven P. DenBaars, and Larry A. Coldren, "A Widely-tunable high-speed transmitter using an integrated SGDBR Laser-Semiconductor Optical Amplifier and Mach-Zehnder Modulator," *Jour. Of Selected Topics in Quant. Elec*., **9**, (5), pp. 1113-1117 (September/October 2003)
4. D.A. Cohen, J.A. Nolde, A. Tauke-Pedretti, C.S. Wang, E. J. Skogen, and L.A. Coldren , "Sensitivity and Scattering in a Monolithic Heterodyned Laser Biochemical Sensor,", *Jour. Of Selected Topics in Quant. Elec*., **9**, (5), pp. 1124-1131 (September/October 2003)
5. J. Raring, E. Skogen, L. Johansson, M. Sysak, J. Barton, Milan L. Masanovic, and L. Coldren , "Demonstration of Widely-Tunable Single-Chip 10 Gb/s Laser-Modulators Using Multiple-Bandgap InGaAsP Quantum-Well Intermixing" *Phot. Tech. Let.,* **16,** (7),pp. 1613-1615 (July 2004)
6. J. W. Raring, E. J. Skogen, L. A. Johansson, M. N. Sysak, L. A. Coldren, "Low dispersion penalty at 10 Gb/s, Over 75 km, using a quantum-well-intermixed electroabsorption-modulator/widely-tunable laser transmitter," *Proc. OFC 2004,* PDP13, Los Angeles, CA, (February 22-27, 2004).
7. Erik J. Skogen, Chad S. Wang, James W. Raring, Gordon B. Morrison, and Larry A. Coldren, "Small-Footprint, High-Efficiency, Integrated Transmitters for High-Speed Optical Interconnect Applications," *Proc. Integrated Photonics Research*, paper no. IThD2, San Francisco, CA (June 2004).
8. M.N. Sysak, J.S. Barton, L.A. Johansson, J.W. Raring, E.J. Skogen, M.L. Masanovic, D.J. Blumenthal, and L.A. Coldren, "Single-Chip Wavelength Conversion Using a Photocurrent-Driven EAM Integrated With a Widely Tunable Sampled-Grating DBR Laser," *Phot. Tech. Let.,* **16,** (9),pp. 2093-2095 (September 2004).
9. D. Lofgreen *et. al*., "Enhanced intermixing of InGaAs/GaAs quantum wells using silicon doped InGaP and SiO_2", submitted to *Appl. Phys. Lett.*
10. E. Skogen, et al., "Multiple band-edge quantum well intermixing in the InGaAs/InGaAsP/InGaP material system",Submitted to *Appl. Phys. Letts.*
11. Jonathon S. Barton, Matt Dummer, Anna Tauke-Pedretti, Erik J. Skogen, James Raring, Matt Sysak, Milan Masanovich, Leif A. Johansson, Larry A. Coldren "InP-based Active Photonic Integrated Circuits" *Proc. LEOS annual meeting 2004*, paper no. TuA5, pp. 169-170, Puerto Rico (October 2004).
12. T. Wipiejewski, Y.A. Akulova, G. Fish, C. Schow, P. Koh, A. Karim, S. Nakagawa, A. Dahl, P. Kozodoy, A. Matson, B. Short, C. Turner, S. Penniman, M. Larson, and L.A. Coldren, "Integration of Active Optical Components," *Proc. SPIE,* Vol. 4997A-02 , San Jose, CA (January 2003)

Proc. 63rd Device Research Conference, 1, pp. 11-14, Santa Barbara, CA (June 20-22, 2005)

Widely-Tunable Transmitters and Photonic Integrated Circuits

Larry A. Coldren, James W. Raring, Jonathon S. Barton, Matt Sysak, and Leif Johansson
Electrical &Computer Engineering and Materials Departments, University of California Santa Barbara, CA 93106
and
Agility Communications, Inc., 475 Pine Ave, Santa Barbara, CA 93117
Ph: (805) 893-4486; Fax: (805) 893-4500; email: lcoldren@agility.com

INVITED PAPER

Abstract: Widely-tunable lasers and single-chip transmitters, in which such lasers are integrated with modulators and semiconductor-optical-amplifiers, have recently become the core of practical modules that are gaining wide-spread use in new wavelengh-division-multiplexed systems. More advanced photonic ICs have been demonstrated for use in advanced communication and sensor systems.

1. Introduction

Despite a significant downturn in the market for telecommunication products, certain new enabling components are enjoying rapid market growth as their capabilities to reduce operational costs gain acceptance. One such example is the widely-tunable laser and derivative products that provide a 'one-size-fits all' solution in dense wavelength division multiplexed (DWDM) communication systems. In the future, such devices may also find use in reconfigurable optical add-drop multiplexers (ROADMs), photonic switch architectures, and other elements in dynamically reconfigured networks.

In this paper, we shall summarize recent advances with InP-based single-chip photonic integration techniques that are gaining wide acceptance for such applications[1,2]. Such photonic integration has long been sought after as the next big step toward low-cost, low-size, and low-power dissipation chips with increased capability. Although efforts in this area have been ongoing for decades, only within the past several years have practical photonic integrated circuits (PICs) emerged.

Key to the active PICs to be discussed here are having seamless transitions in absorption edge, so that the various amplifying, modulating, splitting, and passive interconnecting waveguides can be integrated together without loss or reflections. As illustrated in Fig. 1 various approaches have been developed. The first, butt-joint regrowth, requires an extra regrowth, but the waveguide properties can be chosen nearly arbitrarily. The other three require no regrowths, but are somewhat restricted due to the inherent relationships between the sections. Nevertheless, such approaches are being widely used because of the relative simplicity of the fabrication process and the fact that relatively good properties for the various elements of many PICs can be obtained.

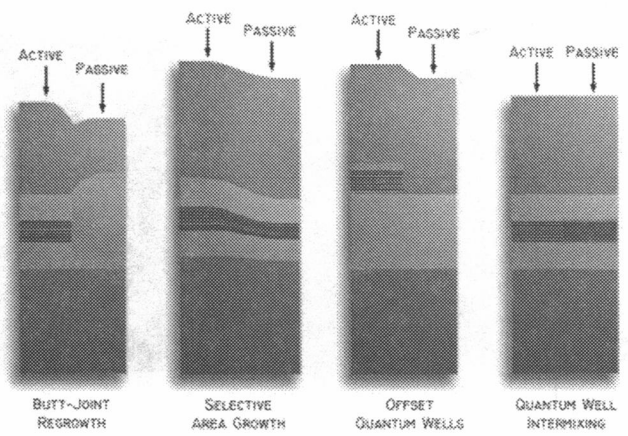

Figure 1. Schematics of active-to-passive waveguide integration techniques.

In principle, there is no limit to the scale of the PICs that can be created, once waveguides of about three or four different different bandgaps can be integrated with high yield. The PICs to be discussed also achieve a high level of

0-7803-9040-7/05/$20.00 ©2005 IEEE

functionality by using only photonic components with no electronics or the interconnections to such electronics required. For example, optical amplifiers (SOAs) are used for power gain and pre-amplification of weak signals, in many cases obviating the need for any electronic components in the entire sub-system.

2. Recent Technology Advances: Quantum-well intermixing

Figure 2 illustrates how quantum-well intermixing (QWI) works and details the process of the novel approach used at UCSB for InGaAsP/InP[1]. In this case, low-energy P^+ ions are implanted near the surface of a sacrificial InP layer to create vacancies, and in a subsequent rapid-thermal-annealing (RTA) step, these are then diffused through this layer and then across the multiple-quantum-well (MQW) active region to intermix this MQW region and increase its effective bandgap energy. Multiple bandgaps are formed by performing multiple short RTAs with intermediate selective etching steps to remove the implanted sacrificial InP, and thus vacancy source, in regions where the bandgap is to be frozen. Finally, all of the sacrificial InP is removed, other processing such as grating formation is performed if desired, and then the top waveguide cladding layers are regrown. Thus, only a single regrowth step, as required for grating reflector formation, is typically carried out.

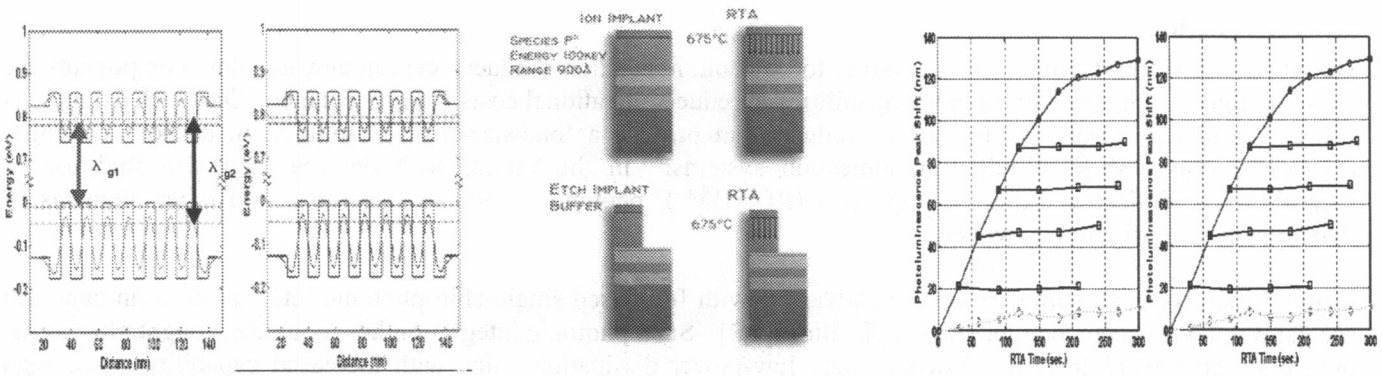

Figure 2. Schematic of QWI in InGaAsP/InP; procedure for multiple bandgaps from one implant; experimental bandgaps vs RTA time after sequential etch steps to remove vacancy source[1].

3. Example Device Advances: Photonic ICs

Figure 3 illustrates a widely-tunable transmitter in the 1550nm wavelength band formed with the QWI process. It includes a widely-tunable laser, a back-side absorber/detector, an electro-absorption-modulator (EAM), and a curved-waveguide output coupler, all monolithically integrated on the same chip with the process described above[3,4]. As shown by the results in Fig. 4 high output power, full C-band tunability, and negative chirp capability is demonstrated with three different QWI bandgaps formed from the single MQW growth.

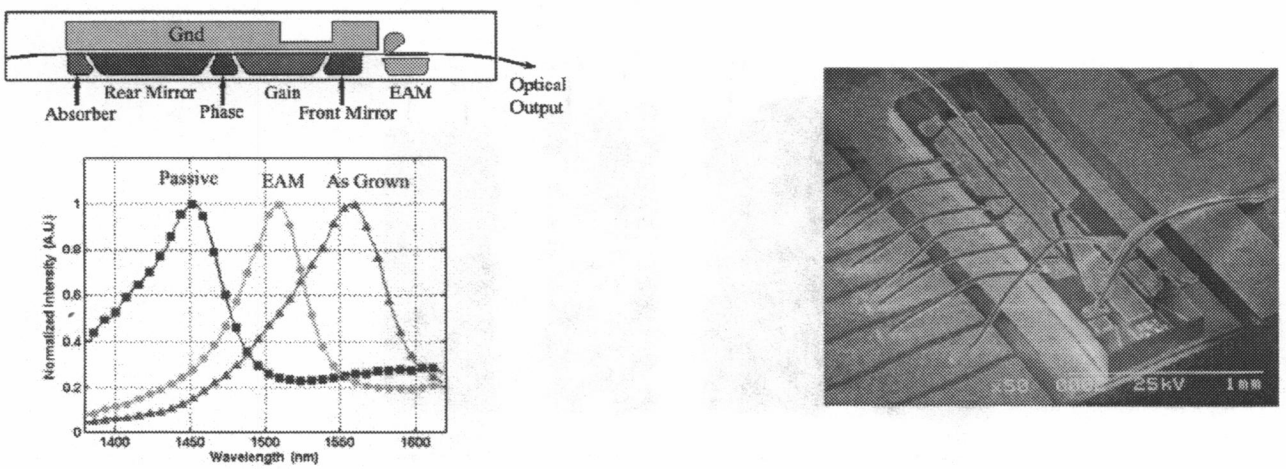

Figure 3. Schematic, SEM and photoluminescence spectra of an integrated SGDBR-EAM transmitter that uses a three-bandgap QWI process. Full C-band tunability with negative chirp demonstrated [3,4].

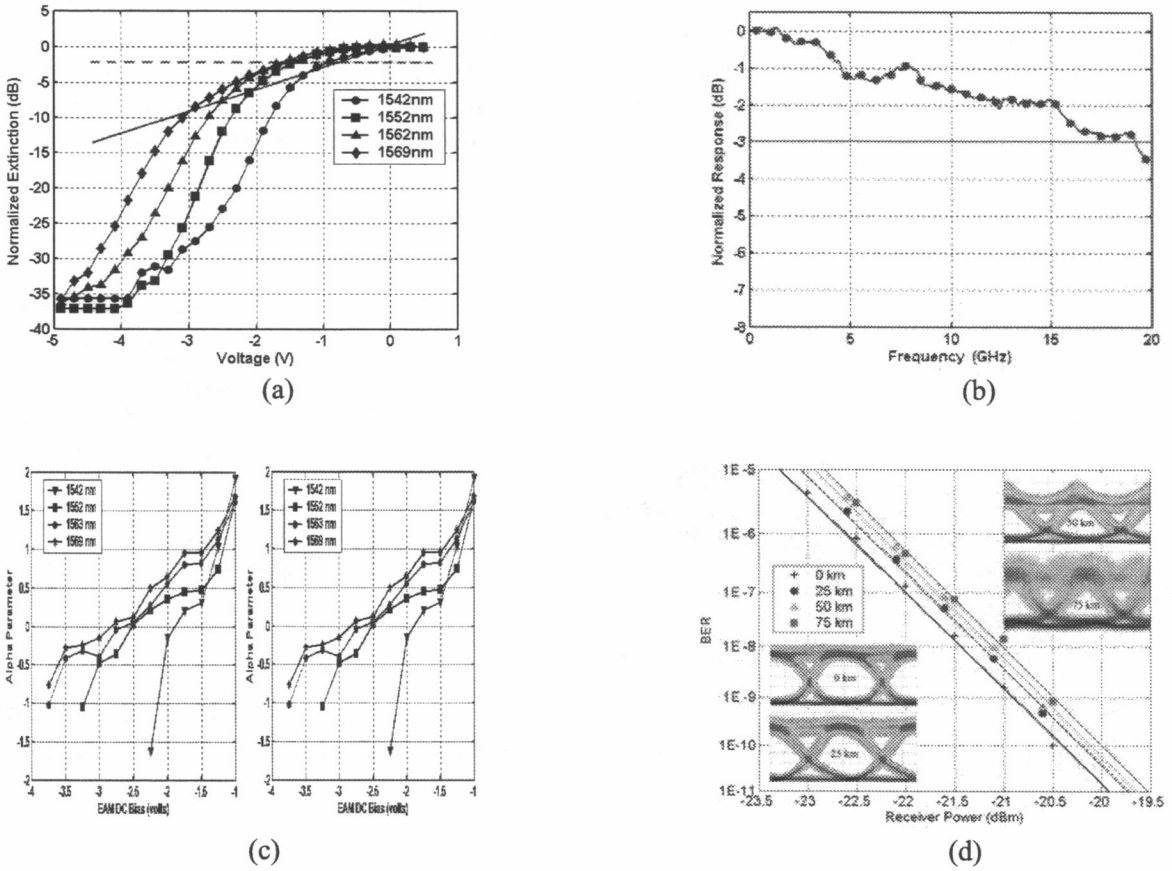

Figure 4. Results of Fig. 3 device: (a) Static electro-absorption characteristics of EAM; (b) small signal bandwidth; (c) large-signal chirp parameter across tuning range; and (d) bit-error-rate vs. receiver power for transmission through various distances of standard fiber with eye-diagrams. [3,4]

Using the QWI process more narrowly tunable laser-EAM PICs have been investigated for optical interconnect applications, in which very high efficiency transmitters are desired[5]. For the expected higher data bandwidths anticipated within the next decade, the laser-modulator configuration will probably be required. Figure 5 illustrates preliminary results for a laser-EAM design formed with the same QWI technology platform as used in Figs. 3 & 4. In this case the EAM was better optimized for the wavelength being used, so very low voltage swing (0.6 V) for 10 dB extinction is possible. The high 3 dB bandwidth (~25GHz) obtained without any traveling-wave structures suggests that 40Gb/s operation should soon be possible with less than 10 mW of power dissipated in the EAM.

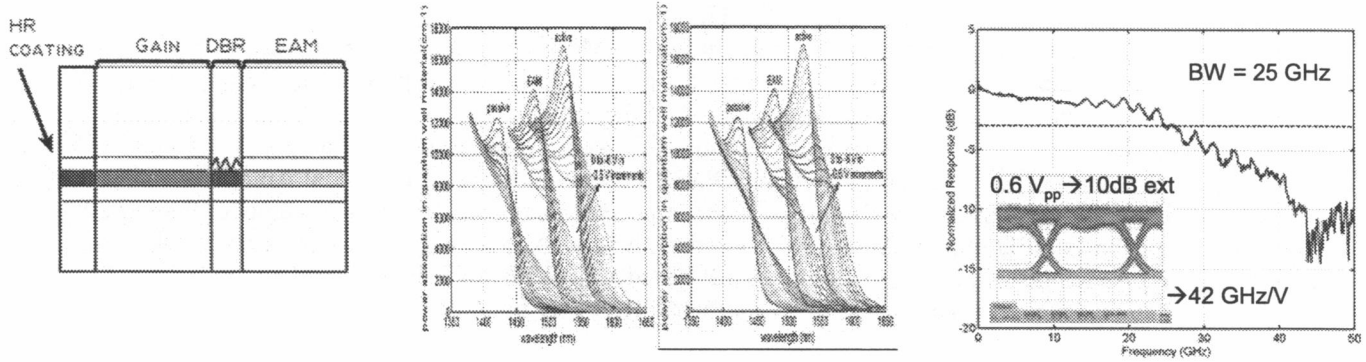

Figure 5. Short-cavity laser-EAM formed with QWI technology at 1550nm and results. The center figure gives the photocurrent for the three sections, and the right side the bandwidth. Laser-L = 150 μm; EAM-L = 125 μm[5].

Figure 6 depicts an SGDBR integrated with a backside detector, an SOA post-amp, and a Mach-Zehnder modulator (MZM) [6,7]. In this case the electrodes of the MZM are formed with 'T-coplanar' series-connected traveling-wave transmission lines. Also, a separate phase section is included in the MZM to establish the zero-bias set point, and a curved output guide suppresses facet reflections. As can be seen the frequency can extend to nearly 40GHz with proper choice of load resistor. Digital data up to 40 Gb/s has been transmitted with such a device along short distances of fiber.

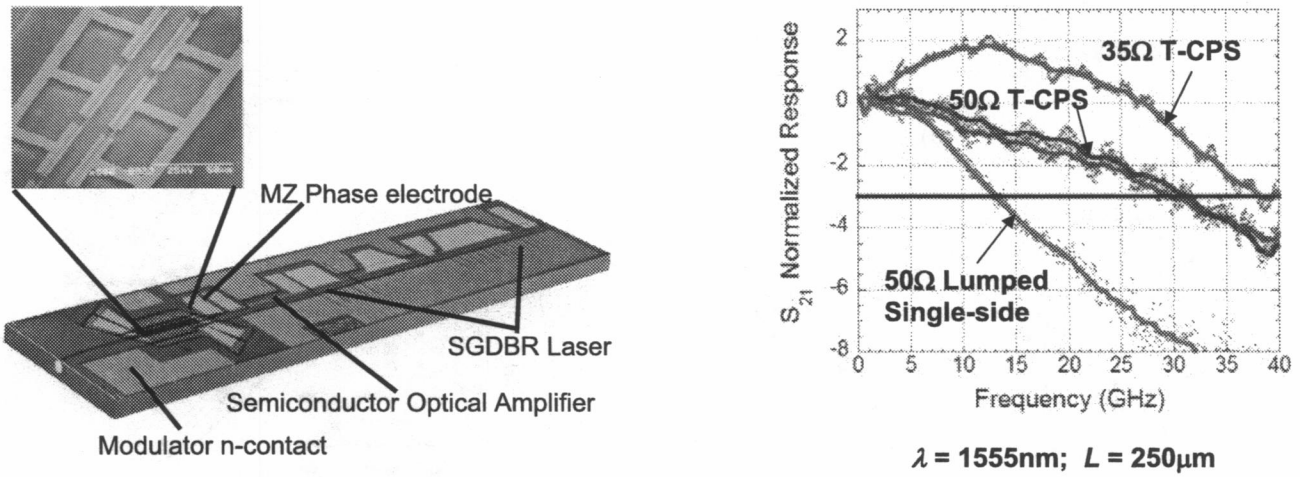

Figure 6. Integrated SGDBR-MZM schematic, inset SEM of T-CPS transmission line, and experimental small-signal modulation response[6,7].

References

1. E. Skogen, J. Raring, J. Barton, S. DenBaars, and L. Coldren, "Post-Growth Control of the Quantum-Well Band Edge for the Monolithic Integration of Widely-Tunable Lasers and Electroabsorption Modulators," *IEEE J. Sel. Topics in Quantum Electron.*, vol. 9, pp. 1183-1190, (September/October 2003).
2. T. Wipiejewski, Y.A. Akulova, G. Fish, C. Schow, P. Koh, A. Karim, S. Nakagawa, A. Dahl, P. Kozodoy, A. Matson, B. Short, C. Turner, S. Penniman, M. Larson, and L.A. Coldren, "Integration of Active Optical Components," *Proc. SPIE,* Vol. 4997A-02 , San Jose, CA (January 2003).
3. J. Raring, E. Skogen, L. Johansson, M. Sysak, J. Barton, Milan L. Masanovic, and L. Coldren , "Demonstration of Widely-Tunable Single-Chip 10 Gb/s Laser-Modulators Using Multiple-Bandgap InGaAsP Quantum-Well Intermixing" *Phot. Tech. Let.,* **16,** (7),pp. 1613-1615 (July 2004).
4. J. W. Raring, E. J. Skogen, L. A. Johansson, M. N. Sysak, L. A. Coldren, "Low dispersion penalty at 10 Gb/s, Over 75 km, using a quantum-well-intermixed electroabsorption-modulator/widely-tunable laser transmitter," *Proc. OFC 2004,* PDP13, Los Angeles, CA, (February 22-27, 2004).
5. Erik J. Skogen, Chad S. Wang, James W. Raring, Gordon B. Morrison, and Larry A. Coldren, "Small-Footprint, High-Efficiency, Integrated Transmitters for High-Speed Optical Interconnect Applications," *Proc. Integrated Photonics Research*, paper no. IThD2, San Francisco, CA (June 2004).
6. Jonathon S. Barton, Erik J. Skogen, Milan L. Masanovic, Steven P. DenBaars, and Larry A. Coldren, "A Widely-tunable high-speed transmitter using an integrated SGDBR Laser-Semiconductor Optical Amplifier and Mach-Zehnder Modulator," *Jour. Of Selected Topics in Quant. Elec.*, **9**, (5), pp. 1113-1117 (September/October 2003)
7. Jonathon S. Barton, Matt Dummer, Anna Tauke-Pedretti, Erik J. Skogen, James Raring, Matt Sysak, Milan Masanovich, Leif A. Johansson, Larry A. Coldren "InP-based Active Photonic Integrated Circuits" *Proc. LEOS annual meeting 2004*, paper no. TuA5, pp. 169-170, Puerto Rico (October 2004).

High Efficiency Widely Tunable SGDBR Lasers for Improved Direct Modulation Performance

Jonathan Klamkin, John M. Hutchinson, Jonathan T. Getty, Leif A. Johansson, *Member, IEEE*, Erik J. Skogen, and Larry A. Coldren, *Fellow, IEEE*

***Abstract*—We report on two novel approaches to improve the differential quantum efficiency (DQE) of widely tunable 1.55-μm lasers: the bipolar cascade sampled grating distributed Bragg reflector (BC-SGDBR) laser and the gain-levered SGDBR (GL-SGDBR) laser. Each is fabricated on a robust InGaAsP/InP photonic integrated circuit platform. The lasers demonstrate improved direct modulation performance over conventional SGDBR lasers. The BC-SGDBR laser was also monolithically integrated with a semiconductor optical amplifier and photodetector receiver in order to perform wavelength conversion. Error free wavelength conversion at 2.5 Gb/s and improvements in conversion efficiency are demonstrated.**

***Index Terms*—Bipolar cascade (BC) laser, gain-levered (GL) laser, sampled grating distributed Bragg reflector (SGDBR) laser, semiconductor laser, wavelength converter.**

I. Introduction

DIRECT MODULATION performance of conventional semiconductor lasers is limited in part by the differential quantum efficiency (DQE) of the laser. Oftentimes the efficiency of the laser is compromised in order to achieve a higher bandwidth. Enhancing the DQE of the laser would therefore improve modulation efficiency. Another issue is impedance matching to a radio frequency (RF) source. In broadband systems applications, impedance matching is usually accomplished with a series-connected resistor, which consumes a significant amount of the RF power. This results in lower modulating laser currents and therefore reduces the modulation efficiency. Alternative impedance matching techniques could improve efficiency.

This paper focuses on two different approaches to enhance the DQE of widely tunable lasers. The first approach integrates a bipolar cascade series-connected laser concept into the gain section of a widely tunable sampled grating distributed Bragg reflector (SGDBR) laser. This approach also simplifies impedance matching because it is possible to tailor the input impedance of the laser. Several cascading techniques have been investigated to improve the DQE of semiconductor lasers including stacked multiple active region vertical-cavity surface-emitting laser (VCSEL) structures [1], in-plane laser arrays [2], and VCSEL arrays [3]. One of the more successful attempts at improving laser DQE is the bipolar cascade segmented Fabry–Perot laser [4]. In this case, an in-plane ridge laser structure is constructed in which electrically isolated segments are series connected to form a chain of diodes sharing the same optical cavity. Current is applied to the p-side of the first stage, extracted from the n-side, and transferred to the p-side of the next stage through a metal interconnect. Ion implantation is used to sufficiently electrically isolate the stages. As a result of driving current through the diodes in series, the same current density is created with nearly $1/N$ (where N is the number of stages) times the current as compared to a single-stage laser. The DQE nearly scales with N. The voltage and input impedance also increase, but the latter can be tailored to meet impedance matching requirements.

Segmenting a laser into several diodes and series connecting them in this manner is very useful if integrated into a single frequency platform. Here, the gain section of SGDBR lasers is segmented and series connected. These multistage devices show superior direct modulation characteristics over conventional single-stage devices. Such a bipolar cascade SGDBR (BC-SGDBR) laser is also monolithically integrated with an input semiconductor optical amplifier (SOA) and photodetector (PD) receiver in order to perform wavelength conversion. Some other photocurrent-driven widely tunable wavelength converters use an external modulation scheme such as an integrated electroabsorption modulator (EAM) or Mach–Zehnder modulator (MZM) [5], [6]. The direct modulation approach to a photocurrent-driven monolithically integrated wavelength converter is simple and linear [7]. Bipolar cascade (BC) lasers should require less receiver photocurrent than conventional lasers for the direct modulation approach due to their enhanced DQE; therefore, improvements in conversion efficiency should be achieved.

The second approach for achieving higher DQE is to incorporate a gain lever into the gain section of a widely tunable SGDBR laser. Gain-levered (GL) lasers demonstrate enhanced DQE and have sharp turn-on lasing characteristics. Bistable laser diodes have been proposed for use in optical networks due to their enhanced differential efficiency, signal regeneration properties, as well as their implementations for all-optical flip-flops [8]. The increased laser DQE can yield an improved noise figure (NF) in microwave fiber-optic links [9]. Sharp turn-on light-current characteristics have been observed in gain-levered Fabry–Perot ridge lasers [10]. Recently, optically injection-locked gain-levered lasers have been reported with enhanced RF performance [11]. Here a widely tunable gain-levered SGDBR

Manuscript received November 18, 2004; revised June 14, 2005. This work was supported by DARPA/MTO CS-WDM under Grant N66001-02-C-8026 and by Intel Corporation under Grant TXA001630000.

J. Klamkin, J. T. Getty, L. A. Johansson, E. J. Skogen, and L. A. Coldren are with the Department of Materials and the Department of Electrical and Computer Engineering, University of California at Santa Barbara, Santa Barbara, CA 93106 USA (e-mail: klamkin@engineering.ucsb.edu).

J. M. Hutchinson is with the Intel Corporation, Strategic Technology, Santa Ana, CA 95052 USA (e-mail: john.hutchinson@intel.com).

Digital Object Identifier 10.1109/JSTQE.2005.853846

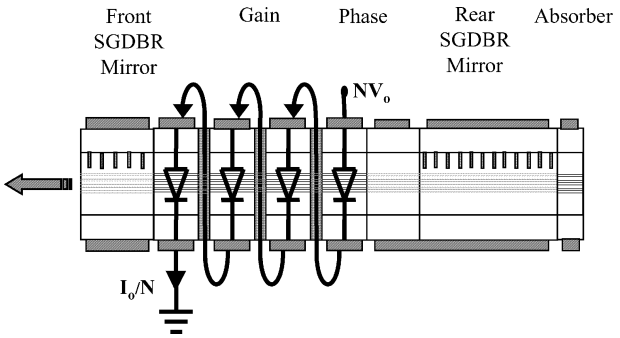

Fig. 1. Circuit schematic of a 4-stage BC-SGDBR laser. Quantum wells in the gain section and absorber section are as grown. Quantum wells in the front mirror, phase, and rear mirror sections are intermixed. The segments in the gain section (shaded) are intermixed and implanted with Helium ions.

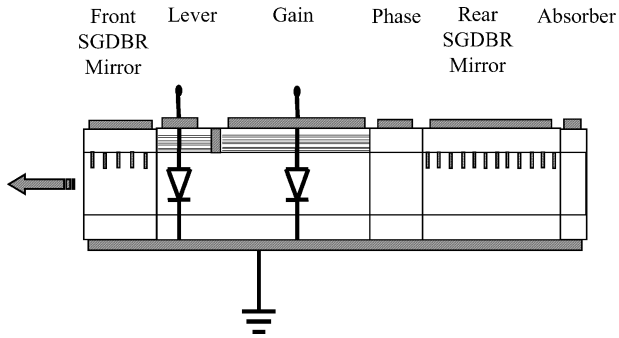

Fig. 2. Circuit schematic of GL-SGDBR laser. The output SOA, which is not shown, is directly in front of the front SGDBR mirror.

(GL-SGDBR) laser is reported which exhibits high DQE and good RF performance.

II. Device Design and Fabrication

A. Bipolar Cascade SGDBR Laser

The SGDBR laser is a five-section device consisting of a gain section, front SGDBR mirror, rear SGDBR mirror, phase section, and rear absorber. Lasers were fabricated with 1, 3, 4, and 8 stages in the gain section, which has a total length of 550 μm for all cases. The front mirror consists of 5 4-μm-wide bursts, and the rear mirror consists of 12 6-μm-wide bursts. The phase section is used for fine tuning. A schematic of a 4-stage gain section device is shown in Fig. 1. Metal interconnects from one stage to the next are shown as wires with arrows. Current is forced through the diodes in series.

The epitaxial base structure is grown on a semi-insulating InP substrate. The growth begins with an n-InP buffer layer followed by an n-InGaAs contact layer, which allows for top-side n-contacts that are necessary to form the metal interconnects in the gain section. Another 1.1 μm of n-InP is grown to separate the InGaAs contact layer from the waveguide. A centered quantum well integration platform is used. The active region consists of seven 70-Å thick InGaAsP quantum wells, and eight 80-Å thick InGaAsP barriers centered between two 1200-Å layers of 1.3-Q waveguide material. A novel implantation-induced quantum well intermixing technique [12] is used to render the quantum wells passive where necessary. This process involves a masked shallow P^+ implant into an undoped sacrificial InP layer, creating vacancies near the surface. This is followed by a 3-min rapid thermal anneal at a temperature of 675° C, which drives the vacancies downward in the implanted regions. In this case, the band edge in the front and rear mirror sections and the phase section is placed so that the relative photoluminescence peak shift is over 100 nm. The sacrificial InP layer is then removed and sampled gratings are defined in the upper portion of the waveguide. A regrowth is performed in which 2 μm of p-doped InP is grown, followed by a 1000-Å p-InGaAs contact layer. After 3-μm-wide ridges are etched, the n-contact layer is exposed and Ni–AuGe–Ni–Au n-contacts are deposited and annealed. It is necessary to perform this anneal prior to the Helium implantation for isolation because the temperature used is sufficiently high to anneal some of the damage created by the implant.

Helium implantation destroys conductivity in both p-type and n-type InP. To isolate stages of the gain section, helium ions are implanted in 3-μm stripes. The quantum wells in the implanted regions are deactivated during the quantum well intermixing step discussed earlier. This is to prevent excess photon absorption in the implanted regions. To allow for alignment tolerance and to account for the straggle of the implant, a 7-μm stripe is intermixed with the implanted stripe centered in this region. Two series of implants are required for isolation. One series is designed to cover the region from the top of the ridge down to the substrate, and the other series is designed for the region beside the ridge, from the top of the waveguide down to the substrate. This supplied over 300 kΩ of isolation between stages. Last, Ti-Pt-Au is deposited and annealed for p-metal contacts and to serve as the interconnects for the series-connected gain section.

B. Gain-Levered SGDBR Laser

The GL-SGDBR laser is illustrated schematically in Fig. 2 and consists of six sections, which are a gain-lever section, front SGDBR mirror, rear SGDBR mirror, phase section, rear absorber, and output SOA. The gain-lever section has a 460 μm-long gain section and a 90-μm-long lever section. The output SOA is 550 μm. The SGDBR mirror design is the same as for the BC-SGDBR laser. The device is fabricated with a common 1.4-Q waveguide. An offset quantum well integration platform is used in which the quantum wells are grown on top of the waveguide, which is 3500 Å thick. The wells and waveguide are separated by a thin InP stop etch layer. Passive sections, such as SGDBR mirrors and the phase section, are formed by selectively etching off the quantum wells using a wet etch process. Once the quantum wells are removed from the mirror sections, the gratings are etched directly into the top of the waveguide. The regrowth is the same as that for the BC-SGDBR laser, a thick p-InP cladding followed by a p-InGaAs cap. Ridges are etched and, just as for the BC-SGDBR process, Ni–AuGe–Ni–Au metal is used for the n-contacts and Ti-Pt-Au is used for the p-contacts. Selectively removing the regrown p-InGaAs and

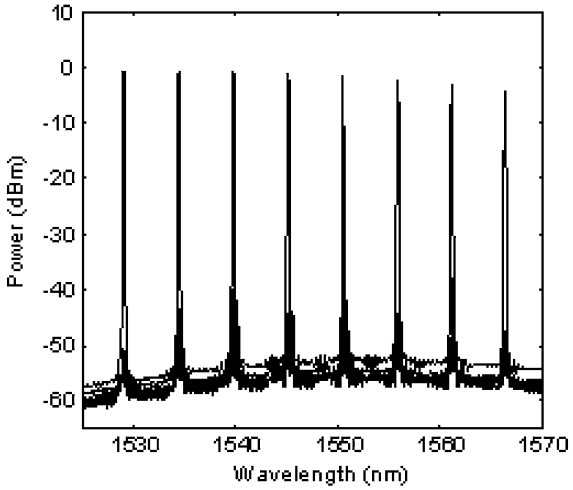

Fig. 3. Superimposed optical spectra for a 3-stage BC-SGDBR laser at varying front mirror currents.

TABLE I
OPTICAL AND ELECTRICAL CHARACTERISTICS OF BC-SGDBR LASERS

Stages	Threshold Current	Differential Efficiency	DC Input Impedance
1	1	1	8.5 Ω
3	0.36	2.8	50 Ω
4	0.26	3.4	77 Ω
8	0.17	4.5	222 Ω

implanting protons provides carrier confinement between adjacent device sections. Unlike the BC-SGDBR, the GL-SGDBR retains an electrically continuous n-type contact between all diodes. More details of the fabrication process are given in [7].

III. RESULTS

A. Bipolar Cascade SGDBR Laser

Continuous wave room temperature light–current–voltage measurements were taken. The normalized threshold current and DQE as well as absolute input impedance for each device are shown in Table I. For the 1-stage laser, the threshold current is 42 mA, and the single-ended DQE is 11%. The threshold current and DQE scale as expected. The 3-stage device has an input impedance of 50 Ω, which has advantages for applications in RF photonics, as will be discussed. The loss for each segment was extracted and is 0.12 dB per pass. This results in a slightly sublinear dependence of DQE on the number of stages. Superimposed optical spectra at varying front mirror currents for a 3-stage SGDBR laser are shown in Fig. 3. The devices have a tuning range of 38 nm with 40 dB or more SMSR over this range.

The small signal modulation response of both a 1-stage and a 3-stage SGDBR laser shown in Fig. 4 was measured with an Agilent 8703A lightwave component analyzer. In both cases, the device was mounted on an AlN submout, and the contact

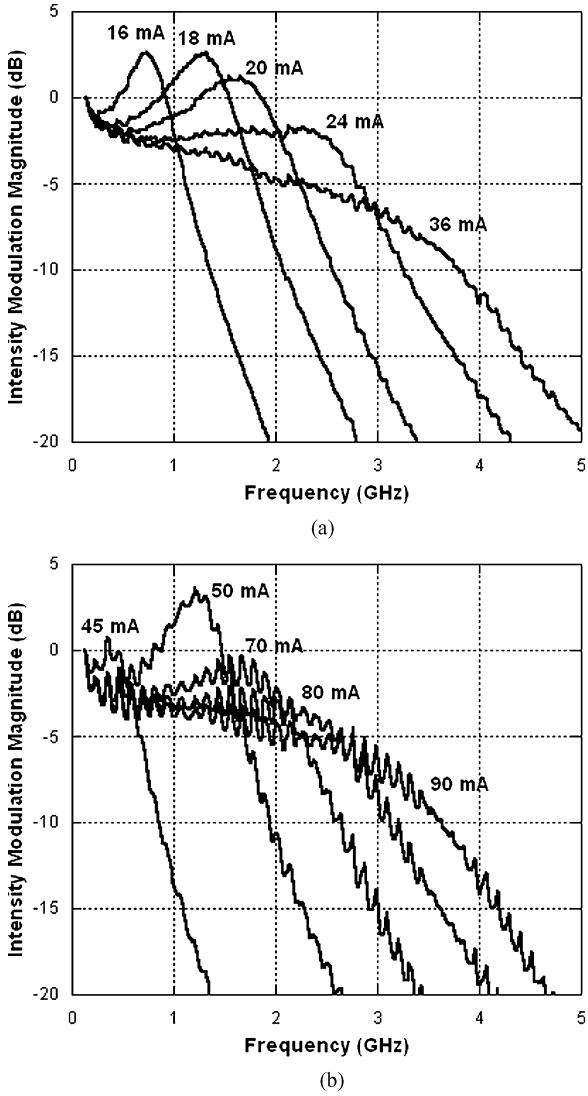

Fig. 4. Small signal modulation response at varying gain section bias currents for (a) 3-stage BC-SGDBR laser and (b) 1-stage BC-SGDBR laser, both operating at 1567 nm. The additional noise in the response for the 1-stage laser could be due to impedance mismatch. For these measurements, both lasers were not terminated.

pads were wire-bonded to a coplanar waveguide line on the submount. The laser was then biased through a bias tee. The response for the 3-stage devices is as good or better than that of the 1-stage devices in terms of 3-dB bandwidth. For applications in optical links, BC-SGDBR lasers can lead to improved link gain and NF. The 3-stage device also has a 50-Ω input impedance, which could simplify broad band matching.

To compare the direct modulation performance of BC-SGDBR lasers to conventional SGDBR lasers, the devices were also digitally modulated with large signal data. Nonreturn to zero (NRZ) pseudorandom bit stream (PRBS) data was provided by an HP 71612B signal generator at a rate of 2.5 Gb/s and a word length of $2^{31} - 1$. The gain section bias current and peak-to-peak modulation voltage were chosen to maximize the extinction ratio (ER). The bias point and voltage swing that generated the deepest modulation depth, that is to say the lowest zero signal level, resulted in the highest ER. Under

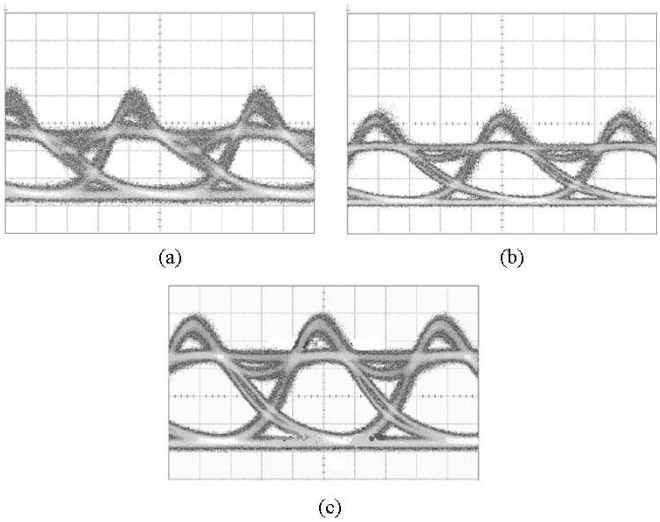

Fig. 5. 2.5-Gb/s NRZ eye patterns for (a) 1-stage device with $I_{bias} = 70$ mA, $V_{p-p} = 1.49$ V, ER = 8.0 dB, (b) 3-stage device with $I_{bias} = 24$ mA, $V_{p-p} = 0.65$ V, ER = 9.6 dB, and (c) 4-stage device with $I_{bias} = 17.5$ mA, $V_{p-p} = 0.6$ V, ER = 8.0 dB.

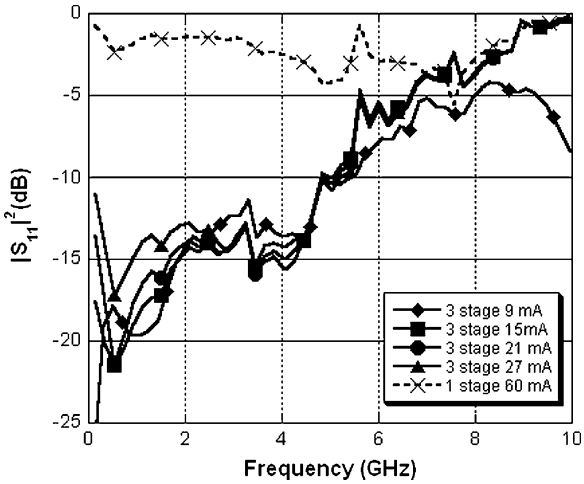

Fig. 6. RF reflection coefficient for a 3-stage device at various gain section biases and for a 1-stage device at a single bias.

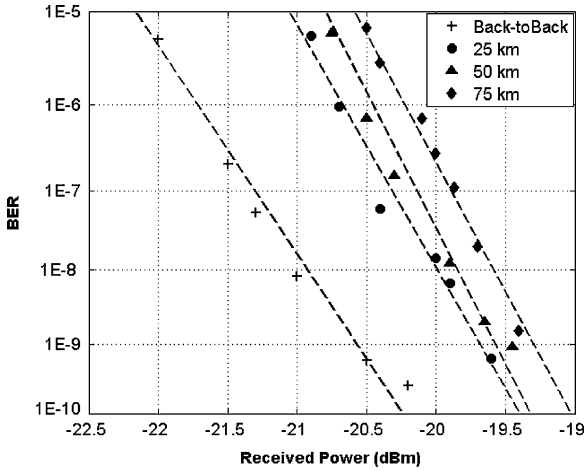

Fig. 7. BER data transmission through back-to-back (0 km), 25 km, 50 km, and 75 km of single mode fiber for a 3-stage SGDBR with $I_{bias} = 22.6$ mA and $V_{p-p} = 0.69$ V.

such conditions, we see some overshoot in the eye diagrams, shown in Fig. 5, due to the relaxation resonance of the lasers. For a 1-stage conventional SGDBR laser, a bias of 70 mA and peak-to-peak voltage swing of 1.49 V resulted in an ER of 8.0 dB. For a 3-stage device, a bias of 24 mA and a peak-to-peak swing of 0.65 V yielded a 9.6-dB ER, and for a 4-stage device a bias of 17.5 mA and peak-to-peak swing of 0.6 V yielded an 8.0-dB ER. For this measurement, the devices were not terminated with series resistors. In the case of the 3-stage device, the input impedance is 50 Ω ; therefore, this device is intrinsically matched to the 50-Ω RF source. If the single-stage device were connected in series with a termination resistor, which is ordinarily required for broad band matching, significantly more voltage swing would be required to achieve the same modulating laser current and subsequently the same output ER. The RF reflection coefficient was also measured for a 3-stage device at various bias currents and for a single-stage device at a single bias current. A plot of this parameter is shown in Fig. 6, displaying the improved response for the 50-Ω input impedance 3-stage laser. To further investigate the transmission properties of the BC-SGDBR lasers, the bit error rate (BER) was measured for transmission through up to 75 km of standard single mode fiber and compared to back-to-back (0 km) data as shown in Fig. 7. The power penalties for error free operation through 25, 50, and 75 km of fiber were 0.8, 0.9, and 1.25 dB, respectively, and are comparable to or better than previously reported data for directly modulated SGDBR lasers [13]. The dispersion penalties are due to the chirping of the laser [14].

B. Gain-Levered SGDBR Laser

Continuous wave room temperature light-lever current measurements were taken as a function of gain section current (Fig. 8). With separately biased gain and lever contacts, threshold current is reduced and DQE near threshold is increased for increasing gain current. For gain currents greater than 35 mA, sharp turn-on lasing was observed at lever currents of less than 2 mA. This is typical of bistable laser diodes. Optical power roll-off with higher currents is due to device heating. A summary of the optical characteristics is shown in Table II. With the gain and lever contacts shorted, the laser threshold current was 30 mA. At high gain currents, the light-current curve showed hysteretic behavior (Fig. 9) indicative of laser bistability. Since the mirror design for the GL-SGDBR laser is the same as that for the BC-SGDBR laser, similar tuning characteristics were observed.

The GL-SGDBR lasers were also mounted on carriers for RF testing. The small signal modulation response was measured on unterminated devices (Fig. 10). Despite the hysteretic behavior of the CW *L–I* characteristic, the modulation bandwidth is at least as good as a conventional laser. The 3-dB bandwidth was measured to be 5.0 GHz for $I_{gain} = 60$ mA and $I_{lever} = 8$ mA.

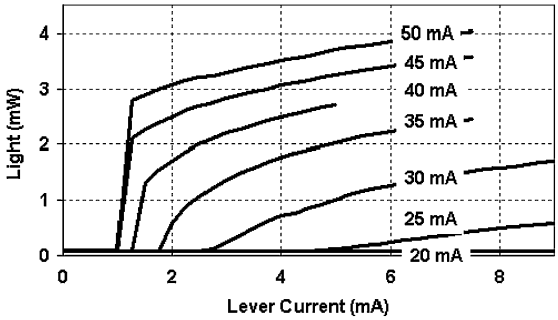

Fig. 8. DC optical power versus lever current with gain current as a parameter for GL-SGDBR laser with $I_{SOA} = 30$ mA.

TABLE II
OPTICAL CHARACTERISTICS OF GL-SGDBR LASERS

Gain Bias	Threshold Current	Differential Efficiency
30 mA	2.5 mA	6.4 %
40 mA	1.6 mA	36 %
50 mA	1.4 mA	68 %

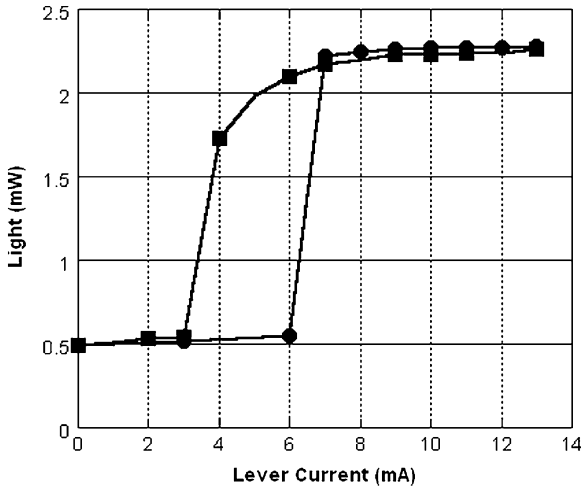

Fig. 9. CW L–I characteristic for GL-SGDBR laser. Hysteresis observed for $I_{SOA} = 70$ mA, $I_{gain} = 70$ mA. Circles are for increasing lever current, squares are for decreasing lever current.

The relative intensity noise (RIN) of the laser was measured (Fig. 11) as a function of lever current for fixed gain current and with the gain and the lever sections shorted together. The RIN appears consistent at similar resonance peaks when driving the lever independently. The RF small-signal bandwidth and the RIN peak scales proportionally with laser output power. The devices were also digitally modulated with an NRZ $2^{31} - 1$ PRBS bit stream at 2.5 Gb/s and demonstrated open eyes as shown in Fig. 12. With $I_{gain} = 60$ mA, $I_{lever} = 11$ mA, and $V_{p-p} = 1.0$ V, the ER is 5.4 dB. This is likely limited by pattern affects created by the output SOA.

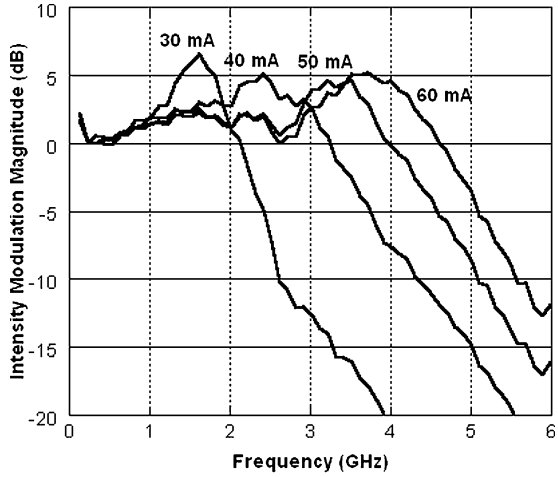

(a)

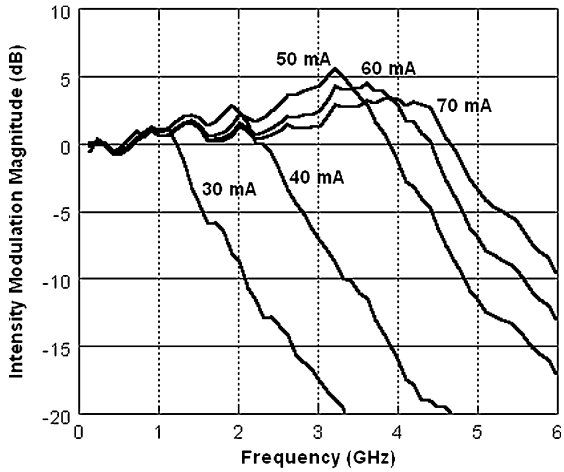

(b)

Fig. 10. Small signal modulation response of GL-SGDBR laser (a) modulating the lever section at $I_{lever} = 8$ mA, I_{gain} as a parameter, and (b) modulating both sections shorted with $I_{gain} + I_{lever}$ as a parameter.

IV. WAVELENGTH CONVERTER

The fabrication process for the BC-SGDBR lasers allows for the monolithic integration of other optical components such as semiconductor optical amplifiers (SOAs) or photodetectors (PDs). Most current wavelength conversion technologies for wavelength-division multiplexing (WDM) applications involve the integration of discrete optical components [15]. In order to reduce the number of times light must be coupled on and off chip and therefore improve performance, devices can be monolithically integrated on the same chip. By increasing the functionality on chip, packaging requirements are also reduced. A monolithic widely tunable wavelength converter can be fabricated by integrating an input SOA and PD receiver with an SGDBR laser transmitter on a common InP platform. In the case of a directly modulated laser transmitter, the photocurrent from the receiver is transferred by way of a metal interconnect to the gain section of the laser. The performance of such a photocurrent-driven monolithically integrated device relies heavily on the amount of photocurrent that can be generated on chip to directly modulate the laser and achieve sufficient ER. It has been demonstrated

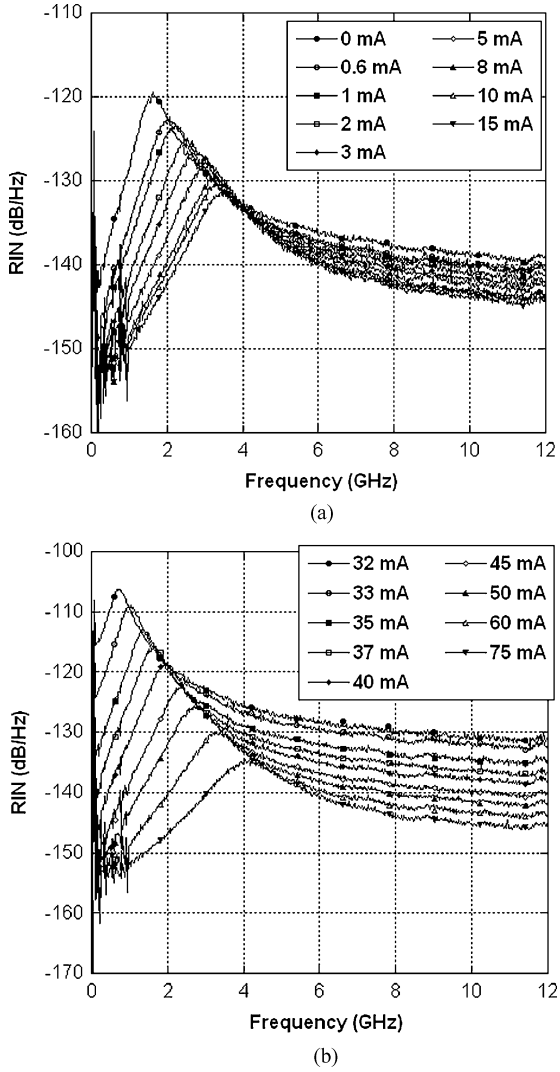

Fig. 11. RIN spectra of GL laser with (a) I_{lever} as parameter, $I_{gain} = 50$ mA, and (b) gain and lever shorted with $I_{gain} + I_{lever}$ as a parameter.

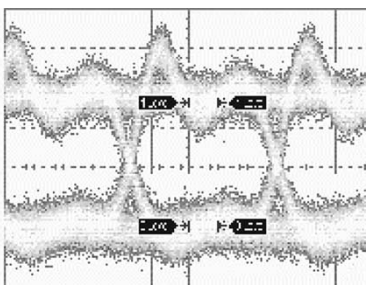

Fig. 12. 2.5-Gb/s NRZ eye diagram for GL-SGDBR laser with $I_{SOA} = 30$ mA, $I_{gain} = 60$ mA, $I_{lever} = 11$ mA, $V_{p-p} = 1.0$ V, ER $= 5.4$ dB.

that bipolar cascade lasers require significantly less modulation current than conventional single-stage lasers to achieve a certain level of ER.

Widely tunable BC-SGDBR lasers have been monolithically integrated with SOA-PD receivers to perform wavelength conversion. A circuit schematic of the wavelength converter is shown in Fig. 13. The receiver consists of a 750-μm-long input

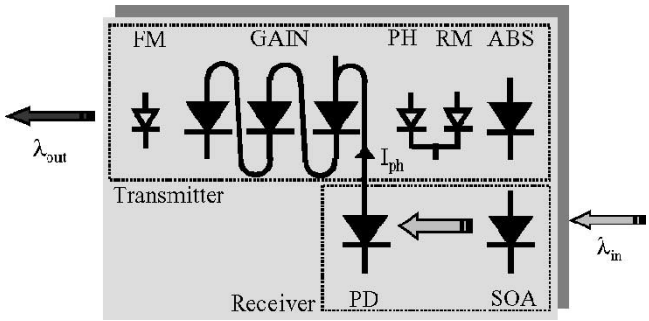

Fig. 13. Circuit schematic of 3-stage BC-SGDBR-based wavelength converter. Large diodes in schematic have as-grown active quantum wells and small diodes have intermixed passive quantum wells. Photocurrent from the PD is transferred to the first stage of the gain section through a metal interconnect.

SOA followed by a 200-μm-long quantum well PD. A metal interconnect provides a means for transferring the photocurrent from the PD to the p-metal pad of the first stage of the laser. These devices were also mounted on AlN carriers. Independent direct current (dc) bias is provided to the laser through an off-chip bias tee.

In order to test wavelength conversion, 2.5-Gb/s NRZ signals were provided to an Agilent lightwave transmitter, which operates at a wavelength of 1548.1 nm. The transmitted optical pulses were then amplified with an erbium doped fiber amplifier (EDFA) and then filtered to suppress some of the amplified spontaneous emission (ASE) noise. The light was then sent through a polarization controller before being input to the on-chip receiver. The wavelength converted output signals are attenuated and then input to an Agilent lightwave receiver. BER measurements are taken with an HP 70843B BER tester (BERT).

The 1-stage, 3-stage, and 8-stage BC-SGDBR wavelength converters were tested. The lasers were biased somewhere near threshold. The bias and input optical power were optimized to maximize the ER of the wavelength converted output signal. Low operating points and low input powers yielded the highest ER and subsequently the lowest power penalties. Wavelength converted output eye diagrams are shown in Fig. 14. The eye patterns are compared in terms of the amount of photocurrent generated in the PD as opposed to input optical power. For the 1-stage wavelength converter, a significant amount of optical input power is required in order to generate enough photocurrent to modulate the laser. The devices are fabricated on a centered quantum well platform; therefore, the confinement factor is fairly high and the SOAs tend to saturate at relatively low input powers. For the 1-stage wavelength converter with 8.2 mA of average photocurrent generated in the PD, the output signal has an ER of only 2.3 dB and exhibits a poorly opened eye. Because of the limited DQE in this conventional laser, not enough current swing was generated to provide a good ER. There is a significant amount of overshoot in the eye diagram because the SOA is saturated. However, by reducing the input power here, the eye closed up even more and there was a very low ER. With a similar amount of average photocurrent, 8.65 mA, the 3-stage device achieved 7.9 dB of ER, however there is overshoot in the eye also due to the saturation of the SOA.

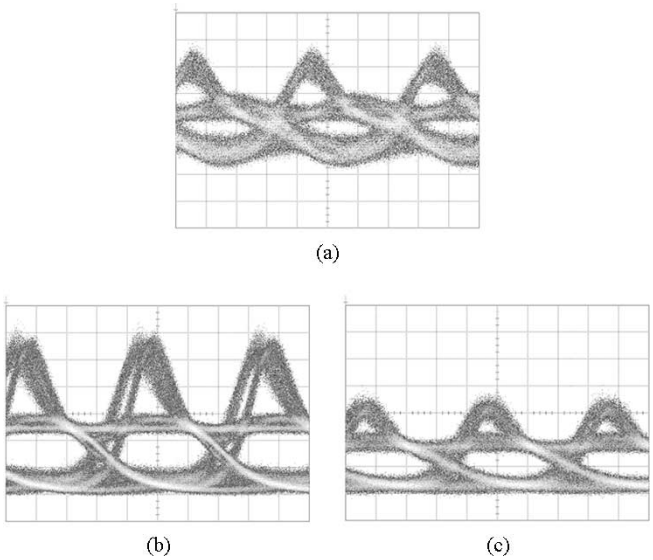

Fig. 14. 2.5-Gb/s wavelength converted output eye diagrams. Input wavelength is 1548.1 nm, and output wavelength is 1565 nm for all cases. (a) 1-stage wavelength converter with $I_{ph}^{avg} = 8.2$ mA, ER $= 2.3$ dB, (b) 3-stage wavelength converter with $I_{ph}^{avg} = 8.65$ mA, ER $= 7.9$ dB, and (c) 8-stage wavelength converter with $I_{ph}^{avg} = 5.5$ mA, ER $= 6.5$ dB.

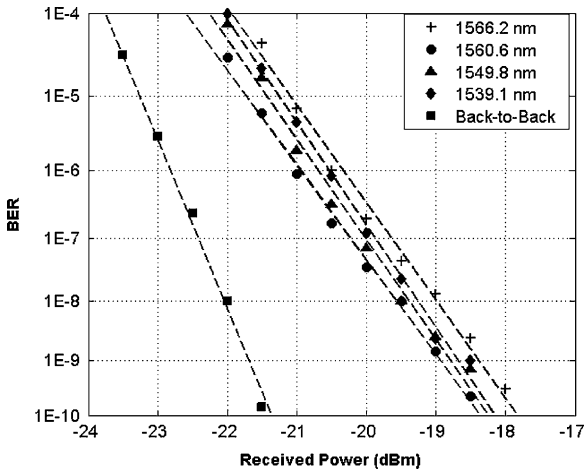

Fig. 15. BER for various converted output wavelengths for 3-stage wavelength converter. The input wavelength is 1548.1 nm.

With lower input powers, this overshoot is suppressed somewhat; however, the ER also decreases. For the 8-stage device, with 5.5 mA of average photocurrent, 6.5 dB was achieved, and the only overshoot seen in the eye pattern is due to the relaxation resonance of the laser. Although the 8-stage device can be operated at low input powers since it has the highest DQE, the ER is limited by the maximum output power of the laser. The maximum output power of the 8-stage laser is slightly less than that of the 1-stage laser or the 3-stage laser, likely due to heating, which causes a roll-over in the *L–I* characteristic. The 3-stage wavelength converter operated the best in terms of ER and BER. BER data is shown in Fig. 15 for several converted output wavelengths. The average input fiber power for this set of data was around 2.5 dBm. The power penalty ranges from 2.7–3.2 dBm. This penalty was slightly reduced for lower input powers, likely due to the suppression of the overshoot in the eye pattern. The conversion efficiency, which is the ratio of output signal power to input signal power, was also measured for the 3-stage wavelength converter. The device provides up to 7 dB of chip gain, where 4–5 dB of loss is incurred at each input and output. The gain could be further enhanced with a better set of lasers that are more efficient, or an improved SOA design.

V. Conclusion

We have described the design, fabrication, and performance of two novel implementations of widely tunable SGDBR lasers. The BC-SGDBR lasers have enhanced DQE allowing for lower drive voltages for direct modulation. A 3-stage BC-SGDBR laser has a 50-Ω input impedance allowing for intrinsic matching to an RF power source. The GL-SGDBR lasers also demonstrate improved DQE and have sharp lasing turn-on characteristics. The BC-SGDBR laser was also monolithically integrated with a receiver to perform wavelength conversion and demonstrates improved conversion efficiency due to the enhanced DQE.

Acknowledgment

The authors acknowledge Prof. M. Huang from the Physics Department of the University at Albany, Albany, NY, for performing the helium implants.

References

[1] J. Kim *et al.*, "Near room-temperature CW operation of electrically pumped, multiple-active-region 1.55 μm VCSEL's with high differential efficiency," *Appl. Phys. Lett.*, vol. 77, pp. 3137–3139, 2000.

[2] S. G. Ayling *et al.*, "Novel integrated laser devices with greatly enhanced quantum efficiency and intrinsic RF matching for low loss, broad band opto-microwave applications," in *Conf. Microwave Photonics*, 1998, pp. 161–164.

[3] K. D. Choquette and E. Young, "Cascade vertical cavity surface emitting laser arrays," Presented at the LEOS 2002 Annu. Meeting, Glasgow, U.K., 2002, Paper TuAA1.

[4] J. T. Getty, L. A. Johansson, E. J. Skogen, and L. A. Coldren, "1.55 μm bipolar cascade segmented ridge lasers," *IEEE J. Sel. Topics Quantum Electron.*, vol. 9, no. 5, pp. 1138–1145, Sep./Oct. 2003.

[5] M. N. Sysak *et al.*, "Single-chip wavelength conversion using a photocurrent-driven EAM integrated with a widely tunable sampled-grating DBR laser," *IEEE Photon. Technol. Lett.*, vol. 16, no. 9, pp. 2093–2095, Sep. 2004.

[6] J. S. Barton *et al.*, "2.5 Gbit/s error-free wavelength conversion using a monolithically-integrated widely-tunable SGDBR-SOA-MZ transmitter and integrated photodetector," *IEEE Photon. Technol. Lett.*, vol. 16, no. 6, pp. 1531–1533, Jun. 2004.

[7] J. M. Hutchinson *et al.*, "Monolithically integrated InP-based tunable wavelength conversion," in *Proc. SPIE Photonics West*, 2004, Paper 5349–5325.

[8] H. Kawaguchi, "Bistable laser diodes and their applications: State of the art," *IEEE J. Sel. Topics Quantum Electron.*, vol. 3, no. 5, pp. 1254–1270, Sep./Oct. 1997.

[9] K. Y. Lau, "Passive microwave fiber-optic links with gain and a very low noise figure," *IEEE Photon. Technol. Lett.*, vol. 3, no. 6, pp. 557–559, Jun. 1991.

[10] J. Lee and P. Zory, "Sharp turn-on diode lasers," in *Proc. 2003 IEEE LEOS Annu. Meeting Conf.*, vol. 2, 2003, pp. 987–988.

[11] H.-K. Sung *et al.*, "Optical injection-locked gain-lever distributed Bragg reflector lasers with enhanced RF performance" in *Proc. Microwave Photonics MWP'04 Conf.*, Oct. 2004, pp. 225–228 Paper TE-1.

[12] E. J. Skogen *et al.*, "A quantum-well intermixing process for wavelength-agile photonic integrated circuits," *IEEE J. Sel. Topics Quantum Electron.*, vol. 8, no. 4, pp. 863–869, Jul./Aug. 2002.

[13] M. L. Majewski *et al*., "Direct intensity modulation in sampled-grating DBR lasers," *IEEE Photon. Technol. Lett*., vol. 14, no. 6, pp. 747–749, Jun. 2002.
[14] S. L. Lee *et al*., "Dynamic responses of widely tunable sampled grating DBR lasers," *IEEE Photon. Technol. Lett*., vol. 8, no. 12, pp. 1597–1599, Dec. 1996.
[15] S. J. B. Yoo, "Wavelength conversion technologies for WDM network applications," *J. Lightw. Technol*., vol. 14, no. 9, pp. 955–966, Sep. 1996.

Jonathan Klamkin was born in Oceanside, NY, in 1980. He received the B.S. degree in electrical and computer engineering from Cornell University, Ithaca, NY, in 2002, and the M.S. degree in electrical and computer engineering from the University of California, Santa Barbara, in 2004. He is currently working toward the Ph.D. degree in materials at the University of California, Santa Barbara.

His current research interests include the design, growth, fabrication, and characterization of widely tunable semiconductor lasers, photodetectors, modulators, and semiconductor optical amplifiers for photonic integrated circuits in the InGaAsP/InP material system.

John M. Hutchinson received the Ph.D. degree in electrical engineering from the University of California, Berkeley, in 1994.

He worked in Intel Corporation's Components Research Department from 1994 to 2001, where his focus was on advanced silicon process technology. He is currently with Intel's Strategic Technology Group, Santa Ana, CA, as a Researcher-in-Residence at the University of California, Santa Barbara. His research focuses on in-plane InP-based optoelectronics design and fabrication technology through design, fabrication, and testing of optical wavelength converters.

Jonathan T. Getty received the B.S. degree in electrical engineering from Cornell University, Ithaca, NY, and worked on satellite transponders at the Jet Propulsion Laboratory before graduate study at the University of California, Santa Barbara. There he received the M.S. degree in 1998 and the Ph.D. degree in 2003, both in electrical and computer engineering.

His current research interests include design, fabrication, and characterization of bipolar cascade modulators and semiconductor lasers, photonic integrated circuits, and novel quantum well intermixing techniques.

Leif A. Johansson (M'04) received the Ph.D. degree in engineering from University College London, London, U.K., in 2002.

He took up a postdoctoral position at the University of California, Santa Barbara, in 2002. His current research interests include design and characterization of integrated photonic devices for analog and digital applications.

Erik J. Skogen was born in Minneapolis, MN, in 1975. He received the B.S. degree in electrical engineering from Iowa State University, Ames, IA, in 1997, and the M.S. and Ph.D. degrees in electrical and computer engineering from the University of California, Santa Barbara, in 1999 and 2003, respectively.

He has authored or coauthored over 50 technical publications and presentations. His current research interests include widely tunable semiconductor lasers, monolithic integration techniques for photonic integrated circuits, growth aspects in the InGaAsP/InP and InGaAsP/GaAs material systems using MOCVD, and quantum well intermixing.

Larry A. Coldren (S'67–M'72–SM'77–F'82) received the Ph.D. degree in electrical engineering from Stanford University, Stanford, CA, in 1972.

In 1984, after 13 years in research at Bell Laboratories, he was appointed Professor of electrical and computer engineering at the University of California, Santa Barbara (UCSB). In 1986, he assumed a joint appointment with the Materials Department, and in 2000 he was awarded the Fred Kavli Chair in Optoelectronics and Sensors. He also serves as Chairman and Chief Scientist at Agility Communications, Inc., a company he co-founded in 1998 to commercialize widely tunable optical transmitters and transponders. At UCSB his research has included work on novel fabrication technology and optoelectronic components, including guided-wave and vertical-cavity modulators and lasers, as well as photonic integrated circuits that incorporate widely tunable lasers with numerous other optical components. He has authored or co-authored over 700 papers, five book chapters, one textbook, and has been issued 36 patents.

Dr. Coldren is a Fellow of the OSA and IEE, U.K., a member of the National Academy of Engineering, and a recipient of the 2004 John Tyndall Award.

Proc. LEOS 2005, The 18th Annual Meeting of the IEEE, paper no. TuBB3, pp. 408-409, Sydney, Australia (October 23-27, 2005)

Monolithic Dual-Quantum-Well 10 Gb/s Mach-Zehnder Transmitter

Anna Tauke-Pedretti, Matthew N. Sysak, Jonathon S. Barton, James W. Raring,
Matthew Dummer and Larry A. Coldren
Departments of Electrical and Computer Engineering and Materials
University of California Santa Barbara
Santa Barbara, CA 93106
Email: atauke@engineering.ucsb.edu

***Abstract*— A 10 Gb/s transmitter composed of a Sampled-Grating DBR (SGDBR) laser and Mach-Zehnder modulator was fabricated on a dual-quantum-well integration platform. The device exhibited error free operation and negative chirp.**

I. Introduction

Transmitters play an important role in fiber optic communication systems. The monolithic integration of the laser and modulator reduces packaging cost and insertion losses while eliminating polarization dependance. Widely tuneable transmitters have the additional advantage of reducing the inventory requirements for providers. While, negative chirp provides the benefits of high bit rates and longer transmission distances.

It is well known the use of quantum-wells within the Mach-Zehnder allows for higher index changes [1]. Previously, a sampled-grating DBR laser (SGDBR) and a Mach-Zehnder modulator has been successfully integrated using bulk InGaAsP in the modulator regions [2]. Building upon this work the first widely tuneable Mach-Zehnder transmitter on a dual-quantum-well integration platform has been fabricated. This devices implements a SGDBR laser and a series-push-pull Mach-Zehnder modulator-as shown in Fig. 1.

II. Device

The transmitter's epitaxial structure is comprised of two sets of quantum-wells identical to that in [3]. A set of offset quantum-wells (photoluminescence = 1550 nm) are used in the gain section of the SGDBR and the SOAs. A separate set of seven quantum-wells (photoluminescence = 1465 nm) centered in the InGaAsP waveguide aid the modulator efficiency. The fabrication of this device requires a single blanket regrowth of the InP cap and InGaAs contact layer following the selective removal of the offset quantum-wells from the passive sections and the etching of holographically defined sampled gratings.

The modulator has a traveling wave electrode segmented into 8-50 μm long T-sections to capacitively load the transmission line allowing for better impedance matching. The ridge width is reduced from 3 μm in the laser and SOA regions to 2 μm within the modulators. In addition to the thinner ridge widths, BCB is used underneath the modulator electrode to reduce the capacitance. An integrated 50 Ω NiCr resistor provides on chip termination. The 400 μm long Mach-Zehnder

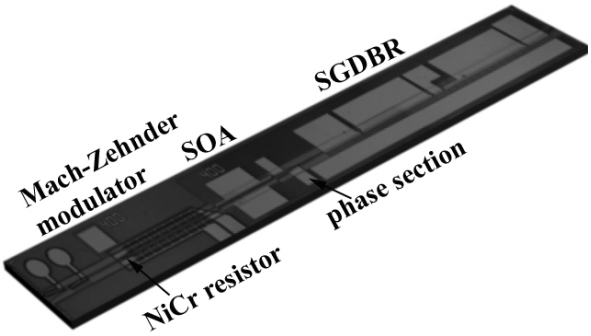

Fig. 1. Diagram of integrated widely tuneable transmitter chip

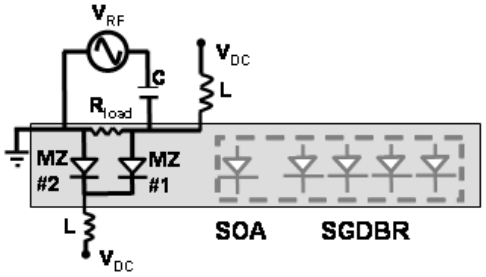

Fig. 2. Schematic of series-push-pull biasing scheme

is operated in a series-push-pull fashion with the RF signal applied across the modulator electrode (Fig. 2). This configuration allows for improved bandwidth, lower modulation voltages and small chirp values [2], [4].

In each arm of the Mach-Zehnder there is a 400 μm SOAs to increase the output power of the device and compensate for propagation losses. Phase sections within the interferometer arms are implemented to allow for biasing to π-phase-shift. A flared and curved output waveguide as well as an AR coating was used to reduce optical reflections and to aid in fiber coupling.

III. Experiments

Following fabrication the devices were thinned, cleaved and mounted onto an aluminum nitride carrier for testing. All DC contacts were wirebonded to the carrier and contacted via a

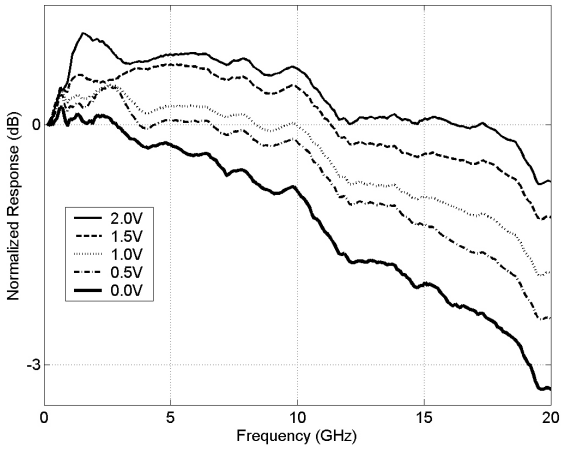

Fig. 3. Bandwidth of transmitter of different Mach-Zehnder biases

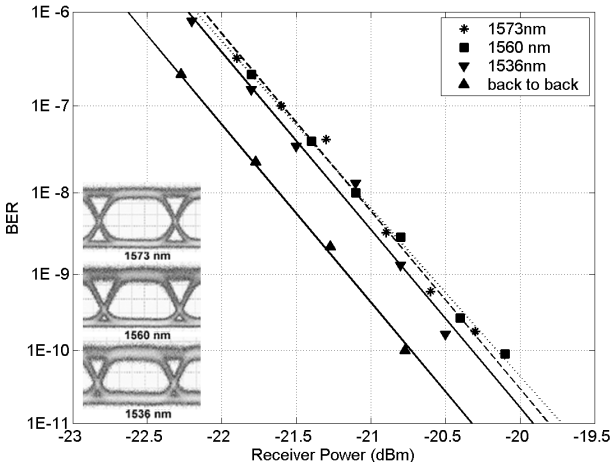

Fig. 4. BER for various wavelengths.

probe card. The modulator was directly probed with a CPS probe to prevent any parasitic effects from wirebonds.

Bandwidth measurements have been taken for various modulator biases. These measurements clearly show greater than 20 GHz bandwidth for all modulator biases greater than 0 V (Fig. 3).

Bit Error Rate testing at 10 Gb/s with a NRZ 2^{31}-1 pseudorandom bit sequence was done for both back-to-back and transmission through 25 km and 50 km of Corning SMF-28 fiber. The modulator was biased at -1 V across each arm and driven with a 1.87 V_{p-p} electrical signal from a HP 70843B BERT. The optical signal from the device was amplified with a high power Erbium Doped Fiber Amplifier (EDFA) followed by an optical filter, fiber for transmission and finally an attenuator before being detected by an HP 83434A 10 Gb/s photoreceiver. Error free operation (better than 1e-9 BER) and extinction ratios in excess of 10 dB were achieved for a wavelength range greater than 35 nm (Fig. 4). Transmission measurements show negative chirp across the wavelength range with a trend towards more negative chirp at lower wavelengths (Fig. 5).

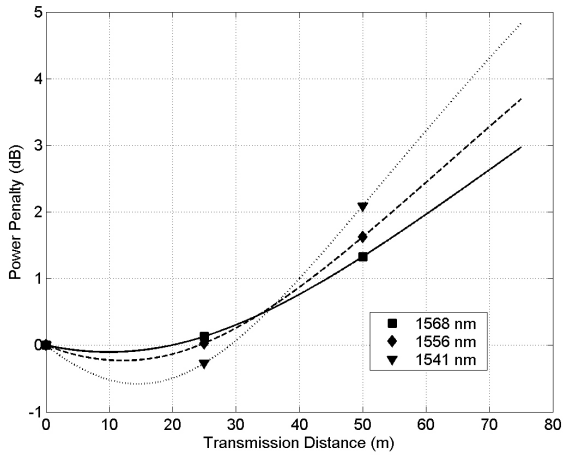

Fig. 5. Power penalty vs. transmission distance for various wavelengths. BER measurements were taken for transmission through 0 km, 25 km and 50 km of Corning SMF-28 fiber

IV. Conclusion

For the first time a widely tunable Mach-Zehnder transmitter has been fabricated on a dual-quantum-well platform using a single blanket regrowth. The device demonstrates over 35 nm of tuning and bandwidth in excess of 20 GHz. The low DC bias of 1 V for this device means there is minimal insertion losses and low power consumption. Error free operation has been demonstrated for up to 50 km of transmission through fiber and all wavelengths have negative chirp with a 1.87 V_{p-p} drive voltage.

Acknowledgment

The authors would like to thank DARPA-LASOR for funding and Agility Communications for AR coatings.

References

[1] W. Bardyszewski, D. Yevick, L. Yong, C. Rolland, and S. Bradshaw, "Theoretical and experimental analysis of mach-zehnder quantum-well modulators," *Journal of Applied Physics*, vol. 80, pp. 1136–41, July 1996.

[2] J. S. Barton, M. L. Masanovic, A. Tauke-Pedretti, E. J. Skogen, and L. A. Coldren, "Monolithically-integrated 40gbit/s widely-tunable transmitter using series push-pull mach-zehnder modulator soa and sampled-grating dbr laser," in *Optical Fiber Communication Conference and Exposition and The National Fiber Optic Engineers Conference*, Anaheim, CA USA, March 2005, paper OTuM3.

[3] M. N. Sysak, J. S. Barton, J. W. Raring, M. Dummer, A. Tauke-Pedretti, D. J. Blumenthal, and L. A. Coldren, "10 gb/s photocurrent driven, widely tunable electroaborption modulator based wavelength converter," in *Optical Fiber Communication Conference and Exposition and The National Fiber Optic Engineers Conference*, Anaheim, CA USA, March 2005, paper OTuM4.

[4] R. G. Walker, "High-speed iii-v semiconductor intensity modulators," *IEEE J. Quantum Electron.*, vol. 27, pp. 654–667, Mar. 1991.

I. Photonic Integrated Circuits (PICs) and Related Technology

C. Wavelength Converter Technology

Proc. OFC/NFOEC 2005, paper no. OWK4, Anaheim, CA (March 6-11, 2005)

Programmable Optical Buffering using Fiber Bragg Gratings combined with a Widely-Tunable Wavelength Converter

Chin-Hui Chen, Leif A. Johansson, Vikrant Lal, Milan L. Mašanović,
Daniel J. Blumenthal and Larry. A. Coldren
Department of Electrical and Computer Engineering, University of California, Santa Barbara, CA 93106
janet@ece.ucsb.edu

Abstract: A 40Gbps RZ all-optical buffering method implemented by FBG and tunable wavelength converter is presented. Preliminary results of time-delay up to 7 μs and pulse broadening were measured. System measurements at 10Gbps show desired delay programmability.

OCIS codes: (060.2330) Fiber Optics Communications; (060.2360) Fiber Optics links and subsystems

1. Introduction

In proposed all-optical packet-s witched networks [1], optical buffering is required to avoid contention issues. Contention occurs when more than one packet of the same wavelength competes for the same output port at the same time. Thus, buffering is essential to many optical packet switch implementations. In order to eliminate the extra optoelectronic conversions and the inefficiency of existing electronic system, all-optical buffering is being widely investigated.

In this paper a method of all-optical buffering that can provide a large number of rapid selectable [2] discrete delay values with low insertion loss and long available maximum delay is presented and demonstrated. The main idea is illustrated in Fig.1 in which Fiber Bragg Gratings (FBG) and wavelength converters (WC) are used to implement wavelength-dependent delay lines. In the proposed method an incoming packet is converted by a rapid-tunable WC to a specific wavelength which is controlled by an external decision signal, and the desired delay value is mapped to the wavelength domain by cascaded FBG elements. Various implementations of wavelength conversion have been presented [3,4,5], specifically the wavelength converter, integrated with SGDBR, used in this work is described in [6].

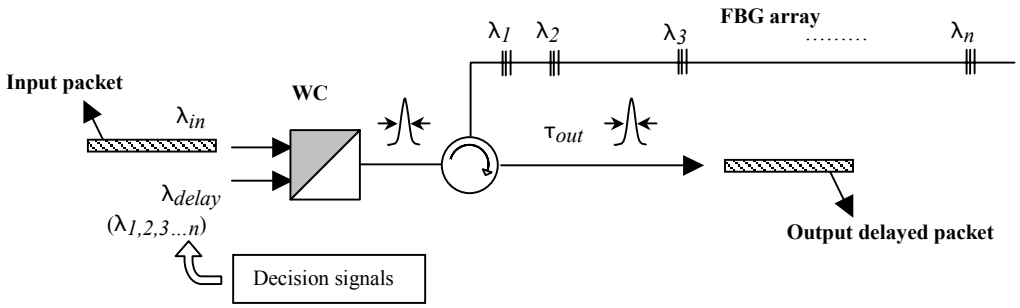

Fig. 1. System concept for optical buffering implemented by FBGs and wavelength converters (WC).

2. FBG buffer design

This system was designed to be compatible with a 40Gbps RZ communication system, in which less than 12.5ps reflected pulse width is required, and therefore a grating bandwidth ≥100GHz is needed. A 200GHz channel spacing was chosen to keep adjacent channel crosstalk below –20dB. With the selected channel spacing, up to 25 discrete delay values can be reached using an all-optical wavelength converter based on a rapid-switchable widely-tunable SG-DBR laser with a tuning range exceeding 40nm [6]. The design was aimed at satisfying performance targets of low group velocity delay (GVD) and moderately low loss, using a relatively simple structure suitable for low-cost manufacturing, considering of future expansion. A central tradeoff in the grating design is between peak reflectivity and GVD, by the means of changing grating burst length. Fortunately, for reflection-type delay line application, high in-band extinction is not necessary allowing the use of shorter gratings with less than the typical 99.9% peak reflectivity.

The final specifications of the FBG was a 2.5mm grating burst, raised cosine apodization and with an index contrast of Δn= 0.0008. The use of a non-chirped grating was found to ensure low GVD and simple manufacturing. The modeled performance of the grating includes <5ps group delay variation and 80.9% peak reflectivity, resulting in less than 1dB insertion loss and a calculated impulse response with 6.3ps FWHM.

3. FBG buffer characterization

To demonstrate the functional feasibility, a system of four-FBG connected to a three-port circulator was established for the initial demonstration. The four FBGs with serial center wavelengths at 200GHz spacing were physically arranged on the order of 1552.5nm(FBG1), 1549.2nm(FBG2), 1550.9nm(FBG3), and 1553.8nm(FBG4). They were placed out of wavelength sequence in order to make the crosstalk measurement easily implemented. The fiber lengths among FBGs were designed to have logarithmic increments.

To demonstrate the achieved range of delay times, a relatively wide pulse (with ~7ns width) at a specific wavelength, equal to one of the FBG center wavelengths, was sent into the input port of the circulator, and the reflected delayed signal was checked by an oscilloscope. The result is shown on Fig. 2. and the time delay differences between the FBG1 and others are 29ns, 1.06μs, and 7.02μs, respectively. The non-uniform pulse intensity is here limited by the loss of each connection between components. The insertion loss can ultimately be reduced to the limit of the fiber transmission loss (<0.2 dB/km), which enables realization of very large buffer depths. Also shown in Fig. 2 is the combined reflection spectrum from the four FBGs. No grating crosstalk was evident in the time-domain data that was limited by the 30dB SNR of the measurement.

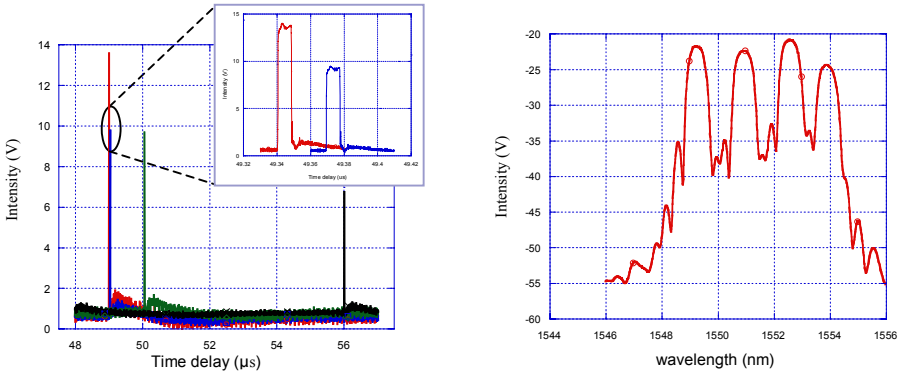

Fig. 2. **Left:** Different time delay values correspond to four discrete FBGs. The delay time differences between the FBG1 and others are 29ns, 1.06μs, and 7.02μs, respectively. The inset is the detail of the first two reflected pulse. **Right:** The reflection spectrum from the four FBGs. The non-uniform peak intensity of each FBG is here mainly due to interconnect loss.

To measure the dispersion properties of the buffer a narrow pulse source was used. The pulse width was measured by an autocorrelator. Two measurements were performed. In the first measurement, a tunable wideband pulse source with the pulse width of 1.24ps at a selected wavelength was sent into the system, the output signal was passed through a filter to define the specific wavelength, and then was received by an autocorrelator. The obtained data is shown in Table 1. The raised-cosine FBG weighting function provides a Gaussian-like reflected pulse with no apparent side lobes in the time domain. The broadened pulse width is around 5ps for shorter lengths of fiber, which confirms the simulation and the initial design. For the 5-6 ps pulse widths achieved using the all-optical wavelength converters reported elsewhere [5], the resulting delayed pulse-width will remain well within the 12.5 ps FWHM requirement stated above. At the longest buffer time delay, 7.02μs, some excess pulse broadening is observed due to fiber dispersion. If even longer buffer delays need to be achieved, dispersion managed fibers, possibly combined with some amplification, could be used to preserve the signal.

In the second measurement, a negatively chirped pulse with 12.47ps width was used as the input signal, and a compressed output pulse width of 10.47ps was obtained. Since the FBG has a positive dispersion characteristic, as it combines with a negatively chirped pulse source, the pulse was compressed by the grating. Pulse broadening depends on pulse chirp, fiber and FBG dispersion, and FBG bandwidth, therefore, pulse compression is possible with a proper combination of FBG dispersion and pulse characteristics, and was realized in this experiment.

Table 1. Measurements summary

	FBG1 1552.5nm	FBG2 1549.2nm	FBG3 1550.9nm	FBG4 1553.8nm
Δ(Time delay) to FBG1	0	0.029μs	1.06μs	7.02μs
Fiber length to FBG1	0	2.9m	106m	702m
Pulse width τ_{out} (1.24ps wideband input)	5.97ps	4.49ps	5.48ps	8.14ps
Compressed pulse widthτ_{out} (12.47ps negatively-chirped input)	-	-	-	10.47ps

4. Systems demonstration

To demonstrate the proposed buffering function, a preliminary 10Gbps system is presented here. A modulated signal at λ_{in} is sent in to a rapidly-tunable WC and converted to a desired wavelength λ_{delay} which equals to one of the FBG center wavelengths by tuning the front and back mirror and phase sections of the SGDBR integrated in WC. A filter is placed to ensure no undesired signal exists and the output is fed to an oscilloscope. The system setup and results are shown in Fig.3. In the eye diagrams, a promising result is demonstrated that no apparent degradation is found after sending into the FBG array. It can be further confirmed by extinction ratio that after WC conversion it is measured to be 10.5dB and keeps unchanged for all the system. It is noticed that the eye of FBG4 is a little bit noisier than other channels due to the additional interconnect loss and could be improved by a better connection.

Based on this systematic demonstration combined with the time delay and pulse broadening measurements, a programmable optical buffering method has been established and demonstrated. It is also believed in the future success at 40 Gbps systems.

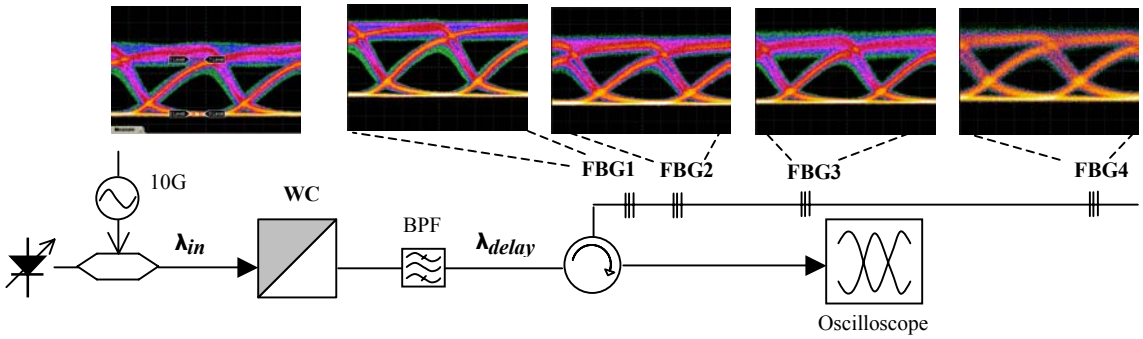

Fig. 3. Optical buffering in 10Gbps system setup and the eye diagrams of the input and four output channels.

5. Conclusion

A large number of rapidly selectable discrete delay values with low insertion loss and long available maximum delay can be achieved by the proposed method of all-optical buffering using FBGs and rapidly-tunable WCs. A FBG buffer working at 40Gbps for an RZ system has been designed and programmable time delays from tens of nanoseconds to microseconds have been obtained. It is also confirmed that the pulse broadening effect is within an acceptable range for a 40Gbps RZ system. A preliminary 10Gbps four-element FBG system has been built to demonstrate its functionality and a promising result of no apparent degradation is also achieved. According to these initial measurements and demonstrations, it is believed that the proposed method has a great possibility to work at 40Gbps.

This work is supported by the DARPA/MTO LASOR Program under Grant No. W911NF-9-0001.

6. References

[1] Blumenthal, D.J. *et al*. Communications Magazine, IEEE, vol. 41, No. 2 , Feb. (2003)
[2] John E. *et al*. IEEE *Photonics Technology Letters*, vol. 15, No. 8, Aug. (2003)
[3] N. Edagawa *et al*. Conference on Optical Fiber Communication. OSA Technical Digest Series. vol. 6, (1997)
[4] P.S. Cho *et al*. IEEE *Photonics Technology Letters,* vol. 11, pp1662-4, (1999)
[5] Sysak, M.N. *et al*. *Photonics Technology Letters*, IEEE, vol. 16, No. 9, Sept. (2004)
[6] M. L. Mašanović *et al*. IEEE *Photonics Technology Letters*, vol. 16, No. 10, (2004)
[7] V. Lal *et al*. submitted to OFC (2005)

Proc. OFC/NFOEC 2005, paper no. OtuM4, Anaheim, CA (March 6-11, 2005)

10 Gb/s Photocurrent Driven, Widely Tunable Electroaborption Modulator Based Wavelength Converter

Matthew N. Sysak, Jonathon S. Barton, James W. Raring, Matthew Dummer, Anna Tauke-Pedretti, Daniel J. Blumenthal, Larry A. Coldren

University of California Santa Barbara, Engineering II Santa Barbara, CA 93106
Tel: (805)893-8465, FAX: (805) 893-4500, email: mnsysak@engineering.ucsb.edu

Abstract: An electroaborption modulator based photocurrent driven wavelength converter has been characterized. Bit Error Rate measurements at 10 Gb/s show less than 2.5 dB Power penalty over 30 nm with 10 dB extinction and input fiber-coupled power less than 2 mW.

OCIS codes: (250.5300) Photonic Integrated Circuits; (250.3140) Integrated Optoelectronic Circuits

1. Introduction

Wavelength agile photonic integrated circuits are key components for increased functionality in next generation optical networks. As these functionalities drive to higher bit rates and complexity levels, the benefits of monolithic integration such as scalability and reduced packaging costs become increasingly important. In particular, components such as wavelength converters that have the potential to reduce blocking probabilities and provide dynamic wavelength management in high traffic WDM networks have become more and more attractive. Recently, wavelength converters based on photocurrent technology, where an input optical signal is detected and used to drive a reverse biased Electroabsorption modulator, have been shown to support data rates up to 320 Gb/s [1]. Of particular interest is the single-chip, monolithically integrated photocurrent driven device where an optically preamplified receiver is used to reduce power requirements for wavelength conversion with no additional drive electronics. Such devices have been demonstrated using a common InGaAsP/InP materials platform with both Electroabsorption and Mach Zehnder Modulators integrated with a widely tunable Sampled Grating DBR (SGDBR) laser, Semiconductor Optical Amplifiers (SOA), and a photodetector. Data rates up to 2.5 Gb/s have been demonstrated with wide tunability [2, 3]. However, this approach has suffered from high input power requirements. In this work a shallow multi quantum well stack has been introduced into the modulator epi-layer for higher modulation efficiency without a corresponding increase in capacitance compared to previously reported results [2]. In addition, a high gain optical pre-amplifier has been included for lower input power requirements.

2. Device architecture and epi-layer

The wavelength converter architecture consists of two neighboring ridges interconnected with a coupling capacitor and terminated with a load resistor. A transmitter ridge consists of a standard four section sampled grating DBR laser [4] monolithically integrated with a 300-μm-long SOA and a 400 um EAM. A receiver ridge contains a monolithically integrated input optical pre-amplifier and OQW photodetector. The pre-amplifier is 600 um long and has been flared from 3 um to 9 um wide for high saturation power and gain. The reverse biased photodetector is 50 long and is tapered from 9 to 6 um. For operation, the EAM and the photodetector were individually probed with an integrated 50-Ω probe on the photodetector and an open circuit probe on the EAM. The two devices were interconnected with a high-speed RF cable and individual Bias-T's. A schematic is shown in figure 1. The transmitter epi-layer structure incorporates a dual quantum well stack design. A set of Offset Quantum Wells (OQW) [4] provides gain in the laser (Photoluminescence = 1550 nm) while a separate set of quantum wells, centered in the InGaAsP quaternary waveguide (PL = 1300 nm), provides broadband modulation efficiency when reverse biased in the EAM. The centered QW stack contains 7 x 90 A compressively strained wells and 6 x 50 A tensile strained barriers (PL = 1465 nm). The receiver epi-layer structure consists of the same OQW stack, but does not have the centered wells that are present in the transmitter. Though currently, the receiver and transmitter are not monolithically integrated, the low PL (1465 nm) of the transmitter wells and the fact that the both sections have identical InP regrowth and fabrication steps, shows that the dual quantum well base structure should be well suited for single chip wavelength converter fabrication. A schematic of the CQW and OQW transmitter layer stack is shown in figure 1.

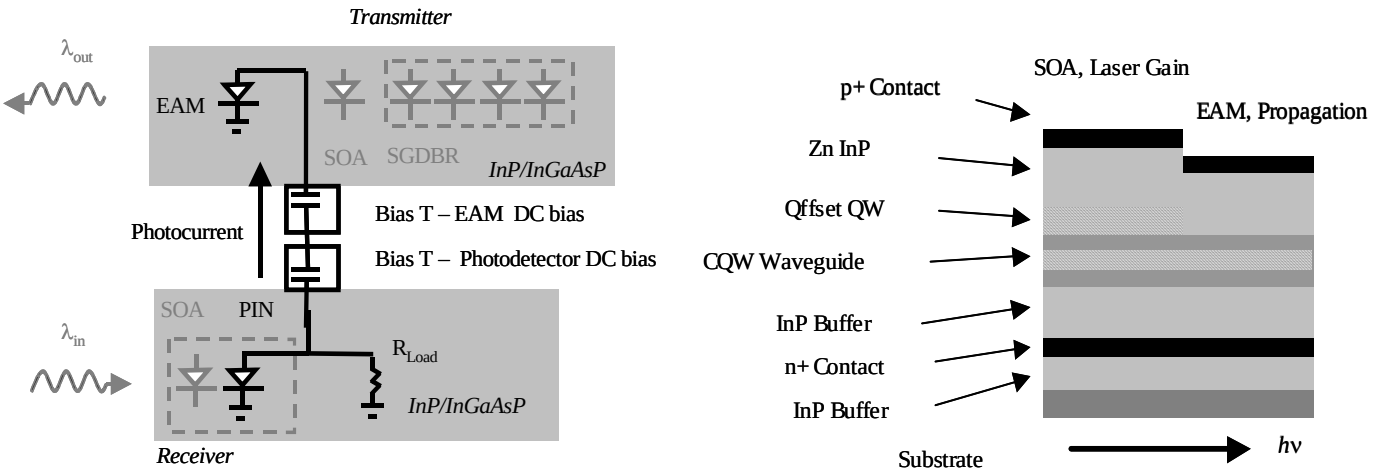

Figure 1. Wavelength Converter Bias schematic (left) and Transmitter epi-layer stack (right).

3. Results

DC extinction curves, receiver characteristics, bandwidth measurements and BER curves have been generated for the 50 Ω terminated EA based wavelength converter device. In these experiments, the laser gain section, pre-amplifier SOA, and transmitter SOA are biased at 160 mA, 250 mA, and 120 mA respectively and the device was maintained at 16^0 C with a thermoelectric cooler. DC extinction measurements for the 400 um EAM show greater than 20 dB extinction over 30 nm with less than –4V bias. Results are shown in figure 2. Receivers were characterized by measuring the voltage swing over the 50-ohm loaded probe on the photodetector through the RF cable and both Bias-T's as shown in figure 1. A 1548.1 nm input optical signal at various optical power levels was fed into the optical pre-amplifier under various SOA bias currents. The photodetector was biased to –4.5 V for maximum efficiency. A peak-to-peak voltage swing of greater than 2.5 V can be seen with waveguide powers up to 3 dBm. A summary of the results can be seen in figure 2.

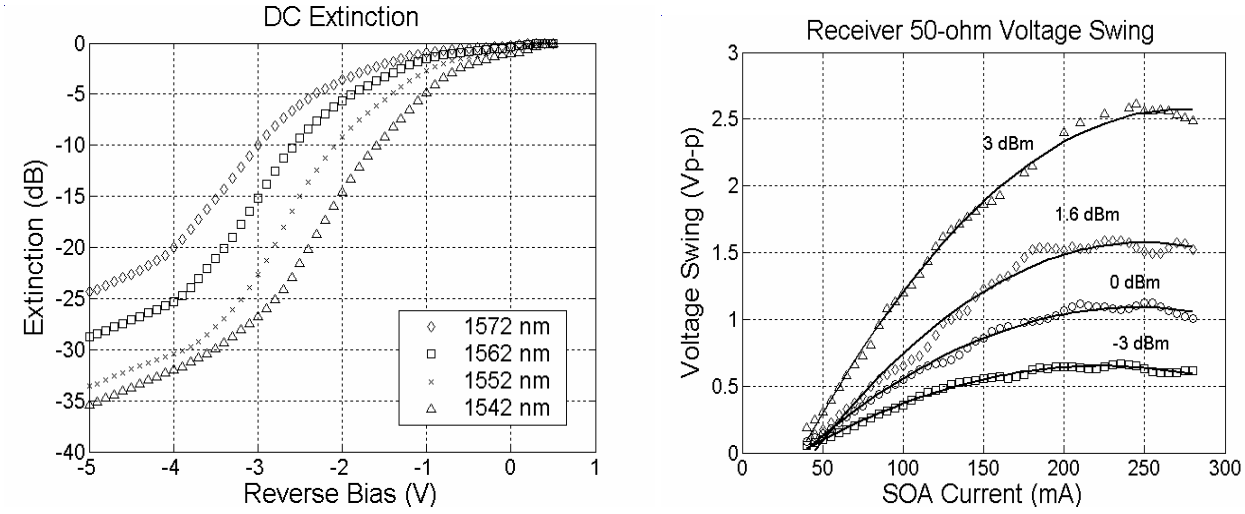

Figure 2. DC Extinction Characteristics for EA Wavelength Converter (left) and 50 ohm terminated Receiver Characteristics (right). Receiver input wavelength is 1548.1 nm and is performed at 10 Gb/s with 2^7-1 NRZ data. Waveguide power levels are indicated for various SOA bias currents.

Bandwidth measurements were performed for 50 Ω terminated discrete EA modulator, photodetector and for the integrated wavelength converter. S_{21} results showed ~10 GHz and ~20 GHz bandwidth for modulator and photodetector respectively and ~7 GHz optical to optical bandwidth for the wavelength converter (1548.1 nm to 1565 nm). For these experiments, the photodetector bias was again set at –4.5V. Bit-error-rate (BER) curves with

eye diagrams have been generated. For the BER measurements a nonreturn-to-zero $2^7 - 1$ pseudorandom bit stream at 10 Gb/s from a 10 Gb/s BER tester transmitter (Agilent 83433A) at a wavelength of 1548.1 nm was input into a high power Erbium Doped Fiber Amplifier (EDFA) followed by a polarization controller and an optical filter and transmitted to the device under test using a conically tipped lensed fiber. In this experiment, 4.9 mW of optical fiber power was used and the extinction ratio of the input signal was 14 dB. Input and output coupling losses are estimated to be 5 dB and 3 dB respectively. The output optical signal of the WC was then input into a variable optical attenuator before entering the PIN Receiver. Note that no optical output filtering or amplification was required. Error-free operation has been achieved with a power penalty of less than 2.5 dB at 10 Gb/s. Results for Extinction Ratio and output power over wavelength as well as BER curves are shown in figure 3.

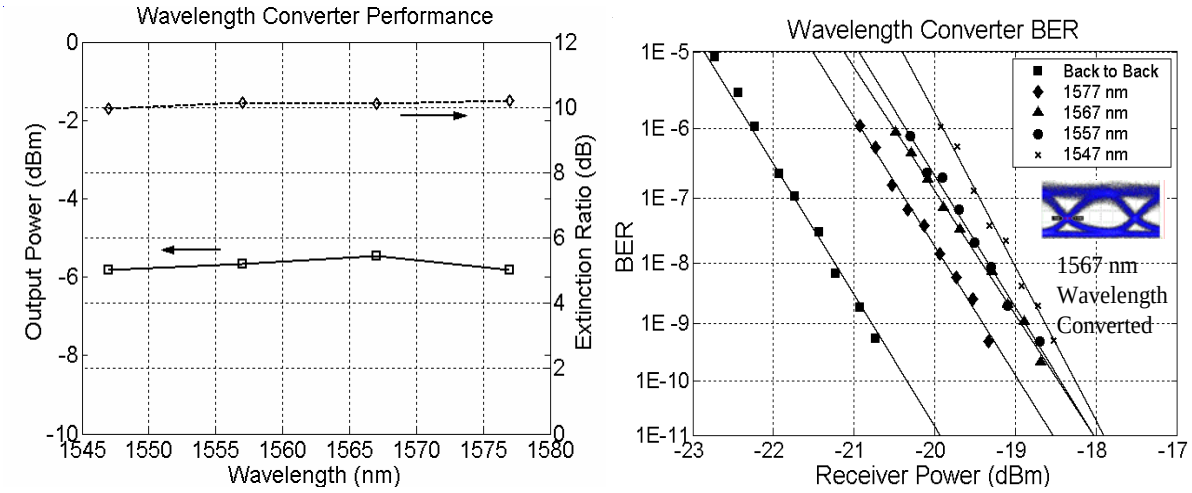

Figure 3. Extinction Ratio and average output power (left) and 10 Gb/s BER curves for 50 Ω terminated EAM based wavelength converter (right). Input wavelength is 1548.1 nm with wavguide power level of 1.7 mW. Converted wavelength is indicated

4. Discussion

We have demonstrated wavelength conversion over 30 nm at 10 Gb/s with 10 dB optical extinction and less than 2.5 dB power penalty. Wavelength conversion required less than 5 mW (+6.8 dBm) of input fiber power and less than 2 mW (+2.3 dBm) of waveguide input power. If coupling is neglected, overall device efficiency is estimated at approximately -5 dB with integrated high power receivers and centered QW layer stack. This is a significant improvement over previously reported results for EA modulator based widely tunable wavelength converters.

5. Acknowledgements

The authors would like to acknowledge Agility Communications for regrowth and AR coatings.

6. References

[1] S. Kodama, T. Yoshimatsu and H. Ito, "320 Gbit/s optical gate monolithically integrating photodiode and electroabsorption modulator," *Electronics Lett.*, vol.39, no.4, pp.383-5, Feb. 2003.

[2] M.N Sysak, J.S. Barton, L.A. Johansson, J.W. Raring, E.J. Skogen, M.L. Masanovic, D.J. Blumenthal and L.A. Coldren. "Single-Chip Wavelength Conversion Using a Photocurrent-Driven EAM Integrated With a Widely Tunable Sampled-Grating DBR Laser" *IEEE Photon.Technol. Lett.*, vol. 16, pp.2093-2095, Sept. 2004.

[3] J.S. Barton, E.J. Skogen, M.L. Masanovic, M.N. Sysak, D.J. Blumenthal and L.A. Coldren. "2.5 Gbit/s error-free wavelength conversion using a monolithically-integrated widely-tunable SGDBR-SOA-MZ transmitter and integrated photodetector" *IEEE Photon.Technol. Lett.*, vol. 16, pp.1531-1533, June 2004.

[4] B. Mason, J. Barton, G. Fish, and L. Coldren, "Design of Sampled Grating DBR Lasers with Integrated Semiconductor Optical Amplifiers," *IEEE Photon. Technol. Lett.*, vol. 12, pp. 762-764, July 2000.

Widely Tunable Monolithically Integrated All-Optical Wavelength Converters in InP

Milan L. Mašanović, *Member, IEEE*, Vikrant Lal, *Student Member, IEEE*, Joseph A. Summers, *Student Member, IEEE*, Jonathon S. Barton, *Student Member, IEEE*, Erik J. Skogen, Lavanya G. Rau, Larry A. Coldren, *Fellow, IEEE, Fellow, OSA*, and Daniel J. Blumenthal, *Fellow, IEEE, Member, OSA*

***Abstract*—Design, fabrication, and characterization of monolithically integrated widely tunable all-optical wavelength converters in InP is reported. The devices are based on the SGDBR laser integrated with different MZI-SOA wavelength converters. Error-free wavelength conversion at 2.5 Gbps was demonstrated over 50 nm input and 22 nm output wavelength range. Static operation, extinction ratio enhancement, signal reamplification, dynamic range, and chirp properties were characterized as well.**

***Index Terms*—Mach-Zehnder interferometer (MZI), photonic integrated circuits (PICs), tunable laser, tunable wavelength converter, wavelength conversion, wavelength converter.**

I. Introduction

THE further development of photonic integrated circuits (PICs) with increased functional complexity, monolithically integrated on a single chip, is a critical step for the future deployment of optical networks. Monolithically integrated widely tunable wavelength converters are a family of PICs whose function is essential for wavelength division multiplexing (WDM) systems, particularly in functions like optical switching, wavelength routing and add/drop multiplexing. The integration of tunable lasers and all-optical wavelength converters solves one of the last obstacles for all-optical switching to have the functionality and flexibility needed to be a serious candidate to replace electronic switches. Tunable all-optical wavelength converters allow data to be transferred from an input wavelength to a tunable output wavelength without passing the signal through electronics. Semiconductor optical amplifier Mach-Zehnder interferometer (SOA-MZI) wavelength converters represent an important class of integrated wavelength converters that work for both RZ and NRZ data formats while also acting as 2R signal regenerators due to their nonlinear transfer functions. Integration of SOA-MZIs in InP has been reported previously [1]–[3]. In addition, an SOA-MZI wavelength converter was integrated with a nontunable DFB laser, but it had severe performance tradeoffs due to reflections from the MZI back to the laser [4]. Recent attempts at an integrated multifrequency laser/MZI-SOA wavelength converter have shown an interesting device design concept, but have yet failed to produce a fully operational wavelength converter [5].

The devices reported in this paper consist of a widely tunable sampled grating distributed Bragg reflector (SGDBR) laser [6], monolithically integrated with different SOA-MZI wavelength converters [7], [8].

The SGDBR laser represents an enabling technology for widely tunable photonic integrated circuits. First, it is well suited for integration, as its lithographically defined mirrors enable lasing without a facet reflection [6]. Second, because the laser consists of a combination of active and passive waveguides, additional elements can be integrated on the same chip without increasing the level of complexity of the fabrication process. To illustrate the usefulness of SGDBR lasers, it is worth noting that in addition to our work described here, functional integration with other components has been reported for SOAs [9], EAMs [10], Mach-Zehnder modulators [11], and recently photocurrent-driven widely tunable wavelength converters [12], [13].

The fabrication platform used in this work, offset quantum wells, represents a versatile integration platform that enables simplicity in fabrication and high efficiency in transition between active and passive waveguides. Additionally, this platform, with its low contrast waveguides and the continuous quaternary waveguide layer throughout the entire device, is particularly suitable for reflection minimization and control, which is one of the key requirements for high-density PIC integration involving on-chip lasers. Using this platform, a single epitaxial overgrowth of p-InP is required to fabricate the devices, which makes the fabrication process simple, reproducible, and robust.

The level of chip-scale integration demonstrated in our tunable wavelength converters offers a number of benefits, some of which are: reduced coupling loss between the laser and the converter, reduced polarization control requirements, improved converter noise figure, higher conversion efficiency, and, ultimately, reduced size, simplified packaging, reduced footprint, and lower cost of the entire component.

II. Device Design and Fabrication

The integrated tunable wavelength converter consists of an InP SGDBR laser [6], monolithically integrated with an SOA-based MZI wavelength converter. The schematics of the two different device generations that have been designed, fabricated, tested, and are being described in this work are given in Figs. 2

Manuscript received November 14, 2003; revised August 28, 2004. This work was supported by DARPA/MTO CS-WDM Program by Grant N66001-02-C-8026.

M. L. Mašanović, V. Lal, J. A. Summers, J. S. Barton, L. A. Coldren, and D. J. Blumenthal are with the Electrical and Computer Engineering Department, University of California, Santa Barbara, CA 93106 USA (e-mail: mashan@ece.ucsb.edu).

E. J. Skogen is with the Sandia National Laboratories, Albuquerque, NM 87185 USA.

L. G. Rau is with the California Institute for Telecommunications and Information Technology, University of California, Irvine, CA 92697 USA.

Digital Object Identifier 10.1109/JLT.2005.843464

and 3. Both device generations use identical tunable laser designs and differ in the interferometric wavelength converter designs.

A. Tunable Laser Design

The SGDBR laser is 1.5 mm long and has five sections: front mirror, gain section, phase section, back mirror, and back facet detector. The back facet detector has been monolithically integrated for measurement of optical power and to decrease the requirements of the backside antireflective coating.

The laser's mirrors are made of periodically sampled DBR gratings that form a comb-like reflectivity spectrum which enables for wide tuning range using the Vernier effect [6]. The front mirror consists of five 4 μm long bursts spaced by 61.5 μm. The back mirror consists of twelve bursts that are 6 μm long and spaced by 46 μm. Since the sampling periods of the two mirrors differ, the peak reflectivity spacings are different, so that only one set of reflectivity peaks for both mirrors is aligned at one time. By differentially tuning the front or the back mirrors using electrical current injection, adjacent reflectivity peaks can be aligned, and the laser will operate at this new wavelength [6]. To achieve the wavelength coverage between the mirror peaks, both mirrors need to be tuned simultaneously.

B. MZI-SOA Design

The role of the MZI-SOAs is to behave as nonlinear elements and to enable the interaction between the continuous wave and the input data signals through the gain compression and phase change, which are used to achieve the wavelength converter operation. Two main MZI-SOA parameters of interest are the amount of phase change attainable, and the gain recovery lifetime, which will limit the maximum speed of operation. The dynamic response of an SOA depends on the material parameters of the SOA (differential gain), the level of electrical pumping, the confinement factor, the optical power in the SOA, as well as the length of the SOA through the effects of high-pass filtering [24]. While our material parameters (i.e., the gain as a function of carrier density) and the confinement factor (6%) are set by the choice of the integration platform, the other parameters can be adjusted, primarily by controlling the SOA's bias current, input optical power into the SOA and the length of the SOA.

Simulated total phase change in an SOA as a function of the optical power levels and the SOA lengths is shown in Fig. 1. The amount of the phase change will depend on the amount of index change, which in turn depends on the amount of the gain and carrier concentration change in the SOA. One disadvantage in using the offset quantum well platform is in the fact that the optical mode overlap with the active region is only 6%, and most of the index change happens in the active region (assuming large release times from the quantum wells). As a result, according to the simulation, large pump power variations are needed to achieve a full π rad phase shift. Analyzing Fig. 1, we conclude that increasing the length of the SOA beyond 1 mm will not significantly improve the phase change abilities. On the other hand, to utilize the full benefits of the self-filtering effect [24], the SOA length should be at least 1 mm. Extended SOA lengths will have an adverse effect in terms of possible back-reflections into the laser, heating, device power consumption and the chip

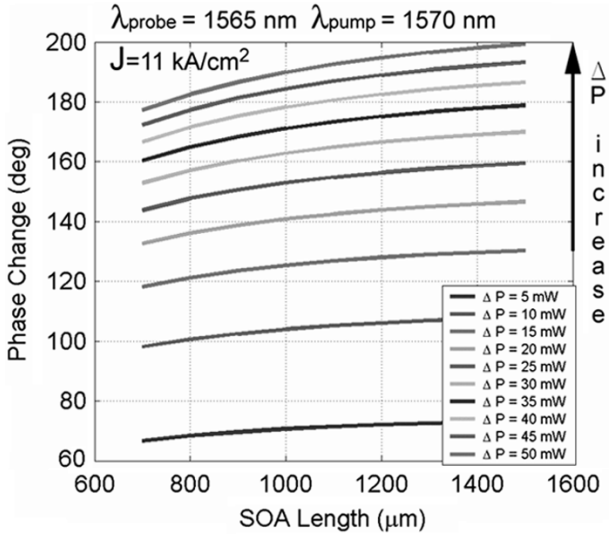

Fig. 1. Simulated phase change in a SOA as a function of the SOA length. The probe signal is kept constant at 4 mW and the power of the pump signal is varied.

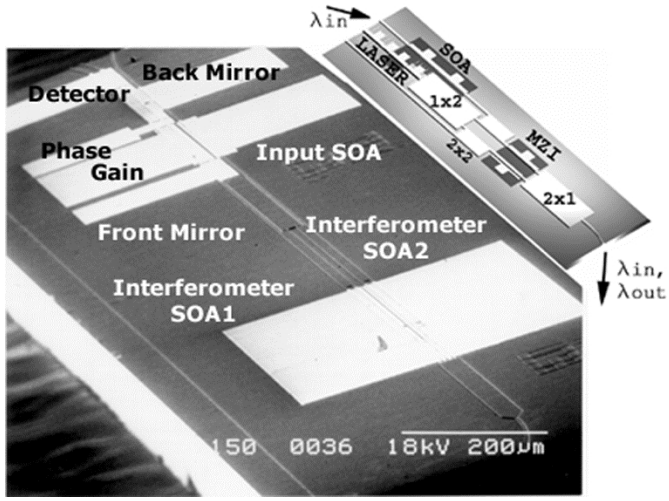

Fig. 2. Tunable all-optical MMI-MZI-based wavelength conveter (TAOMI-WC).

size. Taking all of these requirements and tradeoffs of our design into account, the optimum SOA length was chosen to be 1 mm.

C. Generation I—Tunable All-Optical MMI-MZI Wavelength Converter (TAOMI-WC)

In this device implementation, the interferometer is defined by a combination of two 16 μm wide and 760 μm long multimode interference (MMI) based 1×2 light splitters [15], in combination with 2 MMI based 2×2 couplers that are 12 μm wide [15], straight waveguides and 1 mm long SOAs (Fig. 2). The total waveguide separation in the interferometer is 17 μm. This value is determined primarily by the fabrication tolerances for the minimum separation of the two MZI-SOA electrodes. The input signal is coupled onto the chip through a tapered, angled input waveguide, and then amplified by an 800 μm long input semiconductor optical amplifier. The 2×2 MMI coupler is used to mix the input signal with the continuous wave signal generated by the SGDBR laser in one of the interferometer's

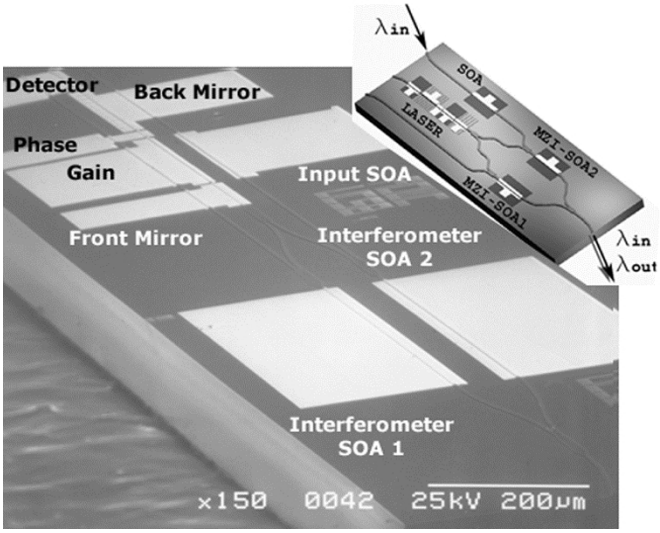

Fig. 3. Tunable all-optical MZI-based wavelength converter (TAO-WC).

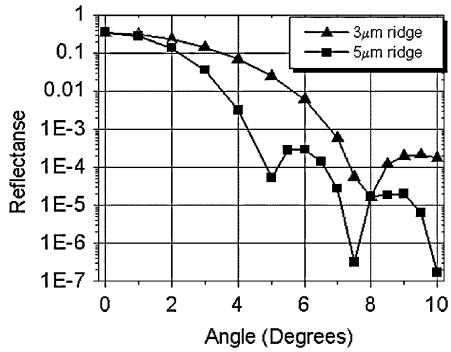

Fig. 4. Modal reflectance as function of the output waveguide width and angle.

SOAs. This SOA, where the interaction between the input data and the CW signal occurs, will be referred to as "common SOA" in the rest of this paper. The unused output branch of the 2×2 MMI coupler extends into the unpumped active region and is adiabatically tapered into a point to absorb all of the stray light. This is done to prevent any back reflections that could destabilize the laser. The output waveguide of the MZI is tapered and angled to reduce the AR coating requirements. The total device length is 5.2 mm.

D. Generation II—Tunable All-Optical MZI Wavelength Converter (TAO-WC)

The interferometer is defined by a combination of four 1×2 MMI light splitters and combiners (180 μm long and 13 μm wide), by S-bends with curvature radii of 2 mm and by two 1 mm long SOAs (Fig. 3). The laser and the interferometer are connected via a 1×2 MMI splitter and the total waveguide separation in the interferometer is 70 μm. This insures that there is no thermal crosstalk between the two branches of the interferometer. The input signal is coupled onto the chip through a tapered input waveguide, and then amplified by an 800 μm long input semiconductor optical amplifier. The same MMI splitter/combiner design is used to connect the input waveguide and the SGDBR signal with the common interferometer SOA, as well as to combine the light from the two branches at the interferometer output. The output waveguide is tapered and angled to reduce the AR coating requirements. The total device length is 4.9 mm.

E. Coherent Reflection Suppression

One of the critical design issues for PICs that include an integrated laser is the suppression of coherent back reflections. Low levels of coherent back-reflection will lead to an increase of the laser linewidth, while large back-reflections levels will be completely detrimental for device performance.

Several possible sources of reflection exist on our chips and they all require careful minimization. The potential sources of backreflection are the output facet, multimode interference based light splitters and combiners and the active-passive waveguide interfaces. The offset quantum-well integration platform, used in this paper, with its low refractive index contrast waveguides and the continuous quarternary waveguide layer throughout the entire device structure, is particularly suitable for reflection minimization and control.

The dominant source of back reflections is the output facet of the device. The SOAs of the Mach-Zehnder act as amplifiers for any reflections from the output facet. However, due to their operation in saturation, the amount of gain that they provide is limited to less than 8 dB. Taking into account the amplifier gain, to insure for linewidth change of less than 10%, the requirement for reflectance of the output facet is that it be better than 10^{-5}. This level of reflectance cannot be achieved by simple anti-reflection coating, rather, the output waveguide design has to minimize the amount of reflection. As has been proposed in [16], [17], angled output waveguides have significantly smaller modal reflectances than the corresponding straight waveguides. In addition, increasing the waveguide width further reduces the back reflection coupled into the original mode. Analiticaly, the reflectance of a Gaussian mode at an interface will have an exponential dependence on the angle of incidence and on the width of the mode [16]. Conversely, widening the output waveguide increases the ellipticity of the output mode, thereby complicating the coupling scheme required for high coupling efficiency. Fig. 4 shows the calculation of the modal reflectances [17] in function of the output waveguide angle, for two different output waveguide widths—3 μm and 5 μm. The values of the parameters in the calculation are based on the InP/InGaAsP material system used in this work. For the output angle of 6.5 degrees or higher, with the ridge with of 5 μm, the envelope of the modal reflectance will be lower than 10^{-4}. Therefore, applying a multilayer AR coating on this type of the output facet can provide for the broadband reflectance that meets our design requirements.

MMI-based components are a potential source of severe reflections, so care must be taken to optimize their design. This is especially true in integration platforms that utilize high index contrast waveguides [18]. Our fabrication platform, on the other hand, is based on the weakly guiding waveguides and employs no semiconductor-air interfaces. The MMI lengths in our structures are optimized for minimum back reflections according to [15], and all MMI components are tapered at both inputs and outputs so that reflections are not coupled back into the laser

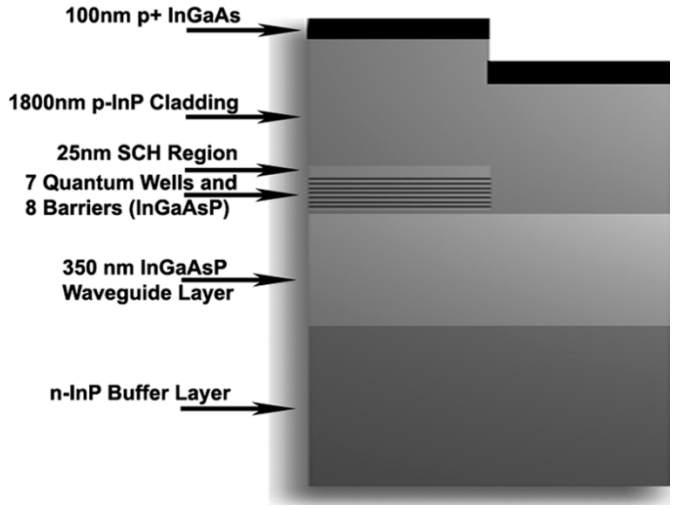

Fig. 5. Offset quantum well integration platform.

cavity. We found that this approach was easy to implement and as effective as the approach suggested in [19].

Low reflection, low loss transitions between the active and passive waveguides in our fabrication platform are achieved by employing techniques similar to those already discussed for the output waveguide design. Active-passive interfaces in the device are angled to avoid coupling of the reflected light into the waveguide mode. Moreover, the quarternary waveguide layer is continuous throughout the device structure, thereby avoiding potential index discontinuities such as those that can be introduced when using butt-joint growth techniques.

F. Fabrication

Devices are fabricated using an offset quantum well integration platform in InP. All growths are performed using the MOCVD crystal growth technology. The device cross section at the active-passive interface is shown in Fig. 5.

The layer formation of the base epitaxial structure consists of a 350 nm thick quarternary waveguide, followed by a 7 quantum well/8 barrier active region and a thin InP cap. The first step of the process is to selectively etch off the quantum wells in the future passive sections of the device. Subsequently, gratings are lithographically defined in the mirror sections using holography and then etched directly into the top of the waveguide layer using reactive ion etching (RIE). The surface of the sample is then regrown with a 1.8 μm thick p-doped InP upper cladding layer and a 100 nm p^+-InGaAs contact layer (Fig. 5). It is important to emphasize that this is the only regrowth step required in the entire process.

After the regrowth, ridges in InP are formed using a combination of RIE/crystallographic wet chemical etching. The surface of the sample is isolated with a dielectric film and the top metal contacts (Ti/Pt/Au—20/40/1000 nm) are evaporated using E-beam evaporation, followed by a proton implant to electrically isolate the different electrodes. After the sample is thinned down, identical back side (Ti/Pt/Au) contacts are evaporated and the sample is strip annealed at 420 °C. In conclusion, there are no additional major processing steps required to fabricate this device beyond the standard SGDBR fabrication process, which demonstrates the versatility of our integration platform.

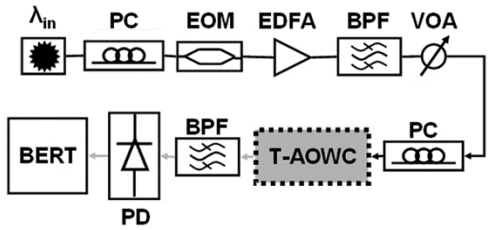

Fig. 6. Schematic of the test setup.

III. Experimental Procedure

All of the experiments are performed with the devices soldered on aluminum nitride submounts, wirebonded, vacuum clamped onto a gold-plated copper stage and cooled to 17 °C using a thermoelectric cooler. The light is coupled to and out of the devices using conical-tipped lensed-fibers mounted on the piezo-controlled translational stages. The tapered waveguides at device inputs and outputs improve the coupling to the device; we measured 4 dB of coupling loss to the waveguides on the chip. The input signal is generated using an external cavity tunable laser source and modulated using a lithium-niobate electrooptic modulator. Polarization controllers are used at both the input to the modulator and the wavelength converter because the device active regions are polarization sensitive. For static measurements, the output of the device is optically filtered and fed into an optical power meter. For wavelength conversion, the data is generated using a BERT with NRZ $2^{31}-1$ pseudorandom bit sequence (PRBS) data at 2.5 Gbps. The converted output wavelength is filtered using a 0.4-nm thin-film tunable filter and detected with a PIN receiver. The test setup schematic is shown in Fig. 6.

IV. Static Performance

The integrated tunable wavelength converter's lasers have a tuning range of about 22 nm—overlapped spectra for TAOMI-WC and TAO-WC devices are shown in Fig. 7(a) and (b). These spectra were recorded through the output facet of the device, with laser gain sections biased at 85 mA and both MZI SOAs biased at 200 mA. The tuning range is determined by the sampled mirror design, and could be extended to 40 nm by further optimization. The grating depth for TAOMI-WC devices is lower than for the TAO-WC devices, resulting in lower presence of the light reflected from the laser's rear mirror peaks in the overlapped spectra, shown in Fig. 7(b).

The output of the interferometer can be turned off by adjusting the bias of the SOA in one of the interferometer branches, in order to achieve π relative phase shift between the two branches. Fig. 8 shows an extinction map as a function of the currents applied to the SOAs in the interferometer arms. No input signal was present for these measurements. In the region of low bias currents ($<$120 mA), for one SOA current set, there exists a combination of currents where the extinction ratio is greater than or equal to 20 dB. However, with the increase in the SOA bias currents, the extinction ratio is reduced to as low as

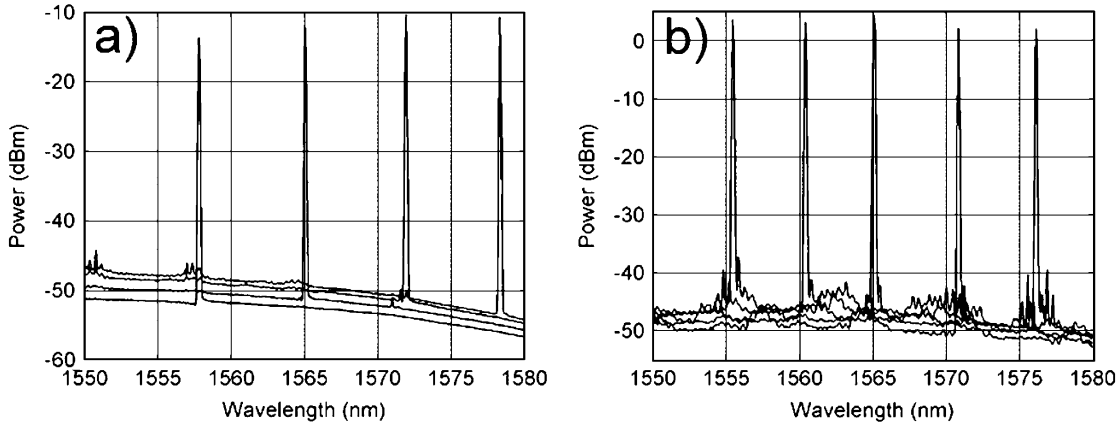

Fig. 7. Overlapped spectra for TAOMI-WC and TAO-WC devices.

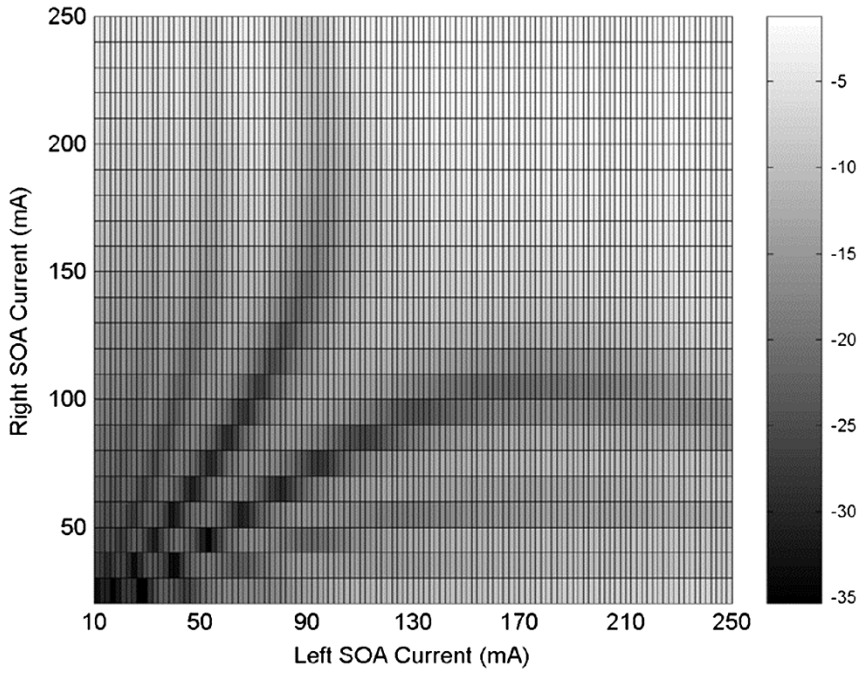

Fig. 8. Extinction map for electrical control of the TAO-WC.

10 dB at 250 mA on either of the SOAs. This can be explained by noting that the large difference in power levels emitted from the two branches of the interferometer when added, even with totally opposite phase, still yields significant power coming out of the interferometer. Hence the performance of the device could be improved by running the SOAs in the interferometer in deeper saturation, i.e., by increasing the optical power of the incoming light, while maintaining the same amount of phase change.

Fig. 9 shows the static electrical transfer functions of the interferometer as a function of integrated laser wavelength. Again, no input signal was present for these measurements. The bias current to the common SOA was kept constant at 200 mA while the bias current to the other SOA in the MZI was varied. As can be seen, the extinction peaks around the material gain peak wavelength (which is approximately 1555 nm).

Typical optical transfer curves for both inverting and noninverting modes of operation, for different input wavelengths, are shown in Fig. 10. In these measurements, the bias of the input preamplifier was kept constant at 80 mA. The interferometer set points were chosen based on the static optical characteristics in Fig. 9, at the minimum for noninverting operation (determined by the bias current of 80 mA), and at the maximum on the left size of the main electrical characteristic notch for inverting mode of operation (55 mA, Fig. 9). Then, the power of the input signal was varied and the output power of the device recorded. Static extinction ratios measured are better than 8 dB in the noninverting and better than 16 dB in the inverting mode of operation. As the transfer curves are highly nonlinear, it is possible to achieve input signal extinction ratio enhancement, as long as the extinction ratio of the input signal is lower that the maximum attainable extinction ratio of the wavelength converter.

The difference in extinction ratios measured for the inverting and noninverting modes of operation can be explained by analyzing the device principle of operation. Due to the cross-gain

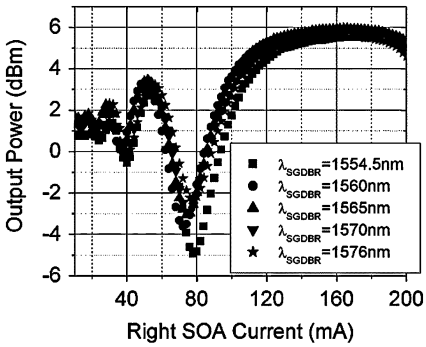

Fig. 9. Static electrical transfer function as a function of wavelength (TAO-WC).

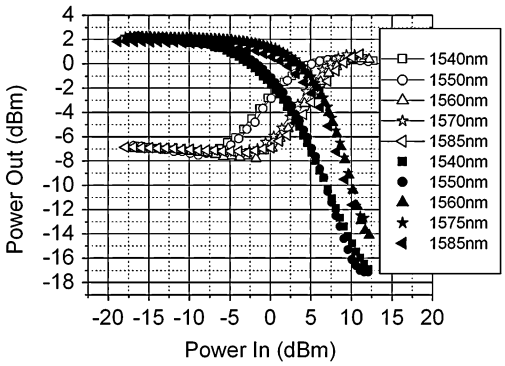

Fig. 10. Optical transfer functions for inverting and noninverting modes of operation (TAO-WC).

effects in the common SOA of the Mach-Zehnder (Fig. 11), the device always yields a higher output extinction ratio in the inverting mode of operation.

For the inverting mode of operation, the output of the MZI is on the high level with no probe signal present (Fig. 12). To reduce the carrier lifetime as much as possible, the bias current of the common SOA should be the higher of the two MZI-SOA bias currents. This bias scheme will result in higher CW signal power at the output of the common SOA. Once the probe signal enters the common SOA, the gain compression will reduce the power of the pump signal in the common MZI branch. This causes two effects—the phase change for the CW signal and the power level equalization between the two branches of the MZI, which therefore allow for better extinction, due to better cancellation of the fields of similar power coming from the two branches of the SOA. In conclusion, in the inverting mode of operation, the two signals are added together when they both carry more power and subtracted when they have similar power levels therefore yielding high extinction ratio. This is illustrated in Fig. 12.

For the noninverting mode of operation, the output of the MZI is on the low level with no probe signal present. To turn the interferometer off, the two SOAs in the MZI have to be biased differently, to yield a relative π phase shift. However, these different bias levels will limit the output extinction at the low level, due to significantly different field intensities in the two interferometer branches (Fig. 11). Once the probe signal enters the common SOA, it will cause the gain compression effect which will reduce the power of the pump signal in the common SOA and the

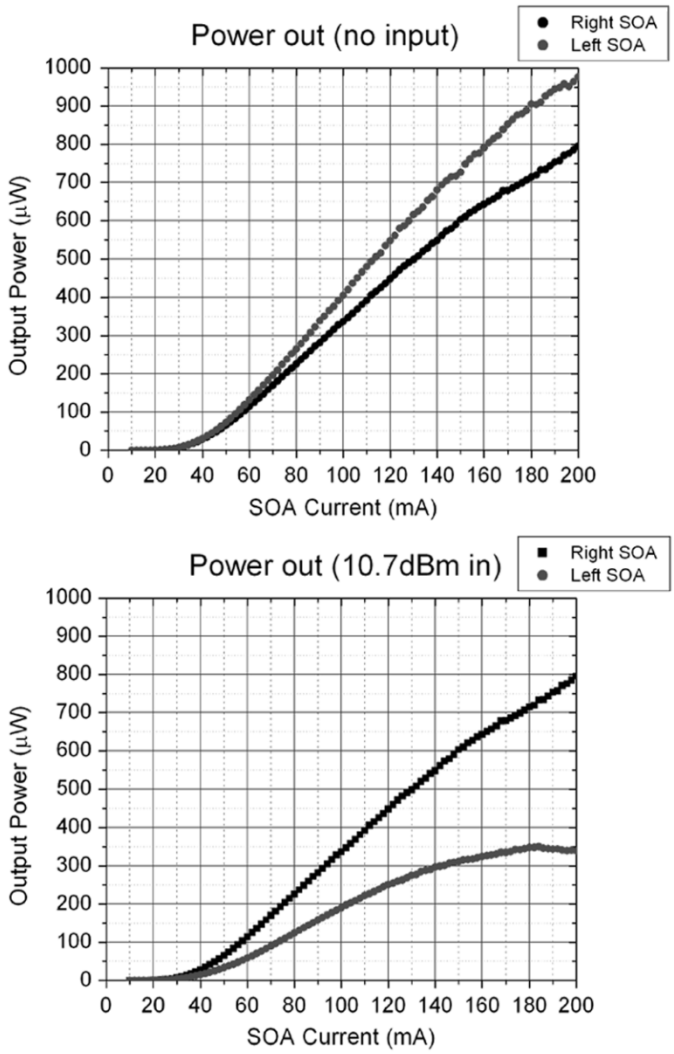

Fig. 11. Gain compression in the common SOA (top) no external signal (bottom) with external signal (TAO-WC).

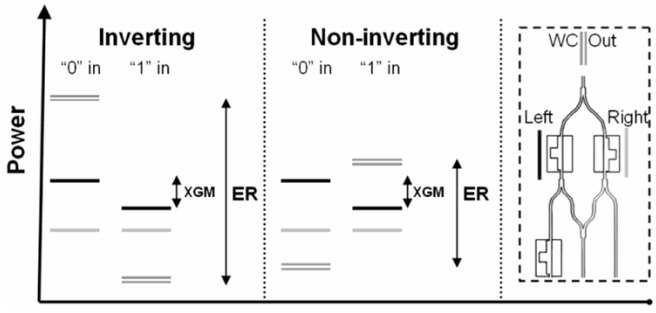

Fig. 12. Extinction ratio analysis for inverting and noninverting modes of operation.

phase change. Consequently, signals from two MZI branches will be added together when power of one of them is reduced by the cross-gain effects of the probe signal. Accordingly, in the noninverting mode of operation, the two signals are being added when they both carry lower optical power, and subtracted when their power levels are different, due to the necessary difference in SOA bias currents to achieve the interferometer OFF state. This effect reduces the maximum obtainable extinction in the noninverting case (Fig. 12).

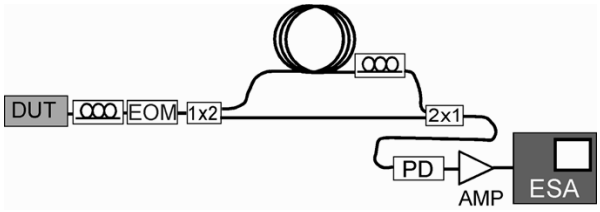

Fig. 13. Linewidth measurement setup.

We can conclude this analysis of the static performance of the wavelength converter by noting that the extinction of the MZI can be improved with the capability of adjusting the phase and the power in the MZI branches independently, as has been done in [20]. That capability would also reduce the differences in output extinction ratios between inverting and noninverting modes of operation.

This extinction ratio analysis holds for the dynamic operation of the wavelength converter as well.

V. Dynamic Performance

As pointed out previously, the key issue for PICs that incorporate integrated lasers is the suppression of coherent back reflections. Even low levels of back reflections can cause significant changes in the laser linewidth, which can degrade the device performance in transmission.

In the first part of this section, TAO-WC linewidth measurement results are presented. Then, results of bit-error rate measurements, the input signal dynamic range, wavelength sensitivity of the wavelength conversion process, bias sensitivity of the wavelength conversion process, dynamic extinction ratio and signal regeneration are discussed.

A. Linewidth

Measuring the linewidth of the device provides useful information about the limitations of the device performance in real networks. Relative intensity noise measured after transmission through fiber indicates that high-frequency white noise determines the transmission properties of a device [21]. In this paper, we determine the linewidth of the TAO-WC device directly by measuring the autocorrelation function of the output light beam. Direct comparison of our results with the linewidth of a commercial widely tunable SGDBR laser enable us to assess the wavelength converter properties as well as investigate the potential back reflection issues with the chip. Although optical low-coherence reflectometry can be used as a more accurate tool to investigate the origins of particular back reflections on chip, the information on the linewidth represents a good way of verifying whether any detrimental reflections are present in the device at all.

The linewidth of a light source can be determined by measuring the autocorrelation function of the output light beam [23]. If the electric field from the output of the device is mixed with the version of the same field that is delayed by some time t, as long as the phases of two fields are well correlated, the fields will add coherently [23].

The schematic of the experimental setup used to measure the linewidth is shown in Fig. 13. The gain section of the tunable wavelength converter's laser is biased at 90 mA, the booster—SOAs are biased at 45 mA, and the MZI-SOAs are biased at 200 mA. The light from the output is coupled through a lens with a built-in isolator, then modulated with a sinusoidal signal whose frequency is 1 GHz. Then the light is split between the two branches of the interferometer, decorrelated by passing the signal from one branch through a spool of fiber, and finally detected by a photodiode, amplified by an electrical amplifier and led to an electrical spectrum analyzer. The reason for spectrally shifting the signal is to eliminate the influence of the $1/f$ noise. The two recombined incoherent fields generate a difference frequency signal which contains the combined FM field noise from both light sources. Therefore, the full width at half maximum of the spectrum measured represents twice the laser linewidth, due to the properties of the Lorentzian line shape [23].

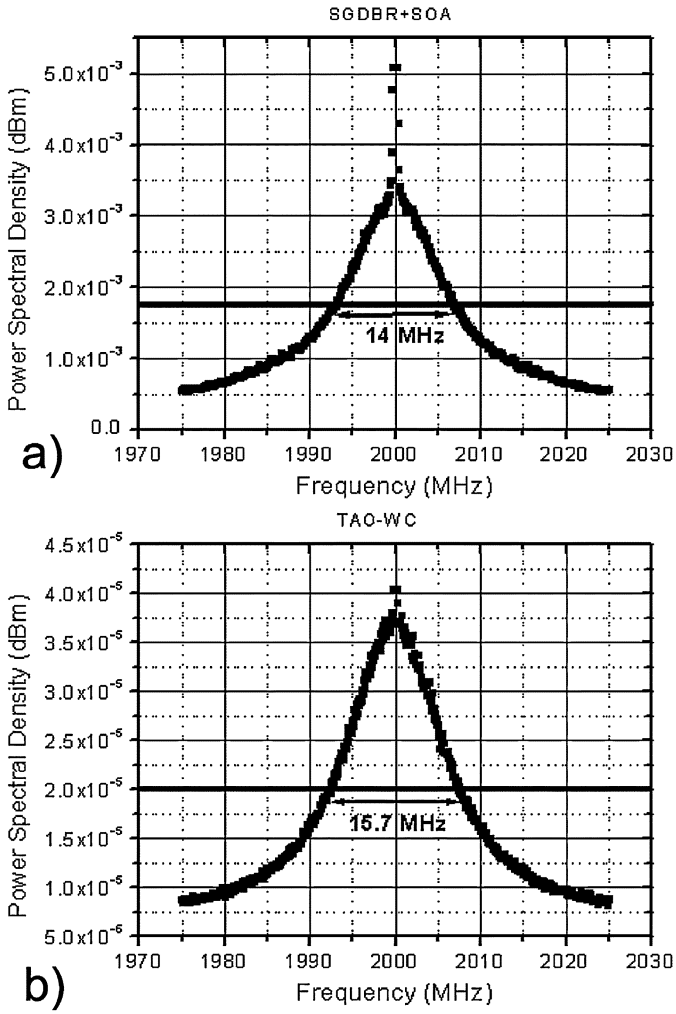

Fig. 14. Linewidth measurement results (a) commercial SGDBR laser. (b) TAO-WC device.

Fig. 14(b) shows the measured FM noise spectrum for the TAO-WC wavelength converter. The linewidth of the device corresponding to this measurement is 7.85 MHz. For comparison, Fig. 14(a) shows the measured FM noise spectrum for an etalon commercial SGDBR laser using the same test setup. The linewidth corresponding to this measurement is 7 MHz. The value measured is consistent with the linewidth values that are

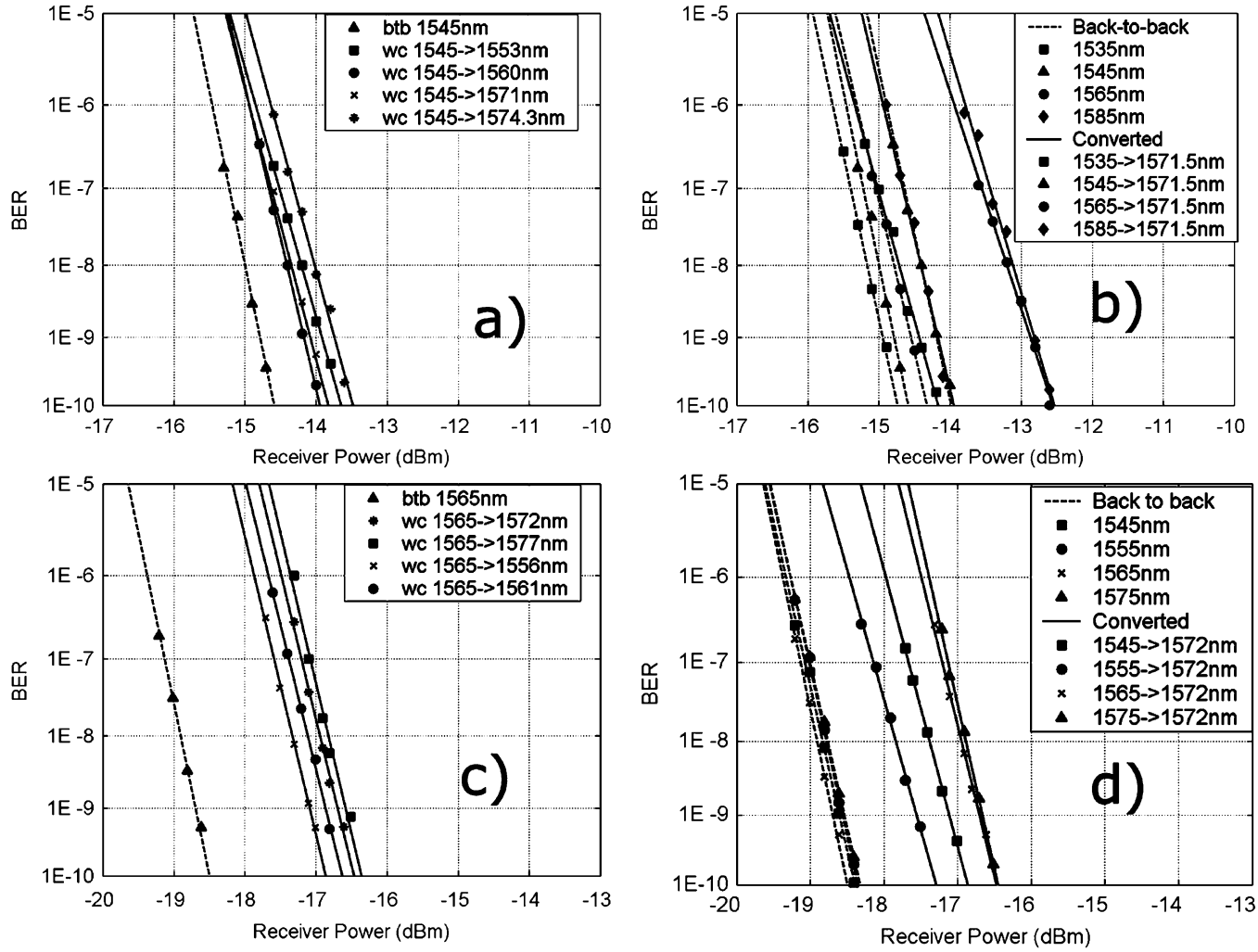

Fig. 15. Results of BER testing for TAOMI and TAO-WC.

specified for this type of laser product. Therefore, the performance of the tunable wavelength converter is free of any influences from coherent back reflections and it is in no way limited by this factor.

B. 2.5 Gbps Wavelength Conversion

The performance of the first generation of the devices (TAOMI-WC) is tested using an Agilent photodiode receiver with a sensitivity of -15 dBm. The input power to the wavelength converter is kept at 4 dBm. The output power of the converter is relatively low (-8 dBm) due to the thermal effects on the MZI-SOA gain, as well as the longer MZI passive sections, when compared to the TAO-WC design. For the first set of measurements, one input wavelength (1545 nm) is chosen, and 2.5 Gbps NRZ $2^{31}-1$ PRBS data are converted onto four different output wavelengths, set by the device (21 nm range). Error-free conversion is obtained with maximum power penalty of 1 dB for the inverting mode of operation, Fig. 15(a). The bias point of the MZI is adjusted for every pair of wavelengths in order to maximize the extinction, thus minimizing the power penalty.

In the subsequent set of measurements, NRZ $2^{31}-1$ PRBS data streams at 2.5 Gbps from different input wavelengths are converted onto one device output wavelength (1571.5 nm). The Mach-Zehnder bias is again optimized for best extinction at each input wavelength. BER curves [Fig. 15(b)] indicate error-free operation over 50 nm input wavelength range, with a maximum power penalty of 1.6 dB. While the upper limit of the input wavelength was set by cross-phase modulation degradation due to finite SOA gain bandwidth, the lower limit was set by the filters available to us (1535 nm). Increase in power penalty and eye noise for input wavelengths above 1565 nm can be attributed, in part, to the input signal-to-noise ratio (SNR) degradation due to our nonoptimum L-band amplifier. Gain in the L band was achieved by using an additional 10 meter long spool of erbium doped fiber in line with our standard C-band EDFA. This noise did not affect our back-to-back measurements, since those were performed without the EDFA. Another cause for power penalty increase in this wavelength range would be higher ASE noise levels as the laser is tuned away from the SOA gain peak.

The second generation of devices (TAO-WC) is tested using a Nortel photodiode receiver with a built-in electrical amplifier, which had a sensitivity of about -18.8 dBm. The output power of the converter is significantly higher in this case (-2 dBm). The main reason for output power increase is the reduced heating of the SOAs in the MZI, due to their larger lat-

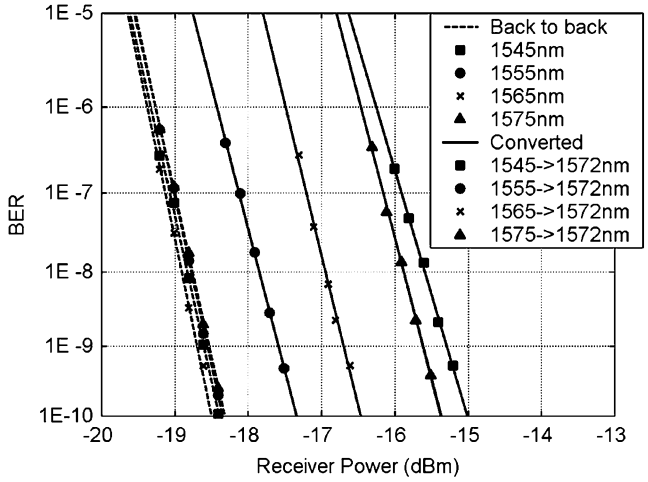

Fig. 16. Wavelength dependence of the BER for TAO-WC.

eral separation (70 μm for TAO-WC, as compared to 17 μm for TAOMI-WC). For the first set of measurements, one input wavelength (1565 nm) is chosen, and 2.5 Gbps data are converted onto 4 different output wavelengths of the device (21 nm range). The bias point of the MZI is adjusted for every pair of wavelengths in order to maximize the extinction, thus minimizing the power penalty. BER curves [Fig. 15(c)] indicate error-free operation with little variation in power penalty as a function of output wavelength. The maximum power penalty was 2 dB. In the subsequent set of measurements, the data streams at 2.5 Gbps from different input wavelengths are converted onto one device output wavelength (1572 nm), again, with optimization of the operating conditions for every wavelength pair. The maximum power penalty again is about 2 dB.

Finally, to investigate the change of power penalty as a function of input wavelength, the TAO-WC is operated with fixed bias currents and input signal powers, and the wavelength of the input signal is varied (Fig. 16). The best power penalty of 1 dB was obtained for the input signal closest to the gain peak of the SOAs at 1555 nm. For this wavelength, the on-chip preamplifier SOA would give the highest possible gain at the input and the effects of gain compression and cross phase modulation in the common SOA of the MZI would be the most pronounced. The power penalty was primarily caused by extinction ratio degradation wavelength dependence, due to finite extinction at the output of <12 dB. The maximum power penalty obtained at far ends of the gain peak was as much as 3 dB, due to further decrease in conversion efficiency and output extinction ratio. Additional power penalty is caused by the pattern dependence of the SOA preamplifiers on chip. The length of the preamplifier SOAs determines the device sensitivity, with longer SOAs decreasing the propagation loss of the input signal. However, long SOAs will always run in saturation, thereby distorting the input signal and introducing the pattern dependence in the converted eye (as seen in Figs. 17 and 18).

C. Device Dynamic Range

Dynamic range of operation can be controlled by the input SOA length and bias, as well as by the bias set point of the MZI. Fig. 17 shows the maximum ER values measured as a function of the data input power. High extinction ratio, greater than 10 dB, can be maintained over 16 dB of input signal power variation. The inset of Fig. 17 also shows the converted eye for -6 dBm input fiber power to a TAO-WC device, corresponding to the converted signal output power of -4 dB in fiber, thereby reamplifying the signal by 2 dB. Different slopes in the eye diagram are due to the different rise and fall times of the pulses, associated with gain recovery time. The input signal wavelength was 1555 nm, and the output signal wavelength was 1565 nm.

The current dynamic range is limited by the passive waveguide propagation losses and available gain of the input SOA. Optimizing the epitaxial heterostructure could yield higher output powers and lower input power requirements, thus increasing the dynamic range and the amount of reamplification. However, care needs to be taken to minimize the pattern dependence effects introduced by the proper design of the preamplifier SOA.

D. Regenerative Properties

Regenerative properties of the SOA-MZI based wavelength converters are based on their highly nonlinear optical transfer characteristics. To quantify the regenerative properties of the tunable wavelength converter (TAO-WC), the input signal's extinction ratio was degraded in a controllable manner by adjusting the EOM bias and the polarization of the light at the input of the electrooptic modulator used to encode the data. This signal, with reduced extinction ratio, was then coupled into the wavelength converter. Significant improvements in the output extinction ratio are obtained—for input ER of 6.33 dB, the converted signal had an extinction of 12.06 dB in the noninverting and 12.33 dB in the inverting mode of operation, Fig. 18. However, decreasing the extinction of the input signal increased the average input power into the common SOA in the MZI and thereby reduced the number of carriers and the gain of the laser signal. Consequently, 6 dBm of input optical power resulted in only -4.4 dBm of the output optical power of the converted signal. On the other hand, device excitation with the high ER signal at the input (12 dB) provided the conversion gain of around 2 dB, with -4 dBm at the optical input and -2 dBm in the converted signal. We believe that this effect could be overcome by increasing the power of the SGDBR laser going into the MZI, thereby constantly keeping the SOAs in the Mach-Zehnder in deep saturation. That would enable the simultaneous signal reamplification and extinction ratio improvement which would qualify the tunable wavelength converter as a 2R regenerator.

E. Chirp Properties

Chirp is the frequency shift occurring in the output pulses of the wavelength converter. This frequency shift appears mainly at the edges of pulses, and is caused by the refractive index modulation in the MZI SOAs. Output chirp is an important parameter for any type of optical regenerator as it will dictate the dispersion-limited transmission distance and/or number of regenerator spans. Low chirp or negative chirp is required for long distance transmission over standard single mode fiber.

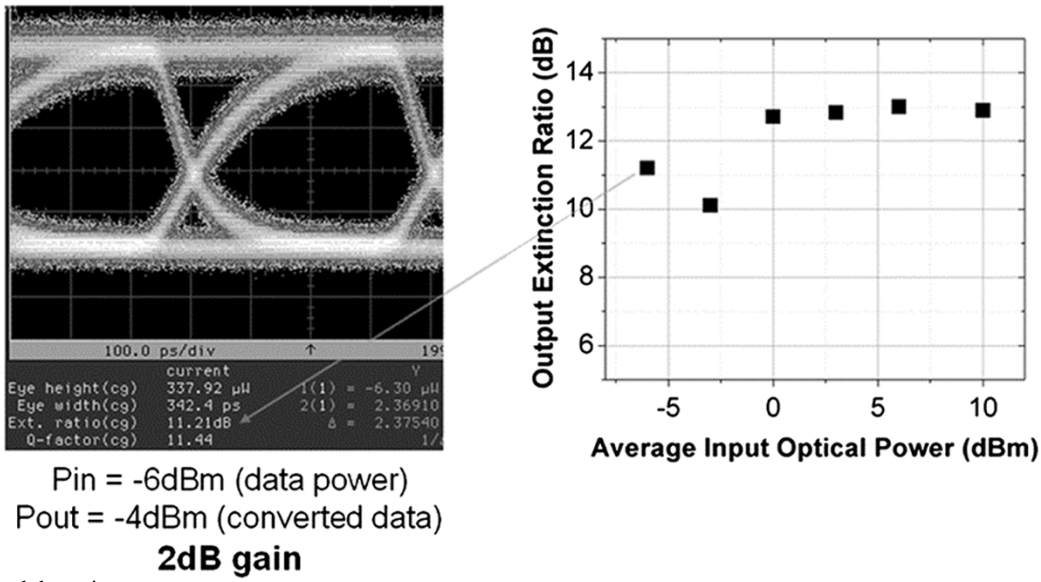

Fig. 17. Input signal dynamic range.

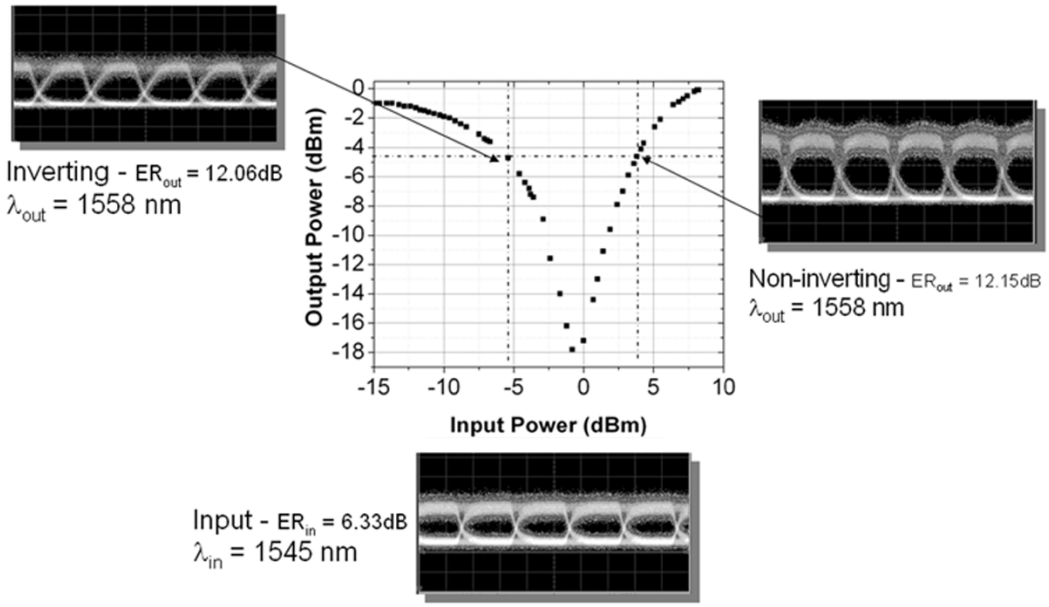

Fig. 18. Example of extinction ratio improvement.

For time-resolved chirp measurements, the TAO-WC MZI's bias currents are optimized for maximum extinction ratio in either inverting or noninverting mode of operation at 2.5 Gb/s. The output of the device is optically filtered and then led into a time-resolved chirp test instrument. The interferometric method used for chirp measurement is based on frequency and amplitude change measurements on two different slopes of the interferometer, in order to obtain the time-resolved frequency change [21]. The optical output from the instrument is connected to a high-speed digital oscilloscope, which is used as part of the setup to perform measurements on the data pattern.

Time-resolved chirp is measured as a function of the input wavelength, output wavelength (set by the integrated on-chip laser) and interferometer bias point (inverting, noninverting and in between). Examples of time-resolved results measured for noninverting (top) and inverting (bottom) mode of operation are shown in Fig. 19. Little input–output wavelength dependence of chirp parameter values is observed across the entire data set. Chirp parameter value and sign depend on the slope of the transfer function of the wavelength converter in the selected regime of operation. For noninverting operation, the average chirp parameter is measured to be -2 for 40 nm input and 22 nm output wavelength range. For inverting mode of operation, the average chirp parameter is measured to be 1–3 for the same output wavelength range. Thus, the performance of the wavelength converter in transmission should consistently reduce the dispersion power penalty if operated in the suitable mode of operation (based on the fiber dispersion parameter). The chirp parameter sign measured is consistent with theoretical predictions [23] and previous results for an XPM-SOA based wavelength converter [25].

F. Dynamic Performance Analysis

Carrier dynamics in the SOAs of the MZI limited the wavelength converter bandwidth to 7 Gbps (for TAO-WC). Dynamic behavior of the chips is a result of the confinement factor of the

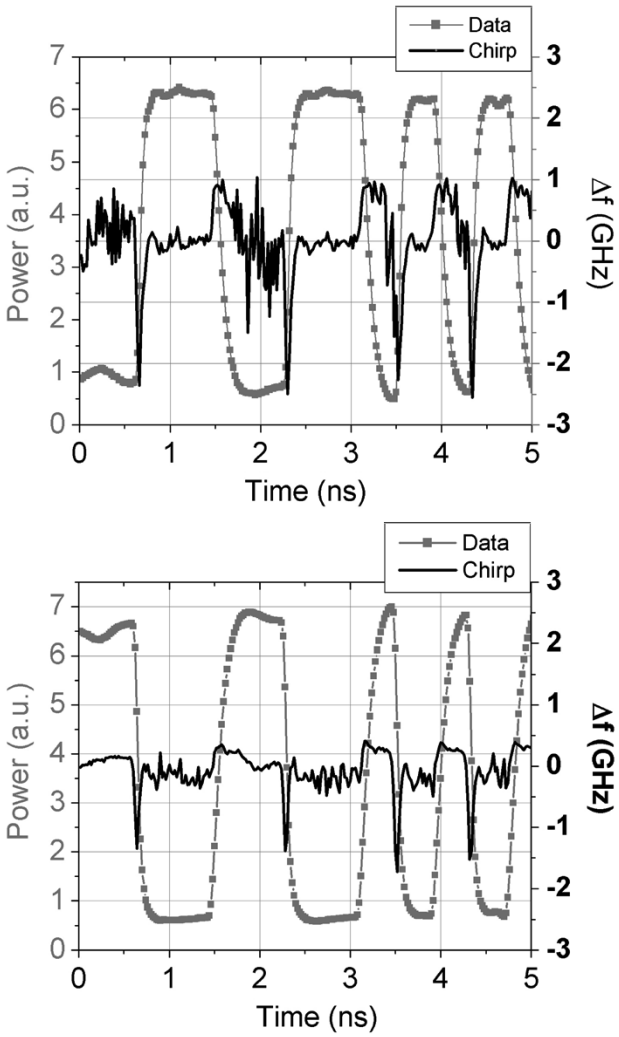

Fig. 19. Examples of time resolved chirp measured: (top) noninverting and (bottom) inverting modes of operation.

SOAs, the gain properties of the quantum wells used, the SOA pump current and the photon density in the SOAs. Increasing the SOA pump currents eventually changes the bandstructure of the quantum wells through thermal effects, which then leads to the reduction in differential gain, thereby increasing the gain recovery time. Therefore, there is an optimum bias current setpoint for the MZI-SOA operation.

The operating speeds observed for TAO-WC device type are higher than those for TAOMI-WC device due to several differences in the device design. First, the length of the passive sections preceeding the MZI-SOA in the TAO-WC design is shorter than that in the TAOMI-WC design, allowing for higher SGDBR-generated CW light intensities to reach the MZI. This high photon density helps to reduce the gain recovery time by increasing the optical pumping of the SOAs in the MZI. The higher speeds are observed in part due to the wider separation of the MZI SOAs in the TAO-WC device, which leads to lower heating of these SOAs, causing the differential gain to remain high.

The main mechanism that can be used to enhance the bandwidth of operation in the offset quantum-well platform is further increase of the photon density in the MZI-SOAs. This has been demonstrated with an improved device design and operation at 10 Gbps in our more recent work [26].

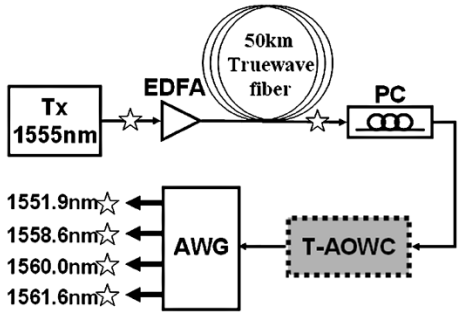

Fig. 20. Schematic of the wavelength routing experiment.

VI. Wavelength Routing Demonstration

As discussed in the introduction, one of the main applications of tunable wavelength converters is for the implementation of optical wavelength routing. Hence, a tunable wavelength converter must be able to reliably convert received signals between different channels in a WDM network, such as the channels determined by the ports of an arrayed waveguide grating router (AWGR). As part of this work, a demonstration of wavelength routing using the TAO-WC device is shown through four different ports in an AWGR, as indicated in the experimental setup schematic, Fig. 20.

A. Experiment

The transmitter consists of a tunable laser operating at 1555 nm, a polarization controller, and a lithium niobate electro-optic modulator. An EDFA is placed after the transmitter to amplify the signal for transmission through 50 km of dispersion shifted Truewave fiber.

Two conical-tipped lensed-fibers on piezo-controlled translational stages are used to couple light into and out of the device. Four wavelengths (1551.9, 1558.6, 1560.0, 1561.6 nm), each corresponding to a different port on the AWGR, are chosen for their placement in the C-band and for their relation to the input wavelength of 1555 nm. Tuning of the device's output wavelength is achieved by current injection through the front, phase, and back mirror sections of the integrated SGDBR laser.

B. Results

For the experimental demonstration, the $2^{31}-1$ PRBS data at 2.5 Gbps is generated using a BERT pattern generator. The optical power measured in the fiber at the input to the device is -2.5 dBm. For each output wavelength, the currents injected through the SOAs of the device's MZI arms are adjusted to maximize the extinction ratio of the wavelength converted signal. The extinction ratio is calculated using the eye diagram obtained by a digital sampling oscilloscope.

Extinction ratios of 12 dB or greater are measured for each of the wavelength converted signals. BER measurements are taken after the transmitter, after the 50 km spool of fiber, and at the output ports of the AWGR for each wavelength using an optically preamplified receiver whose sensitivity was -34.5 dBm. Results of the BER measurements are shown in Fig. 21. Less

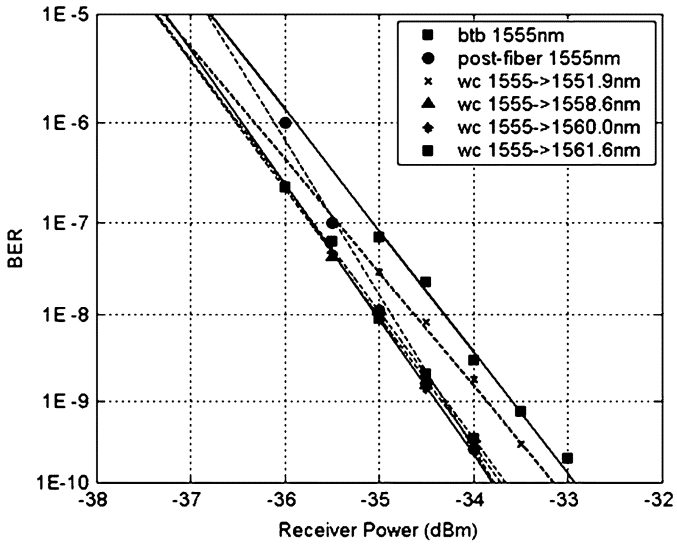

Fig. 21. BER results for the wavelength routing experiment.

than 1 dB of power penalty is observed at a bit-error rate of 10^{-9} for each of the wavelength converted signals.

VII. Conclusion

Monolithically integrated widely tunable wavelength converters are PICs whose function is essential for WDM systems, particularly in applications like optical switching, wavelength routing, and add/drop multiplexing.

In this paper, we discussed the design, fabrication, and characterization of the first fully functional monolithically integrated widely tunable all-optical wavelength converters, based on the SGDBR laser monolithically integrated with MZI-SOA wavelength converters. Error-free wavelength conversion at 2.5 Gbps is demonstrated over 50 nm input and 22 nm output wavelength range, with extinction ratio enhancement and signal reamplification. The devices show linewidth comparable to that of commercial SGDBR lasers, as well as low negative chirp.

By further optimizing the device design, it is possible to additionally improve the device performance, including the maximum data rate, the output wavelength tuning range and input and output powers, while keeping the same simple and robust integration platform and the single-regrowth fabrication process. This has been demonstrated with an improved device design operating over a 35 nm output wavelength range and at 10 Gbps in our more recent work [26].

Acknowledgment

The authors acknowledge Agility Communications for providing growth/AR coating services.

References

[1] X. Pan, J. M. Wiesenfeld, J. S. Perino, T. L. Koch, G. Raybon, U. Koren, M. Chien, M. Young, B. I. Miller, and C. A. Burrus, "Dynamic operation of a three-port, integrated Mach-Zehnder wavelength converter," *IEEE Photon. Technol. Lett.*, vol. 7, pp. 995–997, 1995.

[2] W. Idler, K. Daub, G. Laube, M. Schilling, P. Wiedemann, K. Dutting, M. Klenk, E. Lach, and K. Wunstel, "10 Gb/s wavelength conversion with integrated multiquantum-well 3-port Mach-Zehnder interferometer," *IEEE Photon. Technol. Lett.*, vol. 8, pp. 1163–1165, 1996.

[3] C. Janz, F. Poingt, F. Pommereau, W. Grieshaber, F. Gaborit, D. Leclerc, I. Guillemot, and M. Renaud, "New all active dual order mode (DOMO) Mach-Zehnder wavelength converter for 10 Gbit/s operation," in *ECOC 99*, Nice, France.

[4] L. Spiekman, U. Koren, M. Chien, B. Miller, J. Wiesenfeld, and J. Perino, "All-optical Mach-Zehnder wavelength converter with monolithically integrated DFB probe source," *IEEE Photon. Technol. Lett.*, vol. 9, pp. 1349–1351, 1997.

[5] R. Broeke and M. Smit, "A wavelength converter with integrated tunable laser," in *IPR 2003*, Washington, DC, 2003.

[6] V. Jayaraman, Z. Chuang, and L. Coldren, "Theory, design, and performance of extended tuning range semiconductor lasers with sampled gratings," *IEEE J. Quantum Electron.*, vol. 29, pp. 1824–1834, 1993.

[7] M. Mašanović, V. Lal, J. Barton, E. Skogen, L. Coldren, and D. Blumenthal, "Monolithically integrated Mach-Zehnder interferometer wavelength converter and widely-tunable laser in InP," *IEEE Photon. Technol. Lett.*, vol. 15, pp. 1117–1119, 2003.

[8] M. Mašanović, V. Lal, J. Barton, L. Coldren, and D. Blumenthal, "Wavelength conversion over a 50 nm input and 21 nm output wavelength range using a monolithically integrated tunable all-optical MMI-MZI (TAOMI) wavelength converter," in *Eur. Conf. Optical Commun., ECOC 2003*, Rimini, Italy, Sep. 2003.

[9] B. Mason, J. S. Barton, G. A. Fish, L. A. Coldren, and S. P. Denbaars, "Design of sampled grating DBR lasers with integrated semiconductor optical amplifiers," *IEEE Photon. Technol. Lett.*, vol. 12, pp. 762–764, 2000.

[10] Y. Akulova, G. Fish, K. Ping-Chiek, C. Schow, P. Kozodoy, A. Dahl, S. Nakagawa, M. Larson, M. Mack, T. Strand, C. Coldren, E. Hegblom, S. Penniman, T. Wipiejewski, and L. Coldren, "Widely-tunable electroabsorption-modulated sampled-grating DBR laser transmitter," *IEEE J. Sel. Topics Quantum Electron.*, vol. 8, pp. 1349–1357, 2002.

[11] J. Barton, E. Skogen, M. Mašanović, and L. Coldren, "Widely-tunable high-speed transmitters using integrated SGDBR's and Mach-Zehnder modulators," *IEEE J. Sel. Topics Quantum Electron.*, Sep. 2003.

[12] J. Barton, M. Mašanović, M. Sysak, E. Skogen, J. Hutchinson, D. Blumenthal, and L. Coldren, "A novel, monolithically integrated widely-tunable wavelength converter based on a SGDBR-SOA-MZI transmitter and integrated photodetector," in *Photonics in Switching 2003*, Versailles, France.

[13] J. Hutchinson, J. Henness, L. Johansson, J. Barton, M. Mašanović, and L. Coldren, "2.5 Gb/sec wavelength conversion using monolithically-integrated photodetector and directly modulated widely-tunable SGDBR laser," in *LEOS Annual Meet. 2003*, Tucson, AZ.

[14] C. Joergensen, S. Danielsen, K. Stubkjaer, M. Schilling, K. Daub, P. Doussiere, F. Pommerau, P. Hansen, H. Poulsen, A. Kloch, M. Vaa, B. Mikkelsen, E. Lach, G. Laube, W. Idler, and K. Wunstel, "All-optical wavelength conversion at bit rates above 10 Gb/s using semiconductor optical amplifiers," *IEEE J. Sel. Topics Quantum Electron.*, pp. 1168–1180, 1997.

[15] L. Soldano and E. Pennings, "Optical multi-mode interference devices based on self-imaging: Principles and applications," *J. Lightw. Technol.*, vol. 13, pp. 615–627, 1995.

[16] D. Marcuse, "Reflection loss of laser mode from tilted end mirror," *J. Lightw. Technol.*, vol. 7, pp. 336–339, 1989.

[17] B. Jaskorzynska, J. Nilsson, and L. Thylen, "Modal reflectivity of uptapered, tilted-facet, and antireflection-coated diode-laser amplifiers," *J. Opt. Soc. Amer. B-Opt. Phys.*, vol. 8, pp. 484–493, 1991.

[18] E. Pennings, R. van Roijen, M. van Stralen, P. de Waard, R. Koumans, and B. Verbeck, "Reflection properties of multimode interference devices," *IEEE Photon. Technol. Lett.*, vol. 6, pp. 715–718, 1994.

[19] Y. Gottesman, E. Rao, and B. Dagens, "A novel design proposal to minimize reflections in deep-ridge multimode interference couplers," *IEEE Photon. Technol. Lett.*, vol. 12, no. 12, pp. 1662–1664, Dec. 2000.

[20] E. Gini, E. Gamper, W. Vogt, and H. Melchior, "Monolithic integration of passive waveguides with active SOA's and phase shifters for $\mathrm{lambda} = 1.55\ \mu\mathrm{m}$ using four step LP-MOVPE growth," in *Proc. 25th Europ. Conf. Opt. Commun. ECOC'99 Conf. Soc. Electr. Electron*, vol. 1, Paris, France, 1999, pp. 174–5.

[21] S. Nakagawa, G. Fish, G. A. Dahl, P. Koh, C. Schow, M. Mack, L. Wang, and R. Yu, "Phase noise of widely-tunable SG-DBR laser," in *Optical Fiber Communications Conf. (OFC). (Trends in Optics and Photonics Series Vol. 86) Tech. Dig. (IEEE Cat. 03CH37403). Opt. Soc. Amer.*, vol. 2, Wash., DC, 2003, pp. 461–2.

[22] R. Saunders, J. King, and I. Hardcastle, "Wideband chirp measurement technique for high bit rate sources," *Inst. Elect. Eng. Electron. Lett.*, vol. 30, pp. 1336–1338, 1994.

[23] L. A. Coldren and S. W. Corzine, *Diode Lasers and Photonic Integrated Circuits*. New York: Wiley-Interscience, 1995.

[24] T. Durhuus, B. Mikkelsen, C. Joergensen, S. L. Danielsen, and K. Stubkjaer, "All-optical wavelength conversion by semiconductor optical amplifiers," *J. Lightw. Technol.*, vol. 14, pp. 942–954, 1996.

[25] S. Cao and J. Cartledge, "Characterization of the chirp and intensity modulation properties of an SOA-MZI wavelength converter," *J. Lightw. Technol.*, vol. 20, pp. 689–695, 2002.

[26] M. L. Mašanović, V. Lal, J. A. Summers, J. S. Barton, E. J. Skogen, L. A. Coldren, and D. J. Blumenthal, "Design and performance of a monolithically-integrated widely-tunable all-optical wavelength converter with independent phase control," *IEEE Photon. Technol. Lett.*, vol. 12, Oct. 2004.

Milan L. Mašanović (S'98–M'04) graduated as a valedictorian from the School of Electrical Engineering, University of Belgrade, Yugoslavia, in 1998. He received the M.S. degree in 2000 and the Ph.D. degree in electrical engineering from the University of California, Santa Barbara, in 2004.

He is currently a Research Scientist at the University of California at Santa Barbara. He authored or coauthored more than 50 papers in the field. His research interests are in the area of InP photonic integration with emphasis on integrated tunable wavelength converters and optical wavelength routing for novel all-optical networks.

Dr. Mašanović received the 2004 IEEE Lasers & Electro-Optics Society (LEOS) Graduate Student Fellowship award as well as the 2003 Best Student Paper Award at Indium Phosphide and Related Materials Conference.

Vikrant Lal (S'00) received the B.S. degree in electrical engineering in August 1999 from the Indian Institute of Technology, Delhi, and the Master's degree in communications engineering from the Electrical and Computer Engineering Department from the University of Maryland, College Park, in August 2001.

He is currently a Ph.D. student in electrical and computer engineering at the University of California, Santa Barbara, working under Prof. D. Blumenthal. His research interests include optical networking, photonic integrated circuits, and all-optical switching.

Joseph A. Summers (S'00) received the B.S. degree in electrical engineering from Northwestern University, Chicago, IL, in 2000 (minor in economics).

He is currently working toward the Ph.D. degree in electrical and computer engineering at the University of California, Santa Barbara. His interests include high-density photonic integrated circuits, and academic outreach.

Jonathon S. Barton (S'00) was born in Sacramento, CA, in 1975. He received the B.S. degree in electrical engineering and material science in 1998 from the University of California, Davis, and the Ph.D. degree in material science from the University of California, Santa Barbara, in 2004.

He is currently a Research Scientist at the University of California at Santa Barbara. His research interests focus on photonic integrated circuits—integrating tunable lasers with semiconductor optical amplifiers and modulators.

Erik J. Skogen was born in Minneapolis, MN, in 1975. He received the B.S. degree from Iowa State University in 1997, and the M.S. and Ph.D. degrees from the University of California, Santa Barbara, in 1999 and 2003, respectively.

After working as a Research Scientist at the University of California, Santa Barbara, he joined Sandia National Laboratories, Albuquerque, NM, in January 2005. His research interests include widely tunable semiconductor lasers, monolithic integration for photonic integrated circuits, crystal growth by MOCVD, and quantum-well intermixing.

Lavanya G. Rau received the Ph.D. degree from the University of California, Santa Barbara (UCSB), in 2003. Her dissertation focused on ultrafast wavelength conversion using cross-phase modulation in nonlinear fiber and its application in future high-speed photonic networks.

She is currently a Postdoctoral Researcher with the California Institute for Telecommunications and Information Technology, University of California at Irvine. Her present work involves evaluating the regenerative nature of all-optical 3R regenerators in the presence of jitter and noise.

Larry A. Coldren (S'67–M'72–SM'77–F'82) received the Ph.D. degree in electrical engineering from Stanford University, CA, in 1972.

After 13 years in the research area at Bell Laboratories, he was appointed Professor of Electrical and Computer Engineering at the University of California at Santa Barbara (UCSB) in 1984. In 1986, he assumed a joint appointment with Materials and Electrical and Computer Engineering and, in 2000, the Fred Kavli Chair in Optoelectronics and Sensors. He is also Chairman and Chief Technology Officer of Agility Communications, Inc. At UCSB, his efforts have included work on novel guided-wave and vertical-cavity modulators and lasers, as well as the underlying materials growth and fabrication technology. He is now investigating the integration of various optoelectronic devices, including optical amplifiers and modulators, tunable lasers, wavelength converters, and surface-emitting lasers. He has authored or coauthored more than 500 papers, five book chapters, and one textbook, and has been issued 32 patents.

Dr. Coldren is a Fellow of the Optical Society of America (OSA) and a Member of the National Academy of Engineering.

Daniel J. Blumenthal (M'97–F'03) received the B.S.E.E. degree from the University of Rochester, New York, in 1981, the M.S.E.E. degree from Columbia University, New York, in 1988, and the Ph.D. degree from the University of Colorado, Boulder, in 1993.

In 1981, he worked at StorageTek, Louisville, CO, and from 1993 to 1997, he was Assistant Professor with the School of Electrical and Computer Engineering, Georgia Institute of Technology, Atlanta. He is currently a Professor with the Department of Electrical and Computer Engineering, University of California at Santa Barbara. He is the Principle Investigator for the Defense Advanced Research Projects Agency (DARPA) Department of Defense (DoD)-N LASOR project and currently serves on the Board of Directors for National LambdaRail (NLR), a national footprint optical network research infrastructure. His research areas are optical communications, photonic packet-switched and all-optical networks, all-optical wavelength conversion, optical subcarrier multiplexing, integrated optic chip-scale wavelength-division multiplexing (WDM), and nanophotonic technologies. He has authored or coauthored more than 160 papers in these and related areas, as well as coauthored the book *Tunable Laser Diodes and Related Optical Sources*.

Dr. Blumenthal is a Member of the Optical Society of America (OSA). He is the recipient of a 1999 Presidential Early Career Award for Scientists and Engineers (PECASE) from the White House and the DoD, a 1994 NSF Young Investigator (NYI) Award, and a 1997 Office of Naval Research Young Investigator Program (YIP) Award. He is an Associate Editor for the IEEE PHOTONICS TECHNOLOGY LETTERS and has served as Associate Editor for the IEEE TRANSACTIONS ON COMMUNICATIONS. He was a Guest Editor for the JOURNAL OF LIGHTWAVE TECHNOLOGY Special Issue on Photonic Packet Switching Systems (December 1998) and Guest Editor for the IEEE JOURNAL OF SELECTED AREAS IN COMMUNICATIONS Special Issue on High-Performance Optical/Electronic Switches/Routers for High-Speed Internet. He also served on numerous other technical program committees, including the Conference on Optical Fiber Communications (OFC) from 1997 to 2000 and the Conference on Lasers and Electro-Optics (CLEO) from 1999 to 2000.

Device Physics of an Optoelectronic Integrated Wavelength Converter

J. Piprek,[i] V. Lal, J. Hutchinson,[*] J. Henness, A. Tauke Pedretti, M. Dummer, and L. Coldren

Electrical and Computer Engineering Department
University of California, Santa Barbara, CA 93106
[*] Intel Corporation, Portland, OR

ABSTRACT

An InP-based tunable wavelength converter is investigated which monolithically combines a waveguide photodetector with a sampled-grating distributed Bragg reflector laser diode. We employ advanced device simulation to study internal physical mechanisms and performance limitations. Our three-dimensional finite-element model self-consistently combines carrier transport, optical waveguiding, and nanoscale many-body theory to accurately account for optical transitions within the quantum wells. Good agreement with measurements is achieved. The validity of several model simplification options is discussed.

Keywords: Optoelectronic integrated circuit, wavelength converter, semiconductor optical amplifier, many-body theory, three-dimensional device simulation, rate equation model

1. INTRODUCTION

Wavelength converters are of interest for wavelength-division multiplexing (WDM) fiber-optic communication systems to transfer signals from one channel to another. We investigate a monolithic InP-based tunable wavelength converter which combines a waveguide photodetector with a sampled-grating distributed Bragg reflector (SGDBR) laser diode.[1] Table 1 lists the epitaxial structure including the multi-quantum well (MQW) active region. Figure 1 shows a schematic layout of the entire converter. The receiver integrates signal pre-amplification by a semiconductor optical amplifier (SOA) and signal detection by a waveguide photodiode (WPD). The optical signal is converted into an electrical signal that directly modulates the tunable SGDBR laser diode which is integrated with a semiconductor optical amplifier for signal enhancement. Further experimental details are given elsewhere.[2]

Layer	Material	Thickness nm	Doping 10^{18} cm^{-3}
p-contact	InGaAs	100	30 (p)
upper cladding	InP	1600	1 (p)
upper cladding	InP	200	0.3 (p)
doping setback	InP	50	-
quantum barrier (8x)	$In_{0.685}Ga_{0.315}As_{0.595}P_{0.405}$	8	-
quantum well (7x)	$In_{0.685}Ga_{0.315}As_{0.864}P_{0.136}$	6.5	-
etch stop	InP	10	-
waveguide	$In_{0.612}Ga_{0.338}As_{0.728}P_{0.272}$	350	0.1 (n)
lower cladding	InP	1400	1 (n)
etch stop / n-contact	InGaAs	100	1 (n)
Buffer	InP	1000	-

Tab. 1 Epitaxial layer sequence of the monolithic device.

[i] Corresponding author, e-mail: piprek@ieee.org

Optoelectronic Integrated Circuits VII, edited by Louay A. Eldada, El-Hang Lee, Proc. of SPIE Vol. 5729
(SPIE, Bellingham, WA, 2005) · 0277-786X/05/$15 · doi: 10.1117/12.584570

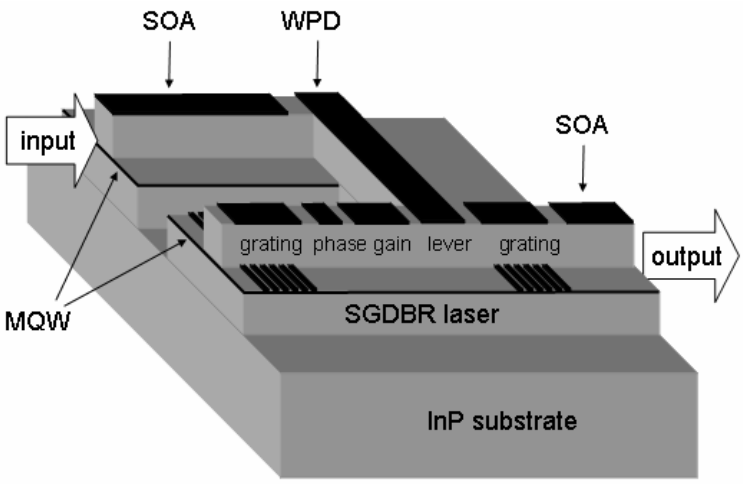

Fig. 1: Schematic view of the optoelectronic integrated wavelength converter.

We here analyze internal physical processes of this device using advanced numerical simulation that is in good agreement with our measurements. Section 2 compares different models for optical transitions within the quantum wells. Section 3 outlines the three-dimensional (3D) device model and introduces a more simple rate equation model for the amplifier. Section 4 compares the simulation results from both models to SOA saturation measurements.

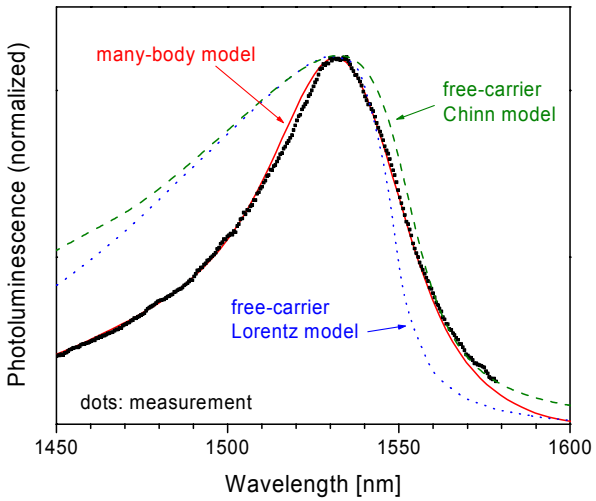

Fig. 2: Comparison of measured and calculated photoluminescence spectra.

2. QUANTUM WELL MODELING

The accurate modeling of quantum well properties, in particular the optical transition rates (spontaneous emission, gain, absorption) are prerequisite for a realistic simulation of the wavelength converter. We initially employed a simple free-carrier model based on 4x4 kp band structure calculations and using a Lorentz energy broadening function.[3] However, this approach did not give consistent agreement with experimental results.[4] A comparison to the measured photoluminescence spectrum is shown in Fig. 2 revealing discrepancies on both sides of the spectrum. The energy broadening model by Chinn et al.[5] is considered an improvement over the Lorentz model as it describes the low-energy tail of the Lorentz function by a more appropriate Gaussian function. Indeed, this spectrum shows better agreement for

low energies in Fig. 2 (dashed line), however, both free-carrier models deviate substantially from the measurement at high energies. Thus, energy broadening effects by many-body interactions require more careful consideration using advanced many-body theory.[6] This many-body model provides excellent agreement across the entire spectrum (solid curve in Fig. 2) which is of paramount importance for predictions of our device performance for all possible wavelengths (1525 nm - 1565 nm). Carrier-carrier and carrier-phonon interactions seem to have a non-trivial influence on the optical transition probabilities and cannot be represented by simple broadening functions.

Figure 3 plots calculated gain vs. density characteristics for different wavelengths. In agreement with experimental observations, the many-body model (solid line) gives almost constant gain across the wavelength range of interest. The free-carrier Chinn model (dashed lines) shows considerable gain variations within the same wavelength range. It comes close to the many-body results only for wavelengths near 1553 nm.

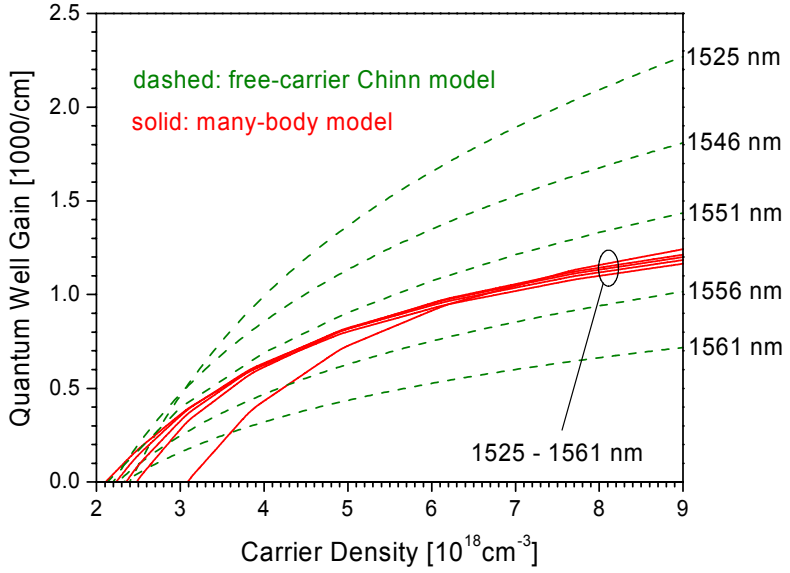

Fig. 3: Gain vs. carrier density characteristics from both models at different wavelength.

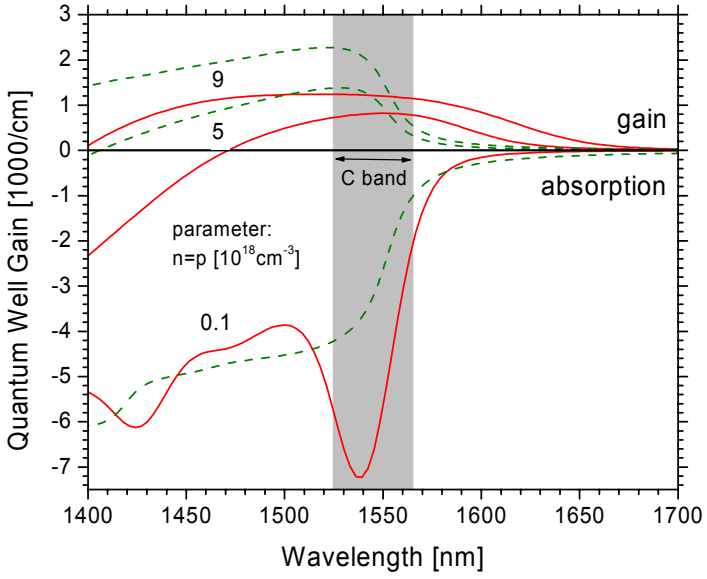

Fig. 4: Gain spectra from both models at different carrier densities.

Full gain/absorption spectra are compared in Fig. 4 for three carrier densities. At higher densities, the spectra cross each other at 1552 nm and 1554 nm, respectively, and reasonable agreement of device simulations can only be expected in close proximity to those wavelengths. Near the short-wavelength boundary of the C-band, the two models differ by a factor of two. With very low quantum well carrier densities, as in photodetectors, the absorption spectra also show significant differences. While the calculated bulk absorptions at higher energies are relatively close, the main differences occur near the band edge due to exciton transitions. Such electron-hole interactions are fully considered in the many-body model and cause a strong absorption peak, which is missing in the free-carrier model.

3. DEVICE SIMULATION

We now implement the precalculated many-body spectra into the 3D device simulation code PICS3D.[7] This software self-consistently combines the carrier transport (including Fermi statistics and thermionic emission) with optical wave-guiding. Details of the 3D model and of the many-body spectra integration are published elsewhere.[8] This novel simulation approach results in excellent agreement with a variety of device measurements, as reported earlier. [9,10]

In the following, we outline a more simple rate equation model for the SOA which will be shown to give good agreement with the 3D model as long as the same many-body spectra are implemented. The carrier rate equation for the MQW active region is given by

$$\frac{\partial N(t)}{\partial t} = \frac{\eta_i I}{qV} - (AN + BN^2 + CN^3) - \frac{\Gamma}{wd\hbar}\frac{g(N,\omega_s)}{\omega_s}P_s(t)$$

where

N	is the electron density (assumed equal to hole density)
η_i	is the injection efficiency
I	is the injected current
V	is the volume of the active region
A,B,C	are the recombination parameters
Γ	is the overlap of the optical mode with the active material
w,d	are the active region width and height resp.
P_s	is the input signal power
ω_s	is the signal frequency
g	is the material gain at carrier density N and frequency ω

This type of a description works well for a resonant or gain-clamped SOA, but for a traveling wave type SOA where there are no facet reflections, carrier density and power distributions are non-uniform along the length of the SOA, and models that approximate the entire SOA with a single average carrier density do not work well. For this reason, we break our SOA region into a number of much smaller elements, within which we can approximate the carrier density as uniform. This approach is depicted in Fig 5.

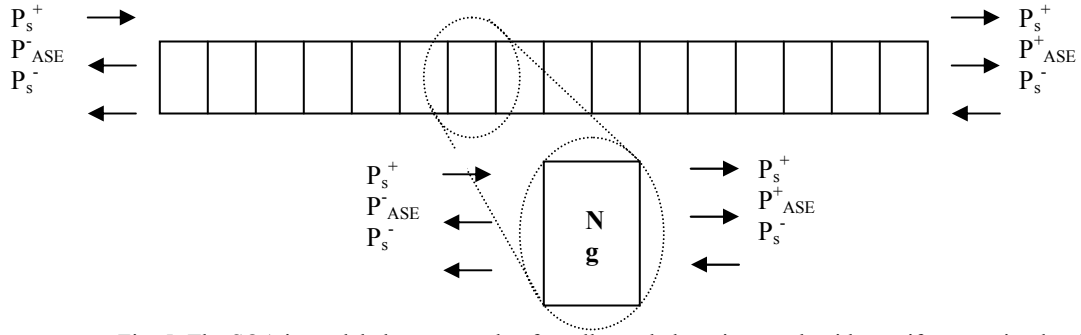

Fig. 5: The SOA is modeled as a cascade of small coupled sections each with a uniform carrier density

Each section of the SOA can then be described using the following three equations:

$$\frac{\partial N(z,t)}{\partial t} = \frac{\eta_i J}{qd} - (AN + BN^2 + CN^3) - \frac{\Gamma}{wd\hbar}\left[\sum_k \frac{g(N,\omega_s)}{\omega_s} P_s(z,t) + \int \frac{g(N,\omega)}{\omega}(P^{ASE+} + P^{ASE-})d\omega\right]$$

$$\frac{1}{v_g}\frac{\partial P_s^{\pm}}{\partial t} \pm \frac{\partial P_s^{\pm}}{\partial z} = \left[\Gamma g(N,\omega_s) - \alpha_i\right]P_s^{\pm} \qquad \forall k$$

$$\frac{1}{v_g}\frac{\partial P^{ASE\pm}}{\partial t} \pm \frac{\partial P^{ASE\pm}}{\partial z} = \left[\Gamma g(N,\omega) - \alpha_i\right]P^{ASE\pm} + \beta R_{sp}(N,\omega)A\hbar\omega \quad \forall \omega$$

where,

$P^{ASE+/-}$	is the power spectral density of the ASE traveling in the + or – direction
J	is current density in the particular section of the SOA
v_g	is the signal group velocity
β	is the spontaneous emission factor
R_{sp}	is the spontaneous emission rate

The first equation describes the rate of change of electron/hole density in the given SOA section, which depends on the signal power and the amplified spontaneous emission (ASE) power present in the section. The summation is over all signals propagating in both the positive and negative direction, and the ASE is integrated over its entire spectrum. The second equation describes the propagation of the signal across a gain medium. Finally, the third equation describes the evolution of the ASE power spectral density. The βR_{sp} term is the generated spontaneous emission that couples into the guided modes of the SOA. For index guided traveling wave SOAs, that do not have resonant modes in the longitudinal direction, β is given by

$$\beta = (2\pi n)^{-2}\frac{\lambda_o^2}{S_o}$$

with S_o being the optical mode area. The equations can be easily solved iteratively to compute the gain, signal, and ASE in different sections of the SOA. However, ASE is found negligible in our example.

4. COMPARISON TO AMPLIFIER MEASUREMENTS

We now compare the results of both device models, including many-body spectra, to saturation measurements on our amplifier structure. The SOA is 600 μm long and its ridge width is 3 μm. The same parameters are used in both models.[8] The injection efficiency η_i=0.82 and the optical confinement factor Γ = 0.06 are extracted from the full 3D simulation. The internal optical loss is assumed as α_i = 10/cm, additional intervalence band absorption is neglected here. Figure 6 plots the calculated SOA output power vs. input power in comparison to the measurement (dots).

The agreement between both device models is surprisingly good, indicating that the quantum well recombination processes dominate the SOA performance. The carrier transport to the MQW as well as the carrier distribution within the MQW do not seem very important, as both are neglected in the rate equation model. Only slight deviations are observed at higher power. The full 3D simulation gives slightly stronger non-linearity which may be attributed to differences in the recombination rates. While Auger coefficients and SRH lifetimes are identical in both models, the spontaneous recombination rate is computed differently. The rate equation model uses the common coefficient B = 10^{-10} cm^3/s whereas PICS3D integrates the many-body spectra for the spontaneous emission. At low power, the full 3D model gives a slightly higher gain than the rate equation model. This is identified as numerical artifact which can be avoided by reducing the initial input power of the PICS3D simulation.

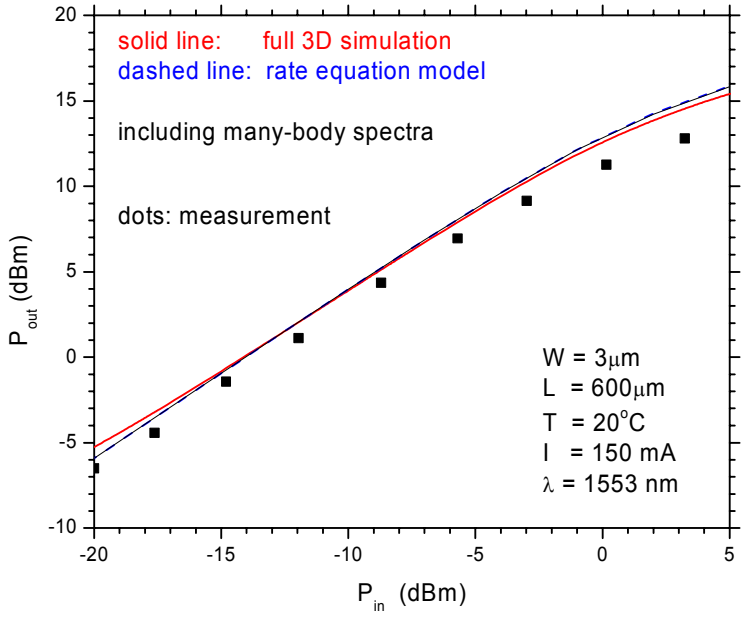

Fig. 6: Amplifier output power vs. input power at 8.3 kA/cm^2 current density.

By employing advanced many-body theory, both models give good agreement with the measurement in Fig. 6. The remaining small deviation can have multiple reasons, e.g., additional optical losses and/or self-heating of the device, which is neglected in both models. 3D thermal simulations show an active region temperature rise of about 15K at 150mA current assuming a thermal resistance of 100 K/W for substrate and heat sink.

5. SUMMARY

Different simulation approaches are compared to achieve a realistic representation of internal device physics in our wavelength converter. The application of many-body theory to the calculation of quantum well optical spectra is identified as most essential element of the model. Carrier transport and distribution effects seem less important.

ACKNOWLEDGMENT

This research project was sponsored by the Semiconductor Research Corporation (Award 2001-NJ-968) and by the Intel Corporation. Supercomputer calculations of the many-body spectra have been performed by Nonlinear Control Strategies, Inc., Tucson, AZ.

REFERENCES

[1] V. Jayaraman, A. Mathur, L. A. Coldren, and P. D. Dapkus, "Theory, design, and performance of extended tuning range in sampled grating DBR lasers," IEEE J. Quantum Electron., vol. 29, pp. 1824–1834, 1993.

[2] J. Hutchinson, J. Barton, M. Masanovic, M. Sysak, J. Henness, L. Johansson, D. Blumenthal, and L. A. Coldren, "Monolithically integrated InP-based tunable wavelength conversion." In: *Physics and Simulation of Optoelectronic Devices XII,* SPIE Proc. Vol. 5349, pp. 176-184, 2004.

[3] S. L. Chuang, *Physics of Optoelectronic Devices,* Wiley, New York 1995.

[4] J. Piprek, N. Trenado, J. Hutchinson, J. Henness, and L. A. Coldren, "3D Simulation of an integrated wavelength converter." In: *Physics and Simulation of Optoelectronic Devices XII,* SPIE Proc. Vol. 5349, pp. 185-196, 2004.

[5] S. Chinn, P. Zory, and A. Reisinger, IEEE J. Quantum Electron., vol. 24, pp. 2191-2214 (1988)

[6] S.W. Koch, J. Hader, A. Tränhardt, and J.V. Moloney, "Gain and Absorption: Many-Body Effects," Chapter 1 in: *Optoelectronic Devices – Advanced Simulation and Analysis*, J. Piprek (ed.), Springer Verlag, New York, 2004.

[7] PICS3D by Crosslight Software (www.crosslight.com)

[8] J. Piprek, S. Li, P. Mensz, and J. Hader, "Monolithic Wavelength Converter," Chapter 14 in: *Optoelectronic Devices – Advanced Simulation and Analysis*, J. Piprek (ed.), Springer Verlag, New York, 2004.

[9] J. Piprek, J. Hutchinson, J. Henness, L. Coldren, and J. Hader; "Many-Body Effects on InP-based Optoelectronic Wavelength Converters for WDM Applications" (postdeadline) 4th IEEE/LEOS Int. Conf. on *Numerical Simulation of Optoelectronic Devices*, Santa Barbara, August 2004.

[10] J. Piprek, J. Hutchinson, J. Henness, M. Masanovic, and L. A. Coldren; "Saturation Analysis of a Monolithic Wavelength Converter," in: *Physics and Applications of Optoelectronic Devices*, SPIE Proc. 5594, pp. 102-109, 2004.

Proc. SPIE Photonics West, 5729, pp. 177-191, San Jose, CA (March 2005)

Widely-tunable photocurrent-driven wavelength converters

Jonathon S. Barton, Matthew N. Sysak, Anna Tauke-Pedretti, Matthew Dummer, Jonathan Klamkin, Jonathan Getty, Erik J. Skogen, James Raring, Leif A. Johansson, Milan L. Mašanović, Larry A. Coldren

Materials and Electrical and Computer Engineering Depts., University of California, Santa Barbara, 93106
jsbarton@engineering.ucsb.edu

ABSTRACT

Wavelength converters are seen as important to the scalability, flexibility, and cost of future optical networks. These devices have opportunities for deployment in optical switches, routers and add/drop multiplexers. This talk will outline the latest results of monolithic and hybrid photocurrent-driven wavelength converters (PD-WC) based on either the direct modulation of a bipolar cascade SGDBR laser or by external modulation using an Electro-absorption (EA), or Mach-Zehnder (MZ) modulator using integration building blocks such as a semiconductor optical amplifiers (SOA), SGDBR lasers, PIN detectors and EA and MZ modulators. As the input and output waveguides are separate in this configuration of wavelength converter, an optical filter is not required to reject the input signal at the output which is desirable particularly with wavelength tunable applications where the response time of a filter could limit system performance.

Keywords: Wavelength conversion, high-speed modulators, optically controlled gate, tunable laser, semiconductor optical amplifier, Electro-absorption modulator, Mach-Zehnder modulator, direct modulation, Bipolar cascade

I. INTRODUCTION

In today's point-to-point fiber networks, wavelength conversion is performed using conventional transponders and optical—electrical—optical (OEO) conversion. Unfortunately, these OEO devices often consume large amounts of power at high bit rates, have a large footprint, and due to the electronics involved, lack bit-rate transparency[1-3]. The cost penalty associated with upgrading to higher bit rates is seen as prohibitive. As networks transition to complex optical-mesh networks from point-to-point networks, monolithic wavelength converters are billed as important to reduce costs by eliminating wavelength blocking, improve the flexibility of network management and routing, and offering data regeneration possibilities. These new networks will require reconfigurability that may be obtained using wavelength converters in add/drop multiplexers and de-multiplexers to reroute data to new fiber links when conflicts arise at network nodes. Due to the above issues with standard OEO conversion, a number of different approaches have been explored to transfer data from one wavelength to another without passing the data through electronics and are outlined in table 1. Typical approaches use either semiconductor optical amplifiers (SOAs) or Electro-absorption (EA) modulators with cross-gain modulation (XGM)[4], Four-Wave Mixing (FWM)[5], Difference Frequency Generation(DFG)[6], Nonlinear Optical Loop Mirror (NOLM)[7], or cross-phase modulation in 'all optical' SOA based Mach-Zehnder[8,9], SAGNAC[10], or Michelson interferometer[11] structures (XPM). Some laser integrated devices include the TAO-WC[12] 'all optical' wavelength converter, wavelength selectable laser with all-optical wavelength converter[20], and SSGDBR[17] and GCSR[18] lasers using gain suppression by direct injection into a laser cavity.

Wavelength converter device performance is impacted by a number of different issues, for example, insertion losses/coupling losses, wavelength dependence of output power, extinction ratio, input and output optical bandwidth, input power dynamic range, power dissipation particularly with arrays, optical filtering of the input wavelength, bandwidth limitations such as carrier lifetime, cascadability, and chirp. Effective design needs to attempt to achieve adequate performance of all these metrics simultaneously.

This paper will address devices that improve on the level of integration by fabricating a monolithic wavelength converter with a widely-tunable transmitter and receiver on a common integration platform. This builds on the optical gating concept comprised of vertically coupled Uni-Traveling Carrier (UTC) detectors and EAMs which has been demonstrated with bit-rates as high as 320Gbit/s[14]. Here we explore a number of planar photocurrent-driven (PD) widely-tunable wavelength converters (WCs) that incorporate an integrated Sampled Grating Distributed Bragg Reflector (SGDBR) based agile source and amplified receiver simultaneously reducing the footprint size, eliminating the coupling losses and complexity of three fiber connections, and reducing manufacturing costs. PD-WC refer to devices that rely on the generation of photocurrent from an incident light signal in a detecting region to change the voltage on a transmitting region at an output wavelength.

Table 1. Examples of Widely-tunable wavelength converter approaches

Approach	Polarity Inv or non-inv	Demon. Max. Bandwidth	Advantages	Disadvantages	Ref []
DISCRETE					
OEO Transponder	Non	40G	3R regeneration possible, low input power req.	Not bit rate transparent, expensive, scalability?, high power consumption	
SOA XGM	Inv	40G-100G	Efficient , simple	Extinction ratio degrades for long wavelengths, requires filter, large chirp, conversion to same λ only in counter propagating mode	[4,12]
SOA FWM and DFG	Non	40G-100G	Format transparency, chirp inversion	Not efficient	[5,6]
MZ SOA XPM	Inv/Non	20G-40G	Lower signal power req. than XGM 40G in differential mode. 3R regeneration capabilities	Require filter in copropagating direction	[8,9]
Optical Gate UTC detector + TW EAM	Non	320G	Compact/Fast/no filter required	Requires large input power	[13,14]
EAM (XAM) or PAW	Non	10G-40G	Single waveguide-high bandwidth	High power req. Converted power low	[15]
NOLM	Non	40G	Fiber SAGNAC interferometer	Only amplitude mod formats	[7]
Fiber (XPM)	Inv/Non	40G	Simple	Similar to SOA case	[16]
TUNABLE LASER INTEGRATED					
Laser SSGDBR	Inv	10G /20G	Simple very wide tuning (90nm)	Requires filter, cannot convert to same λ, high chirp	[17]
GCSR	Inv	10G	Simple wide tuning (nm)	Requires filter cannot convert to same λ, high chirp	[18]
Wavelength selectable Laser + All optical WC	Inv/Non	1G	High functionality	Low power/ narrow tuning, optical feedback limited	[19]
TAO-WC	Inv/Non	10G	40G in differential mode	Requires filter	[20]
PHOTOCURRENT- DRIVEN TUNABLE LASER INTEGRATED					
SGDBR – SOA-PIN Receiver	Non	2.5G	Simple, can convert to same λ,	High chirp, low input SOA gain	[21]
BC-SGDBR – SOA-PIN Reciever	Non	2.5G	Very efficient, high conversion effic., can convert to same λ, no output SOA required.	Input SOA low saturation power	[23]
MZ-SGDBR – PIN detector	Inv/Non	2.5G	Single regrowth, can convert to same λ, low photocurrent generation in modulator	High input power req. Non inverted has positive chirp	[24]
SPP-MZ-SGDBR – SOA-PIN Reciever	Inv/Non	10G	0 Chirp, low input power req., single regrowth low photocurrent generation in modulator	More complicated bias circuitry	[25]
EAM-SGDBR – SOA-PIN Receiver	Non	10G	Low positive chirp, single regrowth, good transfer characteristic	Photocurrent competition in modulator	[27,29]

All three of the devices in this paper use the same SGDBR mirror design using a front Sampled Grating mirror (FM) with 5 4μm bursts with a 68.5μm sampling period, a 75um long phase section (Ph), as well as 12 6μm bursts with a

FM Ph RM

61.5μm sampling period Rear mirror (RM) similar to described previously[24]. This design yields over 38nm of tuning before wrap around. Externally modulated devices have an output SOA that is 400μm long that use the same material as the gain section of the laser.

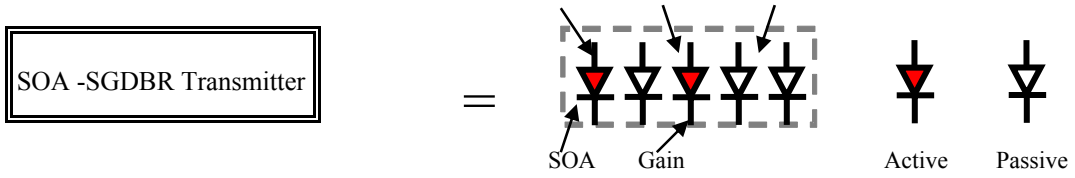

Fig 1. SGDBR block diagram

These transmitting regions can involve either the modulation of a single gain region[21] or bipolar cascade of gain regions[23], an external modulator such as an Electro-absorption(EA)[27,29] or Mach-Zehnder(MZ)[12] as shown in fig.2.

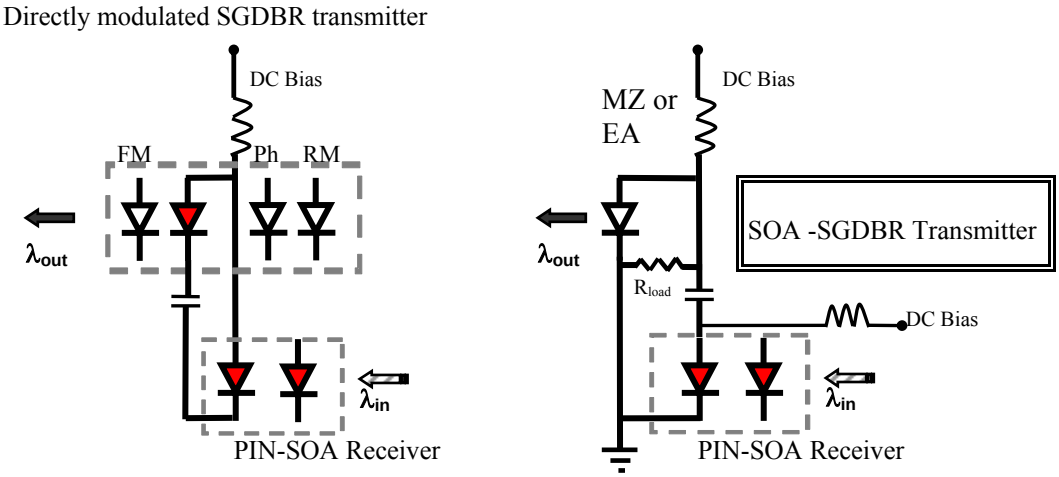

Fig. 2 Widely-tunable photocurrent-driven wavelength converter equivalent circuit diagrams using a directly modulated SGDBR laser or external modulation using single-side MZ or EA Modulator.

Wavelength conversion is achieved through electrically routing photocurrent, generated in the receiver section, via a metal trace on chip to directly drive the laser or change the voltage across a load resistor connected to an EA/MZ modulator. These integrated PD wavelength converters make use of an optically pre-amplified receiver to eliminate the need for electrical amplification in the device. Also, PD-WCs do not require an optical filter to reject the input signal at the output which is desirable particularly with wavelength tunable applications where the response time of a filter could limit system performance. Additionally, they have the potential of exhibiting less dissipated power than conventional SOA based all-optical WC devices with smaller SOA biases required.

II. INTEGRATION PLATFORMS

Throughout this work we have explored a number of different integration platforms as shown in fig. 3. Commercially, the offset QW structure has been employed with great success to fabricate both EAM and MZM based SGDBR transmitters due to the simplicity of defining active-passive interfaces[31]. Monolithically integrated widely-tunable 2.5Gbit/s wavelength conversion have also been demonstrated using an offset-QW materials platform with both EA[31] and MZ[24] modulators integrated with a SGDBR laser, Semiconductor Optical Amplifiers (SOA), and a photodetector. However, up till now, this approach has suffered from high input power requirements. By using a more optimized SOA

receiver design, input power requirements have been reduced considerably – down to approximately 1.3mW for a 600um long linearly tapered SOA.

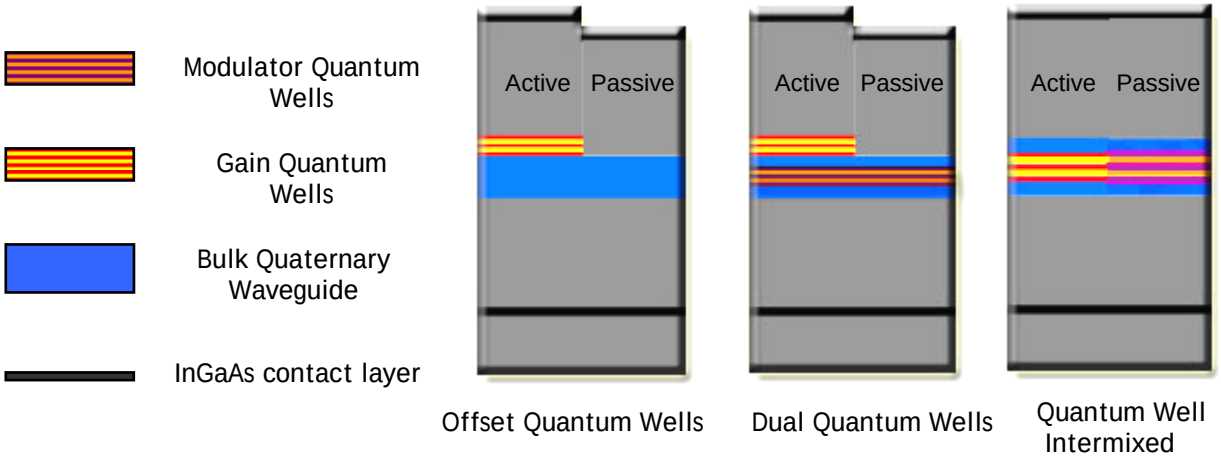

Fig. 3 InP/InGaAsP Integration platforms used for widely-tunable device fabrication

It is well known that by implementing QWs in a modulator structure, one can improve the efficiency of modulation at lower DC biases on the modulator. The challenges are in simultaneously achieving low propagation losses and wavelength independence. We can take advantage of this added performance by using a dual QW structure in which offset gain QWs are used in the SOA and gain section of a SGDBR tunable laser, and wide and shallow centered QWs are used for the modulation and tuning regions. This approach improves the modulation efficiency considerably without increasing the propagation losses, or excessively restricting the wide wavelength range.

By using a impurity free quantum well intermixing process[28], WC device design can be further optimized as multiple bandgaps are possible in each section. Different components such as detectors and modulator on a chip can benefit from the optimization of the growth structure. This integration platform has shown promise in exhibiting negative chirp EAM devices[29], as well as high gain SGDBRs. The devices outlined in this paper will explore three different wavelength converter designs using the three integration platforms outlined previously. First we will look at a Quantum Well Intermixed (QWI) device that uses direct modulation, then an EA modulator based device using the Dual Quantum Well (DQW) technology, and a Mach-Zehnder modulator device using the Offset Quantum Well (OQW) technology.

III. DIRECT MODULATION

Using the direct modulation of a SGDBR gain region provides a fairly simple configuration, linear response and high conversion efficiency. Work has been done to demonstrate photocurrent-driven direct modulation based wavelength conversion using SGDBRs[21], however it is difficult to achieve a high extinction ratio and high bandwidth simultaneously. More recently we have been pursuing a design involving a bipolar cascade series connected laser into the gain section of a widely-tunable SGDBR laser. The integration scheme utilizes the centered QWI approach as mentioned earlier. The bipolar cascade concept is advantageous as it is an approach that can improve the differential quantum efficiency (DQE) of the laser as compared to conventional single stage lasers. Enhancing the DQE of the laser also improves the modulation efficiency as has been demonstrated with segmented Fabry-Perot lasers[22]. In this case an in-plane ridge laser structure is constructed in which electrically isolated segments are series connected to form a chain of diodes sharing the same optical cavity. Both proton and helium ion implantation are used to electrically isolate the stages. As a result of driving current through the diodes in series, the same current density is created with nearly 1/N (where N is the number of stages) times the current as compared to a single-stage laser. The DQE nearly scales with N. The voltage and input impedance also increase, but the latter can be tailored to meet impedance matching requirements. The performance of such a photocurrent driven monolithically integrated device relies heavily on the amount of photocurrent that can be generated on chip to directly modulate the laser and achieve sufficient

extinction ratio. It has been demonstrated that bipolar cascade lasers require significantly less modulation current than conventional single stage lasers to achieve a certain level of ER.

The design and operation of the tunable bipolar cascade SGDBR laser transmitters used in this work are described in [23]. The laser consists of a front SGDBR mirror (FM), bipolar cascade gain section, phase section (PH), rear SGDBR mirror (RM), and rear absorber (ABS) as shown in Fig. 4.

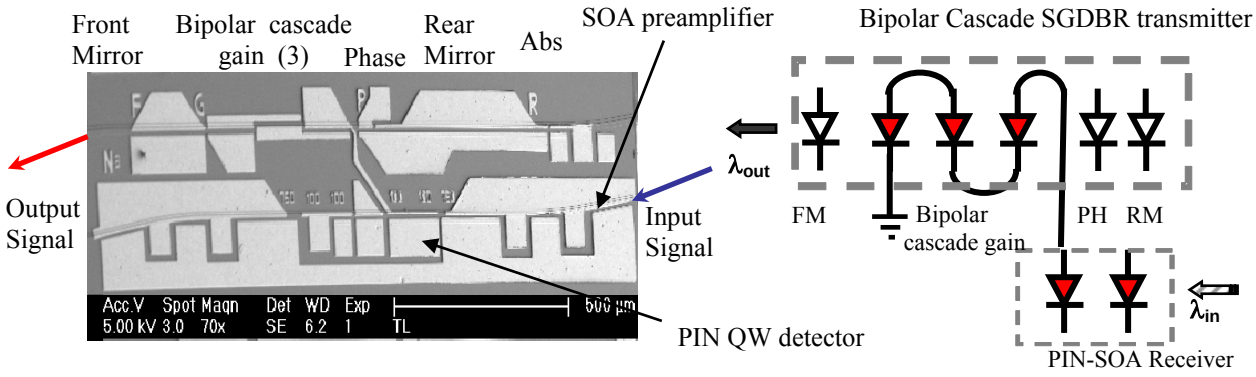

Fig. 4 SEM of Monolithic three-stage Bipolar-Cascade SGDBR Wavelength converter with circuit diagram

The integrated input optical receiver consists of a 3µm wide 750µm long SOA followed by a 200µm long PD. A metal interconnect provides a means for transferring the photocurrent from the PD to the p-metal pad of the first stage of the laser. Independent bias is provided to the laser through an off-chip bias-T to a metal pad shared by the laser and PD allowing the detector to be reverse-biased and the laser forward biased. The bias and input optical power were optimized to maximize the extinction ratio (ER) of the wavelength converted output signal. Low operating points and low input powers yielded the highest extinction ratio and subsequently the lowest power penalties.

A comparison of wavelength converted output eye diagrams are shown in Fig. 5 for devices having 1-stage, 3-stage, and 8-stage bipolar cascade gain sections in the SGDBR laser.

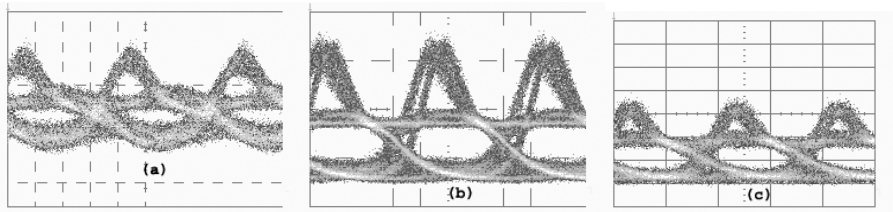

Fig. 5. 2.5 Gb/s wavelength converted output eye diagrams. Input wavelength is 1548.1 nm, and output wavelength is 1565 nm for all cases. (a) 1-stage wavelength converter with I_{ph}^{avg} = 8.2 mA, ER = 2.3 dB, (b) 3-stage wavelength converter with I_{ph}^{avg} = 8.65 mA, ER = 7.9 dB, and (c) 8-stage wavelength converter with I_{ph}^{avg} = 5.5 mA, ER = 6.5 dB.

The eye patterns are compared in terms of the amount of photocurrent generated in the PD as opposed to input optical power. For the 1-stage wavelength converter, a significant amount of optical input power is required in order to generate enough photocurrent to modulate the laser. As the devices are fabricated on a centered QWI platform, the confinement factor is fairly high and the SOAs tend to saturate at relatively low input powers. The fabrication process is however compatible with the OQW integration platform which results in a lower confinement factor. Also a high power receiver design, as will be described in the next section could be integrated to further improve performance. For the 1-stage wavelength converter with 8.2 mA of average photocurrent generated in the PD, the output signal has an extinction ratio (ER) of only 2.3 dB and exhibits a poorly opened eye. Because of the limited DQE in this conventional laser, insufficient current swing was generated to provide good ER. There is a significant amount of overshoot in the eye diagram mostly due to SOA saturation, however, some overshoot is expected due to the relaxation resonance of the

laser. With a similar amount of average photocurrent, (8.65 mA), the 3-stage device achieved 7.9 dB of ER, however there is overshoot in the eye also due to the saturation of the SOA. With lower input powers, this overshoot is suppressed somewhat, however the ER also decreases. For the 8-stage device, with 5.5 mA of average photocurrent, 6.5 dB was achieved, and the only overshoot seen in the eye pattern is due to the relaxation resonance of the laser. Although the 8-stage device can be operated at low input powers since it has the highest DQE, the ER is limited by the maximum output power of the laser which was slightly less than that for the one stage or three stage laser.

Wavelength conversion with a 2.5 Gb/s NRZ PRBS 2^{31}-1 signal was performed using an Agilent lightwave transmitter, which operates at a wavelength of 1548.1 nm. The transmitted optical pulses were then amplified with an Erbium Doped Fiber Amplifier (EDFA) and then filtered to suppress some of the amplified spontaneous emission (ASE) noise. The light was then sent through a polarization controller before being input to the on-chip receiver. The wavelength converted output signals were attenuated and then input to an Agilent lightwave receiver. Bit error rate (BER) measurements were taken with an HP 70843B bit error rate tester (BERT). BER data is shown in Fig. 6 for several converted output wavelengths. For the 3-stage wavelength converter up to 7dB of chip conversion gain is achieved. Although promising for applications within the limits of the relaxation resonance of the laser, more complex external modulation solutions show potential when there are higher bandwidth and chirp requirements. Next we will explore the receiver design used for hybrid device testing.

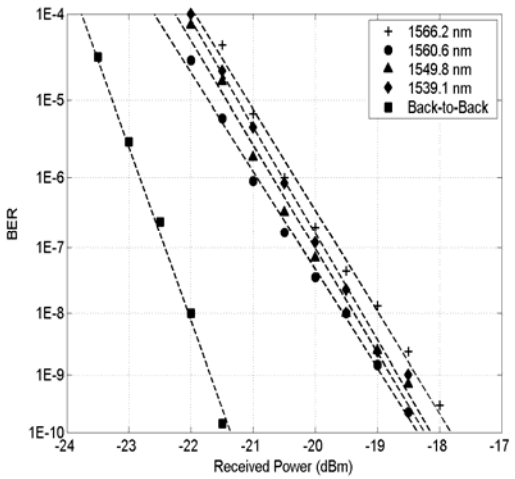

Fig. 6. BER for various converted output wavelengths for 3-stage wavelength converter. The input wavelength is 1548.1 nm.

IV. RECEIVER DESIGN

Although 2.5Gbit/s error free transmission has been demonstrated with monolithic MZ and EA modulator PD-WC devices, these designs contained either no optical pre-amplifier at all, or short amplifiers (300 μm) which provided little or no gain. This lead to high input power requirements as data rates were increased. Recent attempts to improve the WC characteristics by developing higher gain, higher saturation power SOAs using an Offset QW structure to improve the device sensitivity and noise characteristics. The challenge is to achieve maximum gain and maximum output power levels without introducing large pattern dependent effects through carrier lifetime. The receiver for the two subsequent hybrid experiments consisted of a 600μm long SOA pre-amplifier with a single electrode followed by a 50 μm long detector as illustrated in fig. 7. The pre-amplifier is composed of a 200 μm long straight (3 μm wide) section followed by a 400 μm long linearly tapered region (from 3μm to 9μm). The 50μm long detector is an offset-QW detector that was tapered down from 9μm to 6μm and nominally reverse-biased to -4.5V.

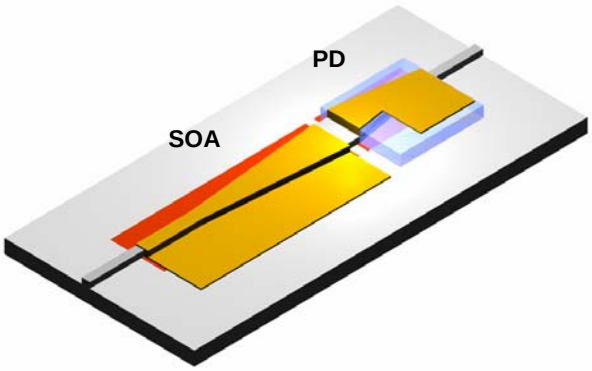

Fig. 7 Receiver with Flared SOA and PIN detector

As an optical input signal is fed into the receiver, photocurrent is generated resulting in a voltage swing applied to the transmitter. This voltage swing was measured at 10Gbit/s across 50ohms as a function of the coupled input power. Due to the bias T's used in the hybrid scheme, approximately 2dB of electrical loss at 10GHz was present. A peak-to-peak voltage swing of greater than 2.5 V can be seen in fig. 8a with waveguide powers up to 3 dBm. Also, small-signal gain curves are shown in fig. 8b.

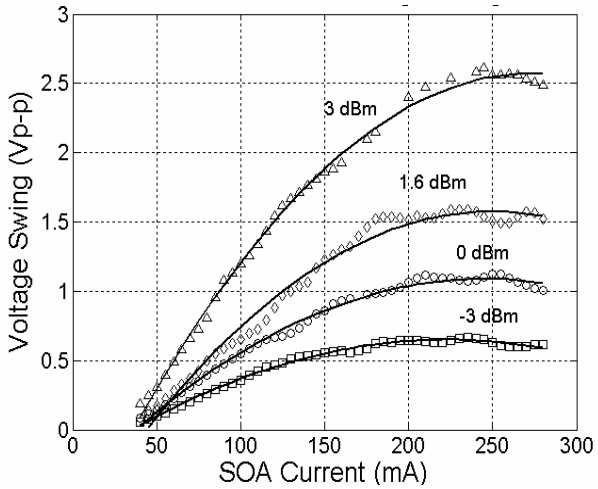

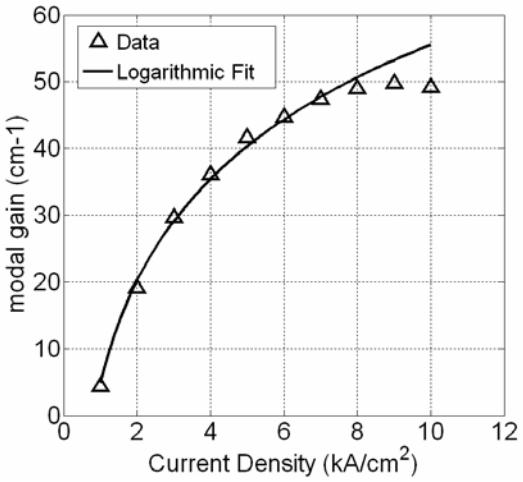

Fig. 8a Voltage swing vs. SOA current and input optical power at 1548nm
Fig. 8b Small-signal optical gain vs current density for OQW gain material at 1548nm

This added gain improves the operation sensitivity of a photocurrent driven wavelength converter significantly as compared with previous work allowing successful operation with only 1.3mW coupled input power. The last two wavelength converters have been connected in a co-packaged hybrid configuration to explore the added performance of using flared SOA and detector regions. Although not monolithically integrated at this time, the growth and processing steps are 100% compatible for both the transmitter and receiver.

V. ELECTROABSORPTION BASED DEVICES

Electro-absorption modulator based PD-WCs have been fabricated and tested utilizing each of the three above mentioned integration platforms. In the standard tunable laser OQW integration platform, bulk InGaAsP Franz-Keldysh waveguide modulators are fabricated very simply since the EAM material structure can be the same as the mirror sections and phase section of the laser. However, since it is advantageous for the laser to have low loss waveguides, the waveguide bandgap is large (InGaAsP Bandgap wavelength = 1.4 μm) relative to the laser operating wavelengths. As a result, this approach suffers from a lack of modulation efficiency, positive chirp, and in general, requires high DC bias voltages.

However, as a proof of concept for a fully monolithic EAM based PD-WC, a single chip, Franz-Keldysh based device was fabricated and tested. Results from this device showed greater than 10 dB optical extinction ratio with 12.6dBm of input fiber power required at 2.5 Gb/s. BER measurements at this data rate showed less than 2.5 dB power penalties over 40 nm of operation [27]. Unfortunately, due to high waveguide doping levels (Nd = 2e17 cm-3), and a high waveguide bandgap energy (λ_b 1.4 um), the Franz-Keldysh based devices did not prove to scale well to higher data rates. It is possible to lower the waveguide bandgap energy and reduce waveguide doping in order to increase modulation efficiency and reduce device junction capacitance. However, this leads to higher propagation loss discussed previously and inherently lower peak fields overlapping the optical mode, resulting in modulation efficiencies that are not significantly improved over high bandgap energy devices.

In an effort to achieve data rate scaling and maintain the critical functions of the single chip PD-WC, a second, new base structure was designed that incorporates quantum wells as an absorption mechanism instead of the bulk Franz-Keldysh effect. A schematic of the new dual quantum well base structure is shown in fig. 9 with specific details summarized in table 2.

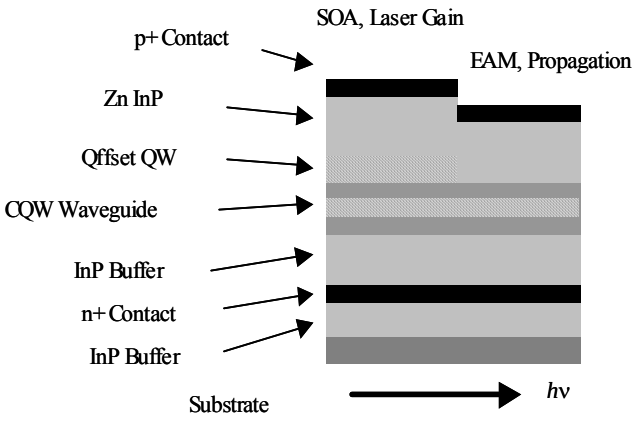

Fig. 9 Schematic of Dual QW Materials Platform

Table. 2 Dual Quantum Well and Franz Keldysh epitaxial growth structure

	Dual QW		**Franz Keldysh**	
Layer	**Doping**	**Thickness**	**Doping**	**Thickness**
p-InGaAs	1e19 cm^{-3} Zn	100nm	1e19 cm^{-3} Zn	100nm
Zn InP	1e18 cm^{-3} Zn	2μm	1e18 cm^{-3} Zn	2μm
Offset QW	Uid	106.5nm	Uid	106.5nm
Waveguide	5e161e19 cm^{-3} Zn	126nm	5e161e19 cm^{-3} Zn	187.5nm
Centered MQW	Uid	93nm	Uid	0nm
Waveguide	5e16 cm^{-3} Zn	126nm	5e16 cm^{-3} Zn	187.5nm
InP Buffer	1e18 cm^{-3} Zn	1.8μm	1e18 cm^{-3} Zn	1.8μm
N InGaAs	1e18 cm^{-3} Zn	100nm	1e18 cm^{-3} Zn	100nm
InP buffer	1e18 cm^{-3} Zn	0.5μm	1e18 cm^{-3} Zn	0.5μm
Substrate	Fe Semi-insulating	100μm	Fe Semi-insulating	100μm

The base structure is almost identical to the standard Franz-Keldysh(FK) structure, except for a multi-quantum well region centered in the optical waveguide layer. The centered QW stack contains 7 x 9nm compressively strained (0.33 %) wells and 6 x 5nm tensile strained (0.075 %) barriers and has a photoluminescence peak at 1485 nm. With the proper design of the CQW stack, it is possible to achieve low propagation loss, high modulation efficiency and broad optical modulation bandwidths. In addition, by utilizing shallow QW for the CQW stack, devices can operate under high waveguide optical power levels (>30 mW) without degradation of optical bandwidth and introduction of pattern dependent effects. It is also very important that the tuning characteristics of the SGDBR is also improved slightly, that the injection efficiency for the offset quantum well stack is not affected, and that optical amplifiers still maintain good

performance with the inclusion of the quantum wells in the waveguide. Pulsed measurements have been performed and show an injection efficiency of 69 % and propagation loss as low as 6 cm-1.

For fabrication of integrated components in the Dual QW base structure, the same offset QW removal techniques used in the standard FK device process have been incorporated. This approach enables high gain, OQWs described previously for use as a gain medium in the laser and in the amplifiers, and centered EAM QWs in the waveguide and EAM regions for modulation efficiency. Using this approach, processing for PD-WC devices using the new dual QW integration platform has been completed and devices have been tested. DC extinction curves and slope efficiency (dT(dB)/dV) from a 400 μm long dual QW EAM integrated with an SGDBR tunable laser is shown in fig. 10. For comparison, a dT/dV curve for a 400 μm long FK EAM ($\lambda_{InGaAsP}$ = 1.4 μm) device at 1550 nm is also included. Significant improvements in slope efficiencies for the dual quantum well stack base structure EAMs can be seen over FK devices.

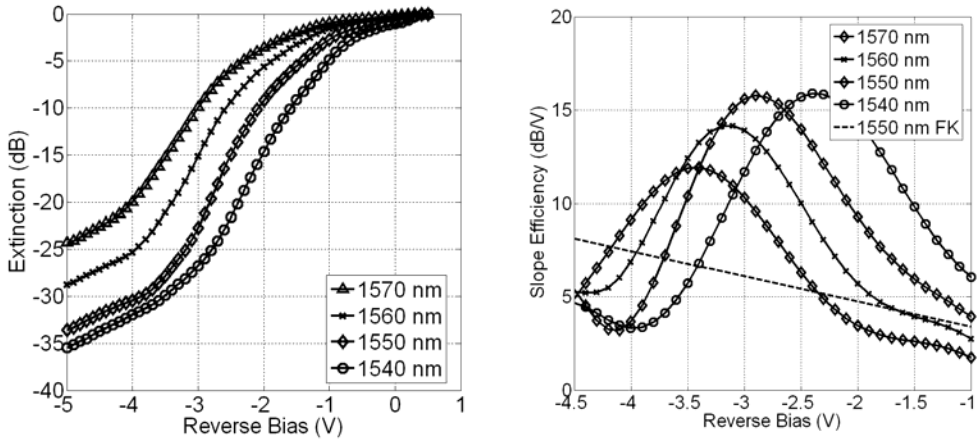

Fig. 10a DC Extinction Curves for 400 μm dual QW EAM from 1540 nm to 1570 nm.
Fig. 10b Slope Efficiencies (dT(dB)/dV) for dual QW EAM from 1540 to 1570 nm with Franz Keldysh Data for reference.

As a further comparison, bandwidth as a function of EAM length for both Franz Keldysh based materials platform and Dual QW platform has been examined and results can be seen in fig. 11. Due to the reduced doping (5e16 cm-3 Si) in the waveguide region of the Dual QW base structure, there is a significant bandwidth increase over Franz Keldysh devices.

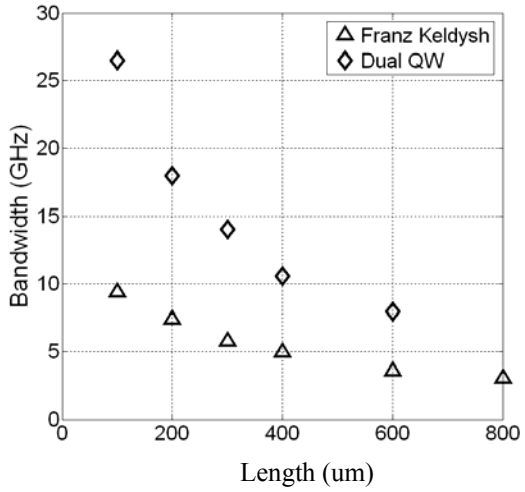

Fig. 11 Bandwidth vs. Length(um) for both Franz Keldysh and Dual QW materials platforms using 50 ohm termination

For the full PD-WC devices using the dual QW base structure, unfortunately, fabricated device designs did not incorporate the high efficiency receivers that have been mentioned earlier in this paper. As a proof of concept for the integration platform, a transmitter consisting of a standard four section SGDBR laser monolithically integrated with a 300-μm-long input SOA and 400μm EAM has been connected in a hybrid arrangement with the OQW receiver described in section IV. The EAM and the photodetector were individually high speed probed with a parallel 50-Ω termination on the photodetector. The two devices were interconnected with a high-speed RF cable and individual Bias-T's. A schematic is shown in fig. 12. Though currently the receiver and transmitter are not monolithically integrated, the low propagation loss of the dual QW base structure, and the fact that the both sections have identical InP regrowth and fabrication steps, shows that the dual quantum well base structure should be well suited for single chip wavelength converter fabrication. A picture of the fabricated hybrid PD-WC is included below

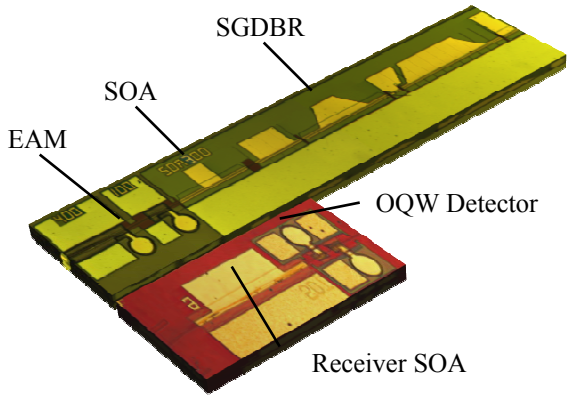

Fig 12 Hybrid EAM- Receiver PD-WC

High speed measurements have been made on this hybrid device. Bandwidth measurements and BER curves have been generated for the EA based wavelength converter device. In these experiments, the laser gain section, pre-amplifier SOA, and transmitter SOA are biased at 160 mA, 250 mA, and 120 mA respectively and the device was maintained at 16^0C with a thermoelectric cooler. For the receiver section the pre-amplifier was biased to 250 mA and the photodetector was biased to -4.5 V for maximum efficiency.
Results from optical bandwidth measurements for a 50 Ω terminated discrete EA modulator, photodetector and integrated wavelength converter have been measured. Results show S_{21} of ~10 GHz, ~20 GHz, and ~7 GHz respectively. Bit-Error-Rate (BER) curves with eye diagrams were generated from a nonreturn-to-zero $2^7 - 1$ pseudorandom bit stream at 10 Gb/s from a 10 Gb/s BER tester transmitter (Agilent 83433A) operating at a wavelength of 1548.1 nm. In the experiment, this signal was input into a high power Erbium Doped Fiber Amplifier (EDFA) followed by a polarization controller and an optical filter and transmitted to the device under test using a conically tipped lensed fiber. Approximately 4.9 mW of input optical fiber power was used and the extinction ratio of the signal into the on-chip pre-amplifier was 14 dB. Input and output coupling losses are estimated to be 5 dB and 3 dB respectively. The output optical signal of the WC was then input into a variable optical attenuator before entering the PIN Receiver. Note that no optical output filtering or amplification was required. Error-free operation has been achieved with a power penalty of less than 2.5 dB at 10 Gb/s. Results for Extinction Ratio and output power over wavelength as well as BER curves are shown in fig. 13 below.

PD-WC based on EAM technology have been fabricated and tested with both Franz Keldysh and dual QW materials platforms. With the introduction of the QW stack in the center of the waveguide, it has been shown that an improvement in the bandwidth efficiency product is possible for the EAMs while maintaining high injection efficiency and low propagation losses in the laser section. We have demonstrated wavelength conversion over 30 nm at 10 Gb/s with 10 dB optical extinction and less than 2.5 dB power penalty.

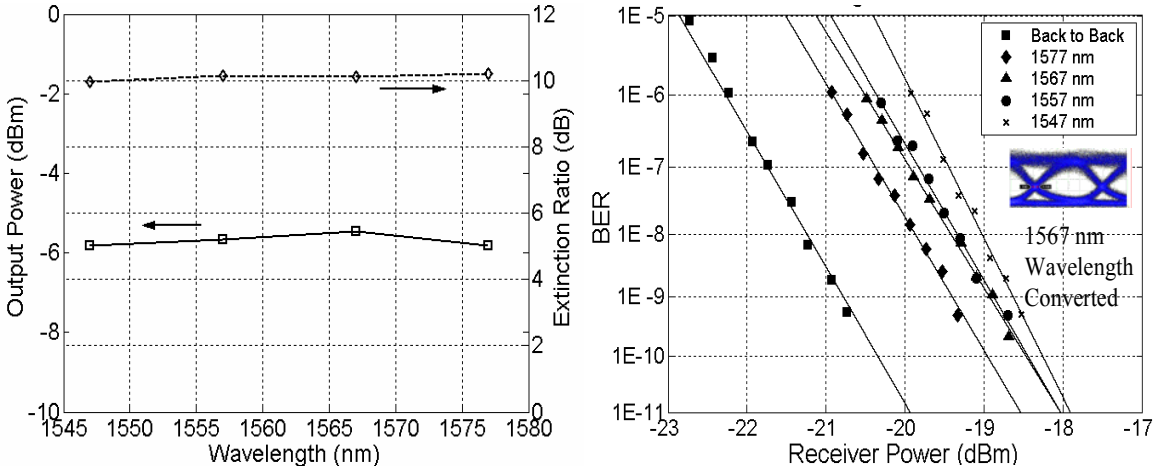

Fig 13. Extinction Ratio and average output power (left) and 10 Gb/s BER curves for 50 Ω terminated EAM based wavelength converter (right). Input wavelength is 1548.1 nm with waveguide power level of 1.7 mW. Converted wavelength is indicated

Wavelength conversion required less than 5 mW (+6.8 dBm) of input fiber power and less than 2 mW (+2.3 dBm) of waveguide input power. If coupling is neglected, overall device efficiency is estimated at approximately -5 dB with integrated high power receivers and centered QW layer stack. This is a significant improvement over previously reported results for EA modulator based widely tunable wavelength converters.

VI. MACH-ZEHDNER BASED DEVICES

Two types of Mach-Zehnder based photocurrent-driven wavelength converters have been demonstrated recently. The first configuration used photocurrent generated in a high saturation power passive region photodiode to drive a single side of a Mach-Zehnder – SOA-SGDBR laser transmitter[24]. Due to the parallel connection of diodes, the optical bandwidth of the device can be limited particularly without traveling-wave electrodes. Also, as with an EA modulator, photocurrent competition between the photodiode and the induced electro-absorption in the modulator will effectively diminish the drive voltage. This means that either the input light intensity must be much larger than the output, the bias on the detector needs to be significantly larger than the modulator requiring a capacitor between them (as shown in Fig. 14b, or the materials need to be sufficiently different in the two subcomponents (detector and modulator) in order to have good performance. One way to get around these limitations is to use a SOA-PIN receiver (as described previously) to drive a series push-pull (SPP) modulator as shown in fig. 14a&b.

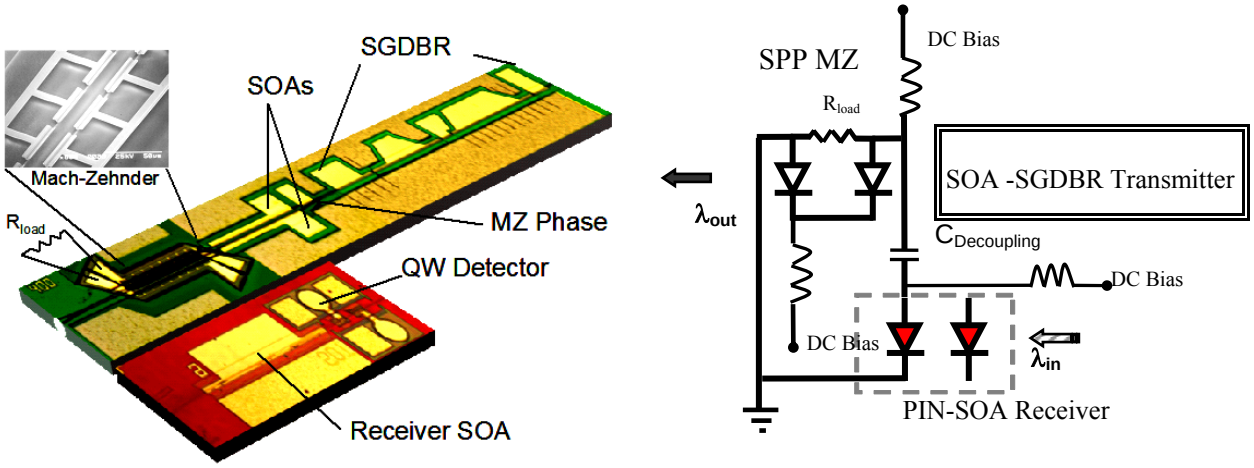

Fig. 14a Hybrid SPP-MZ-SOA-SGDBR transmitter receiver Layout
Fig. 14b Series Push-pull (SPP) MZ photocurrent-driven wavelength converter configuration

A tunable transmitter using a 400μm long series push-pull driven Mach-Zehnder modulator electrode structure was fabricated using the OQW structure mentioned earlier. The total footprint of the chips is less than 1mm x 3.8mm. The bias configuration is shown in fig. 14b and uses a load resistor termination at the end of the electrode as shown in fig 14a. The detector and the front end of the modulator were both probed with separate bias Ts. This allows the Mach-Zehnder modulator to operate at low bias (-0.5V), favoring reduced insertion losses and the detector to be reverse-biased higher (-4.5V) for improved efficiency.

The use of a Mach-Zehnder modulator reduces the photocurrent competition as less light is absorbed when compared with a EA modulator since the light is split into two branches, and typically bulk quaternary waveguide material that is far from the operating wavelength is used(1.4μm bandgap wavelength) resulting in less absorption for a given reverse bias. As can be seen in fig.14b, a decoupling capacitor is used to maintain different DC biases on the detector and modulator sections. This can be implemented on either the p-side (as shown in fig 14b.) or on the n-side contact of the diode. This allows a large bias to be applied on the detector to maintain high speed and high photocurrent, and a lower bias on the MZ branches to reduce the insertion losses of the output modulated signal. Each DC bias has a RF blocking inductor connection.

Most types of wavelength converters induce chirp in the output wavelength. At high bit rates the dispersion in optical fibers will reduce the reach that is possible for a sub-optimal chirp parameter. A standard SOA based All-optical Mach-Zehnder interferometer uses mostly cross-phase modulation in one branch of the modulator to produce negative chirp in the non-inverting operation and positive chirp in the inverting operation. A tunable photocurrent-driven wavelength converter using a single-side drive Mach-Zehnder modulator will provide negative chirp with inverting operation and positive chirp with non-inverting operation[24]. Despite some additional bias circuitry, by using a series push-pull configuration Mach-Zehnder modulator, zero chirp may be achieved in both non-inverting and inverting operation. Also with this device configuration, the device may be biased so that no DC current will flow through the termination resistor. This structure can improve the bandwidth of the modulator by roughly a factor of two compared with a single-side drive configuration[26]. Additionally, by using a push-pull scheme – only one branch of the MZ experiences photocurrent competition. Capitalizing on the nonlinear MZ response, with sufficient output power swing one can achieve regeneration of the signal at the output.

VII. SPP-MZ WAVELENGTH CONVERSION RESULTS

The small-signal optical-to-optical bandwidth (S_{21}) was measured for the wavelength converter with an input signal at 1548nm and converted signal at 1555nm for various biases on each branch of the Mach-Zehnder modulator. The 50ohm terminated 3dB bandwidth corresponding to the modulator and detector independently were ~30GHz and ~20GHz respectively. The optical-to-optical wavelength converter bandwidth is given in fig. 15. As can be seen in fig. 15, an optical bandwidth suitable for 10Gbit/s operation is obtained with a 50ohm termination on the detector and modulator. Modest voltage dependence of the bandwidth is due to the depletion of the PN junction in the waveguide of the MZ structure. The fiber-to-fiber insertion loss of the device is approximately 10dB, however, is only 0dB without input and output fiber coupling loss.

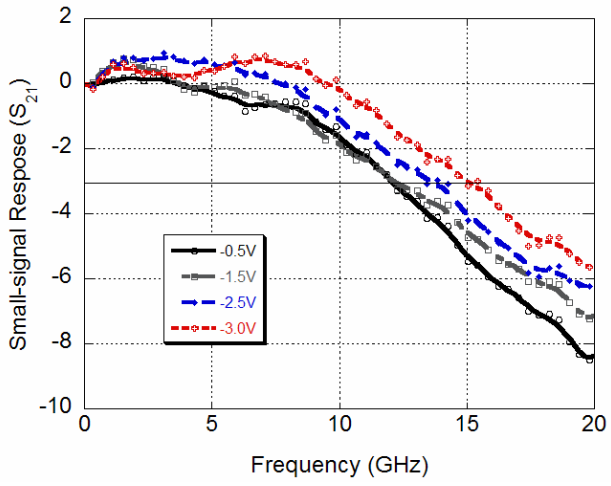

Fig 15. Optical-to optical small-signal response of WC with 50ohm termination. Detector biased at -4.5, MZ bias varied as shown in figure with the same bias on each branch.

Transmission though the wavelength converter was measured for NRZ 2^7-1 PRBS 10Gbit/s data generated at an input wavelength of 1548.1nm using a 12 Gbit/s BERT and Agilent 83433A transmitter. An EFDA was used to boost the power to 8dBm fiber power, in which the signal was optically filtered and the polarization controlled to achieve 1.3mW of coupled optical power in the receiver waveguide. The converted signal from the integrated transmitter at λ_2 was measured using an Agilent 11982A receiver without preamplification. Typical back-to-back bit error rate (BER) measurements are shown in fig. 16.

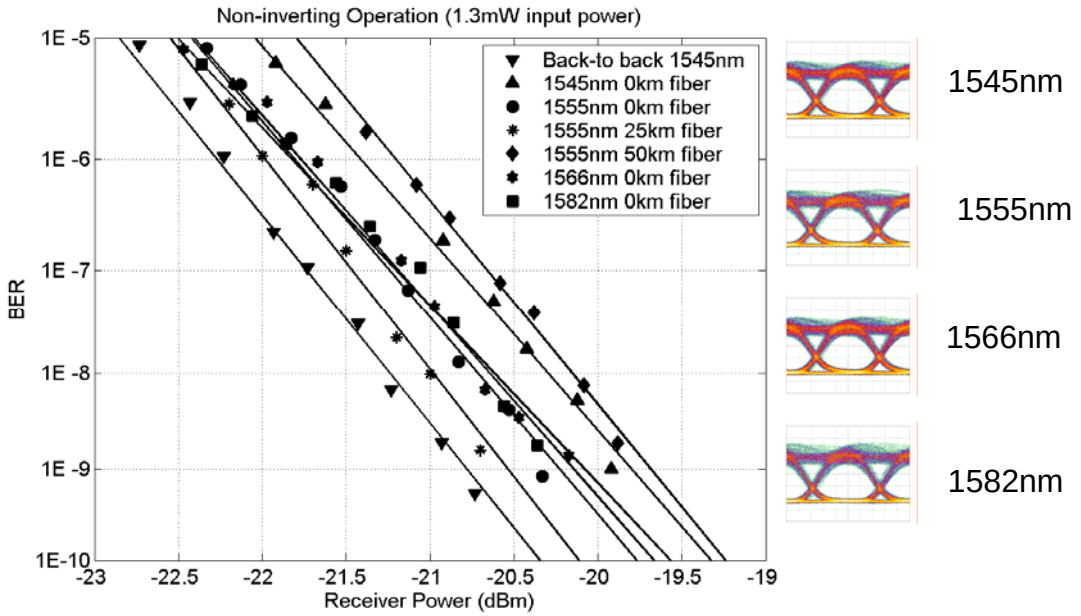

Fig. 16 BER at 10Gbit/s NRZ 2^7-1 PRBS for multiple wavelengths back-to-back and through 25km and 50km of Corning SMF-28 fiber.

Error-free wavelength conversion was achieved over a wide range (37nm output) with less than 1dB power penalty. Transmission through Corning SMF-28 fiber was also measured for 25km and 50km distances at 1555nm yielding <1.2dB power penalty as shown in fig. 16.

VIII. CONCLUSION

Our objective was met by demonstrating three tunable laser integrated wavelength converters using three different integration platforms. Externally modulated hybrid EA and MZ devices can achieve 10Gbit/s operation with over 10dB of RF extinction. The use of high-gain, high saturation power receivers coupled with high bandwidth efficient modulators have been shown to allow the realization of viable wavelength conversion at high bit rates. Dual QW integrated EAM PD-WCs have demonstrated wavelength conversion over 30 nm at 10 Gb/s with 10 dB optical extinction and less than 2.5 dB power penalty. Series push-pull MZ PD-WCs have demonstrated error-free wavelength conversion over 37nm with <1dB power penalty, and low input power (1.3mW). Both transmitter and receiver chips utilize the same epitaxial platform and processing steps leading to simple integration in the future.

IX. ACKNOWLEDGMENTS

This work was supported by Intel Corporation grant # TXA001630000 and DARPA MTO – CS-WDM grant #N66001-02-C-8026. We acknowledge Agility Communications for the growth of some of the material, and all the AR coating of the devices.

X. REFERENCES

1. Yoo S.J.B., "Wavelength Conversion Technologies for WDM Network Applications", IEEE J. Lightwave Technology, 14, 944-966 (1996).
2. Stubkjaer KE, Kloch A, Bukhave Hansen P, Poulsen HN, Wolfson D, Stockholm Jepsen K, Clausen AT, Limal E, Buxens A. "Wavelength converter technology." *IEICE Transactions on Electronics, vol.E82-C, no.2, Feb. 1999, pp.338-48. Publisher: Inst. Electron. Inf. & Commun. Eng, Japan.*
3. Yates Jennifer M., Michael P Rumsewicz, Jonathan P.R. Lacey, "Wavelength converters in dynamically reconfigurable WDM networks" IEEE Communications Surveys Second Quarter 1999.
4. Nesset D, Kelly T, Marcenac D. All-optical wavelength conversion using SOA nonlinearities. *IEEE Communications Magazine, vol.36, no.12, Dec. 1998, pp.56-61.*
5. Geraghty David F., Robert B. Lee, Marc Verdiell, Mehrdad Ziari, Atul Mathur, and Kerry J. Vahala,"Wavelength Conversion for WDM Communication Systems Using Four-Wave Mixing in Semiconductor Optical Amplifiers", IEEE Journal of Selected Topics in Quantum Electronics, Vol. 3, No. 5, Oct. 1997
6. C. Q. Xu, H. Okayama, and M. Kawahara, "1.5 pin band efficient broadband wavelength conversion by difference frequency generation in a periodically domain-inverted LiNbOs channel waveguide," ***Appl.*** *Phy. Lett,* vol. 63, p. 3559, 1993.
7. Cao, X.D. Jiang, M. Dasika, P. Islam, M.N. Evans, A.F. Hawk, R.M. Nolan, D.A. Pastel, D.A. Weidman, D.L. Moodie, D.G., "All-optical 40 GHz demultiplexing in a NOLM with sub-pJ switching energy" 1997. CLEO '97., Vol. 11, pp. 446-447, 18-23 May 1997.
8. Wolfson D, Hansen PB, Kloch A, Fjelde T, Janz C, Coquelin A, Guillemot I, Garorit F, Poingt F, Renaud M. All-optical 2R regeneration at 40 Gbit/s in an SOA-based Mach-Zehnder interferometer. *OFC/IOOC'99. Optical Fiber Communication Conference and the International Conference on Integrated Optics and Optical Fiber Communications (Cat. No.99CH36322). IEEE. Part Suppl., 1999, pp.PD36/1-3 Suppl.. Piscataway, NJ, USA.*
9. Spiekman LH, Koren U, Chien MD, Miller BI, Wiesenfeld JM, Perino JS. All-optical Mach-Zehnder wavelength converter with monolithically integrated DFB probe source. *IEEE Photonics Technology Letters, vol.9, no.10, Oct. 1997, pp.1349-51.*
10. Suzuki Y, Ito T, Shibata Y. "Monolithically integrated wavelength converter: Sagnac interferometer integrated with parallel-amplifier structure (SIPAS) and its application." 2002 LEOS Summer Topical Meetings IEEE.2002, ppWB2-12.
11. Wolfson D, Fjelde T, Kloch A, Janz C, Poingt F, Pommereau F, Guillemot I, Gaborit F, Renaud M. Detailed experimental investigation of all-active dual-order mode Mach-Zehnder wavelength converter. Electronics Letters, vol.36, no.15, 20 July 2000, pp.1296-7.
12. Leuthold J., C.H. Joyner, B. Mikkelsen, G. Raybon, J.L.Pleumeekers, B.I. Miller, K. Dreyer and C.A. Burrus 100Gbit/s all-optical wavelength conversion with integrated SOA delayed-interference configuration, Elect. Letts. Vol. 33, pp. 2137 (1997).
13. Demir HV, Sabnis VA, Jun-Fei Zheng, Fidaner O, Harris JS Jr, Miller DAB. "Scalable wavelength-converting crossbar switches." *IEEE Photonics Technology Letters, vol.16, no.10, Oct. 2004, pp.2305-7. IEEE.*
14. Kodama S, Yoshimatsu T, Ito H. 320 Gbit/s error-free demultiplexing using ultrafast optical gate monolithically integrating a photodiode and electroabsorption modulator. Electronics Letters, vol.39, no.17, 21 Aug. 2003, pp.1269-70. Publisher: IEE, UK.
15. Hsu-Feng Chou, Yi-Jen Chiu, Adrian Keating, John E. Bowers, and Daniel J. Blumenthal, "Photocurrent-AssistedWavelength (PAW) Conversion With Electrical Monitoring Capability Using a Traveling-Wave Electroabsorption Modulator", IEEE. Photonics Technology Letters, Vol. 16, No. 2, February 2004.

16. Olsson B-E, Ohlen P, Rau L, Blumenthal DJ. A simple and robust 40-Gb/s wavelength converter using fiber cross-phase modulation and optical filtering. IEEE Photonics Technology Letters, vol.12, no.7, July 2000, pp.846-8.
17. Yasaka H, Sanjoh H, Ishii H, Yoshikuni Y, Oe K. Finely tunable wavelength conversion of high bit-rate signals by using a superstructure-grating distributed Bragg reflector laser. *Journal of Lightwave Technology, vol.15, no.2, Feb. 1997, pp.334-41. IEEE.*
18. Lavrova OA, Rau L, Blumenthal DJ. "10-Gb/s agile wavelength conversion with nanosecond tuning times using a multisection widely tunable laser." *Journal of Lightwave Technology, vol.20, no.4, April 2002, pp.712-17 .IEEE.*
19. Broeke RG, Smit MK. "A wavelength converter with integrated tunable laser." *Integrated Photonics Research (Trends in Optics and Photonics Series Vol.91). Optical Soc. of America. 2003, pp.15-17. Washington, DC.*
20. Mašanovic M.L., V. Lal, J.S. Barton, E. J. Skogen, L. A. Coldren, D. J. Blumenthal "Monolithically Integrated Mach-Zehnder Interferometer Wavelength Converter and Widely-Tunable Laser in InP." IEEE Photonics Technology Letters, Aug. 2003.
21. Hutchinson J.M., J. Zheng, J.S. Barton, J.A. Henness, M.L. Mašanovic, M.N. Sysak, L.A. Johansson, D.J. Blumenthal, L.A. Coldren, H.V.Demir, V.A. Sabnis, O. Fidaner, J.S. Harris, and D.A.B. Miller, "Indium Phosphide-Based Optoelectronic Wavelength Conversion for High-Speed Optical networks"
22. Getty J.T., L.A. Johansson, E.J. Skogen, L.A. Coldren, "1.55μm bipolar cascade segmented ridge lasers," *IEEE J. Select. Topics in Quantum Electron.,* vol. 9, pp. 1138-1145, Sept.-Oct. 2003.
23. Klamkin J., L. A. Johansson, J. T. Getty, J. M. Hutchinson, E. J. Skogen and L. A. Coldren, "Photocurrent Driven Widely-Tunable Wavelength Converter based on a Directly Modulated Bipolar Cascade SGDBR Laser ", LEOS 2004.
24. Barton J.S., Masanovic ML, Sysak MN, Hutchinson JM, Skogen EJ, Blumenthal DJ, Coldren LA. 2.5-Gb/s error-free wavelength conversion using a monolithically integrated widely tunable SGDBR-SOA-MZ transmitter and integrated photodetector. *IEEE Photon Tech. Letts, vol.16, no.6, June 2004, pp1531-3*
25. Barton, J.S. Coldren, L.A. "Lumped electrode Series Push-Pull modulated Mach-Zehnder integrated widely-tunable transmitter" Submitted to Journal of Lightwave Technology Sept, 2004
26. Walker RG. "High-speed III-V semiconductor intensity modulators." IEEE Journal of Quantum Electronics, vol.27, no.3, March 1991, pp.654-67.
27. Sysak MN, Barton JS, Johansson LA, Raring JW, Skogen EJ, M. L. Mašanović, Blumenthal DJ, Coldren LA. "Single-chip wavelength conversion using a photocurrent-driven EAM integrated with a widely tunable sampled-grating DBR laser." *IEEE Photonics Technology Letters, vol.16, no.9, Sept. 2004, pp.2093-5.*
28. Skogen E.J. *et al.,* "A quantum-well intermixing process for wavelength-agile photonic integrated circuits," *IEEE J. Select. Topics in Quantum Electron.,* vol. 8, pp. 863-869, July-Aug. 2002.
29. Raring J.W., E. J. Skogen, L. A. Johansson, M. N. Sysak, J. S. Barton, M. L. Mašanović, L. A. Coldren "Demonstration of Widely-Tunable Single-Chip 10 Gb/s Laser-Modulators Using Multiple-Bandgap InGaAsP Quantum-Well Intermixing, Photonics Technology Letts. July 2003.
30. Tauke-Pedretti, Anna, M. M. Dummer, J. S. Barton, M.N. Sysak, J. Raring, and L.A.Coldren," Integrated Photoreceivers with High Saturation Power, High Gain and >20GHz Bandwidth", Submitted to Photonics Tech. Letts. Sept 2004.
31. Simes R. J., G. A. Fish, P. Abraham, Y. A. Akulova, C. W. Coldren, M. Focht, E. M. Hall, M. C. Larson, H. Marchand, P. Kozodoy, A. Dahl, P. C. Koh, and T. Strand "InP chip scale integration platform for high-performance tunable lasers" Proceedings of SPIE, December 2003, pp. 80-94.

Widely-Tunable All-Optical Wavelength Converter Monolithically Integrated with a Total Internal Reflection Corner Mirror Delay Line for 40Gbps RZ Operation

Joseph A. Summers, Vikrant Lal, Milan L. Mašanović,
Nadir Dagli, Larry A. Coldren, Daniel J. Blumenthal
Department of Electrical and Computer Engineering, University of California, Santa Barbara, CA 93106-9560, USA
jsummers@ece.ucsb.edu

Abstract: This paper reports on a novel widely tunable all-optical wavelength converter monolithically integrated with a compact turning mirror delay for differential operation at 40Gbps RZ. Wavelength conversion is achieved over 25nm of device tuning range.

OCIS Codes: (250.5300) Photonic integrated circuits; (230.4040) Mirrors

1. Introduction

Research in photonic integrated circuits (PICs) has been driven by the desire to reproduce and improve the functions of discretely packaged components while reducing their size and cost through monolithic integration. For next generation optical WDM networks, wavelength converters (WCs) are expected to play a significant role by enabling wavelength routing, add/drop multiplexing, and optical switching functions. Several schemes for monolithically integrated wavelength converters in InP have been demonstrated, and among them the Mach-Zehnder interferometer SOA (MZI-SOA) configuration has drawn strong interest due to its fast speed and 2R regeneration [1].

Widely tunable MZI-SOA wavelength converters have been demonstrated for NRZ data rates up to 10Gbps, with the speed of operation limited by the gain recovery lifetime of the SOAs [2]. Faster data rates have been achieved in integrated MZI-SOA WCs for RZ data using a differential time-delay scheme that takes advantage of the fast stimulated carrier lifetime to produce both the rising and falling edges of the converted signal [3-5]. To fully exploit the benefits of this approach, further monolithic integration of a MZI-SOA WC with a widely tunable laser and a time delay for differential operation would improve the stability and simplify the operation, while reducing the coupling losses and making the device practical for real network deployment.

This paper describes a novel design of a widely tunable MZI-SOA all-optical wavelength converter, where the differential on-chip delay has been implemented using TIR corner mirrors. The device has been fabricated using our standard offset quantum well (OQW) integration platform [2,3], with a simple modification to the standard fabrication process used in the past. Wavelength conversion performance of the new wavelength converter at 40 Gbps is described.

2. Design and Fabrication

The wavelength converter described in this paper consists of a widely tunable sampled grating distributed Bragg reflector (SGDBR) laser monolithically integrated with a SOA-based MZI, and a compact on-chip waveguide delay line implemented using deeply-etched TIR corner mirrors (Fig. 1).

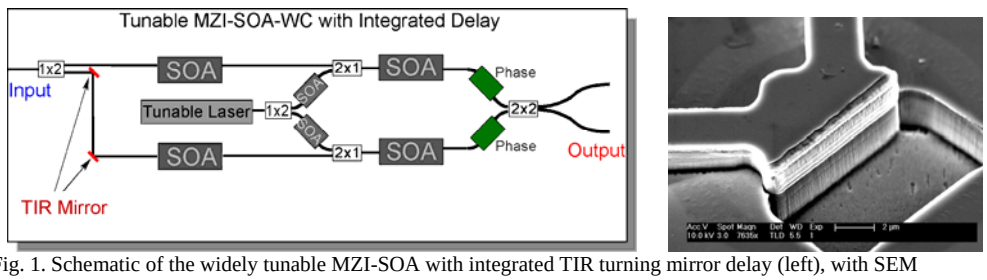

Fig. 1. Schematic of the widely tunable MZI-SOA with integrated TIR turning mirror delay (left), with SEM micrograph of a TIR corner mirror (right).

The device has a single optical input, which is split equally between two arms (top and bottom) using a 1x2 multimode interference (MMI) optical splitter. Each arm has an input SOA for amplification and power balancing, followed by a 2x1 MMI optical combiner to combine with the SGDBR signal before going into a corresponding arm of the MZI. Each MZI arm consists of an SOA operated at high current density for fast cross phase modulation (XPM), and a phase electrode to optimize extinction between the arms. The signals from the two MZI arms are then combined by a 2x2 MMI at the output.

Differential operation of the MZI requires that the input signal in one arm be time-delayed with respect to the other. To make this delay compact, and without increasing the length of the device, deeply etched TIR corner mirrors are used to sharply redirect the light in the bottom arm through an additional section of waveguide. The length of this delay section is designed to be approximately one half of the desired converted pulse width, which for this design was chosen to be 500um (approx. 6ps of delay in InP).

The device was fabricated using an offset quantum well integration platform [2,3]. TIR corner mirrors were integrated into the platform using a self-aligned process to ensure proper placement of the mirror surface with respect to the input and output waveguides [6]. This self-aligned process involves the overlap of two etch masks: one mask to define the waveguide ridge and mirror surface, and the other mask to open up a window over the ridge for deep etching of the mirror. For this device, the ridge mask is first defined in $Si0_2$, which is followed by evaporation and lift-off of SrF_2 to open up a window overlapping the ridge-defined mirror surface. Next, the exposed region is deeply etched past the waveguide layer with RIE to define the TIR corner mirror surface. The SrF_2 is then removed in diluted HCl, leaving the SiO_2 mask to define the ridge. The ridge etch is completed next with RIE, and the SiO_2 mask is removed using HF. The TIR corner mirror process is shown in Fig. 2.

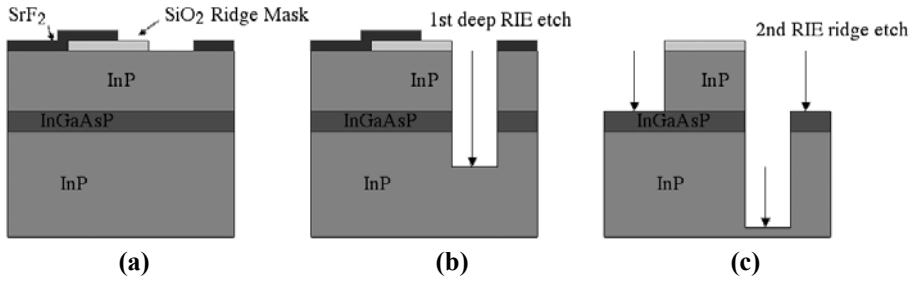

Fig. 2. Schematic of process used for TIR corner mirrors. (a) SrF_2 opens up a window overlapping the SiO_2 for deep etching, (b) Mirror surface is deeply etched past InGaAsP waveguide layer, (c) SrF_2 is removed and ridge is etched.

3. Results

For testing, the devices were soldered onto a copper bar, which was kept at 16° C using a thermo-electric cooler. The device electrodes were probed using DC needle probes, and light was coupled into and out of the device using lensed fibers mounted on piezo-controlled translational stages.

The input signal was produced with a pulsed ring laser operating at 1557nm, which provided output pulses of 2ps FWHM at 10GHz repetition. Data was encoded onto the pulses using a 10Gbps pattern generator and an electro-optic modulator, and then optically multiplexed to 40Gbps before being amplified and coupled to the input waveguide of the device.

The input SOAs in the two arms of the device were operated at different currents to compensate for the delay line loss and to balance the optical power going into the MZI. The extra loss from the delay line was measured to be 2.6dB, which includes the loss from the two TIR corner mirrors and 500um of additional waveguide. The MZI SOAs were operated at equal currents to balance the rise and fall of the converted signal from the differential input, and the MZI phase electrode was biased to maximize extinction of the SGDBR signal with the input signal in the “off” state.

The time delay of the 500um waveguide difference was measured to be 6ps by observing the amplified input signal through each arm, while leaving the other arm unbiased to absorb the light. The two signals, measured with a 50Gbps optical head on a digital communications analyzer, are superimposed for comparison in Fig. 3.

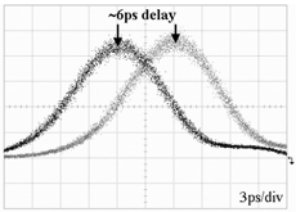

Fig. 3. Observation of the integrated time delay, by capturing the input signal at the device output from each arm with the other arm turned off.

Wavelength conversion was performed at 40Gbps RZ over an output tuning range of greater than 25nm in the C-band. Open eye diagrams at six different output wavelengths are shown in Fig. 4. The tops of the eyes appear noisy due to pattern dependence, which arises from saturation in the input SOAs.

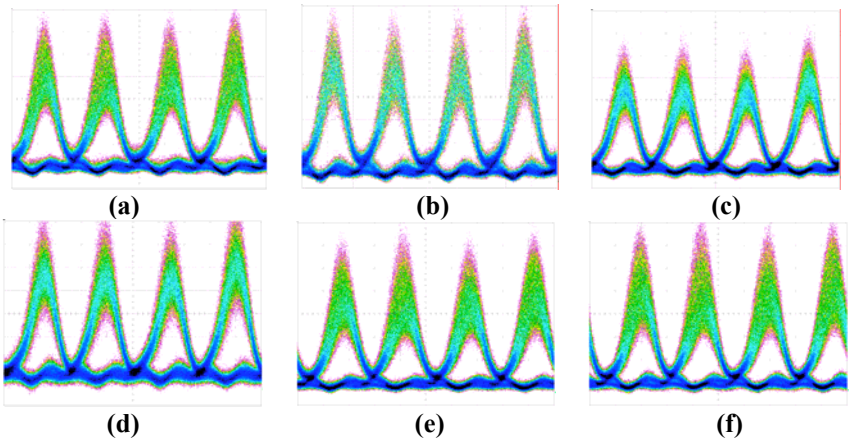

Fig. 4. Wavelength converted eye diagrams at 40Gbps RZ for output wavelengths: (a) 1537 nm, (b) 1542 nm, (c) 1547nm, (d) 1552nm, (e) 1561nm, (f) 1565nm.

4. Conclusions

In this paper, we reported on a novel monolithically integrated widely tunable all-optical wavelength converter with TIR turning mirrors and a time delay for differential operation. Mirror integration was performed in our standard OQW integration platform by a simple modification of the fabrication process. We believe that this successful demonstration of the TIR mirror technology in our platform opens a possibility for achieving significant increases in the PIC integration density in the future. Wavelength conversion at 40 Gbps was demonstrated from an input wavelength of 1557nm to tunable output wavelengths ranging from 1537nm to 1565nm. Future work will focus on mitigating pattern dependence through optimization of the input SOAs.

The authors acknowledge the funding support of the DARPA/MTO DOD-N program under the LASOR project award number W911NF-04-9-0001.

[1] D. Wolfson, T. Fjelde, A. Kloch, C. Janz, F. Poingt, F. Pommereau, I. Guillemot, F. Gaborit, and M. Renaud, “Detailed experimental investigation of all-active dual-order mode Mach-Zehnder wavelength converter,” Electronics Letters **36**, 1296–1297 (2000).

[2] M. L. Masanovic, V. Lal, J. A. Summers, J. S. Barton, E. J. Skogen, L. A. Coldren, and D. J. Blumenthal, "Design and Performance of a Monolithically-Integrated Widely-Tunable All-Optical Wavelength Converter with Independent Phase Control," IEEE Photonics Technology Letters **16** , 2299-2301 (2004)

[3] V. Lal, M. L. Masanovic, J. A. Summers, L. A. Coldren, D. J. Blumenthal, “40Gbps Operation of an Offset Quantum Well Active Region Based Widely-Tunable All-Optical Wavelength Converter,” to be presented at OFC 2005, session OthE.

[4] C. Joergensen, S. L. Danielsen, M. Vaa, B. Mikkelsen, K. E. Stubkjaer, P. Doussiere, F. Pommerau, L. Goldstein, and M. Goix, “40 Gbit/s alloptical wavelength conversion by semiconductor optical amplifiers,” Electronics Letters **32**, 367-368 (1996).

[5] J. Leuthold, B. Mikkelsen, G. Raybon, C. H. Joyner, J. L. Pleumeekers, B. I. Miller, K. Dreyer, and C. A. Burrus, ”All-optical wavelength conversion up to 100 Gbit/s with SOA delayed-interference configuration,” ECOC 2000. 26th European Conference on Optical Communication. VDE Verlag. vol.3, 2000, pp. 119-20.

[6] J. Schneider, M. Moser, K. Affolter, “Low loss corner mirrors in InP/InGaAsP/InP for integrated optics etched with chlorinated gases” Sixth International Conference on Indium Phosphide and Related Materials, 1994. Conference Proceedings, 27-31 March 1994 pp. 216 - 219.

10Gbps Monolithically-Integrated Widely-Tunable Wavelength Converter Using Quantum Well Intermixing

Vikrant Lal, Milan L. Mašanović, Erik J. Skogen, James W. Raring, Joseph A. Summers, Larry A. Coldren and Daniel J. Blumenthal

Electrical and Computer Engineering Department, University of California Santa Barbara, CA 93106-9560, USA
lal@ece.ucsb.edu

Abstract: We report on the implementation and performance of an InP centered quantum well intermixed, MZI-SOA all-optical wavelength-converter monolithically-integrated with an SGDBR. We show error-free operation at 10Gbps, and 3dBm output power over 30nm output tuning.

OCIS codes: (250.5300) Photonic integrated circuits; (230.5590) Quantum-well devices

1. Introduction

Mach-Zehnder interferometer with semiconductor optical amplifier (MZI-SOA) based all-optical wavelength converters represent one important group of integrated devices for wavelength conversion, capable of high-speed operation and signal 2R regeneration. Further integration of tunable laser sources with this converter type on a single chip is a critical step in order to meet performance, yield, cost and footprint requirements of future optical networks and their functions. This high level of integration requires an integration platform that allows optimization of various active and passive chip elements as well as low chip power consumption. In particular, monolithic integration of a laser on the same chip poses strict requirements in terms of on-chip back reflection minimization. Our previous work using a simple Offset Quantum Well integration platform [1,2] resulted in successful demonstrations of monolithically integrated widely tunable all-optical wavelength converters (TAO-WC) which exhibited error-free operation up to 10Gbps over a large tuning range and with 0dBm converted output power. Still, tradeoffs in the MZI-SOA design stemming from the low optical confinement in the offset quantum well active regions limited the device conversion efficiency and maximum operating speed, when compared to the bulk and centered quantum well MZI-SOA-WCs [3].

In this paper, we report on the implementation of a centered quantum well active region based tunable all-optical wavelength converter fabricated using quantum well intermixing (QWI) to overcome these issues.

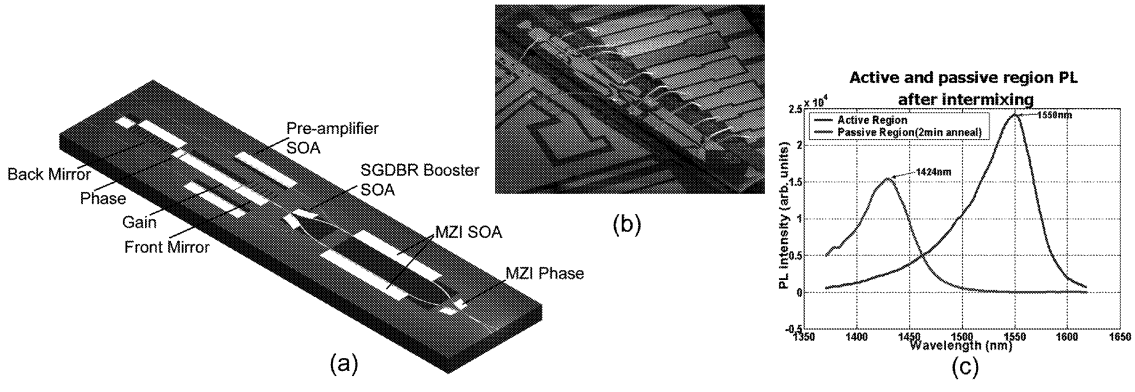

Fig. 1. (a) Schematic and (b) SEM of the quantum well intermixed widely tunable 10 Gbps all-optical wavelength converter. Also shown is (c) the PL spectra from the Active and Passive regions on chip

Quantum well intermixing provides an attractive solution for post-growth bandedge control in complex photonic integrated circuits [4,6], allowing for simple fabrication of active-passive centered quantum well devices without having to resort to complicated growth schemes (selective area growth or butt-joint growth). Furthermore, the value of the confinement factor can be tailored by the choice of the number of quantum wells, and in this

implementation is 50% higher compared to our previous work [1][2]. This platform yields highly-saturated and nonlinear SOAs in the WC part, resulting in the QWI-TAO-WC error-free operation at 10 Gbps data rates with improved rise time, conversion efficiency and average converted output (>3dBm) power compared to our previous work using OQW [1,2], while maintaining over 30nm output tuning range.

2. Device Design and Fabrication Process

The tunable wavelength converter design is similar to the one reported previously [1,2] and consists of a widely tunable sampled grating distributed Bragg reflector (SGDBR) laser monolithically integrated with a MZI-SOA WC, Figure 1. The operation principles of these wavelength converters have been described in detail in [1] [2]. For these QWI-TAO-WC devices an impurity free, vacancy enhanced, quantum well intermixing process is used to create the active and passive bandgap regions on the chip [4][5]. The PL spectra of the active and passive regions after intermixing are shown in Fig 1. The material is selectively ion-implanted with Phosphorus ions, and due to the lattice damage caused by the implant, vacancies are created in the material. The vacancies are then diffused through the quantum wells by rapid thermal annealing the sample. The vacancy diffusion causes the quantum well and barrier materials to intermix, resulting in an increase in the bandgap [5]. The implanted material is then etched away to leave the sample impurity free.

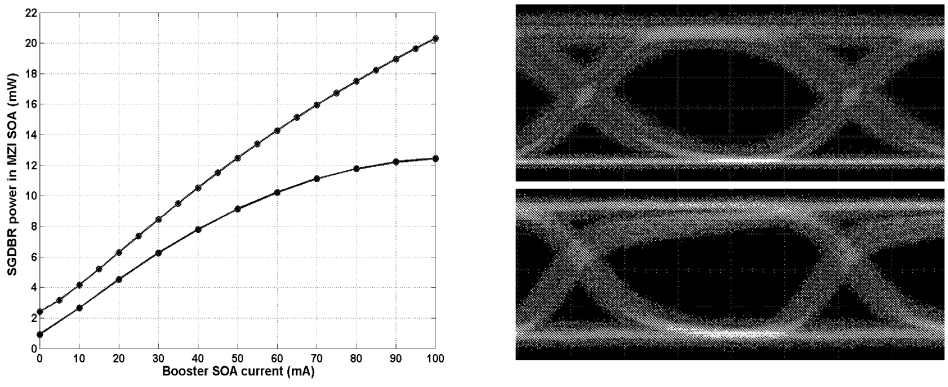

(a) (b)

Fig. 2. Comparison between offset and centered quantum well devices (a) CW power from SGDBR coupled to the MZI higher for CQW devices (b) CQW device eyes(bottom) showing faster lifetimes than the OQW device ones (top)

3. Results

We measured the performance of the device for different input and output wavelengths across the C-band at 10Gbps data rates. We were able to operate the device from 1530 to 1560nm. The EDFAs and thin film filters in our device testing setup limited us to wavelengths below 1560nm, even though the device itself can tune to wavelengths longer than 1560. For the measurements reported in this paper, the device was operated in the inverting mode of operation. For inverting mode of operation, the MZI-SOA bias needs to be adjusted in such a way that the powers of the CW signals in the MZI branches are equal for the high input power level of the incoming data stream [2].

Higher modal gain due to the higher confinement factor of the centered quantum well active region benefits the device operation in two ways: the higher optical power of the on-chip SGDBR laser increases the level of optical pumping in the MZI-SOA, thereby reducing the SOA gain recovery time; lower saturation power of the MZI-SOAs provides for higher SOA nonlinearity, further improving the response time of the SOA and the power of the converted signal. This is illustrated in Fig 2b, where faster response time for a CQW device is clear from the eye diagrams at 10 Gbps shown for an OQW device and a CQW device. Figure 2a) shows the coupled CW power into the MZI-SOA as function of the booster SOA bias [7] for both the OQW and the new CQW devices. Along with the benefits it offers, the increase in the confinement factor also creates additional challenges. The reduction SOA saturation power results in the enhancement of pattern dependence in the preamplifier and MZI SOAs. This causes a pattern dependent power penalty for the current generation of devices. Further research is being done to optimize the SOA designs to overcome this pattern dependence.

We performed two different set of measurements. For the first the input wavelength into the device was held

constant at 1545nm, and the device output was tuned from 1530 to 1560nm. For the second set of measurements, the device output wavelength was help constant at 1545nm, and the input wavelength to the device was varied from 1530 to 1560nm. For both set of measurements, the input data was chosen to be PRBS 2^{31}-1. The measured BER curves are shown in Fig 3.

The power penalty was measured around 4dB for output wavelengths in the range 1530-1560nm. The device performance started to degrade as the input wavelength approached 1530nm, which is close gain bandwidth limit for the quantum wells. We expect that these numbers could improve with future device designs.

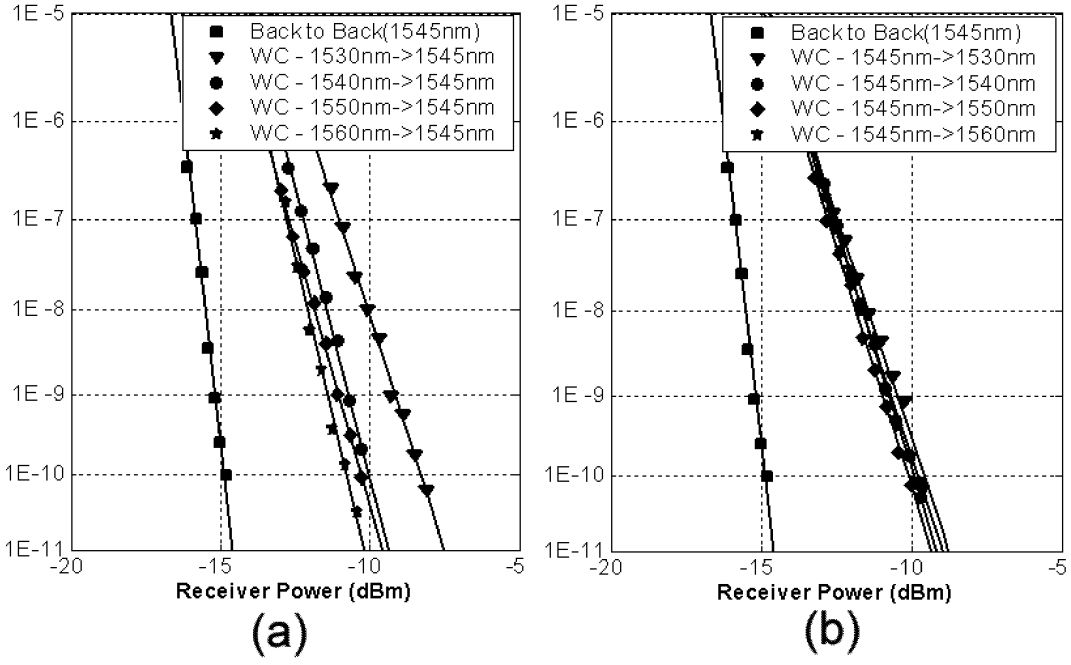

Fig. 3. BER plots for 10Gbps operation for (a) Input: 1530-1560nm, Output: 1545nmm (b) Input: 1545nm, Output: 1530-1560nm

4. Conclusions

We have demonstrated a QWI-based monolithically integrated tunable wavelength converter in InP. Centered quantum wells active regions resulted in the QWI-TAO-WC error-free operation at 10 Gbps data rates with improved rise time, conversion efficiency and average converted output (>3dBm) power compared to our previous work using OQW [1,2]. The operating wavelength range of the device is 30nm (1530-1560nm) for both the input as well as output wavelength. This work is supported by the DARPA/MTO CS-WDM Program under Grant No. N66001-02-C-8026

[1] M. L. Mašanović, „ V. Lal, J. A. Summers, J. S. Barton, E. J. Skogen, L. A. Coldren, and D. J. Blumenthal, "Design and Performance of a Monolithically-Integrated Widely-Tunable All-Optical Wavelength Converter with Independent Phase Control," *IEEE Photonics Technology Letters*, 16 , No. 10, IEEE, (2004)

[2] M. Mašanović, V. Lal, J. A. Summers, J. Barton, E. Skogen, L. Rau, L. Coldren, D. Blumenthal, "Widely-tunable monolithically-integrated all-optical wavelength converters in InP", submitted for publication to *IEEE Journal of Lightwave Technology*.

[3] W. Idler, K. Daub, G. Laube, M. Schilling, P. Wiedemann, K. Dutting, M. Klenk, E. Lach, K. Wunstel, "10 Gb/s Wavelength Conversion with Integrated Multiquantum-Well 3-Port Mach-Zehnder Interferometer" IEEE Photonics Technology Letters, **8**, IEEE, 1163-65. (1996)

[4] E. J. Skogen, J. S. Barton, S. P. Denbaars, L. A. Coldren, "Tunable sampled-grating DBR lasers using quantum-well intermixing" *IEEE Photonics Technology Letters*, 14, No. 9, 1243-1245 (2002)

[5] E. J. Skogen, J. S. Barton, S. P. Denbaars, L. A. Coldren, "A quantum-well-intermixing process for wavelength-agile photonic integrated circuits" *IEEE journal of Sel. Topics in Quantum Elec.* , 8 , No. 4, 863-869 (2002)

[6] J. W. Raring, E. J. Skogen, L. A. Johansson, M. N. Sysak, J. S. Barton, M. L. Masanovic, and L. A. Coldren, "Quantum Well Intermixing for Monolithic Integration: A Demonstration of Novel Widely-Tunable 10Gb/s Transmitters and Wavelength Converters", presented at Integrated Photonics Research Conference, San Francisco, California, USA, 2004.

[7] M. L. Mašanović, V. Lal, E. J. Skogen,J. S. Barton, J. A. Summers,L. A. Coldren, and D. J. Blumenthal, "Detailed Comparison of Cross-phase Modulation Efficiency in Offset Quantum Well and Centered Quantum Well Intermixed Monolithically Integrated Widely-Tunable MZI-SOA Wavelength Converters" *To be presented at OFC 2005*

NOVEL COMPACT InP-BASED MONOLITHIC WIDELY TUNABLE DIFFERENTIAL MACH-ZEHNDER INTERFEROMETER WAVELENGTH CONVERTER FOR 40Gbps OPERATION

Vikrant Lal, Joseph A. Summers, Milan L. Mašanović, Larry A. Coldren and Daniel J. Blumenthal

Electrical and Computer Engineering Department, University of California Santa Barbara, CA 93106-9560
lal@ece.ucsb.edu

Abstract: A novel, compact monolithic widely tunable differential SOA-Mach-Zehnder wavelength converter is described. Total internal reflection mirrors are used to realize on-chip differential delay for 40Gbps operation. This design allows reduced chip area and improved MZI balance.

I. Introduction

High functionality photonic integrated circuits (PIC) are a key technology to meet the cost, footprint and power consumption requirements of future high-speed optical networks. Wavelength conversion, in particular, is an important function for such networks that can be performed using PICs. Wavelength conversion at 40Gbps and higher data rates using InP based PICs has previously been demonstrated using a number of schemes [1-4]. SOA based integrated wavelength converters are a good candidate for systems operating at 40Gbps due to the ultra-fast carrier-depletion induced refractive index changes in an SOA. To overcome the SOA carrier recovery limitation, differential schemes have been shown in which the fast carrier-depletion is used to switch an interferometer on and, after a small delay, turn it back off using the same fast carrier-depletion process [2-4]. SOA based wavelength converters have also been used to perform 2R and 3R on the incoming signal.

In this paper we report on the first design and operation of a fully monolithic, widely-tunable differential Mach-Zehnder interferometer wavelength converter at 40Gbps RZ data rates. The wavelength converter requires only a single input fiber and a single output fiber, with the required CW source and delay being monolithically integrated on-chip, and is shown to operate across an output tuning range of over 25nm. TIR corner mirrors are used in a novel device layout to achieve a compact design that significantly reduces chip area. This device demonstrates the advantages that TIR corner mirror technology can offer for high functionality PICs.

II. Device Design and Results

The device is fabricated in the offset quantum well integration platform [5,6]. The epitaxial structure used in this platform is shown in Fig.1. It shows the active and passive regions formed on-chip by selective etching of the quantum well stack. The device consists of an on-chip widely-tunable SGDBR laser integrated with a differential Mach-Zehnder interferometer.

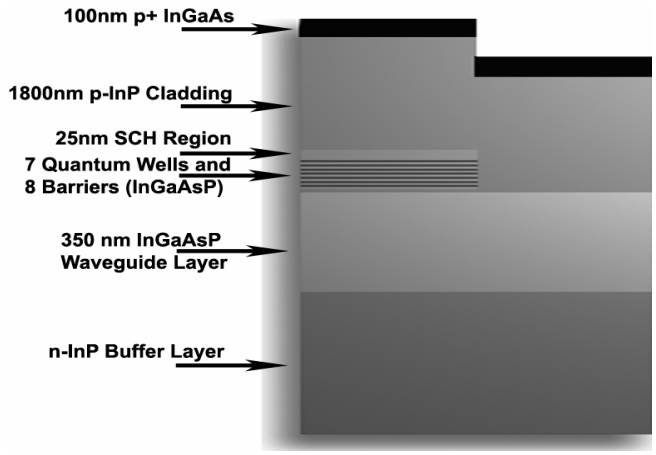

Figure 1. Epitaxial structure for the Offset Quantum Well integration platform

To create a differential Mach-Zehnder, one of the arms of the MZI is made longer than the other by a fraction of the desired output pulse width to achieve the required differential delay. For 40Gbps operation, this delay needs to be typically around 6 to 12ps, depending on the input data pulse width. This delay is approximately 500μm to 1mm of additional length in the InP system. To implement this length difference on-chip with bends, using the same weakly confined waveguides used in the rest of the device, can lead to a very large footprint. To address this problem we use TIR corner mirrors [7]. The TIR mirrors are fabricated using a self aligned two layer process, that allows us to define the mirror facet along with the ridge layer and avoids any potential misalignment issues between the mirror facet and the waveguides.

The device has a single data input and a single output for the converted data. The input signal is amplified using a pre-amplifier SOA and coupled to an on-board widely-tunable SG-DBR laser. The coupled signal is then sent through a differential SOA-MZI. To achieve the required length differential the MZI is folded back towards the input using two TIR corner mirrors in each arm, resulting in one arm

being longer than the other. The length differential can be easily designed by changing the location of the TIR corner mirrors. The device schematic and mirror SEMs are shown in Fig.2.

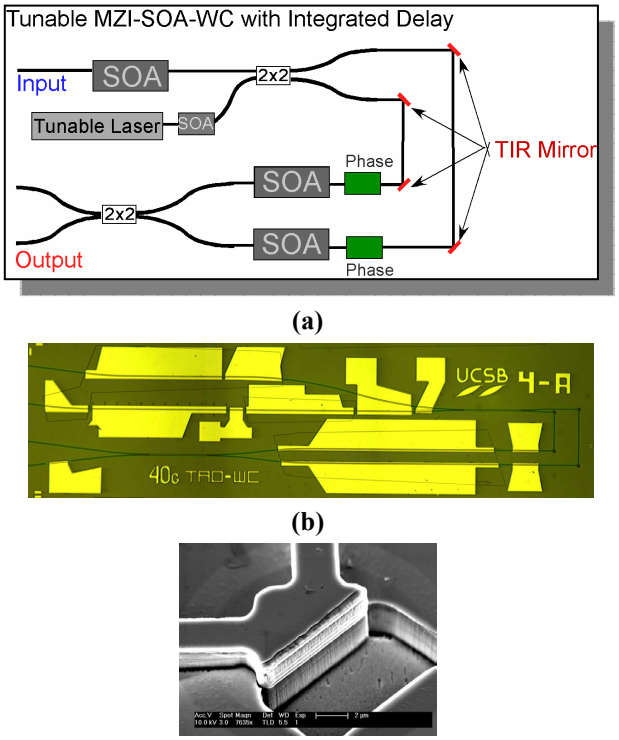

Figure 2. (a) Device Schematic of the 40Gbps differential wavelength converter (b) Device micrograph, and (c) TIR corner mirror SEM

This folded layout results in a compact device that is only 0.8mm wide and 2.9mm long for a total chip area of under 2.4mm^2. The input and output waveguides are on the same facet and so require only a single AR-coating per device. The layout also results in the number of mirrors in each arm being the same, which balances the MZI with respect to any excess loss from the mirrors. This balance is necessary in achieving a high extinction ratio at the output of the MZI.

The on-board SGDBR laser is used to select the outgoing signal wavelength. Fig.3. shows the tuning spectra of the SG-DBR laser. The laser itself can tune by over 35nm, but measurable the operating range of our device is limited by the gain bandwidth of the EDFA used in the receiver. Fig.4. shows he experimental setup used for characterizing these devices. The setup consists of a 40Gbps RZ data transmitter. The data signal is filtered, amplified and coupled into the device. A variable attenuator is used at the input to control the input power level and a polarization controller is used to maximize coupling to the TE polarization state. The output signal from the device is then filtered to remove the input signal and finally the converted data is amplified and sent to a 40Ghz detector. Fig.5. shows the output spectrum of the device for one set of input and output conditions.

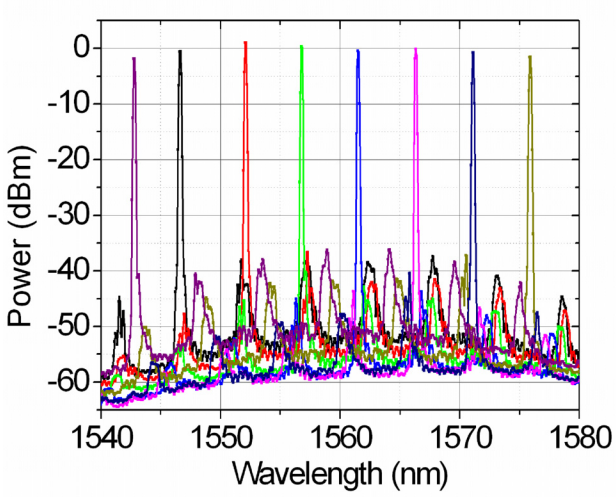

Figure 3. Overlaid spectra of the on board widely-tunable SGDBR laser source

The device operation is shown in Fig.6 for three different output wavelengths. The input wavelength is kept fixed at 1550nm, and the SGDBR is tuned from 1539 to 1563nm. We can see open eye patterns at 40Gbps-RZ for all output wavelengths.

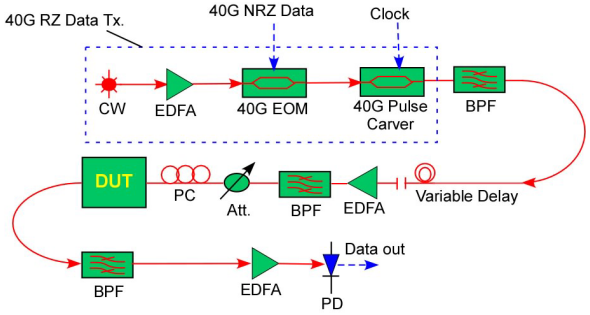

Figure 4. Experimental setup used for 40Gbps wavelength conversion

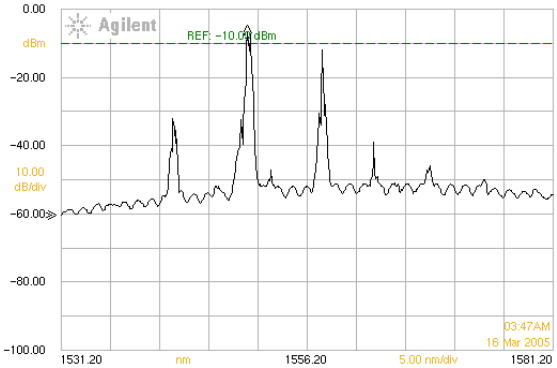

Figure 5. Ouput spectrum from the device showing the input signal at 1550nm and the SGDBR signal at 1558nm

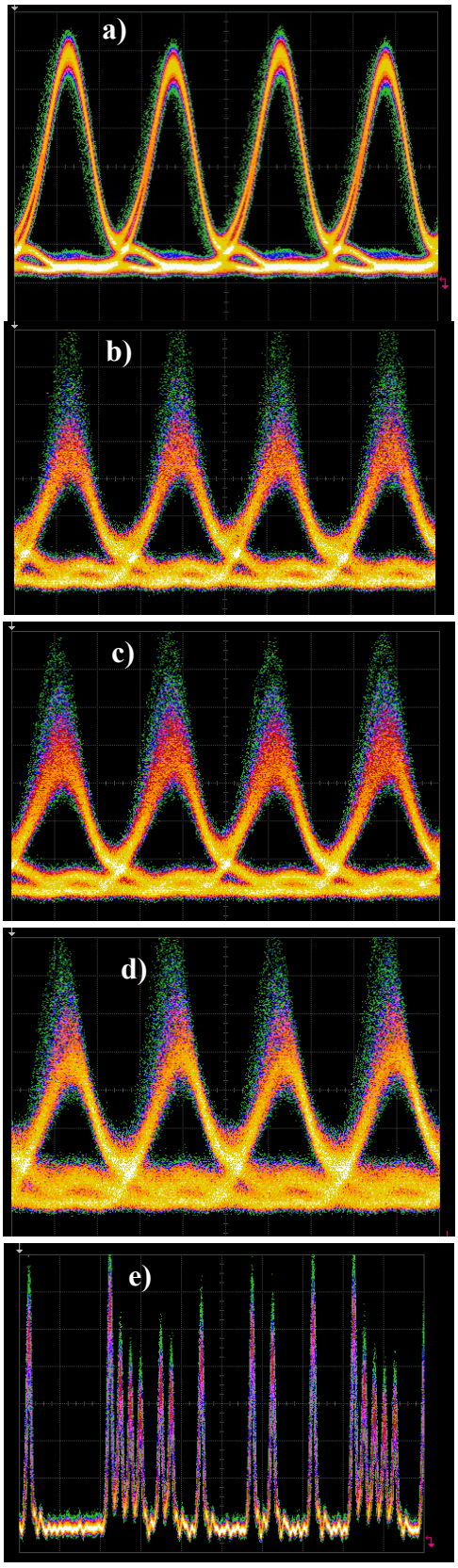

Figure 6. Device performance showing open converted eyes at 40Gbps (a) Input eye at 1550nm (b) Output eye at 1539nm (c) Output eye at 1554nm (d) Output eye at 1563nm (e) Converted data at 1554nm showing pattern dependence

The pre-amplifier SOAs in our current devices induce significant pattern dependence in the input signal, resulting in the eye closure at the high-level. Fig.6e clearly shows the pattern dependence in the output data pattern. Future work will address this issue through optimization of the pre-amplifier designs.

III. Conclusion

In this paper, we demonstrated a compact fully monolithic InP-based tunable differential high-speed wavelength converter. The novel device design incorporates an integrated signal delay of 6ps, designed for 40Gbps-RZ operation. The device also demonstrates the benefits of TIR corner mirror technology in designing compact high functionality PICs. Open eye patterns are shown for the converted signal with 25nm of output tuning range.

The authors acknowledge the funding support of the DARPA/MTO DOD-N program under the LASOR project award number W911NF-04-9-0001.

[1] B. Mikkelsen et al. Electronics Letters, vol. 33, pp. 2137-9, 1997.
[2] V.M. Menon et. al. Photonics Technology Letters, IEEE Volume: 15 , Issue: 2 , Feb. 2003 Pages:254 – 256
[3] M. L. Nielsen et al. Electronics Letters, vol. 39, pp. 385-6, 2003.
[4] J. Leuthold et. al. ECOC 2000. 26th European Conference on Optical Communication. VDE Verlag. Part vol.3, 2000, pp. 119-20 vol.
[5] M. L. Mašanović et. al. *IEEE Photonics Technology Letters*, 16 , No. 10, IEEE, (2004)
[6] V. Lal, et. al. *OFC 2005* session OThE
[7] P. Buchmann et. al. Journal of Lightwave Technology, Volume: 3 , Issue: 4, Pages:785 - 788 Aug 1985

Quantum-Well-Intermixed Monolithically Integrated Widely Tunable All-Optical Wavelength Converter Operating at 10 Gb/s

Vikrant Lal, *Student Member, IEEE*, Milan L. Mašanović, *Member, IEEE*, Erik J. Skogen, *Member, IEEE*, James W. Raring, *Student Member, IEEE*, Joseph A. Summers, *Student Member, IEEE*, Larry A. Coldren, *Fellow, IEEE*, and Daniel J. Blumenthal, *Fellow, IEEE*

***Abstract*—This letter reports on an InP Mach–Zehnder interferometer semiconductor optical amplifier all-optical wavelength converter monolithically integrated with a sampled grating distributed Bragg reflector laser. The device is fabricated using centered quantum wells to achieve a high modal overlap with the active region. The active and passive waveguide regions are defined using an impurity-free quantum-well intermixing technique. The device is shown to perform error-free at 10-Gb/s data rates with a 30-nm output tuning range. The device's output power is also measured to be >3 dBm across the range.**

***Index Terms*—Mach–Zehnder interferometer (MZI), photonic integrated circuit, quantum-well intermixing (QWI), wavelength conversion.**

I. Introduction

TUNABLE wavelength conversion is a key function for reconfigurable wavelength-division-multiplexing networks. Integration of a tunable laser and an all-optical wavelength converter (WC) on a single chip is necessary to meet performance, yield, cost, and footprint requirements of these networks. As the chip level integration density increases and more components are added on chip increasing the level of functionality, it becomes essential to optimize various active and passive elements for required performance as well as reduce overall chip power consumption. Integrating a laser on the same chip poses additional requirements in terms of on-chip back reflection minimization. Therefore, a robust yet flexible integration platform is required.

Previously, we have reported on the successful demonstration of a monolithically integrated widely tunable all-optical WC (TAO-WC) [1], [2] fabricated using a simple offset quantum-well integration platform. While our devices in this platform exhibited error-free operation at 10 Gb/s over a large tuning range and with 0-dBm converted output power, tradeoffs in the semiconductor optical amplifier (SOA) design stemming from the low optical confinement in the active regions limited the device conversion efficiency and maximum operating speed, when compared to the bulk and centered quantum-well Mach–Zehnder interferometer (MZI)-SOA-WCs [3]. In this letter, we report on the implementation of a centered quantum-well active-region-based tunable WC fabricated using quantum-well intermixing (QWI). QWI provides an attractive solution for postgrowth bandgap control in complex photonic integrated circuits [4], [5]. An impurity-free QWI process [5] is used to spatially define the material bandgap to selectively form active and passive regions. It allows simple fabrication of active–passive centered quantum-well devices without having to resort to complicated growth schemes (selective area growth or butt-joint growth). Furthermore, the value of the confinement factor can be tailored by the choice of the number of quantum wells, and in this implementation is 50% higher compared to [1] and [2]. This platform yields highly saturated and nonlinear SOAs in the WC part, higher output power sampled grating distributed Bragg reflector (SGDBR) laser (relative to [2]), and low-loss low-reflection transitions between active and passive regions of the chip.

The devices presented in this letter exhibit error-free operation at 10-Gb/s data rates with improved conversion efficiency relative to [2], over 30-nm output tuning range, and average converted output powers >3 dBm compared to 0 dBm reported in [2].

II. Device Design and Operation

The tunable WC design consists of a widely tunable SGDBR laser monolithically integrated with an SOA-based MZI WC and is shown in Fig. 1. The operation of these WCs has been described in detail in [1] and [2]. For the devices reported in this letter, an impurity-free vacancy-enhanced QWI process is used to create the active and passive bandgap regions on the chip. The material is selectively ion-implanted with phosphorus ions, and due to the lattice damage caused by the implant, vacancies are created in the material. The vacancies are then diffused through the quantum wells by rapid thermal annealing the sample. The vacancy diffusion causes the quantum well and barrier materials to intermix, resulting in an increase in the bandgap [5]. The implanted material is then etched away to leave the sample

Manuscript received February 2, 2005; revised April 20, 2005. This work was supported by the Defense Advanced Reseach Projects Agency (DARPA)/MTO CS-WDM Program under Grant N66001-02-C-8026.

V. Lal, M. L. Mašanović, E. J. Skogen, J. A. Summers, L. A. Coldren, and D. J. Blumenthal are with the Department of Electrical and Computer Engineering, University of California Santa Barbara, Santa Barbara, CA 93106 USA (e-mail: lal@ece.ucsb.edu; mashan@ece.ucsb.edu; skogen@engineering.ucsb.edu; jsummers@ece.ucsb.edu; coldren@ece.ucsb.edu; danb@ece.ucsb.edu).

J. W. Raring is with the Materials Department, University of California Santa Barbara, Santa Barbara, CA 93106 USA (e-mail: jraring@engineering.ucsb.edu).

Digital Object Identifier 10.1109/LPT.2005.851891

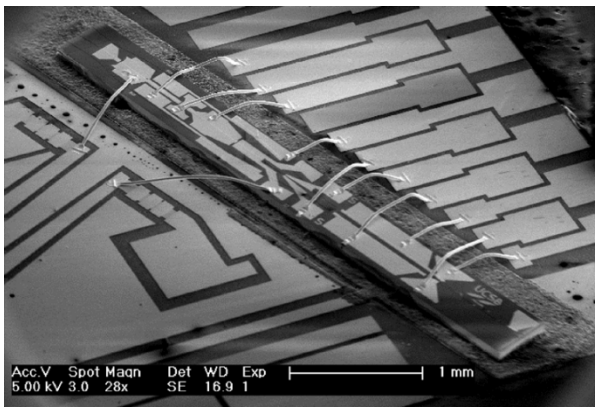

Fig. 1. Scanning electron microscope of the quantum-well-intermixed WC.

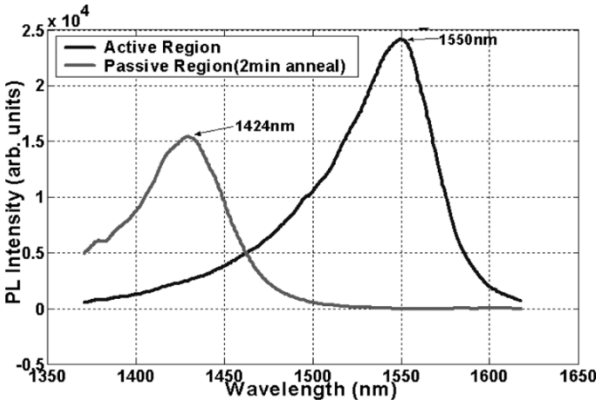

Fig. 2. PL spectra of the active and passive regions on chip after intermixing.

impurity free. This process is described in greater detail in [4] and [5]. Fig. 2 shows the photoluminescence (PL) spectra of the active and passive regions after intermixing. The intermixing process does not lead to any excess loss in the passive waveguides compared to our standard offset quantum-well platform; we measured passive loss around 1.5 dB/mm (or 3.5 cm^{-1}) in both platforms.

The increased confinement factor obtained using centered quantum wells allows us to achieve greater input signal gain, SGDBR power density, and higher phase swing in the MZI [6]. Measurements show continuous-wave power levels (set by the SGDBR laser) of up to 13 dBm in the MZI, compared to 10 dBm in offset quantum-well devices. We also measure a 100% improvement in phase swing as compared to offset quantum-well-based devices for the same input signal and SGDBR power levels, due to the higher modal confinement factor [6]. These improvements can help greatly improve the input dynamic range of these devices and we are working to measure and characterize such benefits.

III. Device Performance

Fig. 3 shows the converted eyes obtained in both modes of operation at pseudorandom binary sequence (PRBS) 2^7-1. We can see clear open eyes with high extinction ratio in both modes of operation. The increased noise at the one-level in the case of the inverting eyes is due to the pattern dependence in the MZI

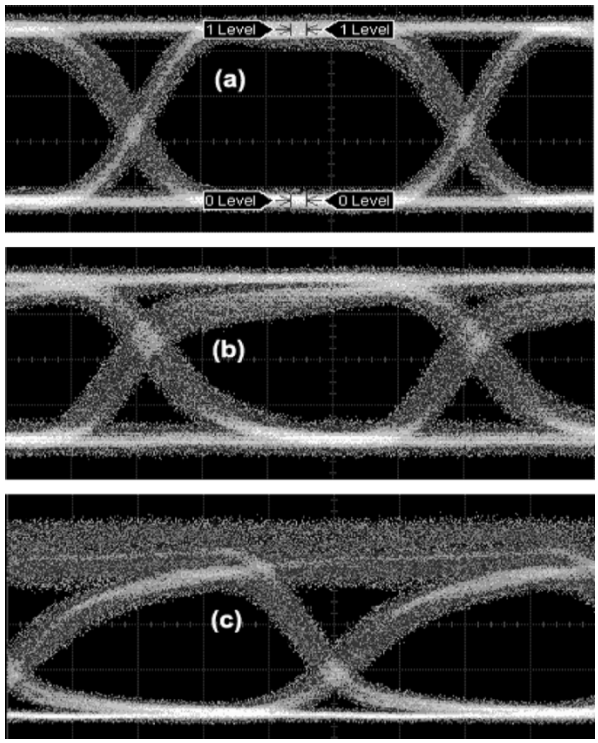

Fig. 3. Eyes of the (a) back-to-back signal and converted signal in (b) noninverting mode (c) inverting mode at PRBS 2^7-1, at 10-Gb/s data rates (time scale on plots 20 ps/div).

SOAs due to a slow gain recovery time. It is not noticeable in the noninverting case since the slow gain recovery is quenched into the zero-level of the converted signal.

We measured the performance of the device for different input and output wavelengths across the C-band at 10-Gb/s data rates. We were able to operate the device from 1530 to 1560 nm, in both the inverting and noninverting modes of operation. Fig. 4(a) shows the error-free operation for both these modes at one set of wavelengths. The erbium-doped fiber amplifiers and thin film filters in our device testing setup limited us to wavelengths below 1560 nm.

Along with the benefit it offers, the increase in the confinement factor also creates additional challenges. The reduction in SOA saturation power results in the enhancement of pattern dependence in the preamplifier and MZI SOAs. This causes a pattern-dependent power penalty for the current generation of devices. As can be seen in Fig. 4(b), for the inverting mode of operation, the power penalty was measured around 1.5 dB for PRBS 2^7-1 and increased to around 4 dB for PRBS $2^{31}-1$, and the bit-error-rate (BER) slope decreased. This was also the case for the noninverting mode of operation.

To estimate the wavelength range of these devices, we performed two different sets of measurements. For the first set, the input wavelength into the device was held constant at 1545 nm, and the device output was tuned from 1530 to 1560 nm. For the second set of measurements, the device output wavelength was help constant at 1545 nm, and the input wavelength to the device was varied from 1530 to 1560 nm. For both sets of measurements, the input data was chosen to be PRBS 2^7-1, and the devices operated in the inverting mode. The measured BER

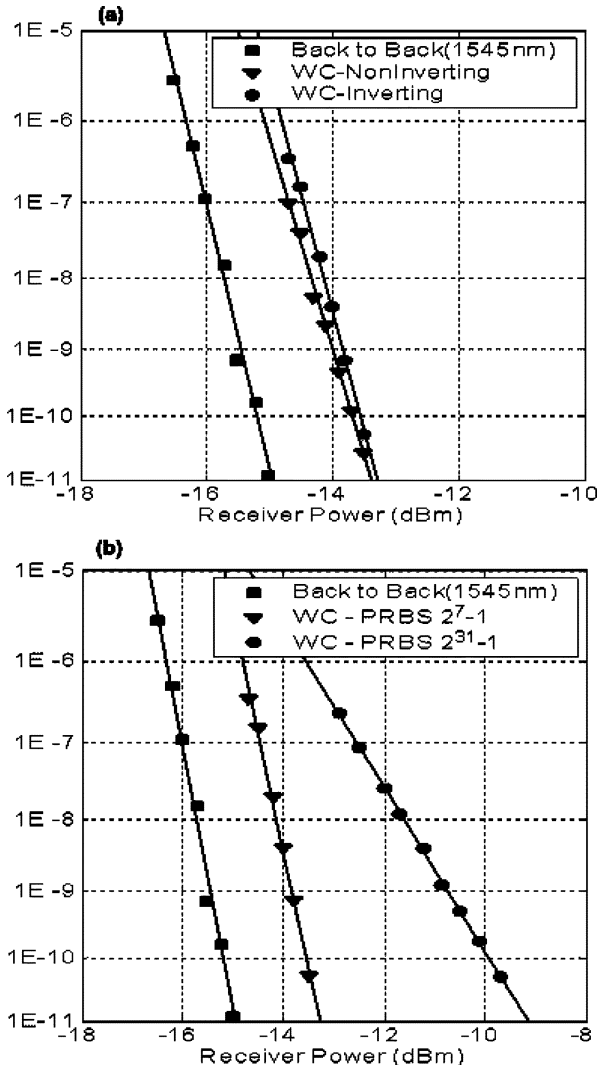

Fig. 4. BER plots for 10-Gb/s operation for (a) noninverting and inverting modes (b) increased power penalty with PRBS $2^{31} - 1$ input. The input wavelength was 1545 nm and output wavelength 1540 nm.

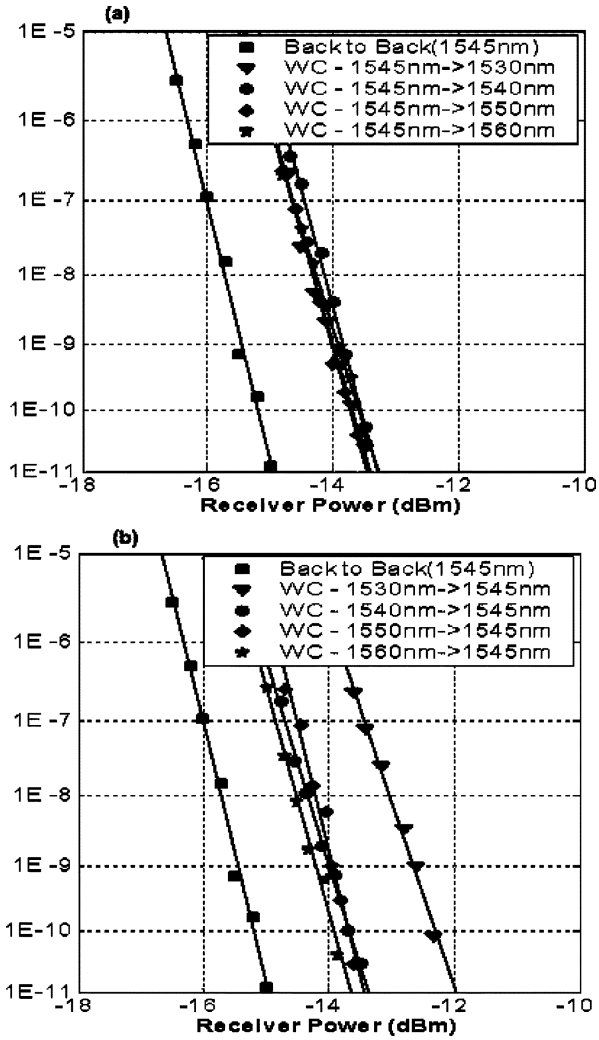

Fig. 5. BER plots for 10-Gb/s operation for (a) input: 1545 nm, output: 1530–1560 nm; (b) input: 1530–1560 nm, output: 1545 nm. The input data was PRBS $2^7 - 1$.

curves are shown in Fig. 5. Device performance degradation is noticeable as the input wavelength approached 1530 nm, which is close gain bandwidth limit for the quantum wells. We expect that these numbers could improve with future device and base epi designs.

IV. Conclusion

We have demonstrated a TAO monolithic WC in InP using a QWI fabrication process. The device exhibits error-free operation at 10 Gb/s. The centered quantum-well-integration platform used to fabricate these devices allows a higher modal overlap with the active region. The increase in the active region confinement factor results in greater phase swing due to cross-phase modulation for the SOAs and also a faster gain recovery lifetime. The operating wavelength range of the device is 30 nm (1530–1560 nm) for both the input as well as output wavelength, and the output power is >3 dBm across the output tuning range.

References

[1] M. L. Mašanović, V. Lal, J. A. Summers, J. S. Barton, E. J. Skogen, L. A. Coldren, and D. J. Blumenthal, "Design and performance of a monolithically integrated widely tunable all-optical wavelength converter with independent phase control," *IEEE Photon. Technol. Lett.*, vol. 16, no. 10, pp. 2299–2301, Oct. 2004.

[2] M. Mašanović, V. Lal, J. A. Summers, J. Barton, E. Skogen, L. Rau, L. Coldren, and D. Blumenthal, "Widely-tunable monolithically-integrated all-optical wavelength converters in InP," *J. Lightw. Technol.*, vol. 23, no. 3, pp. 1350–1362, Mar. 2005.

[3] W. Idler, K. Daub, G. Laube, M. Schilling, P. Wiedemann, K. Dutting, M. Klenk, E. Lach, and K. Wunstel, "10 Gb/s wavelength conversion with integrated multiquantum-well based 3-port Mach–Zehnder interferometer," *IEEE Photon. Technol. Lett.*, vol. 8, no. 9, pp. 1163–1165, Sep. 1996.

[4] E. J. Skogen, J. S. Barton, S. P. Denbaars, and L. A. Coldren, "Tunable sampled-grating DBR lasers using quantum-well intermixing," *IEEE Photon. Technol. Lett.*, vol. 14, no. 9, pp. 1243–1245, Sep. 2002.

[5] ——, "A quantum-well-intermixing process for wavelength-agile photonic integrated circuits," *IEEE J. Sel. Topics Quantum Electron.*, vol. 8, no. 4, pp. 863–869, Jul./Aug. 2002.

[6] M. L. Mašanović, V. Lal, E. J. Skogen, J. S. Barton, J. A. Summers, L. A. Coldren, and D. J. Blumenthal, "Detailed comparison of cross-phase modulation efficiency in offset quantum well and centered quantum well intermixed monolithically integrated widely-tunable MZI-SOA wavelength converters," presented at the Optical Fiber Communication Conf. (OFC 2005), Anaheim, CA, Mar. 2005.

IEEE Photonics Technology Letters, 17, (9), pp. 1902-1904 (September 2005)

10Gbit/s wavelength conversion using a widely-tunable series push-pull photocurrent-driven transmitter

Jonathon S. Barton, *Student Member IEEE,* Anna Tauke-Pedretti, *Student Member, IEEE*, Matt Dummer, *Student Member, IEEE*, Mathew N. Sysak, *Student Member, IEEE*, Milan L. Mašanović, *Student Member, IEEE,* James Raring, *Student Member, IEEE,Erik J. Skogen, Member, IEEE,* Larry. A. Coldren, *Fellow, IEEE*

Abstract— Error-free operation at 10 Gbit/s was demonstrated for a hybrid connected photocurrent-driven series push-pull Mach-Zehnder based wavelength converter (TPDMZ-WC). Back-to-back power penalties of <1dB were measured across the 37nm wavelength tuning range of the SGDBR.

***Index Terms*— Quantum well lasers, photodiodes, optical receivers, optical transmitters, optical planar waveguide components, tunable lasers, optical modulation, wavelength conversion, photocurrent driven wavelength conversion**

I. INTRODUCTION

Widely-tunable wavelength converters are widely regarded as critical to the scalability, flexibility, and cost of future optical networks. These devices have opportunities for deployment in optical switches, routers and add/drop multiplexers. Essentially, they enable Wavelength Division Multiplexed (WDM) signals to be transferred from one wavelength channel to another wavelength channel without requiring off-chip electronic circuitry. Differing approaches have been pursued with devices using cross phase modulation (XPM)[3], differential phase modulation (DPM)[4], and/or cross absorption modulation (XAM) of SOAs. High performance has been obtained with both discrete and monolithically-integrated tunable all-optical wavelength converters (TAO-WC)[6].

Photocurrent-driven (PD-WC) devices have been demonstrated [1,8,9] using either the direct modulation of a laser[9], or external modulation using either an Electro-absorption (EA)[1,9], or Mach- Zehnder modulator.[8] PD-WCs do not require an optical filter to reject the input signal at the output which is desirable particularly with wavelength tunable applications where the response time of a filter could limit system performance. Integrating the SGDBR gives a compact wavelength agile source that requires only two fiber connections – with low-loss coupling between the SGDBR and the modulator. This design ultimately yields a small footprint, low cost, and transmits at high speed.

Manuscript received Sept 30, 2004. This work was supported by Intel Corporation grant # TXA001630000 and DARPA MTO – CS-WDM grant #N66001-02-C-8026. The authors are at the University of California at Santa Barbara, Materials and Electrical and Computer Engineering Dept. 93106 USA (telephone: 805-893-8465, e-mail: jsbarton@engineering.ucsb.edu).

II. WAVELENGTH CONVERTER DESIGN

This particular implementation uses a hybrid-integrated widely-tunable wavelength converter based on a series push-pull SGDBR-SOA-MZ transmitter[10] and offset QW based photo-detector receiver (fig.1&2)[11].

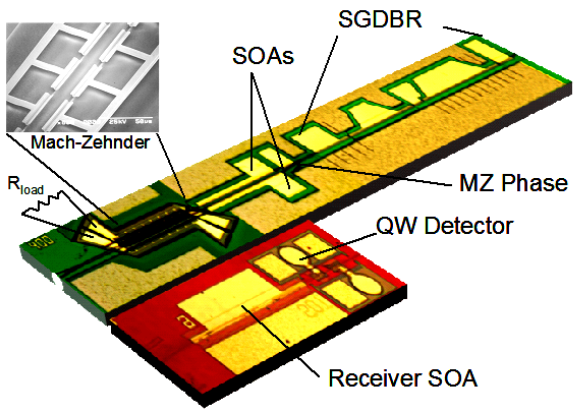

Fig. 1 Device Layout

A tunable transmitter using a 400μm long series push-pull driven Mach-Zehnder modulator electrode structure was fabricated similar to the structure shown in [7]. This structure can improve the bandwidth of the modulator by roughly a factor of two compared with a single-side drive configuration. The receiver for this device consisted of a 600μm long tapered semiconductor optical amplifier (SOA) (from 3μm to 9μm) with a 50μm long offset-QW detector that was tapered down from 9μm to 6μm and nominally reverse-biased to -4.5V[11]. Both devices were fabricated using the same offset-QW base structure[6,8,9] with compatible processing steps and regrowth. The total footprint of the chips is less than 1mm x 3.8mm. The bias configuration is shown in Fig. 2 and uses a load resistor termination at the end of the

electrode as shown in Fig 1. The detector and the front end of the modulator were both probed with separate bias Ts. This allows the Mach-Zehnder modulator to operate at low bias (-0.5V), favoring reduced insertion losses and the detector to be reverse-biased higher (-4.5V) for improved efficiency.

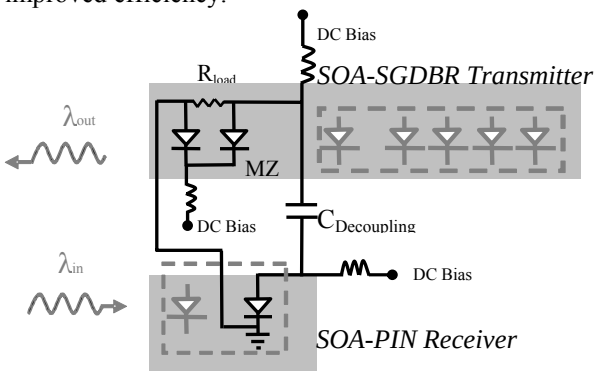

Fig.2. Series Push-pull MZ photocurrent-driven wavelength converter configuration

Despite some additional bias circuitry, this configuration has the added benefit that the device may be biased to achieve zero chirp for inverting and non-inverting operation, and DC power does not dissipate across the resistive load for identical MZ branch biases.

III. RECEIVER CHARACTERISTICS

Integrating the SOA with a detector allows the fabrication of a high-gain, high-saturation power receiver. Figure 3 shows the optical gain at 1548nm for various input optical powers as a function of bias current.

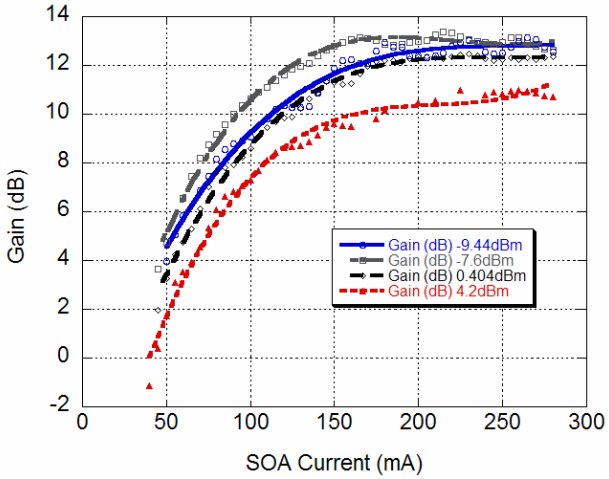

Fig. 3 Optical gain of the SOA in receiver as a function of optical input power at 1548nm. (A current density of 8.33kA/cm corresponds to 250mA bias)

This added gain improves the operation sensitivity of a photocurrent driven wavelength converter significantly as compared with previous work[8,9] allowing successful operation with only 1.3mW coupled input power.

IV. WAVELENGTH CONVERSION RESULTS

As an optical input signal is fed into the receiver, photocurrent is generated resulting in a voltage swing applied to the transmitter. This voltage swing was measured at 10Gbit/s as a function of the coupled input power. Due to the bias T's used in the hybrid scheme, approximately 2dB of electrical loss at 10GHz was present.

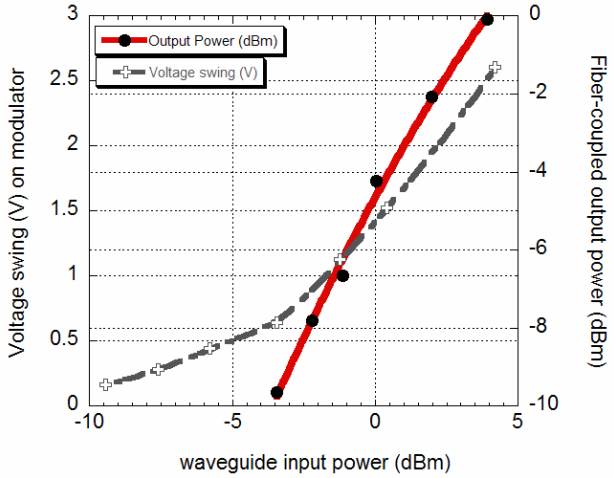

Fig. 4. Voltage swing applied to the modulator and the fiber coupled output power. Input wavelength 1548nm Output 1555nm. Coupling loss for input ~6dB and output ~4dB

The fiber-to-fiber insertion loss of the device is approximately 10dB, however, is only 0dB without input and output fiber coupling loss.

The small-signal optical-to-optical bandwidth (S_{21}) was measured for the wavelength converter with an input signal at 1548nm and converted signal at 1555nm for various biases on each branch of the Mach-Zehnder modulator. The 50ohm terminated 3dB bandwidth corresponding to the modulator and detector independently were ~30GHz and ~20GHz respectively. The optical-to-optical wavelength converter bandwidth is given in fig. 5. As can be seen in fig. 5, an optical bandwidth suitable for 10Gbit/s operation is obtained with a 50ohm termination on the detector and modulator. Modest voltage dependence of the bandwidth is due to the depletion of the PN junction in the waveguide of the MZ structure.

Transmission though the wavelength converter was measured for NRZ 2^7-1 PRBS 10Gbit/s data generated at an input wavelength of 1548.1nm using a 12 Gbit/s BERT and Agilent 83433A transmitter. An EFDA was used to boost the power to 8dBm fiber power, in which the signal was optically filtered and the polarization controlled to achieve 1.3mW of coupled optical power in the receiver waveguide.

IEEE Photonics Technology Letters, 17, (9), pp. 1902-1904 (September 2005)

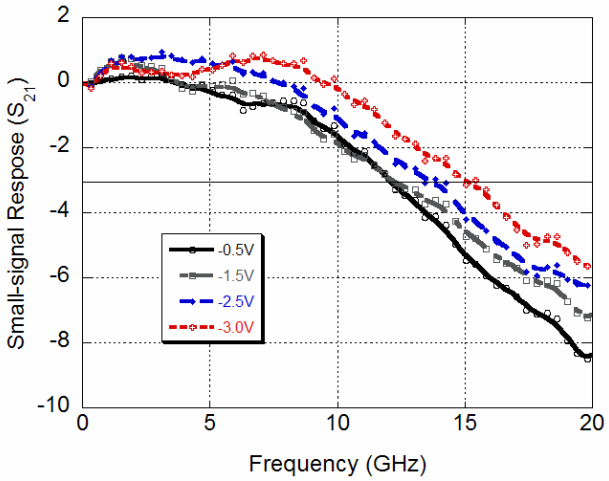

Fig 5. Optical-to optical small-signal response of WC with 50ohm termination. Detector biased at -4.5, MZ bias varied as shown in figure with the same bias on each branch.

The converted signal from the integrated transmitter at λ_2 was measured using an Agilent 11982A receiver without preamplification. Typical back-to-back bit error rate (BER) measurements are shown in fig. 6. The PRBS 10 Gbit/s output waveforms corresponded to 12-13 dB extinction across the wavelength range.

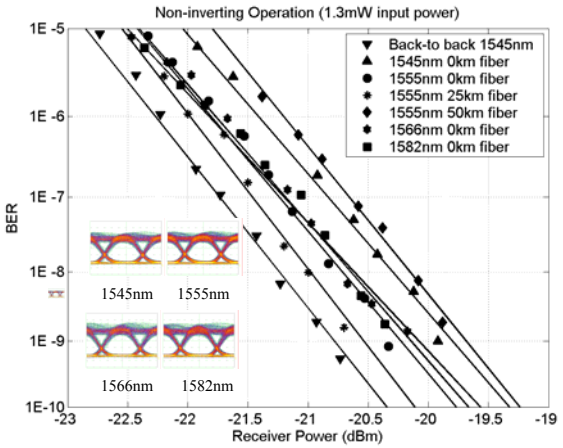

Fig. 6 BER for 10 Gbit/s NRZ 2^7-1 PRBS for different output wavelengths and fiber transmission. Input wavelength = 1548nm >12dB RF extinction for all wavelengths. Gain = 150mA SOA#1 70mA, SOA#2 80mA, FM = 0.5mA, Rear Mirror = 0.5mA, phase = 0mA

Error-free wavelength conversion was achieved over a wide range (37nm output) with less than 1dB power penalty. Transmission through Corning SMF-28 fiber was also measured for 25km and 50km distances at 1555nm yielding <1.2dB power penalty.

V. Conclusion

We demonstrate a hybrid wavelength converter that achieves 10Gbit/s operation. The use of high-gain, high saturation power receivers coupled with high bandwidth efficient modulators have been shown to allow the realization of viable wavelength conversion at high bit rates. We have demonstrated error-free wavelength conversion over 37nm with <1dB power penalty, and low input power (1.3mW) using a novel series push-pull photocurrent driven wavelength converter. Both chips utilize the same epitaxial platform and processing steps leading to simple integration.

Acknowledgement

The authors acknowledge Agility Communications for the regrowth of the transmitter and AR coating of both devices.

References

[1] Kodama S, Yoshimatsu T, Ito H. 320 Gbit/s error-free demultiplexing using ultrafast optical gate monolithically integrating a photodiode and electroabsorption modulator. Electronics Letters, vol.39, no.17, 21 Aug. 2003, pp.1269-70. Publisher: IEE, UK.

[2] Wolfson D, Fjelde T, Kloch A, Janz C, Poingt F, Pommereau F, Guillemot I, Gaborit F, Renaud M. Detailed experimental investigation of all-active dual-order mode Mach-Zehnder wavelength converter. Electronics Letters, vol.36, no.15, 20 July 2000, pp.1296-7.

[3] Olsson B-E, Ohlen P, Rau L, Blumenthal DJ. A simple and robust 40-Gb/s wavelength converter using fiber cross-phase modulation and optical filtering. IEEE Photonics Technology Letters, vol.12, no.7, July 2000, pp.846-8.

[4] Suzuki Y, Ito T, Shibata Y. "Monolithically integrated wavelength converter: Sagnac interferometer integrated with parallel-amplifier structure (SIPAS) and its application." 2002 LEOS Summer Topical Meetings IEEE.2002, ppWB2-12.

[5] Spiekman LH, Koren U, Chien MD, Miller BI, Wiesenfeld JM, Perino JS. All-optical Mach-Zehnder wavelength converter with monolithically integrated DFB probe source. *IEEE Photonics Technology Letters, vol.9, no.10, Oct. 1997, pp.1349-51.*

[6] Mašanovic M.L., V. Lal, J. S. Barton, E. J. Skogen, L. A. Coldren, D. J. Blumenthal "Monolithically Integrated Mach-Zehnder Interferometer Wavelength Converter and Widely-Tunable Laser in InP." IEEE Photonics Technology Letters, Aug. 2003.

[7] Walker RG. "High-speed III-V semiconductor intensity modulators." *IEEE Journal of Quantum Electronics, vol.27, no.3, March 1991, pp.654-67.*

[8] Barton JS, Masanovic ML, Sysak MN, Hutchinson JM, Skogen EJ, Blumenthal DJ, Coldren LA. 2.5-Gb/s error-free wavelength conversion using a monolithically integrated widely tunable SGDBR-SOA-MZ transmitter and integrated photodetector. *IEEE Photonics Technology Letters, vol.16, no.6, June 2004, pp1531-3*

[9] Sysak MN, Barton JS, Johansson LA, Raring JW, Skogen EJ, M. L. Mašanović, Blumenthal DJ, Coldren LA. "Single-chip wavelength conversion using a photocurrent-driven EAM integrated with a widely tunable sampled-grating DBR laser." *IEEE Photonics Technology Letters, vol.16, no.9, Sept. 2004, pp.2093-5.*

[10] Barton, J.S. Coldren, L.A. "Lumped electrode Series Push-Pull modulated Mach-Zehnder integrated widely-tunable transmitter" Submitted to Journal of Lightwave Technology Sept, 2004

[11] Tauke-Pedretti, Anna, M. M. Dummer, J. S. Barton, M.N. Sysak, J. Raring, and L.A.Coldren," Integrated Photoreceivers with High Saturation Power, High Gain and >20GHz Bandwidth", Submitted to Photonics Tech. Letts. Sept 2004.

Proc. IEEE/LEOS International Conference (NUSOD), paper no. ThC2, Berlin, Germany (September 2005)

Broadband Rate-Equation Model including Many-Body Gain for WDM Traveling-Wave SOAs

V. Lal, W. Donat, A. Tauke Pedretti, L. Coldren, D. Blumenthal, and J. Piprek*

Electrical and Computer Engineering Department, University of California, Santa Barbara, CA 93106, U.S.A.
* e-mail: piprek@ieee.org

Abstract – **We present a traveling-wave rate-equation model for wavelength-division multiplexing (WDM) semiconductor optical amplifiers (SOA) which utilizes many-body gain spectra. Good agreement with measurements is obtained across a broad wavelength range.**

I. INTRODUCTION

Broadband semiconductor optical amplifiers (SOAs) are of great interest for wavelength-division multiplexing (WDM) and other multi-wavelength optical communication systems. The wavelength sensitivity of the device performance is of special concern, in our case for a wavelength range from 1525 nm to 1565 nm.

We here present an SOA rate-equation model which gives good agreement with measured device characteristics over a broad wavelength range due to the inclusion of many-body gain spectra. To demonstrate and validate this model, we investigate ridge-waveguide devices with an InGaAsP multi-quantum-well (MQW) active region grown on top of the waveguide layer.[1] Our example SOA is 400μm long and the waveguide ridge is 3μm wide. More device details are given elsewhere.[2]

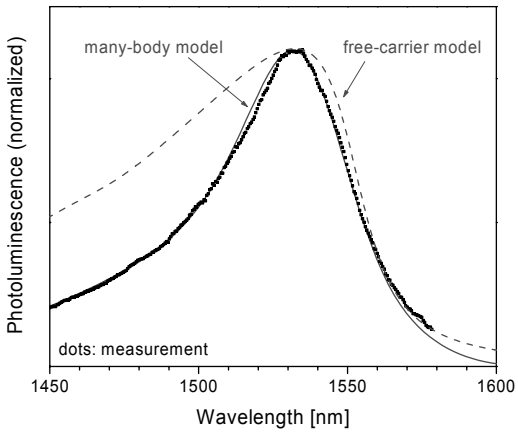

Fig. 1 Photoluminescence spectrum (dots: measured, dashed: free carrier model, solid: many-body model).

II. GAIN MODEL

The accurate modeling of quantum well properties, in particular the optical gain is prerequisite for a realistic simulation of broadband devices. We initially employed the free-carrier gain model by Chinn et al. [3] including 4x4 kp band structure calculations and a Lorentz energy broadening function.[4] However, this approach did not give consistent agreement with experimental results, especially the measured wavelength dependence was not reproduced correctly. This becomes clear from comparison to the measured photoluminescence spectrum (Fig. 1) which exhibits discrepancies on both sides of the spectrum. The many-body gain theory by Koch et al. [5] provides a much better agreement across the entire spectrum (solid curve in Fig. 1). Gain spectra from both models are shown in Fig. 2 which reveal substantial differences not only in shape but also in magnitude. In strong contrast to the free-carrier model, the many-body spectra indicate relatively uniform SOA performance across the C-band, which is in agreement with our experimental observations.

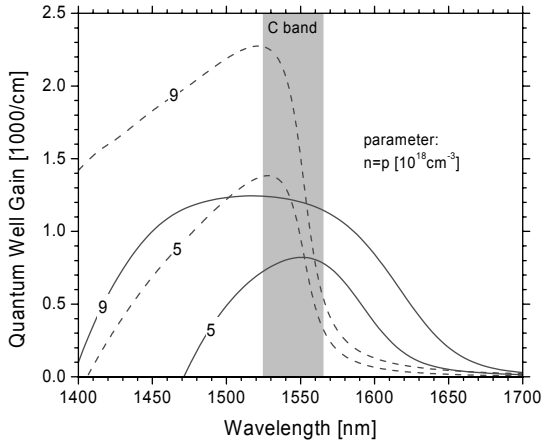

Fig. 2. Calculated gain spectra at two different carrier densities (dashed: free carrier model, solid: many-body model).

III. RATE-EQUATION MODEL

We employ a traditional rate-equation model for the quantum well carrier density and the photon density including non-radiative and spontaneous recombination.[6] As the carrier and photon densities are longitudinally non-uniform in our traveling-wave SOA, we break the active region into a number of much smaller sections, within which we can approximate the densities as uniform. The optical gain in each section is a function of the local carrier density and the signal wavelength.

It is extracted from many-body gain tables purchased from Nonlinear Control Strategies (Tucson, AZ)[7] that have been adjusted to our photoluminescence measurements as described elsewhere.[8]

The rate-equation model employs a number of material parameters which are critical to obtain good agreement with measurements. We assume typical values for the defect recombination lifetime (τ_{SRH} = 20 ns), the spontaneous emission coefficient (B = 0.8 10^{-10} cm^3/s), and the modal loss (α_i = 10 cm^{-1}). The injection efficiency η_i = 82% and the optical confinement factor Γ = 0.06 are extracted from an advanced device simulation.[8] The only fit parameter used here is the Auger coefficient C = 2.4 x 10^{-29} cm^6/s which lies well within the range reported in the literature.[9] Amplified spontaneous emission (ASE) effects are negligibly small.

IV. RESULTS

The fabricated device has a monolithically integrated photodetector at the output of the SOA, which was used to measure the output power.[1] This allows us to measure the output power easily and accurately, eliminating any coupling losses that would results if the detector was off-chip. Figure 3 shows the measured SOA gain (dots) as a function of wavelength along with the simulation result (line). The input power P_{in} is kept low to avoid saturation effects. The simulation is in good agreement with the measured data across a broad wavelength range. The deviation seen at the short-wavelength side may be attributed to slight inaccuracies in the calculated gain spectrum. The injection current density of j = 7.5 kA/cm^2 is sufficiently low to exclude self-heating effects and to assume room temperature in the simulation.

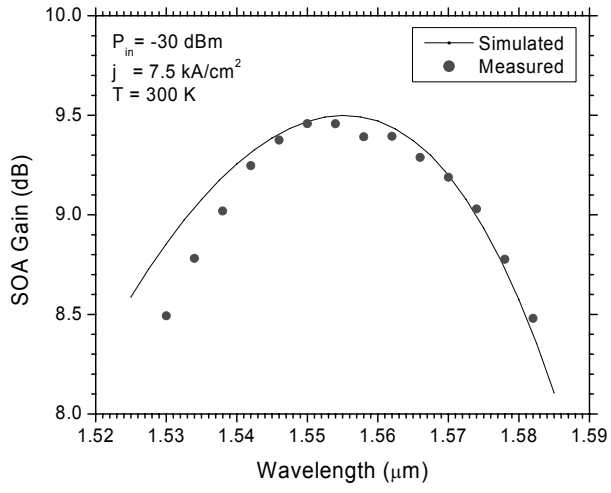

Fig. 3: Unsaturated SOA gain vs. wavelength at low injection current.

Figure 4 shows the output power at 1558 nm as a function of the input power. The measurement is very well reproduced by the model up to about 3 mW output power. Above this power level, saturation sets in as the photon density near the output facet becomes high enough for the stimulated recombination to substantially increase the total carrier recombination rate in the quantum well. Consequently, the carrier density drops and so does the SOA output power. The slight high-power deviation in Fig. 4 shows that the saturation is somewhat stronger in the measurement than calculated, which can be attributed to a slight overestimation of the carrier density in the simulation.

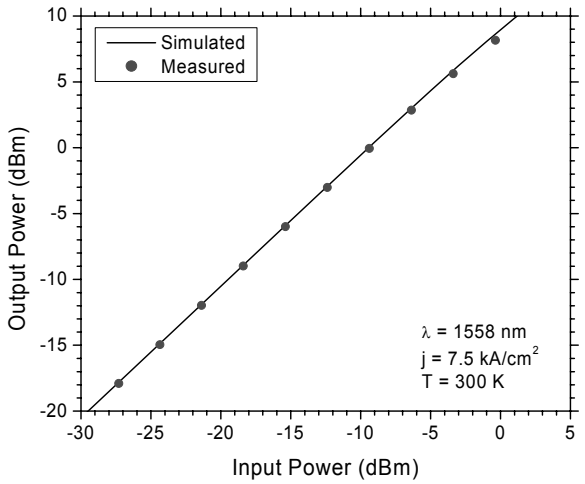

Fig. 4: SOA output power vs. input power.

In summary, we have demonstrated that relatively simple rate-equation models for traveling-wave semiconductor optical amplifiers can deliver realistic performance characteristics across a broad wavelength range by employing an advanced many-body model for the optical gain spectrum.

ACKNOWLEDGEMENT

This work was sponsored in part by the Semiconductor Research Corporation and by the Intel Corporation.

REFERENCES

[1] A. Tauke Pedretti, M. Dummer, J. Barton, M. Sysak, J. Raring, L. Coldren, "Integrated Photoreceivers with High Saturation Power, High Gain and > 20 GHz Bandwidth," to be published in IEEE Phot. Technol.Lett. (2005).

[2] J. Piprek, J. Hutchinson, J. Henness, M. Masanovic, and L. A. Coldren, "Saturation Analysis of a Monolithic Wavelength Converter," in: *Physics and Applications of Optoelectronic Devices*, SPIE Proc. 5594, p. 102, 2004.

[3] S. Chinn, P. Zory, and A. Reisinger, "A Model for GRIN-SCH-SQW Diode Lasers," IEEE J. Quantum Electron., vol. 24, pp. 2191-2214 (1988)

[4] S. L. Chuang, *Physics of Optoelectronic Devices,* Wiley, New York, 1995.

[5] S.W. Koch, J. Hader, A. Tränhardt, and J.V. Moloney, "Gain and Absorption: Many-Body Effects," Ch. 1 in: J. Piprek (ed.), *Optoelectronic Devices: Advanced Simulation and Analysis*, Springer, New York, 2005.

[6] L. A. Coldren and S. W. Corzine, *Diode Lasers and Photonic Integrated Circuits,* Wiley, New York, 1995.

[7] www.nlcstr.com

[8] J. Piprek, S. Li, P. Mensz, and J. Hader, "Monolithic Wavelength Converter," Ch. 14 in: J. Piprek (ed.), *Optoelectronic Devices: Advanced Simulation and Analysis*, Springer, New York, 2005.

[9] J. Piprek, *Semiconductor Optoelectronic Devices: Introduction to Physics and Simulation*, Academic Press, San Diego, 2003.

Proc. LEOS 2005, The 18th Annual Meeting of the IEEE, paper no. TuT2, Sydney, Australia (October 23-27, 2005)

Monolithic Widely-Tunable All-Optical Wavelength Converter with Spatial Filtering of Input and Output Signals for 10Gbps NRZ Operation

Joseph A. Summers, Milan L. Mašanović, Vikrant Lal,
Larry A. Coldren, Daniel J. Blumenthal
Department of Electrical and Computer Engineering, University of California, Santa Barbara, CA 93106-9560, USA
jsummers@ece.ucsb.edu

1. Introduction

Wavelength converters (WCs) are key components of next generation WDM optical networks, enabling functions such as wavelength routing, add/drop multiplexing, contention resolution and signal regeneration. Among the variety of available wavelength conversion schemes, semiconductor-based WCs have generated substantial interest due to their potential for monolithic integration of several components on chip.

Recent integration efforts by our group have successfully demonstrated monolithic integration of widely-tunable SG-DBR lasers with Mach Zehnder Interferometer (MZI) SOA-based WCs using an offset quantum well (OQW) integration platform in InP [1]. These previous integrated designs have relied on the use of an external tunable bandpass filter at the output of the device to remove the input signal from the converted signal. Such filters must be tuned to the output wavelength, introduce additional loss and can cause signal distortion at high bit rates due to the limited bandwidth of the filter function. An external filter also inhibits integration by preventing cascading of WCs with other active components on chip.

To replace the function of an external filter, several schemes have been introduced which spatially filter the input signal from the output signal on chip [2,3,4]. These schemes have proven to be effective at providing >20 dB of separation between the input and output signals and have been demonstrated at speeds up to 10Gbps NRZ.

This paper describes a new approach to a spatially-filtered MZI-SOA based widely-tunable wavelength converter showing error-free operation, and fabricated using our standard OQW integration platform.

2. Design and Operation

A schematic of the wavelength converter design is shown below in Figure 1. The input pump signal enters the device through a waveguide (shown as a black line) on the left and is amplified by a pre-amp SOA before entering a 2x2 MMI splitter/combiner. The MMI evenly distributes the input signal between the top two arms of a three-arm MZI, and combines it with a portion of the CW SG-DBR probe signal. The pump and probe signals co-propagate out of phase in the identical SOAs of the top two arms, and as the pump depletes carriers through stimulated emission, the probe in both arms is modulated by both cross-gain (XGM) and cross-phase (XPM) modulation. The signals from the two arms interfere through a second 2x2 MMI splitter/combiner, which images the probe and the pump to separate waveguides due to their opposite phase as described in [4]. Phase electrodes in the top two arms allow this phase to be tuned to optimize signal separation, or to statically switch them from one output port to the other. To utilize the XPM in the top two arms, the pump signal is routed to an absorber, and the modulated SG-DBR probe signal is recombined with the CW SG-DBR probe signal in the bottom arm of the MZI using a 2x2 MMI splitter/combiner. A phase electrode in the bottom arms allows the extinction of the converted signal to be optimized and the wavelength converter to be switched between inverting and non-inverting modes of operation.

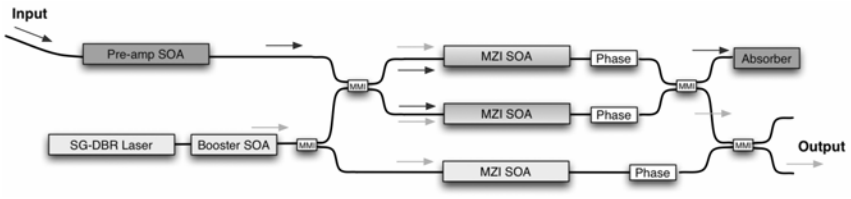

Fig. 1. Schematic of the widely-tunable MZI-SOA wavelength converter with spatial filtering of input and output signals

3. Results

For good thermal and electrical conduction, the device was soldered onto a copper bar and maintained at 16˚C using a thermo-electric cooler. DC needle probes provided current to the SOAs and phase electrodes, and light was coupled into and out of the device using lensed fibers mounted on piezo-controlled translational stages.

The input pump signal was produced by a tunable laser operating at 1550nm and encoded with 2^7-1 PRBS data at 10Gbps NRZ using a pattern generator and an electro-optic modulator. Erbium doped fiber amplifiers (EDFAs) were placed before and after the device to amplify the input and output signals.

The SG-DBR was tuned to several output wavelengths over 30nm, and the phase of the top MZI arm was adjusted to minimize the presence of the input signal at the output of the device for each wavelength. The output spectrum is shown on the left of Figure 2 for conversion from 1550nm to 1555nm. This demonstrates more than 20dB of separation between the input pump and converted probe signals. The corresponding eye diagrams for the input and converted signal are shown on the right of Figure 2, with the device operating in inverting mode.

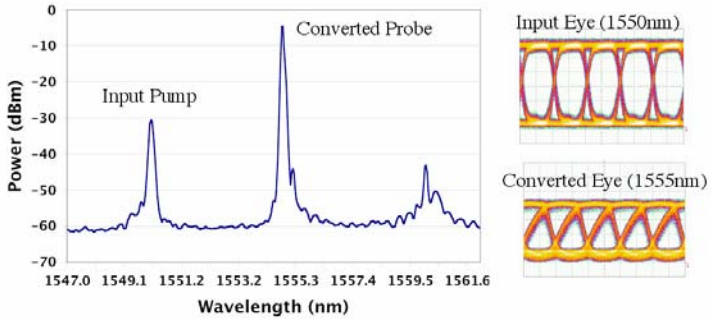

Fig. 2. Output spectra for wavelength conversion from 1550nm to 1555nm (left); with corresponding eye diagrams for the input signal (top right) and converted signal (bottom right)

Bit error rates were performed on the wavelength converter for conversion from 1550nm to two different output wavelengths of 1555nm and 1540nm. These curves are shown in Figure 4, showing approximately 3dB of power penalty from the devices.

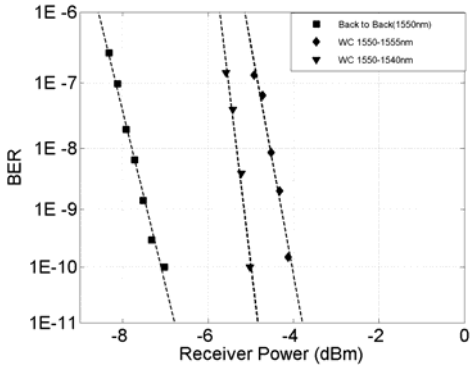

Fig. 3. Bit error rate curves for 2^7-1 PRBS data at 10Gbps NRZ for conversion from 1550nm to 1555nm, and 1550nm to 1540nm.

This work was supported by DARPA/MTO CS-WDM Program under Grant No. N66001-02-C-8026.

[1] M. L. Masanovic, V. Lal, J. A. Summers, J. S. Barton, E. J. Skogen, L. A. Coldren, and D. J. Blumenthal, "Design and Performance of a Monolithically-Integrated Widely-Tunable All-Optical Wavelength Converter with Independent Phase Control," IEEE Photonics Technology Letters **16** , 2299-2301 (2004)

[2] D. Wolfson, T. Fjelde, A. Kloch, C. Janz, F. Poingt, F. Pommereau, I. Guillemot, F. Gaborit, and M. Renaud, "Detailed experimental investigation of all-active dual-order mode Mach-Zehnder wavelength converter," Electronics Letters **36**, 1296–1297 (2000).

[3] J. Leuthold, P-A. Besse, E. Gamper, M. Dülk, S. Fischer, G. Guekos, H. Melchior, "Wavelength Converters and Switches with Integrated Data- and Control-Signal Separation Scheme," Journal of Lightwave Technology **17**, 1056-1066 (1999).

[4] Y. Shibata, N. Kikuchi, S. Oku, T. Ito, H. Okamoto, Y. Kawaguchi, Y. Suzuki, Y. Konudo, "Monolithically Integrated Parallel Amplifiers Structure for Filter-free Wavelength Conversion," Int. Conf. on Indium Phosphide and Related Materials (IPRM, 2001).

Cross-Phase Modulation Efficiency in Offset Quantum-Well and Centered Quantum-Well Semiconductor Optical Amplifiers

Milan L. Mašanović, *Member, IEEE*, Vikrant Lal, *Student Member, IEEE*, Erik J. Skogen, *Member, IEEE*, Jonathon S. Barton, *Member, IEEE*, Joseph A. Summers, *Student Member, IEEE*, James A. Raring, *Student Member, IEEE*, Larry A. Coldren, *Fellow, IEEE*, and Daniel J. Blumenthal, *Fellow, IEEE*

***Abstract*—We conduct an experimental study of cross-phase modulation efficiency for semiconductor optical amplifiers with two different active regions—offset quantum-well (OQW) stack and centered quantum-well (CQW) stack. OQW devices exhibit less than 100° phase change, whereas CQW devices are 60% more efficient for the same pump input power, with more than 200° phase change possible. The input wavelength degrades the phase change significantly outside the 30-nm gain bandwidth window.**

***Index Terms*—Cross-phase modulation (XPM), photonic integrated circuits (PICs), semiconductor optical amplifier (SOA), wavelength conversion, wavelength converter.**

I. Introduction

SEMICONDUCTOR optical amplifiers (SOAs) represent one of the key components of modern photonic integrated circuits (PIC). These devices are used to perform a variety of functions on a chip, such as linear signal preamplification [1], boosting of the signal level of integrated sources [2], optical gating [1], as well as nonlinear functions used in PICs like SOA-based wavelength converters [1]–[4]. Quantification of the SOA nonlinear behavior is presented in this letter, for two commonly used SOA active region structures/integration platforms, employing centered and offset quantum wells (OQWs) [4], [5]. The choice of the SOA active region design depends on the desired application, and will influence the SOA properties such as achievable gain, saturation power, and nonlinearity. The main difference between the offset and centered quantum-well (CQW) platforms is in the extent of overlap of the mode with the active region. Larger overlap, for the case of CQWs, increases the gain and nonlinearity of an SOA, while also reducing the SOAs output saturation power. More details about this can be found elsewhere [1].

Application of SOA nonlinearities is particularly of interest in SOA integrated wavelength converters [2]–[6], which are good candidates for deployment into the future optical networks. These wavelength converters exploit the nonlinear interactions between pump and probe photons at two different wavelengths in the SOA active medium in order to transcribe the original input information onto a new wavelength.

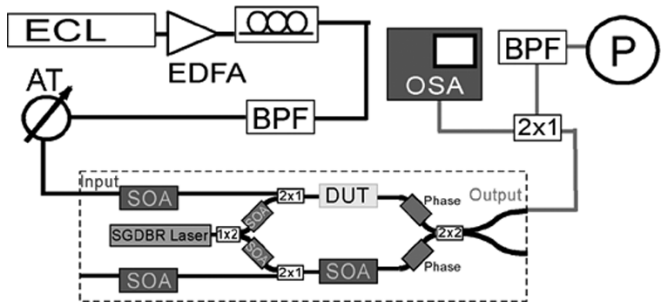

Fig. 1. Experimental setup.

Some of the most promising integrated wavelength converters utilize the effect of cross-phase modulation (XPM) in an SOA. XPM in an SOA is caused by the input bit stream which reduces the carrier density in the active region, compressing the gain of the active region, thereby causing a temporal refractive index change, and as a consequence a temporal optical phase change. This phase change will be imprinted onto a probe continuous-wave signal concurrently propagating through the same SOA [1], [2]. For wavelength conversion of intensity modulated signals, the phase change in the SOA needs to be converted to an amplitude change. This is achieved by using optical filtering, either through an SOA interferometric structure [2], or by using a bandpass filter after the SOA [3].

Despite the popularity of integrated XPM-based SOA wavelength converters, detailed examination of the XPM efficiency of different integration platforms, to the best of our knowledge, has not been reported. This efficiency will directly impact the output power, optical signal-to-noise ratio, and extinction ratio of the SOA based wavelength converters.

We perform a thorough comparison of XPM efficiencies, measured by the amount of achievable optical probe phase change caused by the pump signal power change, for SOAs fabricated in two widely used integration platforms using an OQW active region [6], and using a CQW active region [5].

II. Measurement Method

The phase change measurements are performed indirectly, utilizing two different monolithically integrated widely tunable Mach–Zehnder interferometer (MZI)-SOA wavelength converters (Fig. 1), realized in the OQW platform [4], [6], and also

Manuscript received March 3, 2005; revised July 25, 2005. This work was supported by Defense Advanced Research Projects Agency (DARPA)/MTO CS-WDM Program under Grant N66001-02-C-8026.

The authors are with the Electrical and Computer Engineering Department, University of California Santa Barbara, Santa Barbara, CA 93106 USA (e-mail: mashan@ece.ucsb.edu).

Digital Object Identifier 10.1109/LPT.2005.858162

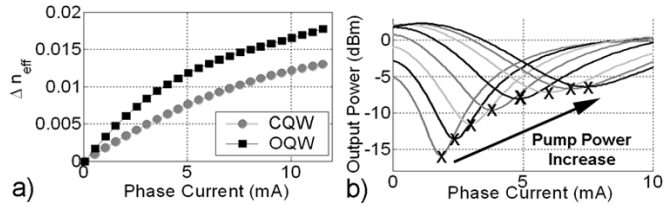

Fig. 2. (a) Effective index change in function of phase current (b) OERC family of curves for increasing pump power.

in the CQW platform that employs quantum-well intermixing [5]. For both device types, OQW and CQW, all SOAs and active regions on chip are realized in the same platform, respectively. The chips also contain a number of passive sections, where the quantum wells have either been etched off (OQW) [4] or intermixed (CQW) [5].

Data about the effective index change as a function of a passive waveguide section's electric bias current can be obtained by observing the shift in the reflected amplified spontaneous emission from the sampled-grating distributed Bragg reflector (SGDBR) laser mirror peaks, while pumping the SGDBR mirror with different current densities [7]. This data is shown in Fig. 2(a), for both OQW and CQW cases.

MZI-SOA interferometer on each device contains the same type of passive waveguide phase section, which enables the interferometer phase control through current injection [4], resulting in a characteristic interferometer optical–electrical response curve (OERC) [4], [6].

Measuring OERC for different optical power levels of the pump signal in the device under test (DUT) yields a family of curves shown in Fig. 2(b). The minima of the curves, as a function of phase electrode current, are shifted due to the different amounts of index change caused by the external pump signal in the DUT. This index change is proportional to the phase electrode current at the minimum of the OERC. Using the relationship between the phase electrode current density and effective index change (Fig. 2(a)) previously obtained, we can relate the total phase change to the optical power level of the pump signal.

III. Experimental Procedure

The XPM efficiency is measured in one of the MZI-SOAs of these integrated devices (labeled DUT in Fig. 1 [6]), which makes the measurements stable and reproducible. The experimental setup is shown in Fig. 1. The input pump signal is generated by an external cavity laser, amplified by an erbium-doped fiber amplifier (EDFA), filtered using a tunable bandpass filter (BPF), and its power is controlled using an optical attenuator. The polarization of the light is controlled before the light is coupled to the input waveguide of the device. The light from the SGDBR laser is equally split on-chip between the two branches of the MZI, and amplified by the booster SOAs before reaching the MZI-SOAs (Fig. 1) [4]. The bias of the DUT (Fig. 1), is controlled by a high precision source meter, which allows for both forward and reverse biasing of the DUT while measuring the current with a precision greater than 1 μA. The output of the interferometer is coupled to a lensed fiber and then split and led to an optical spectrum analyzer, and through an optical BPF to an optical power meter (Fig. 1). Optical power level for the pump signal is controlled by the on-chip preamplifier SOA bias, whereas the probe power level is controlled by the on-chip booster SOA bias [4]. Before each OERC is taken, probe and pump power levels are measured (individually) by reverse biasing the DUT, which then acts as a photodiode with 100% quantum efficiency, and recording the photocurrent. Knowing the quantum efficiency and the responsivity of this photodiode allows for translation of this photocurrent into the optical power. Finally, families of OERCs are taken for different power level, DUT bias, and pump–probe wavelength combinations. The other MZI-SOA's bias current is kept constant, as well as the probe power, throughout the given measurement. This data is analyzed and converted into the phase change data as explained in the Section II.

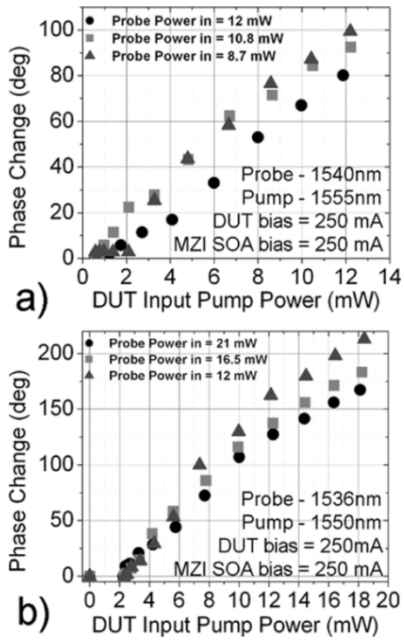

Fig. 3. XPM efficiency as function of probe power (for varied pump powers) (a) OQW (b) CQW.

IV. Results

Fig. 3 shows the results for the DUT phase change as a function of the pump (input signal) power entering the DUT, for different probe (SGDBR) powers coupled into the DUT. Higher probe power results in the lower initial carrier concentration in the DUT, thereby setting the amount of gain compression attainable for the given pump signal power, and thus limiting the maximum phase change. For high-speed wavelength conversion, on the other hand, high photon density caused by the high SGDBR probe power in the DUT is desirable in order to reduce the gain recovery time [1]–[4]. Therefore, a tradeoff exists in order to optimize the speed of operation while maximizing the conversion efficiency. The OQW device experiences a maximum phase change of 100°, whereas the CQW device exhibits a phase change of up to 160° for the same pump power (Fig. 2(a) and (b), respectively). The input pump signal power is limited by the maximum attainable gain in the preamplifier SOA (Fig. 1). Due to higher confinement of about 12% (compared to 7% for the OQW), CQW-based preamplifiers provide more gain at a given amplifier length, thus, phase change data for higher power levels exists for the CQW SOA.

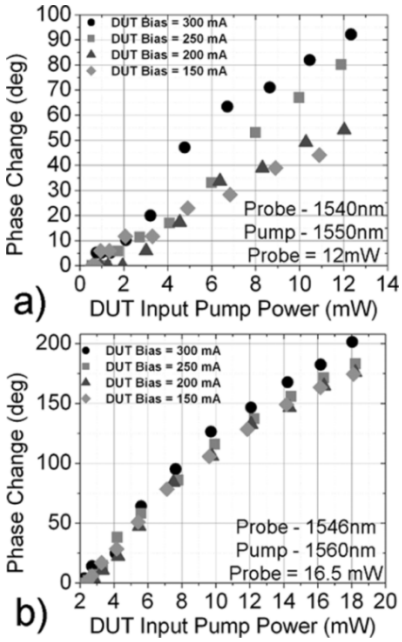

Fig. 4. XPM efficiency as function of DUT bias current (for varied pump power) (a) OQW (b) CQW.

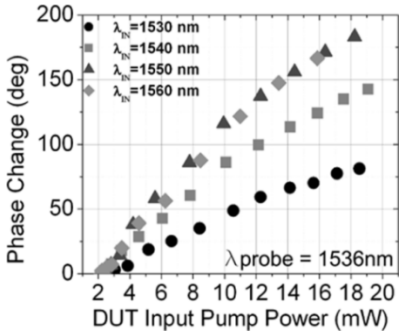

Fig. 5. XPM efficiency wavelength dependence (CQW).

The refractive index change primarily occurs in the active region of the SOA. The modal index then is proportional to this index change and the confinement factor of the mode.

Higher phase change of the CQW SOAs compared to OQW SOAs can be explained by two effects: higher confinement factor, which then increases the modal index change, and higher available gain (over the given SOA length), which allows for more gain compression and more nonlinear behavior of the CQW SOAs.

Fig. 4 shows the XPM efficiency measurements for varying DUT bias current. OQW SOAs exhibit more dependence, primarily due to their higher input saturation power when compared to the CQW SOAs. Increased DUT bias current increases the amount of phase change possible.

High bias current of the DUT is compatible with the high-speed operating conditions of the MZI-SOA WC [1]–[4], so in this case, both efficiency and high-speed operation conditions are satisfied simultaneously.

Wavelength dependence of the XPM of the quantum-well stack used was studied as well, and the results are shown in Fig. 5. The reasons for this dependence is in the wavelength dependence of the quantum-well gain [7]. Since both device realizations utilize the same quantum-well designs, the wavelength dependence will be similar. The results shown are for the CQW case. The XPM efficiency decreases significantly with wavelength change (25% over 20 nm), and is maximum at the gain peak of the quantum wells (1555 nm in this case). The same dependence is expected of the longer wavelength side of the gain peak, but could not be measured due to limited gain bandwidth of the EDFA used.

V. Summary and Conclusion

In this letter, we have reported on the comprehensive investigation of the XPM efficiency for two different types of SOAs, fabricated in two commonly used integration platforms in InP, based on OQW and CQW active regions. The measurements were performed using an interferometric phase measurement method enabled by employing integrated tunable wavelength converter devices [4], [5]. With carrier and photon densities in the DUT set equivalent to conditions that would allow for high-speed wavelength conversion [6], OQW devices exhibit less than 100° phase change, whereas CQW devices are 60% more efficient for the same pump input power, with more than 200° phase change possible. The input wavelength dependence is significant, and the XPM efficiency is limited by the DUT gain bandwidth window. Overall, CQW SOAs are better candidates for realization of the XPM-based wavelength converters [5]. However, OQW devices can provide more linear gain with higher saturation powers due to their lower optical confinement factor [6].

Acknowledgment

The authors would like to thank Agility Communications for metal–organic chemical vapor deposition growth and antireflection coating services.

References

[1] M. J. Conelly, *Semiconductor Optical Amplifiers*. Norwell, MA: Kluwer, 2002.

[2] C. Joergensen, S. L. Danielsen, K. E. Stubkjaer, M. Schilling, K. Daub, P. Doussiere, F. Pommerau, P. B. Hansen, H. N. Poulsen, A. Kloch, M. Vaa, B. Mikkelsen, E. Lach, G. Laube, W. Idler, and K. Wunstel, "All-optical wavelength conversion at bit rates above 10 Gb/s using semiconductor optical amplifiers," *IEEE J. Sel. Topics Quantum Electron.*, vol. 3, no. 5, pp. 1168–1180, Oct. 1997.

[3] J. Leuthold, L. Moller, J. Jaques, S. Cabot, L. Zhang, P. Bernasconi, M. Cappuzzo, L. Gomez, E. Laskowski, E. Chen, A. Wong-Foy, and A. Griffin, "160 Gbit/s SOA all-optical wavelength converter and assessment of its regenerative properties," *Electron. Lett.*, vol. 40, pp. 554–555, 2004.

[4] M. L. Mašanović, V. Lal, J. A. Summers, J. S. Barton, E. J. Skogen, L. A. Coldren, and D. J. Blumenthal, "Design and performance of a monolithically integrated widely tunable all-optical wavelength converter with independent phase control," *IEEE Photon. Technol. Lett.*, vol. 16, no. 10, pp. 2299–2301, Oct. 2004.

[5] V. Lal, M. L. Mašanović, E. J. Skogen, J. W. Raring, J. A. Summers, L. A. Coldren, and D. J. Blumenthal, "Quantum-well-intermixed monolithically integrated widely tunable all-optical wavelength converter operating at 10 Gb/s," *IEEE Photon. Technol. Lett.*, vol. 17, no. 8, pp. 1689–1691, Aug. 2005.

[6] M. L. Mašanović, V. Lal, J. S. Barton, E. J. Skogen, J. A. Summers, L. Rau, L. A. Coldren, and D. J. Blumenthal, "Widely tunable monolithically integrated all-optical wavelength converters in InP," *J. Lightw. Technol.*, vol. 23, no. 3, pp. 1350–1362, Mar. 2005.

[7] L. A. Coldren and S. W. Corzine, *Diode Lasers and Photonic Integrated Circuits*. New York: Wiley, 1995.

I. Photonic Integrated Circuits (PICs) and Related Technology

D. 980nm Edge-Emitter Technology

980 nm DBR Lasers Monolithically Integrated with EA Modulators for Optical Interconnect Applications

Gordon B. Morrison, Chad S. Wang, Erik J. Skogen, Daniel D. Lofgreen, and Larry A. Coldren
ECE Dept. University of California, Santa Barbara, CA 93106

Phone: 805.893.2875, Fax: 805.893.4500, Email: gmorrison@ece.ucsb.edu

Abstract: Short-cavity InGaAs/GaAs/AlGaAs lasers with first order DBRs and integrated EAMs were fabricated using a quantum well intermixing process. >5mW output was achieved at 45mA. DC extinction was >15dB at -1.5V with efficiencies up to 20dB/V.

OCIS codes: (140.5960) Semiconductor lasers; (250.5300) Photonic Integrated Circuits

1. INTRODUCTION

The rapidly increasing complexity of modern computing systems has led to a demand for higher clock frequencies over longer path lengths. Meeting the bandwidth and path length requirements of modern computer systems is becoming increasingly difficult using traditional electrical connections. For this reason, chip to chip optical interconnects (C2OI) are being considered as promising candidates for replacement of electrical interconnects in future computing systems [1]. In addition to having high bandwidth-path length products, optical interconnects exhibit low cross talk, are free from electro-magnetic interference (EMI), and promise lower delay times than their electrical counterparts.

Highly efficient short cavity integrated DBR (distributed Bragg reflector) laser/EAM (electro-absorption modulator) transmitters for C2OI applications have previously been demonstrated at 1550 nm using quantum well intermixing (QWI) [2]. Quantum well intermixing has been demonstrated as an elegant technique for integration of photonic ICs at both 1550 [3] and 980 nm [4]. In the high temperature environment of modern IC's, 980 nm technologies will be required. In this paper we describe the fabrication of novel, short cavity, integrated DBR laser/EAM transmitters operating at 980 nm. The devices are fabricated using a unique QWI technique to monolithically integrate multiple band edges on chip. In addition, a novel immersion holography technique was used to obtain first order 980 nm Bragg reflectors. The devices exhibit single mode operation and have excellent extinction characteristics.

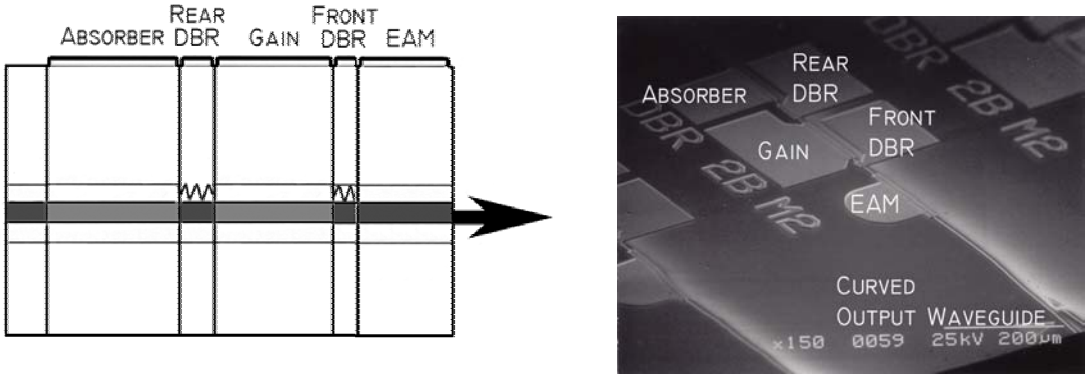

(a) (b)

FIGURE 1. (a) Side view schematic and (b) electron micrograph of the completed short-cavity DBR laser, illustrating the monolithic integration of the Gain, front and rear DBRs, and EAM sections along with a curved output waveguide.

2. EXPERIMENT

Short cavity (110 µm) DBR lasers with first order gratings were designed with 48 µm rear mirrors and 16 µm front mirrors. The laser was integrated with a 125 µm EAM by way of a quantum well intermixing process compatible with regrowth [4]. QWI allows for selective blue shifting of the semiconductor band edge so that each

component of the transmitter can be optimized individually. The first order 980 nm gratings, which require a pitch of approximately 151 nm, were fabricated by an immersion holography technique, which was developed to avoid the expensive and time consuming process of Ebeam lithography. A curved waveguide makes an angle of 8º with the output facet, thereby minimizing unwanted reflective feedback. A side-view schematic and scanning electron micrograph of the device are shown in Fig. 1a and 1b, respectively.

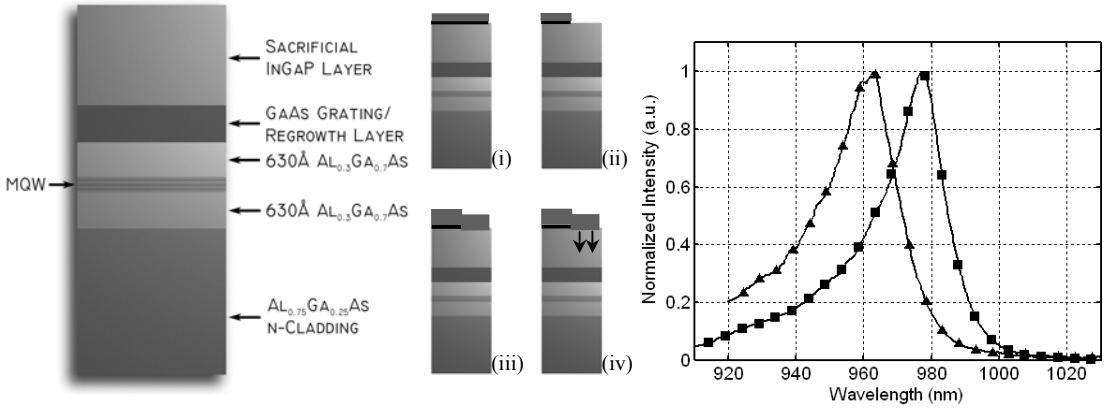

(a) (b)

FIGURE 2. (a) The left shows the epitaxial base structure. The right illustrates the intermixing process used for band edge optimization in this work: (i) surface fluorination followed by SiO_2 deposition; (ii) patterning of the SiO_2 and fluorination layer; (iii) deposition of the second SiO_2 layer; and (iv) rapid thermal annealing to drive vacancies down through the multiple quantum well active region. (b) Normalized photoluminescence spectra for the active (squares) and EAM (triangles) band edges of the device.

3. PROCESS

The epitaxial base structure, as shown in Fig. 2a, was grown on a silicon-doped GaAs substrate by Molecular Beam Epitaxy (MBE). The structure contained an $Al_{0.75}Ga_{0.25}As$ n-cladding region below a multi-quantum well (MQW) active region centered within an $Al_{0.3}Ga_{0.7}As$ waveguide. The MQW consists of 3 InGaAs 8 nm compressively strained quantum wells, separated by 8 nm GaAs barriers. Following the active region, a 65 nm GaAs layer was grown, which serves as part of the grating layer as well as an aluminum-free regrowth interface layer. Finally, a 300 nm sacrificial InGaP layer completed the base structure.

The quantum well intermixing process, as illustrated in Fig. 2a, begins with a surface fluorination treatment of the sacrificial InGaP layer using an SF_6 plasma. A 100 nm layer of SiO_2 is then deposited by plasma enhanced chemical vapor deposition. The SiO_2 is lithographically patterned and etched in BHF so that it only remains where the as-grown band edge is desired. Developer is used to strip the fluorination layer from the semiconductor in regions not protected by the SiO_2. A second, 200 nm layer of SiO_2 is then deposited. In regions where the fluorination layer was removed, the SiO_2 creates vacancies in the InGaP buffer layer. In regions where the fluorination layer remains, the SiO_2 is unable to interact with the semiconductor. The vacancies created in the non-fluorinated parts of the semiconductor are driven into the multiple quantum well active region by rapid thermal annealing at 850 ºC for a time of 5'45". The vacancies promote the diffusion of atoms across the well/barrier interfaces, thereby altering the shape of the quantum wells and producing a blue shift of the band edge. Fig. 2b shows photoluminescence spectra from the as-grown (active) and intermixed (modulator) regions of the device. The active band edge is at $\lambda_{pl} = 977$ nm, and the modulator band edge is at $\lambda_{pl} = 963$ nm.

Following quantum well intermixing, the sacrificial InGaP layer is removed, and gratings are patterned and etched in the GaAs layer. Standard holography techniques using our HeCd 325 nm UV laser cannot produce Bragg gratings with the 151 nm pitch necessary for first order 980 nm DBR gratings. Immersion holography is therefore used to obtain the desired pitch. In this process, photoresist is first spun onto the sample, and a thin layer of index matching fluid is used to adhere the sample to a prism. By this method, the holographic grating pitch is reduced by a factor of *n*, where *n* is the index of the prism. The gratings are then etched into the GaAs using inductively coupled plasma. An MBE regrowth of the $Al_{0.75}Ga_{0.25}As$ upper p-cladding filled in the gratings to achieve a high

index contrast; this was then capped with a highly doped GaAs p-contact layer. Ridge waveguides, 3 μm wide, were patterned and etched. Ti/Pt/Au p-metal contacts were patterned, the wafer was thinned, backside metalized, and the devices were cleaved into bars.

4. RESULTS

Figure 3a shows voltage and optical output power as a function of injection current for the DBR laser operating CW. A low threshold current of 9 mA was measured, and output powers greater than 5 mW were achieved with a gain section current of 45 mA. The optical output power is significantly decreased by attenuation due to the long waveguide associated with the curved output waveguide. The devices demonstrated single mode lasing at 978 nm with >30 dB side mode suppression, as shown in Fig. 3b. Figure 3c presents the DC modal extinction characteristics of the EAM with the laser biased at 40 mA. Greater than 15 dB optical extinction was measured at a reverse bias of -1.5 V. High extinction efficiencies were exhibited, with a maximum efficiency of 20 dB/V at a bias of -1 V.

5. CONCLUSION

Short cavity, 980 nm monolithic integrated laser/modulator devices have been designed, fabricated, and tested. Immersion holography, a faster, simpler, and more cost effective approach compared to Ebeam lithography, was used to obtain first order 980 nm Bragg gratings. The devices were fabricated using QWI for the monolithic integration of the DBR laser and EAM components. The lasers exhibited excellent single mode characteristics, and the 125 μm modulator demonstrated >15 dB DC extinction and high extinction efficiencies.

6. REFERENCES

[1] M.R. Feldman, S.C. Esener, C.C. Guest, and S.H. Lee, "Comparison between optical and electrical interconnects based on power and speed considerations," *Applied Optics*, vol. 27, pp. 1742-1751, 1988.

[2] E.J. Skogen, C.S. Wang, J.W. Raring, G.B Morrison, and L.A. Coldren, "Small Footprint, High-Efficiency, Integrated Transmitters for High Speed Optical Interconnect Applications", *Proc. Integrated Photonics Research*, paper no. IThD2, San Francisco, CA, USA, 2004.

[3] E. Skogen, J. Raring, J. Barton, S. DenBaars, and L. Coldren, "Post-Growth Control of the Quantum-Well Band Edge for the Monolithic Integration of Widely-Tunable Lasers and Electroabsorption Modulators," *IEEE J. Sel. Topics in Quantum Electron*., vol. 9, pp. 1183-1190, 2003.

[4] S. Charbonneau, E.S. Koteles, P.J. Poole, J.J. He, G.C. Aers, J. Haysom, M. Buchanan, Y. Feng, A. Delage, F. Yang, M. Davies, R.D. Goldberg, P.G. Piva, and I.V. Mitchell, "Photonic Integrated Circuits Fabricated Using Ion Implantation," *IEEE J. Sel. Topics in Quantum Electron.*, vol. 4, pp. 772-793, 1998.

[5] D.D. Lofgreen, T.E. Mates, Y.C. Chang, and L.A. Coldren, "Enhanced intermixing of InGaAs/GaAs quantum wells using silicon doped InGaP and SiO_2," *submitted to Applied Physics Letters*.

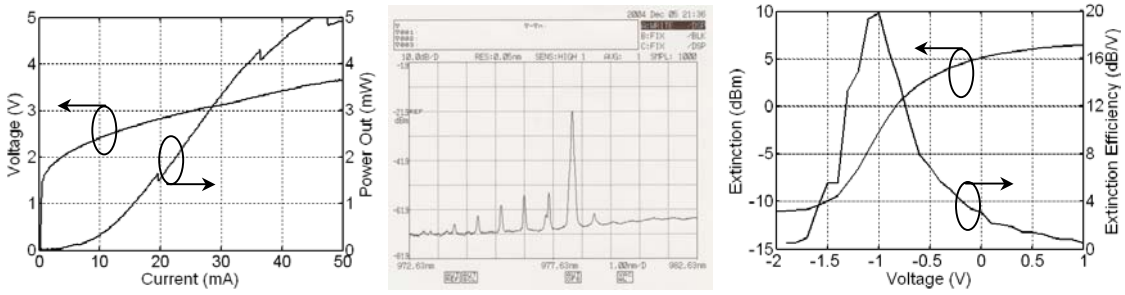

(a) (b) (c)

FIGURE 3. (a) CW voltage vs. injection current and optical power through the modulator vs. injection current. (b) CW lasing spectra showing emission at 978 nm with greater than 30 dB SMSR. (c) DC optical extinction of a 125 μm modulator showing more than 15 dB at -1.5 V. Extinction efficiencies of up to 20 dB/V are found at a –1 V bias.

Fabrication and MBE Regrowth of First Order, High Contrast AlGaAs/GaAs Gratings

Chad S. Wang, Gordon B. Morrison, Erik J. Skogen, and Larry A. Coldren
ECE Dept. University of California, Santa Barbara, CA 93106

Phone: 805.893.7065, Fax: 805.893.4500, Email: cswang@engineering.ucsb.edu

In this paper, we present the fabrication and regrowth of first order, high contrast, AlGaAs/GaAs Bragg gratings for short-wavelength applications. The gratings are employed as reflectors in a distributed Bragg reflector (DBR) laser emitting at 980 nm. We first present a novel immersion holography technique used to fabricate the first order short-wavelength gratings. Next, we discuss a matrix of regrowth experiments used to overgrow high contrast gratings. Solid source Molecular Beam Epitaxy (MBE) was used for regrowth, and atomic force microscopy (AFM) and scanning electron microscope (SEM) were used to characterize the gratings and quality of overgrowth. Finally, results of these gratings monolithically integrated into a DBR laser are presented.

High contrast, first order gratings are important technologically because of the high reflectivity with a small footprint. There are two main methods of patterning diffraction gratings—direct e-beam writing and holography. Standard holography is attractive due to its ease of fabrication, high throughput, and low cost. In our holography setup, a HeCd laser emitting at 325 nm was used as the source. However, to achieve the short grating pitch of ~150 nm necessary for our first-order 980 nm gratings, the wavelength of the laser source was reduced via a prism. Xylene was used to adhere the sample to the prism and also act as an index-matching fluid. This immersion holography technique was thereby effective in patterning uniform gratings at a shorter pitch. The exposed grating pattern is then transferred directly to the semiconductor via dry etching, and the sample is cleaned and prepared for regrowth.

MBE regrowth has generally been considered a difficult or impractical growth technique for smooth overgrowth of gratings. Chemical vapor deposition is more commonly used due to the high mass transport properties [1]. In this work, MBE regrowth has been successfully achieved on patterned gratings. The gratings were targeted to have a high coupling coefficient, $\kappa \sim 650\ cm^{-1}$. Therefore, $Al_{0.75}Ga_{0.25}As$ was used to overgrow GaAs gratings that were ~300 Å deep. Similar to work performed by Pickrell, et. al., we find that a slow growth rate is effective in overgrowing the gratings [2]. By growing at a slow growth rate, pitting defects are greatly reduced. Finally, substrate temperature and Arsenic overpressure were optimized to achieve both smooth overgrowth in non-grating regions as well as filled overgrowth over grating regions.

The high contrast, first order gratings were monolithically integrated into a DBR laser to evaluate its performance as a mirror [3]. The devices demonstrated single mode lasing at 978 nm with >30 dB side mode suppression. The lasers had a threshold current of 9 mA, and had output powers >5 mW.

In summary, first order, high contrast, AlGaAs/GaAs diffraction grating have been developed and implemented into a DBR laser emitting at 980 nm. A novel immersion holography technique has been developed to fabricate highly uniform gratings. Optimum regrowth conditions were found to overgrow and fill in the gratings. These gratings were successfully integrated in a DBR laser structure resulting in single mode emission at 980 nm.

References

[1] E.J. Skogen, J.S. Barton, J.W. Raring, S.P. DenBaars, and L.A. Coldren, "High contrast InP/InGaAsP gratings MOCVD regrowth using TBA and TBP," *J. of Crystal Growth*, vol. 272, pp. 564-569, 2004.

[2] G.W. Pickrell, C.F. Xu, D.A. Louderback, H.C. Lin, M.A. Fish, J.J. Hindi, M.C. Simpson, P.S. Guilfoyle, Z.H. Zhang, K.C. Hsieh, "Molecular beam epitaxy regrowth on diffraction gratings for vertical-cavity, surface-emitting laser-based integrated optoelectronics," *J. of Applied Physics*, vol. 96, no. 8, pp. 4050-4055, 2004.

[3] G.B. Morrison, C.S. Wang, E.J. Skogen, D.D. Lofgreen, and L.A. Coldren, "980 nm DBR Lasers Monolithicallly Integrated with EA Modulators for Optical Interconnect Applications, *Proc. Integrated Photonics Research and Applications*, paper no. IWF2, San Diego, CA, April 11-13, 2005.

II. InP-Based Vertical Cavity Lasers

Available online at www.sciencedirect.com
SCIENCE DIRECT®
Journal of Crystal Growth 277 (2005) 13–20
JOURNAL OF CRYSTAL GROWTH
www.elsevier.com/locate/jcrysgro

>100% output differential efficiency 1.55-μm VCSELs using submonolayer superlattices digital-alloy multiple-active-regions grown by MBE on InP

C.S. Wang[a,*], R. Koda[a], A.S. Huntington[b,c], A.C. Gossard[b], L.A. Coldren[a,b]

[a]*Department of Electrical and Computer Engineering, University of California, Santa Barbara, CA 93106, USA*
[b]*Department of Materials, University of California, Santa Barbara, CA 93106, USA*
[c]*Voxtel, Inc., Beaverton, OR 97005, USA*

Received 30 October 2004; accepted 23 December 2004
Communicated by D.W. Shaw
Available online 1 February 2005

Abstract

High-quality InAlGaAs digital-alloy active regions using submonolayer superlattices were developed and employed in a 3-stage bipolar cascade multiple-active-region vertical cavity surface emitting laser (VCSEL) design. The photoluminescence intensity and linewidth of these active regions were optimized by varying the substrate temperature and digitization period. These active regions exhibit considerable improvement over previously developed digital-alloy active regions and are comparable to analog-alloy active regions. Multiple-active-region VCSELs, grown all-epitaxially by MBE on InP, demonstrate greater than 100% output differential efficiency at 1.55-μm emission. A record high 104% output differential efficiency was achieved for a 3-stage long-wavelength VCSEL.

PACS: 42.55.Px; 78.66.−w; 81.15.Hi

Keywords: A1. Photoluminescence; A3. Molecular beam epitaxy; A3. Quantum wells; B3. Laser diodes; B3. Vertical cavity lasers

1. Introduction

Multiple-active-region (MAR) vertical cavity surface emitting lasers (VCSELs) are a novel approach to develop high output power VCSELs [1,2]. MAR can allow for differential efficiencies greater than unity, which could be used to make low-noise, transparent optical links, or even links with gain [3,4]. In this approach, active region stages are epitaxially stacked in series with Esaki tunnel junctions that effectively 'recycle' current to each stage of the active region, as illustrated in Fig. 1. Electrons injected into an active region can

*Corresponding author. ECE Department, UC Santa Barbara, CA 93117, USA. Tel.: +1 805 893 7065; fax: +1 805 893 4500.
E-mail address: cswang@engineering.ucsb.edu (C.S. Wang).

0022-0248/$ - see front matter © 2005 Elsevier B.V. All rights reserved.
doi:10.1016/j.jcrysgro.2004.12.139

recombine to emit a photon, but can then tunnel into subsequent active region stages. This cascading of N_a active regions with tunnel junctions can theoretically lead to N_a photons for every one electron. Furthermore, the threshold current scales sublinearly with $1/N_a$. Detailed analysis of the scaling properties of MAR devices can be found in Refs. [1,2,5]. To realize high performance MAR VCSELs, high-quality active regions must be developed. This is necessary in order to achieve the high gain necessary for high output efficiency. Previously at 1.55-μm emission, 94% output differential efficiency was shown grown with analog-alloy active regions [2]. In the work presented in this paper, high-quality digital-alloy active regions (DAAR) using submonolayer superlattices (SMS) were developed and implemented into a 3-stage MAR VCSEL with greater than 100% differential efficiency.

The structures were grown by molecular beam epitaxy (MBE), a popular method for all-epitaxial VCSELs due to its precise control over layer thicknesses. The technique of digitally grown alloys also alleviates the need for multiple group III sources or changes in cell temperature during growth. This technique has been successfully used in a wide variety of structures, such as light emitters [6], graded structures [7,8], and distributed Bragg reflectors (DBRs) [9], to name a few. Digital alloys can also be applied to active regions to utilize the control over precise composition and strain. In the long-wavelength regime, InAlGaAs-based quantum wells and barriers can be easily tailored to span across the 1.31–1.55 μm range. Furthermore, InAlGaAs-based active regions are preferred for their high temperature performance [10]. Previous work on long-wavelength DAAR with short period superlattices and SMS has shown improved uniformity and compositional accuracy using a variety of binary and ternary superlattice combinations, such as binary—binary SMS [11,12], lattice-matched ternary (LMT)—strained ternary superlattices [13], and binary—LMT SMS [14,15]. These techniques have demonstrated edge emitting lasers with low threshold current densities. In this work, we use a binary—LMT SMS technique similar to Reddy et. al. due to the relative ease of implementation since the growth depends only on two parameters: ternary lattice matching condition and their growth rates [15]. However, the dependence on the digitization period and growth conditions has not been well studied and documented.

In this paper, we first investigate the growth parameters to optimize the growth of high-quality DAAR using SMS. These active regions, targeted to 1.55-μm, are then applied to an all-epitaxially grown 3-stage MAR VCSEL. The devices demonstrate greater than 100% output differential quantum efficiency, the highest ever reported for a 3stage long-wavelength VCSEL, with low threshold voltages and current densities.

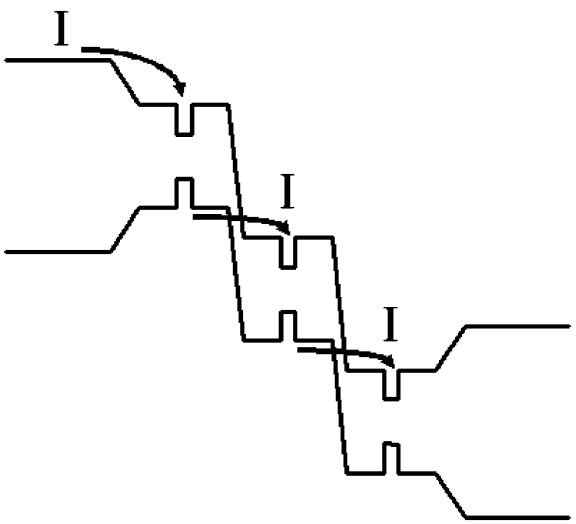

Fig. 1. Schematic illustration of a MAR VCSEL operation.

2. Experimental procedure

The experimental work reported on in this paper first investigates the growth of high quality DAAR using SMS at 1.55-μm. These were optimized for photoluminescence (PL) intensity and linewidth full width half max (FWHM). Then, the structure and growth conditions for a MAR VCSEL using the optimized DAAR is described. Finally, broad area VCSELs were fabricated and tested.

The growths for this work were performed in an ultra-high vacuum Varian Gen II solid-source

MBE system. A valved arsenic cell was the only group V source present for our machine, thus preventing any growth of InP for buffer or heat-spreading layers in the VCSEL.

2.1. Digital-alloy active region optimization

The DAAR were optimized by varying the SMS periodicity, Λ, and the active region substrate temperature, as measured by an optical pyrometer. The substrate temperatures quoted in this work were measured while idling with arsenic overpressure only. (With the group III cells open, the substrate temperature reads 10–20 °C hotter.) Fig. 2 shows the structure grown to evaluate the DAAR. The structure consists of a 200 nm $In_{0.52}Al_{0.48}As$ buffer followed by a 500 nm $In_{0.52}Al_{0.34}Ga_{0.14}As$. This buffer layer, like all other InAlGaAs layers grown in this work, was grown digitally using appropriate amounts of $(In_{0.53}Ga_{0.47}As)_{1-x}(In_{0.52}Al_{0.48}As)_x$. Sandwiched in between $In_{0.52}Al_{0.29}Ga_{0.19}As$ is the active region, nominally designed for 1530 nm emission. The active regions consist of five 70 Å thick, compressively strained $In_{0.70}Al_{0.07}Ga_{0.22}As$ quantum wells with six 50 Å thick, tensile strained $In_{0.44}Al_{0.12}Ga_{0.44}As$ barriers. A matrix of growths was performed varying the active region substrate temperature from 500 °C to 590 °C with a SMS periodicity of 3.5 Å. At active region substrate temperatures of 530 °C and 560 °C, the SMS periodicity was varied from 3.5 Å up to 17 Å. Table 1 lists the digitization schemes used for the SMS. Finally, all buffer layers were grown at 500 °C with an arsenic overpressure of 8×10^{-6} Torr, equivalent to a V/III ratio of 18, as optimized in a separate study for smoothest epitaxial films [16].

The quality of the DAAR was evaluated by room temperature PL for intensity and FWHM, and atomic force microscopy (AFM) for surface roughness. Fig. 3 shows PL curves for a few DAAR grown at varying substrate temperatures. As the active region is grown hotter, the PL wavelength blue shifts due to indium desorption. Figs. 4 and 5 plot the peak PL intensity and FWHM, respectively, as a function of substrate temperature for the entire matrix set. First, for short SMS periodicities ($\Lambda < 10$ Å), the most noticeable trend is that the peak PL intensity is maximized for DAAR grown between 520 °C and 530 °C. Likewise, the FWHM minimizes to around 35 meV at those temperatures. At higher temperatures, the PL begins to degrade and broaden; this corresponded to an increase in material roughness as a result of deviating from the window of smooth growth. However, the dependence on SMS periodicity is less obvious. At the cooler substrate temperatures of 530 °C, the peak PL intensity and FWHM does not degrade until a SMS periodicity of 17 Å. However, for DAAR grown at 560 °C, a SMS periodicity of 17 Å does not significantly differ than those of shorter periodicities. This is due to inhomogeneous material at the colder substrate temperatures. At longer SMS periodicities grown colder, the epitaxial film forms

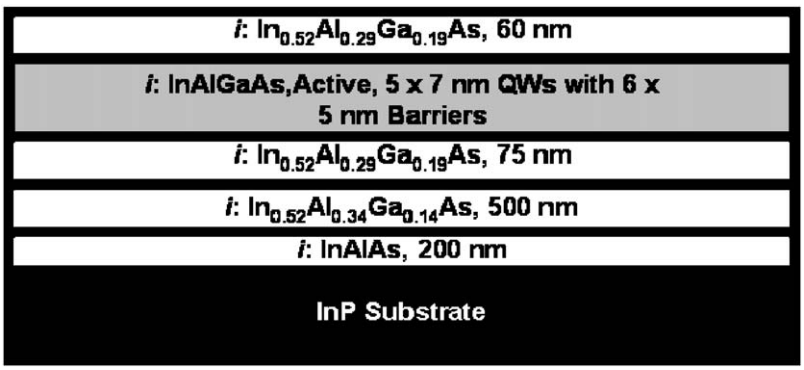

Fig. 2. Epilayer structure used in DAAR optimization study.

Table 1
SMS periodicity, thickness, and layer sequence used in the DAAR

	Thickness (Å)	Target SMS period, Λ (Å)	Actual SMS period, Λ (Å)	Repetitions	SMS layer sequence—thickness (Å)
Barrier	50	3.5	3.572	14	
		5	5.008	10	InGaAs–Λ/3.4182
		7	7.144	7	AlInAs–Λ/4.0
		10	10.0016	6	InGaAs–Λ/3.4182
		17	16.6667	3	GaAs–Λ/6.0645
Quantum well	70	3.5	3.503	20	InGaAs–Λ/4.1802
		5	5.3892	13	InAs–Λ/5.4734
		7	7.0057	10	AlInAs–Λ/6.404
		10	10.0054	7	InGaAs–Λ/4.1802
		17	17.5095	4	InAs–Λ/5.4734

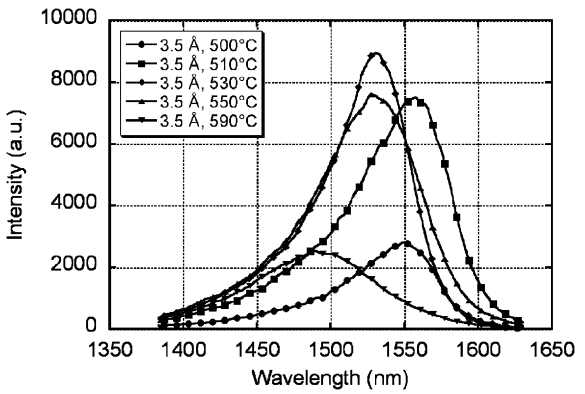

Fig. 3. PL of DAAR grown with a SMS periodicity of $\Lambda = 3.5$ Å at varying substrate temperatures.

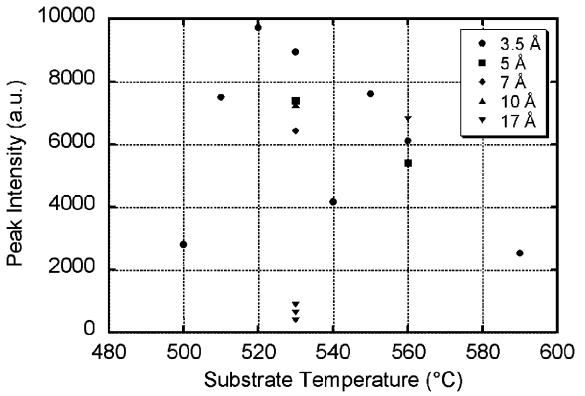

Fig. 4. PL peak intensity of DAAR grown with varying SMS periodicity, Λ, at varying substrate temperatures.

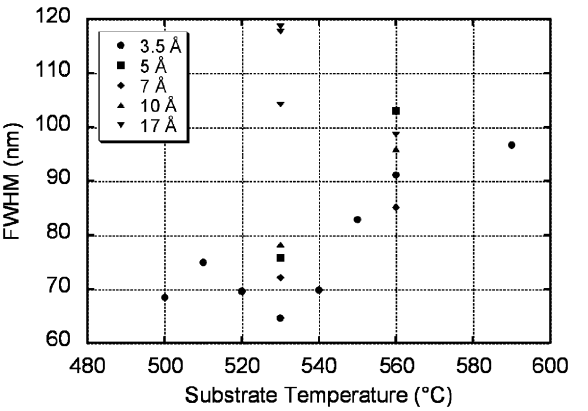

Fig. 5. PL full width half maximum of DAAR grown with varying SMS periodicity, Λ, at varying substrate temperatures.

spontaneous lateral composition modulations due to strain and islanding in the material, leading to poor superlattice [17]. This is confirmed by high surface roughness for these samples, which are in excess of 10 Å rms. However, when grown under hotter conditions, the epitaxial film is given more energy to migrate and form more homogeneous films.

From this experiment, an acceptable growth window for DAAR has been identified. Low SMS periodicities are desirable with substrate temperatures between 520 °C and 530 °C. Of course the periodicity of the SMS is ultimately limited by the speed of the shutter operation. Lastly, bright room temperature PL was observed with FWHM as low

as 33 meV, better than previous DAAR [14,18], and comparable to analog-alloy based active regions [19,20].

2.2. MAR VCSEL growth and fabrication

The technology used for this MAR VCSEL include the use of InAlGaAs/InAlAs DBRs and InAlGaAs active regions, lattice-matched to InP. This material system has the inherent drawback of low thermal impedance and low refractive index contrasts. However, this can be alleviated with the inclusion of InP as a heat spreading layer and well calibrated growth. Nevertheless, this technology was chosen for its capability to be grown all-epitaxially. The epilayers for the bottom emitting MAR VCSEL structure are shown in Fig. 6. The bottom and top DBRs are composed of 35.5 and 45.5 periods, respectively, of $In_{0.53}Al_{0.1}Ga_{0.38}As/In_{0.52}Al_{0.48}As$, and are compositionally graded at the interfaces. This results in reflectivities of 98.9% and 99.9% for the bottom and top DBRs, respectively. The doping in the DBRs is varied n-type from $2.5 \times 10^{18}\,cm^{-3}$ farther away from the active region down to $1 \times 10^{18}\,cm^{-3}$ nearer to the active region. The undoped separate confinement heterostructure (SCH) cladding layers are composed of $In_{0.52}Al_{0.29}Ga_{0.19}As$. The tunnel junctions are 350 Å thick similarly composed of $In_{0.52}Al_{0.29}Ga_{0.19}As$, with 220 Å for the n++-side and 130 Å for the p++-side. Silicon is used as the n-dopant and carbon for the p-dopant. The same active region composition as used in the DAAR optimization experiment was used for the VCSEL.

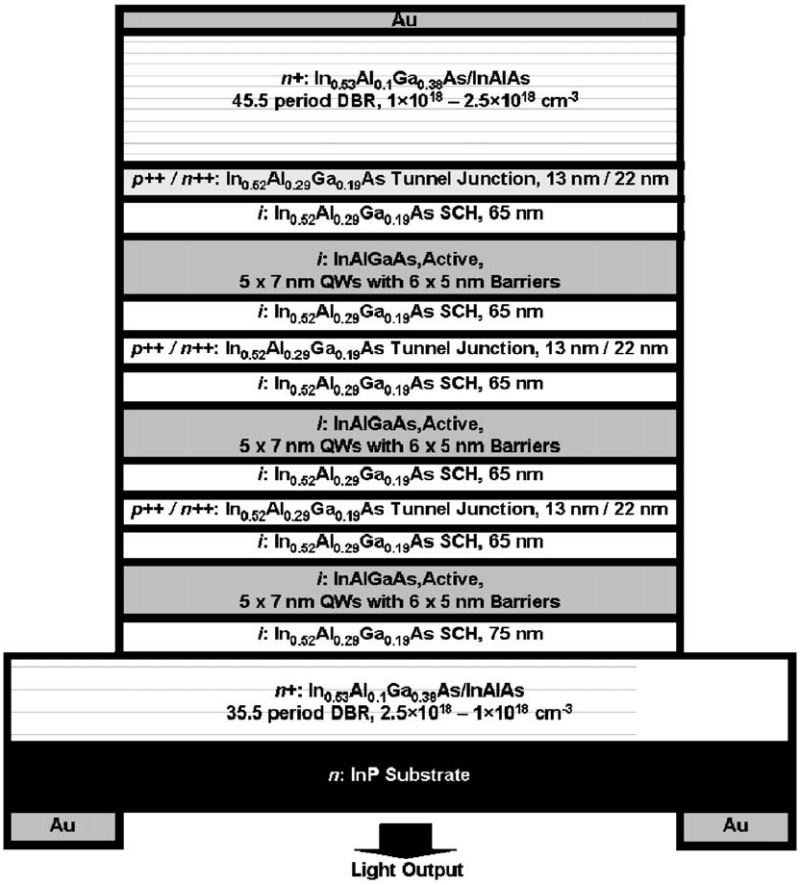

Fig. 6. Epilayer structure for the 3-stage MAR VCSEL.

The epilayers were grown on a sulfur doped n-type InP (1 0 0) wafer. Growth was preceded first with oxide desorption. The substrate was heated under very slight arsenic pressure (5×10^{-7} Torr) to 520 °C, upon which growth commenced while the substrate cooled to its growth temperature of 500 °C. An arsenic overpressure of 8×10^{-6} Torr was used during growth, facilitating a growth rate of 1 μm per hour. During growth of the n-side of the tunnel junction, the substrate temperature was reduced to 450 °C and the arsenic overpressure was increased to 2×10^{-5} Torr. This was found to increase the silicon doping concentration. The active region was grown at 530 °C with a 3.5 Å SMS digitization period.

The measured and designed reflectivity spectra of the MAR VCSEL is shown in Fig. 7, with the measured optical cavity at 1551 nm sandwiched between an approximately 100 nm wide stopband. The decreased reflectivity dip at around 1505 nm is due to absorption from the $In_{0.53}Ga_{0.47}As$ contact layer and the dip at 1580 nm is due to slight misalignment of the top and bottom DBRs. Next, the surface roughness between defects measured by AFM was 2.23 Å, indicating smooth superlattice growth throughout the epilayers. The low surface roughness is necessary for the high-quality active regions and low optical scattering in the DBRs [21].

Broad area pillars ranging from 25- to 100-μm in diameter were fabricated. First, the top mirror contact metal (Ti/Pt/Au) immediately followed by a dielectric etch mask (SrF_2) was deposited and lifted off to form the pillars. Next, a dry etch was used to etch straight sidewall pillars through the active region. After removing the etch mask, backside metal (Ni/AuGe/Ni/Au) was deposited onto the substrate, and the contacts were annealed. Lastly, a MgO anti-reflection (AR) coating was deposited on the substrate output interface.

3. Results and discussion

The devices were tested under room temperature pulsed operation with 500 ns pulses at a repetition rate of 1 kHz. The devices exhibited excellent voltage and light output power characteristics, and all lased multimode at around 1537 nm wavelength. Average output differential efficiencies were 70%, 90%, and 95%, for 25, 50, and 100-μm diameter devices, respectively, as shown in Fig. 8. Fig. 9 shows the best LIV performance at each device size. 104% differential efficiency was achieved for the 100-μm diameter device. Absorption from the 500-μm thick n-doped substrate was not taken into account, leading to approximately 15% more output power [2]. This would result in a record high 119% differential quantum efficiency for a 3-stage long-wavelength VCSEL. The decrease in output efficiency for the 25-μm diameter

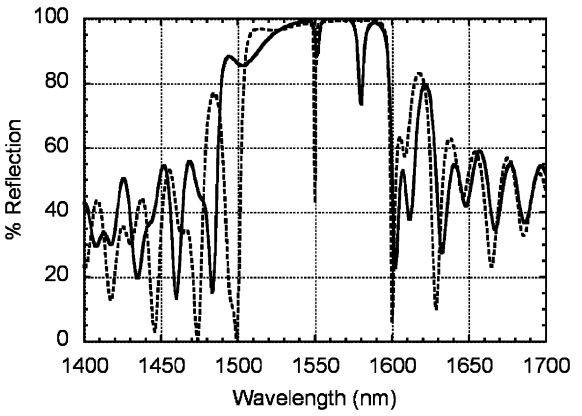

Fig. 7. Measured (solid) and simulated (dashed) reflectivity spectrum of the MAR VCSEL.

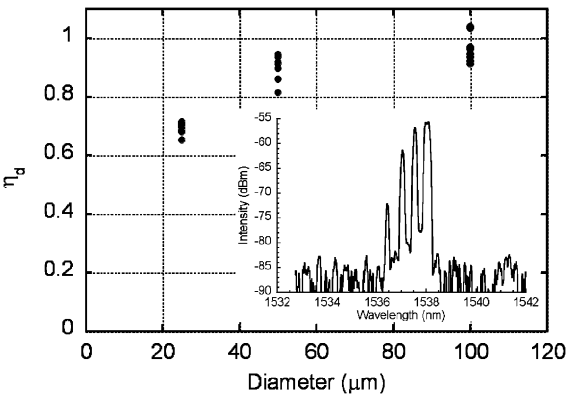

Fig. 8. Light output differential efficiencies for 25, 50, and 100-μm diameter MAR VCSEL devices. The inset shows a spectrum of a 25-μm device biased at 4.5 mA.

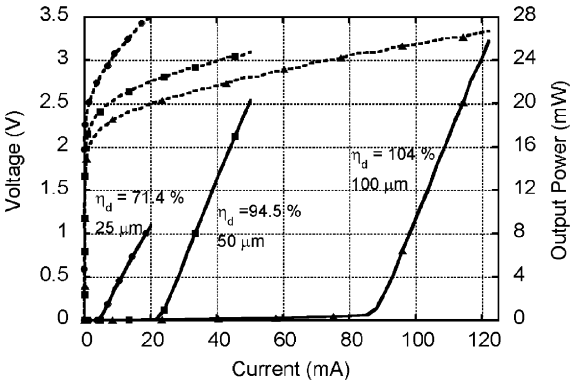

Fig. 9. Light (solid) and voltage (dashed) curves vs. current for a 25-μm (circles), 50-μm (squares), and 100-μm (triangles) diameter device.

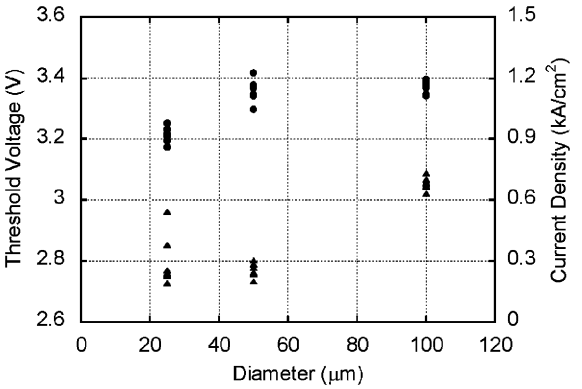

Fig. 10. Threshold voltage (triangles) and threshold current densities (circles) for 25, 50, and 100-μm diameter MAR VCSEL devices.

device is due increased sidewall scattering at smaller device diameters and diffraction loss through bottom DBR. Aperturing the mode would greatly alleviate this scattering and improve towards single mode emission. In addition to the high output efficiency, the devices also exhibited low threshold voltages and threshold current densities, as shown in Fig. 10. For the 25-μm diameter device, threshold voltages were 2.75 V. Subtracting the 2.4 V for the photon energy of a three-stage device, 350 mV remain for the three tunnel junctions and both DBR mirrors. With an estimated 65 mV drop across each tunnel junction measured from a separate investigation, only 155 mV drop across each DBR at a current density of 1 kA/cm^2. This clearly demonstrates both design and growth optimization of each component of the VCSEL to yield low voltage performance. These MAR VCSELs with DAAR, when compared to an identical design using conventional analog-alloy active regions [2], demonstrate comparable performance in terms of output differential efficiency and better performance in terms of voltage and threshold currents. Furthermore, 3-stage MAR edge-emitting lasers with DAAR, fabricated to evaluate active region parameters, performed similarly to previously published MAR edge-emitting lasers with analog-alloy active regions [5]. 3-stage MAR edge-emitting lasers with DAAR exhibited injection efficiencies, η_i, of ~275% and optical losses, α_i, of ~28 cm^{-1}, while those grown with analog-alloy active regions had $\eta_i = 233\%$ and $\alpha_i = 38\,\mathrm{cm}^{-1}$ [5]. This shows that high-quality DAAR with excellent performance can be applied to use in MAR laser structures.

4. Summary

In summary, we have developed high-quality InAlGaAs digital-alloy active regions grown using submonolayer superlattices. These active regions are comparable to their analog counterparts in terms of FWHM. These DAAR were implemented in a 3-stage MAR VCSEL design. The devices exhibited high output differential efficiencies, indicating the good quality and applicability of these DAAR. Greater than 100% output differential quantum efficiencies were achieved along with low voltage and threshold characteristics. Further improvements can be made by including InP, which can be used in the future for ease of aperturing and towards high temperature continuous wave operation.

Acknowledgements

The authors with to thank DARPA for supporting this work via CHIPS. We also want to thank the excellent laboratory support of John English. This work made use of MRL Central Facilities

supported by the MRSEC Program of the National Science Foundation under award No. DMR00-80034.

References

[1] T. Knödl, M. Golling, A. Straub, R. Jäger, R. Michalzik, K.J. Ebeling, IEEE J. Sel. Topics Quantum Electron. 9 (2003) 1406.
[2] J.K. Kim, S. Nakagawa, E. Hall, L.A. Coldren, Appl. Phys. Lett. 75 (2000) 1083.
[3] F. Rana, R.J. Ram, Appl. Phys. Lett. 76 (2000) 1083.
[4] F. Dross, F. van Dijk, B. Vinter., IEEE J. Quantum Electron. 40 (2004) 1003.
[5] J.K. Kim, E. Hall, O. Sjölund, L.A. Coldren, Appl. Phys. Lett. 74 (1999) 3251.
[6] J.G. Cody, D.L. Mathine, R. Droopad, G.N. Maracas, R. Rajesh, R.W. Carpenter, J. Vac. Sci. Technol. B 12 (1994) 1075.
[7] M. Sundaram, A. Wixforth, R.S. Geels, A.C. Gossard, J.H. English, J. Vac. Sci. Technol. B 9 (1991) 1524.
[8] W. Geißelbrecht, U. Pfeiffer, A. Thränhardt, U. Klütz, A.C. Gossard, G.H. Döhler, J. Crystal Growth 201/202 (1999) 163.
[9] M.G. Peters, B.J. Thibeault, D.B. Young, J.W. Scott, F.H. Peters, A.C. Gossard, L.A. Coldren, Appl. Phys. Lett. 63 (1993) 3411.
[10] N. Ohnoki, G. Okazaki, F. Koyama, K. Iga, Electron. Lett. 35 (1999) 51.
[11] S. Jourba, M. Gendry, O. Marty, M. Pitaval, G. Hollinger, Appl. Phys. Lett. 75 (1999) 220.
[12] A.J. Springthorpe, T. Garanzotis, P. Paddon, G. Pakulski, K.I. White, Electron. Lett. 36 (2000) 1031.
[13] G.T. Liu, A. Stintz, E.A. Pease, T.C. Newell, K.J. Malloy, L.F. Lester, IEEE Photon. Tech. Lett. 12 (2000) 4.
[14] M.H.M. Reddy, A. Huntington, D. Buell, R. Koda, E. Hall, L.A. Coldren, Appl. Phys. Lett. 80 (2002) 3509.
[15] M.H.M. Reddy, D.A. Buell, D. Feezell, T. Asano, R. Koda, A.S. Huntington, L.A. Coldren, IEEE Photon. Tech. Lett. 15 (2003) 891.
[16] A.S. Huntington, C.S. Wang, X.G. Zheng, J.C. Campbell, L.A. Coldren, J. Crystal Growth 267 (2004) 458.
[17] A.G. Norman, S.P. Ahrenkiel, H. Moutinho, M.M. Al-Jassim, A. Mascarenhas, J. Mirecki Millunchick, S.R. Lee, R.D. Twesten, D.M. Follstaedt, J.L. Reno, E.D. Jones, Appl. Phys. Lett. 73 (1998) 1844.
[18] J.D. Song, J.M. Kim, J.S. Yu, S.J. Bae, Y.T. Lee, Proceedings of the International Conference on Indium Phosphide and Related Materials, 2002, p. 335.
[19] H. Shimizu, N. Iwai, T. Mukaihara, K. Nishikata, A. Kasukawa, Proceedings of the International Conference on Indium Phosphide and Related Materials, 1997, p. 141.
[20] R. Kiefer, R. Lösch, H. Walcher, M. Walther, S. Weisser, K. Czotscher, W. Benz, J. Rosenzweig, N. Herres, M. Maier, C. Manz, W. Pletschen, J. Braunstein, G. Weimann, Proceedings of the International Conference on Indium Phosphide and Related Materials, 1998, p. 395.
[21] J.M. Elson, J.P. Rahn, J.M. Bennett, Appl. Opt. 22 (1983) 3207.

High-differential-quantum-efficiency, long-wavelength vertical-cavity lasers using five-stage bipolar-cascade active regions

R. Koda[a] and C. S. Wang
Department of Electrical and Computer Engineering, University of California, Santa Barbara, California 93106

D. D. Lofgreen
Raytheon Vision Systems, Goleta, California 93117

L. A. Coldren
Department of Electrical and Computer Engineering, University of California, Santa Barbara, California 93106

(Received 15 October 2004; accepted 6 April 2005; published online 16 May 2005)

We present five-stage bipolar-cascade vertical-cavity surface-emitting lasers emitting at 1.54 μm grown monolithically on an InP substrate by molecular beam epitaxy. A differential quantum efficiency of 120%, was measured with a threshold current density of 767 A/cm^2 and voltage of 4.49 V, only 0.5 V larger than 5×0.8 V, the aggregate photon energy. Diffraction loss study on deeply etched pillars indicates that diffraction loss is a major loss mechanism for such multiple-active region devices larger than 20 μm. We also report a model on the relationship of diffraction loss to the number of active stages. © *2005 American Institute of Physics*.
[DOI: 10.1063/1.1931060]

Long-wavelength vertical-cavity surface-emitting lasers (VCSELs) are a promising low cost alternative to conventional edge-emitting lasers as transmitters for optical communication networks. Several different material systems have been investigated for 1.55 μm VCSELs with viable results by researchers. These include GaAs-based wafer fusion,[1] AlGaAsSb,[2] InP/air-gap distributed Bragg reflector (DBR),[3] and metamorphic DBR.[4] While all of them have high index contrast in DBRs, desirable for VCSELs, difficulties in growth or fabrication exist. An alternative choice is to use the AlInGaAs material system for the mirrors. This is an attractive material since the growth of AlInGaAs on InP is more mature than other material systems, such as AlGaAsSb. The main problem in this material is that the index contrast of the DBRs is relatively low. However, cascading active regions can more than compensate for this problem since a higher gain is possible by recycling of carriers.

Bipolar cascaded active region devices, also known as multiple-active-region (MAR) lasers, can be constructed by epitaxially stacking each stage of the active region in series with Esaki tunnel junctions.[5] A band diagram of a three-stage MAR is shown in Fig. 1. In MAR devices, carriers can be recycled through tunneling Esaki junctions, and as a result, a single electron entering the terminal can provide multiple photons, leading to uniform pumping and higher gain without the penalty of high bias current. Highly doped Esaki junctions can be placed at the null of the standing wave to minimize absorption loss.

Furthermore, bipolar-cascade VCSELs are attractive candidates for transmitters in optical networks where high differential efficiency and low-noise lasers are desirable. High efficiency is possible through the use of lower reflective DBRs[6] and higher signal to noise ratio is expected since the signal is enhanced for the same noise when the active is divided into several stages.[7]

We have previously reported InP-based three-stage bipolar-cascade VCSELs with 94% differential quantum efficiency (η_d) at −10 °C.[5] Threshold voltage was 3.3 V which was only 0.9 V higher than the combined active junction voltages of 2.4 V. Although relatively successful, further optimization of growth and fabrication process was carried out to reduce the voltage drop across the DBRs and tunnel junctions (TJs). These involve band-gap engineering of the DBR interfaces as well as growth optimization for TJs. Air-post VCSELs presented previously are known to suffer from significant diffraction loss since the bottom DBRs possess no waveguiding.[8] An aperture can effectively eliminate such diffraction loss if designed properly, such as tapered oxide apertures used in a GaAs system.[9] The tapered aperture has a graded index, and thus can act as a lens to refocus a reflected mode reducing diffraction loss. However, the development of apertures in long-wavelength VCSELs with a single-growth monolithic approach has been difficult. While aperturing technologies have been developed by several research groups, for example using air gaps[2] or buried TJ apertures,[10] such elements are not very effective in multimode high-power applications where broad area devices are required.[11]

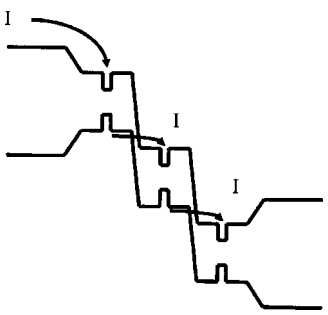

FIG. 1. Illustration of current path in bipolar-cascade lasers.

[a]Electronic mail: rintaro@engineering.ucsb.edu

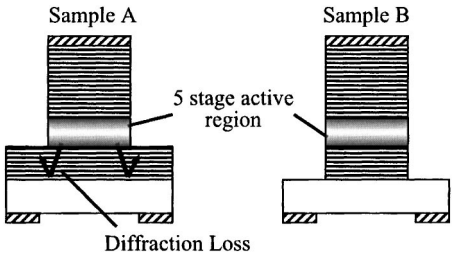

FIG. 2. Schematics of shallow (Sample A) and deeply etched (Sample B) pillars, illustrating diffraction loss from the bottom DBR for Sample A.

In these cases, diffraction loss of the higher-order modes appears to be a limiting factor. In this letter, we present a diffraction loss study of five-stage cascade VCSELs which have record differential efficiencies ~120% and improved low-voltage DBRs and TJs, in which the excess voltage was only 0.5 V higher than the sum of the band-gap energies of 4 V.

A bottom-emitting 1.55 μm VCSEL structure with five-stage MAR was monolithically grown by molecular-beam epitaxy on an *n*-InP substrate. Top and bottom DBRs consisted of $Al_{0.09}In_{0.53}Ga_{0.38}As/Al_{0.48}In_{0.52}As$ with a reflectivity of 99.8% and 98.3%, respectively. The interfaces of each DBR layer were graded over 32 nm to minimize conduction-band discontinuity. Each stage of the active region contained five 7 nm compressively strained quantum wells (QWs) ($Al_{0.17}In_{0.67}Ga_{0.16}As$) and six 5 nm tensile strained barriers ($Al_{0.20}In_{0.40}Ga_{0.40}As$). A 15 nm thick $Al_{0.29}In_{0.52}Ga_{0.19}As$ TJ separated each stage and consisted of a 9 nm layer of Si doped *n*-type to 5×10^{19} cm^{-3} and a 6 nm layer of C doped *p*-type to 2×10^{20} cm^{-3}.

The structure was fabricated as air-post VCSELs where pillars were formed by an inductively coupled plasma etcher at 200 °C. As mentioned before, such a structure would suffer from diffraction loss through the bottom DBRs since no waveguiding is present. The diffraction loss of unguided DBRs is strongly dependent on the index contrast of the two DBR layers because the effective propagation distance is larger for a smaller contrast.[8] To study the effect, we have fabricated two samples: One where the pillar was etched through the active region (Sample A) and the other etched through the bottom DBR (Sample B) as shown in Fig. 2. Index guiding by the bottom DBRs would eliminate the diffraction loss, leading to higher differential efficiency and lower threshold current provided surface roughness is sufficiently small.

Light-current-voltage characteristics for Samples A and B are shown in Fig. 3. Significantly higher differential efficiency (η_d) is clearly seen with Sample B, attributed from the much lower optical loss. The inset of Fig. 3 shows the lasing spectrum at ~1538 nm. The lack of an optical aperture results in a multimode spectrum. Threshold voltages were 4.56 V and 4.57 V for Samples A and B, respectively. This is only 0.6 V higher than the net active region junction voltage of 4 V (5×0.8 V). Separately grown TJ voltages were measured to be around 80 mV at 1 kA/cm^2. Figure 4 shows a plot of differential quantum efficiencies versus pillar diameters. Greater than 100% efficiencies, only possible with cascaded active regions, are seen for a range of device sizes for Sample B. A device with a 31 μm pillar diameter showed 122% efficiency. It can also be mentioned that while η_d sublinearly decreased for Sample A, it remained constant for

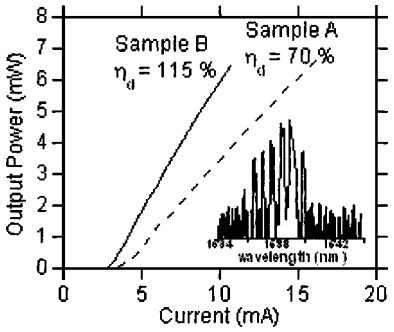

FIG. 3. Light-current-voltage plot of Samples A and B under pulsed operation at 20 °C.

Sample B until the device size became smaller than 20 μm. At this point, sidewall scattering becomes significant and η_d starts to decrease.

While the diffraction-free structure of Sample B is attractive, Sample A may be more practical because heat can dissipate more effectively in Sample A. It is possible to reduce diffraction loss of unguided DBR by using less number of periods. To investigate this, numerical simulation of the diffraction loss was carried out by Fourier decomposition method described in Babic *et al.*[8] First, the fundamental mode of a MAR VCSEL, ψ_I, was calculated by solving a two-dimensional scalar wave equation. The field profile is decomposed into its plane-wave Fourier components which is then multiplied by bottom DBR's angular spectrum. Finally, an overlap integral of the reflected mode, ψ_R, and ψ_I was calculated

$$\kappa = \frac{\int d^2r \psi_R \cdot \psi_I^*}{\int d^2r \psi_I \cdot \psi_I^*}. \tag{1}$$

The diffraction loss can then be calculated from $\delta = 1 - \kappa^* \kappa$. Figure 5 shows the diffraction loss versus the number of DBR pairs for a pillar diameter of 8 μm with corresponding reflectivity shown on the top *x* axis. The reduction of the diffraction loss is clearly seen for lower reflective DBRs. However, ordinary single-stage VCSELs would severely suffer an increase of the threshold gain and current if the output DBR reflectivity is reduced. On the other hand, in bipolar-cascade devices, multiple-active stages can compensate for the increased mirror loss to keep the threshold gain within each QWs approximately the same.

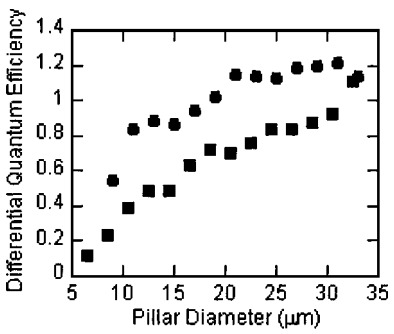

FIG. 4. Differential quantum efficiency vs pillar diameter for Sample A (square) and Sample B (circle).

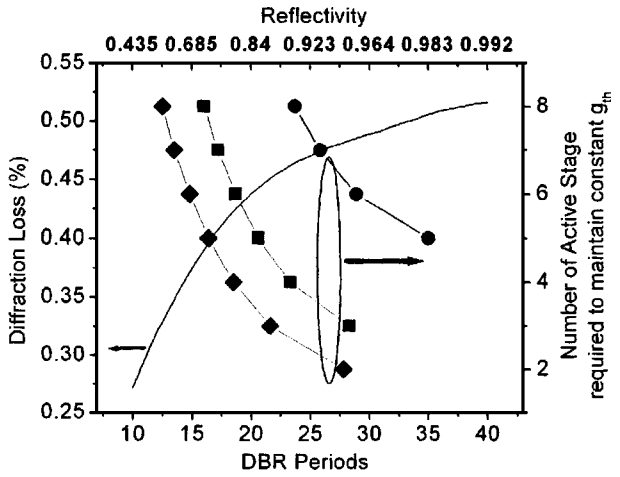

FIG. 5. Simulated diffraction loss for an 8 μm pillar vs number of DBR periods, with the top axis indicating the corresponding reflectivity. The number of active stages required to maintain constant threshold gains of 414 cm^{-1} (circles), 800 cm^{-1} (squares), and 1200 cm^{-1} (diamonds) is also plotted as a function of the number of DBR periods and reflectivity.

The threshold gain within the QWs of bipolar-cascade VCSELs was derived by Knodl *et al.*[6] and shown below as a reference

$$g_{\mathrm{th}} \approx \frac{\tilde{g}_{\mathrm{th}}}{N_a} + \frac{\alpha \Delta L}{N_a \Gamma d} - \frac{\ln \sqrt{\xi}}{N_a \Gamma d}, \tag{2}$$

where $\tilde{g}_{\mathrm{th}}$ is the threshold gain of a single-stage VCSEL with an active thickness of d, N_a is the number of stages, α is the absorption coefficient in the extended active region of ΔL, and Γ is the confinement factor. Output mirror reflectivity of cascaded devices, R_o were related to single-stage one, $\tilde{R}_o$ by $R_o = \xi \tilde{R}_o$. Using Eq. (2), the number of active stages required to maintain a constant threshold gain for different reflectivity was calculated and shown also in Fig. 5. For $g_{\mathrm{th}} = 1200\ cm^{-1}$ (diamonds), more than 20% reduction of diffraction loss is possible by reducing the number of DBR periods from 28 to 15 by changing the number of stages from 2 to 6.

In this letter, we presented a 1550 nm five-stage MAR-VCSEL with greater than 120% efficiency using improved DBRs and TJ voltages. We also have experimentally demonstrated that the diffraction loss has a significant impact on device performance for a broad area air-post VCSEL structure. The increased gain of a MAR-VCSEL can enable a reduction in diffraction loss by the use of fewer periods in the DBRs without suffering the increase of threshold gain. Equations (1) and (2) can be used to estimate diffraction loss and the optimal number of active stage as illustrated in Fig. 5.

This project was funded by ARO through UCSD subcontract and CHIPS through DARPA.

[1] A. Karim, J. Piprek, P. Abraham, D. Lofgreen, Y. J. Chiu, and J. E. Bowers, IEEE J. Sel. Top. Quantum Electron. **7**, 178 (2001).
[2] S. Nakagawa, E. Hall, G. Almuneau, J. K. Kim, D. A. Buell, H. Kroemer, and L. A. Coldren, IEEE J. Sel. Top. Quantum Electron. **7**, 224 (2001).
[3] C. K. Lin, D. P. Bour, Z. Jintian, W. H. Perez, M. H. Leary, A. Tandon, S. W. Corzine, and M. R. T. Tan, IEEE J. Sel. Top. Quantum Electron. **9**, 1415 (2003).
[4] J. Boucart, C. Starck, F. Gaborit, A. Plais, N. Bouche, E. Derouin, L. Goldstein, C. Fortin, D. Carpentier, P. Salet, F. Brillouet, and J. Jacquet, IEEE Photonics Technol. Lett. **11**, 629 (1999).
[5] J. K. Kim, S. Nakagawa, E. Hall, and L. A. Coldren, Appl. Phys. Lett. **77**, 3137 (2000).
[6] T. Knodl, M. Golling, A. Straub, R. Jager, R. Michalzik, and K. J. Ebeling, IEEE J. Sel. Top. Quantum Electron. **9**, 1406 (2003).
[7] P. M. Mayer, F. Rana, and R. J. Ram, Appl. Phys. Lett. **82**, 689 (2003).
[8] D. I. Babic, Y. Chung, N. Dagli, and J. E. Bowers, IEEE J. Sel. Top. Quantum Electron. **29**, 1950 (1993).
[9] M. J. Noble, P. Sotirelis, J. A. Lott, and J. P. Loehr, SPIE-Int. Soc. Opt. Eng. **3944**, 252 (2000).
[10] R. Shau, M. Ortsiefer, J. Rosskopf, G. Bohm, F. Kohler, and M.-C. Amann, Electron. Lett. **37**, 1295 (2001).
[11] M. Miller, M. Grabherr, R. Jager, and K. J. Ebeling, IEEE Photonics Technol. Lett. **13**, 173 (2001).

Proc. 63rd Device Research Conference, post deadline paper, Santa Barbara, CA (June 20-22, 2005)

High Differential Efficiency (>60%) Continuous-Wave Operation of 1.3μm InP-Based VCSELs with Sb-Based DBRs

D. Feezell, D.A. Buell, L.A. Johansson, and L.A. Coldren
University of California, Department of Electrical Engineering, ESB Room 3205B, Santa Barbara, CA 93106
Phone: 805-893-5955, Fax: 805-893-4500, Email: feezell@engineering.ucsb.edu

Long-wavelength vertical-cavity surface-emitting lasers (VCSELs) operating in the important telecommunications window of 1.3 – 1.6μm are attractive light-sources for short to mid-range optical networks. We have previously demonstrated a monolithic all-epitaxial platform utilizing InAlGaAs active regions and AlGaAsSb distributed Bragg reflectors (DBRs) with excellent results at 1.55μm [1]. Here we demonstrate the first continuous-wave (CW) operation of a 1.3μm InP-based VCSEL with Sb-based DBRs. These devices achieved world-record CW differential efficiencies for long-wavelength VCSELs of greater than 60% at room-temperature (RT). Furthermore, we demonstrate the first high-speed modulation for any long-wavelength VCSEL with Sb-based DBRs. These advancements verify that the Sb-based DBR technology can yield high-performance devices spanning the entire 1.3 – 1.6μm wavelength window.

Fig. 1 shows a schematic of the monolithic all-epitaxial VCSEL structure. The device was grown by solid-source molecular beam epitaxy (MBE) in a single growth step and utilizes a thin (350Å) selectively etched tunnel-junction layer to generate efficient optical and electrical confinement. The AlGaAsSb DBRs provide an index contrast of $\Delta n = 0.4$, comparable to GaAs/AlGaAs DBRs. The cavity contains a five quantum-well active region surrounded by InP layers that facilitate current and heat spreading in the device. The total cavity thickness is 4λ. Fig. 2 displays the CW light and voltage vs. current (LIV) curves for a VCSEL device with an 8μm diameter tunnel-junction aperture. CW operation was observed up to 88°C, with an output power >1.5mW at 20°C. These devices lased single-mode at 1.305μm with a side-mode suppression ratio (SMSR) of 46dB, as shown in Fig. 3.

The thin selectively etched tunnel-junction aperture provided low-loss optical confinement, generating the high differential efficiencies demonstrated in Fig. 4. World-record values were achieved, with 64% at RT and greater than 50% at 50°C. This result is an important advancement towards creating higher power devices with low-required drive-currents. Fig. 5 shows the threshold current vs. stage temperature for the device, indicating that the optimal gain-peak to cavity-mode alignment occurred around 20°C. These devices were designed for optimal RT operation, but improved temperature performance can be expected with a higher gain offset.

In order to demonstrate the high speed capabilities of these devices, they were modulated with a 2^{31}-1 prbs at 3.125Gb/s. Light was coupled directly into a single-mode fiber and then into a 10Gb optical receiver. Open eye diagrams were obtained up to 60°C and are shown in Fig. 6. The extinction ratios were derived directly from the optical bit stream and were >8dB for operation up to 60°C with a peak-to-peak drive voltage of only 800mV. Error-free operation was obtained up to 60°C and the bit error rate (BER) curves are shown in Fig. 7.

In conclusion, we have demonstrated the first CW operation of 1.3μm VCSELs with Sb-based DBR technology and have achieved record-high CW differential efficiencies. High speed modulation was also demonstrated for the first time with this technology. Coupled with previous results at 1.55μm, these results clearly demonstrate this platform's ability to generate high-performance monolithic VCSELs spanning the entire 1.3 – 1.6μm wavelength window.

[1] S. Nakagawa, et al., *Applied Physics Letters*, vol. 78, pp. 1337-1339 (2001).

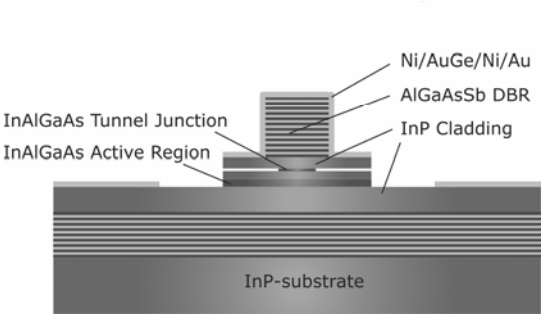

Fig. 1: Schematic of 1.3µm InP-based VCSEL device with selectively etched tunnel-junction aperture.

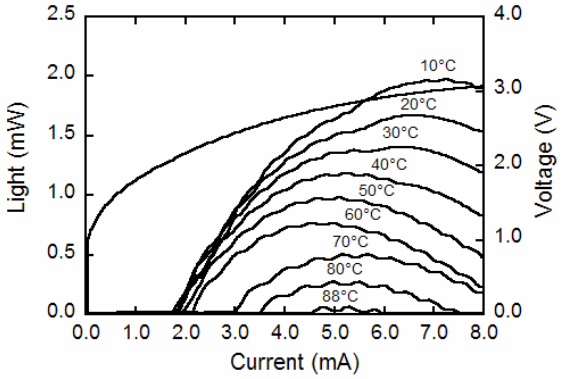

Fig. 2: CW LIV curves for bottom-emitting VCSEL with 8µm aperture at various temperatures showing operation up to 88°C.

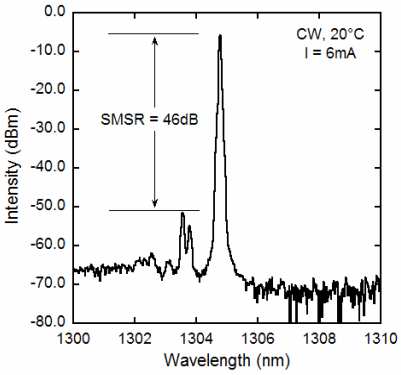

Fig. 3: CW lasing spectrum showing emission at 1.305µm and a 46dB SMSR.

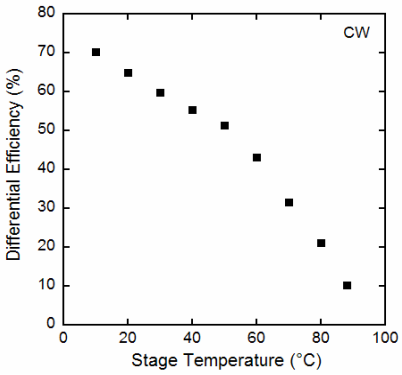

Fig. 4: Differential efficiency vs. stage temperature showing differential efficiency over 50% at 50°C.

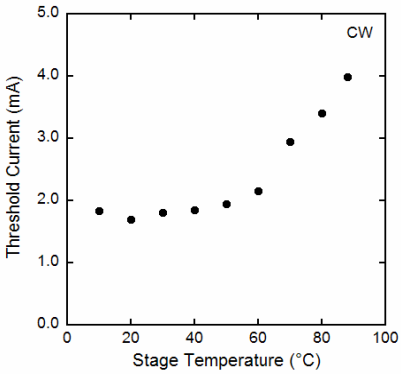

Fig. 5: Threshold current vs. stage temperature for VCSEL device optimized for RT performance.

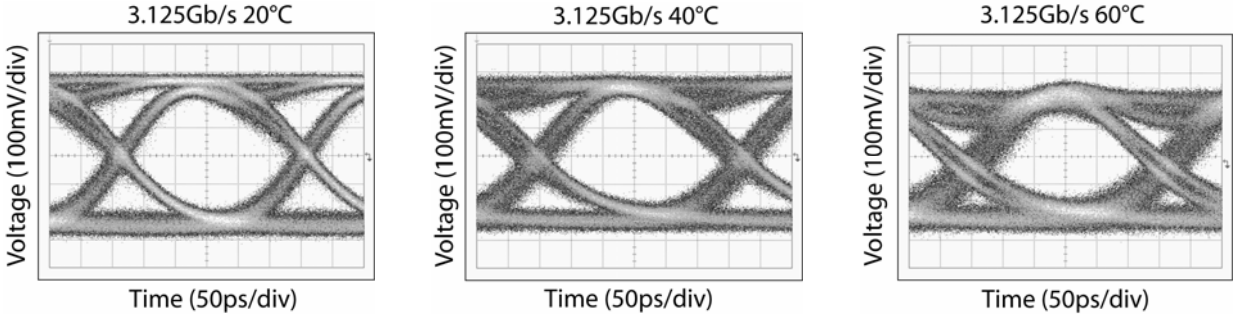

Fig. 6: Eye diagrams at 3.125Gb/s for 20, 40, and 60°C. Extinction is >8dB up to 60°C with a drive voltage of 800mV.

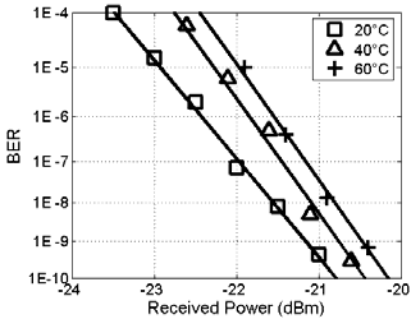

Fig. 7: BER curves at 20, 40, and 60°C for a 2^{31}-1 prbs showing error-free operation up to 60°C.

Proc. Electronic Materials Conference, paper no. NN7, Santa Barbara, CA (June 22-24, 2005)

NN7

Defect Reduction at the AlGaAsSb/InP Interface for Optimized Long-Wavelength Vertical Cavity Lasers

David Buell[1], Danny Feezell[1], Larry Coldren[1]
[1]University of California, Santa Barbara

ABSTRACT

High-performance vertical-cavity lasers operating in the 1310 to 1550 nm range can be realized with a single epitaxial growth on InP substrates by using appropriate materials for the distributed Bragg reflectors (DBRs). One such successful materials system is (Al,Ga)AsSb, which can be grown lattice-matched to InP and which has a large index contrast (~0.4). Devices using this DBR material have been demonstrated to operate at both 1310 and 1550nm. The yield of these devices is limited by point defects and roughness which lead to increased optical scattering losses. The primary source of defects in this system is the InP cladding layer grown on the bottom DBR. These defects are oriented along the [011] direction, and are approximately 5nm high. With sufficient growth these defects coalesce, leading to large-scale roughness detrimental to device performance. This paper will report on techniques developed to reduce the defects formed at this interface, with the goal of improving long-wavelength vertical cavity laser performance. Molecular beam epitaxy was carried out in Varian Gen-II reactor on 2-inch InP substrates. The group-III fluxes were provided by SUMO cells in all cases, increasing stability. The group-V sources are all valved crackers, which allows for stable and reproducible fluxes as well. Transitions between AlGaAsSb and InP are complicated by the fact that both cations and anions are different at the interface, with quaternary material on one side and binary on the other. When changing from AlGaAsSb to InP, a pause is necessary to open the P valve to the appropriate setting. This pause can be done with an overpressure of either As, Sb or both. The time and species have been demonstrated to be important. Additionally, the length of time for P exposure before commencing InP growth is key. Marked differences in surface morphology are apparent with varying any of these conditions. We have found the ideal transition method to be a 15 second As soak followed by a 30 second P soak, done at a temperature of 465ºC as measured by optical pyrometry. This method yields films which have an RMS roughness as measured by AFM of 2.0 Å, and a defect density of less than 200 defects/cm^2. We have used this approach to grow a 12.5period AlGaAsSb DBR centered at 1310 nm with 6000Å of InP which has defect density of 300 cm^-2 and roughness of 2.1 Å. Full vertical cavity lasers grown using this technique have been shown to have roughness of 7 Å for layers approaching 15 microns thick. Device results will be reported using this optimized growth technique.

Continuous-wave operation of all-epitaxial InP-based 1.3 μm VCSELs with 57% differential quantum efficiency

D. Feezell, D.A. Buell and L.A. Coldren

All-epitaxial InP-based 1.3 μm VCSELs with a record-high continuous-wave differential quantum efficiency (57%) for single active region long-wavelength devices are demonstrated. Low-loss optical mode confinement is achieved through a selectively etched undercut tunnel-junction aperture. Singlemode continuous-wave lasing was observed up to 87°C and the room-temperature output power was 1.1 mW at a current of 4.1 mA and a wavelength of 1.305 μm.

Introduction: Vertical-cavity surface-emitting lasers (VCSELs) emitting at 1.3 μm are attractive light sources for short to mid-range telecommunications and high-speed Internet applications. These devices offer many advantages over the existing distributed feedback (DFB) laser infrastructure, including low power consumption, on-wafer testing, low-cost packaging, and high fibre-coupling efficiency.

Recently, long wavelength VCSEL technology has grown to include a wide variety of approaches [1–6]. While excellent results have been reported, the majority of these approaches struggle to demonstrate monolithic all-epitaxial devices that can reliably span the entire 1.3–1.6 μm wavelength range. InP-based devices with AsSb-based distributed Bragg reflectors (DBRs) are promising candidates to solve this problem. In a previous work, we reported continuous-wave (CW) lasing up to 88°C with 1.55 μm InP-based VCSELs implementing AsSb-based DBRs [7]. In this Letter, we demonstrate the first above room-temperature (RT) CW lasing of 1.3 μm InP-based VCSELs with AsSb-based DBRs. These devices achieve a high CW differential quantum efficiency (DQE) of 57%. To our knowledge, this is the highest reported DQE value for single active region long-wavelength VCSEL devices. A selectively etched undercut tunnel junction was employed to produce a low-loss thin aperture that achieves simultaneous optical and electrical confinement [8]. Singlemode CW lasing was observed up to 87°C and the RT output power was 1.1 mW at a wavelength of 1.305 μm.

Device structure and fabrication: The VCSEL structure was grown monolithically in a single growth step by solid-source molecular beam epitaxy (MBE). Fig. 1 shows a schematic of the bottom-emitting all-epitaxial device with a selectively etched tunnel-junction aperture. The device uses a double intra-cavity contacting scheme to circumvent the high electrical and thermal resistance of the undoped AlGaAsSb DBRs. The top and bottom DBRs are designed to have reflectances of >99.9 and 99.4%, respectively. The VCSEL cavity is 4λ long and consists of a ½λ five quantum well $Al_{0.18}In_{0.67}Ga_{0.15}As$ active region with six $Al_{0.24}In_{0.40}Ga_{0.36}As$ barriers clad on both sides by InP layers that facilitate current spreading and heat removal from the device. The active region is designed for peak photoluminescence at 1275 nm and contains five 1.0% compressively-strained 7 nm quantum wells and six 0.6% tensile-strained 5 nm barriers. Embedded in the upper InP cladding layer is a 350 Å n^{++}-$Al_{0.29}In_{0.52}Ga_{0.19}As/p^{++}$-$Al_{0.29}In_{0.52}Ga_{0.19}As$ tunnel junction (doped Si:3e19 cm^{-3}/C:1e20 cm^{-3}) that is placed at a standing wave null to minimise absorption loss.

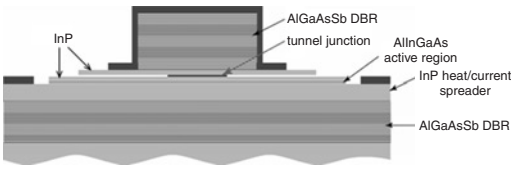

Fig. 1 *Schematic of bottom-emitting 1.3 μm VCSEL structure showing thin tunnel-junction aperture*

Device fabrication consisted of reactive ion etching (RIE) of the top DBR down to the upper InP cladding layer in Cl_2 plasma. Ni/AuGe/Ni/Au and SiO_2 were then evaporated as the top contact and etch mask, respectively. The upper InP cladding was then etched down to the tunnel-junction layer via RIE in CH_4:H_2:Ar_2. The tunnel junction layer was then selectively undercut with respect to InP with a 10:1 mixture of 1M citric acid and 30% hydrogen peroxide to form the thin air-gap aperture. The selectivity of this etch was observed to be greater than 100 to 1 and the diameter of the tunnel-junction aperture was controlled via observation of removal of sacrificial pillars on the chip. Subsequently, the remaining InP cladding was etched down to the active region via RIE. Finally, the active region was wet etched in citric acid and hydrogen peroxide to expose the bottom InP cladding. Ni/AuGe/Ni/Au was then deposited via electron beam evaporation to form the bottom contact.

Results: Fig. 2 shows the CW light and voltage against current (LV) curve at 20°C for a device with a 22 μm pillar and a 6 μm tunnel-junction aperture. This is the first reported RT CW lasing of a 1.3 μm InP-based VCSEL with AsSb-based DBRs. Moreover, the 57% DQE and resulting low required drive current are new milestones. High DQE values are desirable to achieve maximum device output powers at low bias and modulation currents. For this device, over 1 mW output power was demonstrated at the low current of 3.5 mA. The high DQE value is attributed to the implementation of the 350 Å low-loss air-gap tunnel-junction aperture placed at a standing wave null. The low effective index contrast ($\Delta n = 0.01$) afforded by this aperture provides good optical mode confinement with no scattering loss from the rough DBR sidewalls. Fig. 3 shows the CW lasing spectrum of the device at a bias of 4 mA. Singlemode lasing was observed up to the maximum output power and the lasing wavelength at this bias was 1.305 μm. The sidemode suppression ratio (SMSR) was 42 dB. These results clearly indicate the effective optical confinement achieved by the thin tunnel-junction aperture.

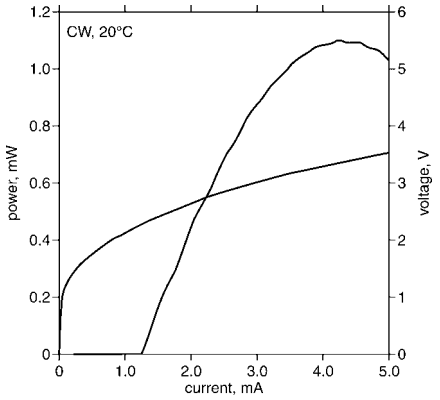

Fig. 2 *CW LIV curve of device with 57% differential quantum efficiency at room temperature*

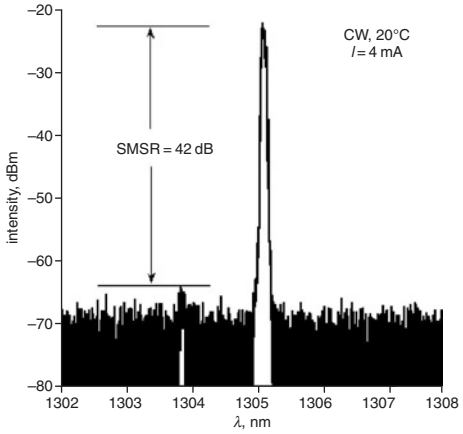

Fig. 3 *CW lasing spectrum at 4 mA of 1.3 μm VCSEL device, showing singlemode operation with 42 dB SMSR*

Fig. 4 shows the light against current (LI) curves for various stage temperatures. The maximum CW lasing temperature achieved was observed to be 87°C. The wavy nature of the LI curves can be attributed to substrate reflections due to an imperfect antireflection coating on the bottom-emitting device. AlInGaAs active regions have been shown to operate up to 134°C with a large (~60 nm) gain peak to cavity-mode offset [2]. For these devices, the highest temperature operation of 87°C can be partly attributed to the relatively small (~30 nm) offset, which was designed for optimum room-temperature device performance. The thermal impedance of the device was measured to be less than 2°C/mW,

indicating that for a potential compromise in RT performance, higher temperature operation would be possible with larger gain peak to cavity-mode offsets.

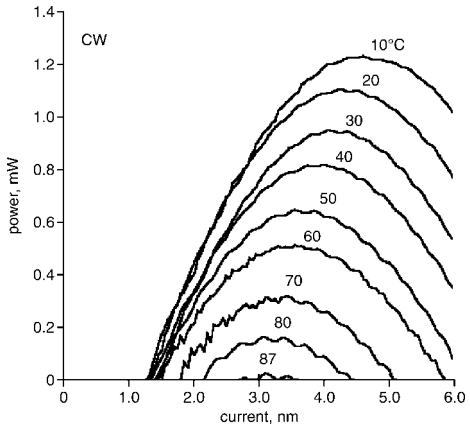

Fig. 4 *LI curves for various stage temperatures, showing CW lasing up to 87°C and over 1 mW output power at 20°C achieved below 4 mA*

Conclusions: We have demonstrated the first above room-temperature CW lasing for an InP-based 1.3 μm VCSEL with AsSb-based DBRs. These all-epitaxial devices achieved a record-high CW differential quantum efficiency (57%). Effective optical mode guiding and current confinement was achieved via a thin selectively etched tunnel-junction aperture. Singlemode operation was observed up to the maximum output power of 1.1 mW at 20°C and showed an SMSR of 42 dB. The maximum CW lasing temperature was shown to be 87°C. The lasing wavelength at 20°C for the maximum output power was 1.305 μm.

18 May 2005
Electronics Letters online no: 20051827
doi: 10.1049/el:20051827

D. Feezell and L.A. Coldren (*Electrical and Computer Engineering Department, University of California Santa Barbara, Engineering Sciences Building Room 3205B, Santa Barbara, CA 93106, USA*)

E-mail: feezell@engineering.ucsb.edu

D.A. Buell (*Materials Department, University of California Santa Barbara, Engineering Building II Room 1231, Santa Barbara, CA 93106, USA*)

References

1 Nishida, T., Takaya, M., Kakinuma, S., Kaneko, T., and Shimoda, T.: '4.2 mW GaInNAs long-wavelength VCSEL grown by metalorganic chemical vapor deposition'. IEEE Semiconductor Laser Conf., Matsue-shi, Japan, 2004

2 Jayaraman, V., Mehta, M., Jackson, A.W., Wu, S., Okuno, Y., Piprek, J., and Bowers, J.E.: 'High-power 1320-nm wafer-bonded VCSELs with tunnel junctions', *IEEE Photonics Technol. Lett.*, 2004, **15**, pp. 1495–1497

3 Nishiyama, N., Caneau, C., Hall, B., Guryanov, G., Hu, M., Liu, X., Bhat, R., and Zah, C.: 'Temperature, modulation, and reliability characteristics of 1.3 μm-VCSELs on InP with AlGaInAs/InP lattice matched DBR'. IEEE Semiconductor Laser Conference, Matsue-shi, Japan, 2004

4 Chang, J., Shieh, C.L., Huang, X., Liu, G., Murty, M.V.R., Lin, C.C., and Xu, D.X.: 'Efficient CW lasing and high-speed modulation of 1.3 μm AlGaInAs VCSELs with good high temperature lasing performance', *IEEE Photonics Technol. Lett.*, 2005, **17**, pp. 7–9

5 Shau, R., Ortsiefer, M., Rosskopf, J., Bohm, G., Kohler, F., and Amann, M.C.: 'Vertical-cavity surface-emitting laser diodes at 1.55 μm with large output power and high operation temperature', *Electron. Lett.*, 2001, **37**, pp. 1295–1296

6 Lin, C.K., Bour, D.P., Zhu, J., Perez, W.H., Leary, M.H., Tandon, A., Corzine, S.W., and Tan, M.R.T.: 'Long wavelength VCSELs with InP/air-gap DBRs', *SPIE Int. Soc. Opt. Eng. Proc.*, 2004, **5364**, pp. 16–24

7 Nakagawa, S., Hall, E., Almuneau, G., Kim, J.K., Buell, D.A., Kroemer, H., and Coldren, L.A.: '88°C, continuous-wave operation of apertured, intracavity contacted, 1.55 μm vertical-cavity surface-emitting lasers', *Appl. Phys. Lett.*, 2001, **78**, pp. 1337–1339

8 Reddy, M.H.M., Asano, T., Feezell, D., Buell, D.A., Huntington, A.S., Koda, R., and Coldren, L.A.: 'Selectively etched tunnel junction for lateral current and optical confinement in InP-based vertical cavity lasers', *J. Electron. Mater.*, 2004, **33**, pp. 118–122

Proc. 23rd North American Conference on Molecular Beam Epitaxy, paper no. WC-1, Santa Barbara, CA (September 11-14, 2005)

Molecular Beam Epitaxy of InP-Based Alloys for Long-Wavelength Vertical-Cavity Lasers

David A. Buell[1], Daniel Feezell[2], Bjørn-Ove Fimland[2,3] and Larry A. Coldren[1,2]

Department of Materials[1], Department of Electrical and Computer Engineering[2]
University of California, Santa Barbara, CA 93106

[3]on leave from Department of Electronics and
Telecommunications, Norwegian University of Science and Technology, NO-7491
Trondheim, Norway

Abstract

In this paper we review the growth, design, and characterization of 1310 nm lattice-matched vertical-cavity lasers which take advantage of AlGaAsSb distributed Bragg reflector and AlInGaAs active regions. The molecular beam epitaxial growth for this structure was particularly challenging due to the various III-V alloys used; in particular the interfaces between them were observed to be a significant source of macroscopic defects and roughness. The AlGaAsSb-InP interface was seen to control the yield and overall quality of device structures, and so was the focus of the crystal growth optimization. InP heat- and current-spreading layers were utilized to offset the thermal and electrical limitations of the AlGaAsSb mirrors; we optimized the defect density and roughness of these epilayers by studying their dependence on growth temperature and P-overpressure. Vertical-cavity lasers grown using these optimized approaches and incorporating a thin, selectively etched tunnel-junction aperture were fabricated and tested, and demonstrated promising characteristics. Operating temperatures up to 90 ºC with single-mode power in excess of 1.6 mW was observed. Differential quantum efficiency of 64% was seen for our best devices, a record for long-wavelength vertical-cavity lasers.

Keywords: Semiconductor lasers, molecular beam epitaxy, crystal growth, antimonides, vertical-cavity surface-emitting lasers, long wavelength.

PACS: 81.05.Ea, 81.07.St, 81.15.Hi, 42.55.Px

INTRODUCTION

Vertical cavity lasers (VCLs) operating in the wavelength space from 1300-1600 nm are interesting datacom and telecom sources for existing fiber-optic networks, since they take advantage of absorption and dispersion minima in conventional silica fiber; their circular output mode shape, low dissipated power, and efficient direct modulation behavior make them favorable for network applications. VCLs operating at shorter wavelengths (780-980nm) have demonstrated excellent performance characteristics for short distance communications [1]. In order to translate these successes to the local-, storage-, and metro-area networks, VCLs operating at 1310 and 1550 nm are desired. There have been two general lines of approach for realizing long-wavelength VCLs to this point: GaAs-based and InP-based. GaAs-based approaches take advantage of AlGaAs/GaAs distributed Bragg reflectors (DBRs) with their associated high index of refraction contrast and thermal conductivity. The optical and current aperturing technology is also well developed, with sub-micron devices incorporating tapered oxide apertures demonstrating high-speed modulation and high differential quantum efficiency. In order to extend the operation of GaAs-based devices from 980nm to 1310 and 1550nm, less mature active region materials such as GaInN(Sb)As or InGaAs quantum dots must be used [2,3]. These active regions are relatively new, and their reliability at longer wavelengths remains in question.

InP-based approaches take the opposite tack: the active region materials, AlInGaAs and InGaAsP, are well developed, having been deployed in commercial long-wavelength edge-

emitting lasers for many years. The DBR and aperturing technology, however, are less well-developed. The conventional lattice-matched alloys to InP, AlInGaAs and InGaAsP, do not have sufficient index contrast to be effective options for DBRs with high reflectivity. This has led to a variety of approaches to realize InP-based VCLs, including wafer-fused AlGaAs/GaAs DBRs [4], metamorphically grown AlGaAs DBRs [5], and dielectric DBRs [6]. Devices with high operating temperature, useful output power, and good differential efficiency have been demonstrated using each of these techniques.

In this paper we report results using an alternative approach, in which we take advantage of the InP lattice-matched material AlGaAsSb. Our group has reported VCLs based on this technology before, both at 1550 nm [7] and more recently at 1310 nm [8]. Prior results at 1550 nm showed operating temperature of 88 ºC and 1.2mW output power at 15 ºC, with 23% differential quantum efficiency. Improvements to the device design and epitaxial growth have led to our most recent results, in which 1310 nm VCLs have been fabricated which operate to 90 ºC, have 1.6 mW single-mode output power, and a record differential quantum efficiency of 64%. The molecular beam epitaxial growth optimization is detailed below.

MOLECULAR BEAM EPITAXY

The vertical-cavity laser structures detailed in this paper were grown using molecular beam epitaxy in a Varian Gen-II reactor, with standard EPI-SUMO effusion cells for group III elements and valved, cracked sources for all group V elements. For our laser structures, AlGaAsSb alloys were used as DBRs, AlInGaAs was used for active regions and tunnel junctions, and InP for heat- and current-spreading layers. The optimization of these different alloys, as well as the interfaces between them, was of utmost importance to successful device

fabrication. A schematic of a fully fabricated VCL is given in Figure 1 to illustrate the relationship between the various alloys and their placement in the device structure.

AlGaAsSb DBR Growth

Lattice-matched $AlAs_{0.56}Sb_{0.44}$ and $GaAs_{0.51}Sb_{0.49}$ has been demonstrated to be a suitable candidate for DBRs in the wavelength span of 1310-1550 nm [9]. We controlled the composition of the AlGaAsSb alloy via short-period superlattices (2.0 nm) with varying duty cycles of AlAsSb and GaAsSb. Using this method we formed alternating ¼ λ layers of $Al_{0.95}Ga_{0.05}As_{0.54}Sb_{0.46}$ and $Al_{0.30}Ga_{0.70}As_{0.52}Sb_{0.48}$, referred to in this paper as 95%AlGaAsSb and 30%AlGaAsSb, respectively. Growth was performed at a temperature of 480 ºC as measured using an Ircon optical pyrometer, and a growth rate of 0.35 nm/s. The lattice matching of the ternaries was achieved using the method we have previously reported, in which the beam flux ratio for As/Sb is fixed to ~6.5, and fine-tuning of the composition was done by adjusting the Al and Ga beam fluxes [10]. Stable lattice-matched conditions were possible using this method, with observed x-ray diffraction (XRD) peaks indicating less than 0.01% strain in the growth direction. Minimum defect density and roughness, as measured using atomic force microscopy (AFM), for samples grown using the above parameters was 150 cm^{-2} and 0.17 nm RMS, respectively. The bottom (output) DBR for the 1310 nm VCL consisted of 27.5 pairs, while the top (highly reflective) DBR used 39.5 pairs.

InP Growth Diagram

Homoepitaxy of InP, compared to GaAs, has a narrow optimal growth window. Previously we had observed that defect density in our bulk layers of InP was sufficient to increase optical

losses and thus decrease device performance. An investigation of the InP growth diagram for our conditions was thus necessary. We have previously found that InP substrate orientation played a large role in the quality of subsequently grown InP epilayers, with optimum films observed on (001) substrates miscut 0.5º towards the (111)A planes. For compatibility with the other requirements of our system, an InP growth rate of 0.15 nm/s was fixed, and other pertinent growth parameters were varied. Below we present the dependence on growth temperature and P_2 beam flux pressure of the macroscopic defect density and RMS roughness. In these experiments an InP growth rate of 0.15 nm/s was achieved using an In beam flux of $3.6x10^{-7}$ Torr.

Growth of InP under $9x10^{-6}$ Torr P_2 overpressure at a temperature of 465 ºC yielded films with defect density equal to 200 cm^{-2} and RMS roughness of 0.17 nm for 1 micron thick epilayers. InP which was grown on the optimized AlGaAsSb DBRs described above, however, suffered from increased defect density and roughness. In order to grow the highest quality devices an investigation into the interface between AlGaAsSb and InP was necessary.

AlGaAsSb-InP Interface

The interface between AlGaAsSb and InP occurred where the bottom DBR and InP heat/current spreading layer met, as seen in Figure 1. This interface involved the transition between a quaternary and binary alloy, with no common anions or cations between them. As a result, many different methods for switching from one material to the next could be imagined. Previously, we transitioned from AlGaAsSb to InP by soaking the static AlGaAsSb surface in both As and Sb beams while adjusting the P valve position for InP growth. We then soaked the AlGaAsSb surface under P_2 flux to pump out excess As and Sb for 30 seconds. InP growth was then initiated. Using this approach (referred to as AsSb-soak) occasionally yielded acceptable

films, including some of our prior VCL results, but was not sufficiently reproducible for reliable usage. Antimony adatoms present on the static surface tended to remain even with subsequent P_2 soaking, due to the relatively cool growth temperature of 465 ºC. This led to the observed defects and roughness. In order to overcome this limitation we developed a transition approach (referred to as P-soak) in which P_2 is the only group-V species present during the growth pause between AlGaAsSb and InP. This transition used a short initial P_2 soak followed by a thin (2.0 nm) InP buffer layer. This buffer layer was then exposed to the P_2 beam for 60 seconds to pump out the excess As and Sb still present. Growth of InP continued using the optimized conditions described above. Using this technique we routinely and repeatedly obtained films with low defect density and roughness. In Table I we summarize and compare the two transition methods.

Using this interface transition technique, in conjunction with the optimized AlGaAsSb and InP bulk heteroepitaxy, a full 1310 nm VCL device layer structures was grown. An AFM image of the wafer surface after this 15 micron-thick growth is given in Figure 3. The RMS roughness of this surface is 0.31 nm.

VERTICAL CAVITY LASER DEVICE STRUCTURE AND RESULTS

Our 1310 nm VCL structure and design have been detailed elsewhere [8]; the major features are described here, with some of the most pertinent device results provided as well. After MBE growth, the completed all-epitaxial laser structure was fabricated using standard lithographic techniques, with the thin tunnel-junction aperture formed by selectively etching the AlInGaAs

with respect to surrounding InP using a solution of citric acid and hydrogen peroxide (10:1 ratio). The devices were then probed on a stage mounted with an InGaAs photodetector, and the light-current-voltage (L-I-V) characteristics measured. In Figure 4 we see L-I curves for a range of temperatures, showing continuous-wave (CW) operation up to a maximum of 90 ºC. Figure 5 shows the L-I-V curves for a device with an aperture diameter of 5 microns at room temperature.

This device has single-mode output power greater than 1.0 mW, and differential quantum efficiency of 60%, and other devices exhibited up to 64%. This efficiency is a record, to the authors' best knowledge, for all long-wavelength vertical cavity lasers. The high differential efficiency can be attributed to low excess optical losses in the structure, thanks to the thin tunnel junction aperture located at the standing wave null of the mode in the optical cavity, along with low free-carrier absorption losses from the mostly n-type doping in the structure, and undoped DBRs. The high temperature operation is limited by the active region injection efficiency, which decreased to zero near 120 ºC. Improvements to the characteristic temperature via redesigning the band structure of the quantum wells and barriers will lead to increased maximum operating temperature for the VCLs. In addition, optimization of the spectral offset between the cavity mode and optical gain peaks should increase the achievable maximum temperature.

CONCLUSIONS

Long-wavelength vertical cavity lasers grown all-epitaxially on InP substrates can take advantage of AlGaAsSb alloys for highly reflective Bragg mirrors and AlInGaAs alloys for quantum well active regions. The interface between AlGaAsSb and InP has been optimized for minimum defect density and roughness. Growth of complete layer structures with 0.31 nm RMS

roughness has been demonstrated with low defect density. 1310 nm VCLs were then fabricated with low-loss thin tunnel-junction apertures for current and optical confinement. Operation at temperatures as high as 90 ºC was observed, with single-mode output power above 1.6 mW. Differential quantum efficiency as high as 64 % was achieved, a record for long-wavelength vertical cavity lasers.

ACKNOWLEDGMENTS

The authors thank Mr. Geir Myrvågnes for discussion on the AlGaAsSb MBE growth. This work made use of MRL Central Facilities supported by the MRSEC Program of the National Science Foundation under award No. DMR00-80034 and was funded by NSF under award No. #ECS-0245426.

REFERENCES

1. Ueki, N., Sakamoto, A., et al, *Photonics Technology Letters* **11**, 1539-1541 (1999).
2. Kondow, M., Kitatani, T., et al, *Journal of Selected Topics in Quantum Electronics* **3**, 719-730 (1997).
3. Gambin, V., Wonhill H., et al, *Journal of Selected Topics in Quantum Electronics* **8**, 794-800 (2002).
4. Jayaraman, V., Mehta, M., et al, *Photonics Technology Letters* **15**, 1495-1497 (2003).
5. Cheng, J., Shieh, C.-L., et al, *Photonics Technology Letters* **15**, 7-9 (2005).
6. Shau, R., Ortsiefer, M., et al, *Electronics Letters* **37**, 1295-1296 (2001).
7. Nakagawa, S., Hall, E., et al, *Journal of Selected Topics in Quantum Electronics* **7**, 224-230 (2001).
8. Feezell, D., Buell, D.A., et al, *Electronics Letters* **14**, (2005).
9. Blum, O., Hafich, M.J., et al, *Appl. Phys. Letters* **67**, 3233-3235 (1995).
10. Reddy, M.H.M., Buell, D.A., et al, *Appl. Phys. Letters* **82**, 1329-1331 (2003).

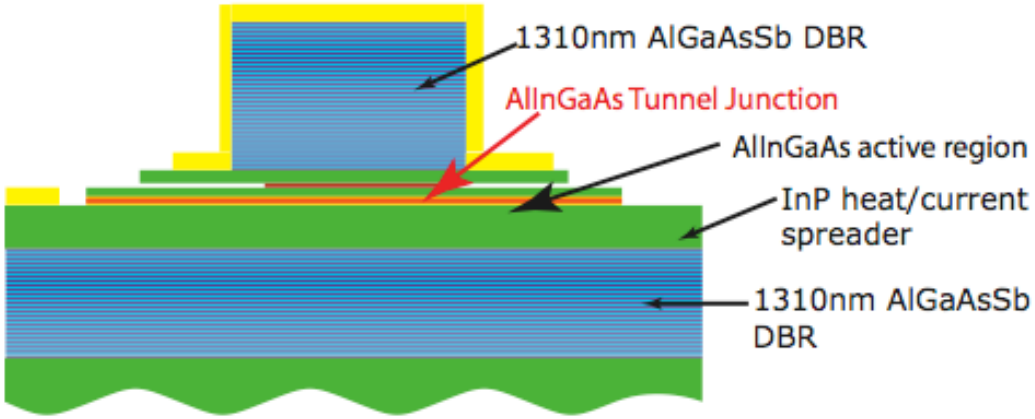
1310nm AlGaAsSb DBR
AlInGaAs Tunnel Junction
AlInGaAs active region
InP heat/current spreader
1310nm AlGaAsSb DBR

Figure 1.

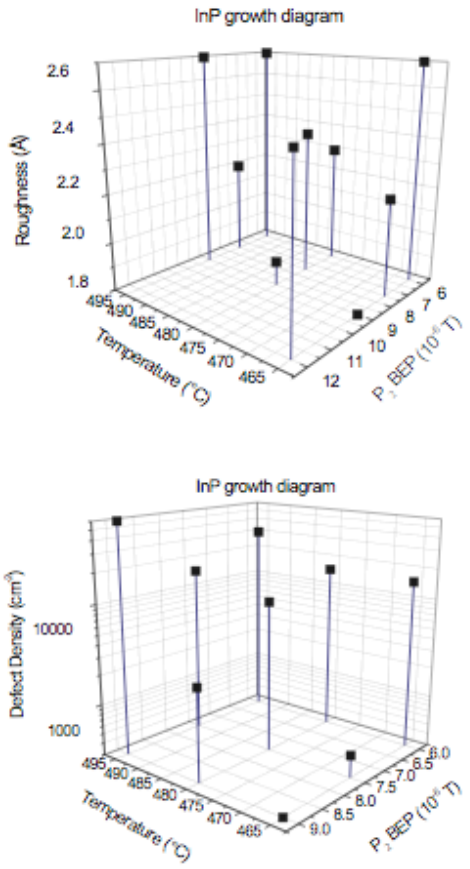
InP growth diagram
Roughness (Å)
2.6
2.4
2.2
2.0
1.8
495
490
485
480
475
470
465
Temperature (°C)
6
7
8
9
10
11
12
P2 BEP (10-6 T)
InP growth diagram
Defect Density (cm-2)
10000
1000
495
490
485
480
475
470
465
Temperature (°C)
6.0
6.5
7.0
7.5
8.0
8.5
9.0
P2 BEP (10-6 T)

Figure 2.

Table I. Transitions between AlGaAsSb - InP

AsSb-soak	**P-soak**
AlGaAsSb DBR growth	AlGaAsSb DBR growth
Soak AsSb surface with both As_2 and Sb_2 flux – 30 seconds	Soak AsSb surface with only P_2 flux – 5 seconds
Open In shutter, grow according to optimized conditions	Grow 2.0 nm InP buffer layer
	Soak InP buffer layer with P_2 flux – 60 seconds
	Grow remaining InP using optimized conditions
Macroscopic Growth Results	
Defect Density: 5000 cm^{-2} RMS roughness: 1.5 nm	Defect Density: 200 cm^{-2} RMS roughness: 0.18 nm

Table 1.

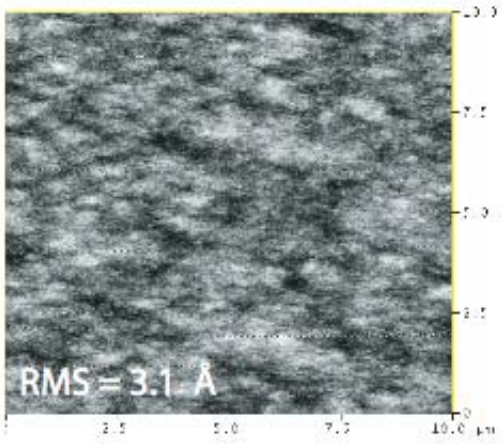

Figure 3.

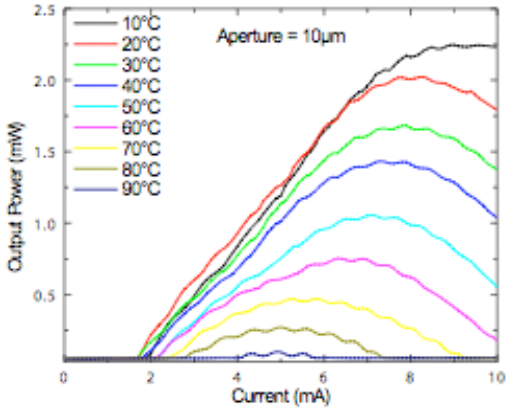
Aperture = 10μm
10°C
20°C
30°C
40°C
50°C
60°C
70°C
80°C
90°C
Output Power (mW)
Current (mA)
0
2
4
6
8
10
0.5
1.0
1.5
2.0
2.5

Figure 4.

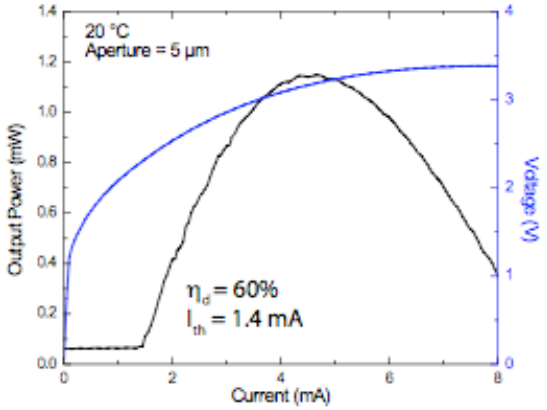
20 °C
Aperture = 5 µm
η_d = 60%
I_{th} = 1.4 mA
Output Power (mW)
Voltage (V)
Current (mA)
0.0
0.2
0.4
0.6
0.8
1.0
1.2
1.4
0
1
2
3
4
0
2
4
6
8

Figure 5.

FIGURE 1. 1310 nm VCL with AlGaAsSb DBRs and AlInGaAs active region, with thin AlInGaAs tunnel junction aperture for current and optical confinement.

FIGURE 2. RMS roughness (top) and defect density (bottom) dependence on InP homoepitaxial layers. Growth rate for InP in all cases is 0.15 nm/second.

FIGURE 3. 10x10 μm AFM image of completed VCL layer structure epilayers. The scale in the image is 5 nm.

FIGURE 1. Light-current curves for a multi-mode 1310 nm VCL operating CW at a range of temperatures. Maximum operating temperature of 90 ºC is observed.

FIGURE 2. L-I-V curves for a single-mode 1310 nm VCL operating CW at room temperature. Maximum output power of 1.1 mW and differential efficiency of 60% is observed.

InP-Based 1.3–1.6-μm VCSELs With Selectively Etched Tunnel-Junction Apertures on a Wavelength Flexible Platform

D. Feezell, D. A. Buell, and L. A. Coldren, *Fellow, IEEE*

***Abstract*—In this letter, the authors demonstrate a wavelength flexible platform for the production of long-wavelength vertical-cavity surface-emitting lasers which provide full wavelength coverage from 1.3–1.6 μm. All-epitaxial InP-based devices with AsSb-based distributed Bragg reflectors were achieved through a common design, process, and growth technology at both the important telecommunications wavelengths of 1.3 and 1.5 μm. Thin selectively etched tunnel junctions were implemented as low-loss apertures and offer scalability to small device dimensions. Devices showed low threshold currents (<2 mA), near single-mode (SMSR > 20 dB) operation, and high differential efficiency (>40% at 1.3 μm and >25% at 1.5 μm).**

***Index Terms*—InP-based, long wavelength, molecular beam epitaxy, optical fiber communications, semiconductor laser processing, semiconductor lasers, tunnel junction, vertical-cavity surface-emitting lasers (VCSELs).**

I. Introduction

LONG wavelength vertical-cavity surface-emitting lasers (VCSELs) operating in the 1.3–1.6-μm wavelength range are attractive light sources for metro, local area, and storage area networks. These devices offer a potential low-cost alternative to existing distributed feedback laser transmitters. In addition, due to simple packaging, high fiber-coupling efficiency, and on-wafer testing, VCSELs offer many inherent advantages over the existing in-plane infrastructure.

Recently, much attention has been devoted to a variety of approaches to long-wavelength VCSEL devices. Structures employing epitaxial, dielectric, and wafer bonded distributed Bragg reflector (DBR) mirrors have all been demonstrated. Various active region designs have also been utilized with success. Several of the most promising material systems include GaInNAs [1], AlInGaAs [2]–[5], and InGaAsP [6]. The underlying drawback to the majority of these approaches, however, is their inability to produce monolithic all-epitaxial devices that span the entire 1.3–1.6-μm wavelength range. From a manufacturability standpoint, this is an important goal.

Previously, we have reported monolithic all-epitaxial InP-based VCSELs with AlGaAsSb DBRs and AlInGaAs active regions [7], [8]. AsSb-based DBRs are lattice matched to InP and offer high reflectivity over a broad wavelength range, thus enabling wavelength selection from 1.3–1.6 μm. In fact, the available index contrast is $\Delta n \approx 0.4$, comparable to that of the GaAs–AlGaAs system. Coupled with the mature AlInGaAs active regions, AsSb-based technology facilitates all-epitaxial InP-based devices spanning the entire long-wavelength range with consistent device design, process flow, and materials growth.

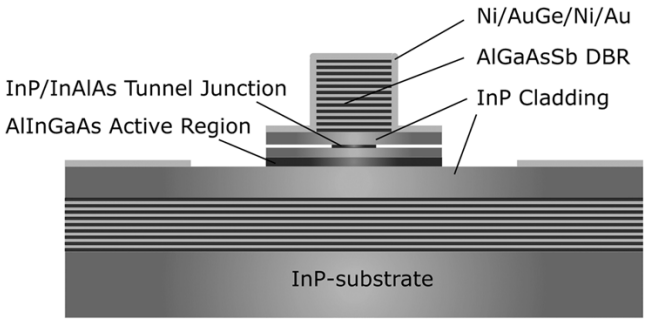

Fig. 1. Schematic of bottom-emitting all-epitaxial VCSEL structure with undercut tunnel-junction aperture.

In addition, we have previously investigated several aperturing techniques [7]–[9]; unfortunately, these aperturing schemes have suffered from high scattering loss, difficult processing steps, or current crowding. Recently, we have demonstrated an improved aperture through selective etching of a thin tunnel junction layer to achieve simultaneous optical and electrical confinement in in-plane lasers [10].

In this letter, we report the fabrication of InP-based 1.3- and 1.5-μm VCSELs with AsSb-based DBRs and selectively etched tunnel-junction apertures. We demonstrate a platform with flexible lasing wavelength and low-loss apertures scalable to small dimensions. This is the first reported 1.3-μm InP-based all-epitaxial VCSEL with AsSb-based DBRs and a selectively etched tunnel-junction aperture. Finally, we show the effectiveness of the thin tunnel-junction apertures in facilitating single mode operation, improving differential efficiency, and reducing threshold current.

II. VCSEL Design and Fabrication

Fig. 1 shows a schematic of the bottom-emitting device structure applicable to both 1.3- and 1.5-μm devices. The VCSEL was grown by solid-source molecular beam epitaxy in a single growth step. A double intracavity contacting scheme is employed to circumvent the high electrical and thermal resistances of the AsSb-based DBRs. The $(1/2) - \lambda$

Manuscript received May 6, 2005; revised June 8, 2005. This work was supported in part by the National Science Foundation.

The authors are with the Department of Electrical and Computer Engineering and the Department of Materials Science, University of California Santa Barbara, Santa Barbara, CA 93106 USA (e-mail: feezell@engineering.ucsb.edu).

Digital Object Identifier 10.1109/LPT.2005.854357

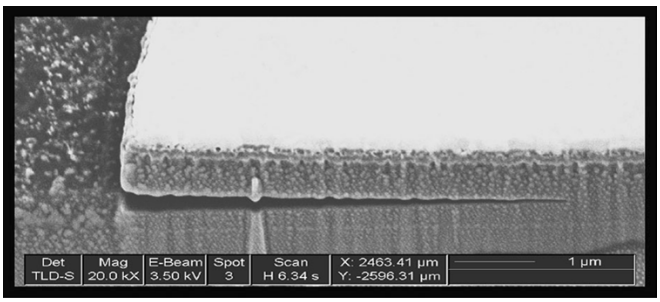

Fig. 2. Cross-sectional SEM of selectively etched InAlAs–InP tunnel-junction aperture in a VCSEL cavity test structure.

AlInGaAs active region contains five 1.0% compressively strained 7-nm quantum wells and six 0.6% tensile-strained 5-nm barriers. Cladding both sides of the active region are InP layers doped 5e17 cm^{-3} that facilitate current spreading and heat removal in the device. The upper InP cladding layer contains a 3e19-cm^{-3} n^{++}-InAlAs/1e20 cm^{-3} p^{++}-InP tunnel-junction layer placed at a standing wave null to minimize absorption loss, which is selectively etched to form the thin aperture. The total cavity thickness is $3.5 - \lambda$. The DBRs are $Al_{0.30}Ga_{0.70}As_{0.53}Sb_{0.47}$–$Al_{0.95}Ga_{0.05}As_{0.51}Sb_{0.49}$ for the 1.3-μm structure and $Al_{0.15}Ga_{0.85}As_{0.54}Sb_{0.46}$–$Al_{0.95}Ga_{0.05}As_{0.51}Sb_{0.49}$ for the 1.5-μm structure. The top and bottom mirrors contain 36.5 and 24.5 pairs for the 1.3-μm devices, respectively, and 34.5 and 24.5 pairs for the 1.5-μm devices, respectively. The major advantage of this structure is that both 1.3- and 1.5-μm devices are realized with parallel design, process, and materials growth technology. This is potentially an excellent platform for coarse wavelength-division-multiplexing (CWDM) applications between 1.3–1.6 μm with 20-nm channel spacing.

Device fabrication involved reactive ion etching (RIE) of the top DBR down to the top InP contact layer in Cl_2 plasma. The upper InP cladding layer, which functions as an etch-stop layer for the upper DBR, was etched down to the tunnel-junction layer via RIE with CH_4-H_2-Ar. Selective lateral etching of the InAlAs portion of the tunnel junction was then performed with a mixture of citric acid and hydrogen peroxide to form the thin air-gap aperture. The selectivity of this etch over InP was observed to be greater than 100 to 1. Subsequently, the remaining InP cladding was etched to the active region via RIE. Finally, the active region was etched with a citric acid and hydrogen peroxide mixture to expose the bottom InP contact layer. Ni–AuGe–Ni–Au was then evaporated on the top and bottom InP contact layers.

A scanning electron microscope (SEM) picture of the selectively etched tunnel-junction air-gap aperture is shown in Fig. 2. The dimensions of the aperture are controlled through observing the removal of sacrificial etch pillars on the wafer.

III. Results and Discussion

The 1.3- and 1.5-μm devices were fabricated and tested. Light output versus current and voltage (L–I–V) curves are shown for both 1.3- and 1.5-μm VCSELs in Figs. 3 and 4, respectively. These devices were each 20-μm diameter pillars with 8-μm diameter tunnel-junction apertures. The spectra at 3 × threshold for both wavelengths are inset in the appropriate figures and

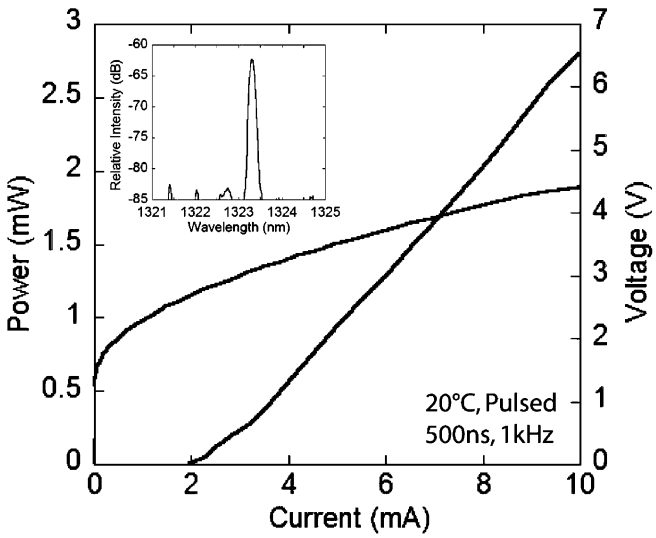

Fig. 3. Room temperature pulsed L–I–V curve for 1.3-μm VCSEL with inset pulsed lasing spectrum. Data was under-sampled due to pulsed measurement restrictions, giving apparent kink in L–I–V curve.

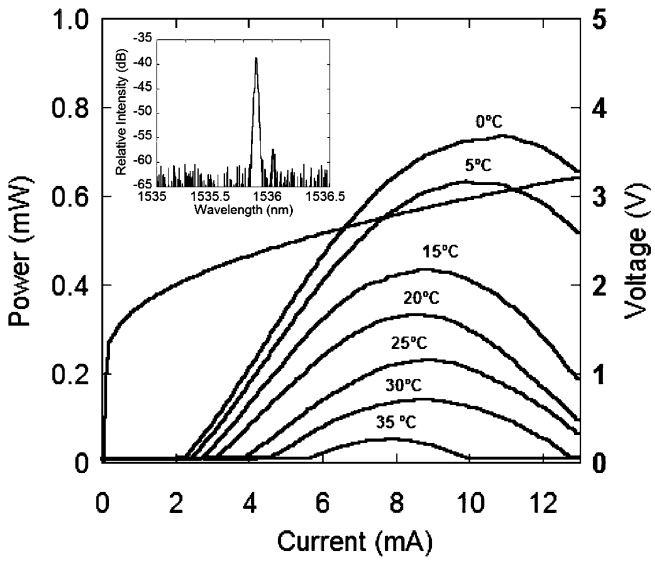

Fig. 4. CW L–I–V curves at various temperatures for 1.5-μm VCSEL with inset CW lasing spectrum.

demonstrate the near single-mode (SMSR $>$ 20 dB) nature of these devices. This operation demonstrates that the thin air-gap aperture placed at a standing wave null provides sufficient index contrast to confine the mode to smaller dimensions without significant scattering loss.

We believe this to be the first report of an InP-based 1.3-μm VCSEL with AsSb-based DBRs and tunnel junction aperturing technology. The 1.3- μm devices lased pulsed (20 °C, 500 ns, 1 kHz) at 1.32 μm and showed a high differential efficiency of greater than 40%, demonstrating that the thin tunnel-junction aperture effectively confines the optical mode away from the rough DBR sidewalls. The 1.3-μm devices only displayed continuous-wave (CW) lasing at 0 °C due to a red shift of the gain peak with respect to the cavity-mode and the low bottom mirror reflectivity ($R \approx 99.1\%$). The 1.5-μm devices lased at 1.54 μm and achieved differential efficiencies above 25%. CW operation

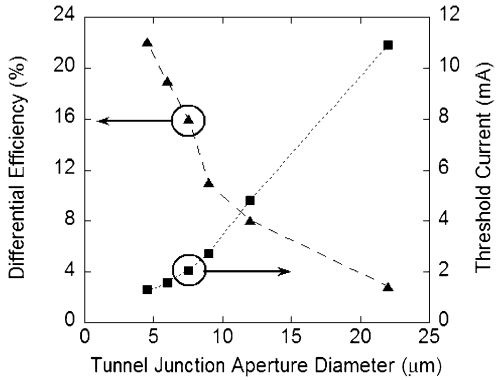

Fig. 5. Differential efficiency and threshold current versus tunnel-junction aperture diameter for a 1.5-μm device, showing scalability of aperturing technology.

was observed for these devices up to 35 °C. Higher temperature performance is expected at both wavelengths with proper adjustment of the gain peak to cavity-mode offset.

The scalability of the thin tunnel-junction apertures to small dimensions is important for low threshold operation and to, therefore, reduced heat generation in the devices. Fig. 5 displays an example of this scalability. A reduction in threshold current is demonstrated in a 1.5-μm device as the tunnel-junction aperture is scaled to smaller dimensions. In fact, both wavelengths of devices displayed very low threshold currents, with a lowest value of 0.67 mA for a 4-μm tunnel junction diameter in a 1.5-μm device, and a lowest value of 1.4 mA for a 6-μm tunnel junction diameter in a 1.3-μm device. This result clearly indicates the effective current confinement achieved by the tunnel-junction apertures.

Fig. 5 also shows a greater than 5 $\times$ improvement in differential efficiency as the aperture is scaled to smaller dimensions, indicating that the thin tunnel-junction aperture achieves mode guiding down to small dimensions without introducing significant scattering loss to the device. The low differential efficiencies for large aperture sizes are due to scattering off the rough pillar sidewalls, as the aperture diameter is still comparable to the pillar diameter. These results are in good correlation with simulations based on an algorithm analogous to the classic work of Fox and Li [11].

IV. Conclusion

We have demonstrated all-epitaxial 1.3- and 1.5-μm InP-based VCSELs on a wavelength flexible platform that utilizes a common design, process, and materials growth technology. This shows excellent promise for CWDM applications. Implementation of a thin selectively etched tunnel-junction aperture provided simultaneous electrical and optical confinement and has led to near single-mode operation. These apertures have exhibited good performance down to small dimensions, generating low threshold currents and high differential efficiencies. Future work will involve optimization of the gain peak to cavity-mode offset and high-speed characterization.

References

[1] T. Nishida, M. Takaya, S. Kakinuma, T. Kaneko, and T. Shimoda, "4.2 mW GaInNAs long-wavelength VCSEL grown by metalorganic chemical vapor deposition," in *IEEE Semiconductor Laser Conf.*, Matsue-shi, Japan, Sep. 2004.

[2] V. Jayaraman, M. Mehta, A. W. Jackson, S. Wu, Y. Okuno, J. Piprek, and J. E. Bowers, "High-Power 1320-nm wafer-bonded VCSELs with tunnel junctions," *IEEE Photon. Technol. Lett.*, vol. 15, no. 11, pp. 1495–1497, Nov. 2004.

[3] N. Nishiyama, C. Caneau, B. Hall, G. Guryanov, M. Hu, X. Liu, R. Bhat, and C. Zah, "Temperature, modulation, and reliability characteristics of 1.3 μm-VCSELs on InP with AlGaInAs/InP lattice matched DBR," in *IEEE Semiconductor Laser Conf.*, Matsue-shi, Japan, Sep. 2004.

[4] J. Chang, C. L. Shieh, X. Huang, G. Liu, M. V. R. Murty, C. C. Lin, and D. X. Xu, "Efficient CW lasing and high-speed modulation of 1.3-μm AlGaInAs VCSELs with good high temperature lasing performance," *IEEE Photon. Technol. Lett.*, vol. 17, no. 1, pp. 7–9, Jan. 2005.

[5] R. Shau, M. Ortsiefer, J. Rosskopf, G. Bohm, F. Kohler, and M. C. Amann, "Vertical-cavity surface-emitting laser diodes at 1.55 μm with large output power and high operation temperature," *Electron. Lett.*, vol. 37, no. 21, pp. 1295–1296, Oct. 2001.

[6] C. K. Lin, D. P. Bour, J. Zhu, W. H. Perez, M. H. Leary, A. Tandon, S. W. Corzine, and M. R. T. Tan, "Long wavelength VCSELs with InP/air-gap DBRs," *SPIE Int. Soc. Opt. Eng. Proc.*, vol. 5364, no. 1, pp. 16–24, 2004.

[7] S. Nakagawa, E. Hall, G. Almuneau, J. K. Kim, D. A. Buell, H. Kroemer, and L. A. Coldren, "88 °C, continuous-wave operation of apertured, intracavity contacted, 1.55 μm vertical-cavity surface-emitting lasers," *Appl. Phys. Lett.*, vol. 78, pp. 1337–1339, 2001.

[8] T. Asano, D. Feezell, R. Koda, M. H. M. Reddy, D. A. Buell, A. S. Huntington, E. Hall, S. Nakagawa, and L. A. Coldren, "InP-based all-epitaxial 1.3 μm VCSELs with selectively etched AlInAs apertures and Sb-based DBRs," *IEEE Photon. Technol. Lett.*, vol. 15, no. 10, pp. 1333–1335, Oct. 2003.

[9] M. H. M. Reddy, D. A. Buell, T. Asano, R. Koda, D. Feezell, A. S. Huntington, and L. A. Coldren, "Lattice-matched $Al_{0.95}Ga_{0.05}AsSb$ oxide for current confinement in InP-based long wavelength VCSELs," *J. Cryst. Growth*, vol. 251, no. 1–4, pp. 766–770, Apr. 2003.

[10] M. H. M. Reddy, T. Asano, D. Feezell, D. A. Buell, A. S. Huntington, R. Koda, and L. A. Coldren, "Selectively etched tunnel junction for lateral current and optical confinement in InP-based vertical cavity lasers," *J. Electron. Mater.*, vol. 33, no. 2, pp. 118–122, 2004.

[11] A. G. Fox and T. Li, "Resonant modes in a maser interferometer," *Bell Syst. Tech. J.*, vol. 40, pp. 453–488, 1961.

Efficient Modulation of InP-Based 1.3-μm VCSELs With AsSb-Based DBRs

D. Feezell, L. A. Johansson, D. A. Buell, and L. A. Coldren, *Fellow, IEEE*

***Abstract*—We demonstrate efficient error-free 3.125-Gb/s modulation of InP-based 1.3-μm vertical-cavity surface-emitting lasers with AsSb-based distributed Bragg reflectors up to 60 °C. These devices demonstrated high differential efficiencies [>60% at room temperature (RT)], which resulted in a required bias current for modulation of only 5.9 mA. The measured extinction ratios were greater than 8 dB up to 60 °C with a peak-to-peak drive voltage of only 800 mV. The 3-dB-down RT small-signal bandwidth was 4.4 GHz at a bias of 5.9 mA.**

***Index Terms*—InP-based, long wavelength, modulation, optical fiber communication, semiconductor laser processing, semiconductor lasers, vertical-cavity surface-emitting lasers (VCSELs).**

I. Introduction

LONG-WAVELENGTH vertical-cavity surface-emitting lasers (VCSELs) operating in the 1.3–1.6-μm wavelength range are expected to provide a low-cost alternative to existing edge-emitting lasers in optical fiber communication systems. With low power consumption, on-wafer testing, and high fiber-coupling efficiency, VCSELs are attractive candidates for short to midrange high data-rate applications such as coarse wavelength-division-multiplexing, metro, and local area networks.

Much of the progress toward more manufacturable long-wavelength VCSELs has been hampered by the necessity to match a reliable high-gain active region with high-index-contrast distributed Bragg reflectors (DBRs) over the full 1.3–1.6-μm wavelength range. Approaches employing GaInAsN active regions have shown excellent characteristics near 1.3 μm but still struggle to replicate that performance at higher wavelengths [1]. Wafer-bonded approaches have also shown promising results, but suffer from difficult processing steps [2]. A variety of methods employing the well-established InAlGaAs active region technology have perhaps shown the best performance [3]–[5]. Unfortunately, most of these approaches require a dielectric DBR and do not produce monolithic all-epitaxial devices, which is an important goal toward a more manufacturable product. Another approach is to utilize InAlGaAs active regions coupled with AlGaAsSb DBRs. InAlGaAs active regions are lattice-matched to InP and have demonstrated reliable high-gain operation over the full long-wavelength range with excellent temperature performance. AlGaAsSb DBRs are also lattice-matched to InP and offer high reflectivity over a broad wavelength range, thus enabling wavelength selection from 1.3 to 1.6 μm. In fact, the available index contrast is $\Delta n \approx 0.4$, comparable to that of the GaAs–AlGaAs system. Previously, we have demonstrated excellent continuous-wave (CW) performance in devices employing AsSb-based DBR technology at both the important telecommunications wavelengths of 1.3 and 1.55 μm [6], [7]. The feasibility of this technology for use in high data-rate applications, however, remains to be demonstrated.

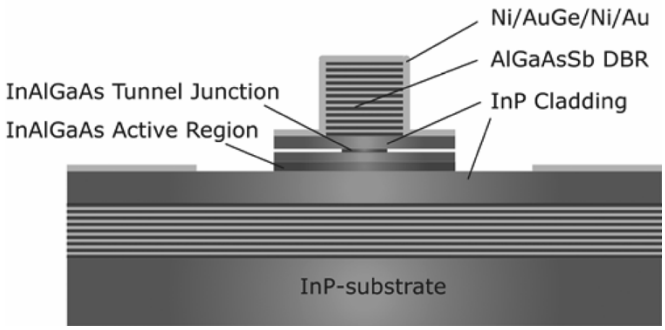

Fig. 1. Schematic of bottom-emitting all-epitaxial VCSEL structure with undercut tunnel-junction aperture.

In this letter, we report the first high-speed modulation of monolithic all-epitaxial 1.3-μm VCSELs with AsSb-based DBRs. Modulation at a data rate of 3.125 Gb/s was demonstrated and error-free operation was obtained up to 60 °C. These devices displayed high differential efficiencies, which resulted in a required bias current for modulation of 5.9 mA. Open eye diagrams were observed at 3.125 Gb/s up to 60 °C. The extinction ratios were extracted and remain >8 dB up to 60 °C for a peak-to-peak drive voltage of only 800 mV. Furthermore, excellent static characteristics were observed. The single-mode CW output power at room-temperature (RT) was >1.6 mW and the differential quantum efficiency was 64%. The threshold current was 1.7 mA and the lasing wavelength was 1.305 μm with a sidemode suppression ratio (SMSR) of 46 dB.

II. Device Structure and Fabrication

The VCSEL structure was grown monolithically in a single growth step by molecular beam epitaxy. Fig. 1 shows a schematic of the bottom-emitting VCSEL device. The device structure is the same as previously reported [7]. The 1/2-λ InAlGaAs multiple-quantum well active region is clad on both

Manuscript received June 15, 2005; revised July 12, 2005. This work was supported in part by the National Science Foundation.

The authors are with the Department of Electrical and Computer Engineering and the Department of Materials, University of California, Santa Barbara, CA 93106 USA (e-mail: feezell@engineering.ucsb.edu; leif@ece.ucsb.edu; dbuell@engineering.ucsb.edu; coldren@ece.ucsb.edu).

Digital Object Identifier 10.1109/LPT.2005.857216

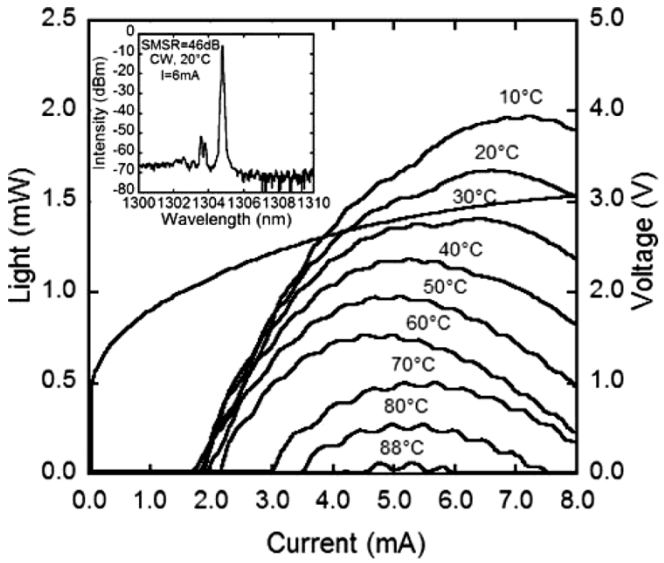

Fig. 2. CW L–I–V curves for bottom-emitting 1.3-μm VCSEL with 8-μm aperture for various stage temperatures. Inset lasing spectrum shows emission at 1.305 μm and 46 dB SMSR. Ripples on L–I curve are due to substrate reflections from bottom-emitting device.

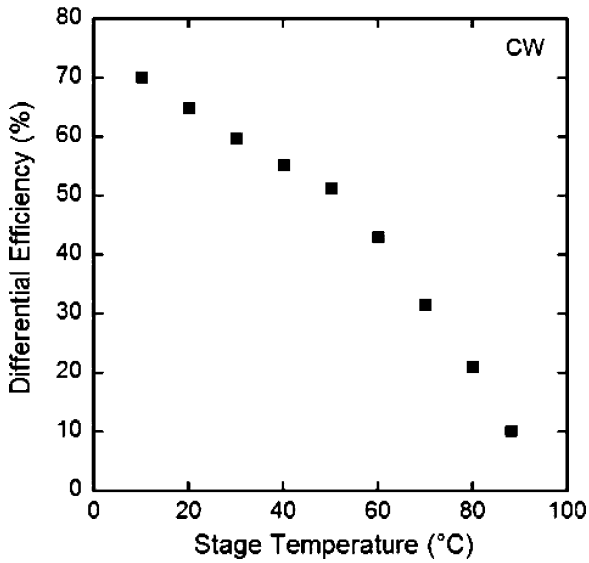

Fig. 3. CW differential efficiency versus stage temperature showing differential efficiency of 64% at RT and over 50% at 50 °C.

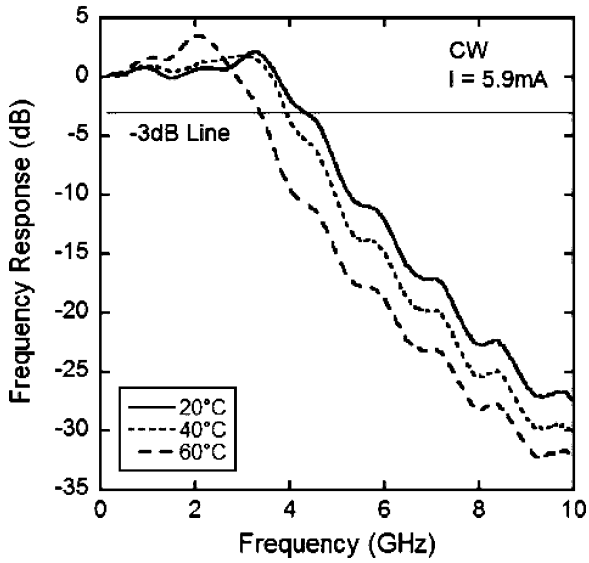

Fig. 4. Small-signal frequency response for VCSEL with 8-μm aperture diameter at 20 °C, 40 °C, and 60 °C at 5.9-, 5.2-, and 4.9-mA drive currents, respectively.

sides by InP layers. These layers facilitate current and heat spreading in the device and serve as intracavity contact layers, allowing for the circumvention of the high electrically and thermally resistive AsSb-based DBRs. The top and bottom DBRs are AlGaAsSb and AlAsSb and contain 39.5 and 25.5 pairs, respectively. Embedded within the upper InP cladding layer at a standing wave null is a 350-Å n^{++}–InAlGaAs/p^{++}InAlGaAs tunnel junction layer that is selectively etched to form a thin low-loss air-gap aperture. This aperture provides excellent optical and electrical confinement in the device [8], [9].

Device fabrication consisted of reactive ion etching (RIE) of the top DBR down to the upper InP-cladding layer in Cl_2 plasma. Ni–AuGe–Ni–Au and SiO_2 were then deposited as the upper contact and etch mask, respectively. The upper InP cladding layer, which functions as an etch-stop layer for the upper DBR, was etched down to the tunnel-junction layer via RIE with CH_4–H_2–Ar. Selective lateral etching of the tunnel junction was then performed with a 10 : 1 mixture of citric acid and hydrogen peroxide to form the thin air-gap aperture. Subsequently, the remaining InP cladding was etched to the active region via RIE. Finally, the active region was etched in citric acid and hydrogen peroxide to expose the bottom InP contact layer. Ni–AuGe–Ni–Au was then evaporated to form the bottom contact.

III. Experiment and Results

Fig. 2 shows the RT static light and voltage versus current (L–I–V) characteristics for a 20-μm VCSEL device with an 8-μm diameter aperture. CW lasing was observed up to 88 °C with an RT output power >1.6 mW and a 64% differential quantum efficiency. These results represent new milestones for AsSb-based long-wavelength VCSELs. The threshold current was 1.7 mA and the device lased single-mode at 1.305 μm with an SMSR of 46 dB. These devices were optimized for RT performance with a gain-mode offset of only 30 nm. With a larger gain-mode offset, the maximum lasing temperature is expected to increase significantly.

Fig. 3 shows the CW differential efficiency versus stage temperature for this device. The differential efficiency remained >50% up to 50 °C. This result is an important advancement toward creating higher power devices with low required drive currents.

Fig. 4 demonstrates the small-signal frequency response of the device at 20 °C, 40 °C, and 60 °C. The maximum RT bandwidth was obtained at a bias of 5.9 mA and is 4.4 GHz. To illustrate the high-speed capabilities of these devices, the VCSELs were modulated using a $2^{31} - 1$ pseudorandom bit sequence (PRBS) at 3.125 Gb/s up to 60 °C. A signal generator and an error performance analyzer provided the data. Light was coupled directly from the device into standard single-mode fiber and then into a 10-Gb optical receiver. Open eye diagrams were

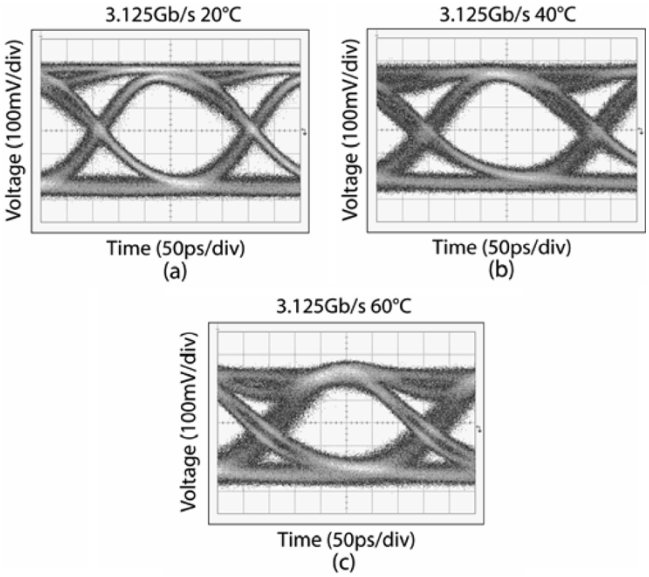

Fig. 5. Eye diagrams for 3.125-Gb/s operation at (a) 20 °C, (b) 40 °C, and (c) 60 °C. Extinction is >8 dB up to 60 °C with a drive voltage of only 800 mV.

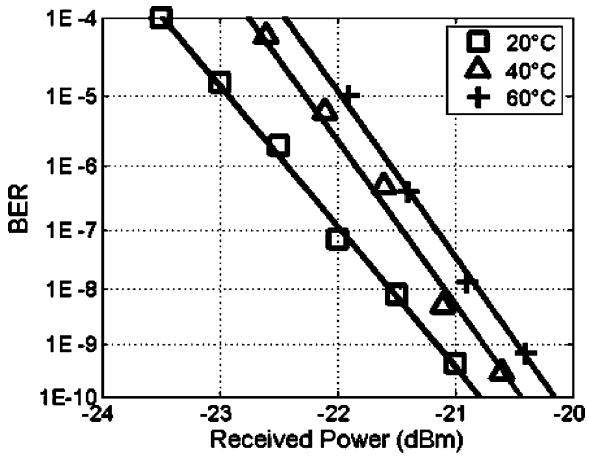

Fig. 6. BER versus received power for 3.125-Gb/s modulation at 20 °C, 40 °C, and 60 °C for a $2^{31} - 1$ PRBS demonstrating error-free operation. Extinction ratio is >8 dB up to 60 °C. Measurements were performed back-to-back.

obtained up to 60 °C. Fig. 5 shows these results. The extinction ratios were derived directly from the optical bit stream and remained >8 dB for operation up to 60 °C with a peak-to-peak drive voltage of only 800 mV. The bias currents at 20 °C, 40 °C, and 60 °C were 5.9, 5.2, and 4.9 mA, respectively.

In order to demonstrate the quality of the eye diagrams at 3.125 Gb/s, bit-error-rate (BER) measurements were performed in a back-to-back configuration. Fig. 6 shows the BER versus received power for 3.125-Gb/s operation at 20 °C, 40 °C, and 60 °C. Error-free operation was demonstrated for a $2^{31} - 1$ PRBS up to a temperature of 60 °C. BERs below 10^{-9} were obtained, indicating that these devices are promising candidates for transmitters at a 3.125-Gb/s data rate.

IV. Conclusion

We have demonstrated the first high-speed modulation for InP-based long-wavelength VCSELs with AsSb-based DBRs. Error-free operation at 3.125 Gb/s was demonstrated up to 60 °C and open eye diagrams were obtained. The extinction ratios were >8 dB up to 60 °C with a peak-to-peak drive voltage of only 800 mV. The high differential efficiencies demonstrated resulted in the low required drive voltages. These results clearly indicate the potential application of this all-epitaxial technology for high-speed data transmitters. Future work will involve larger gain-mode offset devices for improved temperature performance.

References

[1] T. Nishida, M. Takaya, S. Kakinuma, T. Kaneko, and T. Shimoda, "4.2 mW GaInNAs long-wavelength VCSEL grown by metalorganic chemical vapor deposition," presented at the IEEE Semiconductor Laser Conf., Matsue-shi, Japan, Sep. 2004.

[2] V. Jayaraman, M. Mehta, A. W. Jackson, S. Wu, Y. Okuno, J. Piprek, and J. E. Bowers, "High-power 1320-nm wafer-bonded VCSELs with tunnel junctions," *IEEE Photon. Technol. Lett.*, vol. 15, no. 11, pp. 1495–1497, Nov. 2004.

[3] N. Nishiyama, C. Caneau, B. Hall, G. Guryanov, M. Hu, X. Liu, R. Bhat, and C. Zah, "Temperature, modulation, and reliability characteristics of 1.3 μm-VCSELs on InP with AlGaInAs/InP lattice matched DBR," presented at the IEEE Semiconductor Laser Conf., Matsue-shi, Japan, Sep. 2004.

[4] J. Chang, C. L. Shieh, X. Huang, G. Liu, M. V. R. Murty, C. C. Lin, and D. X. Xu, "Efficient CW lasing and high-speed modulation of 1.3 μm AlGaInAs VCSELs with good high temperature lasing performance," *IEEE Photon. Technol. Lett.*, vol. 17, no. 1, pp. 7–9, Jan. 2005.

[5] R. Shau, M. Ortsiefer, J. Rosskopf, G. Bohm, F. Kohler, and M. C. Amann, "Vertical-cavity surface-emitting laser diodes at 1.55 μm with large output power and high operation temperature," *Electron. Lett.*, vol. 37, no. 21, pp. 1295–1296, Oct. 2001.

[6] S. Nakagawa, E. Hall, G. Almuneau, J. K. Kim, D. A. Buell, H. Kroemer, and L. A. Coldren, "88 °C, continuous-wave operation of apertured, intracavity contacted, 1.55 μm vertical-cavity surface-emitting lasers," *Appl. Phys. Lett.*, vol. 78, pp. 1337–1339, 2001.

[7] D. Feezell, D. A. Buell, and L. A. Coldren, "Continuous wave operation of all-epitaxial InP-based 1.3 μm VCSELs with 57% differential quantum efficiency," *Electron. Lett.*, vol. 41, no. 14, pp. 803–804, Jul. 2005.

[8] M. H. M. Reddy, T. Asano, D. Feezell, D. A. Buell, A. S. Huntington, R. Koda, and L. A. Coldren, "Selectively etched tunnel junction for lateral current and optical confinement in InP-based vertical cavity lasers," *J. Elect. Mater.*, vol. 33, no. 2, pp. 118–122, 2004.

[9] D. Feezell, D. A. Buell, and L. A. Coldren, "InP-based 1.3–1.6 μm VCSELs with selectively etched tunnel-junction apertures on a wavelength flexible platform," *IEEE Photon. Technol. Lett.*, vol. 17, no. 10, pp. 2017–2019, Oct. 2005.

III. Avalanche Photodetectors and SOA-PIN Receivers

Detrimental Effect of Impact Ionization in the Absorption Region on the Frequency Response and Excess Noise Performance of InGaAs–InAlAs SACM Avalanche Photodiodes

Ning Duan, S. Wang, X. G. Zheng, X. Li, Ning Li, Joe C. Campbell, *Fellow, IEEE*, Chad Wang, and Larry A. Coldren, *Fellow, IEEE*

***Abstract*—It is shown that optimization of the electric field profile in the absorption region of separate absorption, charge, and multiplication InGaAs–InAlAs avalanche photodiodes is critical to achieve low excess noise and high gain bandwidth product.**

***Index Terms*—Avalanche photodiodes (APDs), excess noise factor, impact ionization, photodetectors.**

I. Introduction

AVALANCHE photodiodes (APDs) are important components in many optical receivers due to the sensitivity margin provided by their internal gain. The seperate absoprtion, charge, and multiplication (SACM) structure APD, which consists of an absorbing region and a multiplication region separated by a charge layer, has the advantage that the photon absorption process and the carrier multiplication process are independent and can be optimized individually to improve both the noise and speed performance [1]. Further, this structure effectively suppresses tunneling in the narrow bandgap-absorbing layer.

$In_{0.53}Ga_{0.47}As$–$In_{0.52}Al_{0.48}As$ (referred to below as InGaAs and InAlAs) APDs have been studied for high-bit-rate optical communication applications [2], [3]. Reduction of the transit time in these APDs can be achieved by utilizing thin absorption layers [4]–[6]. For high responsivity in normal incidence APDs, however, a thick absorption layer is required (the quantum efficiency of a InGaAs–InAlAs SACM APDs with a 1.5-μm InGaAs absorption region is 13% higher than that with a 1-μm InGaAs absorption region), which results in a tradeoff between the sensitivity and the speed. Further, it has been shown for InP–InGaAs separate absorption and multiplication APDs that impact ionization in the absorption region, which is more pronounced for thick absorption regions, can significantly reduce the gain–bandwidth product [7]–[10]. In this paper, we study the speed and noise performance of InGaAs–InAlAs SACM APDs with a thick ($\sim$ 1.5 μm) absorption region. We find that the doping profile in the InGaAs absorption layer influences the level of impact ionization in that layer, which, in turn, significantly affects the gain–bandwidth product and the excess noise.

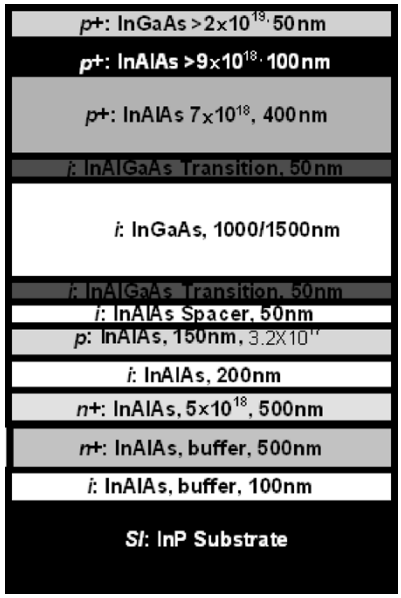

Fig. 1. Schematic layer structure of the InGaAs–InAlAs SACM APD.

II. Device Structure

The structures were grown in a molecular beam epitaxy reactor, on semi-insulating InP substrates. As shown in Fig. 1, the first layer grown was a 100-nm-thick unintentionally doped InAlAs layer to suppress silicon diffusion into the semi-insulating InP substrate from the InAlAs n-contact layer, which can cause excessive parasitic capacitance between contact pads. A 500-nm-thick heavily doped n^+-type (silicon, $\geq 8\times10^{18}$ cm^{-3}) InAlAs layer was grown as a buffer layer and was followed by a 500-nm n^+-type (silicon, $\geq 5\times10^{18}$ cm^{-3}) $In_{0.52}Al_{0.48}As$ contact layer. Following the n-type contact layer, was the multiplication region, an intrinsic InAlAs layer, with a thickness of 200 nm. Next to be deposited was the charge layer, 150-nm-thick p-type (Be-doped) $In_{0.52}Al_{0.48}As$. A 1000 or 1500-nm-thick intrinsic InGaAs, which was sandwiched between two 50-nm-thick unintentionally doped InAlAs spacer

Manuscript received September 30, 2004; revised December 6, 2004.

N. Duan, S. Wang, X. Li, N. Li, and J. C. Campbell are with the Department of Electrical and Computer Engineering, University of Texas at Austin, TX 78713 USA (e-mail: jcc@mail.utexas.edu).

X. G. Zheng is with JDS Uniphase, San Jose, CA 95134 USA.

C. Wang and L. A. Coldren are with the University of California at Santa Barbara, CA 93106 USA.

Digital Object Identifier 10.1109/JQE.2005.843613

TABLE I
PROPERTIES OF APD WAFERS

Parameter	Wafer A	Wafer B	Wafer C
Absorption layer thickness	1μm	1.5μm	1.5μm
Absorption layer doping	Unintentional n-type background doping $2X10^{15}$ cm^{-3}	Unintentional n-type background doping $2X10^{15}$ cm^{-3}	p^- doping of $5X10^{15}cm^{-3}$

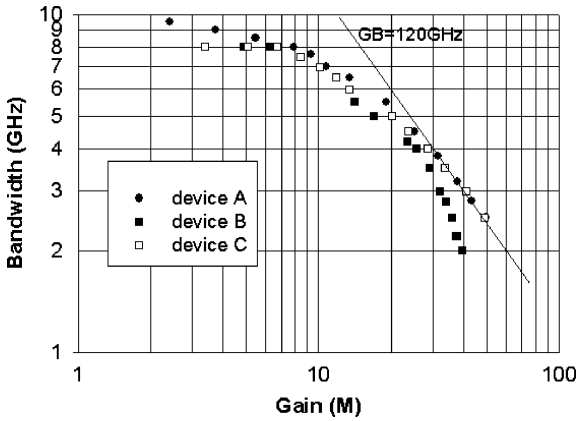

Fig. 2. Measured 3-dB bandwidth versus gain for devices A, B, and C.

layers, was grown as the absorbing layer. The 50-nm undoped InGaAlAs grading layers were inserted to reduce the barrier between InAlAs and InGaAs in order to prevent hole pile-up in the heterointerface. Then a 400-nm-thick p-type (Be-doped, 7×10^{18} cm^{-3}) InAlAs window layer was grown. The p-type contact layers consisted of 100 nm of $In_{0.52}Al_{0.48}As$ (Be: $\geq 2 \times 10^{19}$ cm^{-3}) capped with 50 nm of InGaAs doped at the same level. The wafers studied are compared in Table I. SIMS measurements on all three wafers indicated that, within the measurement accuracy, the structures of wafers A, B, and C were as designed with the same charge doping level of 3.2×10^{17} cm^{-3}. This was also confirmed with capacitance–voltage measurements.

The wafers were fabricated by wet chemical etching into back illuminated mesa structures with diameters in the range 20 to 50 μm. The 50-μm-diameter devices were chosen for speed and noise measurements. The mesas were passivated by plasma-enhanced chemical vapor deposition of SiO_2. The passivation also served as a partial antireflection coating. Ti–Pt–Au metal dot contacts were deposited on the top p-surface of the mesa, and AuGe–Ni–Au contacts were deposited on the n-surface. Conventional photolithography and liftoff metallization techniques were used to define the metal contacts. Microwave contact pads with an air-bridge connection were fabricated for high-speed measurements.

III. RESULTS AND DISCUSSION

S21 Frequency response measurements were made on 50 μm-diameter devices at the wavelength of 1.3 μm. Fig. 2 shows the measured 3-dB bandwidth of devices A, B, and C. If avalanche multiplication is confined to the multiplication region, the gain–bandwidth product should be same for all three devices since they have the same multiplication region.

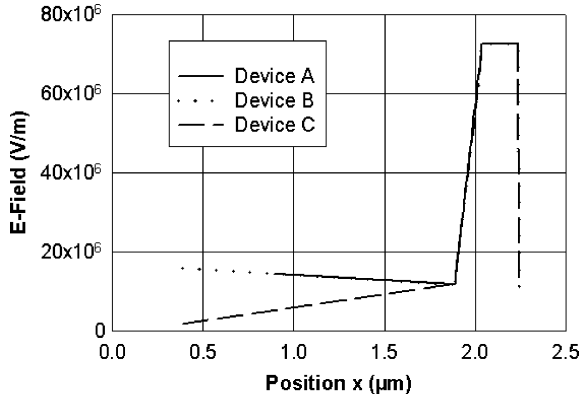

Fig. 3. One-dimensional electric-field profile of devices A, B, and C at gain of 20.

Devices A and C have the same gain–bandwidth product of 120 GHz, an indication that there is insignificant impact ionization in the absorbing layer for these two devices. However, for device B, the bandwidth begins to drop at $M = 15$. This bandwidth degradation compared to devices A and C is due to impact ionization in the thick InGaAs absorption region. In the SACM structure, a high electric field in the multiplication region is required to provide gain, whereas the electric field intensity in the absorbing layer is required to be sufficiently low so as 1) to suppress tunneling and 2) to minimize carrier multiplication in the absorbing region, which is extremely detrimental to APD speed performance [7]–[10]. The electric field strength that causes significant low field carrier multiplication in InGaAs is approximately 150 kV/cm [11], whereas the threshold for tunneling is approximately 220 kV/cm. This speed degradation for device B can be explained by the electric field profile in the absorption region (Fig. 3). The n-type background doping in device B contributes to an electric field profile in which the field in the absorption region closer to the top surface is higher than at the side near the charge layer. When the gain exceeds $\sim$ 15, the electrical field in the absorption region of device B is $\sim$150 kV/cm. With further increase in the electric field, impact ionization becomes more and more significant. Hence, the n-type background doping leads to impact ionization in the portion of the absorption region closer to the top surface where the electric field is higher, which can be extremely detrimental to the speed owing to the effective increase in the total multiplication width for a fraction of the carriers. If the impact ionization in the absorption region occurs in the region near the multiplication region, the speed degradation will not be as serious.

To reduce this bandwidth degradation, we have introduced a p^- doping of 5×10^{15} cm^{-3} in the absorption region of device C in order to keep the electric field low. From Fig. 2 it can be seen that, for device C, the bandwidth for $30 < M < 50$ fits the line of 120-GHz gain–bandwidth product. There is no bandwidth drop similar to that observed for device B, a reflection of the fact that the electrical field in the absorption region of device C remains low (< 150 kV/cm) up to a gain of 50 due to the p^- doping as shown in Fig. 3. Although the electric field profile

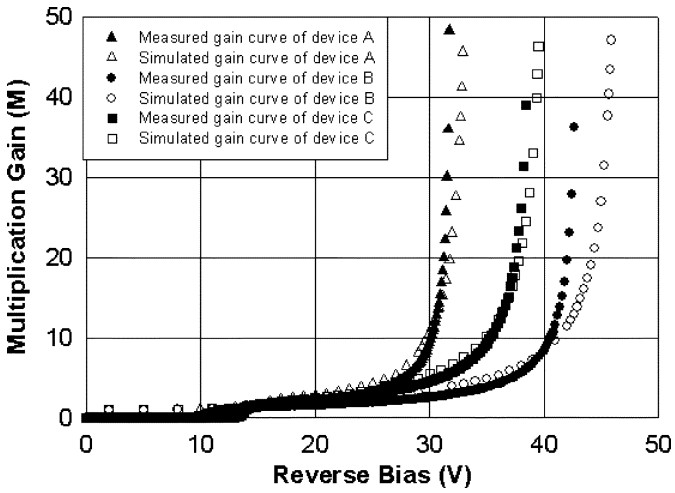

Fig. 4. Measured and simulated gain as a function of reverse bias voltage for devices A, B, and C.

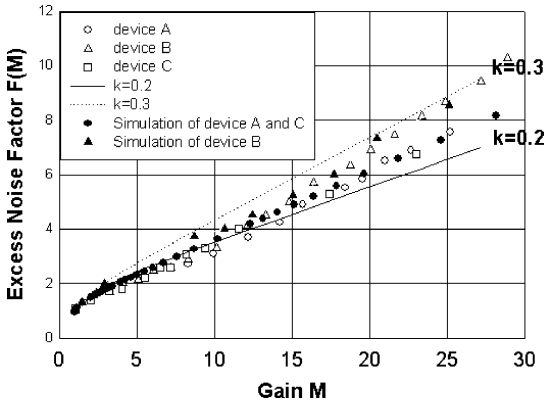

Fig. 5. Simulated and experimental excess noise factor as a function of gain for devices A, B, and C.

of device A is the same as that of device B, there is no significant bandwidth degradation for device A since its absorption region is 0.5 μm thinner than B. Hence, the maximum electric field value in the absorbing region of device A is not as high as that of device B as shown in Fig. 3. The degree of impact ionization is proportional to the product of ionization coefficient and available multiplication width (nonlocal theory). Device A has both lower ionization coefficient and multiplication width.

The gain–bandwidth products of devices A and C are 120 GHz. This value is consistent with previously published results for APDs with similar InAlAs multiplication layer thickness [12]. Devices A and C have the same gain–bandwidth product since they have the same 200-nm-thick InAlAs multiplication region. In the low gain regime, the bandwidth of device A is 9 GHz, while that of device C is 8 GHz. The RC limited bandwidth was estimated by measuring the S11 parameters with a network analyzer. The measured capacitance was $\sim$ 150 fF and total resistance was $\sim$ 70 Ω, yielding an estimated RC-bandwidth of 15 GHz. This frequency is too high to account for the observed 8- and 9-GHz ceilings. The carrier transit-time bandwidth is 13 GHz for devices B and C and 17 GHz for device A if there are no secondary carriers [13]. But for this case, the transit time for the secondary holes to traverse the whole depletion region is important. (The secondary electrons can be neglected since the absorbing layer is much wider than the multiplication region). Taking the transit time of secondary holes into effect, the transit time is $\sim$ 7 ps for devices B and C and $\sim$ 6 ps for device A. Hence we conclude that the observed low gain bandwidths of 8 and 9 GHz are determined by the hole transit time [14]. In the high gain regime ($M > 30$), the bandwidth is dominated by the avalanche buildup time.

According to Emmons' model [15], in the high gain regime, the effective transit time for devices A and C is 1.3 ps.

Using the analytical model described in [16], we simulated the gain curves of devices A, B, and C (Fig. 4). The gain curves were measured using the procedure described in [12]. The measured gain curve of device B is sharper than the simulated gain curve since the simulation assumes no impact ionization in the absorption region, which causes the gain to increase faster. The gain value contributed by a 1.5-μm-thick InGaAs absorbing layer with an electric field of 150 kV/cm is calculated to be 1.13 using the parameters and equations given by [10]. This calculated gain result is consistent with the measured result of [11]. From [17], if a small fraction ε of the secondary holes traveling back across the absorber initiate impact ionization in the absorption region, the total gain is given by

$$M = \frac{M_0}{[1 - \varepsilon(M_0 - 1)]} \tag{1}$$

where M_0 is the electron initiated gain of the InAlAs avalanche region and ε is the feedback factor. At a bias of 42 V as shown in Fig. 4, the measured gain M of device B is 30, while the simulated gain M_0 is 15. The simulated gain of 15 is the gain from the InAlAs multiplication region. Hence, we estimated that the feedback factor ε at this point is 0.036. This shows that if only 3.6% of the secondary holes that traverse the absorbing layer initiate impact ionization, the gain will increase by a factor of two. On the other hand, for devices A and C, the simulated and measured gain curves are coincident. The estimated values of ε are 0.01 and 0.007 for devices A and C, respectively. The small feedback factors for devices A and C explain why there is no bandwidth degradation for these two devices.

To further study the effect of ionization in the absorption layer, the excess noise factor $F(M)$ of these APDs was measured using the procedure described in [18]. A tunable laser operating at 1.55 μm was used as the light source for these measurements. The measured $F(M)$ of devices A, B, and C are shown in Fig. 5. The effective k value was estimated to be 0.2 for both devices A and C. This value is consistent with previously published results for a SACM APD with similar thickness InAlAs multiplication region [19]. The black circle is the simulated $F(M)$ of device A and C using the analytical model described in [16], assuming that impact ionization is confined to the multiplication region. The excess noise of devices A and C follows the simulation. On the other hand, for $M > 15$, the excess noise of device B deviates from the $\mathrm{k} = 0.2$ curve, further confirmation that there is impact ionization in the absorption region. A Monte Carlo simulation [20] confirmed that significant impact ionization occurs in the InGaAs absorption layer;

the simulated noise curve for device B is marked by black triangles in Fig. 5.

In conclusion, we have demonstrated the detrimental effect of impact ionization in the absorption region on the speed and noise performance of InGaAs–InAlAs SACM APDs. We find that the doping profile in the absorption layer strongly influences the amount of impact ionization and thus the gain–bandwidth product and the excess noise.

REFERENCES

[1] H. Nie, K. A. Anselm, C. Hu, S. S. Murtaza, B. G. Streetman, and J. C. Campbell, "High-speed resonant-cavity separate absorption and multiplication avalanche photodiodes with 130 GHz gain-bandwidth product," *Appl. Phys. Lett.*, vol. 70, pp. 161–163, Jan. 1997.

[2] T. Nakata, T. Takeuchi, J. Watanabe, K. Makita, and T. Torikai, "10 Gbit/s high sensitivity, low-voltage-operation avalanche photodiodes with thin InAlAs multiplication layer and waveguide structure," *Electron. Lett.*, vol. 36, pp. 2033–2034, Nov. 2000.

[3] C. Lenox, H. Nie, P. Yuan, G. Kinsey, A. L. Holmes Jr., B. G. Streetman, and J. C. Campbell, "Resonant-cavity InGaAs-InAlAs avalanche photodiodes with gain-bandwidth product of 290 GHz," *IEEE Photon. Technol. Lett.*, vol. 11, no. 9, pp. 1162–1164, Sep. 1999.

[4] G. S. Kinsey, J. C. Campbell, and A. G. Dentai, "Waveguide avalanche photodiode operating at 1.55 μm with a gain-bandwidth product of 320 GHz," *IEEE Photon. Technol. Lett.*, vol. 13, no. 8, pp. 842–844, Aug. 2001.

[5] S. Demiguel, N. Li, X. Li, X. Zheng, J. Kim, J. C. Campbell, H. Lu, and A. Anselm, "Very high-responsivity evanescently coupled photodiodes integrating a short planar multimode waveguide for high-speed applications," *IEEE Photon. Technol. Lett.*, vol. 15, no. 12, pp. 1761–1703, Dec. 2003.

[6] J. Wei, F. Xia, and S. R. Forrest, "A high-responsivity high-bandwidth asymmetric twin-waveguide coupled InGaAs-InP-InAlAs avalanche photodiode," *IEEE Photon. Technol. Lett.*, vol. 14, no. 11, pp. 1590–1592, Nov. 2002.

[7] I. Watanabe, M. Tsuji, K. Makita, and K. Taguchi, "Gain-Bandwidth product analysis of InAlGaAs-InAlAs superlattice avalanche photodiodes," *IEEE Photon. Technol. Lett.*, vol. 8, no. 2, pp. 269–271, Feb. 1996.

[8] L. E. Tarof, J. Yu, R. Bruce, D. G. knight, T. Baird, and B. Oosterbrink, "High-Frequency performance of separate absorption, grading, charge, and multiplication InP/InGaAs avalanche photodiodes," *IEEE Photon. Technol. Lett.*, vol. 5, no. 6, pp. 672–674, Jun. 1993.

[9] G. Kahraman, N. E. A. Saleh, W. L. Sargeant, and M. C. Teich, "Time and frequency response of avalanche photodiodes with arbitrary structure," *IEEE Trans. Electron Devices*, vol. 39, no. 3, pp. 553–560, Mar. 1992.

[10] F. Osaka and T. Mikawa, "Excess noise design of InP–GaInAsP–GaInAs avalanche photodiodes," *IEEE J. Quantum Electron.*, vol. QE-22, no. 3, pp. 471–478, Mar. 1986.

[11] J. S. Ng, C. H. Tan, J. P. R. David, G. Hill, and G. J. Rees, "Dependence of impact ionization coefficients in $In_{0.53}Ga_{0.47}As$," *IEEE Trans. Electron Devices*, vol. 50, no. 4, pp. 901–906, Apr. 2003.

[12] X. G. Zheng, J. S. Hsu, J. B. Hurst, X. Li, S. Wang, X. Sun, A. L. Holmes Jr., J. C. Campbell, A. S. Huntington, and L. A. Goldren, "Long-wavelength InGaAs–InAlAs large-area avalanche photodiodes and arrays," *IEEE J. Quantum Electron.*, vol. 40, no. 8, pp. 1068–1073, Aug. 2004.

[13] K. Kato, "Ultrawide-band/high-frequency photodetectors," *IEEE Trans. Microwave Theory Tech.*, vol. 47, no. 7, pp. 1265–1281, Jul. 1999.

[14] J. C. Campbell, W. T. Tsang, G. J. Qua, and B. C. Johnson, "High speed InP–InGaAsP–InGaAs avalanche photodiodes grown by chemical beam epitaxy," *IEEE J. Quantum Electron.*, vol. 24, no. 3, pp. 496–500, Mar. 1988.

[15] E. B. Emmons, "Avalanche-photodiode frequency response," *J. Appl. Phys.*, vol. 38, pp. 3705–3714, Aug. 1967.

[16] X. Li, X. Zheng, S. Wang, F. Ma, and J. C. Campbell, "Calculation of gain and noise with dead space for GaAs and $Al_xGa_{1-x}As$ avalanche photodiode," *IEEE Trans. Electron Devices*, vol. 49, no. 7, pp. 1112–1117, Jul. 2002.

[17] J. N. Holenhorst, D. T. Ekholm, J. M. Geary, V. D. Mattera Jr., and R. Pawelek, "High frequency performance of planar InGaAs/InP avalanche photodiodes," *Proc. SPIE*, vol. 995, p. 53, Sep. 1988.

[18] S. Wang, R. Sidhu, X. G. Zheng, X. Li, X. Sun, A. L. Holmes Jr., and J. C. Campbell, "Low-noise avalanche photodiodes with graded impact-ionization-engineered multiplication region," *IEEE Photon. Technol. Lett.*, vol. 13, no. 12, pp. 1346–1348, Dec. 2001.

[19] N. Li, R. Sidhu, X. Li, F. Ma, X. Zheng, S. Wang, G. Karve, S. Demiguel, A. L. Holmes Jr., and J. C. Campbell, "InGaAs/InAlAs avalanche photodiode with undepleted absorber," *Appl. Phys. Lett.*, vol. 82, pp. 2175–2177, Mar. 2003.

[20] F. Ma, N. Li, and J. C. Campbell, "Monte Carlo simulation of the bandwidth of InAlAs avalanche photodiodes," *IEEE Trans. Electron Devices*, vol. 50, no. 11, pp. 2291–2294, Nov. 2001.

Ning Duan was born in Neimenggu, China, in 1978. She received the B.S. degree in applied physics and the M.S. degree in optics from Northern Jiaotong University, Beijing, China, in 1999 and 2001, respectively. She is currently working toward the Ph.D. degree in electrical engineering at the Microelectronic Research Center, University of Texas at Austin.

Her research interests are high-speed long-wavelength avalanche photodiodes and high-saturation power p-i-n photodiodes.

S. Wang received the B.S. degree in microelectronics from Beijing University, China, in 1995 and the M.S.E.E. degree from University of Notre Dame, South Bend, IN, in 1999. She received the Ph.D. degree in electrical engineering from the University of Texas at Austin in 2002.

She is currently a Research Scientist in the Microelectronics Research Center at the University of Texas working on high-speed, low-noise avalanche photodiodes.

Dr. Wang is a member of the IEEE Lasers and Electro-Optics Society.

X. G. Zheng received the B.S.E.E. degree from the Beijing Institute of Technology, Beijing, China, in 1985 and the M.S. degree in electrical engineering from the Hebei Semiconductor Research Institute, Hebei, China, in 1991. He received the Ph.D. degree in electrical engineering from the University of Texas at Austin in 2004.

His major research interests are in optoelectronic devices: impact ionization properties of III-V compound materials, high-speed long-wavelength avalanche photodiodes and arrays, and heterogeneous material integration via direct wafer bonding. He is presently employed by JDS Uniphase, San Jose, CA.

X. Li was born in Beijing, China, in 1970. He received the B.S. and M.S. degrees from the Physics Department of Peking University, Beijing, China, in 1994 and 1997, respectively. He received the Ph.D. degree in electrical engineering from the Microelectronic Research Center, University of Texas at Austin in 2004.

His research interests are avalanche process simulations and high saturation power photodetectors for 1.55 μm applications. He is currently working for Applied Materials, University of Texas at Austin.

Ning Li was born in Beijing, China, in 1978. He received the B.S. and M.S. degrees from the Electronic Engineering Department, Tsinghua University, Beijing, China, in 1998 and 2000, respectively. He is currently pursuing the Ph.D. degree in electrical engineering at the Microelectronic Research Center, University of Texas at Austin.

His research interests are waveguide p-i-n and APD photodetectors.

Joe C. Campbell (S'73–M'74–SM'88–F'90) received the B.S. degree in physics from The University of Texas at Austin in 1969 and the M.S. and Ph.D. degrees in physics from the University of Illinois at Urbana-Champaign in 1971 and 1973, respectively.

From 1974 to 1976, he was with Texas Instruments Incorporated, Dallas, TX, where he was involved with integrated optics. In 1976, he joined the staff of AT&T Bell Laboratories, Holmdel, NJ. In the Crawford Hill Laboratory, he worked on a variety of optoelectronic devices including semiconductor lasers, optical modulators, waveguide switches, photonic integrated circuits, and photodetectors with emphasis on high-speed avalanche photodiodes for high-bit-rate lightwave systems. In January 1989, he joined the faculty of The University of Texas at Austin as a Professor of Electrical and Computer Engineering and Cockrell Family Regents Chair in Engineering. At present, he is actively involved in Si-based optoelectronics, high-speed, low-noise avalanche photodiodes, high-power photodiodes, ultraviolet photodetectors, and quantum-dot IR imaging. He has coauthored six book chapters, more than 300 journal publications, and 200 conference presentations.

Prof. Campbell is a member of the National Academy of Engineering, a Fellow of the Optical Society of America, and a Fellow of the American Physical Society.

Chad Wang received the B.S. degree in electrical and computer engineering from the University of Texas at Austin in 2001. He is currently pursuing the Ph.D. degree at the University of California at Santa Barbara.

He is currently working on a novel, high-speed laser-modulator designed for optical interconnects. He is also involved in MBE growth of GaAs material and lattice-matched arsenides to InP for long-wavelength VCSELs and APDs.

Larry A. Coldren (S'67–M'72–SM'77–F'82) received the Ph.D. degree in electrical engineering from Stanford University, Stanford, CA, in 1972.

After 13 years in the research area at Bell Laboratories, he was appointed Professor of Electrical and Computer Engineering at the University of California at Santa Barbara (UCSB) campus in 1984. In 1986, he assumed a joint appointment with Materials and ECE, and in 2000 the Fred Kavli Chair in Optoelectronics and Sensors. He is also Chairman and Chief Technology Officer of Agility Communications, Inc. At UCSB, his efforts have included work on novel guided-wave and vertical-cavity modulators and lasers as well as the underlying materials growth and fabrication technology. He is now investigating the integration of various optoelectronic devices, including optical amplifiers and modulators, tunable lasers, wavelength-converters, and surface-emitting lasers. He has authored or coauthored over 500 papers, five book chapters, one textbook, and has been issued 32 patents.

Prof. Coldren is a Fellow of the Optical Society of America (OSA) and a past Vice-President of IEEE Laser and Electro-Optics Society (LEOS).

High-Speed and Low-Noise SACM Avalanche Photodiodes With an Impact-Ionization-Engineered Multiplication Region

Ning Duan, Shuling Wang, Feng Ma, Ning Li, Joe C. Campbell, Chad Wang, and Larry A. Coldren

***Abstract*—A separate absorption, charge, and multiplication $In_{0.53}Ga_{0.47}As$–$In_{0.52}Al_{0.48}As$ avalanche photodiode with an impact-ionization-engineered multiplication region is reported. By implementing an electric field gradient in the multiplication region, better control of impact-ionization can be achieved. Gain-bandwidth product of 160 GHz and excess noise factor with an equivalent k value of 0.1 are demonstrated.**

***Index Terms*—Avalanche photodiodes (APDs), impact ionization, photodetectors.**

I. Introduction

THE separate absorption, charge, and multiplication (SACM) structure avalanche photodiode (APD), which consists of an absorbing region and a multiplication region separated by a charge layer, has been widely studied for high-bit-rate long-haul wide-band optical communication applications. The SACM APD structure has the advantage that the photon absorption process and the impact ionization multiplication process are independent from each other and can be optimized individually to improve both the noise and speed performance. Further, this structure effectively suppresses tunneling in the narrow bandgap-absorbing layer.

Much of the research on these APDs has focused on achieving lower noise and higher gain-bandwidth products to accommodate the ever-increasing bit rates of fiber-optic systems. Lower noise is usually associated with higher speed, since in the gain distributions, the high-gain tail contributes to both higher noise and longer transit time [1]. Very low noise has been achieved in the GaAs–AlGaAs material system by impact ionization engineering (I^2E) [2], [3]. It is now understood that the role of heterojunctions in lowering the multiplication noise of APDs is to spatially localize impact ionization events even with $\alpha/\beta \sim 1$ [4]. To apply the I^2E concept first demonstrated with AlGaAs–GaAs APDs to more practical "long wavelength" materials that are widely used for fiber-optic components, APDs with I^2E multiplication region using AlInGaAs–InAlAs have been reported for a PIN-type structure [5]. However, incorporation of an I^2E multiplication region into an SACM structure with an InGaAs absorber has not been reported. In this letter, we present the design and successful implementation of an SACM APD with an $In_{0.52}Al_{0.48}As$–$In_{0.53}Ga_{0.17}Al_{0.3}As$ I^2E multiplication region.

Manuscript received April 5, 2005; revised April 26, 2005.

N. Duan, S. Wang, F. Ma, N. Li, and J. C. Campbell are with the University of Texas, Austin, TX 78712 USA (e-mail: jcc@mail.utexas.edu).

C. Wang and L. A. Coldren are with the University of California, Santa Barbara, CA 93106 USA.

Digital Object Identifier 10.1109/LPT.2005.851903

Fig. 1. Schematic layer structure of the SACM APD.

II. Device Structure

The structure was grown in a molecular beam epitaxy reactor, on a semi-insulating InP substrate. As shown in Fig. 1, the first layer grown was a 100-nm-thick unintentionally doped $In_{0.52}Al_{0.48}As$ layer to suppress silicon diffusion into the semi-insulating InP substrate from the $In_{0.52}Al_{0.48}As$ n-contact layer, which can cause excessive parasitic capacitance between contact pads. A 500-nm-thick heavily doped n^+-type (silicon, $\geq 8 \times 10^{18}$ cm^{-3}) $In_{0.52}Al_{0.48}As$ layer was grown as a buffer layer and was followed by a 500-nm n^+-type (silicon, $\geq 5 \times 10^{18}$ cm^{-3}) $In_{0.52}Al_{0.48}As$ contact layer. Following the n-type contact layer was the I^2E multiplication region. The compound multiplication region consisted of an unintentionally doped layer of $In_{0.52}Al_{0.48}As$ with a thickness of 80 nm, an unintentionally doped $In_{0.53}Ga_{0.17}Al_{0.3}As$ layer with a thickness of 80 nm, a P-type (Be, 2.2×10^{17} cm^{-3})

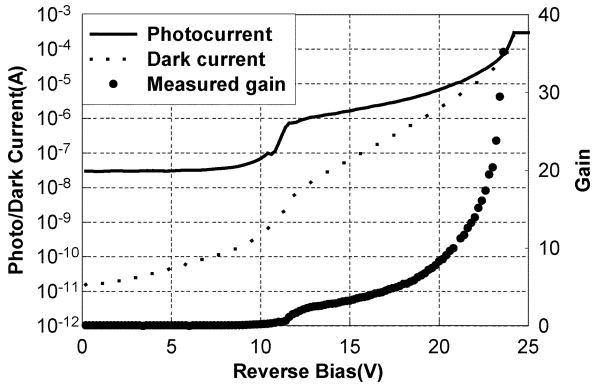

Fig. 2. Current–voltage and gain curves for a 150-μm-mesa-diameter APD.

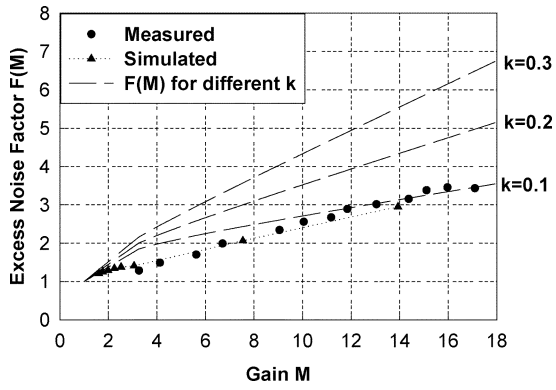

Fig. 3. Simulated and experimental excess noise factor as a function of gain.

120-nm-thick $In_{0.53}Ga_{0.17}Al_{0.3}As$ layer, and an 80-nm-thick $In_{0.52}Al_{0.48}As$ layer with the same P-type doping level. The latter two layers also served as the field control or "charge" region. A 420-nm-thick intrinsic $In_{0.53}Ga_{0.47}As$ layer was grown as the absorbing layer. Undoped InGaAlAs grading layers (50 nm) were inserted to reduce the barrier between $In_{0.52}Al_{0.48}As$ and $In_{0.53}Ga_{0.47}As$ in order to prevent carrier pile-up at the heterointerface. The absorber was slightly p-doped in order to suppress impact ionization in the absorption region [6]. Ideally, the doping in the absorber would be graded to provide a slightly higher field in the direction of the multiplication region. This was approximated by step doping the absorber in two regions, one at $1 \times 10^{16}/\text{cm}^3$ and the other at $4 \times 10^{16}/\text{cm}^3$. After the top grading layer, a 400-nm-thick p-type (Be-doped, 4×10^{18} cm^{-3}) $In_{0.52}Al_{0.48}As$ window layer was grown. The p-type contact layers consisted of 100 nm of $In_{0.52}Al_{0.48}As$ ($\text{Be} : \geq 9 \times 10^{18}$ cm^{-3}) capped with 50 nm of $In_{0.53}Ga_{0.47}As$ doped at the same level.

The wafers were fabricated into back-illuminated mesa structures using the procedure described in [6].

III. Results and Discussion

The photocurrent and dark current curves of an 80-μm-diameter APD are shown in Fig. 2. The punch-through voltage was $\sim$12 V and the breakdown voltage was $\sim$24 V. The photocurrent curve of the APD exhibited a slope after punch-through, an indication of multiplication gain at punch-through. In order to characterize the multiplication gain, the external quantum efficiency (QE) was measured under different bias levels above the punch-through voltage, using a laser operating at 1.55 μm. At a bias of 15 V, the APD was fully depleted and the measured external QE was $\sim$58%. The expected external QE at unity-gain can be estimated by the following expression:

$$\eta_{\text{ext}} = (1 - R) \cdot (1 - e^{-\alpha \cdot d}) \tag{1}$$

where R is the reflection coefficient of the air–semiconductor interface; α is the absorption coefficient of $In_{0.53}Ga_{0.47}As$ at the relevant incident wavelength; and d is the absorption layer thickness. Since the absorption coefficient of $In_{0.53}Ga_{0.47}As$ is 0. 705 μm^{-1} at 1.55 μm [7], for an SACM APD with a 0.42-μm-thick $In_{0.53}Ga_{0.47}As$ absorber, the expected external QE is $\sim$18% assuming an optical transmission of 69% ($R = 0.31$) at the air–semiconductor interface (the SiO_2 AR coating was stripped off during the QE measurement in order to reduce uncertainty in the reflectivity). The measured value ($\sim$58%) at the reference bias of 15 V is 3.2 times higher than the maximum theoretical value ($\sim$18%). We attribute this large QE to the multiplication gain at punch-through, hence the gain at a bias voltage of 15.0 V is estimated to be at least 3.2. The calculated gain curve of an 80-μm-diameter APD is plotted in Fig. 2.

The excess noise factor $F(M)$ was measured following the procedure described in [8]. A semiconductor laser operating at 1.55 μm was used as the light source for these measurements. Since there is multiplication gain at punch-through as discussed above, the determination of $F(M)$ is complicated by the fact that the noise value at unity gain, which is the standard reference for this type of measurement, is unknown. This was addressed by using a Monte Carlo simulation to estimate the excess noise factor at $M = 3.2$. The value obtained was $F(M = 3.2) = 1.41$. This then served as the reference point to determine $F(M)$ at higher gains. The measured and simulated $F(M)$ are shown in Fig. 3. The effective k value was estimated to be 0.1 up to a gain of more than 15. We note that this is consistent with noise measurements on PIN-structure InGaAlAs–InAlAs I^2E APDs [5]. This low noise results from reducing the initial dead space effect for electrons injected from the wide bandgap $In_{0.52}Al_{0.48}As$ into $In_{0.53}Ga_{0.17}Al_{0.3}As$, which has lower threshold energy [9], [10]. The sloped electric field in the multiplication region also plays an important role in achieving low noise [11]. Electrons are injected from the absorption layer to the multiplication region. They start to impact ionize when the electric field in the charge layer becomes sufficiently high. More and more electron-initiated ionizations occur as the electrons are transported into the multiplication region toward higher electric field. On the other hand, hole impact ionizations in the charge layer are suppressed due to the lower and lower electric field they encounter as they travel back toward the absorber. Hence, there is less reliance on noisy feedback ionization to provide multiplication.

Shown in Fig. 4 is a Monte Carlo simulation of the distribution of impact ionization events in the multiplication region at an average gain of 14. It can be seen that most of the ionization events occur in the $In_{0.53}Ga_{0.17}Al_{0.3}As$-well layer. Photon generated electrons drift from the absorption layer toward the charge layer. They gain kinetic energy

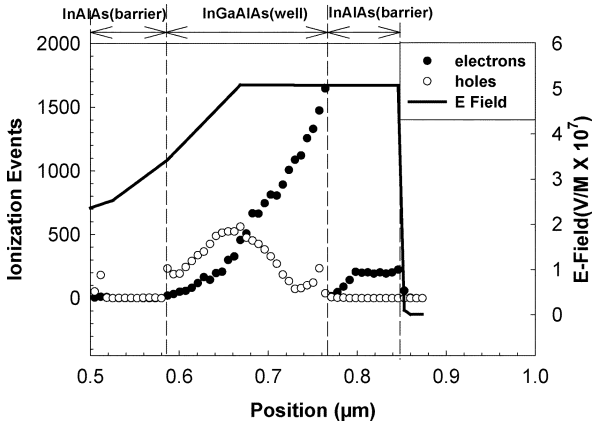

Fig. 4. Simulated impact ionization events distribution and electric field profile as a function of position.

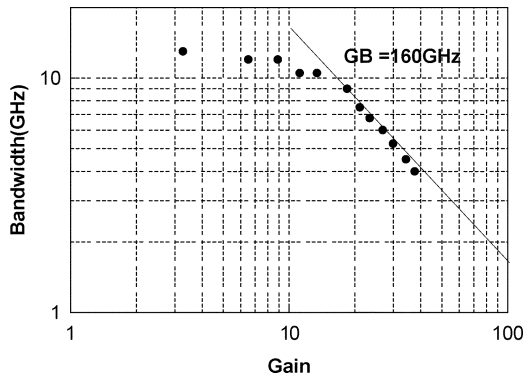

Fig. 5. Measured 3-dB bandwidth versus gain for a 20-μm-mesa-diameter APD.

in the $In_{0.52}Al_{0.48}As$ charge layer where impact ionization events are rare as a result of the large carrier ionization threshold energy in $In_{0.52}Al_{0.48}As$. Once the electrons reach the $In_{0.53}Ga_{0.17}Al_{0.3}As$ charge layer, where the threshold energy is lower, they ionize quickly. As the electrons travel through the $In_{0.53}Ga_{0.17}Al_{0.3}As$ charge layer, they encounter higher and higher electric field and initiate more and more impact ionizations. In the undoped $In_{0.53}Ga_{0.17}Al_{0.3}As$ multiplication layer, the electric field reaches its highest value and the electrons continue to ionize. Once they reach the undoped $In_{0.52}Al_{0.48}As$ layer, although the electric field remains constant, the impact ionization events decrease dramatically due to the higher threshold energy in $In_{0.52}Al_{0.48}As$. Holes generated by electron initiated impact ionization in the $In_{0.53}Ga_{0.17}Al_{0.3}As$ multiplication region travel in the opposite direction toward the p-contact. However, the hole initiated impact ionization events decrease once holes reach the $In_{0.53}Ga_{0.17}Al_{0.3}As$ charge layer due to the lower and lower electric field they encounter. This spatial modulation of electron and hole impact ionization events by utilizing the I^2E structure combined with a graded electric field in the multiplication region results in lower excess noise.

S21 RF amplitude measures were made on 20-μm-diameter devices. Fig. 5 shows the 3-dB bandwidth as a function of gain. This device structure is shown to have a gain-bandwidth product of 160 GHz up to a gain of 40. This gain-bandwidth product is higher than an SACM APD with bulk $In_{0.52}Al_{0.48}As$ multiplication region that has similar multiplication-region-thickness [6]. This is due to the fact that the suppression of hole initiated impact ionization results in reduction of the long tail in the pulse response. The low-gain bandwidth of a typical 20-μm-diameter device is 14 GHz. The calculated resistance–capacitance (*RC*) limited bandwidth was 15 GHz, which indicates that the bandwidth at low gain was *RC* limited.

IV. Conclusion

We have designed and studied an SACM APD structure that was grown on InP substrate with impact-ionization-engineered multiplication region. Lower noise $(k = 0.1)$ and higher speed performance $(\text{gain} - \text{bandwidth product} = 160\ \text{GHz})$ compared to SACM APDs with bulk InAlAs multiplication layer have been achieved.

References

[1] F. Ma, N. Li, and J. C. Campbell, "Monte Carlo simulations of the bandwidth of InAlAs avalanche photodiodes," *IEEE Trans. Electron Devices*, vol. 50, no. 11, pp. 2291–2294, Nov. 2003.

[2] P. Yuan, S. Wang, X. Sun, X. Zheng, A. L. Holmes Jr., and J. C. Campbell, "Avalanche photodiodes with an impact-ionization-engineered multiplication region," *IEEE Photon. Technol. Lett.*, vol. 12, no. 10, pp. 1370–1372, Oct. 2000.

[3] S. Wang, F. Ma, X. Li, R. Sidhu, X. G. Zheng, S. Sun, A. L. Holmes Jr., and J. C. Campbell, "Ultra-low noise avalanche photodiodes with a 'centered-well' multiplication region," *IEEE J. Quantum Electron.*, vol. 39, no. 2, pp. 375–378, Feb. 2003.

[4] F. Ma, S. Wang, X. Li, K. A. Anselm, X.-G. Zheng, A. L. Holmes Jr., and J. C. Campbell, "Monte Carlo simulation of low-noise avalanche photodiodes with heterojunctions," *J. Appl. Phys.*, vol. 92, pp. 4791–4795, Oct. 2002.

[5] S. Wang, J. B. Hurst, F. Ma, R. Sidhu, X. Sun, X. Zheng, A. L. Holmes Jr., and J. C. Campbell, "Low-noise impact-ionization-engineered avalanche photodiodes grown on InP substrates," *IEEE Photon. Technol. Lett.*, vol. 14, no. 12, pp. 1722–1724, Dec. 2002.

[6] N. Duan, S. Wang, X. G. Zheng, X. Li, N. Li, J. C. Campbell, C. Wang, and L. A. Coldren, "Detrimental effect of impact ionization in the absorption region on the frequency response and excess noise performance of InGaAs/InAlAs SACM avalanche photodiodes," *IEEE J. Quantum Electron.*, vol. 41, no. 4, pp. 568–572, Apr. 2005.

[7] X. G. Zheng, J. Hsu, X. Sun, J. B. Hurst, X. Li, S. Wang, A. L. Holmes Jr., J. C. Campbell, A. S. Huntington, and L. A. Coldren, "A 12 _ 12 In Ga As-In Al As avalanche photodiode array," *IEEE J. Quantum Electron.*, vol. 38, no. 11, pp. 1536–1540, Nov. 2002.

[8] S. Wang, R. Sidhu, X. G. Zheng, X. Li, X. Sun, A. L. Holmes Jr., and J. C. Campbell, "Low-noise avalanche photodiodes with graded impact-ionization-engineered multiplication region," *IEEE Photon. Technol. Lett.*, vol. 13, no. 12, pp. 1346–1348, Dec. 2001.

[9] O.-H. Kwon, M. M. Hayat, S. Wang, J. C. Campbell, A. Holmes Jr., Y. Pan, B. E. A. Saleh, and M. C. Teich, "Optimal excess noise reduction in thin heterojunction Al0:6Ga0:4As-GaAs avalanche photodiodes," *IEEE J. Quantum Electron.*, vol. 39, no. 10, pp. 1287–1296, Oct. 2003.

[10] C. Groves, C. K. Chia, R. C. Tozer, J. P. R. David, and G. J. Rees, "Avalanche noise characteristics of single AlxGa1 xAs$(0 : 3 < x < 0 : 6)$-GaAs heterojunction APDs," *IEEE J. Quantum Electron.*, vol. 41, no. 1, pp. 70–75, Jan. 2005.

[11] S. A. Plimmer, C. H. Tan, J. P. R. David, R. Grey, K. F. Li, and G. J. Rees, "The effect of an electric-field gradient on avalanche noise," *Appl. Phys. Lett.*, vol. 75, pp. 2963–2965, Nov. 1999.

High Saturation Power and High Gain Integrated Photoreceivers

Anna Tauke-Pedretti, *Student Member, IEEE*, Matthew Dummer, *Student Member, IEEE*, Jonathon S. Barton, *Member, IEEE*, Matthew N. Sysak, *Student Member, IEEE*, James W. Raring, *Student Member, IEEE*, and Larry A. Coldren, *Fellow, IEEE*

***Abstract*—A novel monolithically integrated semiconductor optical amplifier (SOA) receiver is presented. This receiver implements a flared SOA and tapered quantum-well detector. SOAs exhibited 22-dB unsaturated gain and 15.7-dBm output power at the 1-dB gain compression point while the receiver demonstrated 15-GHz bandwidth and −10.5-dBm sensitivity.**

***Index Terms*—Offset quantum well, optical receivers, saturation power, semiconductor optical amplifiers (SOAs), waveguide photodiodes, wavelength conversion.**

I. Introduction

MONOLITHICALLY integrated photoreceivers which combine amplification and detection elements are advantageous over discrete devices by producing greater sensitivity, decreased coupling loss, simplified packaging, and reduced cost. Although high performance semiconductor optical amplifier (SOA)-PINs have been fabricated with bandwidths up to 40 GHz, typically they produce low output powers (~ 200 mV$_{p\text{-}p}$) requiring the signal to be electronically amplified for many applications [1], [2].

As optical device integration density continues to increase, it becomes desirable to develop integration platforms that are compatible with tunable lasers as well as receivers. One such photonic integrated circuit of interest is a photocurrent driven wavelength converter. These devices use photocurrent from detected input light to drive optical modulators. For size and packaging considerations of wavelength converters, it is desirable to monolithically integrate the receivers and transmitters, thus constraining the material used to be compatible with the fabrication of lasers. To maintain small footprints and minimize parasitic effects in monolithic wavelength converters, it is beneficial to avoid the use of electrical amplification. In past devices, the conversion efficiency and the extinction of the converted signal have been limited by the gain and low saturation powers of the photoreceiver used [3], [4]. These limitations can be overcome with the use of the photoreceivers presented in this letter [5].

Waveguide photodetectors allow for efficient detection of light and are easy to integrate with SOAs; however, they often suffer from saturation problems and degrade at high optical powers due to the high optical power density/photocurrent at the front end of the detector. The detector presented here achieves acceptable power densities at the front end and minimum capacitance through the use of lateral tapering.

It is well known that the high optical power density in SOAs will deplete active region carriers creating gain saturation. When modulated light is amplified, it is desirable to operate at power levels below saturation to prevent signal distortion. The saturation power levels can be increased through gain clamping, reducing the power density [6], or increasing carrier density [7]. In this letter, the SOA has been laterally flared to keep the optical power density below saturation while the power grows.

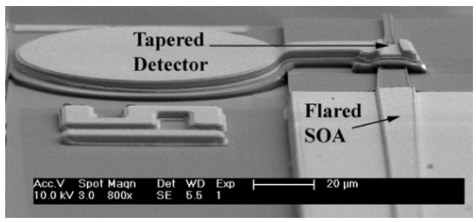

Fig. 1. Scanning electron microscope (SEM) of integrated photoreceiver.

II. Device

The photoreceiver consists of a monolithically integrated SOA and quantum-well absorber, as shown in Fig. 1.

The SOA is designed as a two-stage amplifier. A 200-μm-long by 3-μm-wide section provides gain to low input powers while keeping amplified spontaneous emission noise to a minimum. This is followed by a 400-μm-long section, which linearly flares from 3 to 9 μm. The flaring is implemented to reduce the optical power density, thus increasing the SOA saturation power. The 50-μm-long photodetector employs a linear ridge taper from 9 to 3 μm to prevent front-end saturation effects at high optical powers. Photo-bis-benzocyclobutene (BCB) is used under the detector pads in order to reduce the parasitic pad capacitance.

The device is fabricated using an offset quantum-well material structure with a single regrowth. The fabrication process is completely compatible with that of a sampled-grating distributed-Bragg-reflector transmitter and requires no additional steps [3]–[5]. A curved and flared input waveguide is used to aid in fiber coupling as well as to reduce optical reflections. In addition, a multilayer antireflection coating is applied to further reduce the optical reflections. Seven quantum wells provide the

Manuscript received January 19, 2005; revised June 2, 2005. This work was supported by Intel Corporation Grant TXA001630000 and by Defense Advanced Research Projects Agency (DARPA) MTO-LASOR Grant W911NF-04-9-0001.

The authors are with the Department of Electrical Engineering and the Department of Materials Engineering, University of California Santa Barbara, Santa Barbara, CA 93106 USA (e-mail: atauke@engineering.ucsb.edu; dummer@engineering.ucsb.edu; jsbarton@engineering.ucsb.edu; mnsysak@engineering.ucsb.edu; jraring@engineering.ucsb.edu; coldren@ece.ucsb.edu).

Digital Object Identifier 10.1109/LPT.2005.854422

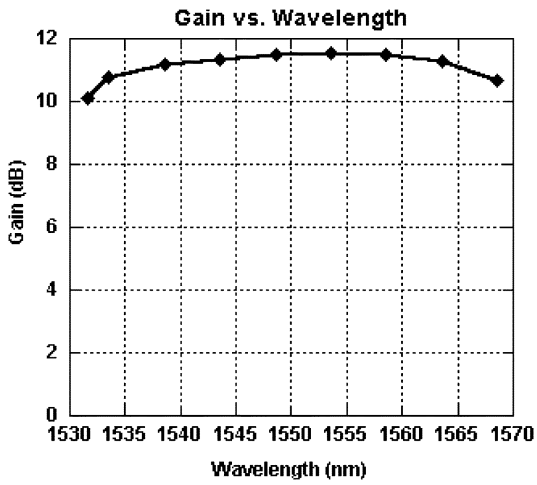

Fig. 2. Gain versus wavelength plot for receiver. ($I_{\rm SOA} = 250$ mA (8.33 kA/cm^2), $V_{\rm detector} = -4$ V, and $P_{\rm in} = 0.8$ mW).

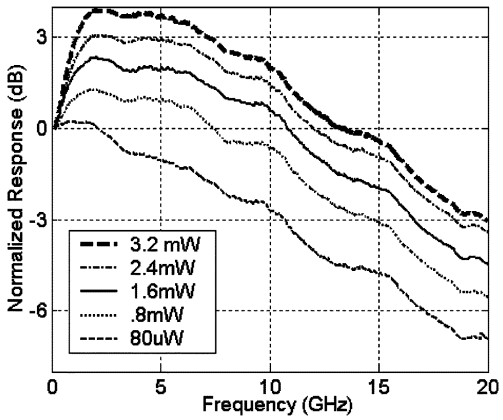

Fig. 3. Input power dependence of the frequency response of the receiver. ($I_{\rm SOA} = 250$ mA (8.33 kA/cm^2) and $V_{\rm detector} = -4$ V).

gain for the forward-biased SOA and the same wells provide a high absorption coefficient in the reverse biased detector.

III. Results

The devices were thinned, cleaved, and mounted onto an aluminum nitride carrier for testing. All dc contacts were wirebonded to the carrier and contacted via a probe card. The detector was directly probed by a coplanar stripline probe to prevent any parasitic effects from wirebonds. In all cases, input powers quoted were for light coupled into the waveguide. The compressively strained quantum wells used in this device are highly polarization-dependent; therefore, the polarization was adjusted to transverse electric to allow for maximum gain during all measurements. This polarization dependence is typical of devices that implement strained quantum wells and can be eliminated with redesigned quantum wells or bulk active material [2].

The dependence of dc gain on wavelength was measured. As shown in Fig. 2, the device exhibited less than 1.5-dB gain variation between 1530 and 1570 nm. This wavelength dependence can be attributed to the optical bandwidth of the quantum wells used for gain in the SOA and absorption in the detector.

The radio-frequency (RF) characteristics of the receiver were also measured. For all measurements, the input wavelength was

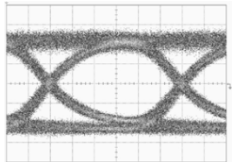

Fig. 4. 20-Gb/s eye for 2^{31}-1 pseudorandom binary sequence (PRBS). ($I_{\rm SOA} = 250$ mA, $V_{\rm detector} = -5$ V, and $P_{\rm in} = 0.8$ mW).

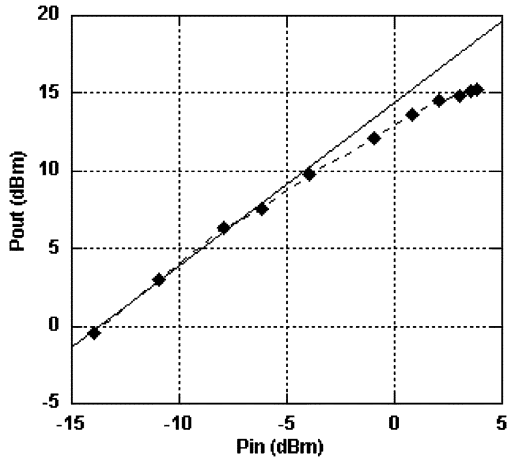

Fig. 5. Optical $P_{\rm in}$ versus optical $P_{\rm out} \propto I_{\rm photocurrent}$ at 10 Gb/s. ($I_{\rm SOA} = 250$ mA (8.33 kA/cm^2) and $V_{\rm detector} = -4$ V).

1548.1 nm and the detector was terminated with 50 Ω. The device has demonstrated a 3-dB bandwidth of 15 GHz for Pin = 0.8 mW (Fig. 3). It is believed the frequency response peaking between 1 and 5 GHz is caused by the input optical signal modulating the carrier density when the SOA experiences gain saturation. Similar peaking was also seen in the frequency response of electrically modulated gain-saturated SOAs [8]. Typically, photodetector saturation will manifest itself through a steeper bandwidth rolloff for high powers. In this case, there was no bandwidth degradation, thus confirming unsaturated photodetector operation. The 20-Gb/s eye diagrams were open and lacking pattern dependence (Fig. 4).

Greater than 14 dB of optical gain was realized at 10-Gb/s operation and the 1-dB gain compression point was reached at 12 dBm of output power (Fig. 5). This translates into ∼16 mA of unsaturated photocurrent, which allows for unsaturated voltage swings up to 0.8 $V_{p\text{-}p}$ when terminated with 50 Ω. It should be noted the RF gain was slightly higher than the dc gain due to additional heating effects at dc.

Bit-error-rate (BER) testing at 10 Gb/s with a nonreturn-to-zero 2^{31}-1 pseudorandom bit sequence was used to demonstrate the −10.5-dBm sensitivity of the receiver (Fig. 6). The BER testing utilized a 10-Gb/s transmitter (Agilent 83 433A) at a wavelength of 1548.1 nm. The signal from the transmitter went through a high power erbium-doped fiber amplifier followed by a polarization controller, an optical filter, and finally an attenuator before being coupled into the device.

The receiver is less sensitive than the −17-dBm sensitivity reported for similar devices in literature [1]. The wider ridge of the receiver presented here is necessary to improve the saturation power; however, this also increases the spontaneous emission therefore limiting the device's sensitivity.

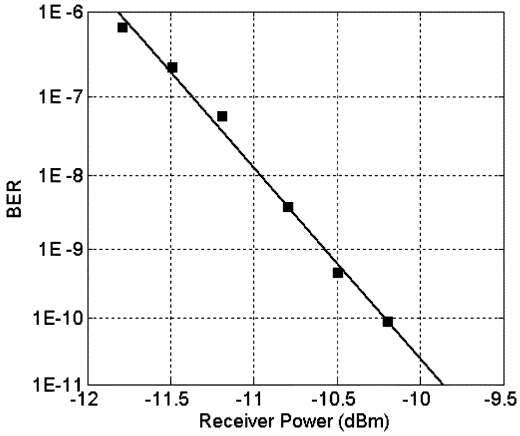

Fig. 6. BER curve for a input signal at 10 Gb/s and 2^{31}-1 PRBS. ($I_{\rm SOA} = 200$ mA and $V_{\rm detector} = -5$ V).

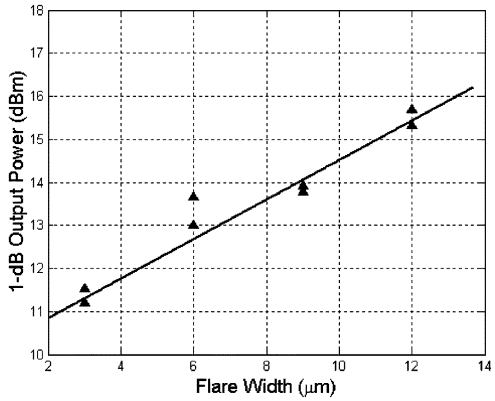

Fig. 7. Output power for 1-dB gain compression point versus the final flare width. ($J_{\rm SOA} = 8.33$ kA/cm^2).

IV. Design Studies

To aid in future receiver designs, the effects of SOA length and flare width have been examined. The SOAs studied were identical to the receiver's SOA except for variations in the length or flare width. These SOAs were integrated with detectors and characterized with dc testing.

The SOAs demonstrated a linear dependence of output saturation power with flare width (Fig. 7). A maximum 1-dB compression point of 15.7 dBm was achieved with a 12-μm flare width.

Gain versus length was characterized for straight 3-μm-wide SOAs. The unsaturated gain for different lengths and current densities was measured with the integrated detector. This data shows excellent linearity with length achieving up to 22 dB of gain, as shown in Fig. 8.

V. Conclusion

A monolithically integrated photoreceiver has been successfully fabricated on a simple offset quantum-well platform requiring only a single regrowth. The 600-μm-long flared SOA has produced greater than 14 dB of gain and 1-dB output saturation power of 12 dBm. However, additional design studies have indicated that improvements in the SOA saturation power and gain are possible. The tapered photodetector biased at -4 V has shown no signs of saturation and has demonstrated a 15-GHz bandwidth and a sensitivity of -10.5 dBm. In conclusion, the high saturation power and significant gain of these receivers make them an excellent choice for the photocurrent driven wavelength converter as well as other applications.

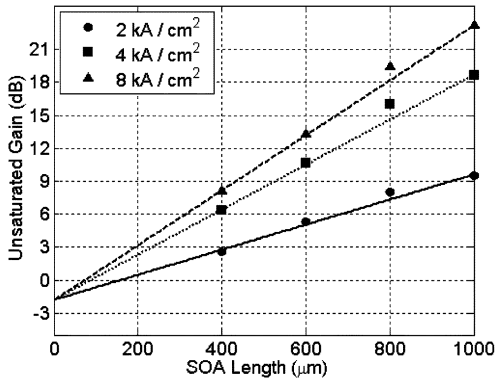

Fig. 8. Unsaturated gain versus length for three different current densities.

Acknowledgment

The authors would like to acknowledge C. Wang for SEM images and Agility Communications for antireflection coatings.

References

[1] B. Mason, J. M. Geary, J. M. Freund, A. Ougazzaden, C. Lentz, K. Glogovsky, G. Przybylek, L. Peticolas, F. Walters, L. Reynolds, J. Boardman, T. Kercher, M. Rader, D. Monroe, and L. Ketelsen, "40 Gb/s photonic integrated receiver with -17 dBm sensitivity," in *Optical Fiber Communications (OFC 2002)*, vol. 2, Mar. 17–22, 2002, Postdeadline Papers, pp. FB10-1–3.

[2] D. Wake, S. N. Judge, T. P. Spooner, M. J. Harlow, W. J. Duncan, I. D. Henning, and M. J. O'Mahony, "Monolithic integration of 1.5 μm optical preamplifier and PIN photodetector with a gain of 20 dB and a bandwidth of 35 GHz," *Electron. Lett.*, vol. 26, pp. 1166–1168, Jul. 1990.

[3] M. N. Sysak, J. S. Barton, L. A. Johansson, J. W. Raring, E. J. Skogen, M. L. Masanovic, D. J. Blumenthal, and L. A. Coldren, "Single-chip wavelength conversion using a photocurrent-driven EAM integrated with a widely tunable sampled-grating DBR laser," *IEEE Photon. Technol. Lett.*, vol. 16, no. 9, pp. 2093–2095, Sep. 2004.

[4] J. S. Barton, M. L. Masanovic, M. N. Sysak, J. M. Hutchinson, E. J. Skogen, D. J. Blumenthal, and L. A. Coldren, "2.5-Gb/s error-free wavelength conversion using a monolithically integrated widely tunable SGDBR-SOA-MZ transmitter and integrated photodetector," *IEEE Photon. Technol. Lett.*, vol. 16, no. 6, pp. 1531–1533, Jun. 2004.

[5] J. S. Barton, A. Tauke-Pedretti, M. Dummer, M. N. Sysak, M. L. Masanovic, J. Raring, E. J. Skogen, and L. A. Coldren, "10 Gbit/s wavelength conversion using a widely-tunable series push-pull photocurrent-driven transmitter," *IEEE Photon. Technol. Lett.*, vol. 17, no. 9, pp. 1902–1904, Sep. 2005.

[6] M. Connelly, *Semiconductor Optical Amplifiers*. Boston, MA: Kluwer Academic, 2002, ch. 2–3.

[7] S. S. Saini, J. Bowser, R. Enck, V. Luciani, P. J. S. Helm, and M. Dagenais, "A semiconductor optical amplifier with high saturation power, low noise figure and low polarization dependent gain over the C-band," in *17th Annu. Meeting IEEE Lasers and Electro-Optics Society (LEOS 2004)*, vol. 1, Nov. 8–9, 2004, pp. 102–103.

[8] L. San-Liang, M. E. Heimbuch, D. A. Cohen, L. A. Coldren, and S. P. DenBaars, "Integration of semiconductor laser amplifiers with sampled grating tunable lasers for WDM applications," *IEEE J. Sel. Topics Quantum Electron.*, vol. 3, no. 2, pp. 615–27, Apr. 1997.

Comments and Corrections

Correction to "Recent Advances in Avalanche Photodiodes"

Joe C. Campbell, *Fellow, IEEE*, Stephane Demiguel, Feng Ma, Ariane Beck, Xiangyi Guo, Shuling Wang, Xiaoguang Zheng, Xiaowei Li, Jeffrey D. Beck, *Senior Member, IEEE*, Michael A. Kinch, Andrew Huntington, Larry A. Coldren, *Fellow, IEEE*, Jean Decobert, and Nadine Tscherptner

In [1], the graphic in Fig.10 was incorrect. Therefore, in Figs. 11–18, the captions did not match the correct figures. The following are the figures with the correct captions.

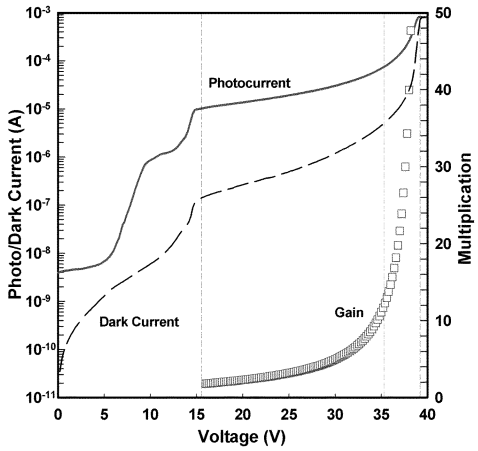

Fig. 10. Photocurrent, dark current, and gain curves for an $Al_{0.48}In_{0.52}As/In_{0.53}Ga_{0.47}As$ SACM APD.

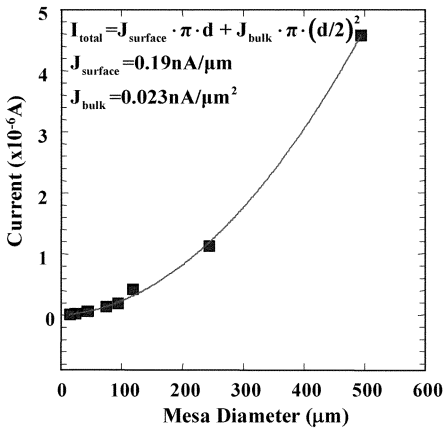

Fig. 11. Measured dark current and quadratic fit versus mesa diameter for $Al_{0.48}In_{0.52}As/In_{0.53}Ga_{0.47}As$ SACM APDs.

Manuscript received December 13, 2004.

J. C. Campbell, S. Demiguel, F. Ma, A. Beck, X. Guo, S. Wang, X. Zheng, and X. Li are with the Microelectronics Research Center, The University of Texas at Austin, Austin, TX 78712 USA (e-mail: jcc@mail.utexas.edu).

J. D. Beck and M. A. Kinch are with DRS Infrared Technologies, LP, Dallas, TX 75374 USA.

A. Huntington and L. A. Coldren are with the Materials Department, Optoelectronics Technology Center, University of California at Santa Barbara, Santa Barbara, CA 93106 USA.

J. Decobert and N. Tscherptner are with Alcatel R&I, 91460 Marcoussis, France.

Digital Object Identifier 10.1109/JSTQE.2004.842288

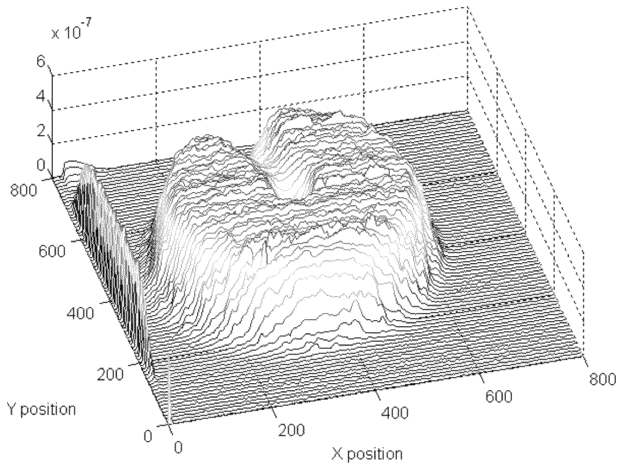

Fig. 12. Raster scan of photoresponse of a 500-μm-diameter $Al_{0.48}In_{0.52}As/In_{0.53}Ga_{0.47}As$ SACM APD for M $\sim$ 20.

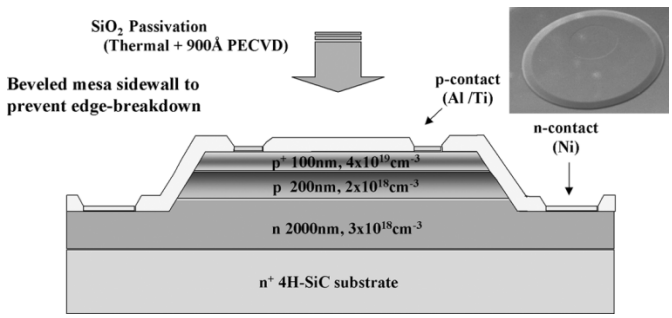

Fig. 13. Schematic cross section of 4H-SiC APD. The inset shows an SEM photograph of the etched mesa.

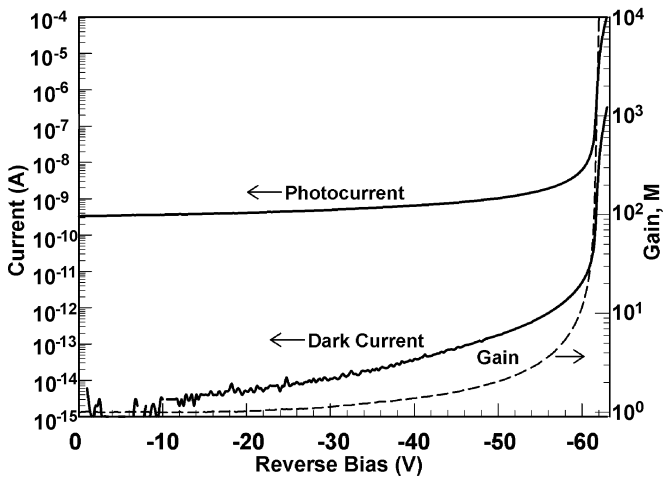

Fig. 14. Photocurrent, dark current, and gain of 100-μm-diameter 4H-SiC APD.

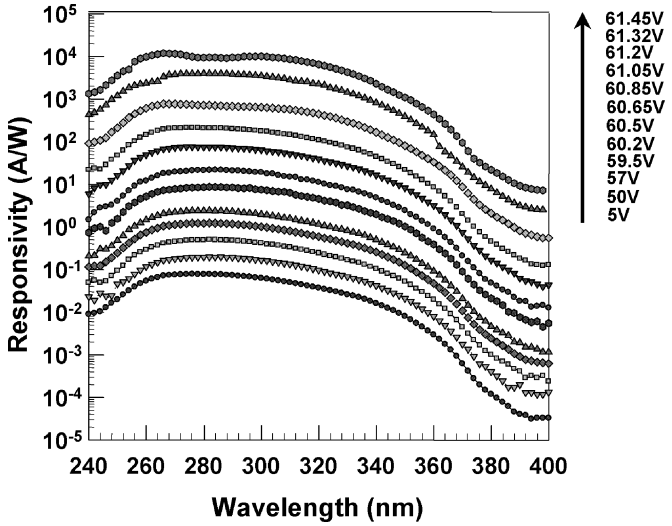

Fig. 15. Spectral response of 4H-SiC APD for a range of bias voltages.

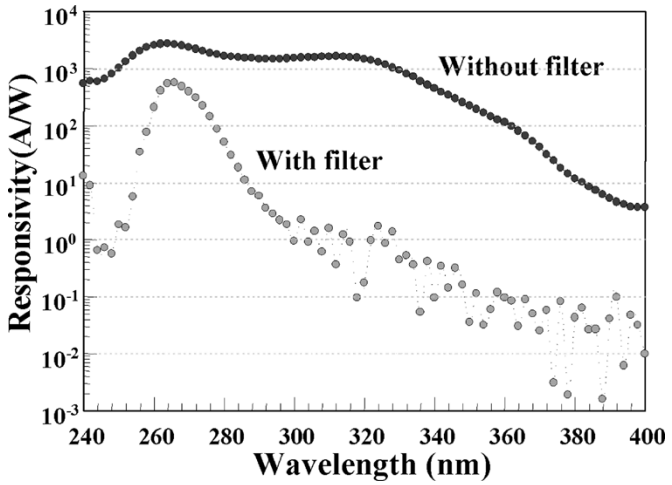

Fig. 16. Responsivity of 4H-SiC APD with and without a 266-nm "laser line" filter.

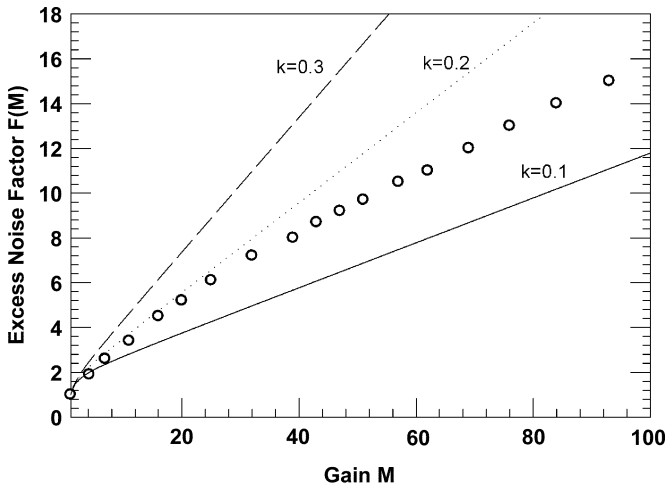

Fig. 18. Measured excess noise, F(M), of a SiC APD versus gain, M. The excess noise corresponds to a k value of 0.15.

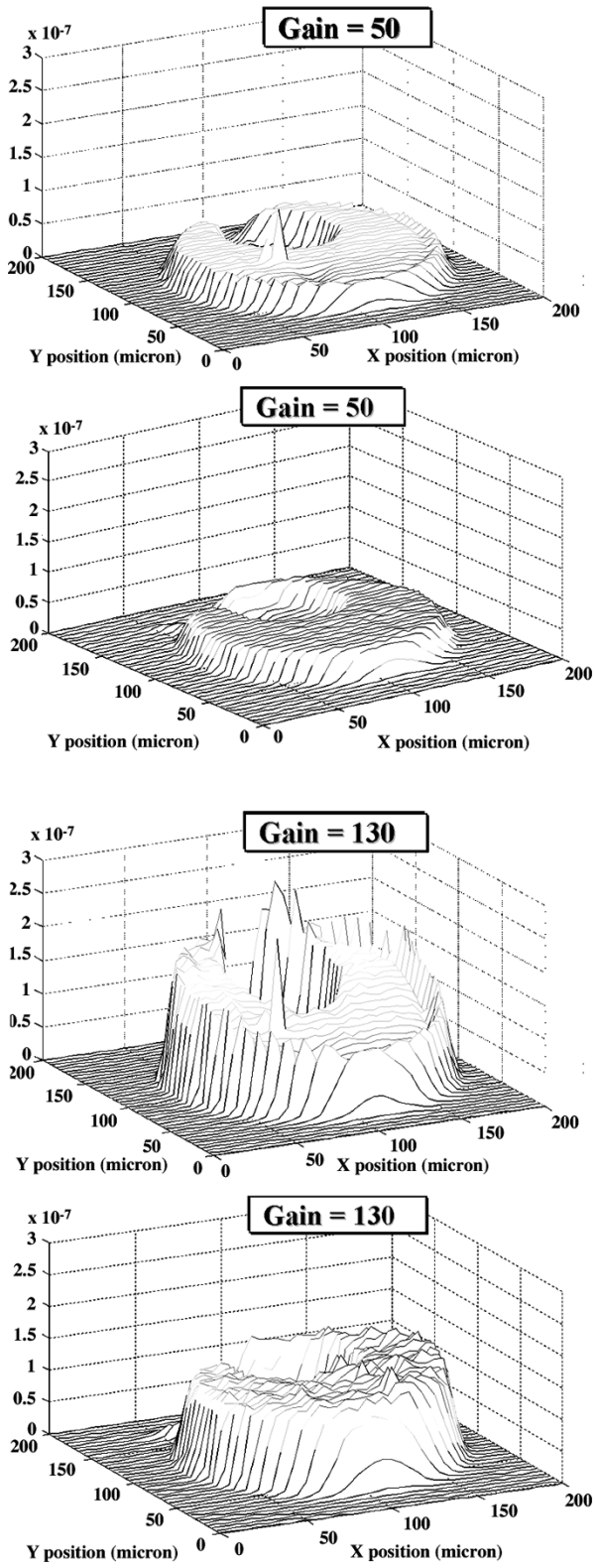

Fig. 17. Raster scans of the photocurrent of (a) nonbeveled and (b) beveled mesa-structure SiC APDs.

REFERENCES

[1] J. C.J. C. Campbell, S.Stephane Demiguel, F.F. Ma, A.A. Beck, X.X. Guo, S.S. Wang, X.X. Zheng, X.X. Li, J. D.J. D. Beck, M. A.M. A. Kinch, A.A. Huntington, L. A.L. A. Coldren, J.Jean Decobert, and N.Nadine Tscherptner, "Recent advances in avalanche photodiodes," *IEEE J. Select Topics Quantum Electron.*, vol. 10, pp. 777–787, July/Aug. 2004.

IV. Terahertz Technology, Microcavities, and Quantum Coherence

Proc. 2005 American Physical Society March Meeting, abstract no. C1.00011, Los Angeles, CA (March 21-25, 2005)

Abstract Submitted
for the MAR05 Meeting of
The American Physical Society

Sorting Category: 13.6 (E)

Cavity Quantum Electrodynamics with Single Quantum Dots in Microcavities MATTHEW RAKHER, Department of Physics, University of California at Santa Barbara, STEFAN STRAUF, Department of Physics and Materials Department, UCSB, NICK STOLZ, Materials Department, UCSB, KEVIN HENNESSY, ECE Department, UCSB, ANTONIO BADOLATO, Materials Department, UCSB, EVELYN HU, Materials Department and ECE Department, UCSB, LARRY COLDREN, Materials Department, UCSB, PIERRE PETROFF, Materials Department and ECE Department, UCSB, DIRK BOUWMEESTER, Department of Physics, UCSB — Several proposals for solid-state cavity quantum electrodynamics rely on a strong interaction between the cavity mode and an embedded single atom or a single quantum dot (QD). In order to achieve a strong light-matter interaction, the cavity must have a small mode volume while maintaining a large quality factor. To this end, InAs/GaAs QDs in GaAs-based microcavities have been investigated using micro-photoluminescence spectroscopy and photon statistics measurements. Individual QDs in these devices have been identified by their photon anti-bunching signatures. Pronounced enhancement of the single QD lifetime has been measured, with some lifetimes limited by the detector resolution (200 ps), corresponding to a Purcell factor of more than 10. Together with active spatial positioning schemes of QDs, these devices are promising avenues to reach the strong coupling regime with individual solid state emitters.

Matthew Rakher
rakher@physics.ucsb.edu
Department of Physics, University of California at Santa Barbara

☐ Prefer Oral Session
☒ Prefer Poster Session

Date submitted: 01 Dec 2004 Electronic form version 1.4

Proc. International Quantum Electronics Conference, paper no. QTuI1, Baltimore, MD (May 22-27, 2005)

Excitonic Autler-Townes splitting induced by an intense Terahertz field

S. G. Carter, V. Ciulin*, and M. S. Sherwin
Physics Department and iQUEST, Broida Hall Building 572,Room 3410, University of California, Santa Barbara, California 93106
scarter@physics.ucsb.edu

C. S. Wang and L. A. Coldren
Electrical and Computer Engineering Department, University of California, Santa Barbara, California 93106

A. V. Maslov
Center for Nanotechnology, NASA Ames Research Center, MS 229-1, Moffett Field, California 94035

Abstract: An InGaAs quantum well driven by a strong THz field has exhibited a splitting of the exciton line, due to strong coupling of hole states. This effect is closely-related to the Autler-Townes effect and electromagnetically-induced-transparency.

OCIS Codes: (190.5970) Semiconductor nonlinear optics including MQW; (270.1670) Coherent optical effects

The effect of a Terahertz (THz) electric field on quantum well (QW) interband absorption has been given a great deal of theoretical attention due to interest in THz-dressed states and in ultrafast optical modulation,[1,2] but few experimental results have been published.[3] We have measured the effect of a strong THz field from the UCSB Free Electron Laser on the linear interband absorption of InGaAs QWs at low-temperature. The results demonstrate a THz-induced splitting of the exciton absorption analogous to Autler-Townes splitting in atomic systems.[4]

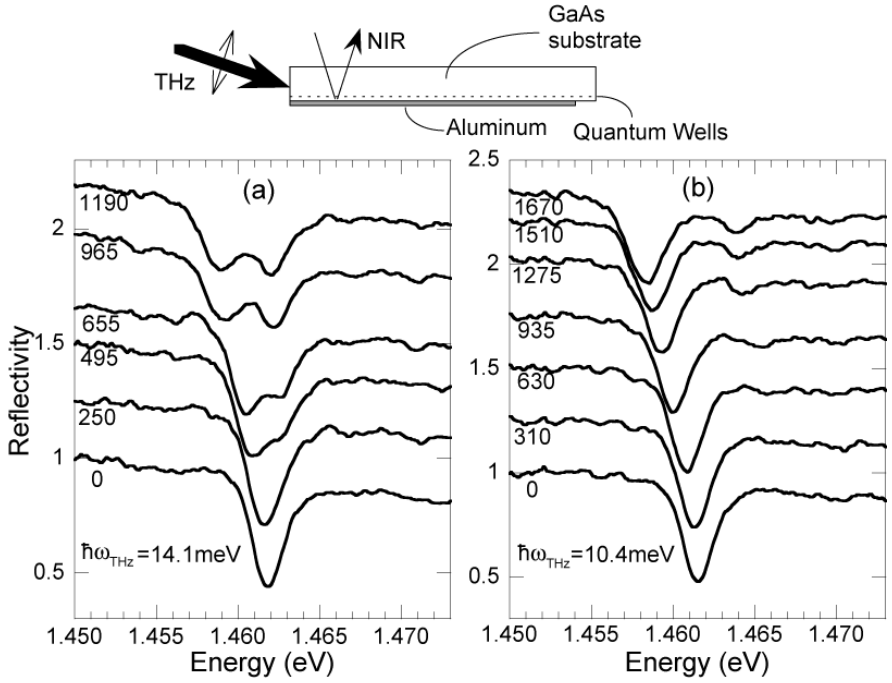

Fig. 1. Reflectivity spectra at 10 K for a series of THz powers at (a) $\hbar\omega_{THz}$ = 14.1 meV and (b) $\hbar\omega_{THz}$ = 10.4 meV. The spectra are offset and labelled according the the THz power (in Watts). A schematic of the sample and experimental geometry is displayed above.

The sample consists of 10 undoped 14.3 nm $In_{0.06}Ga_{0.94}As$ QWs separated by 30 nm $Al_{0.3}Ga_{0.7}As$ barriers. The experimental geometry is shown above Fig. 1. The interband probe beam, from a near-infrared (NIR) LED, passed through the GaAs substrate, through the QWs, and then reflected off of an Al layer evaporated on the

surface. This Al layer gave a strong growth-direction THz field and prevented any in-plane fields, a significant improvement over previous THz-coupling methods.[5]

Figure 1 displays a series of NIR reflectivity spectra taken at increasing THz powers for (a) $\hbar\omega_{THz}$ = 14.1 meV and (b) 10.4 meV. Without the THz field (lowest spectra), the reflectivity shows absorption by the lowest exciton state, e1hh1X. The e1hh2X state is optically forbidden in these symmetric QWs and is expected to be ~13.5 meV above e1hh1X. Higher electron and heavy-hole states are expected to be sufficiently far away that they can be ignored. The lowest light hole exciton appears to be shifted out of the way due to strain.

In the presence of the THz field, the changes in absorption were quite striking. For $\hbar\omega_{THz}$ = 14.1 meV, which was near the e1hh1X-e1hh2X resonance, there was a clear splitting of the exciton line, which increased as a function of power. For $\hbar\omega_{THz}$ = 10.4 meV, which was below the resonance, the splitting was more asymmetric, with a weaker absorption line appearing above the undriven exciton line. This splitting has been predicted by several authors for QWs driven by a strong intersubband pump,[1,6] but has never before been observed. These results show for the first time clear evidence of Autler-Townes splitting of excitons in a THz-driven QW. Fig. 2(a) displays the exciton splitting schematically.

Reflectivity measurements were performed for many THz frequencies at a series of powers. The spectra taken at a THz power near 550 W were fitted to two Lorentzians, and the results are plotted in Fig. 2(b). The absorption strength is represented on a greyscale for each marker. The existence of the two absorption lines is due to the two dressed (Floquet) states created by the THz field. On resonance, the oscillator strength is shared equally between the two dressed states and thus, the two absorption peaks are equal in magnitude. Off-resonance, the oscillator strength is strongest for the absorption line nearest the undriven exciton line. Using a Rabi splitting model, the energies of these dressed states are $E_{\pm} = E_0 - (1/2)(\Delta \mp \sqrt{\Delta^2 + (2\mu E_{THz})^2})$, where E_0 is the undriven exciton energy, Δ is the detuning from resonance, μ is the intersubband dipole moment, and E_{THz} is the THz field. The measured absorption energies fit very well to this simple formula. A much more sophisticated model using the semiconductor Bloch equations has also been applied to this system, giving similar results.

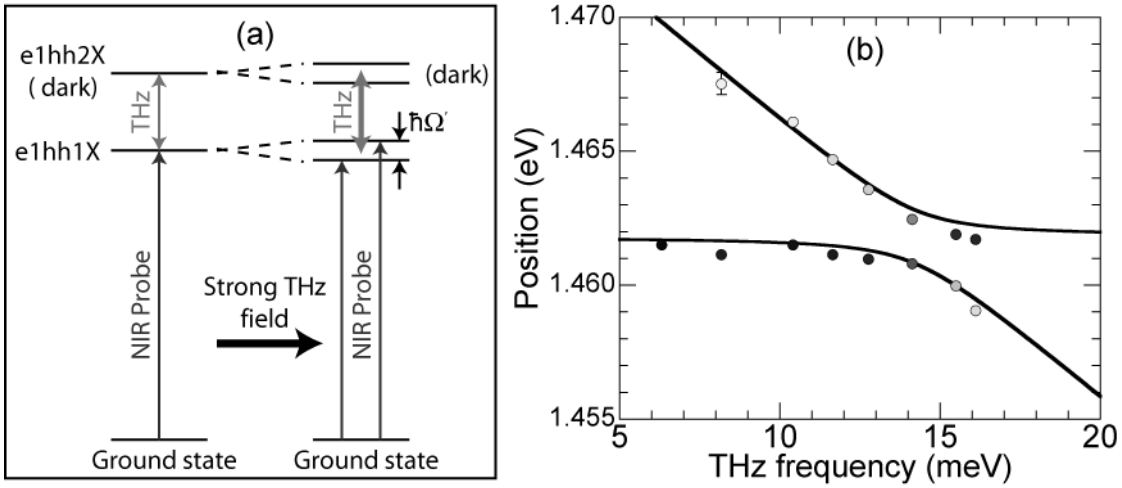

Fig. 2. (a) Schematic exciton energy level diagram showing the splitting that occurs in the presence of a resonant THz field. (b) Absorption line positions vs. THz frequency, showing the anticrossing behavior. The absorption strength for each point is represented on a greyscale. A completely black dot indicates the absorption strength was the same as the undriven absorption strength, while a white dot indicates very small absorption. The lines are plots of $E_{\pm}$ from the Rabi model with μE_{THz} = 2 meV.

The observation of THz-dressed excitons in this system is particularly interesting since the dressed states can be observed for detunings that are a significant fraction of the level spacing. This comes from the fact that the Rabi frequency can be comparable to the THz frequency, making a number of nonperturbative strong-field effects potentially observable.[7] This system is also technologically interesting as it is essentially a QW modulator driven at THz frequencies. The presence of quantum coherence in a QW modulator may enable fascinating new functionalities. This work was supported by the NSF and SUN Microsystems.

* Present address: V. Birkedal née Ciulin, Department of Chemistry, University of Aarhus, Langelandsgade 140, DK-8000 Aarhus C, Denmark.

[1] A. V. Maslov and D. S. Citrin, "Optical absorption and sideband generation in quantum wells driven by a terahertz electric field," Phys. Rev. B **62**, 16686-91 (2000).
[2] K. Johnsen and A.-P. Jauho, "Quasienergy Spectroscopy of Excitons," Phys. Rev. Lett. **83**, 1207-10 (1999).
[3] K. B. Nordstrom, K. Johnsen, S. J. Allen, A. –P. Jauho, B. Birnir, J. Kono, T. Noda, H. Akiyama, and H. Sakaki, "Excitonic dynamical Franz-Keldysh effect," Phys. Rev. Lett. **81**, 457-60 (1998).
[4] S. H. Autler and C. H. Townes, "Stark effect in rapidly varying fields," Phys. Rev. **100**, 703-22 (1955).
[5] V. Ciulin, S. G. Carter, M. S. Sherwin, A. Huntington, and L. A. Coldren, "Terahertz optical mixing in biased GaAs single quantum wells," Phys. Rev. B **70**, 115312 (2004).
[6] A. Liu and C. Z. Ning, "Exciton absorption in semiconductor quantum wells driven by a strong intersubband pump field," J. Opt. Soc. Am. B **17**, 433-9 (2000).
[7] A. V. Maslov and D. S. Citrin, "Mutual transparency of coherent laser beams through a terahertz-field-driven quantum well," J. Opt. Soc. Am B 1**9**, 1905-9 (2002).

High-quality factor optical microcavities using oxide apertured micropillars

N. G. Stoltz,[a),b)] M. Rakher,[c)] S. Strauf,[b),c)] A. Badolato,[d)] D. D. Lofgreen,[d),e)] P. M. Petroff,[b),d)] L. A. Coldren,[b),d)] and D. Bouwmeester[c)]
University of California, Santa Barbara, California 93106

(Received 28 February 2005; accepted 7 June 2005; published online 12 July 2005)

An oxide aperture is used to confine optical modes in a micropillar structure. This method overcomes the limitations due to sidewall scattering loss typical in semiconductor etched micropillars. High cavity quality factors (Q) up to 48 000 are determined by external Fabry–Perot cavity scanning measurements, a significantly higher value than prior work in III-V etched micropillars. Measured Q values and estimated mode volumes correspond to a maximum Purcell factor figure of merit value of 72. © *2005 American Institute of Physics*. [DOI: 10.1063/1.1999843]

Optical microcavities combined with active emitters provide a great opportunity to study the light-matter interaction at a fundamental level. To produce a high-quality microcavity, it is necessary to confine light to precise resonance frequencies with little or no optical loss.[1] The measure of this optical confinement is referred to as the cavity quality factor (Q). In order to limit the number of optical modes present in a cavity, it is important to reduce the effective optical mode volume (V_{eff}). Figures of merit for optical microcavity applications are proportional to the ratio of these two values Q/V_{eff}.[2] Potential applications include solid-state cavity quantum electrodynamics (CQED) experiments, modification of single-emitter lifetimes, and single-photon emitters and detectors for quantum cryptography.[1,2]

Several solid-state microcavity architectures including microdisks,[3,4] photonic crystals,[5–7] and micropillars[8,9] have shown CQED effects in III-V semiconductors using self-assembled quantum dots (QDs) as active emitters. Among these architectures, micropillars couple light normal to the semiconductor in a single-lobed Gaussian pattern that is easily fiber coupled.[10] This high photon collection efficiency makes micropillars a better alternative for device applications. However, micropillars exhibit higher $V_{\text{eff}}[\sim 5(\lambda/n)^3]$ and lower Qs($\sim$2000–10 000) when compared with photonic crystals.[1,9] V_{eff} can be reduced by decreasing pillar diameter, but scattering losses due to sidewall roughness have been shown to limit achievable Q values.[1,11]

Here, we present an alternative approach, using oxide apertured micropillars in order to reduce V_{eff} while maintaining high Q values. Oxidized micropillars have been used for vertical cavity laser applications to produce low threshold laser devices that are fabricated into inexpensive arrays for optical data networks.[12] By confining the optical mode with a laterally oxidized aperture layer these structures simultaneously provide optical mode and electrical current confinement while eliminating the scattering loss due to sidewall roughness inherent to etched pillar structures. This method has been applied to the field of QD-microcavity coupling with limited success due to very low Qs ($<$1000) as well as high $V_{\text{eff}}[\sim 35(\lambda/n)^3]$ when compared with conventional micropillars.[13,14] If these values are improved, the advantages in ease of fabrication will make oxide apertured micropillars very attractive for coupled QD-microcavity applications.

Micropillar samples investigated in this study were grown by molecular-beam epitaxy on a semi-insulating GaAs (100) substrate with a 0.1 μm buffer layer. There are four independent sections in the structure: The bottom mirror, the active region, the aperture region, and the top mirror as shown schematically in Fig. 1(a). Mirrors consist of alternating one-quarter optical thickness distributed Bragg reflector (DBR) layers of GaAs and $Al_{0.9}Ga_{0.1}As$. 32 pairs of $Al_{0.9}Ga_{0.1}As$/GaAs layers with thicknesses of 79.8/68.4 nm, respectively, form the bottom DBR mirror, while the top DBR mirror is made of 23 pairs. The active region is one optical wavelength in thickness, with two 135.4 nm layers of GaAs embedding a centered InGaAs/GaAs QD layer. QDs self-assemble during epitaxy operating in the Stranski–Krastanov growth mode. InGaAs islands are partially covered with GaAs and annealed before completely capped with GaAs. This procedure blueshifts the QDs emission wavelengths[15] toward the spectral region where Si-based de-

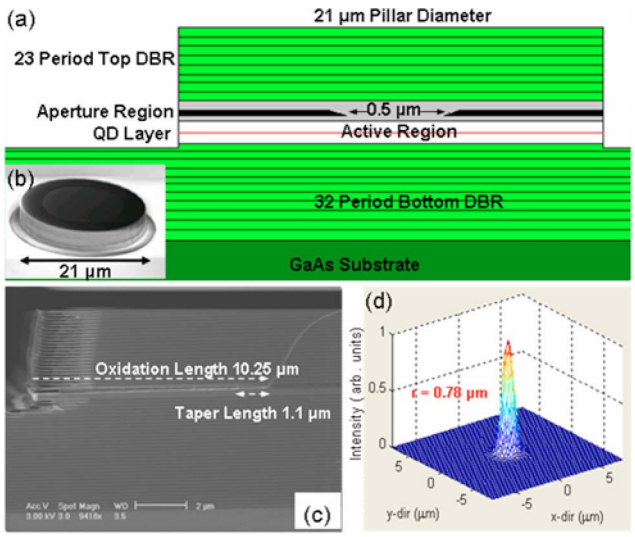

FIG. 1. (Color online) (a) Schematic and layer structure for oxide apertured micropillars. (b) SEM image of a fully processed 21 μm micropillar. (c) SEM cross section image of an oxidized mesa showing actual layer structure depicted in (a). (d) The theoretical fundamental mode profile for the 21 μm micropillar modeled in this study with a Gaussian mode radius of 0.78 μm.

[a)]Electronic mail: stoltzie@engineering.ucsb.edu
[b)]Materials Department.
[c)]Physics Department.
[d)]Electrical Engineering Department.
[e)]Currently at: Raytheon Visions Systems, Goleta, CA 93117.

tectors are more efficient. The thickness of the aperture region is three-quarters optical wavelength and consists of a pure AlAs layer sandwiched by $Al_{0.89}Ga_{0.11}As$ and $Al_{0.75}Ga_{0.25}As$ in order to produce the desired aperture qualities. It is designed to give a change in effective index, $\Delta n_{\text{eff}}=0.08$, between the fully oxidized and unoxidized regions of the micropillar in addition to a linear oxide taper with a length of 1.1 μm after an approximate 10 μm oxidation. A scanning electron microscopy (SEM) image of a fabricated oxide apertured microcavity is shown in Fig. 1(b), while Fig. 1(c) shows a cross-sectional SEM image of an oxidized mesa calibration sample with mirror, active, and aperture regions corresponding to Fig. 1(a). Samples are fabricated by optical lithography and reactive ion etch in Cl_2 plasma penetrating approximately five mirror periods into the bottom DBR. Micropillars are fabricated in large arrays with diameters varying from 21–25 μm. The wet lateral oxidation is performed at 430 °C in order to oxidize the aperture region by converting AlAs into Al_xO_y.

Microphotoluminescence (μ-PL) measurements are performed using a He-flow cryostat (4–300 K). QDs are excited nonresonantly by a continuous-wave 780 nm laser diode focused to a spot size of 2.5 μm using a microscope objective with numerical aperture of 0.55. μ-PL emission is collected through the same objective and recorded with a 1.25 m spectrometer equipped with a charge-coupled device with 30 μeV spectral resolution at 900 nm. A scanning Fabry–Perot cavity along with a single photon counting avalanche photodiode detector and an integrated counting unit are used to experimentally determine linewidths beyond the resolution of the spectrometer.

A two-dimensional model of the cavity has been developed based on the experimentally determined values for the oxide aperture taper length and core width from SEM images (Fig. 1) along with the one-dimensional reflectivity spectrum of the unprocessed sample. This produces a two-dimensional index profile determined by the effective index (n_{eff}) in the growth direction for the unoxidized and oxidized layer stack. The Δn_{eff} between the unoxidized and oxidized regions is evaluated by replacing the AlAs and $Al_{0.89}Ga_{0.11}As$ with $Al_xO_y(n=1.5)$. It has been demonstrated[16] that the linear oxide taper shown in Fig. 1(c) corresponds to a parabolic index grade over the length of the taper.

We used this model to solve for the eigenmodes of the two-dimensional scalar wave equation using a finite difference technique with a nonuniform mesh.[17] The solution for the fundamental mode of a 21 μm pillar is shown in Fig. 1(d) and has a Gaussian mode radius of approximately 0.78 μm. Scattering and radiation losses are determined by propagating a scalar field around the unfolded cavity until the field no longer changes shape. This procedure is analogous to the classic work of Fox and Li.[18]

Mirror, scattering, and radiation losses determine the empty or cold cavity linewidth of the apertured micropillar. Assuming that undoped AlGaAs regions have no internal optical loss at 4 K, the only optical loss mechanisms in the cavity are due to mirror loss (α_m), radiation loss (α_{rad}), and aperture scattering losses (α_{scat}).[17] Furthermore, α_{rad} and α_{scat} are very small for the fundamental mode, $1.7e-3$ and 1.7 cm^{-1}, respectively. This leaves photon escape through the top DBR mirror as the dominating loss mechanism in the cavity, calculated as 13.9 cm^{-1}. Cold cavity (Q_{cold}) values are determined by cavity losses according to $\omega/Q_{\text{cold}}=1/\tau_p$

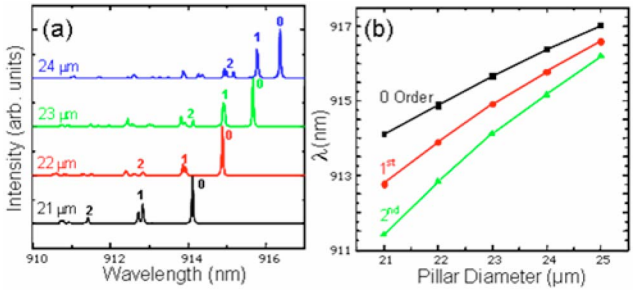

FIG. 2. (Color online) (a) Normalized optical mode spectra for 21–25 um micropillars measured by μ–PL at 4 K are shown. Fundamental, first-, and second-order modes are labeled 0, 1, and 2, respectively. (b) Mode position is shown as a function of pillar diameter for fundamental, first-, and second-order modes.

$=v_g\Gamma g_{\text{th}}=v_g(\alpha_{\text{scat}}+\alpha_{\text{rad}}+\alpha_m)$.[17] Here, τ_p is cavity lifetime, v_g is group velocity, ω is the frequency, Γ is the confinement factor, and g_{th} is the threshold material gain. The estimated Q_{cold} for a 21 μm micropillar is 14 500.

Experimental mode spectra for 21–25 μm diameter pillars are shown in Fig. 2(a) with mode orders 0, 1, and 2 labeled. The lifting of higher-order mode degeneracy is due to asymmetry in the fabrication process. μ–PL data shows cavity modes with lower fundamental energies and increasing mode spacing as pillar diameter decreases. This effect is shown in Fig. 2(b) for varying pillar diameters. In addition, intensity decreases are observed for higher-order modes due to increased scattering losses, an intentional effect produced by the oxide aperture and the larger effective radii of multilobed higher-order modes.

A Fabry–Perot scanning cavity is used to determine experimental Q values. A reference laser is used to calibrate the maximum measurable Q for the Fabry–Perot cavity as 600 000, shown in Fig. 3(a). The fundamental cavity mode is then directed through a 1 nm bandpass filter into the detector for sample measurement. Experimental quality factor (Q_{exp}) is determined to be approximately 48 000 for a 21 μm pillar as shown in Fig. 3(b). This value is larger than the theoretical

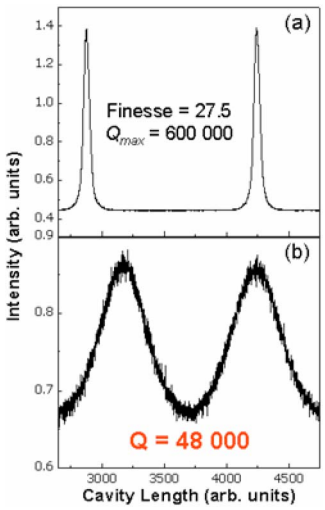

FIG. 3. (Color online) (a) Transmission through a Fabry–Perot cavity as a function of cavity length for a reference laser. Using the given free spectral range of the measurement cavity, the reference laser has $Q>600\,000$ giving a maximum measurable Q. (b) The Fabry–Perot measurement of the fundamental mode linewidth of a 21 μm micropillar cavity. This measurement was done at 50 μW pump power at 4 K.

cold cavity value due to linewidth narrowing caused by modal gain from the QD active region. The experimental gain (g_{exp}) is determined by the relationship between Q_{cold} and Q_{exp} values according to $\omega/Q_{exp}=(\omega/Q_{cold})-v_g\Gamma g_{exp}$.[17]

Q values show little change for pump powers above 10 μW and no laser threshold behavior is observed up to 50 μW pump power. This indicates that material gain in the QD layer saturates before the threshold condition is achieved. Estimated values show that g_{exp} saturates at approximately 10.44 cm^{-1}, corresponding to approximately 2864 cm^{-1} material gain from the active region. This is a reasonable value for the single QD layer in this cavity.[19] At low pump powers, Q values are expected to increase as the optically pumped QD region provides gain and causes linewidth narrowing. For the small lateral area and narrow spectral linewidths in these devices, the modal gain provided by the QD single-exciton emission saturates at pump powers below 1 μW.[6] In this regime, a slight linewidth narrowing from 0.06 to the observed 0.02 nm is expected to occur. However, it is difficult to resolve this linewidth narrowing with a scanning Fabry–Perot cavity at these low pump powers.

The Purcell factor determines the figure of merit for a coupled QD microcavity in the weak coupling regime. Using the theoretical $V_{eff}(\lambda/n_{eff})^{-3}$ of 51 and experimental Q_{exp} values, it is possible to estimate the maximum achievable F_p according to $F_p=(3/4\pi^2)(Q(\lambda/n_{eff})^3/V_{eff})$.[20] Experimentally observed values are decreased due to spectral and spatial detuning. Estimating the Purcell factor with experimental linewidths gives a maximum value of 72.

Oxidized micropillars have a promising outlook for QD-microcavity coupling due to high Q values. Further improvement for these devices could be achieved by reducing V_{eff}. Although oxide aperture micropillars reduce two-dimensional mode areas while maintaining high Q values, V_{eff} remains relatively high. This is due to the large effective cavity length in the growth direction of this structure, approximately 1.39 μm. Improvement lies in reducing this value, potentially by replacing AlGaAs/GaAs DBR mirrors with Al_xO_y/GaAs DBR mirrors having reduced mirror penetration depths.

Experimental data show very high Q (48 000) optical microcavities using an oxide apertured micropillar architecture. Devices exhibit controlled mode positions and sizes down to core widths of approximately 0.5 μm. Unlike etched air interface micropillars, which can be difficult to fabricate with acceptable loss values at smaller diameters, apertured micropillars accomplish this in a controllable and repeatable fashion. Cavities exhibit low loss values resulting from gain related linewidth narrowing effects due to stimulated emission from the QD active region. Apertured micropillars show promise for QD-microcavity coupling applications due to these high experimental Q values producing a maximum Purcell factor of 72.

This work was supported by NSF NIRT Grant No. 0304678 and DARPA Grant No. MDA 972-01-1-0027. One of the authors, S. Strauf acknowledges support from the Max-Kade Foundation.

[1] J. M. Gerard, in *Single Quantum Dots: Fundamentals, Applications, and New Concepts*, edited by P. Michler (Springer, Berlin, 2003), Vol. 90, Chap. 4, pp. 269–314.
[2] K. J. Vahala, Nature (London) **424**, 839 (2003).
[3] A. Kiraz, P. Michler, C. Becher, B. Gayral, A. Imamoglu, L. Zhang, W. V. Schoenfeld, and P. M. Petroff, Appl. Phys. Lett. **78**, 3932 (2001).
[4] E. Peter, P. Senellart, D. Martrou, A. Lemaitre, J. Bloch, J. Hours, and J. M. Gerard, available at http://xxx.lanl.gov/abs/quant-ph/0411076.
[5] T. D. Happ, I. I. Tartakovski, V. D. Kulakovskii, J.-P. Reithmaier, M. Kamp, and A. Forchel, Phys. Rev. B **66**, 041303 (2002).
[6] A. Badolato, K. Hennessy, M. Atature, J. Dreiser, E. Hu, P. M. Petroff, and A. Imamoglu, Science **308**, 1158 (2005).
[7] T. Yoshie, A. Scherer, J. Hendrickson, G. Khitrova, H. M. Gibbs, G. Rupper, C. Ell, O. B. Shchekin, and D. G. Deppe, Nature (London) **432**, 200 (2004).
[8] B. Gayral, J. M. Gérard, A. Lemaître, C. Dupuis, L. Manin, and J. L. Pelouard, Appl. Phys. Lett. **75**, 1908 (1999).
[9] J. P. Reithmaier, G. Sek, A. Loffler, C. Hofmann, S. Kuhn, S. Reitzenstein, L. V. Keldysh, V. D. Kulakovski, T. L. Reinecke, and A. Forchel, Nature (London) **432**, 197 (2004).
[10] M. Pelton, J. Vukovic, G. S. Solomon, A. Scherer, and Y. Yamamoto, IEEE J. Quantum Electron. **38**, 170 (2002).
[11] T. Rivera, J.–P. Debray, J. M. Gerard, B. Legrand, L. Manin-Ferlazzo, and J. L. Oudar, Appl. Phys. Lett. **74**, 911 (1999).
[12] L. A. Coldren, H. Temkin, and C. W. Wilmsen, *Vertical-Cavity Surface-Emitting Lasers*, 1st ed. (Cambridge University Press, Cambridge, UK, 1999), Vol. 1, Chap. 1 , p.1.
[13] L. A. Graham, D. L. Huffaker, and D. G. Deppe, Appl. Phys. Lett. **74**, 2408 (1999).
[14] D. G. Deppe, L. A. Graham, and D. L. Huffaker, IEEE J. Quantum Electron. **35**, 1502 (1999).
[15] P. M. Petroff, A. Lorke, and A. Imamoglu, Phys. Today **54**, 46 (2001).
[16] E. R. Hegblom, N. M. Margalit, A. Fiore, and L. A. Coldren, IEEE J. Sel. Top. Quantum Electron. **5**, 553 (1999).
[17] L. A. Coldren and S. W. Corzine, in *Diode Lasers and Photonic Integrated Circuits*, 1st ed. edited by K. Chang (Wiley, New York, 1995), Vol. 1, Chap. 16 Apps. 4,16, pp.188, 226, 444, 563–567.
[18] A. G. Fox and T. Li, Bell Syst. Tech. J. **40**, 453 (1961).
[19] S. Schneider, P. Borri, W. Langbein, U. Woggon, R. L. Sellin, D. Ouyang, and D. Bimberg, IEEE J. Quantum Electron. **40**, 1423 (2004).
[20] E. M. Purcell, Phys. Rev. **69**, 681 (1946).

12. M. Greiner, C. A. Regal, J. T. Stewart, D. S. Jin, *Phys. Rev. Lett.* **94**, 110401 (2005).
13. M. Henny *et al.*, *Science* **284**, 296 (1999).
14. W. D. Oliver, J. Kim, R. C. Liu, Y. Yamamoto, *Science* **284**, 299 (1999).
15. H. Kiesel, A. Renz, F. Hasselbach, *Nature* **418**, 392 (2002).
16. Y. Kagan, B. V. Svistunov, G. V. Shlyapnikov, *Sov. Phys. JETP* **42**, 209 (1985).
17. E. A. Burt *et al.*, *Phys. Rev. Lett.* **79**, 337 (1997).
18. B. Laburthe Tolra *et al.*, *Phys. Rev. Lett.* **92**, 190401 (2004).
19. A. Robert *et al.*, *Science* **292**, 461 (2001); published online 22 March 2001 (10.1126/science.1060622).
20. O. Jagutzki *et al.*, *Nucl. Instrum. Methods Phys. Res. A* **477**, 244 (2004).
21. See supporting online materials on *Science* Online for details.
22. M. Naraschewski, R. Glauber, *Phys. Rev. A* **59**, 4595 (1999).
23. L. Deng *et al.*, *Nature* **398**, 218 (1999).
24. J. Vogels, K. Xu, W. Ketterle, *Phys. Rev. Lett.* **89**, 020401 (2002).
25. R. Stas, J. McNamara, W. Hogervorst, W. Vassen, *Phys. Rev. Lett.* **93**, 053001 (2004).
26. A. Öttl, S. Ritter, M. Köhl, T. Esslinger, *Phys. Rev. Lett.* **95**, 090404 (2005).
27. After submission of this manuscript, we became aware of a related experiment concerning atom correlations in an atom laser (*26*). We thank R. Sellem of the Détection Temps, Position Image Technology Division (supported by the Mission Ressources et Compétences Technologiques–CNRS Federation FR2764 and by the Université Paris-Sud) for a decisive role in the development of the time-to-digital converter, and O. Jagutzki for advice on delay lines.

Supporting Online Material
www.sciencemag.org/cgi/content/full/1118024/DC1
SOM Text

27 July 2005; accepted 5 September 2005
Published online 15 September 2005;
10.1126/science.1118024
Include this information when citing this paper.

Quantum Coherence in an Optical Modulator

S. G. Carter,[1]* V. Birkedal,[1]† C. S. Wang,[2] L. A. Coldren,[2] A. V. Maslov,[3] D. S. Citrin,[4,5] M. S. Sherwin[1]‡

Semiconductor quantum well electroabsorption modulators are widely used to modulate near-infrared (NIR) radiation at frequencies below 0.1 terahertz (THz). Here, the NIR absorption of undoped quantum wells was modulated by strong electric fields with frequencies between 1.5 and 3.9 THz. The THz field coupled two excited states (excitons) of the quantum wells, as manifested by a new THz frequency- and power-dependent NIR absorption line. Nonperturbative theory and experiment indicate that the THz field generated a coherent quantum superposition of an absorbing and a nonabsorbing exciton. This quantum coherence may yield new applications for quantum well modulators in optical communications.

Quantum three-state systems in which two of the states are strongly coupled by an intense laser field have been widely studied in atomic and molecular systems (*1*). The energies of the quantum states are altered as they are "dressed" by the strong light-matter interaction. Such dressed states were first observed by Autler and Townes (AT) in a molecular system driven by a strong radio-frequency field and probed by weak microwaves (*2*). When a radio-frequency resonance occurred, the microwave absorption line split in two. In three-state systems with weak coupling to the environment, AT splitting can evolve into electromagnetically induced transparency (EIT), in which a strong coupling beam induces transparency at a resonance at which the undriven system is opaque (*3*). This transparency is due to quantum interference between the dressed states. EIT is the basis for slow (*4*) and stopped light (*5*, *6*) in atomic systems.

A variety of quantum systems similar to atomic three-state systems can be engineered in semiconductor quantum wells (QWs). A QW is a layer of one semiconductor grown between semiconductors with larger band gaps (*7*). The layer with the smaller gap is sufficiently thin that well-defined sets of quantized states, or subbands, are associated with electron motion parallel to the growth direction. Within each subband, there is a continuum of states associated with different momenta parallel to the plane of the QW (perpendicular to the growth direction). AT-like splitting (*8*), quantum interference (*9*, *10*), and EIT (*11*, *12*) have been reported in QWs, but their observation has been more difficult than in atoms and molecules. This is in part because of much larger absorption linewidths, which result from disorder, from stronger coupling to the environment, or from scattering between subbands.

We have fabricated a particularly simple three-level system in undoped QWs (Fig. 1). The excitation with the lowest frequency occurs at about 350 THz (wavelength 857 nm or energy 1.46 eV) when an electron is promoted from the filled valence subband of highest energy (labeled h1) to the empty conduction subband of lowest energy (labeled e1). The excited electron binds with the hole it left behind to form an exciton with a hydrogen-like wave function in the QW plane. Transitions between different in-plane states (e.g., the 1s and 2p states) are allowed only for in-plane THz polarizations (*13*, *14*), which are not present in the experiments discussed here. The lowest exciton state is labeled h1X. The next exciton state, h2X, consists of an electron from e1 and a hole from the second highest valence subband, h2. NIR transitions between the crystal ground state and h2X are not allowed because of quantum mechanical selection rules. However, intersubband transitions from h1X to h2X are allowed for THz radiation polarized in the growth direction. The three states analogous to those in an AT picture are the crystal ground state, the lowest exciton h1X, and the second exciton h2X (*15*).

This report explores the NIR absorption of undoped QWs at low temperatures (~10 K) when they are driven by strong electric fields polarized in the growth direction with frequencies between 1.5 and 3.9 THz. Because the frequency of the THz laser is about 1% of that required to create an exciton, the strong laser field does not alter the populations of the quantum states of the system. Near 3.4 THz, the drive frequency is resonant with the transition between the two lowest exciton states. The AT splitting of excitons driven by strong intersubband radiation is experimentally observed, and theoretical predictions (*16*, *17*) are confirmed.

The sample consists of 10 $In_{0.06}Ga_{0.94}As$ QWs (each 143 Å) separated by $Al_{0.3}Ga_{0.7}As$ barriers (300 Å). InGaAs QWs were used instead of GaAs QWs so that the GaAs substrate was transparent for NIR light near the exciton energies. A 100-nm layer of aluminum was deposited on the surface of the sample on which the QWs were grown. The metallic boundary condition improved THz coupling and ensured that the THz field at the QWs was polarized almost perfectly in the growth direction (*18*). The interband absorption was probed using broadband, incoherent, NIR light from an 850-nm light-emitting diode focused onto the sample backside to a spot size ~250 μm in diameter. The NIR intensity was less than 0.3 W/cm^2. As illustrated in Fig. 1, the NIR beam was transmitted through the transparent substrate, interacted with the QWs, was reflected off of the Al layer, and was then collected and sent to a monochromator with an intensified charge-coupled device detector. The reflected NIR beam was measured during the 1 to 1.5 μs at the peak of the THz

[1]Physics Department and Institute for Quantum and Complex Dynamics (iQCD), Broida Hall Building 572, Room 3410, [2]Electrical and Computer Engineering Department, University of California, Santa Barbara, CA 93106, USA. [3]Center for Nanotechnology, NASA Ames Research Center, MS 229-1, Moffett Field, CA 94035, USA. [4]Electrical and Computer Engineering, Georgia Institute of Technology, Atlanta, GA 30332, USA. [5]Georgia Tech Lorraine, Metz Technopole, 2-3 rue Marconi, 57070 Metz, France.

*Present address: JILA, University of Colorado, 440 UCB, Boulder, CO 80309, USA.
†née Ciulin. Present address: Department of Chemistry, University of Aarhus, Langelandsgade 140, DK-8000 Århus C, Denmark.
‡To whom correspondence should be addressed. E-mail: sherwin@physics.ucsb.edu

pulse (fig. S2). The sample was mounted in a closed-cycle refrigerator and maintained at a temperature near 10 K. The lowest curves in Fig. 1, A to C, display the NIR reflectivity measured without the THz field. (The reflectivity is essentially double-pass transmission in this geometry.) The strong absorption line is from h1X. As expected, no absorption is observed from h2X. The energy of h2X is expected to be ~3.34 THz (13.8 meV) above h1X from calculations (*19*).

The THz radiation, given by the UCSB Free-Electron Lasers, was focused onto the edge of the sample with an off-axis parabolic mirror. The spot size was ~400 μm in diameter for THz frequencies between 2.5 and 3.9 THz, near the h1X-h2X resonance. The THz beam was on for ~4 μs with a repetition rate near 1 Hz. The maximum peak power incident on the sample was ~2 kW, giving a maximum intensity in the sample of ~1 MW/cm^2 (~15 kV/cm electric field amplitude). [This estimate of the electric field ignores propagation inside the sample and the Al coating on the surface (*18*)].

The effect of the THz field on the sample reflectivity was quite striking (Fig. 1, A to C). Each graph displays the reflectivity for a series of THz intensities. In Fig. 1A the THz frequency is f_{THz} = 2.52 THz, below the expected h1X-h2X resonance. As the THz intensity increased, the absorption line redshifted and a weaker absorption line appeared above the undriven exciton energy. Near the expected resonance, at f_{THz} = 3.42 THz (Fig. 1B), there was a clear symmetric splitting of the exciton line, which increased as a function of intensity. Just above the resonance, at f_{THz} = 3.90 THz (Fig. 1C), a weaker absorption line appeared below the undriven exciton energy. These measurements were carried out at ~10 K, but the splitting at f_{THz} = 3.42 THz was observed at temperatures up to 78 K.

The calculated reflectivity of a THz-driven QW is shown in Fig. 2 for THz intensities that give spectra comparable to those in Fig. 1. These results were obtained by numerically solving the Schrödinger equation for the dynamics of an optically created electron-hole pair in an infinitely deep QW. The quantization of the electron-hole states, the Coulomb interaction, and the THz field are all treated on an equal footing, without resorting to perturbation theory [see (*20*) for more details]. In essence, the THz field rocks the QW potential, which couples the various confined QW states in a dynamic fashion. All of the QW states are included in the calculations. This approach is equivalent to solving the polarization equation of the semiconductor Bloch equations (SBEs) in the low-density limit (*21*). The reflectivity is defined as the fraction of the incident optical power at a given NIR frequency that is not absorbed.

For these calculations, the absorption strength and energy position of h1X for zero

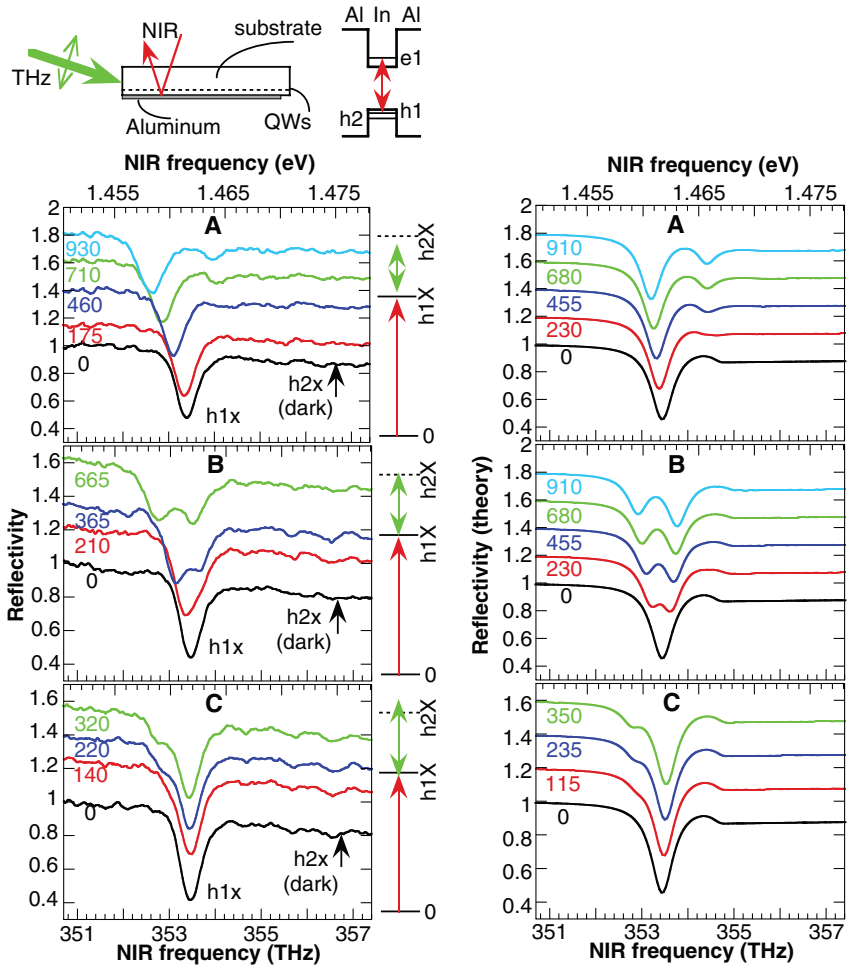

Fig. 1 (left). Reflectivity spectra for a series of THz intensities at f_{THz} = (**A**) 2.52 THz, (**B**) 3.42 THz, and (**C**) 3.90 THz. The spectra are offset and labeled according to the THz intensities (in kW/cm^2). Level diagrams illustrating the detuning from the expected h1X-h2X resonance are shown to the right of each graph. A schematic of the experimental geometry and the band diagram of a QW along with the relevant subband energies are displayed above. The red arrow represents the lowest excitation of the system, the h1X exciton. The AlGaAs barriers are labeled "Al" and the InGaAs layer is labeled "In." **Fig. 2 (right).** Calculated reflectivity spectra for a series of THz intensities at f_{THz} = (**A**) 2.52 THz, (**B**) 3.42 THz, and (**C**) 3.90 THz. The spectra are offset and labeled according to the THz intensity (in kW/cm^2). The absorption strength and energy position of the spectrum for zero THz field were set to best fit the measured reflectivity.

THz field were set to best fit the measured reflectivity. The calculated reflectivity in the presence of the THz field is qualitatively similar to the measured reflectivity, although small differences can be seen. It appears that the calculated splitting at 3.42 THz is more asymmetric than that observed experimentally, indicating that the experimental h1X-h2X resonance is closer to 3.42 THz than 3.34 THz. Also, there is an overall redshift of the measured reflectivity with increasing THz intensity that does not appear in the calculated spectra. This redshift is most likely due to heating by the THz beam and can clearly be seen in fig. S1A, where the absorption line positions are plotted as a function of intensity. The separation between the two absorption lines on resonance at f_{THz} = 3.42 THz is plotted as a function of intensity in fig. S1B. The splitting is discernible over a factor of ~4 in THz intensity (~2 in THz field). Theory and experiment are not far from one another over this limited range, although the dependence of the splitting on THz intensity is closer to a line than the square root function predicted by theory. More work must be done to characterize and understand the dependence of the splitting on THz intensity (*18*).

The reflectivity was measured at many THz frequencies from f_{THz} = 1.53 to 3.90 THz. Absorption spectra for f_{THz} = 2.82 through 3.90 THz (Fig. 3) were obtained by subtracting a linear decrease in reflectivity over the measured NIR frequency span and then calculating the negative natural logarithm of the reflectivity. These absorption spectra were then fit to two Lorentzians. The spectra at f_{THz} = 1.53, 1.98, and 2.52 THz (not shown) were more difficult to fit because the second absorption line was so weak. Differential spectra (spec-

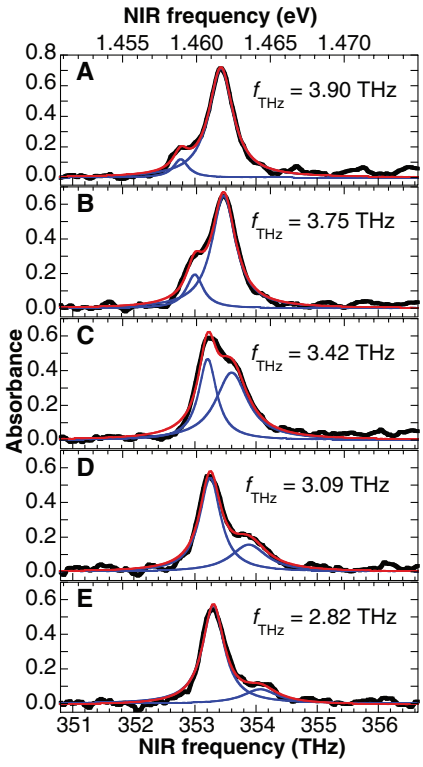

Fig. 3. Absorption spectra and fits for f_{THz} = 3.90 THz (**A**) to 2.82 THz (**E**). The black lines represent the absorption obtained from the reflectivity spectra by correcting for the downward slope due to continuum absorption and by taking the negative natural logarithm. The red curves are fits to two Lorentzians; the blue curves are the individual Lorentzians.

trum with THz field minus spectrum without THz field divided by spectrum without THz field) were used to determine the absorption line positions.

Figure 4 displays the absorption line positions as a function of THz frequency. The spectra used were all obtained with a THz intensity near 300 kW/cm^2 (within 10%), relatively low because this was the highest available intensity at f_{THz} = 3.75 THz and 3.90 THz. The anticrossing behavior in Fig. 4 near the h1X-h2X resonance is expected for the AT effect. The two absorption lines are associated with the two excitons dressed by the THz field. On resonance, the oscillator strength is shared equally between the two dressed states and the two absorption peaks are equal in magnitude. Off-resonance, the oscillator strength is strongest for the absorption line nearest the undriven exciton line. For low THz frequencies, the weaker peak approaches the h2X energy. The data points connected by solid lines in Fig. 4 are the results of calculations using the model equivalent to the SBE for an intensity of 375 kW/cm^2, which agree well with the measurements. The disagreement at 1.53 and 1.98 THz (lower positions) may be due to uncertainty in the THz intensity (*18*).

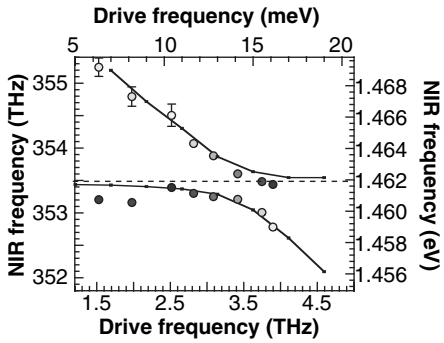

Fig. 4. Measured absorption line positions (large circles) versus THz frequency for a THz intensity of ~300 kW/cm^2. The absorption strength for each point is represented on a grayscale; darker circles indicate stronger absorption. The standard error of the positions from fitting is indicated by error bars except where smaller than the circle diameter. The data points and solid line represent the calculated absorption positions at a THz intensity of 375 kW/cm^2. Near the resonance at f_{THz} = 3.4 THz, the calculated spectra were fit to two Lorentzians to determine absorption positions; away from resonance, the positions were taken at the minimum of the reflectivity for each peak. The horizontal dashed line marks the undriven exciton line position.

Quantum wells driven by growth-direction electric fields are already important as electroabsorption modulators for fiber-optic communications operating with bandwidths <100 GHz (0.1 THz) (*22*). The basis for the QW modulators (QWMs) is the dc quantum-confined Stark effect, wherein a dc electric field polarized in the growth direction causes a redshift of the h1x absorption (*23*). The operating frequencies of QWMs are smaller than the exciton's linewidth. Thus, the response is adiabatic: The NIR absorption spectrum at any instant is determined only by the electric field at that same instant, and not by the modulation frequency. Modulation at higher frequencies is desirable given the 50-THz bandwidth of optical fibers.

Our results show that fascinating quantum effects occur when QWMs are driven in the high-frequency diabatic limit. Most important, AT splitting of excitons due to a strong THz field has been observed. The decrease in absorption at the undriven exciton resonance in the presence of the THz field is certainly suggestive of EIT, although the linewidth of h2X is not expected to be narrow enough for the required quantum interference effects.

The observation of dressed states in this system is noteworthy for several reasons. First, the effects have been observed over a wide range of THz frequencies, where the detuning from the resonance was comparable to the drive frequency. Observation of dressed states at large detunings is possible because the Rabi frequency (half the splitting on resonance) is relatively large, up to 20% of the drive frequency on resonance. Second, the THz driving field does not generate any excited-state population, in part because it is at a much lower frequency than the probe. The driving field is also quasi–continuous wave, which is rare for observations of coherent strong-field effects in semiconductors. Finally, applications to optical communications have been proposed for the THz-driven QW. Two NIR lasers resonant with different dressed states of this system interact strongly (*24*), leading to mutual transparency of the beams depending on their relative phases. This effect could be used for intermodulation of laser beams at arbitrarily low NIR intensities.

References and Notes

1. M. O. Scully, M. S. Zubairy, *Quantum Optics* (Cambridge Univ. Press, New York, 1997), chap. 7.
2. S. H. Autler, C. H. Townes, *Phys. Rev.* **100**, 703 (1955).
3. S. E. Harris, *Phys. Today* **50**, 36 (July 1997).
4. L. V. Hau, S. E. Harris, Z. Dutton, C. H. Behroozi, *Nature* **397**, 594 (1999).
5. C. Liu, Z. Dutton, C. H. Behroozi, L. V. Hau, *Nature* **409**, 490 (2001).
6. D. F. Phillips, A. Fleischhauer, A. Mair, R. L. Walsworth, M. D. Lukin, *Phys. Rev. Lett.* **86**, 783 (2001).
7. J. H. Davies, *The Physics of Low-Dimensional Semiconductors, an Introduction* (Cambridge Univ. Press, New York, 1998).
8. J. F. Dynes, M. D. Frogley, M. Beck, J. Faist, C. C. Phillips, *Phys. Rev. Lett.* **94**, 157403 (2005).
9. J. Faist *et al.*, *Opt. Lett.* **21**, 985 (1996).
10. H. Schmidt, K. L. Campman, A. C. Gossard, A. Imamoglu, *Appl. Phys. Lett.* **70**, 3455 (1997).
11. G. B. Serapiglia, E. Paspalakis, C. Sirtori, K. L. Vodopyanov, C. C. Phillips, *Phys. Rev. Lett.* **84**, 1019 (2000).
12. M. C. Phillips *et al.*, *Phys. Rev. Lett.* **91**, 183602 (2003).
13. K. B. Nordstrom *et al.*, *Phys. Rev. Lett.* **81**, 457 (1998).
14. S. Hughes, D. S. Citrin, *Phys. Rev. B* **59**, R5288 (1999).
15. The exciton states discussed are those with a 1s in-plane wave function, as these dominate the NIR spectra. The subbands h1 and h2 are "heavy hole" subbands because of their high effective masses. Excitons formed from the valence subbands with a lighter effective mass ("light hole" subbands) are shifted to higher energies as a result of strain and do not appear in the measured spectra. Excitons associated with higher subbands (e2, h3) are sufficiently far away in energy that they should only weakly couple to h1X.
16. A. Liu, C. Z. Ning, *J. Opt. Soc. Am. B* **17**, 433 (2000).
17. A. V. Maslov, D. S. Citrin, *Phys. Rev. B* **62**, 16686 (2000).
18. See supporting data on *Science* Online.
19. All calculations were performed for a 150 Å QW with infinite barriers. The electron and hole effective masses (for the growth direction) were 0.067 m_0 and 0.36 m_0, respectively.
20. A. V. Maslov, D. S. Citrin, *IEEE J. Sel. Top. Quantum Electron.* **8**, 457 (2002).
21. H. Haug, S. W. Koch, *Quantum Theory of the Optical and Electronic Properties of Semiconductors* (World Scientific, River Edge, NJ, ed. 4, 2004).
22. D. A. B. Miller, *Opt. Photon. News* **1**, 7 (1990).
23. S. Schmitt-Rink, D. Chemla, D. A. B. Miller, *Adv. Phys.* **38**, 89 (1989).
24. A. V. Maslov, D. S. Citrin, *J. Opt. Soc. Am. B* **19**, 1905 (2002).

25. Supported by NSF grants DMR 0244390 (S.G.C., V.B., M.S.S.) and DMR 0305524 (D.S.C.) and by Sun Microsystems. We thank D. Allen, R. Owings, D. Bouwmeester, and A. Wodtke for helpful feedback on the manuscript, and D. Enyeart for skillful operation of the UCSB Free-Electron Lasers.

Supporting Online Material

www.sciencemag.org/cgi/content/full/310/5748/651/DC1
SOM Text
Figs. S1 and S2

16 June 2005; accepted 21 September 2005
10.1126/science.1116195

Terahertz-optical mixing in undoped and doped GaAs quantum wells: From excitonic to electronic intersubband transitions

S. G. Carter,[1,*] V. Ciulin,[1,†] M. Hanson,[2] A. S. Huntington,[2,‡] C. S. Wang,[3] A. C. Gossard,[2,3] L. A. Coldren,[2,3] and M. S. Sherwin[1]

[1]*Physics Department and iQUEST, University of California, Santa Barbara, California 93106, USA*

[2]*Materials Department, University of California, Santa Barbara, California 93106, USA*

[3]*Electrical and Computer Engineering Department, University of California, Santa Barbara, California 93106, USA*

(Received 20 April 2005; revised manuscript received 30 June 2005; published 13 October 2005)

The mixing of near-infrared and terahertz (THz) beams has been observed in *n*-doped GaAs quantum wells (QWs) and is shown to be quite different from that in undoped QWs. The resonant behavior of the sidebands demonstrates that mixing in doped QWs is primarily sensitive to electronic intersubband transitions while that in undoped QWs is due to excitonic intersubband transitions. These results demonstrate that THz-optical mixing can be used to probe the collective dynamics of a driven electron gas.

DOI: 10.1103/PhysRevB.72.155309 PACS number(s): 78.67.De, 42.65.−k, 73.21.Fg, 78.20.Jq

Nonlinear spectroscopy has become a powerful tool in studying a variety of different systems. In semiconductors, nonlinear techniques are routinely used to explore the dynamics of electrons.[1] These experiments provide far more information on the fundamental physics of semiconductors than linear spectroscopy alone and demonstrate methods of controlling optical processes. In this paper, nonlinear mixing of terahertz (THz) and near-infrared (NIR) radiation in doped GaAs quantum wells (QWs) is studied.

Previous experiments[2–7] and theories[8,9] have examined THz-optical mixing in undoped QWs. In these cases, excitonic interband resonances dominated the NIR spectra. The THz field did not drive a real intersubband (ISB) polarization as there were no free carriers. The mixing occurred as the THz field excited excitonic ISB transitions as part of a parametric process. The result of the mixing was that sidebands were generated at $\omega_{SB}=\omega_{NIR}+n\omega_{THz}$, where $n=\pm1,2,\ldots$. The intensity of the sidebands was greatly enhanced when the NIR laser and/or sideband frequencies matched those of sharp ($\sim$1 meV wide) excitonic resonances. The $n=+1$ sidebands have been used to demonstrate the potential of THz-optical mixing for voltage-controlled, all-optical wavelength conversion.[4–6] In strong THz fields, sidebands have been used to study nonperturbative effects induced by "dressing" the exciton states with the THz field.[7,9]

One might expect THz-optical mixing to be weaker in doped quantum wells since excitons are screened, interband resonances are much broader, and some NIR transitions are Pauli blocked by the Fermi sea at low temperatures. However, in doped quantum wells, the THz radiation can excite an intersubband polarization directly, leading to a channel for sideband generation that has not been previously investigated. In this communication, THz-optical mixing is shown to be quite different in the presence of free carriers but, surprisingly, of similar strength. The differences are illustrated by the resonant structure of the $n=+1$ sideband. Instead of having several sharp excitonic resonances as in an equivalent undoped sample, there is only one broad resonance in the doped sample. The frequency of this resonance matches that of the independently measured intersubband plasmon, the collective intersubband oscillation which couples to THz light. Thus sidebands at NIR frequencies can probe the coherent dynamics of electrons driven at much lower THz frequencies. The results are explained qualitatively in terms of a second order nonlinear susceptibility ($\chi^{(2)}$) model.

The samples consist of ten periods of double GaAs QWs, nominally 100 and 120 Å wide and separated by a 25 Å $Al_{0.2}Ga_{0.8}As$ tunnel barrier. The sample structure is displayed at the top of Fig. 1. Each pair of wells is separated by a 410 Å (920 Å) $Al_{0.3}Ga_{0.7}As$ barrier for the undoped (doped) sample. The difference between the widths of the GaAs wells breaks inversion symmetry in the growth direction, thus allowing the generation of $n=+1$ sidebands at zero bias. Furthermore, the tunnel-splitting produces a spacing between electron subbands in the range of our THz source, the University of California-Santa Barbara (UCSB) free electron laser. In the doped sample, there is silicon δ doping in the middle of the 920 Å barriers between each pair of coupled wells. This gives $\sim 1.2\times10^{11}e/\mathrm{cm}^2$ per well, as determined by capacitance-voltage measurements. Some band bending in the vicinity of the doped double QWs is calculated due to space-charge fields, but the potentials and charge densities are nearly identical for each double QW except for the one closest to the surface. This active region is grown in-between two doped, 70 Å wide QWs. These QWs are contacted ohmically and used to apply a growth-direction electric field (E_{bias}) to the sample, tuning the ISB collective mode frequency [as measured by Fourier-transform infrared (FTIR) spectroscopy and plotted in the inset of Fig. 1(b)] and the optical properties. For most measurements the electric field was pulsed for less than 1 ms to avoid tunneling between wells. The active region and gate QWs are grown on a 30-period distributed Bragg reflector (DBR), designed to reflect the incident laser and the sidebands, which would otherwise be absorbed in the semi-insulating GaAs substrate. In order to maximize interaction with the NIR beam, the coupled wells in the doped sample are placed at the nodes produced by interference between the incident and reflected NIR beams.

The photoluminescence (PL) and reflectivity of the two

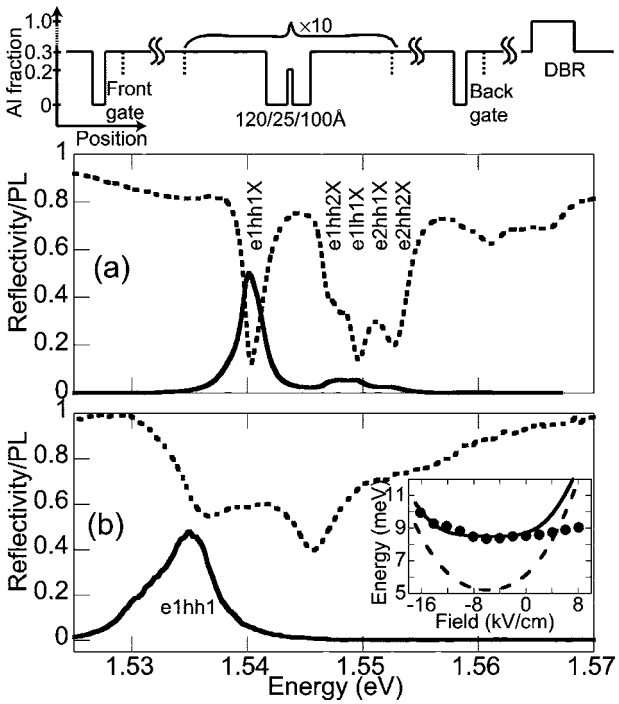

FIG. 1. PL (solid line) and reflectivity (dashed line) of the (a) undoped and (b) doped samples at zero bias taken at ~11 K. For PL, the samples were excited at 777 nm with an intensity of ~9 W/cm^2 for the undoped sample and ~30 W/cm^2 for the doped sample, and both were normalized to 0.5. The interband transitions in (a) are labeled according to theory, but the assignments are uncertain near 1.55 eV because several absorption lines overlap. The doped sample structure is displayed above (a). Doping is indicated by vertical dashed lines. In the undoped sample, the doping adjacent to the coupled quantum wells is absent. The inset in (b) plots the ISB absorption tuning as measured by FTIR (solid dots) along with the calculated dressed (solid line) and bare (dashed line) ISB frequencies. Band bending due to space-charge fields is included in the calculations.

samples are shown in Fig. 1, where the reflectivity is similar to a transmission measurement due to the DBR. In the undoped sample [Fig. 1(a)] there is sharp PL from the lowest state, $e1hh1X$, and a number of sharp, exciton absorption lines (labeled by theory).[5] In the doped sample [Fig. 1(b)], the absorption is much broader as continuum absorption plays more of a role due to exciton screening.[10] The onset of absorption, at ~1.534 eV, can be taken as the Fermi edge, which is near the peak of the PL. The width of the PL reflects the fact that electrons from the Fermi energy to the bottom of the conduction band (a width of ~4.2 meV based on the charge density) can recombine with holes. The obvious shift in PL between the doped and undoped samples may be due to band gap renormalization.[11]

The geometry for sideband experiments is illustrated on the right side of Fig. 2. The sample was mounted in a closed-cycle He cryostat, where its temperature was kept constant between 10 and 16 K. The THz beam was coupled into the edge of the sample with its polarization perpendicular to the QW plane, allowing ISB transitions. The dielectric waveguide modes of the sample give in-plane electric fields and

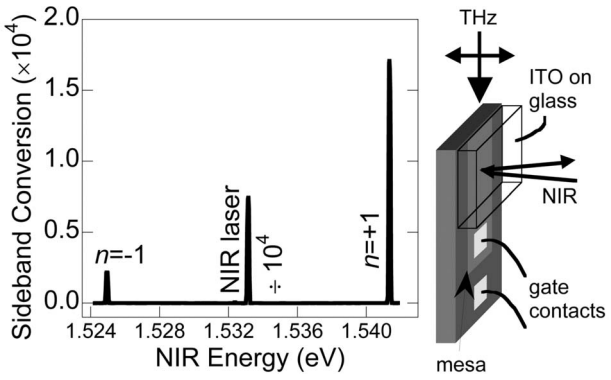

FIG. 2. Sideband spectrum taken at ~11 K with ω_{THz} =2.0 THz (8.2 meV) at ~730 kW/cm^2. The NIR laser signal is divided by $\sim 1\times 10^4$. E_{bias}=5.8 kV/cm. The experimental geometry is to the right of the figure.

substantially reduce the electric field at the surface. Glass coated with indium tin oxide (which conducts at THz frequencies) was pressed onto the sample frontside, improving the surface electric field while leaving the frontside transparent to NIR light. The THz beam was on for about 4 μs at a repetition rate of 1.5 Hz with a maximum power of ~3 kW. It was focused onto the sample with an off-axis parabolic mirror (f/2.4) to a spot measured to be between 0.3 and 1.2 mm in diameter, for THz frequencies between 3.4 and 0.66 THz, respectively. Typically, the intensity was attenuated to ~40 kW/cm^2 (just outside the sample).

The NIR beam, which came from a cw tunable Ti:sapphire laser, was incident perpendicular to the sample and typically focused to an intensity of roughly 25 W/cm^2. It then made a double pass through the sample active region, by reflecting off the DBR, and was sent to a 0.85 m double monochromator, where it was detected by a photomultiplier tube.

Figure 2 displays a typical sideband spectrum for the

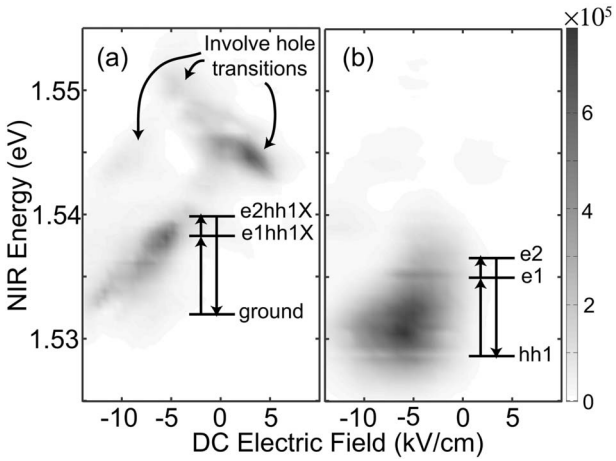

FIG. 3. The $n=+1$ sideband resonance maps of (a) the undoped and (b) doped samples at ω_{THz}=2.0 THz (8.2 meV), taken by varying ω_{NIR} and E_{bias}, while always measuring the $n=+1$ sideband. The sideband conversion for each point is represented on a grey scale, displayed on the right. The maps were taken at ~12 K with a THz intensity of ~18 kW/cm^2 and a NIR intensity of ~25 W/cm^2.

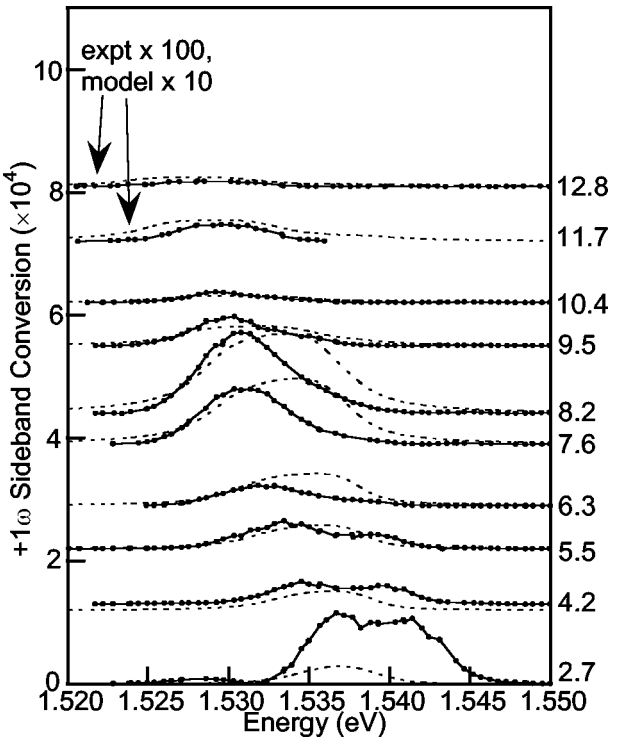

FIG. 4. The $n=+1$ sideband resonance spectra (solid dots and lines) of the doped sample taken with various THz frequencies, all with intensities near 40 kW/cm^2. The temperature was between 11 and 16 K, and E_{bias} was at 5.8 kV/cm. Each point represents the sideband signal when ω_{NIR} is tuned to the value on the horizontal axis. The spectra are vertically offset and labeled according to ω_{THz}. $\chi^{(2)}$ model calculations (dashed lines) are plotted for comparison. Spectra at $\omega_{THz}=11.7$ and 12.8 meV are multiplied by 100 and their model curves are multiplied by 10 for clarity.

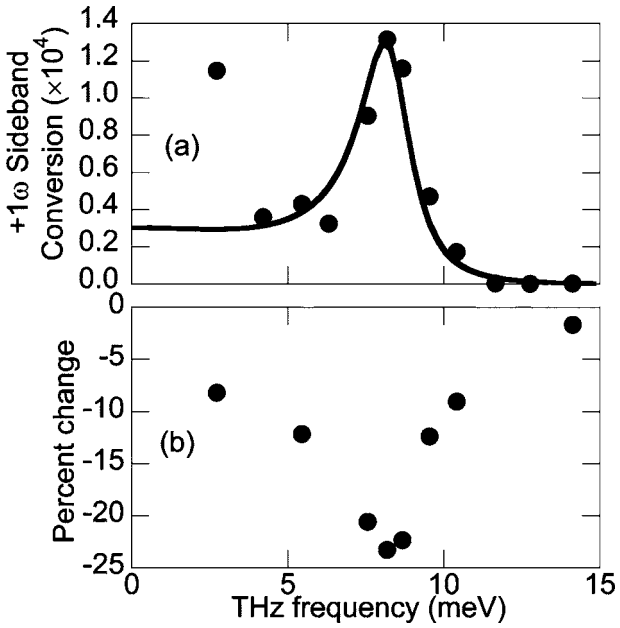

FIG. 5. (a) Peak values of the $n=+1$ sideband resonance spectra (solid dots) for the doped sample and the peak values of the $\chi^{(2)}$ model curves (solid line) plotted vs ω_{THz}. (b) Percent change in the integrated PL of the doped sample with the THz field on at an intensity of ~40 kW/cm^2.

doped sample. The reflected NIR laser (attenuated by 10^4) is at 1.533 eV with $n=\pm1$ sidebands offset by 8.2 meV, the THz frequency. The ratio of the $n=+1$ sideband power to the incident laser power, called the conversion efficiency, is measured to be $\sim1.7\times10^{-4}$. This is the same order of magnitude conversion efficiency as in the undoped sample. Higher order sidebands were extremely small under these conditions.

Sideband generation is strongest when the NIR and THz frequencies (ω_{NIR} and ω_{THz}) are resonant with interband (IB) and ISB transitions, respectively. Figures 3(a) and 3(b) display $n=+1$ sideband resonance maps for the undoped and doped samples. These are obtained by scanning E_{bias} and ω_{NIR} while measuring the sideband. Scanning E_{bias} varies the ISB spacing, bringing it into resonance with ω_{THz}, while scanning ω_{NIR} brings it into resonance with IB transitions. There are several sharp excitonic resonances for the undoped sample, which have been studied previously and assigned to particular transitions.[5] The lower-energy resonance only involves a change in electron state while the other resonances involve hole transitions. In the doped sample, only the resonance involving electron transitions remains significant. The resonance is much broader in NIR frequency as it involves continuum states instead of exciton states, and broader in E_{bias} as ISB tuning is screened somewhat by the electron gas.

For the doped sample, the sideband intensity (on resonance) increased linearly with NIR intensity up to the highest NIR intensity available, ~1500 W/cm^2. In the undoped sample saturation began at ~160 W/cm^2. This difference likely occurred because the sideband resonance in the doped sample is just below the absorption edge, so few carriers were generated. Also, the addition of optically excited carriers in the doped well should have little effect since there is already significant charge density. As a function of THz intensity, both undoped and doped samples began to saturate at ~80 kW/cm^2. This is surprising since resonant ISB absorption has been shown to start saturating at only ~1 W/cm^2.[12]

Valuable information can be obtained by measuring the sideband signal as a function of ω_{THz}. Figure 4 displays the $n=+1$ sideband resonance scans at many different THz frequencies. These data were taken with $E_{bias}=\sim5.8$ kV/cm, where the ISB absorption was measured to be at ~8.3 meV [see inset of Fig. 1(b)]. The resonance scan at 8.2 meV was closest to this frequency and had only a single resonance centered below the PL peak, despite the many IB resonances shown in Fig. 1. Resonance scans near 8.2 meV and at higher ω_{THz} had only one significant resonance that redshifted as ω_{THz} increased. For lower ω_{THz}, there were several resonances at higher ω_{NIR}. Figure 5(a) plots the peak of each sideband resonance scan as a function of ω_{THz}, showing the resonance at the ISB absorption frequency as well as a significant low frequency response. A similar behavior was seen in undoped square QWs but was due to purely IB processes.[4]

Sideband generation is a measure of the coherent response of the QW, but we have also probed the incoherent response by measuring the change in PL when the THz field is present. The electron gas is heated up by the THz beam, quenching the PL and shifting the Fermi distribution as seen

in similar systems.[13,14] Figure 5(b) displays the percent change in the integrated PL as a function of the THz frequency. A single resonance near the ISB absorption is visible, as would be expected when the dominant heating mechanism is ISB absorption.

A qualitative understanding of THz-optical mixing in the doped sample can be obtained from a $\chi^{(2)}$ model. We will only consider three subbands: heavy hole 1 ($hh1$), electron 1 ($e1$), and electron 2 ($e2$). This approximation makes sense as the sideband resonance spectra with $\omega_{THz} > 5.5$ meV have one dominant resonance near the $e1$-$hh1$ transition. This model has been applied to doped GaAs QWs previously.[15] Taking an expression for $\chi^{(2)}$ from Ref. 16 and applying it to this system, the result after eliminating nonresonant and dipole forbidden terms is

$$\chi^{(2)}_{xzx}(\omega_{NIR}+\omega_{THz}) \propto \mu^x_{1n}\mu^z_{n\nu}\mu^x_{\nu 1}\sum_{n,\nu=2,3}\int_0^\infty kdk\frac{\rho_{11}(k)-\rho_{\nu\nu}(k)}{[E_{n1}(k)-\omega_{SB}-i\gamma_{n1}][E_{\nu 1}(k)-\omega_{NIR}-i\gamma_{\nu 1}]} - \frac{\rho_{\nu\nu}(k)-\rho_{nn}(k)}{[E_{n1}(k)-\omega_{SB}-i\gamma_{n1}][E_{n\nu}(k)-\omega_{THz}-i\gamma_{n\nu}]}. \quad (1)$$

The indices 1, 2, and 3 represent the $hh1$, $e1$, and $e2$ subbands, respectively, and k is the in-plane wave vector. $E_{lm}(k)$ is the energy of the lth subband minus the mth subband, both at wave vector k, and μ^x (μ^z) is an IB (ISB) dipole matrix element. $\rho_{mm}(k)$ is the equilibrium occupation function of the mth subband, and γ_{lm} represents the dephasing rate between subbands l and m.

The first term contains IB population differences and IB resonant denominators, and will be nonzero even without doping. A similar term was used in modelling sidebands in undoped QWs.[4] When $n \neq \nu$, the first term is in resonance when ω_{NIR} and $\omega_{sideband}$ match up with IB transitions, giving an indirect ISB resonance. When $n=\nu$, the first term can only be in resonance for $\omega_{THz} < \gamma_{\nu 1}$, and it only involves one IB matrix element and the asymmetry, $\mu^z_{\nu\nu}$. For these reasons, the $n=\nu$ first term is interpreted as resulting from the quasistatic modulation of the IB absorption, and gives rise to the low ω_{THz} sidebands. The second term in Eq. (1) requires an ISB population difference and has one ISB resonant denominator, so it represents sidebands due to ISB excitations. Near the ISB transition, this second term is significantly larger than the others for a Fermi energy of several milli-electron-volts, as in these experiments. Thus, as ω_{THz} is varied, there is an interplay between sidebands due to excitations of the electron gas, and those due to IB processes.

A complication when evaluating Eq. (1) is that the Coulomb interaction strongly modifies the potential well and the subband energies.[17] The Schrödinger equation must be satisfied with Poisson's equation self-consistently in order to correctly include the Coulomb interaction. The ISB spacing (or bare ISB frequency) was calculated by such a self-consistent program as a function of the dc electric field and is plotted in the inset of Fig. 1(b).[18] However, the Coulomb interaction also modifies the dynamics of the QW, such that a driving field induces collective excitations of the electron gas called "intersubband plasmons"[17] ["charge density excitations" in the literature on Raman spectroscopy of two-dimensional electron gases (2DEGs)].[19] The frequency of this collective excitation, called the dressed frequency, along with the measured absorption, is also plotted in the inset of Fig. 1(b). The disagreement between the two at positive voltages is not well understood.

A simple way to correct the $\chi^{(2)}$ model is to use the dressed frequency, 8.3 meV, for the ISB term while using the bare ISB frequency, ~5.2 meV, for the IB terms [see inset of Fig. 1(b)]. Using this correction, Eq. (1) was evaluated using dipole matrix elements calculated for an empty well and with $\gamma_{IB}=2$ meV and $\gamma_{ISB}=1$ meV, values which gave the best fit. The 2D band gap was also adjusted to fit the lower edge of the measured PL at 1.532 eV. The subband occupation function of $e1$ was approximated as a step function while $hh1$ and $e2$ were treated as full and empty, respectively. The intensity of the $n=+1$ sideband is proportional to $|\chi^{(2)}|^2$, which is plotted next to the experimental data in Fig. 4. The maxima of $|\chi^{(2)}|^2$ are plotted as a function of ω_{THz} in Fig. 5(a).

The model accurately predicts the strong resonance near the dressed ISB frequency and the significant signal at low frequencies. It also predicts the redshift of the NIR resonance as ω_{THz} increases. However, the signal at $\omega_{THz}=2.7$ meV is significantly stronger than predicted, and the signal above $\omega_{THz}=10.4$ meV is much weaker than predicted. It may be that comparing the spectra with the same intensity outside the sample introduces this type of error as the intensity coupled to the QW layers may depend on the ω_{THz}. The extra resonances at low ω_{THz} are likely due to higher states similar to those in Fig. 3(a), which are not considered in the model. Finally, the widths and positions of the NIR resonances near $\omega_{THz}=8.3$ meV are quite different from the model and cannot be improved by adjusting the γ's. A challenge remains to fully explain the experimental results, perhaps using a theory which includes the electron-electron and electron-hole interactions *ab initio*.

THz-optical mixing has been measured for the first time in doped QWs, showing strikingly different resonant behavior than in undoped QWs. The most important distinction is that sidebands in doped QWs are primarily sensitive to the collective excitations of the electron gas, as demonstrated by the large resonance at the dressed ISB frequency. This fact allows the use of THz-optical mixing to probe ISB dynamics, providing a useful diagnostic for ISB devices such as THz quantum cascade lasers.[20] The THz fields in these devices are comparable to those used in these experiments.[21] Using NIR light as opposed to FIR light has the advantage of being able

to probe very small areas, to use mature NIR optics, detectors, spectrometers, and to target specific QWs based on their IB transitions. These benefits are similar to those of Raman scattering,[19] but sideband generation is uniquely suited to probe the *coherent* response of electrons to THz driving. Additionally, exciting effects have been predicted for doped QWs in strong THz fields, such as period-doubling bifurcations to chaos,[22] which may be more easily observed using THz-optical mixing. The $\chi^{(2)}$ model provides a good qualitative understanding of THz-optical mixing and reproduces many of the experimental trends.

We thank D. S. Citrin for useful discussions on this subject and acknowledge support from NSF Grant No. DMR 0244390 and Sun Microsystems.

*Present address: JILA, University of Colorado, Boulder, CO 80309, USA.
†Present address: V. Birkedal née Ciulin, Department of Chemistry, University of Aarhus, Langelandsgade 140, DK-8000 Aarhus C, Denmark.
‡Present address: Voxtel, Inc., Beaverton, OR 97005, USA.

[1] J. Shah, *Ultrafast Spectroscopy of Semiconductors and Semiconductor Nanostructures* (Springer, New York, 1996).
[2] J. Cerne, J. Kono, T. Inoshita, M. Sherwin, M. Sundaram, and A. C. Gossard, Appl. Phys. Lett. **70**, 3543 (1997).
[3] J. Kono, M. Y. Su, T. Inoshita, T. Noda, M. S. Sherwin, S. J. Allen, and H. Sakaki, Phys. Rev. Lett. **79**, 1758 (1997).
[4] V. Ciulin, S. G. Carter, M. S. Sherwin, A. Huntington, and L. A. Coldren, Phys. Rev. B **70**, 115312 (2004).
[5] M. Y. Su, S. G. Carter, M. S. Sherwin, A. Huntington, and L. A. Coldren, Appl. Phys. Lett. **81**, 1564 (2002).
[6] S. G. Carter, V. Ciulin, M. S. Sherwin, M. Hanson, A. Huntington, L. A. Coldren, and A. C. Gossard, Appl. Phys. Lett. **84**, 840 (2004).
[7] M. Y. Su, S. G. Carter, M. S. Sherwin, A. Huntington, and L. A. Coldren, Phys. Rev. B **67**, 125307 (2003).
[8] T. Inoshita and H. Sakaki, Physica B **249–251**, 534 (1998).
[9] A. V. Maslov and D. S. Citrin, Phys. Rev. B **62**, 16686 (2000).
[10] C. Delalande, J. Orgonasi, J. A. Brum, G. Bastard, M. Voos, G. Weimann, and W. Schlapp, Appl. Phys. Lett. **51**, 1346 (1987).
[11] D. A. Kleinman and R. C. Miller, Phys. Rev. B **32**, 2266 (1985).
[12] K. Craig, B. Galdrikian, J. N. Heyman, A. G. Markelz, J. B. Williams, M. S. Sherwin, K. Campman, P. F. Hopkins, and A. C. Gossard, Phys. Rev. Lett. **76**, 2382 (1996).
[13] R. Romestain and C. Weisbuch, Phys. Rev. Lett. **45**, 2067 (1980).
[14] N. G. Asmar, J. Cerne, A. G. Markelz, E. G. Gwinn, M. S. Sherwin, K. L. Campman, and A. C. Gossard, Appl. Phys. Lett. **68**, 829 (1996).
[15] A. Neogi, Y. Takahashi, and H. Kawaguchi, J. Opt. Soc. Am. B **14**, 570 (1997).
[16] R. W. Boyd, *Nonlinear Optics* (Academic, San Diego, 1992), Chap. 3, p. 137.
[17] M. Helm, Semicond. Semimetals **62**, 1 (2000).
[18] In these calculations, the tunnel barrier was made 12% wider to better fit the experimental data. The $Al_{0.3}Ga_{0.7}As$ and $Al_{0.2}Ga_{0.8}As$ conduction band offsets were set as 300 and 200 meV, respectively.
[19] G. Abstreiter, R. Merlin, and A. Pinczuk, IEEE J. Quantum Electron. **QE-22**, 1771 (1986).
[20] R. Kohler, A. Tredicucci, F. Beltram, H. E. Beere, E. H. Linfield, A. G. Davies, D. A. Ritchie, R. C. Iotti, and F. Rossi, Nature (London) **417**, 156 (2002).
[21] D. S. Citrin (private communication).
[22] B. Galdrikian and B. Birnir, Phys. Rev. Lett. **76**, 3308 (1996).